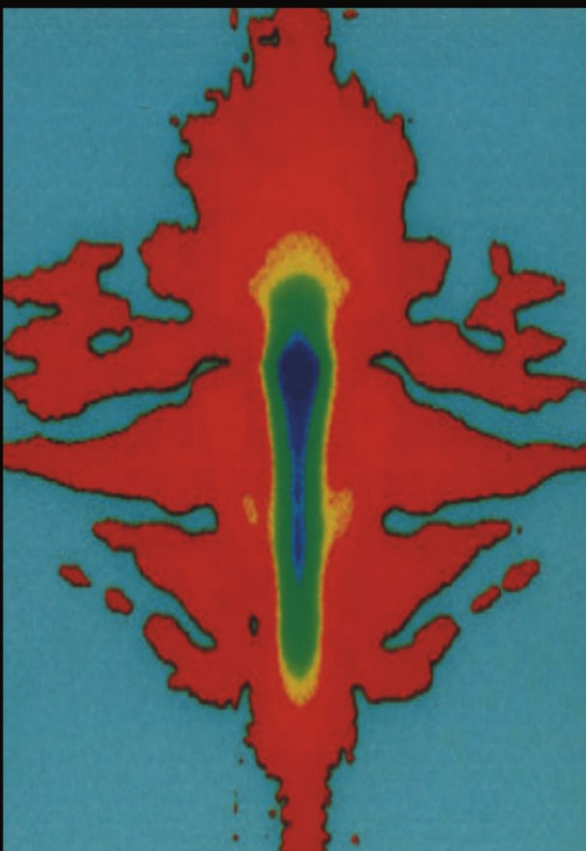


Frequency-Resolved Optical Gating: The Measurement of Ultrashort Laser Pulses



Rick Trebino

***Frequency-Resolved Optical Gating:
The Measurement of Ultrashort
Laser Pulses***

If you haven't measured it, you haven't made it.

Wayne Knox

Frequency-Resolved Optical Gating:

The Measurement of Ultrashort Laser Pulses

Rick Trebino

Georgia Institute of Technology

School of Physics

Atlanta, GA 30332

rick.trebino@physics.gatech.edu



SPRINGER SCIENCE+BUSINESS MEDIA, LLC

Trebino, R.

Frequency-resolved optical gating : the measurement of ultrashort laser pulses / Rick Trebino.

p. cm.

Includes bibliographical references and index.

ISBN 978-1-4613-5432-1 ISBN 978-1-4615-1181-6 (eBook)

DOI 10.1007/978-1-4615-1181-6

1. Laser pulses. Ultrashort—Measurement. I. Title: Measurement of ultrashort laser pulses. II. Title.

QC689.5.L37T74 2002

621.36'6—dc21

2002021855

Copyright © 2000 by Springer Science+Business Media New York

Originally published by Kluwer Academic Publishers in 2000

Softcover reprint of the hardcover 1st edition 2000

All rights reserved. No part of this publication may be reproduced, stored in a retrieval system or transmitted in any form or by any means, mechanical, photo-copying, recording, or otherwise, without the prior written permission of the publisher, Springer Science+Business Media, LLC.

Printed on acid-free paper.

*To Linda Leigh, whose love and enthusiasm made this
work—and everything else—possible.*

Contents

Authors and Contributors	ix
0. Read Me! (Preface)	xiii
1. The Dilemma <i>Rick Trebino</i>	1
2. Ultrashort Laser Pulses <i>Rick Trebino and Erik Zeek</i>	11
3. Nonlinear Optics <i>Rick Trebino and John Buck</i>	37
4. The Autocorrelation, the Spectrum, and Phase Retrieval <i>Rick Trebino and Erik Zeek</i>	61
5. FROG <i>Rick Trebino</i>	101
6. FROG Beam Geometries <i>Rick Trebino</i>	117
7. Geometrical Issues: Single-shot FROG <i>Rick Trebino</i>	141
8. The FROG Algorithm <i>Marco A. Krumbuegel and Rick Trebino</i>	157
9. Noise: Its Effects and Suppression <i>David N. Fittinghoff and Michael Munroe</i>	179
10. Practical Issues, Marginals, Error Checks, and Error Correction <i>Greg Taft and Ken DeLong</i>	203
11. Improvisation in FROG <i>Rick Trebino</i>	219
12. Very Simple FROG Apparatus: GRENOUILLE <i>Rick Trebino, Patrick O'Shea, Mark Kimmel, and Xun Gu</i>	229
13. Ultraviolet and High-Power Pulse Measurement <i>Sterling Backus and Charles Durfee</i>	237

14. FROG in the Single-Cycle Regime <i>Andrius Baltuska, Maxim S. Pshenichnikov, and Douwe A. Wiersma</i>	257
15. FROG Characterization of Complex Pulses <i>John M. Dudley</i>	305
16. XFROG—Cross-correlation Frequency-resolved Optical Gating <i>Stefan Linden, Jürgen Kuhl, and Harald Giessen</i>	313
17. Measuring Extremely Complex Pulses <i>Rick Trebino, Xun Gu, Erik Zeek, and Mark Kimmel</i>	323
18. Non-instantaneous Nonlinearities <i>Rick Trebino</i>	331
19. Fiber-FROG <i>John M. Dudley, John D. Harvey and Mark D. Thomson</i>	337
20. Blind FROG <i>Rick Trebino</i>	345
21. Principal Component Generalized Projections FROG Algorithm <i>Daniel J. Kane</i>	357
22. Measuring Ultraweak Pulses: TADPOLE <i>David N. Fittinghoff</i>	367
23. Measuring Ultrafast Polarization Dynamics: POLLIWOG <i>Arthur L. Smirl</i>	375
24. Multi-pulse Interferometric FROG <i>Craig W. Siders and Antoinette J. Taylor</i>	391
25. The Future of Pulse Measurement <i>Rick Trebino</i>	411
Index	421

Authors and Contributors

Erik Zeek (chapters 2, 4, and 17)

Georgia Institute of Technology
Atlanta, GA 30332

John Buck (chapter 3)

Georgia Institute of Technology
Atlanta, GA 30332

Andrew Millard (contributor to chapter 6)

University of California at San Diego
La Jolla, CA 92093

Michiel Müller (contributor to chapter 6)

University of California at San Diego
La Jolla, CA 92093

Jeff Squier (contributor to chapter 6)

Colorado School of Mines
Golden, CO 80401

Marco A. Krumbuegel (chapter 8)

KLA-Tencor
Alamo, CA 94507

David Fittinghoff (chapters 9, 22, and contributor to chapter 6)

Lawrence Livermore National Labs
Livermore, CA 94550

Michael Munroe (chapter 9)

Mahi Networks
Petaluma, CA 94954

Greg Taft (chapter 10)

University of Wisconsin
Stevens Point, WI 54481

Ken DeLong (chapter 10, contributor to chapters 18 and 20)

Femtosoftware Technologies
Oakland, CA 94619

Mark Kimmel (chapters 12 and 17)

Georgia Institute of Technology
Atlanta, GA 30332

Patrick O’Shea (chapter 12)

Georgia Institute of Technology
Atlanta, GA 30332

Xun Gu (chapters 12 and 17)
Georgia Institute of Technology
Atlanta, GA 30332

Sterling Backus (chapter 13)
University of Colorado at Boulder
Boulder, CO 80309-0440

Charles Durfee (chapter 13)
Colorado School of Mines
Golden, CO 80401

Andrius Baltuska (chapter 14)
University of Tokyo
Tokyo, Japan

Maxim S. Pshenichnikov (chapter 14, contributor to chapter 25)
State University of Groningen
Groningen, The Netherlands

Douwe A. Wiersma (chapter 14)
State University of Groningen
Groningen, The Netherlands

John Dudley (chapters 15 and 19)
Université de Franche-Comté
Besançon cedex, France

Stefan Linden (chapter 16)
Max-Planck-Institut für Festkörperforschung
Stuttgart, Germany

Jürgen Kuhl (chapter 16)
Max-Planck-Institut für Festkörperforschung
Stuttgart, Germany

Harald Giessen (chapter 16)
Philipps-Universität
Marburg, Germany

John D. Harvey (chapter 19)
University of Auckland
Auckland, New Zealand

Mark D. Thomson (chapter 19)
Johann Wolfgang Goethe Universitaet
Frankfurt, Germany

Daniel J. Kane (chapter 21)
Southwest Sciences, Inc.
Santa Fe, NM 87501

Arthur L. Smirl (chapter 23)
University of Iowa
Iowa City, IA 52242

Craig W. Siders (chapter 24)
University of Central Florida
Orlando, FL 32816

Antoinette J. Taylor (chapter 24)
Los Alamos National Lab
Los Alamos, NM 87545

Pascal Kockaert (French translations of slides)
Université libre de Bruxelles CP 194/5
Bruxelles, Belgium

O. Read Me

I don't know about you, but whenever I try to read a scientific book for more than a few minutes, I fall asleep. Scientific writing is dull. Indeed, scientists have a well-deserved reputation for being dull people who write dull books for other dull scientists.

I hate this.

So in writing and editing this book, I've tried something different. I've tried, not only to teach you the science of ultrashort-laser-pulse measurement, but also to convey to you the excitement and fun I've experienced in learning and discovering these ideas. For example, when I heard about the idea of phase retrieval, I dropped everything I'd been doing and spent an entire week in the library reading everything I could find on this amazing topic. So I've tried to convey that enthusiasm to you whenever possible. I've also tried to use some writing techniques that make reading a novel fun. For example, you may notice some recurring themes and direct addresses. (Lucky for you I don't know anything about symbolism.) And I've just written whatever I've felt like writing in places and not bothered to edit it out. Fortunately, the wonderful folks at Kluwer Academic Publishers have encouraged this. I've had a lot of fun writing my share of this book, and I hope this means that you'll have some fun reading it.

But that's not all that makes this book different from the other scientific books on your shelf. I've included a CD that's full of cool full-color stuff for you to play with and lecture from.

The CD contains the FROG software (for the PC and Mac) that retrieves pulses from traces. This software is fun to play with even if you haven't set up a FROG; you can have it try theoretical (or experimental) traces and watch it work. Ken DeLong and Marco Krumbuegel (the authors of this software and both former post-docs in my group) sell this software for a few hundred dollars, so they've disabled the 'save' functions on these free versions. Please buy a copy from their companies (Femtosoft or MakTech) if you plan to do anything serious with it. They're nice guys who aren't making much money from this endeavor; they're mostly doing it for the benefit of humankind.

The CD also contains five hours of full-color PowerPoint lectures (for the PC and Mac in English and in French) that I give to my Ultrafast Optics class on ultrashort pulses and their measurement. So if you're teaching such a class, you just saved 200 hours of lecture preparation time when you bought this book! Indeed, I'm hoping that my supplying these polished files might persuade you to make the transition to high-tech teaching. Gone are the days when the most important attribute of a professor was his penmanship on the blackboard. Why don't all textbooks do this? I don't know. Okay, it might have something to do with those 200 hours it took to create them. Nevertheless, I think they should. Supplying prepared lectures along with a textbook could free up some time for teachers to actually improve the lectures, help students, do research, or maybe just relax.

And there's yet a third innovation in this book. I've written a couple of hundred pages, but the life of a professor is in busy one, and I don't have time to write about everything I'd like included in this book. So I've asked several other scientists to supply chapters on important relevant subjects on which they're the world's leading experts. In this way, we can cover everything, but still get this book to you in a reasonable amount of time. The result is that this is not a single-author book, but it's also not an edited book of independent chapters; it's a hybrid. Whatever works. I've tried to edit the style of these additional chapters to better match mine, but my style is sufficiently weird that I exhibited some restraint here to avoid irritating these wonderful folks who were kind enough to provide chapters.

The result is that roughly the first half of the book—which I mainly wrote—is more general, simpler, more informal, and about right for an advanced undergrad or a first- or second-year grad student, who's just learning about the fascinating world of ultrafast optics and who'd like to know the basic concepts of ultrashort pulses and their measurement. The second half—by the additional authors—is more specialized, more advanced, more formal, and about right for an older grad student or researcher who has to worry about the details of a specific pulse-measurement project. The book is so long that, if you start it your first year in grad school, you'll probably not get through it until a few years later when you're about to graduate, so things may work out just right.

Coincidentally, that's about the same time scale over which the research described in this book occurred. Only a decade ago, it wasn't possible to measure an ultrashort pulse. Autocorrelators provided a rough measure, but that was about it. FROG emerged in 1991, and it's changed the way ultrafast scientists think about their lasers and helped to provide an understanding of these lasers that has led to ever-shorter pulses.

This book is mainly about FROG, which has allowed us to measure an ultrashort laser pulse's complete intensity and phase vs. time and to do it very well and in a very general way. But it also discusses in some detail autocorrelators, partly for historical reasons, but also because an autocorrelator is a key component of a FROG. There's also some discussion of spectrometers for the same reasons. We also cover spectral interferometry (SI) because it nicely complements FROG: it's extremely sensitive (FROG isn't); it's linear (FROG is nonlinear); it requires a well-characterized reference pulse, and FROG, which doesn't, is the best way to obtain one.

Some people have asked me about including other methods, which (in my completely unbiased opinion...) are less well known, less general, less accurate, and more complex. Actually, that *was* my original plan, but I realized that all such methods are used by at most a few groups (usually just the group that invented it) for highly specialized purposes, and they already know about them. Typically, these methods are prohibitively complex: they often begin with a FROG, and then add numerous additional components—including such complex devices as interferometers and pulse stretchers!—seriously

complicating an already nontrivial measurement. One involves an interferometer within an interferometer! (If you know someone who's using such a method, ask him which device he re-aligns when his pulse isn't short enough, the laser or the measurement device. I'll bet it's the latter...) Since these other methods are not in general use, there are only a few papers on each of them, and it's easy to do a quick literature search and read everything there is to know about them; a book on them is unnecessary. Many of them don't actually work or only work on a limited class of pulses—a fact that might not be evident from the papers—so consider yourself warned!

Also, FROG isn't just one technique; it's a class of powerful techniques, each with many variations. In addition, there are many clever things you can do with FROG that you can't do with other methods. For example, FROG has reliable independent checks on the measurement, something not present in any other method. These independent checks are very important because the corollary to Wayne's quotation on the first page of this book is that "If you measured it badly, you probably made it badly, too." Which suggests the following joke:

Question: What's a poorly measured 5-femtosecond pulse?

Answer: A 10-femtosecond pulse.

FROG can even measure the most complex ultrashort pulses ever generated (with a time-bandwidth product in excess of 1000); this is about three orders of magnitude more complex than the most complex pulse ever measured with any other method. Even its alleged weaknesses are in fact advantages: FROG's relatively slow (few-second) iterative algorithm makes it much more versatile than any other method. And its over-determination of the pulse allows such niceties as automatically calculated error bars and the correction for systematic error. More than 300 scientific papers describe FROG and its variations, features, and applications. And, as you can see, just covering FROG has required more than 400 pages—and we had to leave lots of stuff out! In the final analysis, I'd rather do one or two things well than a bunch badly.

In fact, if you feel that I've omitted something—like a reference to a paper—let me know, and I'll include it in the next edition. Keeping up with the literature—even just the FROG literature!—is becoming harder and harder everyday, so I'd appreciate the help.

Finally, when a professor writes a book, the folks who really pay the price are his grad students, who, as a result, are neglected so badly that their graduations can be delayed by as much as a year or more. I'm sensitive to this issue, so I've carefully avoided doing that. In view of the fact that scientists are even duller public speakers than they are writers, I took a different approach, and here's the resulting disclaimer:

No graduate-student careers were harmed in the writing of this book. I wrote my share while pretending to take notes during dull

conference talks when the rest of the audience—and in some cases the speaker—were asleep.

Rick Trebino
Georgia Research Alliance-Eminent Scholar
Chair of Ultrafast Optical Physics

Thanks to Dan Kane for co-inventing FROG with me and pursuing it, despite the fact that it eventually cost us both our jobs. Thanks to my numerous incredibly talented post-docs over the years, Ken DeLong, David Fittinghoff, Marco Krumbuegel, John Sweetser, Bruce Richman, and Erik Zeek, several of whom are still working on FROG several years after receiving their last paycheck from me and after moving on to projects with much less silly names. Thanks to Mark Kimmel for his clever implementations of FROG in three different time zones. Thanks to Alfred Kwok and Luis Ladera for traveling many miles to work on FROG with me. Thanks to Larry Rahn, Don Sweeney, and Bob Gallagher, who supported this research when other managers considered it subversive. Thanks to Georgia Tech and the School of Physics for actually paying me to do what I love. Thanks to those who contributed chapters to this book (don't worry; I hereby take the blame for everything I've done to your chapters). Thanks to my research group, whose enthusiasm for even unfinished chapters bogged down the Georgia Tech email system. And thanks to Kluwer's Michael Hackett for encouraging and overseeing this book project. And thanks again to all these folks for their infinite enthusiasm and patience for this work and book, which, like anything worth doing, wasn't just worth doing well, but also ended up being worth doing well for far more hours than anyone ever imagined. And finally thanks to the Department of Energy and the National Science Foundation for generously supporting this work.

Text and figures were reprinted with permission from numerous articles by the authors: Trebino and Kane, IEEE J. Quant. Electron., 1999. **35**(4): p. 418–420; Trebino, et al., Rev. Sci. Instr., 1997. **68**(9): p. 3277–3295; Tóth, C., et al., in *Ultrafast Phenomena XI*, 1998, Springer: Berlin. p. 109–111; Fittinghoff, et al., IEEE J. Quant. Electron., 1999. **35**(4): p. 479–486; Kane, IEEE J. Quant. Electron., 1999. **35**(4): p. 421–431; Fittinghoff, et al., J. Opt. Soc. Amer. B, 1995. **12**(10): p. 1955–1967; DeLong, et al., IEEE J. Quant. Electron., 1996. **32**(7): p. 1253–1264; Taft, et al., Selected Topics in Quantum Electronics, 1996. **2**, p. 575–585; Zeek et al., *Simultaneous Automatic Calibration and Direction-of-Time Removal in Frequency-Resolved Optical Gating*. Appl. Phys. B, 2002 in press; O'Shea, et al., Opt. Lett., 2001. **26**: p. 932; Trebino, et al., Optics & Photonics News, June 2001; Backus, et al., Optics Letters, 1996. **21**(9): p. 665–667; Wang, et al., J. Opt. Soc. Amer. B, 1999. **16**(10): p. 1790–4; Baltuska, et al., Opt. Lett., 1998. **23**(18): p. 1474–6; Baltuska, et al., IEEE J. Quant. Electron., 1999. **35**(4): p. 459–478; Baltuska, et al., J. Phys. Chem., 1999. **A103**: p. 10065–82; Linden, et al.,

Physica Status Solidi B (Germany), 1998. **206**(1): p. 119–24; Linden, et al., Opt. Lett., 1999. **24**(8): p. 569–71; Gu, X., Opt. Lett., 2002 in press; DeLong, et al., Optics Letters, 1995. **20**(5): p. 486–488; Dudley, et al., IEEE J. Quant. Electron., 1999. **35**(4): p. 441–450.; Thomson, et al., Opt. Lett., 1998. **23**(20): p. 1582–4; DeLong, et al., J. Opt. Soc. Am. B, 1995. **12**(12): p. 2463–2466; Fittinghoff, et al., Optics Letters, 1996. **21**(12): p. 884–886; Walecki, et al., Optics Letters, 1997. **22**(2): p. 81–83; Siders, et al., Opt. Lett., 1997. **22**(9): p. 624–626; Siders, et al., IEEE J. Quant. Electron., 1999. **35**(4): p. 432–440; Fittinghoff, et al., Opt. Lett. **23** (1998), p. 1046–1048; Fittinghoff, et al., IEEE J. Quant. Electron., **35**, 479 (1999). If only a figure or two were used (with permission) from a source, they're referenced in the caption or text.

1. *The Dilemma*

Rick Trebino

In order to measure an event in time, you must use a shorter one. But then, to measure the shorter event, you must use an even shorter one. And so on. So, now, how do you measure the shortest event ever created?

No, this isn't one of those age-old unresolvable dilemmas, the kind that frustrated ancient Greek philosophers. True, it's reminiscent of Zeno's paradox, which considered how finely one may divide distances, rather than durations of time. And it's equally confounding. But, in fact, the above dilemma is a recently solved optical measurement problem, which, until a few years ago, badly frustrated modern laser scientists.

And, unlike the conundra pondered by the ancient Greeks, which were of little practical value, the above dilemma has proven eminently practical. Indeed, to see the action in any fast event, whether it's a computer chip switching states, dynamite exploding, or a simple soap bubble popping, requires a strobe light with a shorter duration in order to freeze the action. But then to measure the strobe-light pulse requires a light sensor whose response time is even faster. And then to measure the light-sensor response time requires an even shorter pulse of light. Clearly, this process continues until we arrive at the shortest event ever created.

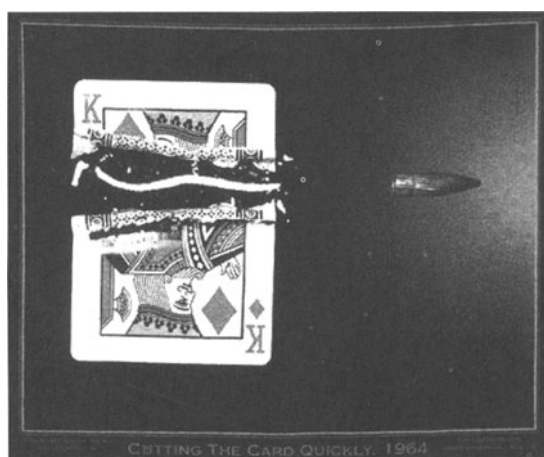


Fig. 1.1: A very short event. Measuring it requires an even shorter event: a strobe light only a few microseconds long. So then, how do you measure the strobe light? (Figure reprinted courtesy of Harold Edgerton collection).

And this event is the ultrashort light pulse.

Ultrashort light pulses as short as a few femtoseconds (1 femtosecond = 1 fs = 1×10^{-15} sec) have been generated with lasers, and it is now routine to generate pulses less than 100 fs long. Here's some perspective on the mind-boggling brevity of these durations: 30 fs is to 1 second as 1 second is to a million years. Or, recalling the well-known fact that time is money, if one second corresponds to the current U.S. national debt (\$5 trillion), then 10 fs corresponds to a mere nickel!

Now you might think that events this short would have little use; what happens on such short time scales that needs to be measured? The answer is: *A lot!* Key processes in biology—photosynthesis, vision, protein-folding, to name a few—all contain events that occur on fs time scales. Key processes in chemistry—molecular vibrations, re-orientations, and liquid-phase collisions, to name a few—also occur on this time scale. And key events in physics and engineering—high-lying excited-state lifetimes, photo-ionization, and electron-hole relaxation times that determine the response times of light detectors and electronics—are also ultrafast. The scientific literature of all of these fields contains many more.

Okay, so there's much to measure with these pulses. But why worry about the pulses themselves? Isn't that a problem of interest only to philosophers? The answer is: *No!* To begin with, we always need to check that a light pulse is in fact shorter than the event we're measuring with it. And if we actually know the precise pulse shape, we can use a pulse only slightly shorter than the event we're measuring with it, rather than one significantly shorter. Second, in many experiments—studies of molecular vibrations, for example—additional details of the pulse's structure play an important role in determining the outcome of the experiment. Of particular importance is the variation of color, or frequency, during the pulse, known as *chirp*. For example, chirped pulses can cause much greater molecular photo-dissociation than unchirped pulses [1]. Also, when a batch of molecules are excited, they make transitions to an excited state and then emit light whose color depends on the separation in energy between the excited state and ground state. Molecules are best described by *potential surfaces*, which are functions of the separation between nuclei in the molecule. As shown in Fig. 1.2, the color of the emitted light will change with time as the molecule vibrates or dissociates. Measuring such light tells us a great deal about the molecule. Third, we'd like to understand the physics of the lasers that emit these pulses, and, to verify theoretical models, we require precise knowledge of the pulse's properties [2–5]. And, in particular, to make even shorter pulses, we must understand the distortions that limit the length of currently available pulses [4,5]. Fourth, many new material-characterization techniques depend heavily on the ability to precisely characterize an ultrashort pulse experimentally. More detailed material information can be discerned by fully characterizing the input and output pulses in such methods [6,7]. Fifth, numerous applications have emerged for *shaped* ultrashort pulses [8,9]. A particularly interesting example of such an

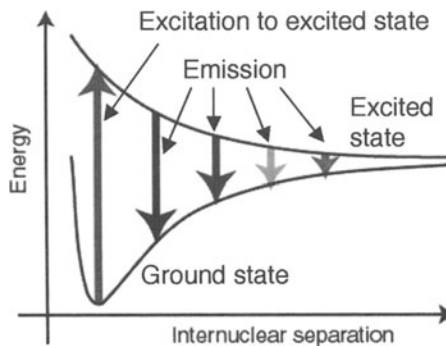


Fig. 1.2: Potential surface diagram for a generic molecule, showing that the emission color (here various shades of gray) changes with time after excitation (the upward-pointing arrow) from the ground to an excited-state surface. Knowledge of the time-resolved luminescence frequency yields important information about the potential surfaces, not available from a mere spectrum or intensity vs. time. This is especially the case for complex molecules—with more complex surfaces than those shown here.

application is the use of chirped pulses to generate novel states of matter unique to the quantum world and having no classical analog. Of course, in all such applications, one must verify that the correct pulse has been used. In general, *any optical measurement of a medium is ultimately limited by the ability to measure the light into and the light out of the medium*, so better light measurement techniques are a generally good idea.

So being able to measure ultrashort light pulses is of great practical value. But philosophical interest is nothing to be ashamed of. And we're not short of that here. Indeed, the measurement of fast events has fascinated humans since the dawn of time [10]. The ancients measured time intervals in days and developed devices such as sundials to measure shorter intervals. The hour-glass and dripping-water methods eventually improved temporal resolution to better than 100 seconds. In the seventeenth century, Galileo Galilei used his heartbeat as a clock in his classic pendulum experiments, achieving an accuracy of close to 0.1 seconds. In 1819, de la Tour devised a standard of time based on sound. He noted that, because the human ear can hear sonic frequencies of greater than 10^4 Hz, periodic intervals transformed into sound waves by some means could be detected by ear to achieve a resolution of 0.0001 seconds. This method transformed the problem of time-measurement into the frequency domain. Many subsequently developed methods also made use of the frequency domain, reducing the problem of time-interval measurement to the often easier measurement of differences in frequency. Charles Wheatstone used electric discharges to ionize air and produced a momentary spark that could “freeze” motion. Henry Fox Talbot invented “instantaneous” photography in 1851, when he made an image of a newspaper on a spinning disk using a spark-discharge flash. Mid-nineteenth-century rotating-mirror streak techniques and excite-probe spark photography achieved microsecond resolution, largely due to the work of Ernst Mach (of Mach-number fame). By

the turn of the century, Abraham and Lemoine had demonstrated nanosecond resolution with a electrical-gate technique employing the dc Kerr effect. And in the middle years of the 20th century Harold Edgerton at MIT developed this work to a fine art (literally) with the development of high-speed strobe lights.

Modern electronic light detectors have pushed the limit of experimental temporal accuracy to picoseconds ($1 \text{ picosecond} = 1 \text{ ps} = 1 \times 10^{-12} \text{ sec}$). And finally, ultrashort-laser-pulse techniques, first developed in the 1970's, are rapidly approaching single-fs resolution. A good fraction of these methods were developed simply because "they were there." Indeed, nineteenth-century photographer, Muybridge, developed the first high-speed movie technology simply to *settle a bet* as to whether a galloping horse's feet all left the ground at once. Many ultrafast scientists, myself included, proudly trace the history of their field back to this event.

So how do we measure ultrashort laser pulses? Obviously, we don't have the required shorter event—a shorter pulse. And even if we did, we'd have the even harder problem of measuring this even shorter pulse. So it wouldn't really help. Clearly, the shortest event available for measuring the pulse is *the pulse itself*. Indeed, early on, it was realized that we must use the pulse to measure itself. But, of course, that's not good enough. As you might expect, techniques that have used the pulse to measure itself have yielded blurry pictures of the pulse: smeared out quantities that mask dips and bumps in the temporal shape of the pulse, just as the use of too slow a camera shutter speed yields a blurry picture of a moving object.

As a result, the development of a technique simply to measure the pulse intensity vs. time remained an unsolved problem for many years, lagging badly behind humankind's ability to create such pulses. The problem of measuring the pulse phase (or, equivalently, its frequency or color) vs. time seemed beyond reach. As late as 1990, these two problems, which together comprise the task at hand, remained unsolved, despite the publication of hundreds of scientific papers on this topic by then.

Interestingly, these problems have recently been solved. The *Frequency-Resolved Optical Gating (FROG)* class of techniques, introduced in 1991 by Daniel J. Kane and Rick Trebino, can measure the full time-dependent intensity and phase of ultrashort light pulses in a wide variety of circumstances. FROG is rigorous, robust, and general; it works over a wide range of wavelengths, pulse energies, and pulse lengths. Using FROG, it's now possible to measure even the shortest pulse. It's possible to measure extremely complicated pulses. It's possible to measure a single pulse. It's even fairly easy, and it just recently became even easier. To give an idea of the current level of sophistication, FROG in conjunction with another technique, spectral interferometry, has measured a train of pulses with considerably less than a photon each.

And all without a shorter event.* It's an interesting story. It's a story with twists and turns, of seemingly unrelated ideas in fields ranging from acoustics to astronomy to number theory, working together to yield an elegant and robust solution. A key role will be played by the musical score, or rather, its mathematically rigorous cousin, the spectrogram. And an unlikely hero will emerge: *a theorem that fails in higher dimensions*. In fact, it's this failure that saves the day. It's almost an adventure story.

It's a story that involves FROGs, TADPOLEs, and POLLIWOGs. No it's not a nature story; these are actually the rather frivolous acronyms for some of the more successful techniques. Despite their silly names, however, these techniques offer great measurement potential and capability unavailable previously. And they're finding applications in many labs around the world.

In order to tell this story, we'll first describe ultrashort laser pulses and define just what it is that we need to measure. This comprises the intensity and phase of a pulse vs. time or frequency. We'll also mention some assumptions that are implicit in pulse-measurement techniques and some properties of the temporal and spectral phase. That'll be Chapter 2.

In Chapter 3, we'll introduce the basic concepts of nonlinear optics in case you haven't seen these ideas before; this is essential because all ultrashort-light-pulse measurements require the use of nonlinear optics.

In Chapter 4, we'll describe the autocorrelation and spectrum, the old standards of short-pulse measurement, and the limited information available from them. These techniques are important because they're the building blocks for FROG, which is simply the spectrum of the autocorrelation (no, I don't know why no one thought of it before, either[†]). It turns out that the retrieval of the pulse intensity and phase from the spectrum is an example of the *one-dimensional phase-retrieval problem*. It's the attempt to reconstruct a function of one variable from the magnitude of its Fourier transform (without knowing the phase). This isn't possible unless additional information is available. Typically, we might also know that the function is of finite duration. Unfortunately, even with this additional information, it's generally not possible to reconstruct the function. Indeed, the one-dimensional phase-retrieval problem is a notorious problem, well known to be unsolvable in almost all cases. Its unsolvability is very fundamental: it follows from the *Fundamental Theorem of Algebra*, which guarantees that we can factor polynomials of one variable. Coincidentally, the retrieval of the pulse intensity from the autocorrelation is also an example of the one-dimensional phase-retrieval problem.

* Actually, a medium with a more rapidly responding event (usually, a non-resonant electronic response) is, in fact, required. But this event is not harnessed in the same sense as a strobe light. The strobe in these techniques is, in fact, the convolution of the electronic response and the light pulse, that is, an event on the order of the pulse itself.

[†] Actually, Ishida and coworkers [13,14] made spectrally resolved autocorrelations (i.e., FROG measurements) in the 1980's but did not attempt to extract the pulse intensity and phase from them.

In Chapter 5, we'll introduce the important notion of the *time-frequency domain* [11], the domain in which the most successful new techniques operate. Unlike the autocorrelation and the spectrum, which are pure time- or frequency-domain quantities, the time-frequency domain involves making measurements with both time- and frequency-resolution, *simultaneously*. We'll do some serious pulse measurement in Chapter 5, when we discuss the specifics of the FROG technique. We'll also discuss the *two-dimensional phase-retrieval problem*. This problem commonly occurs in astronomy and x-ray diffraction. Quite counter-intuitively, two-dimensional phase retrieval, unlike its one-dimensional cousin, *is* a solvable problem when some additional information is available. Two-dimensional phase retrieval turns out to be possible because the Fundamental Theorem of Algebra *fails* for polynomials of two variables. This fascinating and highly unintuitive fact was only discovered in the late 1970's [12]. And it'll turn out that FROG succeeds because the *retrieval of the pulse intensity and phase from the FROG trace is equivalent to the two-dimensional phase-retrieval problem*. We'll show how to make a FROG trace of a pulse and how to interpret it. And we'll discuss how FROG avoids the dilemma at the beginning of this chapter.

In Chapter 6, we'll discuss various beam geometries for FROG, which make it the versatile technique that it is. We'll also give the details you need to decide which geometry is right for you and how to set it up.

It's also possible to measure the intensity and phase of a *single* ultrashort laser pulse. This is accomplished simply by crossing beams at a large angle. The entire trace can then be obtained on a single camera image (Chapter 7). Such geometrical effects are not always desirable, however, and Chapter 7 also includes a discussion of these effects, which can almost always be avoided but should nevertheless be understood.

FROG traces can often be interpreted by simple visual inspection. Nevertheless, it's important to be able to retrieve the mathematical form of the pulse intensity and phase from them. Doing so requires an iterative algorithm. Fortunately, there are several, most derived from phase-retrieval algorithms. These algorithms are the subject of Chapter 8.

FROG is extremely insensitive to noise. This results from the great over-determination of the pulse. The FROG trace is an $N \times N$ array, used to determine only N intensity and N phase points, or $2N$ points. This over-determination has many advantages, one of which is noise reduction. Even better, it allows simple filtering techniques, which can improve the signal-to-noise ratio of retrieved pulses tremendously. This work is the subject of Chapter 9, and you shouldn't do FROG measurements without first having read this chapter!

Measurements of ultrashort laser pulses are prone to many types of errors. As a result, John Dudley likes to say that there are two kinds of ultrashort-laser pulse measurements: *those with independent checks and those that are wrong*. In Chapter 10, we'll discuss some practical issues in making FROG measurements, such as independent checks. We'll show how to verify that

measured traces are consistent with other data, such as the spectrum and autocorrelation. An important aspect of FROG is that such checks are available; they're not in autocorrelation and spectral measurements or in other intensity-and-phase measurement techniques, where it isn't possible to know whether the measurement you just made is correct and free of systematic error.

A number of additional simple tricks exist that make building and using a FROG not only easy, but also more accurate, and they're the subject of Chapter 11. One such trick allows us to automatically calibrate a FROG. It also removes the ambiguity in the direction of time that occurs in one of the FROG beam geometries.

FROG is a relatively simple measurement technique experimentally, only slightly more complex than an autocorrelator. But that doesn't mean that FROG can't be simplified further. Quite surprisingly, a FROG trace of a pulse can be produced by an almost trivial device composed of as few as five simple optical elements. This extremely simple device is called GRating-Eliminated No-nonsense Observation of Ultrafast Incident Laser Light E-fields (GRENOUILLE). Whereas an autocorrelator has four sensitive alignment parameters, GRENOUILLE has *no sensitive alignment parameters at all!* It can be set up in minutes, making it the simplest ultrashort-pulse-measurement device in history. It almost fits in your pocket. And it works. Furthermore, it has much better sensitivity than any other technique, including FROG. Oh, by the way, if you don't speak French, "grenouille" is French for "frog," but you probably could've guessed that. Chapter 12 will discuss this recent development.

Okay, so we've told you everything you can possibly need to know about the FROG technique, in general. What about its use in practical—and difficult—situations, such as measuring UV and high-power pulses? The numerous beam geometries available for FROG measurements become important in these regimes, and Chapter 13 summarizes this issue.

FROG is also ideal for measuring extremely, incredibly, unbelievably short pulses (that is, shorter than merely ultrashort; clearly, we're running out of superlatives), only a few fs long. Indeed, at the time of this writing, the shortest event ever created is an ultrashort laser pulse only 4.5 fs long, and it was measured using FROG. Chapter 14 discusses in detail the issues associated with measuring such extremely short pulses.

Most researchers assume that their pulses are smooth and single-peaked. This is usually not true, however, and it was not until the development of FROG that this has become apparent because autocorrelation tends to mask and smooth out pulse structure. FROG is the only method that is capable of measuring complex pulses. This is because a FROG trace's large number of points ($\sim 10,000$ in a 100×100 trace) give it the information capacity to measure a pulse with a large amount of structure. Indeed, no other technique has ever measured the intensity and phase of a pulse with a time-bandwidth product greater than about 3. And FROG has measured pulses with

time-bandwidth products approaching 100. Chapter 15 will discuss the issues involved in such measurements.

The big advantage of FROG is that it requires no reference pulse—the pulse can measure itself. This is great because there usually aren't any reference pulses lying around. But occasionally there are. Occasionally, a laser emits a fairly smooth pulse, which can be measured using FROG, and which then undergoes some sort of optical torture, becoming a ragged and disheveled mess as a result. As we mentioned above, such a pulse can often be measured using FROG, but why bother? A much more intuitive trace results when measuring the ragged pulse with the smooth, known reference pulse. This variation on FROG, which yields a traditional spectrogram, is usually referred to as *Cross-FROG (XFROG)*, and it's the subject of Chapter 16.

When you need to measure really complex pulses, it's better to use XFROG. Interestingly, it's only recently become possible to generate extremely complex ultrashort pulses—with time-bandwidth products in excess of 1000. While the measurement of such pulses may seem impossible, in fact, XFROG has been used to measure such pulses; this is the subject of Chapter 17.

Amazingly, it's even possible to measure pulses using a medium with an arbitrary response. Because FROG uses a very versatile iterative algorithm, it can easily be modified to deal with almost any situation, including one in which the nonlinear-optical medium is slow. Chapter 18 will show how to do this.

An example of such a situation is *Fiber-FROG*, which makes FROG measurements inside an optical fiber. Chapter 19 will show how. Fiber-FROG is most useful for measuring pulses of 1.5 μm in wavelength.

Okay, so measuring an ultrashort pulse is becoming almost routine. So how about a much harder problem. How about measuring two pulses? At the same time? And how about doing so using not much more than the apparatus already sitting on the table? And just to really complicate the problem, let's do so at the sample medium in an ultrafast spectroscopy apparatus. In this case, we can actually measure both pulses in a manner that actually takes advantage of the apparatus that's being used to do an ultrafast spectroscopy experiment. This method is often called *Blind FROG*, because it's equivalent to the mathematical problem called *Blind De-convolution*. It's the subject of Chapter 20.

The algorithm for Blind FROG is similar to the standard FROG algorithm, but Dan Kane has developed a technique called *principal components generalized projections*, which can, not only retrieve pulses from Blind FROG traces, but also retrieve them from standard FROG traces and do so very rapidly. In fact, his new algorithm (Chapter 21) is so fast that it can retrieve pulses in real time.

What about the measurement of very weak ultrashort pulses? Making a FROG trace of a train of ultrashort laser pulses with less than about a picojoule of energy each is difficult because FROG (and any other such technique) requires the use of a nonlinear-optical process. And nonlinear-optical

processes require fairly intense pulses and hence cannot work for such weak pulses. A *linear-optical* method is thus required. But it can be shown that linear-optical methods cannot completely measure ultrashort pulses. So in Chapter 22 we discuss the problem of measuring weak pulses. The solution in most cases is to realize that weak pulses are not created “in a vacuum;” they are almost always created from stronger pulses. Indeed, in order to create an ultrashort laser pulse in the first place, the laser must use nonlinear-optical processes. As a result, the pulse directly from the laser is almost always intense enough to be measured using FROG, and then it can act as a reference pulse for measuring the weak pulse. One option is XFROG. But when such a well-characterized reference pulse is available, linear-optical methods also suffice. A particularly simple and useful method, *spectral interferometry*, is available. Use of spectral interferometry in this manner, in conjunction with FROG to measure the reference pulse—a technique called *Temporal Analysis by Dispersing a Pair Of Light E-fields, or TADPOLE*—has succeeded in measuring a train of pulses with less than a photon per pulse!

Chapter 23 discusses an even more difficult-sounding problem: the measurement of the ultrafast variation of a pulse’s polarization state. Indeed, this problem sounds impossible—isn’t this what is meant by “unpolarized light,” that is, light whose polarization state varies too quickly to be resolved? If we throw in the additional difficulty that the light happens to be very weak, as well, the problem becomes quite a challenge. But a very simple approach, involving simultaneous TADPOLE measurements of both polarizations of the light, yields the solution. This relative of TADPOLE is appropriately referred to as *POLarization-Labeled Interference vs. Wavelength for Only a Glint (POLIWOG)*. Okay, I admit it; I stayed up really late one night coming up with that name.

In addition, it’s occasionally important to combine the advantages of both FROG and spectral interferometry. FROG has the advantage of incorporating an ultrafast gate, which eliminates any continuous background light that may be present. But because FROG involves the pulse gating itself, it doesn’t measure the arrival time of a pulse. Usually, this information is undesirable; who cares how far it is from the laser to the FROG? And who would like to take the massive effort to accurately stabilize this distance? But occasionally, for example, in spectroscopic measurements in plasmas, these quantities are crucial. Spectral interferometry, can yield the arrival time easily, but it does not involve any gating, and so spectral interferometry measurements can be badly contaminated by continuous background. A combination technique, called *Multipulse-Interferometric FROG (MIFROG)*, offers the best of both worlds and is the subject of Chapter 24.

Finally, in Chapter 25, we conclude by mentioning a few issues to be considered in the future: future applications for FROG, variations that would be welcome, and unsolved pulse-measurement problems.

Many interesting applications have been found for FROG, but it is important to limit the length of this book, and so we’ve chosen to limit our discussion

to the technique, its implementation, and its variations, and leave it to you to find additional clever applications for it.

References

1. B. Kohler, V. V. Yakovlev, J. Che, J. L. Krause, M. Messina, K. R. Wilson, N. Schwentner, R. M. Whitnell, and Y. Yan, "Quantum Control of Wave Packet Evolution with Tailored Femtosecond Pulses," *Phys. Rev. Lett.*, vol. 74, pp. 3360–63, 1995.
2. J. C. M. Diels, J. J. Fontaine, I. C. McMichael, and F. Simoni, "Control and Measurement of Ultrashort Pulse Shapes (in Amplitude and Phase) with Femtosecond Accuracy," *Appl. Opt.*, vol. 24, pp. 1270–82, 1985.
3. M. Beck and I. A. Walmsley, "The Role of Amplitude and Phase Shaping in the Dispersive-Pulse Regime of a Passively Mode-Locked Dye Laser," *J. Quant. Electron.*, vol. 28, pp. 2274–84, 1992.
4. I. P. Christov, M. M. Murnane, H. C. Kapteyn, J. P. Zhou, and C. P. Huang, "Fourth-Order Dispersion Limited Solitary Pulses," *Opt. Lett.*, vol. 19, pp. 1465–67, 1994.
5. J. D. Harvey, J. M. Dudley, P. F. Curley, C. Spielmann, and F. Krausz, "Coherent Effects in a Self-Modelocked Ti:sapphire Laser," *Opt. Lett.*, vol. 19, pp. 972, 1994.
6. P. Zhou, H. Schulz, and P. Kohns, "Atomic spectroscopy with ultrashort laser pulses using frequency-resolved optical gating," *Opt. Comm.*, vol. 123, pp. 501–4, 1996.
7. T. S. Clement, G. Rodriguez, W. M. Wood, and A. J. Taylor, "Characterization of ultrafast interactions with materials through direct measurement of the optical phase," in *Generation, Amplification, and Measurement of Ultrashort Laser Pulses III*, vol. 2701: SPIE, 1996, pp. 229–34.
8. M. Dugan, J. X. Tull, J.-K. Rhee, and W. S. Warren, "High-Resolution Ultrafast Laser Pulse Shaping for Quantum Control and Terabit per Second Communications," in *Ultrafast Phenomena X*, vol. 62, P. F. Barbara, J. G. Fujimoto, W. H. Knox, and W. Zinth, Eds. Berlin: Springer-Verlag, 1996, pp. 26–27.
9. A. M. Weiner, "Femtosecond Optical Pulse Shaping and Processing," *Progress in Quantum Electronics*, 1995.
10. E. P. Ippen and C. V. Shank, *Ultrashort Light Pulses—Picosecond Techniques and Applications*. Berlin: Springer-Verlag, 1977.
11. L. Cohen, "Time-Frequency Distributions—A Review," *Proc. IEEE*, vol. 77, pp. 941–81, 1989.
12. Y. M. Bruck and L. G. Sodin, "On the Ambiguity of the Image Reconstruction Problem," *Opt. Commun.*, vol. 30, pp. 304–8, 1979.
13. A. Watanabe, S. Tanaka, H. Kobayashi, Y. Ishida, and T. Yajima, "Microcomputer-Based Spectrum-Resolved Second Harmonic Generation Correlator for Fast Measurement of Ultrashort Pulses," *Rev. Sci. Instrum.*, vol. 56, pp. 2259–62, 1985.
14. A. Watanabe, H. Saito, Y. Ishida, and T. Yajima, "Computer-Assisted Spectrum-Resolved SHG Auto-correlator for Monitoring Phase Characteristics of Femtosecond Pulses," *Opt. Commun.*, vol. 63, pp. 320–4, 1987.

2. Ultrashort Laser Pulses

Rick Trebino and Erik Zeek

The Basics

What exactly is an ultrashort laser pulse anyway? Quite simply, it's a very very short burst of electro-magnetic energy.

The pulse, like any light wave, is defined by its electric field as a function of space and time, $\mathcal{E}(x, y, z, t)$. You may be more familiar with a continuous beam, whose electric field is sinusoidal in time. The difference is that an ultrashort pulse comprises only a few cycles of a sine wave (more precisely, less than about a million for visible light). Indeed, our expression for an ultrashort pulse will be the product of a sine wave and a pulse-envelope function. So ultrashort laser pulses are not really much different from other types of laser light, just shorter. A lot shorter.

New issues do arise, however, in dealing with ultrashort pulses, and, in particular, in measuring them. For example, the shorter the pulse, the broader its spectrum, that is, the greater the range of colors (the *bandwidth*) present. And, despite the incredibly short duration of these pulses, the color can change rapidly during one. Indeed, the pulse can begin as one color and end as quite another. Simply passing through a material—even air—can modify the color variation of a pulse in time. We'll need to be able to measure this variation—which is contained in the pulse *phase*—as well as variations in the pulse intensity.

We won't concern ourselves with how such pulses are created, a subject that could fill another entire book (and has! [1–4]). Their measurement will prove adequate subject matter for us.

The Intensity and Phase vs. Time

For the sake of simplicity, we'll treat the electric field as linearly polarized, so we need consider only one component of it. This is called the *scalar approximation*, in which we ignore the pulse electric field's vector character. The electric field of the pulse can potentially be a complicated function of space and time, but, as we're mainly interested in the temporal features of the pulse, we'll ignore the spatial portion of the field and write the temporal dependence of the pulse electric field as:

$$\mathcal{E}(t) = \frac{1}{2} \sqrt{I(t)} \exp\{i [\omega t - \phi(t)]\} + c.c. \quad (2.1)$$

where t is time in the reference frame of the pulse, ω_0 is a carrier angular frequency on the order of 10^{15} sec $^{-1}$, and $I(t)$ and $\phi(t)$ are the time-dependent intensity and phase of the pulse.

Notice that we've removed the rapidly varying *carrier wave* $\exp(i\omega_0 t)$ from the intensity and phase. This saves us the trouble of plotting all the oscillations of the pulse field.

Sometimes, we refer to $I(t)$ and $\phi(t)$ as the *temporal* intensity and phase of the pulse to distinguish them for their *spectral* counterparts that we'll define next. We assume that, despite their ultrafast nature, $I(t)$ and $\phi(t)$ vary slowly compared to $\exp(i\omega_0 t)$ —a good assumption for all but the shortest pulses. As usual, “c.c.” means *complex conjugate* and is required to make the pulse field real. But, in this book (as in most other publications), we'll make what's called the *analytic signal* approximation and ignore the complex-conjugate term. This yields a complex pulse field, but it simplifies the mathematics significantly.

We refer to the *complex amplitude* of this wave as:

$$E(t) \equiv \sqrt{I(t)} \exp[-i\phi(t)] \quad (2.2)$$

$E(t)$ is simply $\mathcal{E}(t)$ but without the “Re” and the rapidly varying $\exp(i\omega_0 t)$ factor and multiplied by 2. Equation (2.2) is the quantity we'll be measuring for the rest of this book. Some people refer to $\sqrt{I(t)}$ as the “amplitude,” with the word “real” suppressed (see Fig. 2.1).

We can solve for the intensity, given the field:

$$I(t) = |E(t)|^2 \quad (2.3)$$

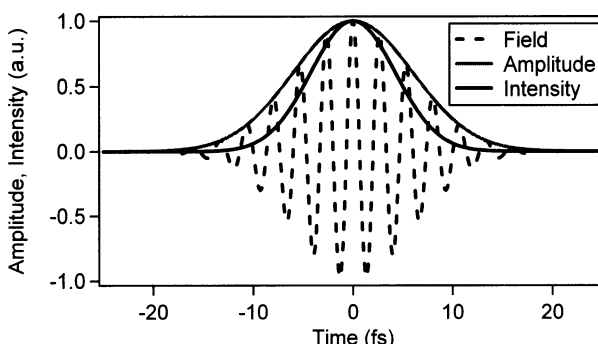


Fig. 2.1: The electric field, intensity, (real) amplitude, and intensity of a Gaussian pulse. The intensity of a Gaussian pulse is $\sqrt{2}$ shorter than its real amplitude. The phase of this pulse is a constant, $\phi(t) = 0$, and is not plotted.

where we don't care about the absolute magnitude of the intensity (the irradiance); instead we only care about the *shape*, so, in Eq. (2.3), we've omitted constants like the permittivity and the speed of light.

We can also solve for the phase:

$$\phi(t) = -\arctan \left\{ \frac{\text{Im}[E(t)]}{\text{Re}[E(t)]} \right\} \quad (2.4)$$

An equivalent formula for the phase is:

$$\phi(t) = -\text{Im}\{\ln[E(t)]\} \quad (2.5)$$

The Intensity and Phase vs. Frequency

The pulse field in the frequency domain is the Fourier transform the time-domain field, $\mathcal{E}(t)$:

$$\tilde{\mathcal{E}}(\omega) = \int_{-\infty}^{\infty} \mathcal{E}(t) \exp(-i\omega t) dt \quad (2.6)$$

where we'll use the tilde ($\tilde{\cdot}$) over a function to indicate that it's the Fourier transform. Also, the inverse Fourier transform is:

$$\mathcal{E}(t) = \frac{1}{2\pi} \int_{-\infty}^{\infty} \tilde{\mathcal{E}}(\omega) \exp(i\omega t) d\omega \quad (2.7)$$

Separating $\tilde{\mathcal{E}}(\omega)$ into its intensity and phase yields:

$$\tilde{\mathcal{E}}(\omega) = \sqrt{S(\omega)} \exp[-i\varphi(\omega)] \quad (2.8)$$

where $S(\omega)$ is the spectrum and $\varphi(\omega)$ is the spectral phase. Note that, while the temporal phase (ϕ) and spectral phase (φ) are both called "phi," we've actually used different Greek characters to distinguish them. The spectrum and spectral phase typically have nonzero regions for both positive and negative frequencies (see Fig. 2.2). Because $\mathcal{E}(t)$ is real, the two regions contain equivalent information, so everyone always ignores the negative-frequency region.

We could've defined the spectrum and spectral phase in terms of the Fourier transform of the complex pulse amplitude, $E(t)$, rather than the entire field, $\mathcal{E}(t)$:

$$\tilde{E}(\omega - \omega_0) = \sqrt{S(\omega - \omega_0)} \exp[-i\varphi(\omega - \omega_0)] \quad (2.9)$$

where $S(\omega - \omega_0)$ would've been the spectrum, and $\varphi(\omega - \omega_0)$ would've been the spectral phase. These are the same functions as above, but the center

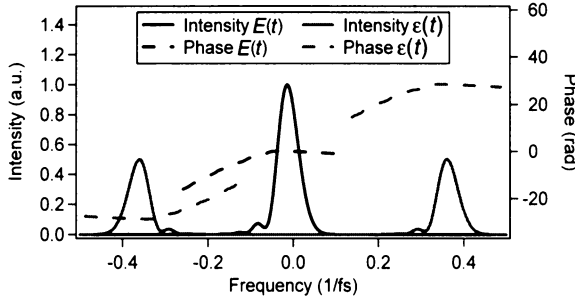


Fig. 2.2: The spectrum and spectral phase corresponding to the real pulse (gray) and the complex amplitude (black). Note that the real pulse spectrum has both positive and negative frequency components, centered on $+\omega_0$ and $-\omega_0$, respectively (in this plot, $\omega_0 \approx 0.38/\text{fs}$). The spectrum and spectral phase corresponding to the pulse complex amplitude have only one component, centered on zero frequency.

frequency of the spectrum and spectral phase would've been shifted to zero. Also, the negative-frequency component is *explicitly* removed in Eq. (2.9) because the complex conjugate does not occur in the complex field envelope (see Fig. 2.2). This is done occasionally, and a few plots in this book will use this definition.

Most the time, we won't do this simply because ultrafast optics researchers generally don't. We're sorry if it may be a bit confusing that the time-domain field in general use is the complex field envelope, while the frequency-domain field is the Fourier transform, not of the complex field envelope, but of the full real electric field (in which the negative frequency component is ignored). The reason for this usage is that people like their spectra centered on the actual center wavelength—not zero—but they don't like their temporal waveforms rapidly oscillating, as would be required to be rigorously consistent. Just memorize this, and don't complain; it's a lot easier than remembering all those PIN numbers banks keep sending you.

Notice that the spectrum is given by:

$$S(\omega) = |\tilde{\mathcal{E}}(\omega)|^2 \quad (2.10)$$

The spectral phase is given by expressions analogous to those for the temporal phase:

$$\varphi(\omega) = -\arctan \left\{ \frac{\text{Im}[\tilde{\mathcal{E}}(\omega)]}{\text{Re}[\tilde{\mathcal{E}}(\omega)]} \right\} \quad (2.11)$$

or, equivalently:

$$\varphi(\omega) = -\text{Im}\{\ln[\tilde{\mathcal{E}}(\omega)]\} \quad (2.12)$$

Finally, the spectrum can also be written in terms of the wavelength. $S_\lambda(\lambda)$ and $S_\omega(\omega)$ can be quite different for broadband functions because, for example, the frequency range extending from zero to some very low frequency extends in wavelength from a finite wavelength out to infinity. So the spectrum plotted vs. wavelength must take on considerably lower values for such large wavelengths to make sense.

We must be able to transform between frequency and wavelength because theoretical work (involving Fourier transforms) uses the frequency, while experiments (involving spectrometers) use the wavelength. The phase vs. wavelength is related to the phase vs. frequency:

$$\varphi_\lambda(\lambda) = \varphi_\omega(2\pi c/\lambda) \quad (2.13)$$

since $\omega = 2\pi c/\lambda$, and where we've added subscripts to indicate the relevant domain (frequency or wavelength). This result simply rescales the phase. But because the frequency scale and wavelength scale aren't linearly related, the phase looks different in the two cases (see Fig. 2.3).

The spectrum is a little trickier. The easiest way to see how these two quantities are related is to note that the spectral energy is equal whether we calculate it vs. frequency or wavelength:

$$\int_{-\infty}^{\infty} S_\lambda(\lambda) d\lambda = \int_{-\infty}^{\infty} S_\omega(\omega) d\omega \quad (2.14)$$

Let's now rewrite the left side of this equation by transforming variables, $\omega = 2\pi c/\lambda$, and noting that $d\omega = -2\pi c/\lambda^2 d\lambda$. We have:

$$\int_{-\infty}^{\infty} S_\lambda(\lambda) d\lambda = \int_{\infty}^{-\infty} S_\omega(2\pi c/\lambda) \frac{-2\pi c}{\lambda^2} d\lambda \quad (2.15)$$

$$= \int_{-\infty}^{\infty} S_\omega(2\pi c/\lambda) \frac{2\pi c}{\lambda^2} d\lambda \quad (2.16)$$

This means that:

$$S_\lambda = S_\omega(2\pi c/\lambda) \frac{2\pi c}{\lambda^2} \quad (2.17)$$

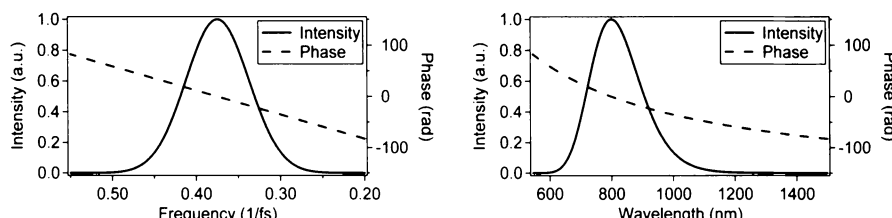


Fig. 2.3: Two identical spectra and spectral phases of a few-fs (i.e., broadband) pulse, plotted vs. frequency (left) and vs. wavelength (right). Note the different shapes of both curves, due to rescaling between frequency and wavelength.

The Phase, Instantaneous Frequency, and Group Velocity

The temporal phase, $\phi(t)$, contains frequency vs. time information, and the pulse *instantaneous angular frequency*, $\omega_{\text{inst}}(t)$, is defined as:

$$\omega_{\text{inst}}(t) \equiv \omega_0 - d\phi/dt \quad (2.18)$$

This is easy to see. At some time, t , consider the total phase of the wave. Call this quantity ϕ_0 :

$$\phi_0 = \omega_0 t - \phi(t) \quad (2.19)$$

Exactly one period, T , later, the total phase will (by definition) increase to $\phi_0 + 2\pi$:

$$\phi_0 + 2\pi = \omega_0(t + T) - \phi(t + T) \quad (2.20)$$

where $\phi(t + T)$ is the slowly varying phase at the time, $t + T$. Subtracting Eq. (2.19) from Eq. (2.20):

$$2\pi = \omega_0 T - [\phi(t + T) - \phi(t)] \quad (2.21)$$

Dividing by T and recognizing that $2\pi/T$ is a frequency, call it $\omega_{\text{inst}}(t)$:

$$\omega_{\text{inst}}(t) = 2\pi/T = \omega_0 - [\phi(t + T) - \phi(t)]/T \quad (2.22)$$

But T is small, so $[\phi(t + T) - \phi(t)]/T$ is the derivative, $d\phi/dt$. So we're done!

Usually, however, we'll think in terms of the *instantaneous frequency*, $v_{\text{inst}}(t)$, so we'll need to divide by 2π :

$$v_{\text{inst}}(t) = \omega_0 - [d\phi/dt]/2\pi \quad (2.23)$$

We can write a Taylor series for the $\phi(t)$ about the time $t = 0$:

$$\phi(t) = \phi_0 + t\phi_1 + t^2\phi_2/2 + \dots \quad (2.24)$$

where only the first few terms are required to describe well-behaved pulses.

While the temporal phase contains frequency vs. time information, the spectral phase contains time vs. frequency information. So we can define the *group delay vs. frequency*, $t_{\text{group}}(\omega)$, given by:

$$t_{\text{group}}(\omega) = d\phi/d\omega \quad (2.25)$$

A similar derivation to the above one for the instantaneous frequency can show that this definition is reasonable. Also, we'll typically use this result, which is a real time (the rad's cancel out), and never $d\phi/dv$, which isn't. Lastly, always remember that $t_{\text{group}}(\omega)$ is *not* the inverse of $\omega_{\text{inst}}(t)$.

It's also common practice to write a Taylor series for $\varphi(\omega)$:

$$\varphi(\omega) = \varphi_0 + (\omega - \omega_0) \varphi_1 + (\omega - \omega_0)^2 \varphi_2/2 + \dots \quad (2.26)$$

where, as in the time domain, only the first few terms are typically required to describe well-behaved pulses. Of course, we'll want to measure badly behaved pulses, which have higher-order terms in $\phi(t)$ and $\varphi(\omega)$.

Unfortunately, these definitions aren't completely satisfying. In particular, they don't always correspond to our intuitive ideas of what the instantaneous frequency and group delay should be for light. Consider the simple case of light with two frequencies:

$$\mathcal{E}(t) = \exp(i\omega_1 t) + \exp(i\omega_2 t) + \text{c.c.} \quad (2.27)$$

Recalling that this is a simple case of "beats," the instantaneous frequency obtained by the definition given above is:

$$\omega_{\text{inst}}(t) = (\omega_1 + \omega_2)/2 \quad (2.28)$$

a frequency that never actually occurs in the beam (only ω_1 and ω_2 do). But, for most ultrashort-pulse applications, there's a broad continuous range of frequencies, and the above definitions prove reasonable.

Phase Distortions in Time and Frequency

Phase Wrapping, Unwrapping, and Blanking

Before we discuss the various phase distortions that occur in ultrashort pulses, we should mention a couple of points that you should always keep in mind when you deal with the phase.

First, because $\exp[i\phi] = \exp[i(\phi + 2\pi)] = \exp[i(\phi + 4\pi)] = \dots$, the phase could be different by any integer times 2π , and the light pulse will still be exactly the same. What this means is that infinitely many different phases vs. time (or frequency) correspond to precisely the same pulse. So how do we decide which phase to use?

There are two preferred methods. The first is to simply force the phase to always remain between 0 and 2π (or $-\pi$ and $+\pi$). This way, there's only one possible phase that yields a given pulse (once the intensity is determined). This is the method you'll be implementing if you simply ask your computer to compute the phase, given the real and imaginary parts of the pulse using Eqs. (2.4), (2.5), (2.11), or (2.12).

The problem with this approach is that, well, it's ugly. When the phase exceeds 2π , it jumps to zero, and a great big discontinuity opens up in the phase. See Fig. 2.4. And this can happen many times over the pulse's life.

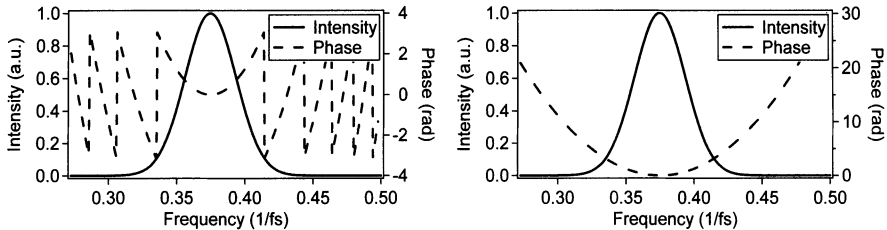


Fig. 2.4: Left: A pulse whose phase has not been phase-unwrapped. Right: The same pulse after phase-unwrapping. Note the different phase scales in each plot.

The solution to this aesthetics problem is to *phase-unwrap*. It involves adding or subtracting the appropriate number of multiples of 2π to the phase at each discontinuity, so that it remains continuous over its entire range. This yields much prettier phases, but the price you pay is the need for a phase-unwrapping routine, which makes these decisions. Fortunately, phase-unwrapping routines work well, and this is the preferred approach in ultrafast optics labs everywhere (including this book).

But be careful, as under-sampling a phase that varies a lot will confuse any phase-unwrapping routine. At a discontinuity, the routine has to decide whether to add 2π to or subtract 2π from the next point. This is easy if the previous two points were 6.276 and 6.280, respectively, and the next point is 0.001: in this case, the routine adds 2π to the 0.001. But if the next point is 2.9 because you didn't sample the points densely enough, it'll just guess. As a result, you could get a really strange-looking phase plot. It'd still be correct, but no one would take you seriously.

Another issue to keep in mind is that, when the intensity goes to zero, the phase is *completely meaningless*. After all, if an arrow has zero length, what possible meaning could there be in its direction? None. Unfortunately, computers are still too dumb to just ignore the phase in this case, and they'll typically simply spew out a blather of random numbers (or worse, error messages) for the phase, even when the intensity is zero.

When this happens, here's something you should *never* do. Do *not* try to fit the resulting random numbers to a polynomial and then call me complaining that your pulse's phase is so complex that even a 500th-order polynomial didn't quite do it (yes, someone did this). Okay, you can do the polynomial fit if you really want to; just don't call me.

The solution to this problem is to *phase-blank*. When the intensity is zero (or so close to zero that it's in the noise), it's customary to simply not plot the phase, instead of plotting random numbers. See Fig. 2.5. The commercial FROG code allows you to decide at what intensity the phase becomes meaningless for your data and hence when to phase-blank. But you can always simply erase these points from your plot.

Finally, there are additional subtleties involving the phase of a pulse. It turns out that a given pulse doesn't necessarily have a unique representation

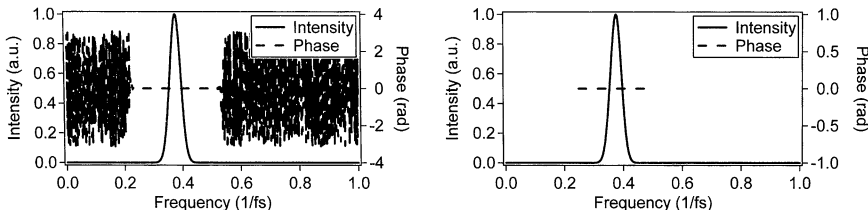


Fig. 2.5: Left: A typical pulse (spectrum and spectral phase) that has not been phase-blanked. The phase takes on random values where the intensity is near zero because the phase is not defined where the intensity is zero. Right: The same pulse after phase-blanking.

in terms of intensity and phase. In other words, different combinations of intensities and phases can yield the same real electric field. Even beyond the above ambiguities, the phase can have additional possible values if we also allow the intensity to vary to compensate. For example, if we artificially modify the intensity slightly by introducing a little bump in it for a very short range of times (think less than one period of the light wave), we can simply adjust the phase at those times to compensate to yield the same real electric field. Don't think too hard about this issue, or you'll have to transfer to a mathematics department.

In fact, to keep us all on the same wavelength, let's all agree to use $S(\omega) = |\mathcal{E}(\omega)|^2$ for the spectrum, $I(t) = |E(t)|^2$ for the intensity, and the corresponding formulas for the phase and spectral phase.

Zeroth-order Phase: The Absolute Phase

First, it's important to realize that the zeroth-order phase is the same in both domains: $\phi_0 = \varphi_0$. This is because the Fourier Transform is linear, and a constant times a function Fourier-Transforms to the same constant times the Fourier Transform of that function. Thus, the zeroth-order phase term, which corresponds to multiplication by a complex constant, is the same in both domains: $E(t) \exp(i\phi_0)$ Fourier-Transforms to $\tilde{E}(\omega) \exp(i\phi_0)$.

The zeroth-order phase term is often called the *absolute phase*. It's something of a misnomer, as it's really a relative phase: the relative phase of the carrier wave with respect to the envelope. Simply stated, it's the phase of the carrier at the peak of the pulse envelope or some other reference time.

Having said that we desire to measure all orders of the phase, including high ones, we now point out that, in reality, we don't usually care much about the lowest-order term. This is because, when the pulse is many carrier-wave cycles long, variation in the absolute phase shifts the carrier wave from the peak of the envelope to a value only slightly different and hence changes the pulse field very little. Figure 2.6 (top) shows the full real field of a 5-cycle pulse with both a 0 and π values of the absolute phase. Note that it is quite difficult to distinguish the two pulses.

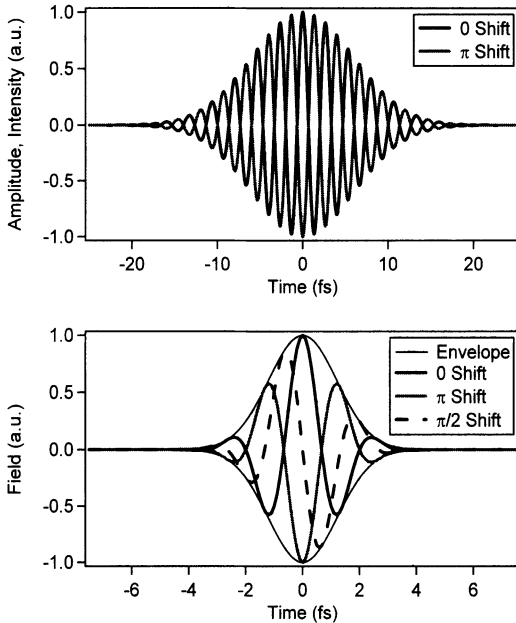


Fig. 2.6: Top: the full real electric field of two 10-fs near-IR pulses, one with zero absolute phase and the other with π absolute phase. Bottom: the full real field of single-cycle near-IR pulses with various absolute phases. Note how different single-cycle pulses look when their absolute phase shifts.

When the pulse is only one cycle long, however, the absolute phase matters. While this effect could be important, we won't consider it in this text.

First-order Phase: A Shift in Time or Frequency

Recall the *Fourier Transform Shift Theorem*, which says that: $E(t - \tau)$ Fourier Transforms to $\tilde{E}(\omega) \exp(-i\omega\tau)$. So a linear term in the spectral phase, $\varphi_1 \equiv \tau$, corresponds to a shift in time, i.e., a delay (see Fig. 2.7). Generally, we care only about the pulse's *shape*, not when it arrives. Indeed, if our measurement technique were sensitive a delay of the pulse, we'd have to maintain high stability of its path length, and hence of all beam-steering optics between the source and measurement device. And that would just further complicate our already complicated lives.

Occasionally, the delay is of interest, and interferometric methods can be used in this case (see chapters 22–24). But the first-order term in the spectral phase, φ_1 , is generally uninteresting.

Since the Shift Theorem also applies to the inverse Fourier Transform, as well, $\tilde{E}(\omega - \omega_0)$ inverse-Fourier-Transforms to $E(t) \exp(i\omega_0 t)$. So a linear term in the temporal phase, ϕ_1 , corresponds to frequency shift (see Fig. 2.7).

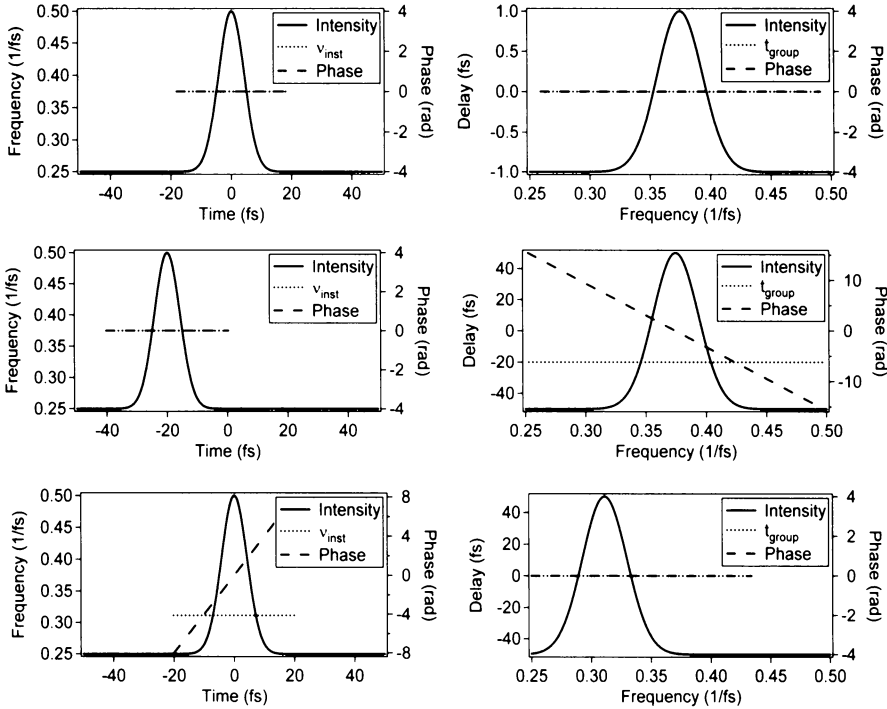


Fig. 2.7: Effect of linear phase. Top row: A Gaussian-intensity, flat-phase pulse. Middle row: the same pulse, but delayed in time, corresponding to a linear spectral phase. Bottom row: the same pulse, but with a linear phase in time, corresponding to a shift of the spectrum. In these plots and all others in this chapter, the frequency scales are measured in cycles per fs, not radians per fs.

bottom row). A spectral shift is often interesting. It is, however, easily measured with a spectrometer.

Second-order Phase: Linear Chirp

Quadratic variation of $\phi(t)$, that is, a nonzero value of ϕ_2 , represents a linear ramp of frequency vs. time and so we say that the pulse is *linearly chirped*. (See Fig. 2.8). Consider a pulse with a Gaussian intensity and quadratic temporal phase:

$$E(t) = [E_0 \exp(-at^2)] \exp(ibt^2) \quad (2.29)$$

where E_0 is a constant, $1/\sqrt{a}$ is roughly the pulse duration, and b is the *chirp parameter*. Here the intensity is:

$$I(t) = |E_0|^2 \exp(-2at^2) \quad (2.30)$$

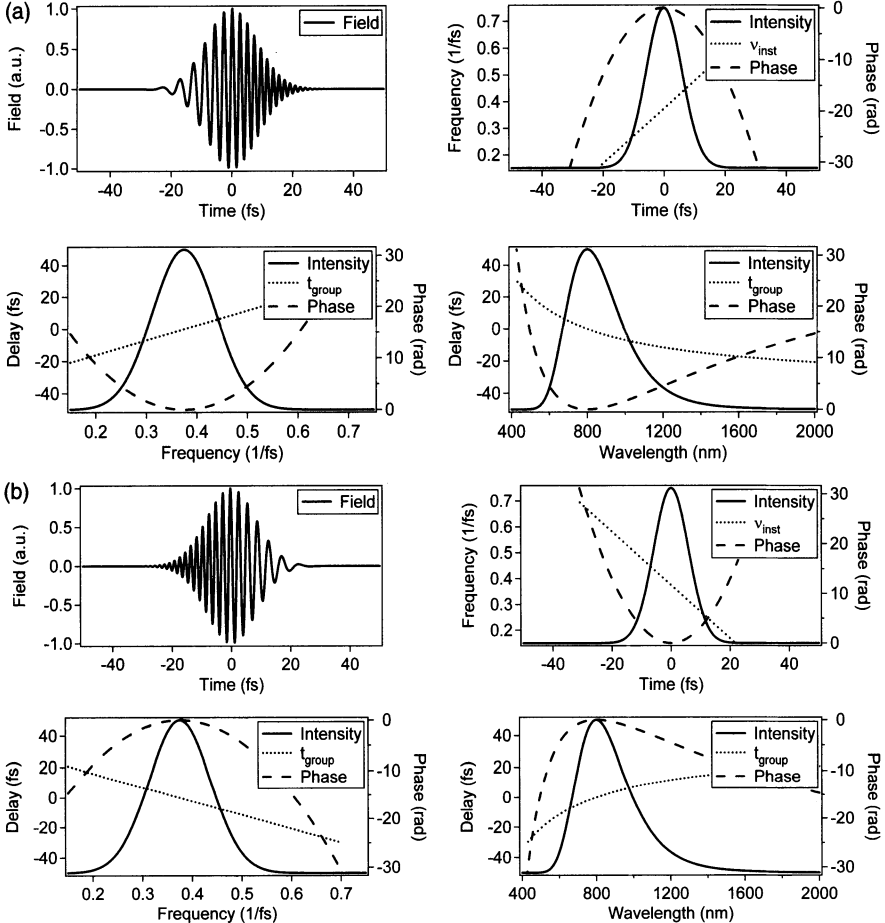


Fig. 2.8: (a) 20-fs Gaussian-intensity pulse w/ quadratic temporal phase, $\phi_2 = -0.032 \text{ rad fs}^2$ or $\varphi_2 = 290 \text{ rad fs}^2$. Here the quadratic phase has stretched what would have been a 3-fs pulse (given the spectrum) to a 13.9-fs one. Top left: the field. Note the increase in frequency with time. Top right: the intensity, phase, and instantaneous frequency vs. time. Bottom row: the spectrum, spectral phase, and group delay vs. frequency and wavelength. Like their time-domain relatives here, the spectrum, spectral phase, and group delay vs. frequency are also Gaussian, quadratic, and linear, respectively, but, plotted vs. wavelength, they are somewhat distorted. (b) Same as Fig. 2.8a, but for a pulse with negative chirp, $\phi_2 = 0.032 \text{ rad/fs}^2$ or $\varphi_2 = -290 \text{ rad fs}^2$.

and the temporal phase is simply:

$$\phi(t) = -bt^2 \quad (2.31)$$

The Fourier transform of this field is:

$$\tilde{E}(\omega) = \frac{\sqrt{\pi}}{a - ib} \exp \left[-\frac{\omega^2}{4(a - ib)} \right] \quad (2.32)$$

Separated into the spectrum and spectral phase, the frequency-domain field can be written:

$$S(\omega) = \frac{\pi}{a^2 + b^2} \exp\left[-\frac{a\omega^2}{2(a^2 + b^2)}\right] \quad (2.33)$$

which is also a Gaussian. And the spectral phase is also quadratic:

$$\varphi(\omega) = \frac{b}{a^2 + b^2} \omega^2 \quad (2.34)$$

As a result, quadratic variation of $\phi(t)$ corresponds to quadratic variation of $\varphi(\omega)$. Note that ϕ_2 and φ_2 have opposite signs. This is a result of the various sign conventions, which are fairly standard.

Propagation through materials usually causes (positive) linear chirp, so if an ultrashort laser pulse doesn't have linear chirp at one point, it will a little further on. In fact, a negatively chirped pulse will shorten as it propagates through material.

Third-order Phase: Quadratic Chirp

Materials have higher-order dispersion, so they also induce higher-order phase distortions, as well. Above second order, distortions in the phase are usually considered in the frequency domain. This is because the spectrum is easily measured, and the intensity vs. time is not, so determination of the spectral phase yields the full pulse field, whereas the temporal phase doesn't. Also, it's quite intuitive to think in terms of how much delay is required for a given frequency to compensate for its distortion in spectral phase.

Third-order spectral phase means a quadratic group delay vs. frequency. This means that the central frequency of the pulse arrives first, say, while frequencies on either side of the central frequency, $\omega_0 \pm \delta\omega$, arrive later. The two slightly different frequencies cause beats in the intensity vs. time, so pulses with cubic spectral phase distortion have oscillations after a main pulse (or before it, if the sign of the third-order coefficient, φ_3 , is negative). See Figs. 2.9a and b. Also, you might want to take a peak at Chapter 17, where we'll measure the mother of all cubic-spectral-phase pulses.

Higher-order Phase

Higher-order terms yield additional distortions, which can give rise to extremely complex pulses. Figures 2.10 and 2.11 show pulse shapes with quartic (fourth-order) and quintic (fifth-order) spectral phase.

For example, the nonlinear-optical process, self-phase modulation, yields a temporal phase proportional to the input pulse intensity vs. time. This distortion can be quite complex, especially when considered in the frequency domain (see Figure 2.12).

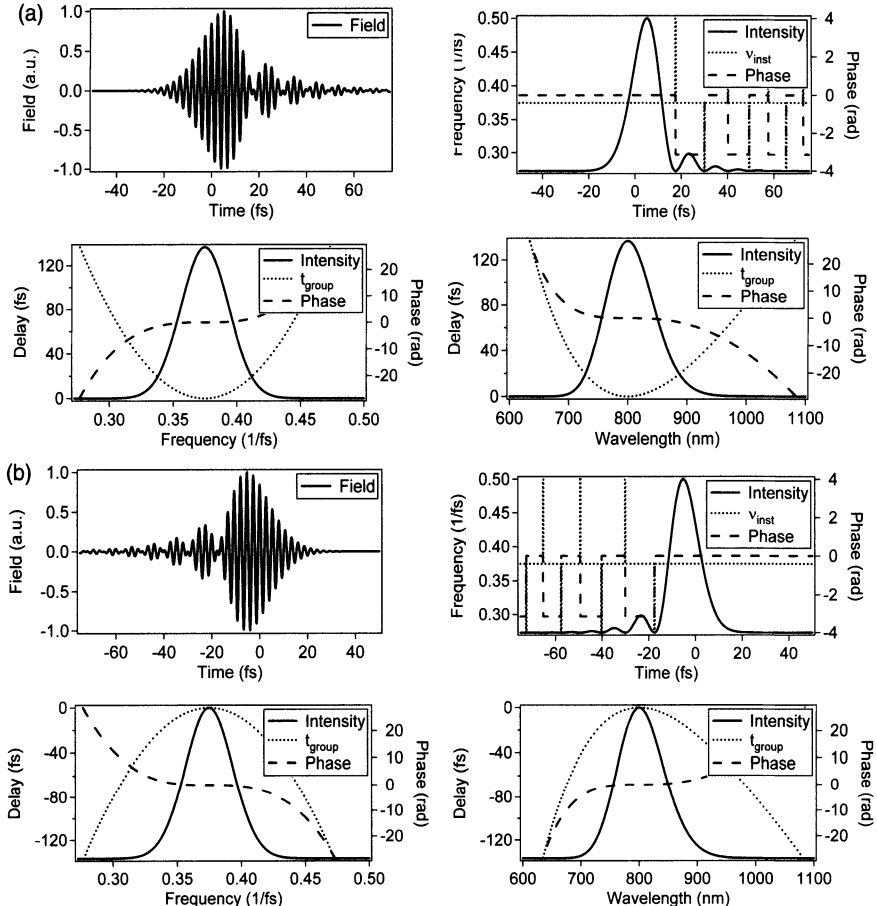


Fig. 2.9: (a) Cubic Spectral phase. Top left: the electric field vs. time for a pulse with a Gaussian spectrum and cubic spectral phase, with $\varphi_3 = 3 \times 10^4 \text{ rad fs}^3$. Top right: the intensity, phase, and instantaneous frequency vs. time. Note that phase jumps correspond to meaningless discontinuities in the instantaneous frequency. Bottom row: The spectrum, spectral phase, and group delay vs. frequency (left) and wavelength (right). (b) Same as Fig. 2.9a, but with negative cubic spectral phase of the same magnitude as in Fig. 2.9a.

Also, propagation through long distances of fiber can result in higher-order dispersion of the fiber becoming evident in the form of higher-order pulse phase distortions, and nonlinear-optical processes can further distort the pulse phase, as well as the intensity, in both domains.

Finally, to repeat a point we made earlier, it's often tempting to take a phase vs. time or frequency and fit it to a high-order polynomial, as inspired by Eqs. (2.24) or (2.26). While this may be reasonable, it is important to realize that when the intensity is zero, the phase is undefined and hence *meaningless*. And, when the intensity is *near* zero, the phase is *nearly* meaningless, which is probably not too different from *totally* meaningless. Thus, it's important

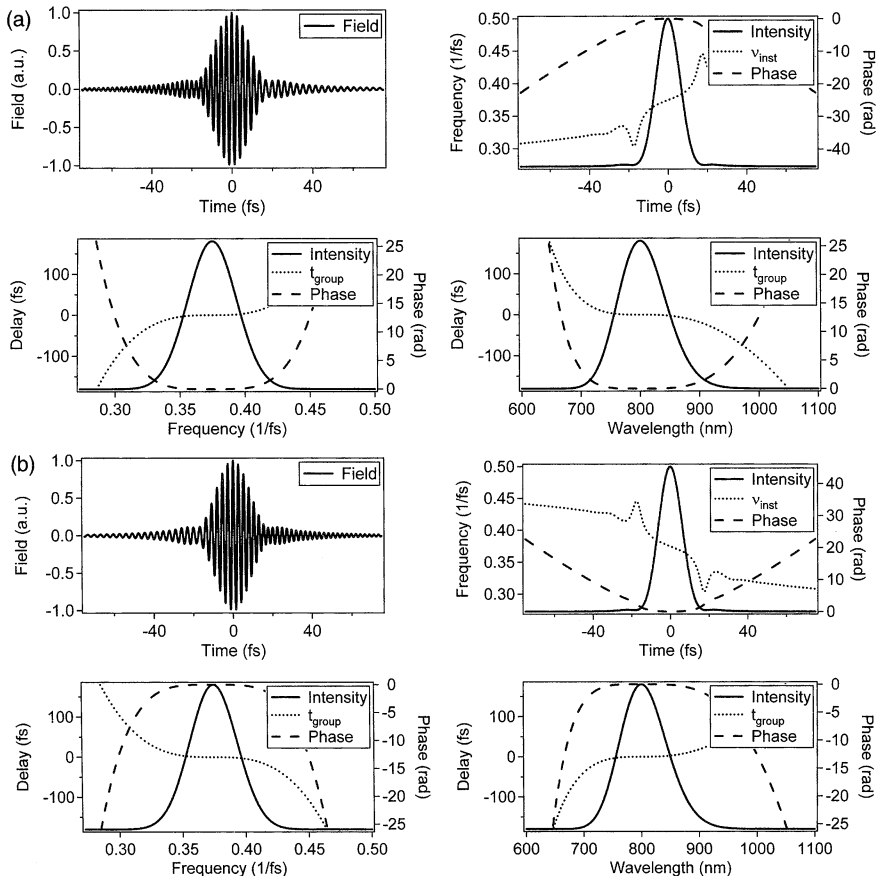


Fig. 2.10: (a) Quartic phase. Top left: the electric field vs. time for a pulse with Gaussian spectrum and positive quartic spectral phase, $\varphi_4 = 4 \times 10^5 \text{ rad fs}^4$. Top right: The intensity, phase, and instantaneous frequency vs. time. Bottom row: and the spectrum, spectral phase, and group delay vs. frequency (left) and wavelength (right). (b) Same as Fig. 2.10a, but with negative quartic spectral phase of the same magnitude as in Fig. 2.10a.

to crop the phase (to phase-blank) at values of the intensity that are within an error bar of zero, often at about 1% of the peak intensity. Or better, when fitting the phase to a high-order polynomial, use an intensity-weighted fit, which places low emphasis on the phase at times or frequencies where the intensity is weak.

Relative Importance of the Intensity and Phase

Finally, while it's obviously true that both the intensity and phase (in either domain) are required to fully specify a function, in some sense the more

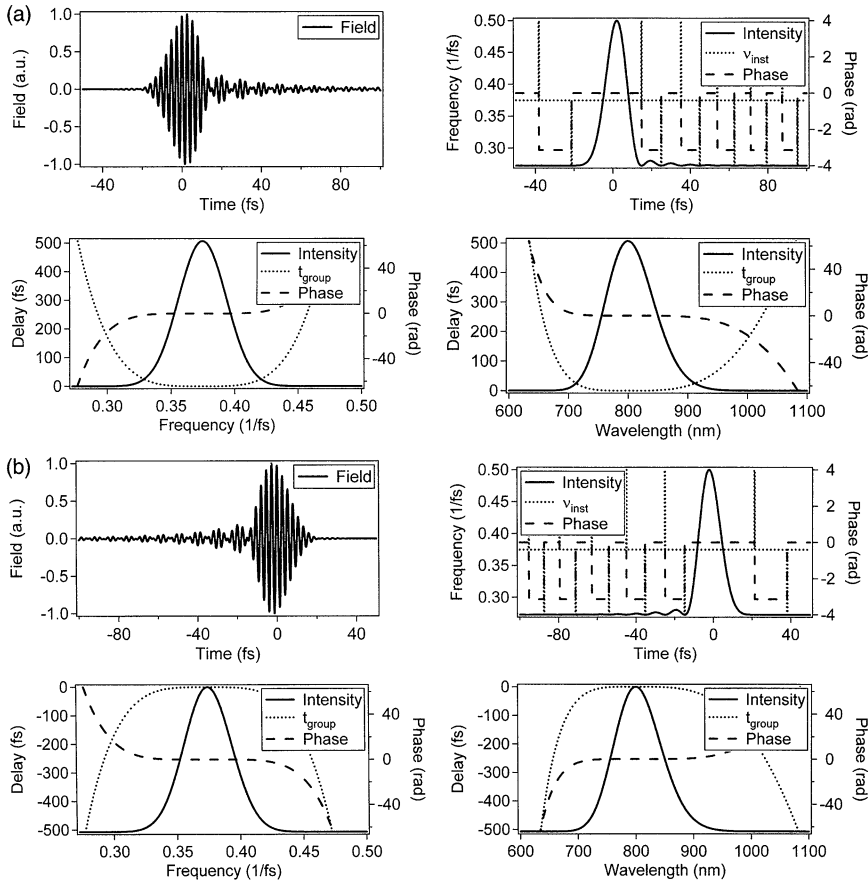


Fig. 2.11: (a) Quintic spectral phase. Top left: the electric field vs. time for a pulse with Gaussian spectrum and $\varphi_5 = 7 \times 10^6 \text{ rad fs}^5$. Top right: The intensity, phase, and instantaneous frequency vs. time. Bottom: the spectrum, spectral phase, and group delay vs. frequency and wavelength. (b) Same as Fig. 2.11a, but with negative quintic spectral phase of the same magnitude as in Fig. 2.11a.

important of the two quantities is the *phase*. To see this [5], take the *magnitude* of the two-dimensional Fourier Transform of a photograph and combine it with the *phase* from the two-dimensional Fourier Transform of a *different* photograph. This composite image, transformed back to the space domain, tends to look much more like the photograph that supplies the Fourier phase than the photograph that supplies the Fourier magnitude. We've reproduced this example in Fig. 2.13 using different photographs. Note that the composite images look almost nothing like the pictures that supply the Fourier magnitude, and instead both look very much like the picture supplying the Fourier phase!

This fact is also evident in recent work in the generation of near-single-cycle pulses. Spectra of such pulses are often quite structured, but, as long

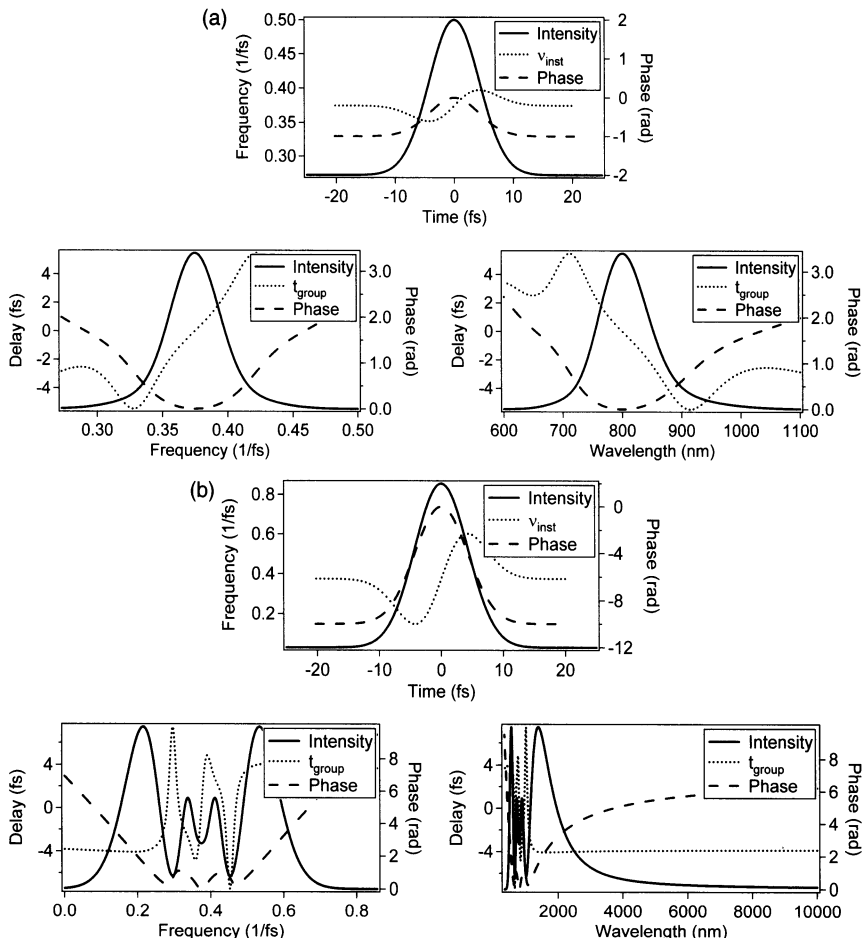


Fig. 2.12: (a) Top: Temporal intensity, phase, and instantaneous frequency of a 10-fs, 800-nm pulse that's experienced self-phase modulation with a peak magnitude of 1 radian. Bottom: spectrum, spectral phase, and group delay vs. frequency and wavelength. All plots use a Gaussian temporal intensity. The pulse is slightly spectrally broadened. (b) Top: Temporal intensity, phase, and instantaneous frequency of a 10-fs, 800-nm pulse that's experienced self-phase modulation with a peak magnitude of 10 radians. Bottom: spectrum, spectral phase, and group delay vs. frequency and wavelength. All plots use a Gaussian temporal intensity. The pulse is massively spectrally broadened.

as a nearly constant spectral phase is achieved, a few-cycle pulse can be produced. The spectral structure causes only small ripples in the wings of the pulse intensity vs. time. See Chapter 14.

Pulse Propagation

We've set up all this terminology to describe potentially very complex ultrashort light pulses. Why have we done this? How do pulses become distorted?

The answer is that light is often created with complex intensity and phase, but, even if it's a simple flat-phase Gaussian pulse to begin with, propagation through materials will distort it.

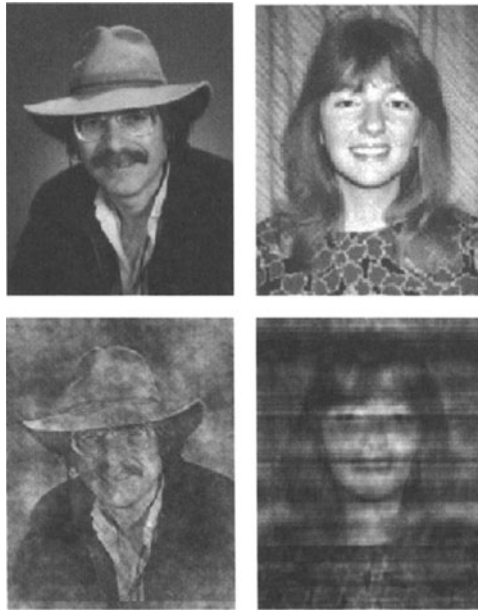


Fig. 2.13: Top: Photographs of the Rick Trebino (left) and his wife, Linda (right). If we 2D-Fourier-transform (FT) each of these pictures, and use the 2D FT magnitude of one photograph in conjunction with the *other photograph*'s FT phase, after inverse FT, we make the composite photographs shown on the bottom row. Bottom left: Photograph produced using the FT-magnitude of Linda and FT-phase of Rick. Bottom right: Photograph produced using the FT-magnitude of Rick and FT-phase of Linda. Note that these composite photographs look nothing like the photographs whose FT-magnitude was used, and they look very similar to the photograph whose FT phase was used.

When a pulse propagates through a medium, its various frequencies have different phase and group velocities due to the medium's frequency-dependent refractive index, $n(\omega)$, that is, its *dispersion*. The absorption coefficient, $\alpha(\omega)$, varies also. These effects are easily and accurately modeled. If L is the length of the medium, the frequency-domain output field, $\tilde{E}_{\text{out}}(\omega)$, will be related to the frequency-domain input field, $\tilde{E}_{\text{in}}(\omega)$, by:

$$\tilde{E}_{\text{out}}(\omega) = \tilde{E}_{\text{in}}(\omega) \exp[-\alpha(\omega)L/2] \exp[in(\omega)kL] \quad (2.35)$$

$$= \tilde{E}_{\text{in}}(\omega) \exp[-\alpha(\omega)L/2] \exp \left[in(\omega) \frac{\omega}{c} L \right] \quad (2.36)$$

Absorption will modify the pulse's spectrum, and dispersion will modify the pulse's spectral phase:

$$S_{\text{out}}(\omega) = S_{\text{in}}(\omega) \exp[-\alpha(\omega)L] \quad (2.37)$$

$$\varphi_{\text{out}}(\omega) = \varphi_{\text{in}}(\omega) + i n(\omega) \frac{\omega}{c} L \quad (2.38)$$

Absorption can narrow the spectrum, which could broaden the pulse. On the other hand, occasionally someone attempts to broaden a pulse spectrum by preferentially absorbing its peak frequencies.

We've seen that phase is usually the more interesting quantity. To a reasonably good approximation, propagation through a medium adds first- and second-order terms to the pulse phase. Since, as we have seen, first-order phase vs. ω corresponds to a simple delay, it isn't very interesting. Thus, it's fairly accurate to say that propagation through a material introduces (positive) chirp into a pulse. A flat-phase pulse becomes positively chirped, and a negatively chirped pulse actually shortens. If the pulse is particularly broadband, however, then third, fourth, and possibly fifth-order phase terms must be considered.

Also, if a pulse propagates through some material on its way to your pulse-measurement device, and you really desire to know the pulse's intensity and phase before it propagates through the material, then you can compensate for the distortions introduced by the material using this result. Of course, you can only do this if you're measuring the complete pulse field, $E(t)$ or, equivalently, $\tilde{E}(\omega)$.

The Pulse Length and Spectral Width

Our goal is to measure the pulse complex amplitude $E(t)$ (or $\tilde{E}(\omega)$) completely, that is, to measure both the intensity and phase, expressed in either domain. We must be able to do so even when the pulse has significant intensity structure and highly nonlinear chirp. In addition, we'd like not to have to make assumptions about the pulse.

Unfortunately, this has turned out to be difficult. As a result, researchers have had to make do with considerably less information than they would've liked for many years. A modest request is to be able simply to measure about how long the pulse is. Analogously, we'd like to be able to know how broad the spectrum is. Unfortunately, researchers haven't settled on a single definition of the *pulse length* (also referred to as the *pulse width*) and the *spectral width* (but, for some reason, never referred to as the "spectral length"). Several definitions exist, and each has its advantages and adherents. Here are the most common definitions.

***Full-width-half-maximum* (τ_{FWHM}):** This is the time between the most-separated points that have half of the pulse's peak intensity (see Fig. 2.14). This

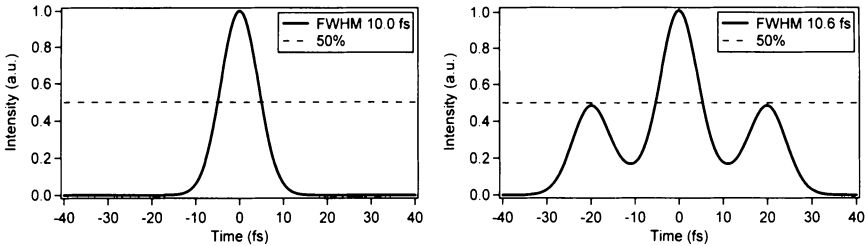


Fig. 2.14: Left: A pulse and its full-width-half-maximum (FWHM). This is a good measure of the pulse width, except when pulse structure exists. Right: A pulse with satellites with 49% of the peak of the pulse, for which this pulse-width definition produces misleading information.

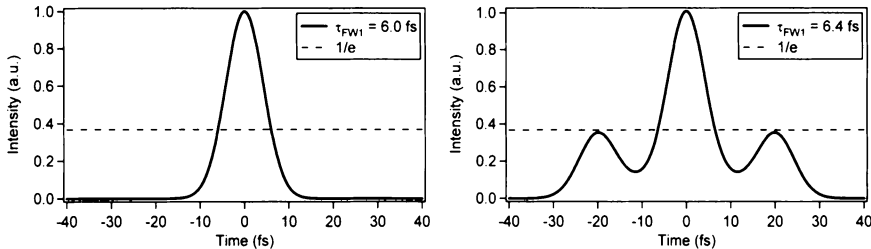


Fig. 2.15: Left: A pulse and its half-width-1/e (HW1/e). Right: This is also a good measure of the pulse width, except when pulse structure exists.

is the most intuitive definition, and it's the rule in experimental measurements, since it's easy to pull τ_{FWHM} off a plot. It's not the most convenient for calculations, however. Also, small variations in the pulse can yield huge changes in τ_{FWHM} . Consider, for example, a pulse with a satellite pulse .49 times as large as the main pulse; if the satellite pulse increases by 1%, the pulse length can increase by a large factor.

For a simple Gaussian-intensity pulse, these issues aren't a problem, and the electric field can be written in terms of τ_{FWHM} :

$$E(t) = E_0 \exp[-2 \ln 2 (t/\tau_{FWHM})^2] = E_0 \exp[-1.38(t/\tau_{FWHM})^2] \quad (2.39)$$

Half-width-1/e ($\tau_{HW1/e}$): This pulse width (see Fig. 2.15) is the amount of time between the pulse's maximum intensity and the time the intensity drops to 1/e (about 0.36) of the maximum value. Especially useful when the pulse is a Gaussian in time or frequency, this definition allows us to write a simple expression for the pulse, with no messy constants. Theorists like this because it makes it easier to write down expressions in calculations. In terms of this definition, a Gaussian pulse field is written:

$$E(t) = E_0 \exp[-\frac{1}{2}(t/\tau_{HW1/e})^2] \quad (2.40)$$

The factor of 1/2 is required so the intensity will lack such constants:

$$I(t) = |E_0|^2 \exp[-(t/\tau_{HW1/e})^2] \quad (2.41)$$

Keep in mind that the HW1/e width is considerably less than the FWHM, so be careful to specify which pulse width definition you're using, especially in a conversation between theorists and experimentalists.

Root-mean-squared pulse width (τ_{rms}): This width is the easiest to prove theorems about. It's the second-order moment about the mean arrival time of the pulse:

$$\tau_{\text{rms}}^2 \equiv \langle t - \langle t \rangle^2 \rangle = \langle t^2 \rangle - \langle t \rangle^2 \quad (2.42)$$

where:

$$\langle t^n \rangle \equiv \int_{-\infty}^{\infty} t^n I(t) dt \quad (2.43)$$

and $I(t)$ is assumed normalized so that its time integral is 1 (so it should have dimensions of inverse time). While the FWHM ignores any values of the pulse intensity as long as they're less than one half the pulse maximum intensity, the rms width emphasizes values far from the center of the pulse, and therefore is a good indicator of "wings" in the pulse.

Equivalent pulse width (τ_e): This definition (see Fig. 2.16) considers that the pulse has a width (τ_e) and a height (I_{max}). And the product of these two quantities should be the area under the intensity (the integral of $I(t)$):

$$\tau_e = \frac{1}{I_{\text{max}}} \int_{-\infty}^{\infty} I(t) dt \quad (2.44)$$

This pulse-width definition is most useful when the pulse is complicated, with many sub-pulses and structure.

We define spectral widths, ω_{FWHM} , $\omega_{\text{HW1/e}}$, ω_{rms} , and ω_e , analogously. And spectral widths in cycles per second are $v_{\text{FWHM}} = \omega_{\text{FWHM}}/2\pi$, etc.

The Time-Bandwidth Product

Now that we've defined the temporal and spectral widths, we can define the *time-bandwidth product*, or TBP, of a pulse, which is just what it sounds like:

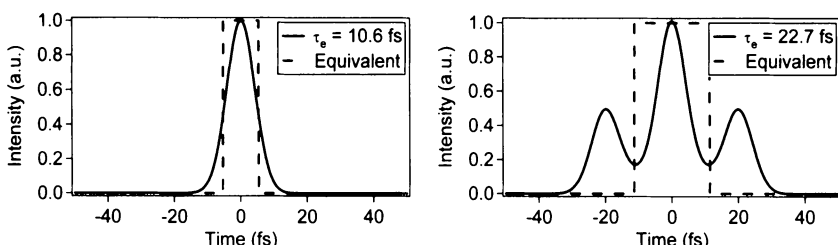


Fig. 2.16: Illustration of the equivalent pulse width for two different pulses. The peak of the dashed rectangular "equivalent" pulse is set equal to the peak of the pulse. The width of the dashed rectangular pulse is then chosen so that its area is equal to that of the solid curve pulse.

the product of the temporal width and the spectral width. If all you can have about a pulse is a single parameter, the parameter you'd like to have is the TBP. Since the units of the pulse width are seconds, and those of the spectral width (ω_{FWHM}) are rad/s, or inverse seconds, the TBP is dimensionless. As a result, it's a good figure of merit for a pulse. The smaller the TBP, the "cleaner" or simpler the pulse. In addition, since the pulse coherence time, τ_c (roughly the length of the shortest structure within a pulse), is the reciprocal of the bandwidth, the TBP is the ratio of the pulse width and the coherence time. So the TBP is the approximate number of sub-pulses in the pulse. For pulses whose main distortion is a low-order phase distortion, however, such as linear chirp, the TBP can be large even when there is no substructure in the pulse. Whatever the source of distortions, laser builders and manufacturers and researchers try very hard to make the simplest pulses with the lowest TBP.

Depending on the definition chosen, the minimum possible TBP ranges from about .1 to 1, and it increases with increasing pulse complexity (see Figs. 2.17 and 2.18).

It would seem reasonable that a pulse with a flat phase would have a smaller TBP than a pulse with a complicated phase. Is this always the case? Or is it possible to have a pulse with, say, a complicated spectrum, for which some complicated spectral phase yields a smaller pulse length and hence a smaller TBP than does a constant phase? It turns out that, for *any* spectrum, the shortest pulse in time, and hence the smallest TBP, *always* occurs for a flat spectral phase. Similarly, for any pulse intensity vs. time, the narrowest spectrum, and hence the smallest TBP, always occurs for a flat temporal phase. These conclusions require that we use the rms temporal and spectral widths and follow easily from the result given by Cohen in his excellent book, *Time-Frequency Analysis* [6,7]:

$$\omega_{\text{rms}}^2 = \int_{-\infty}^{\infty} A'(t)^2 dt + \int_{-\infty}^{\infty} A(t)^2 \phi'(t)^2 dt \quad (2.45)$$

where the real amplitude $A(t) = \sqrt{I(t)}$, intensity is assumed normalized to have unity time integral, the prime means the derivative, and the mean frequency is assumed subtracted from $\phi'(t)$.

This result writes the rms bandwidth as something like the Pythagorean sum of a contribution due to variations in the amplitude and a contribution due to variations in the phase (weighted by the intensity). Note that both integrands and integrals are always positive, so variations in the amplitude only increase the bandwidth and, likewise, variations in the phase also only increase the bandwidth.

Since the Fourier Transform is symmetrical, the same holds for the rms pulse width in terms of the spectral variations:

$$\tau_{\text{rms}}^2 = \int_{-\infty}^{\infty} B'(\omega)^2 d\omega + \int_{-\infty}^{\infty} B(\omega)^2 \varphi'(\omega)^2 d\omega \quad (2.46)$$

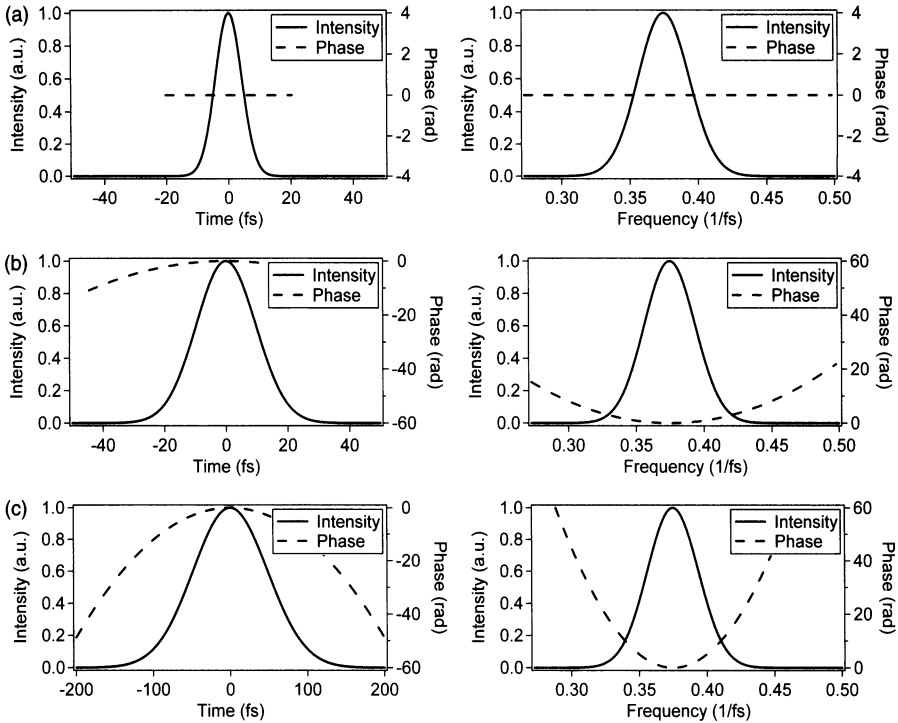


Fig. 2.17: (a) Gaussian-intensity pulse with constant phase and minimal TBP. The intensity and phase vs. time (left); the spectrum and spectral phase vs. frequency (right). For the different definitions of the widths: $TBP_{rms} = \tau_{rms} \omega_{rms} = 0.5$, $TBP_e = 3.14$, $TBP_{HW1/e} = 1$, $TBP_{FWHM} = 2.76$. Divide by 2π for $\tau_{rms} \nu_{rms}$, etc. (b) Same as Fig. 2.17a, except a longer pulse (note the change in scale of the phase axis) with chirp and hence a larger TBP. $TBP_{rms} = 1.13$, $TBP_e = 7.01$, $TBP_{HW1/e} = 2.26$, $TBP_{FWHM} = 6.28$. Divide by 2π for $\tau_{rms} \nu_{rms}$, etc. (c) Same as Fig. 2.17a, except an even longer pulse (note the change in scale of the time axis) with more chirp and hence a larger TBP. $TBP_{rms} = 5.65$, $TBP_e = 35.5$, $TBP_{HW1/e} = 11.3$, $TBP_{FWHM} = 31.3$. Divide by 2π for $\tau_{rms} \nu_{rms}$, etc.

where the spectral amplitude is $B(\omega) = \sqrt{S(\omega)}$, $S(\omega)$ is assumed normalized to have unity area, prime means derivative, and the mean pulse time is assumed subtracted from $\varphi'(\omega)$.

Thus, for a given spectrum, $S(\omega)$, variations in the spectral phase can only increase the rms pulse width over that corresponding to a flat spectral phase.

Spatio-Temporal Pulse Characteristics

In writing Eq. (2.1), we've ignored the spatial dependence of the beam. More specifically, we've tacitly assumed that the complex pulse field, which is actually a function of both time and space, separates into the product of spatial and temporal factors, and we have simply ignored the spatial component. This assumption is valid for the fairly smooth pulses emitted by most

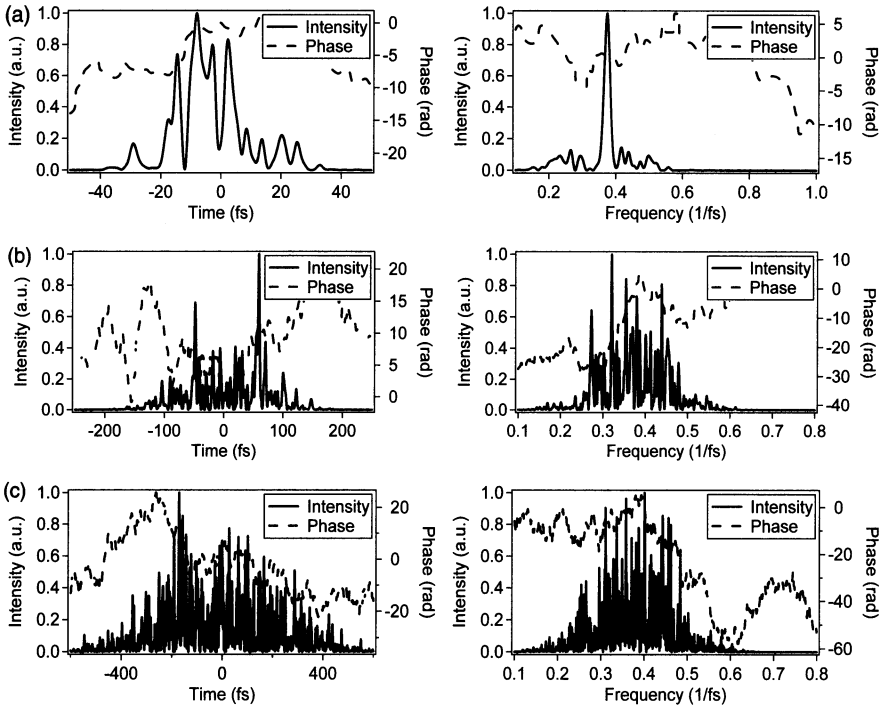


Fig. 2.18: (a) A pulse with random intensity and phase structure. The intensity and phase vs. time (left) the spectrum and spectral phase vs. frequency (right). This pulse has a near-unity TBP. For the various definitions of the pulse and spectral widths, the TBP is: $TBP_{rms} = 6.09$, $TBP_e = 4.02$, $TBP_{HW1/e} = 0.82$, $TBP_{FWHM} = 2.57$. Divide by 2π for $\tau_{rms} \nu_{rms}$, etc. (b) Same as Fig. 2.18a, except a pulse with more structure and hence a larger TBP. $TBP_{rms} = 32.9$, $TBP_e = 10.7$, $TBP_{HW1/e} = 35.2$, $TBP_{FWHM} = 116$. Divide by 2π for $\tau_{rms} \nu_{rms}$, etc. (c) Same as Fig. 2.18a, except a pulse with even more structure and hence an even larger TBP. $TBP_{rms} = 122$, $TBP_e = 44.8$, $TBP_{HW1/e} = 213$, $TBP_{FWHM} = 567$. Divide by 2π for $\tau_{rms} \nu_{rms}$, etc.

ultrafast lasers. It is, however, fairly easy to generate pulses that violate this assumption (for example, pulse compressors and shapers can introduce angular dispersion into the pulse, so the pulse winds up with its redder colors on one side and the bluer colors on the other, a distortion called *spatial chirp*), and nearly all pulse-measurement techniques get confused in this case. We'll talk about how to measure such complicated pulses later when we discuss the spatio-temporal measurement of a pulse (Chapter 22), but in the meantime, we'll ignore this problem. (If you suspect your pulse has this problem before you get to Chapter 22, just aperture it, and measure a small piece of the beam.)

We've also assumed polarized light, but this also is not necessary. We'll get to the measurement of a polarization-varying pulse later (we'll just measure each polarization independently, but we'll have to measure the relative phase of the two polarizations, as well—see Chapter 23).

References

1. Ippen, E.P. and C.V. Shank, *Ultrashort Light Pulses—Picosecond Techniques and Applications*, ed. S.L. Shapiro. 1977, Berlin: Springer-Verlag.
2. Duling, I.N., ed. *Compact Sources of Ultrashort Pulses*. 1995, Cambridge University Press: Cambridge.
3. Rulliere, C., ed. *Femtosecond Laser Pulses: Principles and Experiments*. 1998, Springer: Heidelberg.
4. Kaiser, W., ed. *Ultrashort Laser Pulses and Applications*. Topics in Applied Physics. Vol. 60. 1988, Springer-Verlag: Berlin.
5. Stark, H., ed. *Image Recovery: Theory and Application*. 1987, Academic Press: Orlando.
6. Cohen, L., *Time-Frequency Distributions—A Review*. Proceedings of the IEEE, 1989. **77**(7): p. 941–81.
7. Cohen, L., *Time-Frequency Analysis*. 1995, Englewood Cliffs, NJ: Prentice-Hall.

3. Nonlinear Optics

Rick Trebino and John Buck

Linear vs. Nonlinear Optics

The great thing about ultrashort laser pulses is that all their energy is crammed into a very short time, so they have very high power and intensity. A typical ultrashort pulse from a Ti : Sapphire laser oscillator has a paltry nanojoule of energy, but it's crammed into 100 fs, so its peak power is 10,000 Watts. And it can be focused to a micron or so, yielding an intensity of 10^{12} W/cm^2 ! And it's easy to amplify such pulses by a factor of 10^6 !

What this means is that ultrashort laser pulses easily experience *high-intensity effects*—effects that we don't ordinarily see because even sunlight on the brightest day doesn't approach the above intensities. And all high-intensity effects fall under the heading of *nonlinear optics* [1–12]. Some of these effects are undesirable, such as optical damage. Others are very desirable, such as *second-harmonic generation*, which allows us to make light at a new frequency, twice that of the input light. Or like *four-wave mixing*, which allows us to generate light with an electric field proportional to $E_1(t) E_2^*(t) E_3(t)$, where $E_1(t)$, $E_2(t)$, and $E_3(t)$ are the complex electric-field amplitudes of three different light waves. Whereas linear optics requires that light beams pass through each other without affecting each other, nonlinear optics allows the opposite. This chapter will describe the basics of nonlinear optics for anyone who hasn't experienced this field, so you can understand the basics of FROG, which is an inherently nonlinear-optical phenomenon.

The fundamental equation of optics—whether linear or nonlinear—is the wave equation:

$$\frac{\partial^2 \mathcal{E}}{\partial z^2} - \frac{1}{c_0^2} \frac{\partial^2 \mathcal{E}}{\partial t^2} = \mu_0 \frac{\partial^2 \mathcal{P}}{\partial t^2} \quad (3.1)$$

where μ_0 is the magnetic permeability of free space, c_0 is the speed of light in vacuum, \mathcal{E} is the real electric field, and \mathcal{P} is the real induced polarization. The induced polarization contains the light's effects on the medium and the medium's effect back on the light wave. It drives the wave equation.

The induced polarization contains linear-optical effects (the absorption coefficient and refractive index) and also nonlinear-optical effects. At low intensity (or low field strength), the induced polarization is proportional to the electric field that is already present:

$$\mathcal{P} = \epsilon_0 \chi^{(1)} \mathcal{E} \quad (3.2)$$

where ϵ_0 is the electric permittivity of free space, and the linear susceptibility, $\chi^{(1)}$, describes the linear-optical effects. This expression follows from the

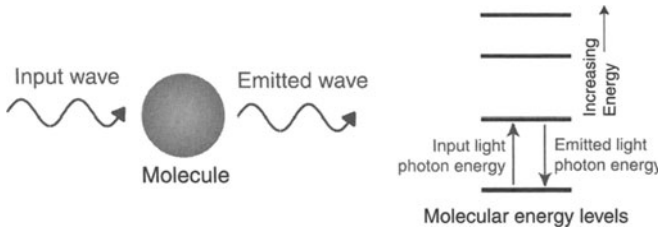


Fig. 3.1: Linear optics. Left: A molecule excited by a light wave oscillates at that frequency and emits only that frequency. Right: This process can be diagrammed by showing the input light wave as exciting ground-state molecules up to an excited level, which re-emits the same frequency.

fact that the light electric field, \mathcal{E} , forces electric dipoles in the medium into oscillation at the frequency of the field; the dipole oscillators then emit an additional electric field at the same frequency. The total electric field (incident plus emitted) is what appears as \mathcal{E} in Eqs. (3.1) and (3.2). If we assume a lossless medium, for example, we find that the electric and polarization field expressions, $\mathcal{E}(z, t) \propto E_0 \cos(\omega t - kz)$ and $\mathcal{P} = \varepsilon_0 \chi^{(1)} E_0 \cos(\omega t - kz)$, will solve the wave equation, provided that $\omega = c k$, and $c = c_0 / (1 + \chi^{(1)})^{1/2}$.

In linear optics, (where Eq. (3.2) applies), the wave equation is linear, so if \mathcal{E} is a sum of more than one beam (field), then so is \mathcal{P} . As a result, \mathcal{P} drives the wave equation to produce light with *only* those frequencies present in \mathcal{P} , and these arise from the original input beams. In other words, light doesn't change color (see Fig. 3.1). Also, with a linear wave equation, the principle of superposition holds, and beams of light can pass through each other and don't affect each other.

Life at low intensity is dull.

Nonlinear-Optical Effects

At high intensity, the induced polarization ceases to be a simple linear function of the electric field. Put simply, like a cheap stereophonic amplifier driven at too much volume, the medium doesn't follow the field perfectly (see Figs. 3.2 through 3.4), and higher-order terms must be included:

$$\mathcal{P} = \varepsilon_0 [\chi^{(1)} \mathcal{E} + \chi^{(2)} \mathcal{E}^2 + \chi^{(3)} \mathcal{E}^3 + \dots] \quad (3.3)$$

where $\chi^{(2)}$ and $\chi^{(3)}$ are called the second- and third-order susceptibilities. $\chi^{(n)}$ is called the n th-order susceptibility.

What do nonlinear-optical effects look like? They're easy to calculate. Recall that the real field, \mathcal{E} , is given by:

$$\mathcal{E}(t) = \frac{1}{2} E(t) \exp(i\omega t) + \frac{1}{2} E^*(t) \exp(-i\omega t) \quad (3.4)$$

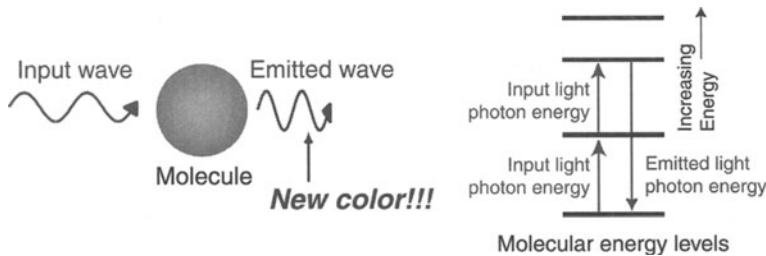


Fig. 3.2: Nonlinear optics. Left: A molecule excited by a light wave oscillates at other frequencies and emits those new frequencies. Right: This process can be diagrammed by showing the input light wave as exciting ground-state molecules up to highly excited levels, which re-emit the new frequencies.

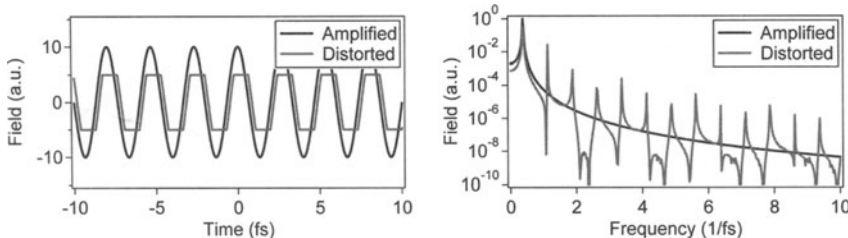


Fig. 3.3: Nonlinear electronic effects in a cheap audio amplifier. The input wave from the audio source is taken here to be a sine wave. In an expensive amplifier, the sine wave is accurately reproduced at higher volume, but, because the cheap amplifier cannot achieve the desired volume, the output wave saturates and begins to look more like a square wave. This produces new frequency components at harmonics of the input wave. Nonlinear-optical effects are analogous: a sine-wave electric wave drives a molecular system, which also does not reproduce the input sine wave accurately, producing new frequencies at harmonics of the input wave. Whereas audiophiles spend a great deal of money to avoid the above nonlinear electronic effects, optical scientists spend a great deal of money to achieve nonlinear-optical effects.

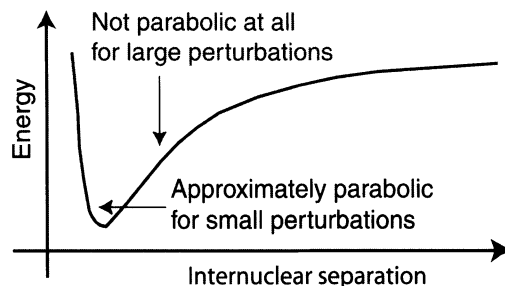


Fig. 3.4: Potential surface of a molecule, showing the energy vs. separation between nuclei. Note that the potential is nearly parabolic near the bottom, but it is far from parabolic for excitations that hit the molecule harder forcing it to vibrate with larger ranges of nuclear separations. This molecule will emit frequencies other than that driving it.

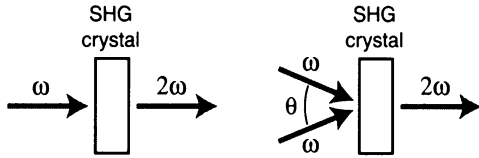


Fig. 3.5: Second-harmonic generation. Left: Collinear beam geometry. Right: Noncollinear beam geometry with an angle, θ , between the two input beams. Such noncollinear beam geometries are possible in nonlinear optics because more than one field is required at the input.

where we have temporarily suppressed the space dependence, and $E(t)$ is the complex field. So squaring this field yields:

$$\mathcal{E}^2(t) = \frac{1}{4} E^2(t) \exp(2i\omega t) + \frac{1}{2} E(t) E^*(t) + \frac{1}{4} E^{*2}(t) \exp(-2i\omega t) \quad (3.5)$$

Notice that this expression includes terms that oscillate at 2ω , the *second harmonic* of the input light frequency. These terms then drive the wave equation to yield light at this new frequency. This process is very important; it's called *second-harmonic generation* (SHG). Optical scientists, especially ultrafast scientists, make great use of SHG to create new frequencies. And it is the single most important effect used to measure ultrashort laser pulses. Figure 3.5 shows a schematic of SHG.

The above expression also contains a zero-frequency term, so light can induce a dc electric field. This effect is called optical rectification; it's generally pretty weak, so we won't say much more about it.

If we consider the presence of two beams and this time don't suppress the spatial dependence, $\mathcal{E}(\vec{r}, t) = \frac{1}{2} E_1(\vec{r}, t) \exp[i(\omega_1 t - \vec{k}_1 \cdot \vec{r})] + \frac{1}{2} E_2(\vec{r}, t) \exp[i(\omega_2 t - \vec{k}_2 \cdot \vec{r})] + c.c.$. In this case, we have:

$$\begin{aligned} \mathcal{E}^2(\vec{r}, t) = & \frac{1}{4} E_1^2 \exp[2i(\omega_1 t - \vec{k}_1 \cdot \vec{r})] \\ & + \frac{1}{2} E_1 E_1^* + \frac{1}{4} E_1^{*2} \exp[-2i(\omega_1 t - \vec{k}_1 \cdot \vec{r})] \\ & + \frac{1}{4} E_2^2 \exp[2i(\omega_2 t - \vec{k}_2 \cdot \vec{r})] + \frac{1}{2} E_2 E_2^* \\ & + \frac{1}{4} E_2^{*2} \exp[-2i(\omega_2 t - \vec{k}_2 \cdot \vec{r})] \\ & + \frac{1}{2} E_1 E_2 \exp\{i[(\omega_1 + \omega_2)t - (\vec{k}_1 + \vec{k}_2) \cdot \vec{r}]\} \\ & + \frac{1}{2} E_1^* E_2^* \exp\{-i[(\omega_1 + \omega_2)t - (\vec{k}_1 + \vec{k}_2) \cdot \vec{r}]\} \\ & + \frac{1}{2} E_1 E_2^* \exp\{i[(\omega_1 - \omega_2)t - (\vec{k}_1 - \vec{k}_2) \cdot \vec{r}]\} \\ & + \frac{1}{2} E_1^* E_2 \exp\{-i[(\omega_1 - \omega_2)t - (\vec{k}_1 + \vec{k}_2) \cdot \vec{r}]\} \end{aligned} \quad (3.6)$$

Okay, this looks like a mess. But the first two lines are already familiar; they're the SHG and optical-rectification terms for the individual fields. The next line

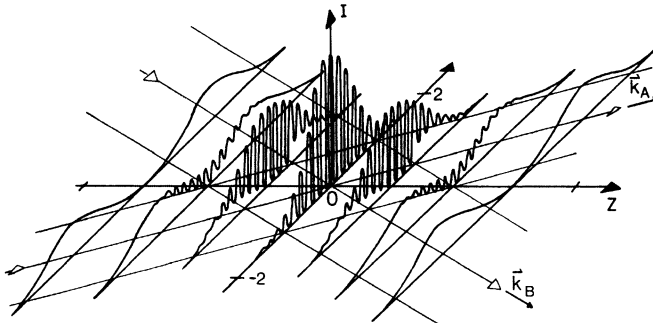


Fig. 3.6: Intensity pattern produced when two beams cross. When the beams cross in a medium, the medium is changed more at the intensity peaks than at the troughs, producing a laser-induced grating [13].

is new: it yields light at the frequency, $\omega_1 + \omega_2$, the sum frequency, and hence is called *sum-frequency generation* (SFG). The last line is also new: it yields light at the frequency, $\omega_1 - \omega_2$, the difference frequency, and hence is called *difference-frequency generation* (DFG). These two processes are also quite important, and they play a key role in techniques to measure pulses, as well.

Notice something else. The new beams are created in new directions, $\vec{k}_1 + \vec{k}_2$ and $\vec{k}_1 - \vec{k}_2$. This can be very convenient if we desire to see these new—potentially weak—beams in the presence of intense input beams that create them.

Third-order effects are collectively referred to as *four-wave-mixing* (4WM) effects because three waves enter the nonlinear medium, and an additional one is created in the process, for a total of four. We won't waste a page and write out the entire third-order induced polarization, but, in third order, as you can probably guess, we see effects including *third-harmonic generation* (THG) and a variety of terms like:

$$\mathcal{P}_i = \frac{3}{4} \varepsilon_0 \chi^{(3)} E_1 E_2^* E_3 \exp \left\{ i[(\omega_1 - \omega_2 + \omega_3)t - (\vec{k}_1 - \vec{k}_2 + \vec{k}_3) \cdot \vec{r}] \right\} \quad (3.7)$$

Notice that, if the factor of the electric field envelope is complex-conjugated, its corresponding frequency and k-vector are both negative, while, if the field is not complex-conjugated, the corresponding frequency and k-vector are both positive. Such third-order effects, in which one k-vector is subtracted, are often called *induced grating* effects because the intensity due to two of the beams, say, E_1 and E_2 , has a sinusoidal spatial dependence (see Fig. 3.6). The sinusoidal intensity pattern affects the medium in some way, creating a sinusoidal modulation of its properties, analogous to those of a diffraction grating. The process can then be modeled as diffraction of the third beam off the induced grating.

Third-order effects include a broad range of interesting phenomena (some useful, some irritating), many beyond the scope of this book. But we'll consider a few that are important for pulse measurement. For example, suppose

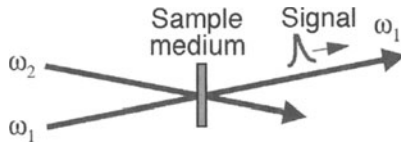


Fig. 3.7: Two-beam coupling. One beam can affect the other in passing through a sample medium. The pulse at the output indicates the signal beam, here collinear with one of the beams and at the same frequency. This idea is the source of a variety of techniques for measuring the properties of the sample medium.

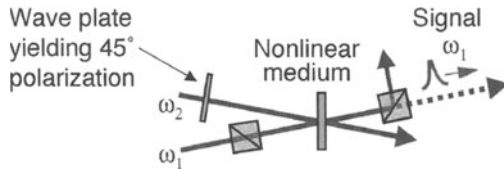


Fig. 3.8: Polarization gating. If the polarizers are oriented at 0° and 90° , respectively, the 45° -polarized beam (at frequency ω_2) induces polarization rotation of the 0° -polarized beam (at frequency ω_1), which can then leak through the second 90° polarizer. The pulse at the output indicates the signal pulse, again collinear with one of the input beams, but here with the orthogonal polarization.

that the second and third beams in the above expression are the same: $E_2 = E_3$ and $\vec{k}_2 = \vec{k}_3$. In this case, the above induced polarization becomes:

$$\mathcal{P}_1 = \frac{3}{4} \varepsilon_0 \chi^{(3)} E_1 |E_2|^2 \exp \{i[\omega_1 t - \vec{k}_1 \cdot \vec{r}]\} + c.c. \quad (3.8)$$

This yields a beam that has the same frequency and direction as beam #1, but allows it to be affected by beam #2 through its mag-squared factor. So beams that pass through each other can affect each other! Of course, the strength of all such effects is zero in empty space ($\chi^{(3)}$ of empty space is zero), but the strength can be quite high in a solid, liquid, or gas. It's often called *two-beam coupling* (see Fig. 3.7).

A particularly useful implementation of the above third-order effect is *polarization gating* (see Fig. 3.8), which involves the use of orthogonal polarizations for E_2 and E_3 . This typically means that these two co-propagating beams combine together to yield a beam polarized at 45° to that of E_1 , which is, say, horizontally polarized. The two vertically polarized beams form a grating, and the horizontally polarized beam diffracts off it, and the diffracted beam maintains horizontal polarization. This creates an induced polarization for the horizontal polarization, i.e., the polarization orthogonal to that of E_1 . This new beam is created in the same direction as beam #1, and with the same frequency, too. As a result, crossed polarizers can be used to separate the new beam from the input beam E_1 . This beam geometry is convenient and easy to set up, and it's much more sensitive than two-beam coupling.

By the way, another process is simultaneously occurring in polarization gating called *induced birefringence*, in which the electrons in the medium oscillate along with the incident field at $+45^\circ$, which stretches the formerly spherical electron cloud into an ellipsoid elongated along the $+45^\circ$ direction. This introduces anisotropy into the medium, typically increasing the refractive index for the $+45^\circ$ direction and decreasing it for the -45° direction. The medium then acts like a wave plate, slightly rotating the polarization of the field, E_1 , allowing some of it to leak through the crossed polarizers.

However you look at it, you get the same answer when the medium responds rapidly.

Another type of induced-grating process is *self diffraction* (see Fig. 3.9). It involves beams #1 and #2 inducing a grating, but beam #1 also diffracting off it. Thus beams #1 and #3 are the same beam. This process has the induced-polarization term:

$$\mathcal{P}_i = \frac{3}{8} \varepsilon_0 \chi^{(3)} E_1^2 E_2^* \exp \{i[(2\omega_1 - \omega_2)t - (2\vec{k}_1 - \vec{k}_2) \cdot \vec{r}]\} + c.c. \quad (3.9)$$

It produces a beam with frequency $2\omega_1 - \omega_2$ and k-vector $2\vec{k}_1 - \vec{k}_2$. This beam geometry is also convenient because only two input beams are required.

And it is also possible to perform third-harmonic generation using more than one beam (or as many as three). An example beam geometry is shown in Fig. 3.10, using two input beams.

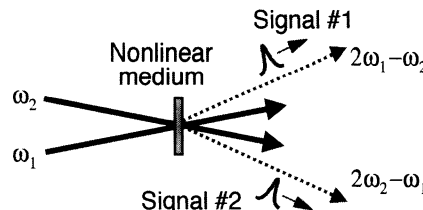


Fig. 3.9: Self diffraction. The two beams yield a sinusoidal intensity pattern, which induces a grating in the medium. Then each beam diffracts off the grating. The pulses at the output indicate the signal pulses, here in the $2\vec{k}_1 - \vec{k}_2$ and $2\vec{k}_2 - \vec{k}_1$ directions.

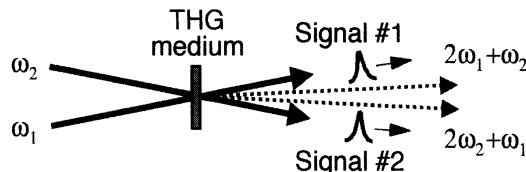


Fig. 3.10: Third-harmonic generation. While each beam individually can produce third harmonic, it can also be produced by two factors of one field and one of the other. These latter two effects are diagrammed here.

Some General Observations about Nonlinear Optics

Nonlinear-optical effects are usually diagrammed as in Fig. 3.11. Upward-pointing arrows indicate fields without complex conjugates and with frequency and k-vector contributions with plus signs. Downward-pointing arrows indicate complex-conjugated fields in the polarization and negative signs in the contributions to the frequency and k-vector of the light created. Unless otherwise specified, ω_0 and k_0 denote the output or *signal* frequency and k-vector.

Notice that, in all of these nonlinear-optical processes, the polarization propagates through the medium just like the light wave does. It has a frequency and k-vector. For a given process of N^{th} order, the signal frequency ω_0 is given by:

$$\boxed{\omega_0 = \pm \omega_1 \pm \omega_2 \pm \cdots \pm \omega_N} \quad (3.10)$$

where the signs obey the above complex-conjugate convention.

The polarization has a k-vector with an analogous expression:

$$\boxed{\vec{k}_0 = \pm \vec{k}_1 \pm \vec{k}_2 \pm \cdots \pm \vec{k}_N} \quad (3.11)$$

where the same signs occur in both Eqs. (3.10) and (3.11).

In all of these nonlinear-optical processes, terms with products of the E-field complex envelopes, such as $E_1^2 E_2^*$, are created. *It is these products that allow us to measure ultrashort laser pulses.* Whether it is simple autocorrelation, FROG, or some new, as yet undiscovered method, it will take advantage of these effects. What we'll be doing, for example, is taking two beams (pulses) and delaying one with respect to the other and considering processes with the

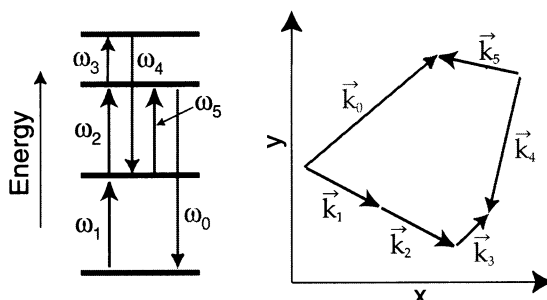


Fig. 3.11: Sample complex nonlinear-optical process, $\mathcal{P} \propto E_1 E_2 E_3 E_4^* E_5$. Here, $\omega_0 = \omega_1 + \omega_2 + \omega_3 - \omega_4 + \omega_5$ and $\vec{k}_0 = \vec{k}_1 + \vec{k}_2 + \vec{k}_3 - \vec{k}_4 + \vec{k}_5$. The k-vectors are shown adding in two-dimensional space, but, in third- and higher-order processes, space's third dimension is potentially also involved. The different frequencies (colors) of the beams are shown as different shades of gray.

product, $E_1(t) E_2(t - \tau)$, where τ is the delay. This multiplication of electric fields will allow one pulse to gate out a temporal piece of another.

The Mathematics of Nonlinear Optics

The Slowly Varying Envelope Approximation

Okay, so there are some interesting induced polarizations going on, but how do we calculate what their effects are? Well, we must substitute into the wave equation, Eq. (3.1), and solve the nonlinear differential equation that results. While this is hard to do exactly, a few tricks and approximations make it quite easy in most cases of practical interest.

The first approximation is that we consider only a range of frequencies near one frequency at a time. We'll write the wave equation for one particular signal frequency, ω_0 , and only consider a small range of nearby frequencies. Anything happening at distant frequencies will alternately be in phase and then out of phase with the fields and polarizations in this range and so should have little effect. We'll also assume that the nonlinear optical process is fairly weak, so it won't affect the input beams. Thus we'll only consider the one signal field of interest. If you're interested in more complex situations, you're probably not measuring pulses, and you should check out a full text on nonlinear optics (see, for example, the list at the end of this chapter).

The second is the *Slowly Varying Envelope Approximation (SVEA)*, which, despite its name, remains a remarkably good approximation for all but the shortest pulses (we'll see it break down in the chapter on few-femtosecond pulses, but the fix will be remarkably simple). It takes advantage of the fact that, as short as they are, most ultrashort laser pulses are still not as short as an optical cycle (about 2 fs for visible wavelengths). Thus the pulse electric field can be written as the product of the carrier sine wave and a relatively slowly varying envelope function. This is what we've been doing, but we haven't explicitly used this fact; now we will. Since the measure of the change of anything is the derivative, we'll now neglect second derivatives of the slowly varying envelope compared to those of the more rapidly varying carrier sine wave. And the wave equation, which is what we must solve to understand any optics problem, is drowning in derivatives.

Assume that the driving polarization propagates along the z-axis, and write the electric field and polarization in terms of slowly varying envelopes:

$$\mathcal{E}(\vec{r}, t) = \frac{1}{2} E(\vec{r}, t) \exp[i(\omega_0 t - k_0 z)] + c.c. \quad (3.12)$$

$$\mathcal{P}(\vec{r}, t) = \frac{1}{2} P(\vec{r}, t) \exp[i(\omega_0 t - k_0 z)] + c.c. \quad (3.13)$$

where we've chosen to consider the creation of light at the same frequency as that of the induced polarization, ω_0 . But we've also assumed that the light field and polarization have the same k-vectors, k_0 , which is a big—and often

unjustified—assumption, as discussed above. But bear with us for now, and we'll come clean in a little while.

Recall that the wave equation calls for taking second derivatives of \mathcal{E} and \mathcal{P} with respect to t and/or z . Let's calculate them:

$$\frac{\partial^2 \mathcal{E}}{\partial t^2} = \frac{1}{2} \left[\frac{\partial^2 E}{\partial t^2} + 2i\omega_0 \frac{\partial E}{\partial t} - \omega_0^2 E \right] \exp[i(\omega_0 t - k_0 z)] + c.c. \quad (3.14)$$

$$\frac{\partial^2 \mathcal{E}}{\partial z^2} = \frac{1}{2} \left[\frac{\partial^2 E}{\partial z^2} - 2ik_0 \frac{\partial E}{\partial z} - k_0^2 E \right] \exp[i(\omega_0 t - k_0 z)] + c.c. \quad (3.15)$$

$$\frac{\partial^2 \mathcal{P}}{\partial t^2} = \frac{1}{2} \left[\frac{\partial^2 P}{\partial t^2} + 2i\omega_0 \frac{\partial P}{\partial t} - \omega_0^2 P \right] \exp[i(\omega_0 t - k_0 z)] + c.c. \quad (3.16)$$

As we mentioned above, we'll assume that derivatives are small and that derivatives of derivatives are even smaller:

$$\left| \frac{\partial^2 E}{\partial t^2} \right| \ll \left| 2i\omega_0 \frac{\partial E}{\partial t} \right| \ll \left| \omega_0^2 E \right| \quad (3.17)$$

Letting $\omega_0 = 2\pi/T$, we find that this condition will be true as long as:

$$\left| \frac{\partial^2 E}{\partial t^2} \right| \ll \left| 2 \frac{2\pi}{T} \frac{\partial E}{\partial t} \right| \ll \left| \frac{4\pi^2}{T} E \right| \quad (3.18)$$

where T is the optical period of the light, again about 2 fs for visible light. These conditions hold if the field envelope is not changing on a time scale of a single cycle, which is nearly always true. So we can neglect the smallest term and keep the larger two.

The same is true for the spatial derivatives. We'll also neglect the second spatial derivative of the electric field envelope.

And the same derivatives arise for the polarization. But since the polarization is small to begin with, we'll neglect both the first and second derivatives.

The wave equation becomes:

$$\begin{aligned} & \left[-2ik_0 \frac{\partial E}{\partial z} - \frac{2i\omega_0}{c^2} \frac{\partial E}{\partial t} - k_0^2 E + \frac{\omega_0^2}{c^2} E \right] \exp[i(\omega_0 t - k_0 z)] \\ &= -\mu_0 \omega_0^2 P \exp[i(\omega_0 t - k_0 z)] \end{aligned} \quad (3.19)$$

since we can factor out the complex exponentials.

We can also cancel the exponentials. Recalling that E satisfies the wave equation by itself, $k_0^2 E = (\omega_0^2/c^2)E$, and those two terms can also be canceled.

Then dividing through by $-2ik$ yields:

$$\frac{\partial E}{dz} + \frac{1}{c} \frac{\partial E}{\partial t} = -i \frac{\mu_0 \omega_0^2}{2k_0} P \quad (3.20)$$

This expression is actually a bit oversimplified. A more accurate inclusion of dispersion (see Diels' and Rudolph's book) yields the same equation, but with the phase velocity of light, c , replaced with the group velocity, v_g :

$$\frac{\partial E}{dz} + \frac{1}{v_g} \frac{\partial E}{\partial t} = -i \frac{\mu_0 \omega_0^2}{2k_0} P \quad (3.21)$$

We can now simplify this equation further by transforming the time coordinate to be centered on the pulse. This involves new space and time coordinates, z_v and t_v , given by: $z_v = z$ and $t_v = t - z/v_g$. To transform to these new co-ordinates requires replacing the derivatives:

$$\frac{\partial E}{\partial z} = \frac{\partial E}{\partial z_v} \frac{\partial z_v}{\partial z} + \frac{\partial E}{\partial t_v} \frac{\partial t_v}{\partial z} \quad (3.22)$$

$$\frac{\partial E}{\partial t} = \frac{\partial E}{\partial z_v} \frac{\partial z_v}{\partial t} + \frac{\partial E}{\partial t_v} \frac{\partial t_v}{\partial t} \quad (3.23)$$

Computing the simple derivatives and substituting, we find:

$$\frac{\partial E}{\partial z} = \frac{\partial E}{\partial z_v} + \frac{\partial E}{\partial t_v} \left[-\frac{1}{v_g} \right] \quad (3.24)$$

$$\frac{\partial E}{\partial t} = 0 + \frac{\partial E}{\partial t_v} \quad (3.25)$$

The time derivative of the polarization is also easily computed. This yields:

$$\frac{\partial E}{\partial z_v} + \frac{\partial E}{\partial t_v} \left[-\frac{1}{v_g} \right] + \frac{1}{v_g} \left[\frac{\partial E}{\partial t_v} \right] = -i \frac{\mu_0 \omega_0^2}{2k_0} P \quad (3.26)$$

Canceling the identical terms leaves:

$$\frac{\partial E}{\partial z} = -i \frac{\mu_0 \omega_0^2}{2k_0} P$$

(3.27)

where we've dropped the subscripts on t and z for simplicity. This nice simple equation is the SVEA equation for most nonlinear-optical processes in the simplest case. Assumptions that we've made to get here include that: (1) the nonlinear effects are weak; (2) the input beams are not affected by the fact that they're creating new beams (okay, so we're violating Conservation of

Energy here, but only by a little); (3) the group velocity is the same for all frequencies in the beams; (4) the beams are uniform spatially; (5) there is no diffraction; and (6) pulse variations occur only on time scales longer than a few cycles in both space and time. And we've assumed that the electric field and the polarization have the same frequency and k-vector. While the other assumptions mentioned above are probably reasonable in practical situations, this last assumption will be wrong in many cases—in fact it's actually difficult to satisfy, and we go to some trouble in order to do so—and we'll consider it in the next section. But the rest of these assumptions are quite reasonable in most pulse-measurement situations.

Solving the Wave Equation in the Slowly Varying Envelope Approximation

If the polarization envelope is constant, then the wave equation in the SVEA is the world's easiest differential equation to solve, and here's the solution:

$$E(z, t) = -i \frac{\mu_0 \omega_0^2}{2k_0} P z \quad (3.28)$$

and we see that the new field grows linearly with distance. Since the intensity is proportional to the mag-squared of the field, the intensity then simply grows quadratically with distance:

$$I(z, t) = \frac{c\mu_0 \omega_0^2}{4} |P|^2 z^2 \quad (3.29)$$

Phase-matching

There is a ubiquitous effect that must always be considered when we perform nonlinear optics and is another reason why nonlinear optics isn't part of our everyday lives. This is *phase-matching*. What it refers to is the tendency, when propagating through a nonlinear-optical medium, of the generated wave to become out of phase with the induced polarization after some distance. If this happens, then the induced polarization will create new light that's out of phase with the light it created earlier, and, instead of making more such light, the two contributions will *cancel out*. The way to avoid this is for the induced polarization and the light it creates to have the same phase velocities. Since they necessarily have the same frequencies, this corresponds to having the same k-vectors, the issue we discussed a couple of sections ago. Then the two waves are always in phase, and the process is orders of magnitude more efficient. In this case, we say that the process is *phase-matched*.

We've been implicitly assuming phase-matching so far by using the variable k_0 for both k-vectors. But because they can be different, let's reserve the variable, k_0 , for the k-vector of the light at frequency ω_0 [$k_0 = \omega_0 n(\omega_0)/c_0$,

where c_0 is the speed of light in vacuum], and we'll now refer to the induced polarization's k-vector, as given by Eq. (3.11), as k_P . We must recognize that k_P won't necessarily equal k_0 , the k-vector of light with the polarization's frequency ω_0 —light that the induced polarization itself creates. Indeed, there's no reason whatsoever for the sum of the k-vectors above, all at different frequencies with their own refractive indices and directions, to equal $\omega_0 n(\omega_0)/c_0$.

Equation (3.27) now becomes:

$$2ik_0 \frac{\partial E}{\partial z} \exp[i(\omega_0 t - k_0 z)] = \mu_0 \omega_0^2 P \exp[i(\omega_0 t - k_P z)] \quad (3.30)$$

Simplifying:

$$\frac{\partial E}{\partial z} = -i \frac{\mu_0 \omega_0^2}{2k} P \exp(i \Delta k z) \quad (3.31)$$

where:

$$\Delta k \equiv k_0 - k_P \quad (3.32)$$

We can solve this differential equation simply also:

$$E(L, t) = -i \frac{\mu_0 \omega_0^2}{2k_0} P \left[\frac{\exp(i \Delta k z)}{i \Delta k} \right]_0^L \quad (3.33)$$

$$= -i \frac{\mu_0 \omega_0^2}{2k_0} P \left[\frac{\exp(i \Delta k L) - 1}{i \Delta k} \right] \quad (3.34)$$

$$= -i \frac{\mu_0 \omega_0^2 L}{k_0} P \exp(i \Delta k L/2) \left[\frac{\exp(i \Delta k L/2) - \exp(-i \Delta k L/2)}{2i \Delta k L} \right] \quad (3.35)$$

The expression in the brackets is $\sin(\Delta k L/2)/(\Delta k L/2)$, which is just the function called $\text{sinc}(\Delta k L/2)$. Ignoring the phase factor, the light electric field after the nonlinear medium will be:

$$E(L, t) = -i \frac{\mu_0 \omega_0^2}{k_0} P L \text{sinc}(\Delta k L/2) \quad (3.36)$$

Mag-squaring to obtain the light irradiance or intensity, I , we have:

$$I(L, t) = \frac{c \mu_0 \omega_0^2}{4} |P|^2 L^2 \text{sinc}^2(\Delta k L/2) \quad (3.37)$$

Since the function, $\text{sinc}^2(x)$, is maximal at $x = 0$, and also highly peaked there (see Fig. 3.12), the nonlinear-optical effect of interest will experience much greater efficiency if $\Delta k = 0$. This confirms what we said earlier, that

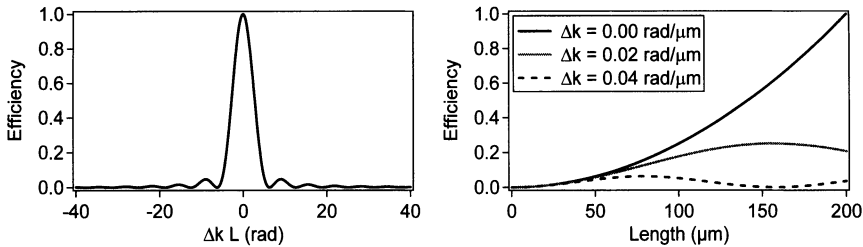


Fig. 3.12: Left: Plot of $\text{sinc}^2(\Delta k L/2)$ vs. $\Delta k L$. Note that the sharp peak at $\Delta k L = 0$. Right: Plot of the generated intensity vs. L , the nonlinear-medium thickness for various values of Δk . Note that, when $\Delta k \neq 0$, the efficiency oscillates sinusoidally with distance and remains minimal for all values of L .

the nonlinear-optical efficiency will be maximized when the polarization and the light it creates remain in phase throughout the nonlinear medium, that is, when the process is *phase-matched*.

Phase-matching is crucial for creating more than just a few photons in a nonlinear-optical process. To summarize, the phase-matching conditions for an N-wave-mixing process are (see Fig. 3.11):

$$\omega_0 = \pm \omega_1 \pm \omega_2 \pm \cdots \pm \omega_N \quad (3.38)$$

$$\vec{k}_0 = \pm \vec{k}_1 \pm \vec{k}_2 \pm \cdots \pm \vec{k}_N \quad (3.39)$$

where k_0 is the k-vector of the beam at frequency, ω_0 , which may or may not naturally equal the sum of the other k-vectors, and it's our job to make it so.

Note that, if we were to multiply these equations by \hbar , they would correspond to energy and momentum conservation for the photons involved in the nonlinear-optical interaction.

Let's consider phase-matching in collinear SHG. Let the input beam (often called the *fundamental beam*) have frequency ω_1 and k-vector, $k_1 = \omega_1 n(\omega_1)/c_0$. The second harmonic occurs at $\omega_0 = 2\omega_1$, which has the k-vector, $k_0 = 2\omega_1 n(2\omega_1)/c_0$. But the induced polarization's k-vector has magnitude, $k_p = 2k_1 = 2\omega_1 n(\omega_1)/c_0$. The phase-matching condition becomes:

$$k_0 = 2k_1 \quad (3.40)$$

which, after canceling common factors ($2\omega_1/c_0$) simplifies to:

$$n(\omega_1) = n(2\omega_1) \quad (3.41)$$

Thus, in order to phase-match SHG, it's necessary to find a nonlinear medium whose refractive indices at ω and 2ω are the same (to several decimal places). Unfortunately—and this is another reason you don't see things like this everyday—all media have dispersion, the tendency of the refractive index

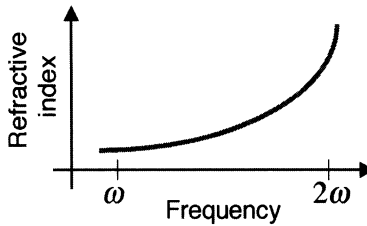


Fig. 3.13: Refractive index vs. wavelength for a typical medium. Because phase-matching SHG requires the refractive indices of the medium to be equal for both ω and 2ω , it is not possible to generate much second harmonic in normal media.

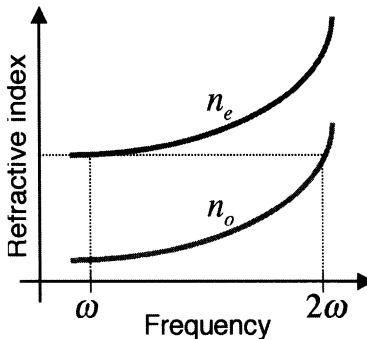


Fig. 3.14: Refractive index vs. wavelength for a typical *birefringent* medium. The two polarizations (say, vertical and horizontal, corresponding to the *ordinary* and *extraordinary* polarizations) see different refractive index curves. As a result, phase-matching of SHG is possible. This is the most common method for achieving phase-matching in SHG. The extraordinary refractive index curve depends on the beam propagation angle (and temperature), and thus can be shifted by varying the crystal angle in order to achieve the phase-matching condition.

to vary with wavelength (see Fig. 3.13). This effect quite effectively prevents seeing SHG in nearly all everyday situations.

It turns out to be possible to achieve phase-matching for birefringent crystals, whose refractive-index curves are different for the two orthogonal polarizations (see Fig. 3.14).

In *noncollinear* SHG, we must consider that there's an angle, θ , between the two beams (see Fig. 3.5). The input vectors have longitudinal and transverse components, but, by symmetry, the transverse components cancel out, leaving only the longitudinal component of the phase-matching equation:

$$k_1 \cos(\theta/2) + k_1 \cos(\theta/2) = k_0 \quad (3.42)$$

Simplifying, we have $2k_1 \cos(\theta/2) = k_0$ as our phase-matching condition. Substituting for the k -vectors, the phase-matching becomes:

$$n(\omega_1) \cos(\theta/2) = n(2\omega_1) \quad (3.43)$$

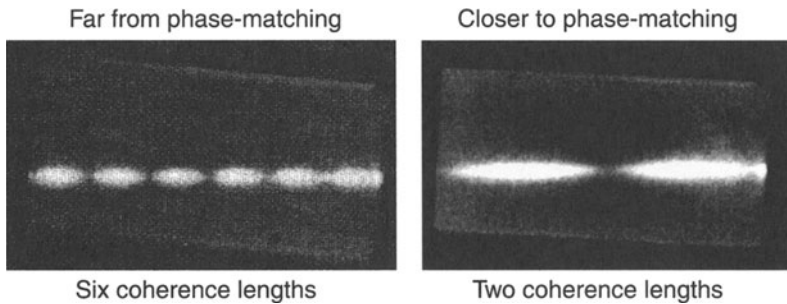


Fig. 3.15: Light inside a SHG crystal for two different amounts of phase-mismatch (i.e., for two different crystal angle orientations). Note that, as the crystal angle approaches the phase-matching condition, the periodicity of the intensity with position decreases, and the intensity increases. At phase-matching, the intensity increases quadratically along the crystal, achieving nearly 100% conversion efficiency in practice [14].

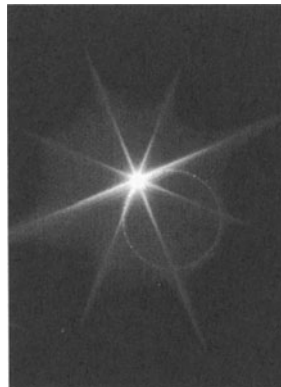


Fig. 3.16: Interesting non-collinear phase-matching effects in second-harmonic generation. (Picture taken by Rick Trebino.)

Figure 3.16 shows a nice display of noncollinear SHG phase-matching processes involving one intense beam and scattered light in essentially all directions. This picture doesn't yield any particular insights for pulse measurement, but it's really pretty, and we thought you might like to see it. By the way, the star isn't really nonlinear-optical; it's just due to the high intensity of the spot at its center (and the "star filter" on the camera lens when the picture was taken). The ring is real, however, and there can be as many as three of them.

Finally, whether a collinear or non-collinear beam geometry, it's also possible to achieve phase-matching using two orthogonal polarizations for the (two) input beams. In other words, the input beam is polarized at a 45° angle to the output SH beam. This is referred to as *Type II phase-matching*, while the above process is called *Type I phase-matching*. Type II phase-matching is

more complex than Type I because the two input beams have different refractive indices, phase velocities, and group velocities, which must be kept in mind when performing measurements using it.

Phase-matching is easier to achieve in third order, largely because we have an extra k-vector to play with. In fact, it can be so easy that it happens automatically. In two-beam coupling and polarization gating, the phase-matching equations become:

$$\omega_0 = \omega_1 - \omega_2 + \omega_2 \quad (3.44)$$

$$\vec{k}_0 = \vec{k}_1 - \vec{k}_2 + \vec{k}_2 \quad (3.45)$$

These equations are *automatically satisfied* when the signal beam has the same frequency and k-vector as beam 1: ω_1 and k_1 , respectively.

For other third-order processes, phase-matching is not automatic, but it can be achieved with a little patience. For some processes, however, it can be impossible, as is the case for self-diffraction. In the latter case, sufficient efficiency can be achieved for most purposes, provided that the medium is kept thin to minimize the phase-mismatch.

Phase-Matching Bandwidth

Direct Calculation

While at most one frequency can be exactly phase-matched at any one time, some nonlinear-optical processes are more forgiving about this condition than others. Since it'll turn out to be important in pulse measurement to achieve efficient SHG (or other nonlinear-optical process) for all frequencies in the pulse, *phase-matching bandwidth* is an important issue. Figures 3.17a, b show the SHG efficiency vs. wavelength for two different crystals and for different incidence angles. Notice the huge variations in phase-matching efficiency for different crystal angles and thicknesses.

We can easily calculate the range of frequencies that will be approximately phase-matched in, for example, SHG. Assuming that the SHG process is exactly phase-matched at the wavelength, λ_0 , the phase-mismatch, Δk , will be a function of wavelength:

$$\Delta k(\lambda) = 2k_1 - k_2 \quad (3.46)$$

$$\Delta k(\lambda) = 2 \left[2\pi \frac{n(\lambda)}{\lambda} \right] - \left[2\pi \frac{n(\lambda/2)}{\lambda/2} \right] \quad (3.47)$$

$$\Delta k(\lambda) = \frac{4\pi}{\lambda} [n(\lambda) - n(\lambda/2)] \quad (3.48)$$

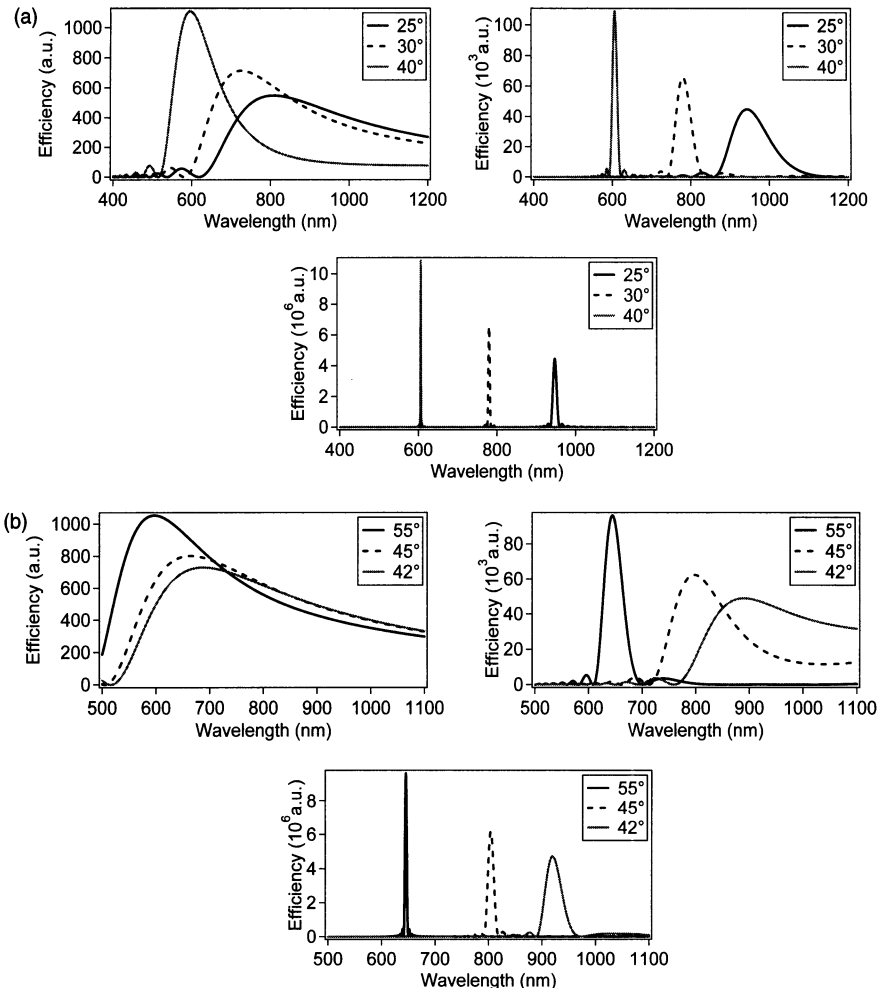


Fig. 3.17: (a) Phase-matching efficiency vs. wavelength for the nonlinear-optical crystal, beta-barium borate (BBO). Top left: a 10 μm thick crystal. Top right: a 100 μm thick crystal. Bottom: a 1000 μm thick crystal. These curves also take into account the ω_0^2 and L^2 factors in Eq. (3.25). While the curves are scaled in arbitrary units, the relative magnitudes can be compared among the three plots. (These curves do not, however, include the nonlinear susceptibility, $\chi^{(2)}$, so comparison of the efficiency curves in Figs. 3.17a and b requires inclusion of this factor.) (b) Same as Fig. 3.17a, except for the nonlinear-optical crystal, potassium di-hydrogen phosphate (KDP). Top left: a 10 μm thick crystal. Top right: a 100 μm thick crystal. Bottom: a 1000 μm thick crystal. The curves for the thin crystal don't fall to zero at long wavelengths because KDP simultaneously phase-matches for two wavelengths, that shown and a longer (IR) wavelength, whose phase-matching ranges begin to overlap when the crystal is thin.

Expanding $1/\lambda$ and the material dispersion to first order in the wavelength,

$$\Delta k(\delta\lambda) = \frac{4\pi}{\lambda_0} \left[1 - \frac{\delta\lambda}{\lambda_0} \right] \left[n(\lambda_0) + \delta\lambda n'(\lambda_0) - n(\lambda_0/2) - \frac{\delta\lambda}{2} n'(\lambda_0/2) \right] \quad (3.49)$$

where $\delta\lambda = \lambda - \lambda_0$, $n'(\lambda) = dn/d\lambda$ and we have taken into account the fact that, when the input wavelength changes by $\delta\lambda$, the second-harmonic wavelength changes by only $\delta\lambda/2$.

Recalling that the process is phase-matched for the input wavelength, λ_0 , we note that $n(\lambda_0/2) - n(\lambda_0) = 0$, and we can simplify this expression:

$$\Delta k(\delta\lambda) = \frac{4\pi}{\lambda_0} \left[\delta\lambda n'(\lambda_0) - \frac{\delta\lambda}{2} n'(\lambda_0/2) \right] \quad (3.50)$$

where we have neglected second-order terms.

The sinc^2 curve will decrease by a factor of 2 when $\Delta k L/2 = \pm 1.39$. So solving for the wavelength range that yields $|\Delta k| < 2.78/L$, we find that the phase-matching bandwidth $\delta\lambda_{\text{FWHM}}$ will be:

$$\delta\lambda_{\text{FWHM}} = \frac{0.44 \lambda_0 / L}{|n'(\lambda_0) - \frac{1}{2}n'(\lambda_0/2)|} \quad (3.51)$$

Notice that $\delta\lambda_{\text{FWHM}}$ is inversely proportional to the thickness of the nonlinear medium. Thus, in order to increase the phase-matching bandwidth, we must use a medium with dispersion such that $n'(\lambda_0) - \frac{1}{2}n'(\lambda_0/2) \approx 0$, or more commonly decrease the medium's thickness (see Fig. 3.18).

Finally, note the factor of 1/2 multiplying the second-harmonic refractive index derivative in Eq. (3.51). This factor does not appear in results appearing in some journal articles. These articles use a different derivative definition for the second harmonic [that is, $dn/d(\lambda/2)$] because the second harmonic necessarily varies by only one half as much as the fundamental wavelength. We, on the other hand, have used the same definition—the standard one, $dn/d\lambda$ —for both derivatives, which, we think, is less confusing, but it yields the factor

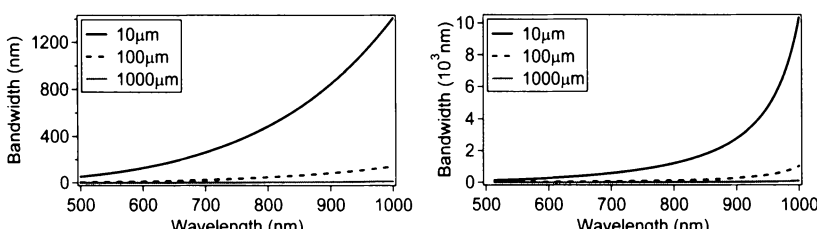


Fig. 3.18: Phase matching bandwidth vs. wavelength for BBO (left) and KDP (right).

of 1/2. It's easy to see that the factor of 1/2 is correct: assuming that the process is phase-matched at λ_0 , maintaining a phase-matched process [i.e., $n(\lambda/2) = n(\lambda)$] requires that the variation in refractive index per unit wavelength near $\lambda_0/2$ be twice as great as that near λ_0 , since the second harmonic wavelength only changes only half as fast as the fundamental wavelength.

Group-velocity Mismatch

There is an alternative approach for calculating the phase-matching bandwidth, which seems like a completely different effect until you realize that you get the same answer, and that it's just a time-domain approach, while the previous approach was in the frequency domain. Consider that the pulse entering the SHG crystal and the SH it creates may have the same phase velocities (they're phase-matched), but they could have different group velocities. This is called *group-velocity mismatch (GVM)*. If so, then the two pulses could cease to overlap after propagating some distance into the crystal; in this case, the efficiency will be reduced because SH light created at the back of the crystal will not coherently combine with SH light created in the front. This effect is illustrated in Fig. 3.19.

We can calculate the bandwidth of the light created when significant GVM occurs. Assuming that a very short pulse enters the crystal, the length of the SH pulse, δt , will be determined by the difference in light-travel times through the crystal:

$$\delta t = \frac{L}{v_g(\lambda_0/2)} - \frac{L}{v_g(\lambda_0)} = L \text{ GVM} \quad (3.52)$$

where $\text{GVM} \equiv 1/v_g(\lambda_0/2) - 1/v_g(\lambda_0)$. This expression can be rewritten using expressions for the group velocity:

$$v_g(\lambda) = \frac{c_0/n(\lambda)}{1 - (\lambda/n(\lambda))n'(\lambda)} \quad (3.53)$$

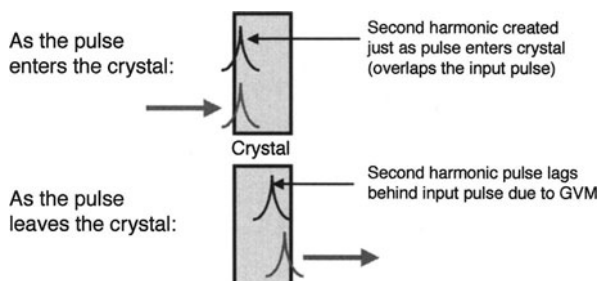


Fig. 3.19: Group-velocity mismatch. The pulse entering the crystal creates SH at the entrance, but this light travels at a different group velocity from that of the fundamental light, and light created at the exit does not coherently add to it.

Substituting for the group velocities in Eq. (3.52), we find:

$$\delta t = \frac{Ln(\lambda_0/2)}{c_0} \left[1 - \frac{\lambda_0/2}{n(\lambda_0/2)} n'(\lambda_0/2) \right] - \frac{Ln(\lambda_0)}{c_0} \left[1 - \frac{\lambda_0}{n(\lambda_0)} n'(\lambda_0) \right] \quad (3.54)$$

Now, recall that we wouldn't be doing this calculation for a process that wasn't phase-matched, so we can take advantage of the fact that $n(\lambda_0/2) = n(\lambda_0)$. Things then simplify considerably:

$$\delta t = \frac{L\lambda_0}{c_0} \left[n'(\lambda_0) - \frac{1}{2} n'(\lambda_0/2) \right] \quad (3.55)$$

Take the second-harmonic pulse to have a Gaussian intensity, for which $\delta t \delta v = 0.44$. Rewriting in terms of the wavelength, $\delta t \delta \lambda = \delta t \delta v [dv/d\lambda]^{-1} = 0.44 [dv/d\lambda]^{-1} = 0.44 \lambda^2/c_0$, where we've neglected the minus sign since we're computing the bandwidth, which is inherently positive. So the bandwidth is:

$$\delta\lambda_{\text{FWHM}} \approx \frac{0.44 \lambda_0 / L}{|n'(\lambda_0) - \frac{1}{2} n'(\lambda_0/2)|} \quad (3.56)$$

Note that the bandwidth calculated from GVM considerations precisely matches that calculated from phase-matching bandwidth considerations.

Phase-matching Bandwidth Conclusions

As we mentioned, in pulse-measurement devices, it's important to achieve efficient (or at least uniform) phase-matching for the entire bandwidth of the pulse. Since ultrashort laser pulses can have extremely large bandwidths (a 10 fs pulse at 800 nm has a bandwidth of over a hundred nm), it'll be necessary to use extremely thin SHG crystals. Crystals as thin as 5 μm have been used to measure few-fs pulses.

But also recall that the intensity of the phase-matched SH produced is proportional to L^2 . So a very thin crystal yields very little signal intensity. Thus there is a nasty trade-off between efficiency and bandwidth. Fortunately, we can usually find a compromise—of just enough bandwidth and efficiency simultaneously. But, as with most compromises, we're not happy about it. As a result, we've spent much time thinking of tricks to beat this trade-off. Chapters 11 and 17 will discuss two different approaches.

Nonlinear-Optical Strengths

Just how strong are nonlinear-optical effects? Clearly they're not so strong that sunlight, even on the brightest day, efficiently produces enough of them for us to see. Of course, phase-matching also isn't happening.

Anyway, what sort of laser intensities are necessary to see these effects? We start with Eq. (3.36), which can be rewritten (with $\omega_0 = 2\omega$) in the form:

$$E^{2\omega}(L, t) = -i \frac{2\mu_0\omega^2 L}{k} P \exp(i\Delta k L/2) \operatorname{sinc}(\Delta k L/2) \quad (3.57)$$

where $P = \frac{1}{2}\varepsilon_0\chi^{(2)}(E^\omega)^2$. Then, we relate intensity to electric field strength through $I = (n/2\eta_0)|E|^2$, where $\eta_0 = \sqrt{\mu_0/\varepsilon_0}$. With these, we re-write Eq. (3.57) in terms of intensities to find:

$$I^{2\omega} = \frac{\eta_0\omega^2(\chi^{(2)})^2(I^\omega)^2 L^2}{2c_0^2 n^3} \operatorname{sinc}^2(\Delta k L/2) \quad (3.58)$$

Next, suppose we consider the best case, in which the process is phase-matched ($\operatorname{sinc}^2(0) = 1$) and re-write Eq. (3.58) in terms of a *SHG efficiency*:

$$\frac{I^{2\omega}}{I^\omega} = \frac{2\eta_0\omega^2 d^2 I^\omega L^2}{c_0^2 n^3} \quad (3.59)$$

where we define the *d-coefficient* as $d = \frac{1}{2}\chi^{(2)}$. d is what we usually find quoted in handbooks. It will depend not only on the material, but also on the field configuration—how the fields are polarized with respect to the crystal orientation. Again, we refer you to a more detailed treatment of nonlinear optics to fully understand these issues. Our concern now is just to get some feel for the numbers involved and what we can hope to achieve in SHG efficiency in the lab. As a quick calculation, suppose we use beta-barium borate (BBO) as our nonlinear crystal, in which $d \approx 2 \times 10^{-12} \text{ m/V}$, and where $n \approx 1.6$ (note that we can get away with approximate values for n when it appears in an amplitude calculation, but we must have *very* accurate values for n when computing phase—or phase mismatch). If we wish to frequency-double an input beam of wavelength, $\lambda = 0.8 \mu\text{m}$, we find from Eq. (3.59):

$$\frac{I^{2\omega}}{I^\omega} \approx 5 \times 10^{-8} I^\omega L^2 \quad (3.60)$$

where I is in W/m^2 and L is in m.

From the small coefficient in front, some pretty high intensities are needed for modest crystal lengths in order to get anything in the way of a decent efficiency! Suppose we consider an ultrafast laser. Basically, if you have an unamplified Ti : Sapphire laser, which produces nanojoule (nJ) pulses, 100 fs long, you have pulses with intensities on the order of 10^{14} W/m^2 (when focusing to a about a $10 \mu\text{m}$ spot diameter). But of course when focusing this tightly, the beam doesn't stay focused for long, which limits the crystal length we can use. Additionally, because ultrashort pulses are broadband, the requirement of phase matching the entire bandwidth limits the SHG crystal thickness to

considerably less than 1 mm, and usually less than 100 μm . Choosing a crystal length of 100 μm , and using the other numbers, we would achieve an efficiency of about 5%. This again is best-case for this configuration because 1) the beam does not stay focused to its minimum size throughout the entire length (as the above calculation assumes), and 2) d is reduced somewhat below its maximum value; this is because the fields are not necessarily at the best orientation within the crystal to most effectively excite the anharmonic oscillators. Phase matching decides the field orientation, and the price is paid through a slightly reduced nonlinear coefficient (known as d_{eff}). So we end up trying to optimize all of these parameters until we're satisfied with the SHG power we are getting. Then we stop.

This brings us to $\chi^{(3)}$. To get an idea of its order of magnitude for non-resonant materials, consider glass. Single mode optical fibers, made of glass, guide light with a cross-sectional beam diameter of slightly less than 10 μm . So we can achieve similar intensities that we saw before in our SHG example, but over much longer distances. In silica glass, $\chi^{(3)} \approx 2.4 \times 10^{-22} \text{ m}^2/\text{V}^2$. One can make a comparison to a second order process by calculating the second and third order polarizations that result at a given light intensity. In our 100 fs 1 nJ pulse, focused to 10 μm diameter, the field strength is $E \approx 2.5 \times 10^8 \text{ V/m}$. Then $\chi^{(3)} E \approx 6 \times 10^{-14} \text{ m/V}$. Compare this to $\chi^{(2)} = 2d \approx 4 \times 10^{-12} \text{ m/V}$ for BBO. From here, the nonlinear polarizations for both processes are found by multiplying these results by the light intensity. As this example demonstrates, third-order processes in non-resonant materials are substantially weaker than second order processes. But this can be made up for sometimes by (1) tuning the frequency of one or more of the interacting waves near a material resonance (but at some cost in higher losses for those waves that are near resonance), or (2) taking advantage of long interactions lengths that may be possible in phase-matched situations (such as in optical fibers). Turning up the intensity will also help. Microjoule pulses can yield more than adequate signal energies from most of the third order nonlinear optical effects mentioned in this chapter. Third order bulk media typically used are fused silica and any glass for the various induced grating effects.

The above illustrations assumed 100 fs pulse intensities on the order of 10^{12} W/cm^2 . However, with the less tight focusing that's practical in the lab, intensities more like 10^9 W/cm^2 are typically available. While this seems high, it's only enough to create barely detectable amounts of second harmonic. How about performing third-order nonlinear optics with such pulses? You can just barely do this in some cases, and it's a struggle. It's better to have a stage of amplification, especially from a regenerative amplifier ("regen"). Microjoule pulses can yield more than adequate signal energies from most of the third-order nonlinear-optical effects mentioned in this chapter. Third-order media typically used are fused silica and any glass for the various induced-grating effects. These media are actually not known for their high nonlinearities, but they are optically very clean and hence are the media of choice for pulse measurement applications.

Nonlinear Optics in 25 Words or Less

Okay, that was a lot to digest. So what's the minimum you need to know to understand the basic ideas of ultrashort-pulse measurement? Not much actually. For the next few chapters, we'll assume perfectly phase-matched interactions, and we won't worry about multiplicative constants, so all you need to remember is that the electric field of the nonlinear-optically generated light wave in this case is given by:

$$E_{\text{sig}}(t) \propto P \quad (3.61)$$

which is a simplified version of Eq. (3.28), and we're referring to the generated wave as the *signal field*, $E_{\text{sig}}(t)$. Also, for pulse-measurement applications, we'll typically be splitting a pulse into two using a beam-splitter (usually a 50%-reflecting mirror) and performing nonlinear optics with the pulse, $E(t)$ and another delayed version of itself, $E(t - \tau)$, where τ is the relative delay between the two pulses. For the various processes we've considered so far, the generated field will be:

$$E_{\text{sig}}(t, \tau) \propto \begin{cases} E(t) E(t - \tau) & \text{for SHG} \\ E(t) |E(t - \tau)|^2 & \text{for PG} \\ E(t)^2 E^*(t - \tau) & \text{for SD} \\ E(t)^2 E(t - \tau) & \text{for THG} \end{cases} \quad (3.62)$$

where we've included the delay in the functional dependence of the signal field. Finally, because we'll be mainly interested only in the pulse *shape*, we'll often neglect proportionality constants and just write, for example, $E(t) = E(t) E(t - \tau)$ for SHG.

That's all you really need to know. But you may still wish to read more on this fascinating subject, so here's a list of relevant books.

References

1. N. Bloembergen, *Nonlinear Optics*, World Scientific Pub. Co., 1996 (original edition: 1965).
2. R.W. Boyd, *Nonlinear Optics*, Academic Press, 1992.
3. P. Butcher and D. Cotter, *The Elements of Nonlinear Optics* Cambridge University Press, 1991.
4. J.-C. Diels and W. Rudolph, *Ultrashort Laser Pulse Phenomena*, Academic Press, 1996.
5. F.A. Hopf and G.I. Stegeman, *Applied Classical Electrodynamics: Nonlinear Optics*, Krieger Pub. Co., reprinted 1992.
6. D.L. Mills, *Nonlinear Optics: Basic Concepts*, 2nd ed., Springer Verlag, 1998.
7. G.G. Gurzadian et al., *Handbook of Nonlinear Optical Crystals*, 3rd ed., Springer Verlag, 1999.
8. K.-S. Ho, S.H. Liu and G.S. He, *Physics of Nonlinear Optics*, World Scientific Pub. Co., 2000.
9. E.G. Sauter, *Nonlinear Optics*, Wiley-Interscience, 1996.
10. Y.R. Shen, *The Principles of Nonlinear Optics*, Wiley-Interscience, 1984.
11. A. Yariv, *Quantum Electronics*, 3rd ed., Wiley, 1989.
12. F. Zernike and J. Midwinter, *Applied Nonlinear Optics*, Wiley-Interscience, 1973 (out of print).
13. H.J. Eichler, et al., *Laser-Induced Dynamic Gratings*, Springer-Verlag, 1986.
14. Christian Rahlff, *Opt. Phot. News*, 8, 4, p. 64 (1997).

4. The Autocorrelation, the Spectrum, and Phase Retrieval

Rick Trebino and Erik Zeek

Time- and Frequency-Domain Measurements

If, to measure a pulse, it's sufficient to measure its intensity and phase in either the time or frequency domains, then it's natural to ask just what measurements can, in fact, be made in each of these domains. And the answer, until recently, was the autocorrelation and spectrum.

The frequency domain is the domain of the spectrometer and, of course, what the spectrometer measures is the spectrum. Indeed the typical off-the-shelf spectrometer is sufficient to measure all the spectral structure and extent of most ultrashort pulses in the visible and near-infrared. Fourier-transform spectrometers do so for mid-infrared pulses. And interferometers are available when higher resolution is desired.

Unfortunately, it hasn't been possible to measure the spectral *phase*. Complex schemes were proposed that yielded the spectral phase over a small spectral range or with only limited accuracy. But these schemes lacked generality, were inaccurate, and did not prove practical.

Later, when we describe the FROG technique, we'll show how to obtain the spectral phase, but it won't be a frequency-domain measurement. As a result, the only frequency-domain information available for a pulse was its spectrum.

How about the time domain? The main device available for characterization of an ultrashort pulse in the time domain has been the intensity autocorrelator, which attempts (but fails) to measure the intensity vs. time [1–3]. Since no shorter event is available, the autocorrelator uses the pulse to measure itself. Obviously, this isn't sufficient, and a smeared-out version of the pulse results. Thus, in the time domain, it has not been possible to measure either the intensity, $I(t)$, or the phase, $\phi(t)$.

We nevertheless should examine these measures, partly for historical reasons, but also because FROG is based on them. What's more, they're interesting, and, even if you're an experienced ultrafast optics researcher, you may be pleasantly surprised by some of the ideas in the remainder of this chapter.

The Frequency Domain: the Spectrum

Measuring the Spectrum

As we mentioned, in the frequency domain, it is generally fairly easy to measure the pulse spectrum, $S(\omega)$. Spectrometers and interferometers perform this task admirably and are readily available. The most common spectrometer

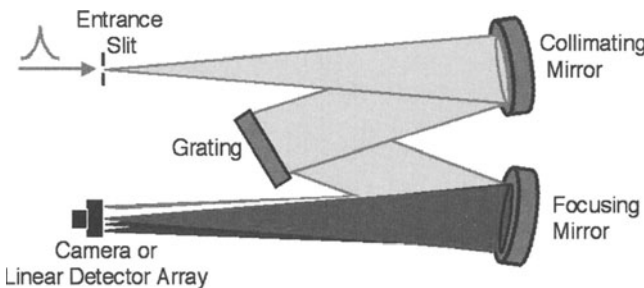


Fig. 4.1: Experimental “Czerny-Turner” layout for a diffraction-grating spectrometer. Additional optics can be added to this device to make it an “imaging spectrometer,” which yields the same spectrum for all entrance positions along the entrance slit.

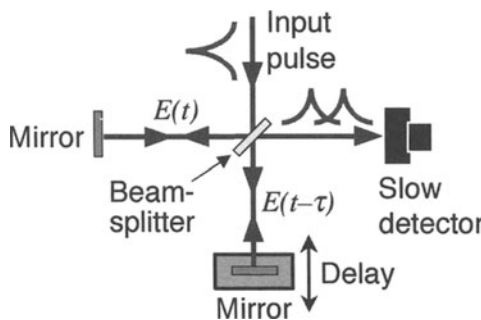


Fig. 4.2: Experimental layout for a Fourier-transform spectrometer.

involves diffracting a collimated beam off a diffraction grating and focusing it onto a camera. See Fig. 4.1.

Fourier-transform spectrometers (Fig. 4.2) operate in the time domain and measure the transmitted integrated intensity from a Michelson interferometer, which is often called the light’s *second-order coherence function*:

$$\Gamma^{(2)}(\tau) = \int_{-\infty}^{\infty} E(t) E^*(t - \tau) dt \quad (4.1)$$

neglecting constant terms. This quantity is also called the *field autocorrelation* and the *interferogram*. Its Fourier transform is simply the spectrum, a result known as the *Autocorrelation Theorem*:

$$\left| \tilde{E}(\omega) \right|^2 = \mathcal{F} \left\{ \int_{-\infty}^{\infty} E(t) E^*(t - \tau) dt \right\} \quad (4.2)$$

Thus, all spectrometers, whether diffraction-grating or Fourier-transform devices, yield the spectrum.

The Spectrum and One-Dimensional Phase Retrieval

So it would seem that, if ever there were a situation that was clear-cut, this is it. The spectrum tells us the spectrum, and that's it. Nothing more and nothing less. What more is there to say?

It's actually more interesting than you might think to ask what information is in fact available from the spectrum. Obviously, if we have only the spectrum, what we lack is precisely the spectral phase. Sounds simple enough. Why belabor this point?

Here's why: what if we have some additional information, such as the knowledge that we're measuring a *pulse*? What if we know that the pulse intensity vs. time is definitely zero outside a finite range of times? Or at least asymptotes quickly to zero as $t \rightarrow \infty$? This is not a great deal of additional information, but it is interesting to ask how much this additional information allows us to limit the possible pulses that correspond to a given spectrum.

Whatever the additional information, this class of problems is called the *one-dimensional phase-retrieval problem* for the obvious reason that we have the spectral magnitude and we are trying to retrieve the spectral phase using this additional information.

It is bad news.

In general, as you probably suspect, the one-dimensional phase-retrieval problem is unsolvable in almost all cases of practical interest, even when the above information is included. There are simply many (usually infinitely many) pulses that correspond to a given spectrum and that satisfy additional constraints such as those mentioned above.

First, there are obvious ambiguities [4]. Clearly, if the complex amplitude $E(t)$ has a given spectrum, then adding a phase shift, yielding $E(t) \exp(i\phi_0)$, also yields the same spectrum. So does a translation, $E(t - t_0)$. Not to mention the complex-conjugated mirror image, $E^*(-t)$, which also corresponds to a time reversal.

Table 4.1: “Trivial ambiguities” in phase retrieval, that is, functions with the same Fourier-transform magnitude as $E(t)$. These ambiguities affect phase-retrieval problems in all dimensions, that is, whether it's a one-dimensional parameter or a multi-dimensional quantity. But we try not to let them bother us.

Function	Type of ambiguity
$E(t) \exp(i\phi_0)$	Absolute-phase shift
$E(t - t_0)$	Translation
$E^*(-t)$	Time-reversal

This last observation, that $E^*(-t)$, which has intensity, $I(-t)$, and phase, $-\phi(-t)$, corresponds to time reversal, is an important fact, so let's check it. Recall that the real electric field is given by:

$$\mathcal{E}(t) = \frac{1}{2}\sqrt{I(t)} \exp\{i[\omega t - \phi(t)]\} + \frac{1}{2}\sqrt{I(t)} \exp\{-i[\omega t - \phi(t)]\} \quad (4.3)$$

where we've written out the complex conjugate. If we replace the intensity and phase with these new quantities, we have a new field, which we'll call $\mathcal{E}'(t)$:

$$\mathcal{E}'(t) = \frac{1}{2}\sqrt{I(-t)} \exp\{i[\omega t + \phi(-t)]\} + \frac{1}{2}\sqrt{I(-t)} \exp\{-i[\omega t + \phi(-t)]\} \quad (4.4)$$

We can rewrite $\mathcal{E}'(t)$, simply rearranging minus signs:

$$\mathcal{E}'(t) = \frac{1}{2}\sqrt{I(-t)} \exp\{-i[\omega(-t) - \phi(-t)]\} + \frac{1}{2}\sqrt{I(-t)} \exp\{i[\omega(-t) - \phi(-t)]\} \quad (4.5)$$

which, referring back to Eq. (4.3) and commuting its two terms, is precisely $\mathcal{E}(-t)$.

Okay, so there are some obvious or *trivial* ambiguities (as they are often called). But what if we can live with them? Indeed, most people can live with them, hence the name. Are there other ambiguities?

Unfortunately, yes. In two classic papers written in 1956 and 1957, E. J. Akutowicz showed that knowledge of the spectrum in conjunction with the additional knowledge that $E(t)$ is of finite duration—often called *finite support*—is still insufficient to uniquely determine $E(t)$ [5,6]. Indeed, he showed that infinitely many pulse fields satisfy these constraints. And he showed how to construct them. You simply multiply the spectral field by “Blaschke products” of the form:

$$B(\omega) = \prod_{m=1}^N \frac{\omega - \omega_m^*}{\omega - \omega_m} \quad (4.6)$$

where the set of ω_m 's are complex zeros of the analytic continuation of the spectrum (i.e., when ω is considered to be complex). Since Blaschke products clearly have unity modulus (when ω is real), they leave the spectrum intact. And Akutowicz also showed that the above values of ω_m leave the pulse with finite duration. And most functions of interest have many such complex zeroes.

Of course, in the ultrashort-laser-pulse-measurement problem, we cannot restrict our attention to finite-duration pulses. Indeed, most pulse shapes of interest are *not* finite in duration and instead merely asymptote to zero (such as a Gaussian or sech^2). You might argue that this issue is merely an academic question, but forcing the pulse to have truly finite support then forces the spectrum to have infinite support. So which assumption is easier to live with, an infinite-support pulse in the time domain or an infinite-support pulse in the frequency domain? Let's just agree to live with both.

When the pulse has potentially infinite support, not only can the ω_m 's take on any value with nonzero imaginary part, but essentially *any* phase function can multiply $\tilde{E}(\omega)$ and still yield the same spectrum.

So the number of ambiguities associated with the measurement of only the pulse spectrum is downright humongous. For example, a Gaussian spectrum can have any linear chirp parameter, and so can correspond to an intensity vs. time that is also Gaussian, but with any pulse width. And of course, it can have any higher-order phase distortion, as well. The number of possible pulses that correspond to a given spectrum isn't just infinity; it's a *higher-order* infinity.

The Time Domain: The Intensity Autocorrelation

Measuring the Intensity Autocorrelation

The *intensity autocorrelation*, $A^{(2)}(\tau)$, is an attempt to measure the pulse's intensity vs. time. It's what results when a pulse is used to measure itself in the time domain [7–15]. It involves splitting the pulse into two, variably delaying one with respect to the other, and spatially overlapping the two pulses in some instantaneously responding nonlinear-optical medium, such as a second-harmonic-generation (SHG) crystal (See Fig. 4.3). A SHG crystal will produce light at twice the frequency of input light with a field that is given by:

$$E_{\text{sig}}^{\text{SHG}}(t, \tau) \propto E(t)E(t - \tau) \quad (4.7)$$

where τ is the delay. This field has an intensity that's proportional to the product of the intensities of the two input pulses:

$$I_{\text{sig}}^{\text{SHG}}(t, \tau) \propto I(t)I(t - \tau) \quad (4.8)$$

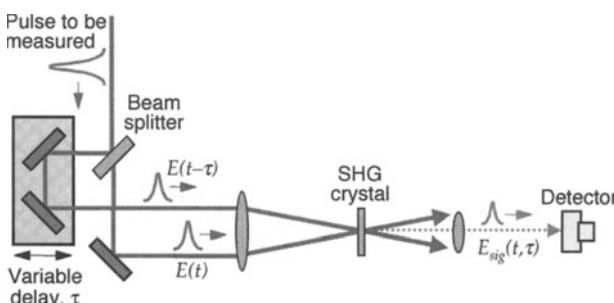


Fig. 4.3: Experimental layout for an intensity autocorrelator using second-harmonic generation. A pulse is split into two, one is variably delayed with respect to the other, and the two pulses are overlapped in an SHG crystal. The SHG pulse energy is measured vs. delay, yielding the autocorrelation trace. Other effects, such as two-photon fluorescence and two-photon absorption can also yield the autocorrelation, using similar beam geometries [2,11,13,14].

Since detectors (even streak cameras) are too slow to time resolve $I_{\text{sig}}^{\text{SHG}}(t, \tau)$, this measurement produces the time integral:

$$A^{(2)}(\tau) = \int_{-\infty}^{\infty} I(t)I(t - \tau) dt \quad (4.9)$$

Equation (4.9) is the definition of the intensity autocorrelation, or, for short, simply the autocorrelation. It's different from the *field* autocorrelation (Eq. (4.1)), which provides only the information contained in the spectrum.

It is clear that an (intensity) autocorrelation yields some measure of the pulse length because no second harmonic intensity will result if the pulses don't overlap in time; thus, a relative delay of one pulse length will typically reduce the SHG intensity by about a factor of two.

Figure 4.4 shows some pulses and their intensity autocorrelations.

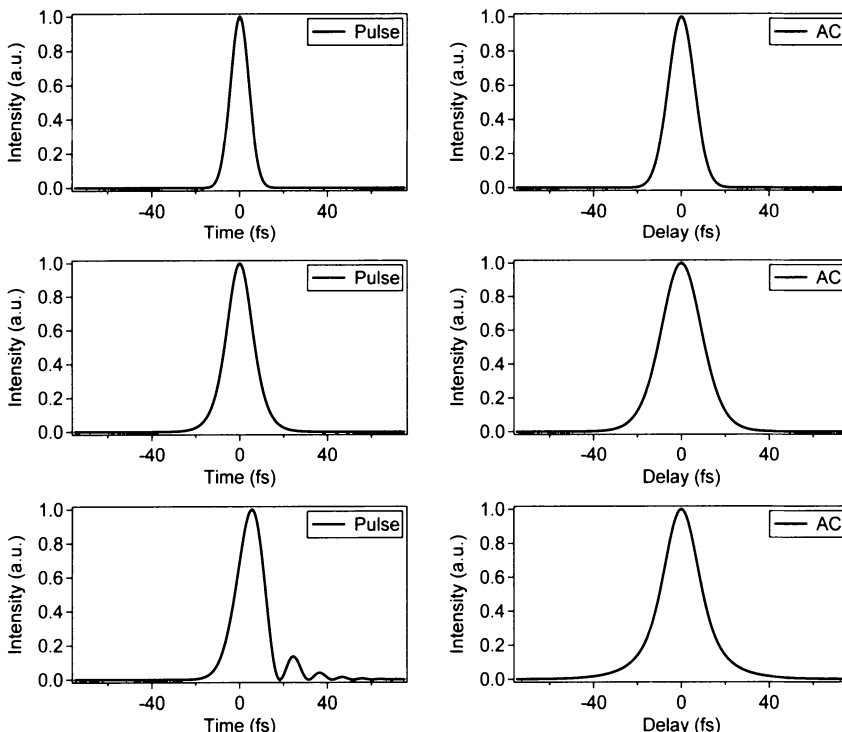


Fig. 4.4: Examples of theoretical pulse intensities and their intensity autocorrelations. Left: Intensities vs. time. Right: The intensity autocorrelation corresponding to the pulse intensity to its left. Top row: A 10-fs Gaussian intensity. Middle row: A 7-fs sech^2 intensity. Bottom row: A pulse whose intensity results from 3rd-order spectral phase. Note that the autocorrelation loses details of the pulse, and, as a result, all of these pulses have similar autocorrelations.

The Autocorrelation and One-Dimensional Phase Retrieval

The autocorrelation always has its maximum at $\tau = 0$, which occurs because you can never have a larger area than when the two factors in the integrand overlap perfectly. In addition, the autocorrelation is always symmetrical, a fact that is easy to prove by changing variables in Eq. (4.9) from t to $t - \tau$, yielding:

$$A^{(2)}(\tau) = \int_{-\infty}^{\infty} I(t + \tau)I(t) dt \quad (4.10)$$

which (when you commute the factors in the integrand) is just the expression for the autocorrelation but with τ replaced by $-\tau$, which means that $A^{(2)}(\tau) = A^{(2)}(-\tau)$. As a result, the autocorrelation cannot distinguish a pulse from its mirror image.

We can learn more about the autocorrelation by applying the Autocorrelation Theorem to it:

$$\tilde{A}^{(2)}(\omega) = |\tilde{I}(\omega)|^2$$

(4.11)

where $\tilde{I}(\omega)$ is the Fourier Transform of the intensity vs. time (note that it's not the spectrum, $S(\omega)$). In words, the Fourier transform of the autocorrelation is the mag-squared Fourier transform of the intensity.

This result is interesting because it says that the Fourier transform of the autocorrelation, $\tilde{A}^{(2)}(\omega)$, is not only real, but also non-negative. That $\tilde{A}^{(2)}(\omega)$ is real is easy to see: $\tilde{A}^{(2)}(\omega)$ is symmetrical, so the $i \sin(\omega t)$ term in the Fourier transform is an integral of an odd function over a symmetrical interval, and hence zero. That $\tilde{A}^{(2)}(\omega)$ is non-negative for all values of ω is not so obvious and is due to the highly centrally peaked nature of $A^{(2)}(t)$ and its tendency to wash out oscillatory structure.

Now you're probably wondering whether, except for the ambiguity in the direction of time, it's possible to uniquely determine the intensity, $I(t)$, from $A^{(2)}(t)$, or, equivalently, from its Fourier transform, $\tilde{A}^{(2)}(\omega)$. From Eq. (4.11), we see that $\tilde{A}^{(2)}(\omega)$ is the squared magnitude of the Fourier transform of $I(t)$. In other words, if we know the autocorrelation of an intensity, we have the magnitude, but not the phase of the Fourier transform of the quantity we wish to find, $I(t)$.

If this sounds familiar, it should. *It's another one-dimensional phase-retrieval problem!*

Immediately, we conclude that autocorrelation can suffer from the trivial ambiguities: absolute-phase shift, translation, and time reversal. However, an absolute phase shift violates the reality constraint, so it can be rejected. And we really don't care about a translation in time. The time-reversal ambiguity is important, but we already know about it, and we decided we can live with it. So the trivial ambiguities aren't a big problem in autocorrelation.

But when we tried to extract the spectral phase from the spectrum, we found that that one-dimensional phase-retrieval problem was plagued with ambiguities. So is extracting the intensity from the autocorrelation as hopeless?

Actually, there are good reasons to believe not. This one-dimensional phase-retrieval problem is different. When we dealt with the spectrum, we were trying to obtain the complete pulse field from the spectrum, and we had little or no additional information. Now, we're not quite as ambitious: we're only trying to find the intensity, $I(t)$, not the entire field. And we're better prepared this time: we know $I(t)$ to be both *real and non-negative*. So, in addition to having a more modest goal, we're now also in a stronger position: we have some fairly serious constraints. Maybe we'll have to take back all those nasty things we said earlier about the one-dimensional phase-retrieval problem.

So does the intensity autocorrelation uniquely yield the intensity?

Autocorrelation Ambiguities

No. While Akutowicz never explicitly considered the non-negativity constraint, he gave a nice example of a simple function that's not only non-negative, but also causal (is zero for negative times), and which has an infinite number of ambiguities [5]. Suppose that the pulse intensity is a decaying exponential:

$$I(t) = \begin{cases} \exp(-\beta t) & \text{if } t \geq 0 \\ 0 & \text{if } t < 0 \end{cases} \quad (4.12)$$

where $\beta > 0$. It's then easy to construct ambiguous intensities, $I'(t)$, that remain not only non-negative, but also causal! Not surprisingly, this construction involves Blaschke products:

$$\tilde{I}'(\omega) = \frac{\omega + \alpha - i\beta}{\omega + \alpha + i\beta} \frac{\omega - \alpha - i\beta}{\omega - \alpha + i\beta} \tilde{I}(\omega) \quad (4.13)$$

but, because we don't have finite support, $\alpha + i\beta$ need not be a complex zero of the analytical continuation of $\tilde{I}(\omega)$. On the other hand, the non-negativity constraint will require instead that $|4\beta/\alpha| < 1$.

Inverse-Fourier-transforming $\tilde{I}'(\omega)$ yields:

$$\begin{aligned} I'(t) &= I(t) - 4\beta \int_0^t \cos[\alpha(t-u)] \exp[-\beta(t-u)] I(u) du \\ &\quad + \frac{4\beta^2}{\alpha} \int_0^t \sin[\alpha(t-u)] \exp[-\beta(t-u)] I(u) du \end{aligned} \quad (4.14)$$

for $t \geq 0$. Performing the integrals yields:

$$I'(t) = \exp(-\beta t) \left\{ \left[1 - \frac{4\beta}{\alpha} \sin(\alpha t) \right] + \frac{4\beta^2}{\alpha^2} [1 - \cos(\alpha t)] \right\} \quad (4.15)$$

So a decaying exponential has the same autocorrelation as infinitely many different decaying sinusoids! Figure 4.5 shows some of these functions.

Okay, so the intensity autocorrelation doesn't uniquely yield the intensity, and there are some dramatic examples of ambiguities. But are there just a few isolated cases of two or more intensities having the same intensity autocorrelation? Perhaps an infinite number of intensities have autocorrelations with ambiguities. But do they represent only a small fraction of all possible intensity autocorrelations? We must also ask whether the ambiguous autocorrelations are distributed in function space in such a way that a measured autocorrelation is always within experimental error of one. If that is

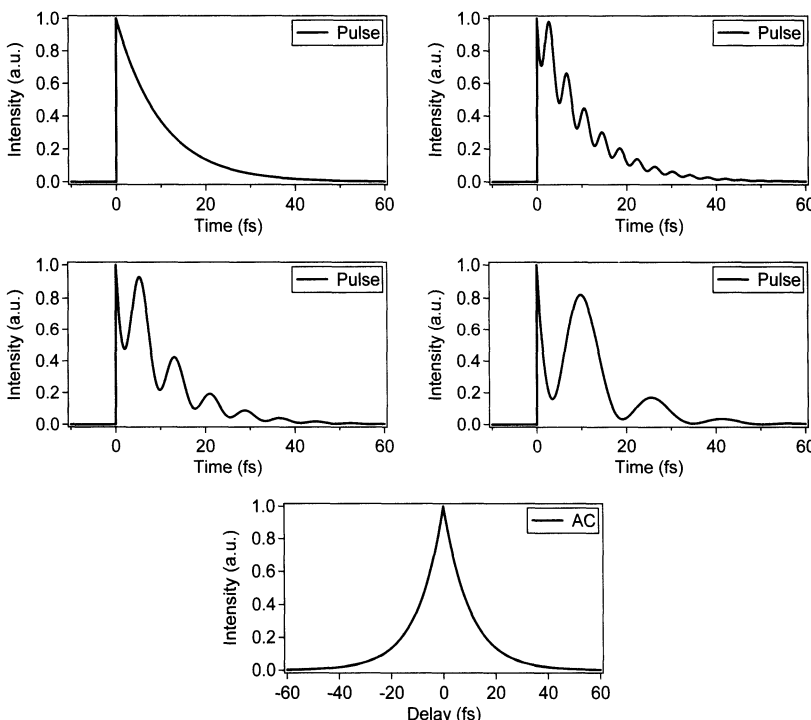


Fig. 4.5: Various intensities (top two rows) given by Eq. (4.15) that all have the same intensity autocorrelation (bottom row). Top left: $\alpha = \infty \text{ fs}^{-1}$ (a decaying exponential); Top right: $\alpha = 1.6 \text{ fs}^{-1}$; Second row left: $\alpha = 0.8 \text{ fs}^{-1}$; Second row right: $\alpha = 0.4 \text{ fs}^{-1}$. In all figures, $\beta = 0.1 \text{ fs}^{-1}$. This autocorrelation is in fact very similar to numerous published ultrashort laser pulse autocorrelations. See, for example, ref [16].

the case, then, even if a measured autocorrelation may uniquely indicate an intensity, the measured autocorrelation is within experimental error of one of the ambiguous autocorrelations, which then yields an ambiguity in the intensity, which cannot be ruled out. A related question is whether there are *approximate* ambiguities, that is, very different intensities that yield almost the same autocorrelations, and hence cannot be distinguished in the presence of experimental error. Finally, in the worst case, perhaps every autocorrelation corresponds to many intensities, or even infinitely many intensities. Unfortunately, these questions don't appear to be resolved at this time. The non-negativity constraint has proven difficult to include.

We can resolve this issue in a practical manner, however, by writing a simple computer program that looks for intensities that yield a given autocorrelation. We've done so and have found that, although it occasionally stagnated (which could mean that the autocorrelation uniquely yielded the intensity in that case but, more likely, that the algorithm simply wasn't powerful enough), our program nearly always finds two or more intensities for a given autocorrelation. Figure 4.6 gives examples of different pulse intensities that have the same autocorrelation to within a rather small rms error (.001).

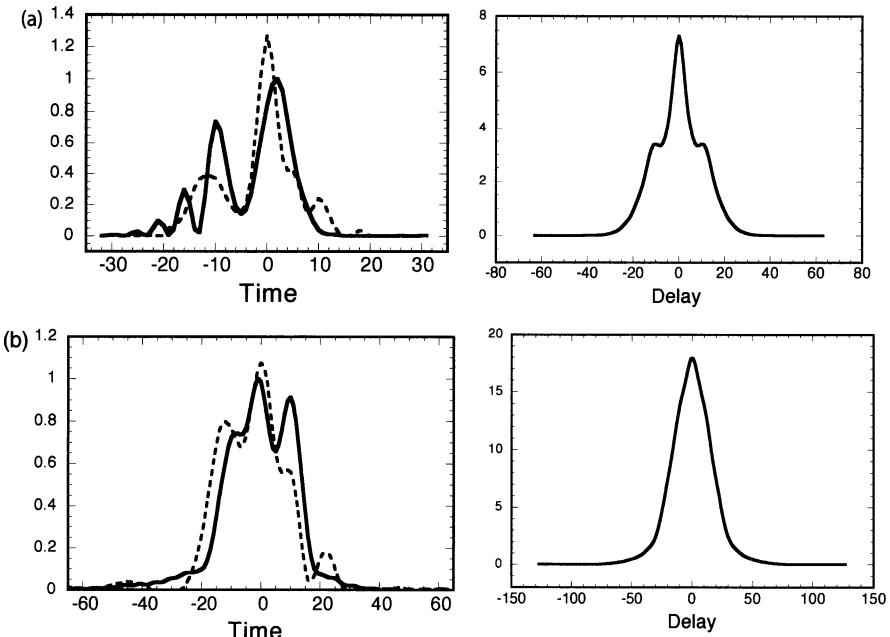


Fig. 4.6: (a) Left: Two pulse intensities that yield numerically equivalent autocorrelations. Right: Their intensity autocorrelation. Both scales are in arbitrary units. (b) Left: Two additional pulse intensities that yield numerically equivalent autocorrelations. Right: Their intensity autocorrelation. In this case, despite their structured shapes, the intensity autocorrelations of these pulses never vary by more than the thickness of the above curve from a Gaussian.

And we conclude that, while it's possible that these ambiguities are merely approximate, it's sufficient for all practical measurement purposes to consider them as ambiguities.

We conclude from these simulations that, in addition to the direction-of-time ambiguity for all autocorrelations, at least some (and probably most) autocorrelations have exact ambiguities. And most (and probably all) autocorrelations have approximate ambiguities that are experimentally indistinguishable. Thus, even if a particular autocorrelation uniquely determined a pulse, a tiny amount of noise in the measurement of that autocorrelation would be almost certain to make it consistent with the autocorrelations of other pulses. Finally, the ambiguous intensities can be quite different.

Autocorrelations of Complex Pulses

Nowhere does the lack of power of the autocorrelation to reveal structure in a pulse reveal itself more than in the measurement of complicated pulses, where, unfortunately, there happens to be a great deal of structure waiting to be revealed. In fact, for complex pulses, it can be shown that, as the intensity increases in complexity, the autocorrelation actually becomes *simpler* and approaches a simple shape of a narrow spike on a pedestal, *independent of the intensity structure* [17].

To see this remarkable fact, we model a complicated pulse field as $E(t) = \sqrt{I_{\text{env}}(t)}u_{\text{noise}}(t)$, that is, the product of complex random noise with unity mean and variance, $u_{\text{noise}}(t)$, and a slowly varying intensity envelope, $\sqrt{I_{\text{env}}(t)}$. The time scale of the rapid variations in the intensity and phase of the random noise is assumed to be much smaller than the width of the envelope. Using higher-order coherence functions, it can be shown that, for a wide range of random-noise models, the autocorrelation of such a pulse can be written:

$$A^{(2)}(\tau) \approx |\Gamma^{(2)}(\tau)|^2 + \int_{-\infty}^{\infty} I_{\text{env}}(t)I_{\text{env}}(t - \tau) dt \quad (4.16)$$

where $\Gamma^{(2)}(\tau)$ is the second-order coherence function of the noise. The width of $|\Gamma^{(2)}(\tau)|^2$ is the pulse coherence time, τ_c , a measure of the width of the finest structure in the noise (and in the pulse intensity, too). For complex pulses, τ_c is much less than the pulse length. The second term in Eq. (4.16) is the autocorrelation of the slowly varying intensity envelope, whose width is roughly the width of the actual pulse. While the details of this calculation are beyond the scope of this book, we should also mention that the two terms in Eq. (4.16) have equal height at $\tau = 0$.

This will produce a trace that contains two components, a narrow central spike (the first term), called the *coherence spike* or *coherence artifact* of approximate width τ_c , sitting on top of a broad *pedestal* or *wings* (the second term) of the approximate width of the envelope τ_p .

Interestingly, this autocorrelation trace simultaneously yields measures of both the pulse spectrum and autocorrelation. Unfortunately, that's all it yields. It says nothing of the intensity structure due to $u_{\text{noise}}(t)$.

So autocorrelations of most complex intensities approach a shape that depends *only* on the pulse spectrum and the slowly varying, average intensity envelope. The autocorrelation thus yields no information on the structure of the pulse intensity. Figure 4.7 shows examples of autocorrelations of complex pulse intensities. Notice that the autocorrelation approaches the above simple form as the pulse complexity increases.

That the autocorrelation doesn't uniquely yield the intensity of complicated pulses is quite an understatement!

Finally, we mentioned that the coherence spike is a measure of the pulse spectrum and the pedestal is a measure of the slowly varying intensity

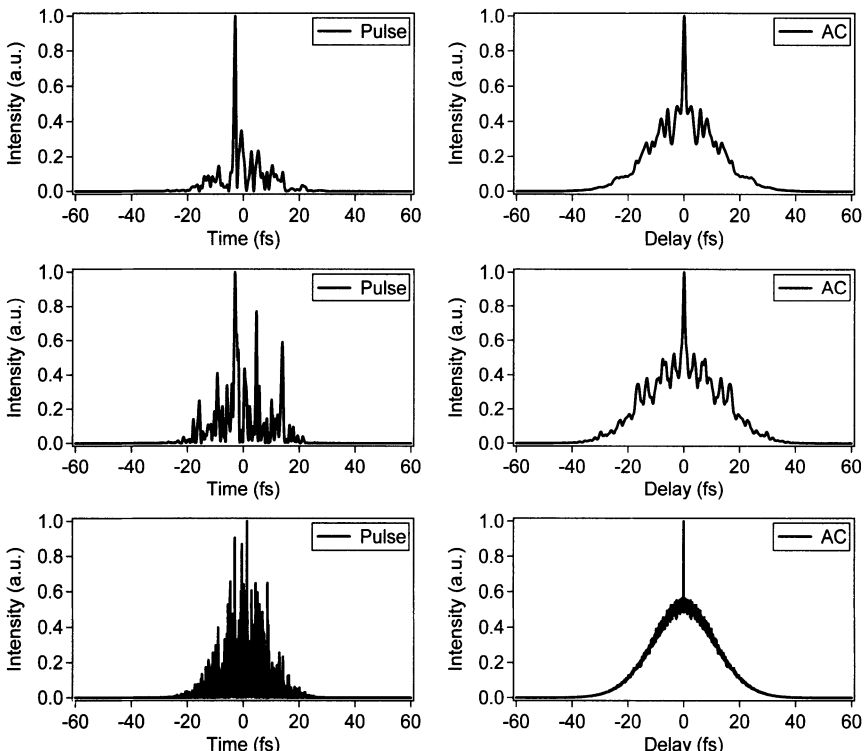


Fig. 4.7: Complex intensities with Gaussian slowly varying envelopes with increasing amounts of intensity structure (left) and their autocorrelations (right). As the pulse increases in complexity (from top to bottom), the autocorrelation approaches the simple coherence-spike-on-a-pedestal shape, independent of the pulse intensity structure. Note that the coherence spike narrows along with the structure, while the pedestal continues to reveal the approximate width of the envelope of the intensity and approaches a perfect Gaussian as the structure increases in complexity.

envelope. And so you're probably wondering about the problem retrieving the spectrum and intensity envelope from the coherence spike and pedestal. Recall that the spectrum and $\Gamma^{(2)}(\tau)$ are a Fourier transform pair. Because the coherence spike is the squared magnitude of $\Gamma^{(2)}(\tau)$, retrieving the spectrum from the coherence spike is equivalent to—you guessed it—*the one-dimensional phase-retrieval problem!* And the pedestal is the autocorrelation of the intensity envelope, so it's also—you guessed it, too—*the one-dimensional phase-retrieval problem!*

Autocorrelations of Noisy Pulse Trains

Even simple pulses can yield autocorrelations of a coherence spike on a pedestal if the measurement averages over a noisy train of them, in which they vary [18]. Consider, for example, double pulses. Figure 4.8 shows some double pulses and their autocorrelations, which have three bumps (and, in general, $2N + 1$ bumps for a series of N pulses).

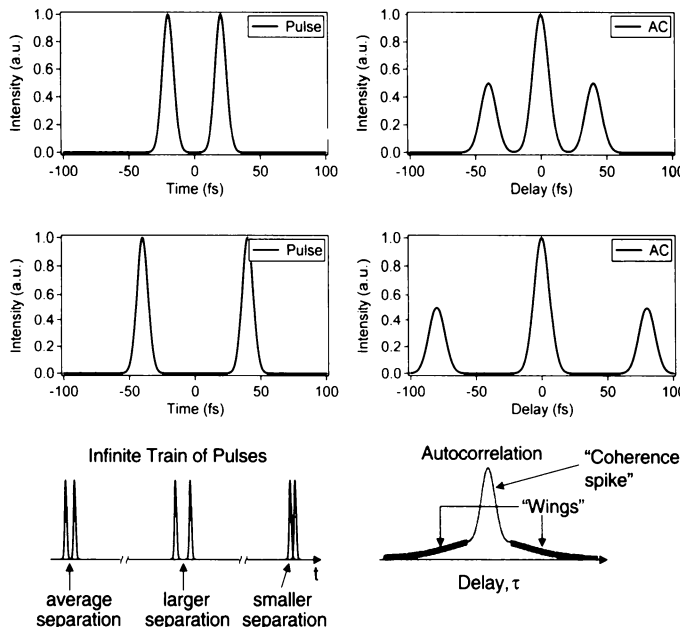


Fig. 4.8: Examples of theoretical double-pulse intensities and their intensity autocorrelations. Left: Intensities vs. time. Right: The intensity autocorrelation corresponding to the intensity to its left. Top row: Two pulses (10 fs Gaussians) separated by four pulse lengths. Second row: The same two pulses separated by eight pulse lengths. Third row: A train of double pulses with varying separation. A multi-shot autocorrelation measurement (third row, right) averages over many double-pulses. Note that the structure has washed out in the autocorrelation due to the averaging over many double pulses in the train, each with its own separation. The pulse length is better estimated by the width of the pedestal than by the width of the coherence spike.

Now, when a laser decides to double-pulse, it typically does so somewhat randomly. It'll often emit a train of double pulses with different, random separations for each double-pulse in the train. Since a typical ultrafast laser emits pulses at a very high repetition rate (100 MHz), and most autocorrelators are multi-shot devices anyway, the autocorrelator will necessarily average over the autocorrelations of many such pulses.

This will also produce a trace that contains two components, a narrow central coherence spike sitting on top of a broad pedestal, whose height will typically be much less than the value of 1/2 we saw in the last section. Clearly the coherence spike is a rough measure of the individual pulses within the double-pulse, and the pedestal indicates the distribution of double-pulse separations. Again, while it would be tempting to try to derive the pulse length from the coherence spike—especially now that the pedestal seems so weak in comparison—the pulse length is related, not to the coherence spike, but to the pedestal. *Even when the pedestal is weak, do not make the mistake of identifying the coherence spike as an indication of the pulse length!*

Now consider a related problem, a pulse whose intensity varies in a complex manner in *space*. Such a pulse should have a similar autocorrelation. Indeed, for pulses with almost any type of complication, the coherence-spike/pedestal shape isn't just a possible autocorrelation trace; it's practically the *only* one!

So what do you do if you're measuring such an autocorrelation trace from your laser? Recognize that your laser is sick, but that this trace is to a laser as a cough is to a human—a cry for better diagnostics.

Finally, you might be wondering how *any* technique can handle such complex cases as an extremely complex pulse or a noisy train of pulses. These are very difficult measurement problems. But they're common, so it's important to address them. And we have. Chapter 17 will describe FROG measurements of extremely complex pulses with $TBP > 1000$ —so complex that it's difficult even to simply plot them. And if that's not challenging enough, we'll measure a *noisy train of them*.

The Autocorrelation and the rms Pulse Length

Despite its shortcomings, the autocorrelation does give us some useful information about the pulse. And it also contains some surprising information you might not expect: it *unambiguously* yields the *rms pulse length*! No assumption of pulse shape is necessary.

This result follows easily from a result well-known in probability theory, that, if $h(t) = f(t) * g(t)$ (a convolution), then the rms widths of these functions are related simply by a Pythagorean sum [19]:

$$(\tau_{\text{rms}})_h^2 = (\tau_{\text{rms}})_f^2 + (\tau_{\text{rms}})_g^2 \quad (4.17)$$

Now the autocorrelation is just the “autoconvolution,” but with an argument reversed: $A^{(2)}(t) = I(t) * I(-t)$. Because reversing the time argument of a

function doesn't change its width, the autocorrelation width, $(\tau_{\text{rms}})_A$, will be:

$$(\tau_{\text{rms}})_A^2 = 2(\tau_{\text{rms}})^2 \quad (4.18)$$

Thus, the autocorrelation rms width is simply $\sqrt{2}$ times the rms pulse width, τ_{rms} . So if all you need is the rms pulse length, you're done!

The Autocorrelation and the FWHM Pulse Length

Unfortunately, we're typically much more interested in the pulse FWHM than the rms. This is because the rms pulse length depends too sensitively on the details of the pulse intensity way out in the wings.

Unfortunately, the autocorrelation isn't as informative in this case. To obtain as little information as the mere FWHM pulse length from the autocorrelation, a guess must be made as to the pulse shape. Once such a guess is made, it's possible to derive a multiplicative factor that relates the autocorrelation full-width-half-maximum to that of the pulse $I(t)$. Unfortunately, this factor varies significantly for different common pulse shapes. J.C. Diels and W. Rudolph give common simple pulse shapes with their autocorrelations in their book, *Ultrashort Laser Pulse Phenomena* [20]. Suffice it to say here that a Gaussian intensity yields an intensity autocorrelation that is $\sqrt{2} = 1.41$ wider, and a $\text{sech}^2(t)$ intensity yields an autocorrelation that is 1.54 times wider.

This lack of power on the part of the autocorrelation has resulted in an unfortunate temptation to choose an “optimistic” pulse shape, such a $\text{sech}^2(t)$, which yields a large multiplicative factor (1.54), rather than a “pessimistic” pulse shape, such as a Gaussian, which has a smaller factor (1.41), in order to obtain a shorter pulse length for a given measured autocorrelation width. Everyone likes to claim the shortest possible pulse.

To see more quantitatively how accurately the autocorrelation determines the pulse length (see Fig. 4.9), Zeek measured real-world unamplified Ti:Sapphire laser pulses (using FROG) and computed their autocorrelations. He then compared the autocorrelation widths (FWHM) and actual

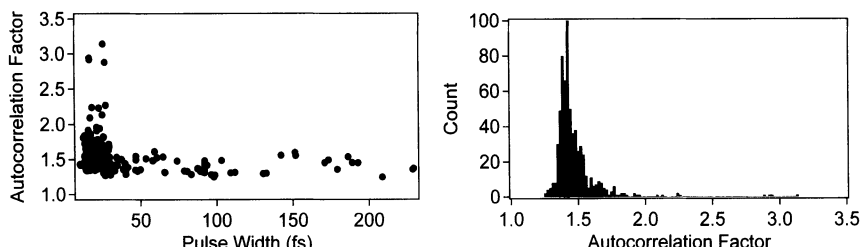


Fig. 4.9: Real pulses from a Ti:Sapphire oscillator (some of which were shaped) and their autocorrelation factors. Left: Autocorrelation factor vs. pulse width. Note that the actual factor was as large as 3.2. Right: a histogram of the autocorrelation factors.

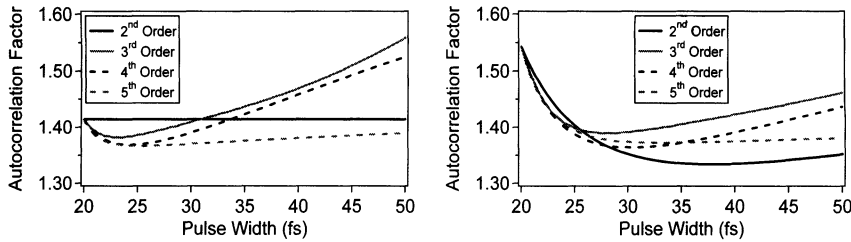


Fig. 4.10: Theoretical autocorrelation factors for non-ideal pulse shapes with various orders of spectral phase distortion for Gaussian (left) and sech^2 (right) spectra. The actual correction factor is plotted against the resulting pulse width.

widths (FWHM). He found that the autocorrelation factor varied considerably. Interestingly, on no occasion did a Gaussian or sech^2 shape intensity ever occur!

In another study (see Fig. 4.10), Zeek compared simple theoretical pulses having low-order spectral-phase distortions with their autocorrelations. Again, the pulse and autocorrelation widths varied significantly. Interestingly, he found that the autocorrelation factor rarely exceeded 1.5, so using 1.54 generally would have under-estimated the pulse length, in agreement with measurements reported by Penman, et al. [21].

In practice, most ultrashort pulses don't have simple intensity profiles. As a result, simply assuming a pulse shape and dividing the measured autocorrelation width by the corresponding factor is irresponsible unless you include a major disclaimer.

So now, if you're at a conference talk and someone claims to determine a pulse length from an autocorrelation, we hope that you'll be quick to object. And if, in addition, the trace has wings, object loudly.

The Third-Order Autocorrelation

The inadequacies of the (second-order) intensity autocorrelation have not been lost on those who use it. As a result, several improvements have emerged over the years, and one simple advance is the *third-order intensity autocorrelation*, or just the *third-order autocorrelation* [22–26].

Third-Order Beam Geometries and Traces

Suppose we could break the symmetry of the autocorrelation. Then we could, at the very least, remove the direction-of time ambiguity. One way to do this is to generate a third-order autocorrelation. This is accomplished by using an instantaneous third-order nonlinear-optical process, instead of SHG, which is a second-order one.

One such third-order autocorrelator uses the polarization-gate (PG) beam geometry, in which one pulse, polarized at 45° , enters an ordinary piece of glass (or other instantaneous medium) and induces some birefringence while it's there. See Fig. 4.11. The glass then becomes a wave plate, but only while this pulse is present, when it'll slightly rotate the polarization of another beam if it's, say, vertically polarized. As a result, some of this second beam will pass through a polarization analyzer placed after the glass and set to reject vertically polarized light. Figs. 4.12 and 4.13 show two more third-order beam geometries.

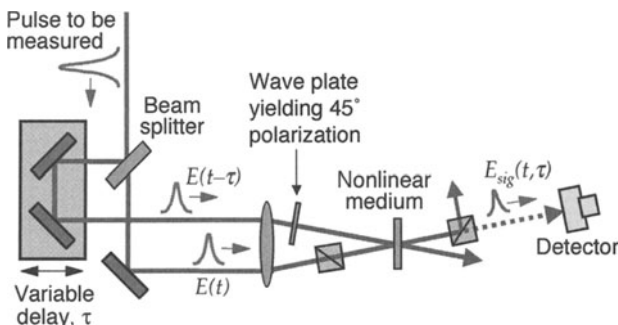


Fig. 4.11: Experimental layout for a third-order intensity autocorrelator using polarization gating. A pulse is split into two, one (the “gate” pulse) has its polarization rotated by 45° and is variably delayed, and the other (the “probe” pulse) passes through crossed polarizers. Then the two pulses are overlapped in a piece of glass. The 45° -polarized gate pulse induces birefringence in the glass, which slightly rotates the polarization of the probe pulse causing it to leak through the polarizers if the pulses overlap in time. The leakage pulse energy is measured with respect to delay, producing the third-order autocorrelation trace.

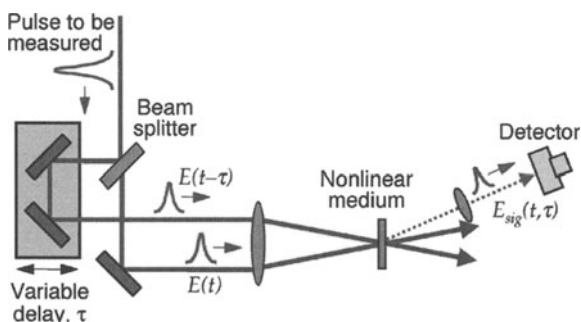


Fig. 4.12: Experimental layout for a third-order intensity autocorrelator using self-diffraction. The pulse is split into two, delayed, and recombined in a third-order nonlinear medium, as in the previous figure, but here, the pulses induce a grating in the glass, which diffracts one of the pulses into a new direction off to the side, at $2k_1 - k_2$. This also produces a third-order autocorrelation trace.

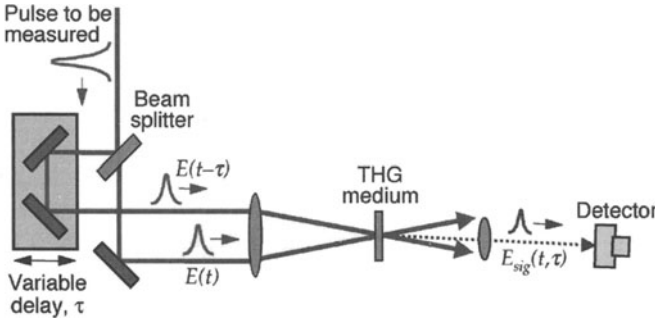


Fig. 4.13: Experimental layout for a third-order intensity autocorrelator using third-harmonic generation (THG). The pulse is split into two, delayed, and recombined in a third-order nonlinear medium, as in the previous figure, but here, the pulses yield the third harmonic. This also produces a third-order autocorrelation trace.

A PG autocorrelator produces a field given by:

$$E_{\text{sig}}^{\text{PG}}(t, \tau) \propto E(t)|E(t - \tau)|^2 \quad (4.19)$$

where $E(t)$ is the vertically polarized pulse and $E(t - \tau)$ is the delayed field of the 45° -polarized pulse. This yields a signal field with three factors of the field, hence the notion of third-order. It then yields a signal intensity that is proportional to three factors of the intensities of the two input pulses:

$$I_{\text{sig}}^{\text{PG}}(t, \tau) \propto I(t)I^2(t - \tau) \quad (4.20)$$

Again, detectors are too slow to time resolve the rapidly varying intensity, $I_{\text{sig}}^{\text{PG}}(t, \tau)$, so this measurement produces a measured quantity, which is the time integral of $I_{\text{sig}}^{\text{PG}}(t, \tau)$:

$$A^{(3)}(\tau) = \int_{-\infty}^{\infty} I(t)I^2(t - \tau) dt \quad (4.21)$$

This result is the third-order autocorrelation.

The other geometries yield different signal fields, but they all yield the same result. For example, self-diffraction (Fig. 4.12) has a signal field given by:

$$E_{\text{sig}}^{\text{SD}}(t, \tau) \propto E^2(t)E^*(t - \tau) \quad (4.22)$$

which has the signal pulse intensity:

$$I_{\text{sig}}^{\text{SD}}(t, \tau) \propto I^2(t)I(t - \tau) \quad (4.23)$$

And its integrated intensity is:

$$A^{(3)}(\tau) = \int_{-\infty}^{\infty} I^2(t)I(t - \tau) dt \quad (4.24)$$

which, with a simple change of variables, $t \rightarrow t - \tau$, yields the same result, except for a reflection about the vertical axis.

Similarly, THG has a signal field:

$$E_{\text{sig}}^{\text{THG}}(t, \tau) \propto E^2(t)E(t - \tau) \quad (4.25)$$

which has the signal pulse intensity:

$$I_{\text{sig}}^{\text{THG}}(t, \tau) \propto I^2(t)I(t - \tau) \quad (4.26)$$

whose time-integral is also the third-order autocorrelation.

Third-order autocorrelations have also been generated using other nonlinear-optical effects, such as three-photon fluorescence [24].

Because $I(t)$ and $I(t - \tau)$ enter into the third-order autocorrelation *asymmetrically* (only one is squared), the change of variables, t to $t - \tau$, no longer yields $A^3(-\tau)$, as was the case for the second-order autocorrelation. So a third-order autocorrelation is symmetrical only if the intensity that produces it is. The asymmetry is not overwhelming, but it is often sufficient. Figure 4.14 shows third-order autocorrelations of some of the same pulses for which we saw second-order autocorrelations in Fig. 4.4.

Third-order nonlinearities are weaker than second-order ones and hence require more pulse energy and do not work well for unamplified pulses from typical ultrafast laser oscillators, but they are useful for amplified pulses and UV pulses (where SHG can't be performed), and will be even more useful when we discuss FROG in the next chapter.

However, the important question for us here is: Does the third-order autocorrelation uniquely determine the pulse intensity?

Third-Order Autocorrelations of Complicated Pulses

That the answer to the above question is “no” is probably clear. But it also follows from the fact that the third-order autocorrelation of a complicated pulse is similar to the second-order autocorrelation of such a pulse: a coherence spike on top of a broad pedestal [17].

Slow Third-Order Autocorrelations of Complicated Pulses

Now imagine creating a third-order autocorrelation in a *very slowly* responding nonlinear medium, a medium whose response time far exceeds the pulse length [27–29]. This violates the assumption we've been making throughout this chapter that an essentially instantaneously responding medium is necessary for an autocorrelation. Indeed, this is an attempt to measure an ultrafast event with an *ultraslow* one.

Consider an induced-grating process whose diffraction is the signal pulse in the third-order interaction. In a slowly responding medium, however, induced-grating fringes have a tendency to wash out as the relative phase of the input

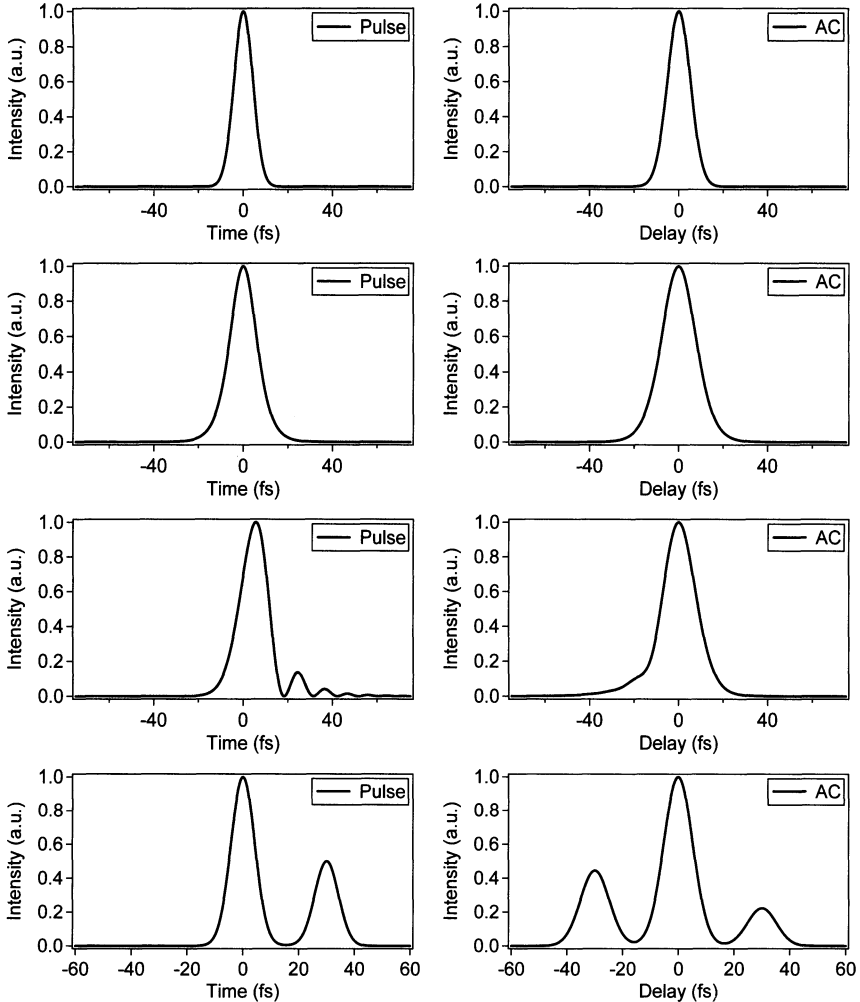


Fig. 4.14: Examples of third-order autocorrelations. Top row: A 10-fs Gaussian intensity. Second row: A 7-fs sech^2 intensity. Third row: A pulse whose intensity results from 3rd-order spectral phase. Fourth row: A double pulse. Note that the third-order autocorrelation also masks structure in the pulse. But it will be slightly asymmetrical if the intensity is.

beams varies and the intensity-fringes sweep back and forth due to pulse phase variations. So not only would it seem that use of a slow medium wouldn't yield ultrafast information, but, worse, its efficiency should be essentially zero, too (except when the delay is zero and the phase fluctuations from the two beams that induce them cancel out). *Interestingly, neither is true* [17].

Consider the same complicated-pulse model as before, consisting of the product of random field noise, $u_{\text{noise}}(t)$, and a slowly varying intensity envelope, $I_{\text{env}}(t)$. As before, the time scale of variations of the random noise is approximately the pulse coherence time, τ_c , which we assume to be much

smaller than the length of the envelope, whose pulse length is τ_p . As with autocorrelations using instantaneous media, we find, for a wide range of noise models, that the third-order autocorrelation using a slowly responding medium can be written as a sum of two terms [17]:

$$A^{(2)}(\tau) \approx |\Gamma^{(2)}(\tau)|^2 + \frac{\tau_c}{\tau_p} \int_{-\infty}^{\infty} I_{env}(t) I_{env}(t - \tau) dt \quad (4.27)$$

where $\Gamma^{(2)}(\tau)$ is the second-order coherence function of the random noise. Recall that the width of $|\Gamma^{(2)}(\tau)|^2$ is the time scale of the fine-scale intensity structure and the pulse coherence time, τ_c .

As before, we find that the measured autocorrelation is the sum of a narrow coherence spike, $|\Gamma^{(2)}(\tau)|^2$, and the autocorrelation of the slowly varying intensity envelope. In this case, however, the pedestal is much smaller: the ratio of the pedestal to the coherence function is τ_c/τ_p , which is much less than one. But it isn't zero. It does go to zero in the limit of an infinitely long pulse, when the grating fringes cancel out perfectly, but it *isn't* zero for a pulse because the induced grating doesn't actually cancel out completely in a finite time, τ_p .

Thus, we find, surprisingly, that a (third-order) autocorrelation trace generated using a *slowly* responding medium yields both a measure of the pulse spectrum and the pulse autocorrelation in one trace.

But again, that's all it yields. And, as in second-order autocorrelations of complex pulses, extracting as little as the spectrum and average intensity requires solving two one-dimensional phase-retrieval problems.

The Triple Correlation

A more informative option is the *triple correlation*:

$$A_3(\tau, \tau') = \int_{-\infty}^{\infty} I(t) I(t - \tau) I(t - \tau') dt \quad (4.28)$$

and which is a function of two different delays, τ and τ' . The triple correlation can be generated by first performing an autocorrelation (using an instantaneous medium). But, instead of simply measuring the signal energy vs. delay, it involves crossing the signal pulse with a third replica of the original pulse in another nonlinear crystal. The signal energy is then measured vs. the delay between the first two pulses *and* the delay between the latter two pulses, in addition. It can also be generated by sending three separate pulse replicas into a third-order medium and independently varying the delays of two of the three pulses.

The Fourier transform of the triple correlation is the *bi-spectrum*:

$$\tilde{A}_3(\omega, \omega') = \int_{-\infty}^{\infty} \int_{-\infty}^{\infty} A_3(\tau, \tau') \exp(-i\omega\tau - i\omega'\tau') d\tau d\tau' \quad (4.29)$$

You may be relieved to learn that, in most cases, the triple correlation uniquely determines the intensity!

Finally, a measure that works!

Unfortunately, the triple correlation is not the most convenient of techniques, requiring two delay lines and three beams. While it does uniquely yield the intensity, most researchers consider it too great a price to pay for this information.

The triple correlation and the bi-spectrum have found application in many other fields, however. For example, it is the mathematics behind speckle interferometry. If you're interested, check out some of the references at the end of this chapter [30–34].

The Autocorrelation and Spectrum—in Combination

If the autocorrelation by itself doesn't determine the intensity, and the spectrum by itself doesn't determine the field, why not just use *both* measures in combination and see what the two quantities *together* yield? Indeed, each can be considered as a fairly strong constraint for the other in their respective one-dimensional phase-retrieval problems. This is precisely what Rundquist and Peatross did in what they called the *Temporal Information Via Intensity* (TIVI) method for finding the intensity and phase of a pulse [35].

Inspired by work well known in the image science and x-ray crystallography communities, they noted that knowledge of the intensity, $I(t)$, and the spectrum, $S(\omega)$, is often sufficient to yield the phase in either (and hence both) domains. The algorithm typically used to find the phase from intensities in both domains is called the Gerchberg-Saxton algorithm, which involves simply making a guess for the phase and Fourier-transforming back and forth between the two domains, replacing the magnitude in the relevant domain with the measured quantity [36,37].

Not only do $I(t)$ and $S(\omega)$ usually yield a unique phase, but the Gerchberg-Saxton algorithm is fairly good at finding it.

Unfortunately, for ultrashort laser pulses, we don't have the intensity and the spectrum. We have the *autocorrelation* and the spectrum.

So Rundquist and Peatross wrote a simple routine to determine an intensity from the autocorrelation. Of course, as we have seen, the autocorrelation doesn't uniquely determine the intensity. So this process can at best yield only *a* possible pulse field, not *the* pulse field.

Nevertheless, it is interesting to ask how well this procedure works. Of course, for very complicated pulses, because the autocorrelation contains so little information, this procedure is clearly doomed to fail.

But what if we assume a simple pulse shape (whose TBP ~ 1)? Unfortunately, no analytical work has been performed on this topic, but recently, Chung and Weiner [38] performed numerical computations to ascertain whether the autocorrelation and spectrum can uniquely determine the pulse

intensity and phase in this regime. And they found numerous nontrivial ambiguities, in addition to the obvious direction-of-time ambiguity. Figures 4.15a and b give examples of ambiguities that they found.

Worse, even if we knew the intensity and spectrum, it wouldn't be sufficient, as knowledge of the intensity and spectrum is not sufficient to yield

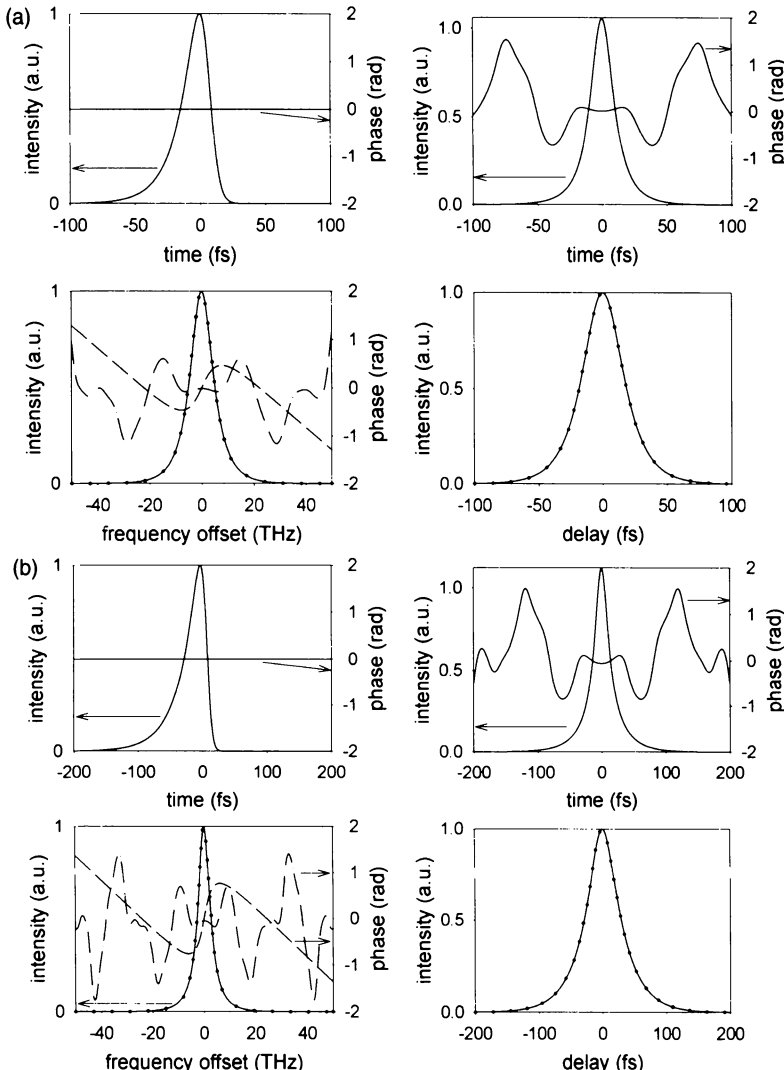


Fig. 4.15: (a) Two pulses (top row) with different intensities and phases, which yield numerically identical autocorrelations (bottom right) and spectra (bottom left). The spectral phase of both pulses is given (dashed curves at bottom left). (b) Two more pulses (top row) with different intensities and phases, which yield numerically identical autocorrelations (bottom right) and spectra (bottom left). The spectral phase of both pulses is given (dashed curves at bottom left).

the phase in all cases of interest. Saxton himself has catalogued numerous cases in which more than one phase is either exactly or approximately consistent with a particular intensity and spectrum [37]. Approximate ambiguities include functions with weak oscillatory components in the phase and whose relative phases are therefore indeterminate. And they also include functions with weak imaginary components. Exact ambiguities result from intensities that are symmetrical in one domain and which cannot distinguish between the correct phase and its complex conjugate in the other domain.

In other words, if we ignore the ambiguities associated with extracting the intensity from the autocorrelation, we still wouldn't be there.

Also, the Gerchberg-Saxton algorithm tends to stagnate [37].

Indeed, even if this procedure worked, it would be difficult to use in practice due to its obvious sensitivity to the presence of noise.

In the end, Rundquist and Peatross instead recommended that their method be used to generate an initial guess for the FROG algorithm (the FROG trace can easily generate the autocorrelation and a quantity related to the spectrum). Because TIVI is a fast algorithm, its use in this manner can effectively speed up the FROG retrieval process.

There are several variations on the TIVI theme out there. While no one has taken the time to evaluate them as Chung and Weiner have the basic TIVI scheme, it is doubtful that they perform any better than TIVI and hence represent a bad career move for any serious scientist.

Fringe-Resolved Autocorrelation

A method that combines quantities related to the autocorrelation and spectrum in a single data trace is the *interferometric autocorrelation*, often called *phase-sensitive autocorrelation* and the *fringe-resolved autocorrelation* (FRAC). It was introduced by Jean-Claude Diels in 1983 [39–45], and it has become very popular. It involves measuring the second-harmonic energy vs. delay from an SHG crystal placed at the output of a Michelson interferometer (see Fig. 4.16). In other words, it involves performing an autocorrelation measurement using collinear beams, so that the second harmonic light created by the interaction of the two different beams combines coherently with that created by each individual beam. As a result, interference occurs due to the coherent addition of the several beams, and interference fringes occur vs. delay. This is in contrast to the usual autocorrelation, which is often referred to as the *background-free autocorrelation* when FRAC is also being discussed.

The expression for the FRAC trace is:

$$I_{FRAC}(\tau) = \int_{-\infty}^{\infty} |[E(t) + E(t - \tau)]^2|^2 dt \quad (4.30)$$

$$= \int_{-\infty}^{\infty} |E(t)^2 + 2 E(t)E(t - \tau) + E(t - \tau)^2|^2 dt \quad (4.31)$$

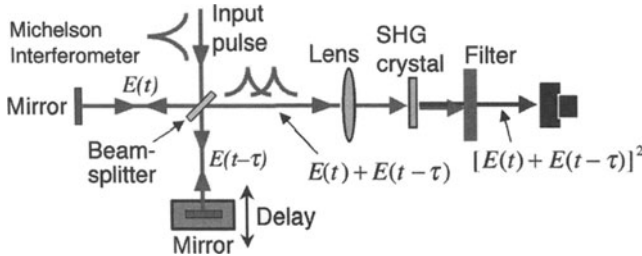


Fig. 4.16: Experimental layout for the Fringe-resolved autocorrelation (FRAC).

Note that, if the $E(t)^2$ and $E(t - \tau)^2$ terms were removed from the above expression, we'd have only the cross term, $2 E(t)E(t - \tau)$, which yields the usual expression for background-free autocorrelation. These new terms, integrals of $E(t)^2$ and $E(t - \tau)^2$, are due to SHG of each individual pulse. And their interference, both with each other and with the cross term, will yield the additional information in the FRAC that is not present in the usual autocorrelation. Indeed, the interference of these new terms with each other will yield an interferogram of the second harmonic of the pulse.

Expanding the above expression:

$$\begin{aligned}
 I_{\text{FRAC}}(\tau) = & \int_{-\infty}^{\infty} \{I(t)^2 + I(t - \tau)^2\} dt \\
 & + \int_{-\infty}^{\infty} \{I(t) + I(t - \tau)\} \operatorname{Re}\{E(t)E^*(t - \tau)\} dt \\
 & + \int_{-\infty}^{\infty} \operatorname{Re}\{E(t)^2 E^*(t - \tau)^2\} dt \\
 & + \int_{-\infty}^{\infty} I(t)I(t - \tau) dt
 \end{aligned} \tag{4.32}$$

In words,

$$\begin{aligned}
 I_{\text{FRAC}}(\tau) = & \text{Constant} \\
 & + \text{Modified interferogram of } E(t) \\
 & + \text{Interferogram of the 2nd harmonic of } E(t) \\
 & + \text{Autocorrelation of } I(t)
 \end{aligned} \tag{4.33}$$

Thus, the FRAC contains a constant, the autocorrelation, something akin to the interferogram (which we refer to here as the “modified interferogram” due to the additional factor, $I(t) + I(t - \tau)$, not present in the interferogram), and the interferogram of the pulse second harmonic. Examples of the FRAC are shown in Fig. 4.17.

We can now dissect this quantity and try to understand it.

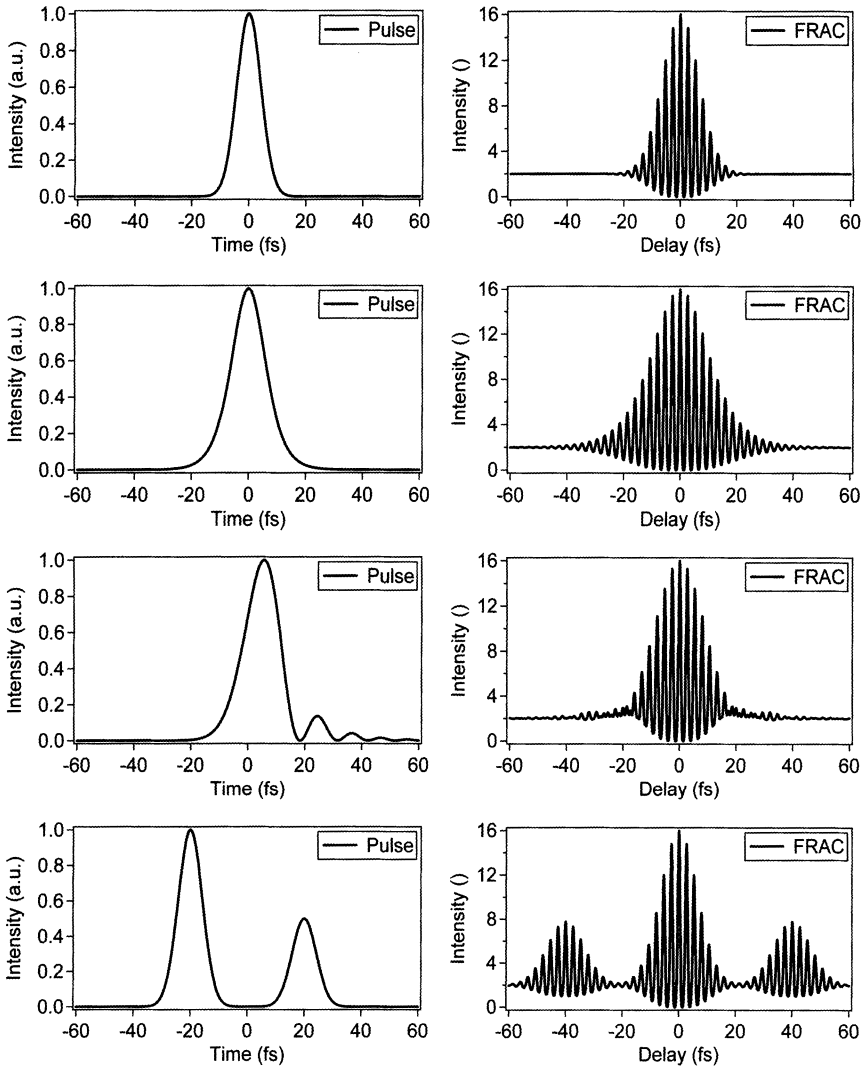


Fig. 4.17: Pulses and their FRAC traces. Top row: A 10-fs Gaussian intensity. Second row: A 7-fs sech^2 intensity. Third row: A pulse whose intensity results from 3rd-order spectral phase. Fourth row: A double pulse. Note that the satellite pulses due to third-order spectral phase, which were invisible in the intensity autocorrelation, actually can be seen in the wings of the FRAC trace.

Let's start with the constant term. Not much information here. Actually, this term is useful for verifying the validity of a measurement. It's easy to show that the peak-to-background ratio in a FRAC trace is 8. If it isn't, then redo the measurement. But this information won't help us determine the pulse. One down, three to go.

Now consider the last term. It's just the autocorrelation, which we're already pretty tired of hearing about by now. Two down, two to go.

Now consider the two interferogram terms. Recall that interferograms yield fringes with respect to delay with the frequency of the light involved. And, in the FRAC trace, there are two interferograms, with such fringes. The fringes in the modified interferogram of $E(t)$ occur at frequency ω . And the fringes in the interferogram of the 2nd harmonic of $E(t)$ occur at frequency 2ω . As a result, except for extremely short pulses of only a few cycles, the various terms can be distinguished by their different carrier frequencies.

Recall that the interferogram is the inverse Fourier transform of the spectrum. Thus, the interferogram of the 2nd harmonic of $E(t)$ simply yields the spectrum of the 2nd harmonic of $E(t)$. Three down, one to go.

Now let us consider the modified interferogram of $E(t)$. This term doesn't correspond to any well-known or intuitive quantity. In the limit that the distortions are mostly in the phase, however, the quantity, $I(t) + I(t - \tau)$, is slowly varying compared to $\text{Re}\{E(t)E^*(t - \tau)\}$, so the remaining integral reduces to the simple interferogram of $E(t)$. In this limit, then, this term is simply equivalent to the pulse spectrum.

So when the distortions are mostly in the phase:

$$\begin{aligned} I_{\text{FRAC}}(\tau) \approx & \text{ Constant} \\ & + \text{Interferogram of } E(t) \\ & + \text{Interferogram of } E^2(t) \\ & + \text{Autocorrelation of } I(t) \end{aligned} \quad (4.34)$$

Now you might think that interferograms/spectra of the fundamental and second harmonic contain equivalent information. But you'd be wrong.

Let's consider the spectrum of the second harmonic. To begin with, the second-harmonic frequency-domain field is the autoconvolution of the fundamental-pulse field:

$$\tilde{E}_2(\omega) \propto \tilde{E}(\omega) * \tilde{E}(\omega) \quad (4.35)$$

since $E_2(t) \propto E(t)^2$. So you might think that the spectrum of the second harmonic is the simple convolution of the pulse spectrum with itself. But it is *not* the case that $S_2(\omega) \propto S(\omega) * S(\omega)$. Here's a counter-example: let $E(t) \propto \text{sinc}(t)$. The second-harmonic field is just the square of the $E(t)$, or $E_2(t) \propto \text{sinc}^2(t)$. The frequency-domain field of $E(t)$ is the Fourier transform of $\text{sinc}(t)$, or $\tilde{E}(\omega) \propto \text{rect}(\omega)$. Since $\text{rect}(\omega)$ is always 0 or 1 (except at isolated points), it's also the case that $S(\omega) \propto \text{rect}(\omega)$. The second-harmonic frequency-domain field, $\tilde{E}_2(\omega)$, is the autoconvolution of $\tilde{E}(\omega)$: $\tilde{E}_2(\omega) \propto \text{triangle}(\omega)$, which when squared yields the second-harmonic spectrum: $S_2(\omega) \propto \text{triangle}^2(\omega)$. But the autoconvolution of the fundamental spectrum is: $S(\omega) * S(\omega) \propto \text{triangle}(\omega)$, not $\text{triangle}^2(\omega)$.

Thus, the FRAC trace contains no less than three interesting measures of a pulse. And, in this limit (when the phase distortions dominate), they have a particularly simple description.

In the limit that the distortions are small, $\{I(t) + I(t - \tau)\}$ varies on a time scale similar to $\text{Re}\{E(t)E^*(t - \tau)\}$ so it must be retained. While this makes the interpretation of the FRAC trace more difficult, it should not hamper any attempt to retrieve the pulse from it because such retrieval necessarily will involve a computer algorithm of some sort.

So what does all this interesting information do for us? Does the FRAC completely determine the pulse field? Unfortunately, no study has been made of what can be retrieved from the FRAC and what ambiguities are present (besides the obvious direction-of-time ambiguity).

Nagunuma has shown that, if the pulse spectrum or interferogram is also included, there is in principle sufficient information present to fully determine the pulse field (except for the direction of time) [46–48]. He also presented an iterative algorithm to find the field. No study has been published on this algorithm's performance, however, and it is rarely used. Researchers who have tried it have found that it tends to stagnate.

Chung and Weiner shed some light on the issue of how well FRAC determines pulses by calculating FRAC traces for the pairs of pulses that yielded ambiguities in TIVI. And they found that the resulting traces of the pairs of pulses had very similar, although not identical, FRAC traces. See Figs. 4.18a and b.

On the other hand, Diels and coworkers showed that the direction of time could be determined by including a second FRAC measurement—actually a fringe-resolved cross-correlation—in which some glass is placed in one of the interferometer arms. This breaks the symmetry and yields an asymmetrical trace. Then, assuming that the dispersion of the glass is known, Diels and coworkers showed that the two FRAC traces could be used to completely determine the pulse field in a few cases. Again, however, no study has been published on this algorithm's performance. On the other hand, Diels gave this method a memorable name, *The Femto-Nitpicker*.

Cross-Correlation

Occasionally, we have a shorter event available to measure a pulse. Then life is good! In this case, we perform a cross-correlation (see Fig. 4.19). The cross-correlation, $C^{(2)}(\tau)$, is given by:

$$C^{(2)}(\tau) = \int_{-\infty}^{\infty} I(t) I_g(t - \tau) dt \quad (4.36)$$

where $I(t)$ is the unknown intensity and $I_g(t)$ is the gate pulse intensity.

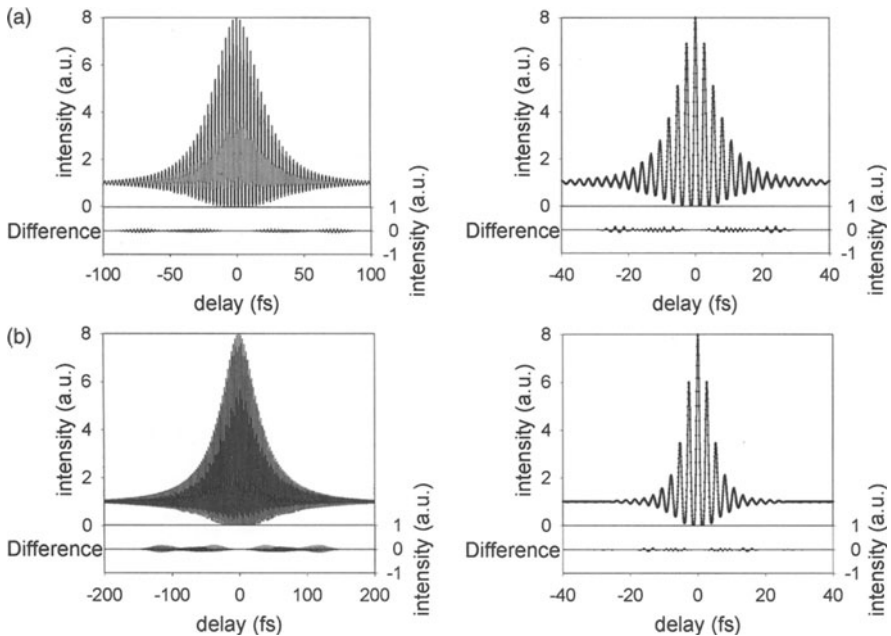


Fig. 4.18: (a) Left: FRAC traces of the pair of pulses from Fig. 4.14a. The difference between the two FRAC traces is plotted below. Right: FRAC traces of the same pulses, but shortened by a factor of 5. Note that, in both cases, the two FRAC traces are very similar. Note also that the FRAC traces are even more difficult to distinguish as the pulse lengths decrease. (b) Left: FRAC traces of the pair of pulses from Fig. 4.10b. The difference between the two FRAC traces is plotted below. Right: FRAC traces of the same pulses, but shortened by a factor of 5. Note that, in both cases, the two FRAC traces are very similar. Note also that the FRAC traces are even more difficult to distinguish as the pulse lengths decrease.

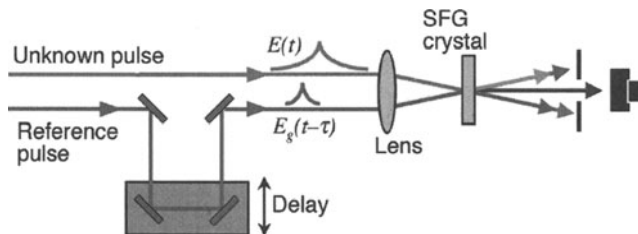


Fig. 4.19: A cross-correlator. A shorter pulse can gate a longer one and yield the intensity.

When a much shorter gate pulse is available, the cross-correlation yields the intensity precisely. Substitution of $\delta(t)$ for $I_g(t)$ easily yields $I(t)$ precisely. In fact, you don't even need to know the gate pulse—just that it's much shorter. The problem is that you don't often have a delta-function pulse lying around the lab.

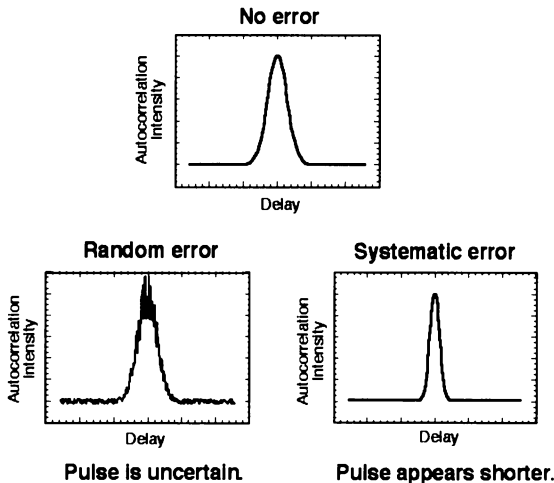


Fig. 4.20: An accurate autocorrelation (top). Bottom: the same trace, but contaminated by random error (left) and nonrandom (systematic) error (right).

Systematic Error in the Autocorrelation and Spectrum

Random vs. Systematic Error

While random error is always an issue in any measurement, it at least announces its presence by having an obvious “noise-like” appearance. In other words, it’s clearly noise, and not the autocorrelation, for example (See Fig. 4.20). On the other hand, nonrandom, or systematic, error will cause the trace to be different from the actual trace, but it leaves no such calling card. As a result, we must be particularly careful to eliminate systematic error in pulse measurements (and all other measurements for that matter). Worse, because small deviations in the autocorrelation can correspond to large deviations in the pulse, systematic error can be quite a problem in such measurements.

Systematic Error in Measurements of the Spectrum

Numerous sources of systematic error plague spectral measurements. Here’s a partial list:

1) *Stray light*: Of course, stray light with a different spectrum can distort a spectral measurement by introducing light at new frequencies or with different relative spectral intensities. But stray light with the *same* spectrum can distort it even more! Suppose that a small fraction of a pulse’s energy, say ε , reflects off an unintended surface and finds its way into the spectrometer after experiencing a delay, τ , with respect to the rest of the pulse. The measured

spectrum will then be:

$$S_{meas}(\omega) = \left| \int_{-\infty}^{\infty} [E(t) + \sqrt{\varepsilon} E(t - \tau)] \exp(-i\omega t) dt \right|^2 \quad (4.37)$$

$$= \left| \tilde{E}(\omega) + \sqrt{\varepsilon} \tilde{E}(\omega) \exp(i\omega\tau) \right|^2 \quad (4.38)$$

$$\approx S(\omega) |1 + \sqrt{\varepsilon} \exp(i\omega\tau)|^2 \quad (4.39)$$

$$\approx S(\omega) \{1 + 2\sqrt{\varepsilon} \cos(\omega\tau)\} \quad (4.40)$$

where we have assumed that ε is small and hence have neglected the ε^2 term. Thus, the stray reflection introduces a modulation at the frequency $2\pi/\tau$ into the measured spectrum (see Fig. 4.21). If τ is large, the fringes will be very closely spaced and possibly beyond the resolution of the spectrometer (and hence would not visibly distort the measured spectrum). For intermediate values of τ , a simple modulation will occur in the spectrum, indicating this effect. And if τ is small, only a fraction of a modulation period may occur over the entire spectrum and hence may not be perceived as a modulation. But it could nevertheless distort the spectrum significantly. Worse, because the modulation amplitude is $2\sqrt{\varepsilon}$, a mere 1% reflection produces a massive 20% amplitude modulation, which is a whopping 40% peak-to-peak modulation, a serious distortion for such a seemingly small amount of stray light.

2) *Spectrally non-uniform efficiencies*: All optical components and devices have transmissions, reflectivities, responsivities, or efficiencies that depend on wavelength. The measured spectrum must be corrected for these non-uniformities.

3) *Improper calibration*: I think you know what we're talking about here. Calibrate your spectrometer using an arc lamp with known emission lines.

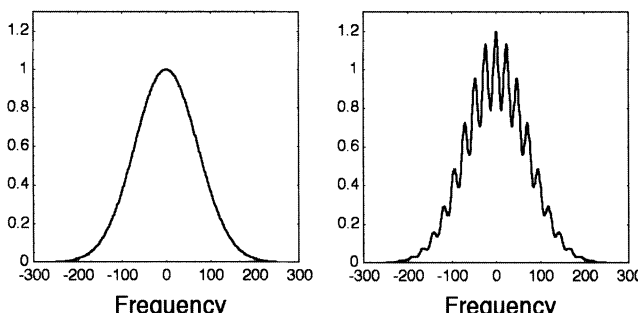


Fig. 4.21: Effects of stray light on measurements of the spectrum. Here we have added to a Gaussian spectrum an additional 1% of light energy with identical spectrum but with a slight delay, yielding frequency fringes of 20% in amplitude. (The spectrum is plotted in arbitrary units against the frequency difference from a center frequency.)

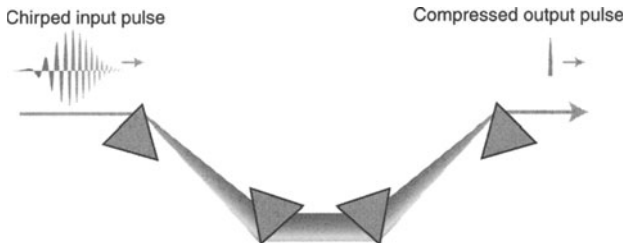


Fig. 4.22: A pulse compressor for removing chirp from a pulse. Note that, after two prisms, there is much spatial chirp in the beam. If this is not precisely compensated, the output pulse will have some spatial chirp. This effect is one of the most common reasons for a poor pulse measurement.

4) *Spatio-temporal effects*: For example, the redder spectral components of the beam could be on the left of a beam and the bluer components could be on the right, a phenomenon referred to as *spatial chirp*, in analogy with temporal chirp. Any dispersive element will introduce this effect into a beam. Of course, it's common practice to compensate for dispersion with another dispersive element, yielding a beam with no angular dispersion, but still with a great deal of spatial chirp. As a result, making a spectral measurement over a small spatial region of the beam will yield different spectra for different positions.

This problem is common. Pulse compressors (see Fig. 4.22) use pairs of gratings or prisms, which introduce dispersion, which must be compensated accurately before any spectral measurement is attempted.

Systematic Error in Measurements of the Autocorrelation

Numerous sources of systematic error can also be present in the measured autocorrelation. Many are due to misalignment effects that can introduce distortions—and it is difficult to know when the measured autocorrelation is free of such effects.

1) *Group-velocity dispersion (GVD)*: Because different wavelengths have different group velocities in media, a pulse will distort as it propagates through any medium, from lenses to the nonlinear medium used to measure the pulse. The pulse can even be distorted by the dielectric coating on a mirror. Even air can distort a pulse whose wavelength is near an air molecule's resonance, which occur in the UV and IR, where, as a result, dispersion (the variation of refractive index with wavelength) is large. The distortion is given by Eq. (2.36) and so is easily modeled. But, because their removal requires knowledge of the full pulse field, these effects cannot be removed from an autocorrelation or FRAC trace.

It's therefore very important to minimize the amount of material in the beam both in the pulse-measurement device and on the way to it. For FROG

measurements, which measure the full pulse field, however, this effect can be corrected using the above equation. Nevertheless, it's best to minimize it in the first place, even when using FROG.

2) *Asymmetry*: The expression for the autocorrelation assumes that the two pulses in the autocorrelator are identical. If one passes through more material than the other, then distortions due to material dispersion will cause asymmetries in the resulting autocorrelation trace. This effect can be difficult to avoid because the required beam splitter reflects one pulse, but transmits the other, causing only the latter to pass through glass. A compensator plate in the other beam is required to equalize the pulses. This is especially important in a FRAC.

3) *Group-velocity mismatch (GVM) or phase-matching bandwidth*: The nonlinear-optical process utilized in a pulse-measurement device must have sufficient bandwidth to efficiently convert the entire spectrum of the pulse to its appropriate signal field. If the nonlinear medium's bandwidth is insufficient, the pulse-measurement device will produce an erroneous result.

It's not correct to think of this effect as causing the device to measure only those frequencies that are phase-matched, which would always yield a narrower-band and hence longer pulse. This is because the effect in question is nonlinear, and we're not measuring the signal pulse, just its energy vs. delay. Indeed, this effect usually produces a measurement indicating a *shorter* pulse length than in reality.

Here's why. Figure 4.23 shows theoretical FROG traces, which are simply spectrally resolved autocorrelations, that is, the spectrum of the autocorrelation signal instead of its mere energy, vs. delay. (We'll explain FROG in much more detail later, but we thought you might like to see some of the power of FROG a bit early.) The three traces are for crystals of three different thicknesses. If α is the ratio of the crystal phase-matching bandwidth to the pulse spectral bandwidth, then a proper measurement requires $\alpha \gg 1$. But in Fig. 4.23 (center and right), we're violating this condition big-time. Since FROG is the spectrally resolved autocorrelation, then un-spectrally-resolving it yields the autocorrelation. Since un-spectrally-resolving means just integrating with respect to frequency, the intensity autocorrelation is just the integral of the FROG traces with respect to frequency. Thus the effect of using a crystal that has too little bandwidth is a simple cropping of the trace in frequency.

Okay, we're ready to interpret the traces below. The trace at left is the correct trace for the pulse measured (a pulse with cubic spectral phase) because the nonlinear-optical bandwidth is sufficient. But notice that, as the bandwidth of the crystal decreases (and α decreases below unity), the trace becomes cropped, and it's the large delay regions that get cropped! Thus the autocorrelation narrows as the crystal increases in thickness—about 30% narrower for the thickest crystal (at right).

Thus, you can usually shorten your pulse simply by using a crystal that's too thick. Of course, the measurement would be wrong.

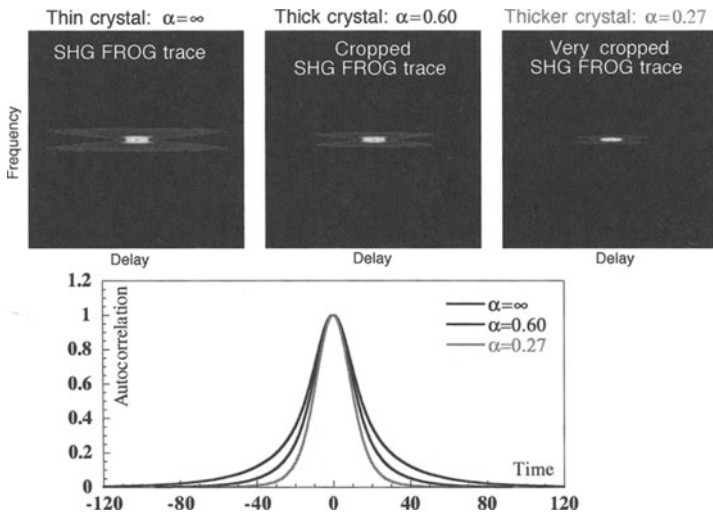


Fig. 4.23: The effect of a thick crystal (and the resulting GVM) on intensity autocorrelation measurements. Typically, using a crystal that is too thick yields a pulse measurement that erroneously indicates a shorter pulse.

By the way, the effect of a thick medium on an autocorrelation is usually considered to be quite mysterious, and the mathematics behind it complex. But the technique we just used to see these effects was quite simple and intuitive. It simply involves computing the FROG trace of the pulse and integrating it with respect to frequency to yield the autocorrelation. Integrations of the FROG trace with respect to one or the other of its co-ordinates, by the way, produce quantities called the “marginals.” We’ll discuss them more in Chapter 10, where you’ll see that they’re very powerful, allowing us to check our FROG measurement for systematic error—and even correct for it.

4) *Pulse-front tilt:* The most general expression for a pulse is $E(x, y, z, t)$, but we usually assume that this function separates into the product of independent functions of space and time. As a result, if we were to put an aperture in the beam and measure the spectrum of only a small region, we’d get the same result no matter where in the beam the aperture was. Unfortunately, this assumption isn’t always satisfied in practice. Any dispersive element will not only introduce angular dispersion into the beam (which obviously violates this assumption), but also pulse-front tilt (see Fig. 4.24). Pulse fronts are the contours of constant intensity (to be distinguished from phase fronts, which are contours of constant phase). Ordinarily, we tend to assume that pulses have pulse fronts that are ellipsoids with axes parallel and perpendicular to the propagation direction. But this isn’t always the case. It’s important to keep this effect in mind when propagating beams inside an autocorrelator because the direction of tilt reverses upon reflection. Thus, if the pulse front is tilted, an

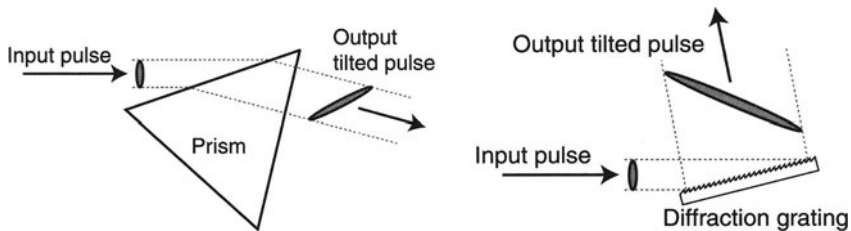


Fig. 4.24: Pulse-front tilt from dispersive elements. Left: In passing through a prism, light that passes near the tip sees less material than does light that passes near the base. While the phase delay vs. transverse position results in the phase fronts remaining perpendicular to the direction of propagation, the group delay is longer and results in pulse fronts having tilt, as shown. Right: In diffracting off a grazing-incidence grating, light takes different paths, and the pulse front tilt is clear from the drawing.

autocorrelator whose two beams have an odd and even number of reflections, respectively, will yield a longer autocorrelation trace than an autocorrelator whose two paths involve, say, an odd and even number of reflections each. We'll have a lot more to say on this subject in Chapter 7.

5) *Spatial variations in pulse spectrum:* Spatial variations in the beam can also confuse an autocorrelator—and any other pulse-measurement device. Spatial chirp is an especially unpleasant effect for pulse-measurement devices because it violates our assumption that the intensity and phase vs. time are the same throughout the beam. Worse, it can often go undiagnosed. Significant spatial chirp usually makes a FRAC trace appear to correspond to a shorter pulse. It also affects the intensity autocorrelation. And it can simply confuse the FROG algorithm, causing it to stagnate. This latter confusion is probably a good thing, however, because, if your pulse has different intensities and phases throughout it, it would be inappropriate for any device to attribute a single intensity and phase to it.

6) *Transverse geometrical distortions:* Using too large an angle between beams in an autocorrelator can yield a geometrical distortion because the delay can vary across the beam, which always lengthens the measured pulse. Chapter 7 has much more to say about this effect, which can always be made to be negligible. Indeed, this effect can be very beneficial: it's the way we achieve single-shot operation.

7) *Misalignment while scanning the delay:* An autocorrelator typically requires scanning the delay by moving a mirror, meanwhile maintaining the precise overlap between the two beams in the nonlinear medium. So it's important that the mirror's motion not misalign this precise overlap by walking the beam to the side. Typically, we align an autocorrelator by setting the delay to zero and then tweaking all the mirrors for maximum signal energy. If the translation stage used to scan the delay wobbles, then the alignment will be best at zero delay and will drop off as the stage moves away from this delay. Thus this effect would yield a shorter pulse than the correct one, and you

might not notice it, unless you scan to a large positive or negative delay and attempt to improve the alignment.

Single-Shot Autocorrelation

For high-repetition-rate ultrashort-pulse lasers, there isn't much variation from pulse to pulse. As a result, a spectrum may be obtained by scanning a monochromator in time or by leaving the shutter open on a camera or diode array at a spectrometer output, and averaging over many pulses. Similarly, the delay in an autocorrelator may be scanned in time with confidence that the pulse hasn't changed during the scan.

Some amplified laser systems have considerably lower repetition rates, however, and non-negligible pulse-to-pulse variations are expected. In this latter case, we must use a single-shot method. It's easy to obtain a single-shot spectrum, simply by opening the spectrometer camera shutter for only a single laser pulse. Single-shot autocorrelation, however, is more complex because the delay must somehow be scanned during a single pulse.

A single-shot autocorrelation trace is obtained by mapping the delay onto position and spatially resolving the autocorrelation signal using a camera or array detector. This involves crossing the two beams in the nonlinear-optical crystal at a large angle, so that, on the left, one pulse precedes the other, and, on the right, the other precedes the one (we'll discuss this in more detail in Chapter 7) [15,49,50]. In this manner, the delay ranges from a negative value on one side of the crystal to a positive value on the other. Usually, we focus with a cylindrical lens, so the beams are line-shaped at the crystal, and the range of delays is greater.

Systematic Error in Single-Shot Autocorrelation

1) *Non-uniform beam profile*: Because single-shot methods map delay onto position, they transform a measurement vs. delay into one vs. position. Basically, such methods turn the spatial profile of the beam into the intensity autocorrelation (or FROG trace). Thus it's important that the beam spatial profile not have structure or variation vs. position in the first place, which could bias the measurement. The beam should be big compared to the resulting beam size produced by the pulse measurement.

2) *Longitudinal geometrical distortions*: The delay between the two pulses can vary along the beam path as the beam propagates through the nonlinear medium. This can cause the trace to spread in delay, leading to a longer measured pulse than would be correct. See Chapter 7 for more details on this distortion. Fortunately, this effect does not occur in SHG-based methods, and it is usually vanishingly small in most other measurements, providing the apparatus is appropriately designed.

Quality Control

It is not sufficient to be able to measure a pulse. It is also necessary to know whether one has done so correctly. And, unfortunately, as we have just seen, there are many things that can go wrong in any measurement. Thus, an important property that a pulse-measurement technique should have is some type of feedback as to whether the measurement has been made correctly.

So what assurances do we have that a measured spectrum, autocorrelation, or FRAC is correct? Unfortunately, not many.

About all we can say about a spectrum is that it shouldn't go negative—which is precious little.

Autocorrelations (second- or higher-order) must have their maxima at zero delay. Second-order autocorrelations must also be symmetrical.

A FRAC must also have its maximum at zero delay and be symmetrical. In addition, the FRAC peak-to-background ratio must be 8. Finally, the fringes in FRAC must occur at the light frequency and twice this number. This allows an automatic calibration. These constraints make FRAC the most reliable of the autocorrelation methods.

Conclusions

Despite drawbacks, ambiguities, and often unknown information content, the autocorrelation and spectrum have remained the standard measures of ultrashort pulses for over twenty-five years, largely for lack of better methods. But they have allowed rough estimates for pulse lengths and time-bandwidth products, and they have helped researchers to make unprecedented progress in the development of sources of ever-shorter light pulses.

References

1. Maier, M., W. Kaiser, and J.A. Giordmaine, Phys. Rev. Lett., 1966. **17**: p. 1275.
2. Giordmaine, J.A., et al., *Two-Photon Excitation of Fluorescence By Picosecond Light Pulses*. Applied Physics Letters, 1967. **11**(7): p. 216–18.
3. Ippen, E.P. and C.V. Shank, *Ultrashort Light Pulses—Picosecond Techniques and Applications*, ed. S.L. Shapiro. 1977, Berlin: Springer-Verlag.
4. Stark, H., ed. *Image Recovery: Theory and Application*. 1987, Academic Press: Orlando.
5. Akutowicz, E.J., *On the Determination of the Phase of a Fourier Integral, I*. Trans. Amer. Math. Soc., 1956. **83**(September): p. 179–92.
6. Akutowicz, E.J., *On the Determination of the Phase of a Fourier Integral, II*. Trans. Amer. Math. Soc., 1957. **84**: p. 234–8.
7. Sala, K.L., G.A. Kenney-Wallace, and G.E. Hall, *CW Autocorrelation Measurements of Picosecond Laser Pulses*. IEEE Journal of Quantum Electronics, 1980. **16**(9): p. 990–6.
8. Rayner, D.M., P.A. Hackett, and C. Willis, *Ultraviolet Laser, Short Pulse-Width Measurement by Multiphoton Ionization Autocorrelation*. Review of Scientific Instruments, 1982. **53**(4): p. 537–8.
9. Kintzer, E.S. and C. Rempel, *Near-Surface Second-Harmonic Generation for Autocorrelation Measurements in the UV*. Applied Physics B, 1987. **42**: p. 91–5.
10. Bourne, O.L. and A.J. Alcock, *Ultraviolet and Visible Single-Shot Autocorrelator Based on Multiphoton Ionization*. Review of Scientific Instruments, 1986. **57**(12): p. 2979–82.

11. Dadap, J.I., et al., *Two-Photon Absorption in Diamond and Its Application to Ultraviolet Femtosecond Pulsewidths Measurement*. OL, 1991. **16**(7): p. 499–501.
12. Dixon, G.J., *Advanced techniques measure ultrashort pulses*. Laser Focus World, 1997. **33**(9): p. 99–102, 104–5.
13. Hutchinson, M.H.R., et al., *Measurement of 248-nm, Subpicosecond Pulse Durations by Two-Photon Fluorescence of Xenon Excimers*. Optics Letters, 1987. **12**(2): p. 102–4.
14. Tünnermann, M.H.R., et al., *Single-Shot Autocorrelator for KrF Subpicosecond Pulses Based on Two-Photon Fluorescence of Cadmium Vapor at $\lambda = 508$ nm*. OL, 1991. **16**(6): p. 402–4.
15. Wyatt, R. and E.E. Marinero, *Versatile Single-Shot Background-Free Pulse Duration Measurement Technique for Pulses of Subnanosecond to Picosecond Duration*. Applied Physics, 1981. **25**: p. 297–301.
16. Ishida, Y., K. Naganuma, and T. Yajima, *Self-Phase Modulation in Hybirdly Mode-Locked CW Dye Lasers*. J. Quantum Electronics, 1985. **21**(1): p. 69–77.
17. Trebino, R., E.K. Gustafson, and A.E. Siegman, *Fourth-Order Partial-Coherence Effects in the Formation of Integrated-Intensity Gratings with Pulsed Light Sources*. J. Opt. Soc. Amer. B, 1986. **3**: p. 1295.
18. Birmontas, A., et al., *Determination of the duration of fluctuating picosecond optical pulses*. Soviet Journal of Quantum Electronics, 1982. **12**(6): p. 792–4.
19. Bracewell, R.N., *The Fourier Transform and Its Applications*. 2nd ed. 1986, New York: McGraw-Hill.
20. Diels, J.C. and W. Rudolph, *Ultrashort Laser Pulse Phenomena*. 1996, San Diego: Academic Press.
21. Penman, Z.E., et al., *Experimental comparison of conventional pulse characterisation techniques and second-harmonic-generation frequency-resolved optical gating*. Optics Communications, 1998. **155**(4–6): p. 297–300.
22. Etchepare, J., G. Grillon, and A. Orszag, *Third Order Autocorrelation Study of Amplified Subpicosecond Laser Pulses*. IEEE Journal of Quantum Electronics, 1983. **19**(5): p. 775–8.
23. Janszky, J. and G. Corradi, *Full Intensity Profile Analysis of Ultrashort Laser Pulses Using Four-Wave Mixing or Third Harmonic Generation*. Optics Communications, 1986. **60**(4): p. 251–6.
24. Sarukura, N., et al., *Single-Shot Measurement of Subpicosecond KrF Pulse Width by Three-Photon Fluorescence of the XeF Visible Transition*. Optics Letters, 1988. **13**(11): p. 996–8.
25. Schulz, H., et al., *Measurement of Intense Ultraviolet Subpicosecond Pulses Using Degenerate Four-Wave Mixing*. IEEE Journal of Quantum Electronics, 1989. **25**(12): p. 2580–5.
26. Fischer, R., J. Gauger, and J. Tilgner, *Fringe Resolved Third-Order Autocorrelation Functions*. Proceedings of American Institute of Physics Conference, 1988. **172**: p. 727–9.
27. Levine, A.M., et al., *Induced-Grating Autocorrelation of Ultrashort Pulses in a Slowly responding Medium*. J. Opt. Soc. Amer. B, 1994. **11**(9): p. 1609–18.
28. Trebino, R., et al., *Chirp and Self-Phase Modulation in Induced-Grating Autocorrelation Measurements of Ultrashort Pulses*. Opt. Lett., 1990. **15**: p. 1079–81.
29. Johnson, A.M., et al., *Microwatt Picosecond Pulse Autocorrelator Using Photorefractive GaAs:Cr*, in *OSA Annual Meeting*. 1988, Optical Society of America: Washington, D.C.
30. Lohmann, A.W., G. Weigelt, and B. Wirnitzer, *Speckle Masking in Astronomy: Triple Correlation Theory and Applications*. Applied Optics, 1983. **22**(24): p. 4028–37.
31. Lohmann, A.W. and B. Wirnitzer, *Triple Correlations*. IEEE Proceedings, 1984. **72**(7): p. 889–901.
32. Paultre, N.G.J. and A.K. Majumdar, *A New Triple Correlator Design for the Measurement of Ultrashort Laser Pulses*. Optics Communications, 1991. **81**(1,2): p. 95–100.
33. Paultre, N.G.J. and A.K. Majumdar, *A New Triple Correlation Technique for Measuring Ultrashort Laser Pulses*. Review of Scientific Instruments, 1991. **62**(3): p. 567–78.
34. Kakarala, R. and G.J. Iverson, *Uniqueness of results for multiple correlations of periodic functions*. Journal of the Optical Society of America A, 1993. **10**(7): p. 1517–28.
35. Peatross, J. and A. Rundquist, *Temporal Decorrelation of short laser pulses*. Journal of the Optical Society of America B, 1998. **15**(1): p. 216–22.
36. Gerchberg, R.W. and W.O. Saxton, *A Practical Algorithm for the Determination of Phase from Image and Diffraction Plane Pictures*. Optik, 1972. **35**: p. 237–46.
37. Saxton, W.O., *Computer Techniques for Image Processing in Electron Microscopy*. 1978, New York: Academic Press.
38. Chung, J.-H. and A.M. Weiner, *Ambiguity of ultrashort pulse shapes retrieved from the intensity autocorrelation and power spectrum*. IEEE Journal on Selected Topics in Quantum Electronics, 2001. **7**(4): p. 656–66.
39. Diels, J.C., J.J. Fontaine, and F. Simoni, *Phase Sensitive Measurements of Femtosecond Laser Pulses From a Ring Cavity*, in *Proceedings of the International Conference on Lasers*. 1983, STS Press: McLean, VA. p. 348–55.

40. Diels, J.C.M., et al., *Control and Measurement of Ultrashort Pulse Shapes (in Amplitude and Phase) with Femtosecond Accuracy*. Applied Optics, 1985. **24**(9): p. 1270–82.
41. Diels, J.C., *Measurement Techniques With Mode-Locked Dye Laser*, in *Ultrashort Pulse Spectroscopy and Applications*. Proceedings of SPIE. 1985, SPIE Press: Bellingham. p. 63–70.
42. Yan, C. and J.C. Diels, *Amplitude and Phase Recording of Ultrashort Pulses*. Journal of the Optical Society of America B, 1991. **8**(6): p. 1259–63.
43. Diels, J.C.M., et al. *The Femto-nippicker*. in *Conference on Lasers & Electro-Optics*. 1987.
44. Le Blanc, S.P., G. Szabo, and R. Sauerbrey, *Femtosecond Single-Shot Phase-Sensitive Autocorrelator for the Ultraviolet*. Optics Letters, 1991. **16**(19): p. 1508–10.
45. Szabo, G., Z. Bor, and A. Muller, *Phase-Sensitive Single-Pulse Autocorrelator for Ultrashort Laser Pulses*. Optics Letters, 1988. **13**(9): p. 746–8.
46. Naganuma, K., K. Mogi, and H. Yamada, *Time Direction Determination of Asymmetric Ultrashort Optical Pulses from Second-Harmonic Generation Autocorrelation Signals*. APL, 1989. **54**(13): p. 1201–2.
47. Naganuma, K., K. Mogi, and H. Yamada, *General Method for Ultrashort Light Pulse Chirp Measurement*. IEEE J. Quant. Electron., 1989. **25**(6): p. 1225–33.
48. Naganuma, K., K. Mogi, and H. Yamada, *Group-Delay Measurement Using the Fourier Transform of an Interferometric Cross Correlation Generated by White Light*. Optics Letters, 1990. **15**(7): p. 393–5.
49. Brun, A., et al., *Single-Shot Characterization of Ultrashort Light Pulses*. J. Phys. D., 1991. **24**: p. 1225–33.
50. Szatmári, S., F.P. Schäfer, and J. Jethwa, *A Single-Shot Autocorrelator for the Ultraviolet with a Variable Time Window*. Review of Scientific Instruments, 1990. **61**(3): p. 998–1003.

5. FROG

Rick Trebino

The Time-Frequency Domain

In the previous chapter, we considered ultrashort-light-pulse measurement techniques that operated purely in the time domain (autocorrelation) and purely in the frequency domain (spectrum). And the results were less than satisfactory. This suggests that we consider a different approach, and the approach that will solve the problem involves a hybrid domain: the *time-frequency domain* [1,2]. This intermediate domain has received much attention in acoustics and applied mathematics research, but it has received only scant use in optics. Nevertheless, even if you don't think you're familiar with it, you are.

Measurements in the time-frequency domain involve both temporal *and* frequency resolution simultaneously. A well-known example of such a measurement is the *musical score*, which is a plot of a sound wave's short-time spectrum vs. time. Specifically, this involves breaking the sound wave up into short pieces and plotting each piece's spectrum (vertically) as a function of time (horizontally). So the musical score is a function of time as well as frequency. See Fig. 5.1. In addition, there's information on the top indicating intensity.

If you think about it, the musical score isn't a bad way to look at a waveform. For simple waveforms containing only one note at a time (we're not talking about symphonies here), it graphically shows the waveform's instantaneous frequency, ω , vs. time, and, even better, it has additional information on the top indicating the approximate intensity vs. time (e.g., fortissimo or pianissimo). Of course, the musical score can handle symphonies, too.

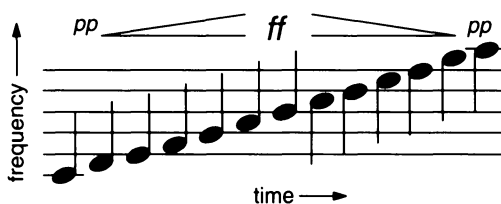


Fig. 5.1: The musical score is a plot of an acoustic waveform's frequency vs. time, with information on top regarding the intensity. Here the wave increases in frequency with time. It also begins at low intensity (pianissimo), increases to a high intensity (fortissimo), and then decreases again. Musicians call this waveform a "scale," but ultrafast laser scientists refer to it as a "linearly chirped pulse."

A mathematically rigorous version of the musical score is the spectrogram, $\Sigma_g(\omega, \tau)$ [3]:

$$\Sigma_g^E(\omega, \tau) \equiv \left| \int_{-\infty}^{\infty} E(t) g(t - \tau) \exp(-i\omega t) dt \right|^2 \quad (5.1)$$

where $g(t - \tau)$ is a variable-delay gate function, and the subscript on the Σ indicates that the spectrogram uses the gate function, $g(t)$. Figure 5.2 is a graphical depiction of the spectrogram, showing a linearly chirped Gaussian pulse and a rectangular gate function, which gates out a piece of the pulse. For the case shown in Fig. 5.2, it gates a relatively weak, low-frequency region in the leading part of the pulse. The spectrogram is the set of spectra of all gated chunks of $E(t)$ as the delay, τ , is varied.

The spectrogram is a highly intuitive display of a waveform. Some examples of it are shown in Fig. 5.3, where you can see that the spectrogram intuitively displays the pulse instantaneous frequency vs. time. And pulse intensity vs. time is also evident in the spectrogram. Indeed, acoustics researchers can easily directly measure the intensity and phase of sound waves, which are many orders of magnitude slower than ultrashort laser pulses, but they often choose to display them using a time-frequency-domain quantity like the spectrogram. Importantly, knowledge of the spectrogram of $E(t)$ is sufficient to essentially completely determine $E(t)$ [3,4] (except for a few unimportant ambiguities, such as the absolute phase, which are typically of little interest in optics problems).

Frequency-Resolved Optical Gating (FROG) measures a spectrogram of the pulse [5–13].

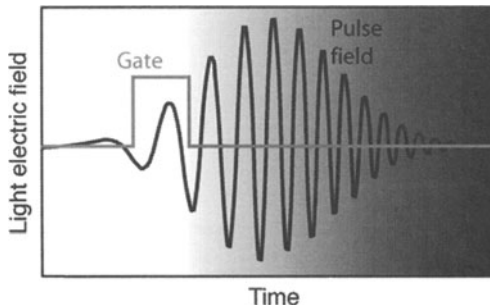


Fig. 5.2: Graphical depiction of the spectrogram. A gate function gates out a piece of the waveform (here a linearly chirped Gaussian pulse), and the spectrum of that piece is measured or computed. The gate is then scanned through the waveform and the process repeated for all values of the gate position (i.e., delay).

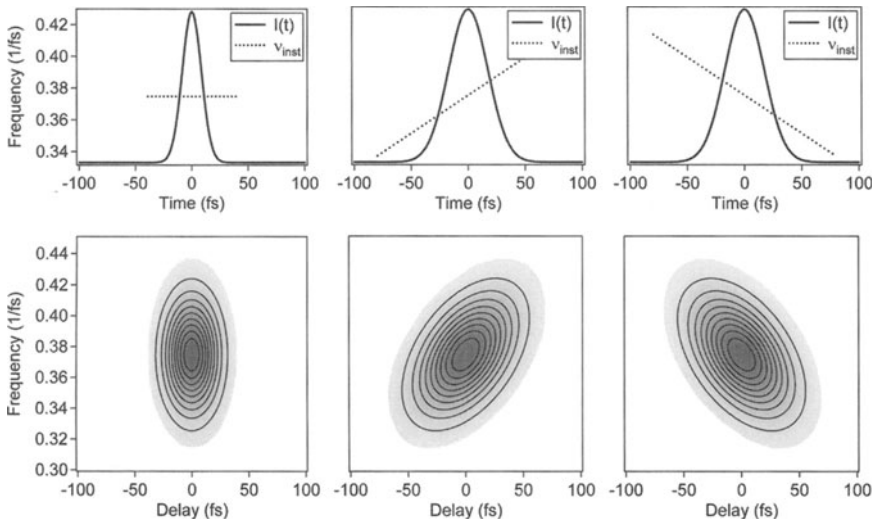


Fig. 5.3: Spectrograms (bottom row) for linearly chirped Gaussian pulses (top row), all with the same Gaussian spectrum and using a Gaussian gate pulse. The spectrogram, like the musical score, reflects the pulse instantaneous frequency vs. time. It also yields the pulse intensity vs. time: notice that the shortest pulse (left) has the narrowest spectrogram. And if we look at the spectrogram sideways, it yields the group delay vs. frequency (as well as the spectrum).

Introduction to FROG

Okay, so a spectrogram is a good idea. But recall the big dilemma of pulse measurement: “In order to measure an event in time, you need a shorter one.” In the spectrogram, then, isn’t the gate function precisely that mythical shorter event, the one we *don’t* have?

Indeed, that is the case.

So, as in autocorrelation, we’ll have to use the pulse to measure itself. We must gate the pulse with itself. And to make a spectrogram of the pulse, we’ll have to spectrally resolve the gated piece of the pulse.

Will this work? It doesn’t sound much better than autocorrelation, which also involves gating the pulse with itself (but without any spectral resolution). And autocorrelation isn’t sufficient to determine even the intensity of the pulse, never mind its phase, too. So how do we resolve the dilemma?

And that’s not the only problem. Even if this approach does somehow resolve the fundamental dilemma of ultrashort pulse measurement, spectrogram inversion algorithms assume that we know the gate function [4]. After all, who would’ve imagined gating a sound wave *with itself* when it’s so easy to do so electronically with detectors because acoustic time scales are so slow? So no one ever considered a spectrogram in which the unknown function gated itself—an idea, it would seem, that could occur to only a seriously disturbed individual. Unfortunately, we have no choice; we *must* gate the

pulse with itself. But by gating the unknown pulse with itself—i.e., a gate that is also unknown—we can't use available spectrogram inversion algorithms. So all those nice things we said about the spectrogram don't necessarily apply to what we're planning to do. How will we avoid these problems?

Hang on. You'll see.

In its simplest form, FROG is any autocorrelation-type measurement in which the autocorrelator signal beam is spectrally resolved [5,8,9]. Instead of measuring the autocorrelator signal energy vs. delay, which yields an autocorrelation, FROG involves measuring the signal *spectrum* vs. delay.

As an example, let's consider, not an SHG autocorrelator, but a polarization-gate (PG) autocorrelation geometry. Ignoring constants, as usual, this third-order autocorrelator's signal field is $E_{\text{sig}}(t, \tau) = E(t)|E(t - \tau)|^2$. Spectrally resolving yields the Fourier Transform of the signal field with respect to time, and we measure the squared magnitude, so the FROG trace is given by:

$$I_{\text{FROG}}^{\text{PG}}(\omega, \tau) = \left| \int_{-\infty}^{\infty} E(t)|E(t - \tau)|^2 \exp(-i\omega t) dt \right|^2 \quad (5.2)$$

Note that the (PG) FROG trace is a spectrogram in which the pulse intensity gates the pulse field. In other words, the pulse gates itself.

So how will we obtain $E(t)$ from its FROG trace?

First, consider $E_{\text{sig}}(t, \tau)$ to be the one-dimensional Fourier transform with respect to τ , *not* t , of a new quantity that we will call $\bar{E}_{\text{sig}}(t, \Omega)$:

$$E_{\text{sig}}(t, \tau) = \int_{-\infty}^{\infty} \bar{E}_{\text{sig}}(t, \Omega) \exp(-i\Omega\tau) d\Omega \quad (5.3)$$

Since this Fourier transform involves τ , and not t , we're using a bar, rather than a tilde, on top of the Fourier-transformed functions here.

Now, it's important to note that, once found, $E_{\text{sig}}(t, \tau)$ or $E_{\text{sig}}(t, \Omega)$ easily yields the pulse field, $E(t)$. Specifically, if we know $\bar{E}_{\text{sig}}(t, \Omega)$, we can inverse-Fourier-transform to obtain $E_{\text{sig}}(t, \tau)$. Then we can substitute $\tau = t$: $E_{\text{sig}}(t, t) = E(t)|E(0)|^2$. Since $|E(0)|^2$ is merely a multiplicative constant, and we don't care about such constants, then as far as we're concerned, $E_{\text{sig}}(t, t) = E(t)$. Thus, to measure $E(t)$, it is sufficient to find $\bar{E}_{\text{sig}}(t, \Omega)$.

We now substitute the above equation for $E_{\text{sig}}(t, \tau)$ into the expression for the FROG trace, which yields an expression for the FROG trace in terms of $\bar{E}_{\text{sig}}(t, \Omega)$:

$$I_{\text{FROG}}^{\text{PG}}(\omega, \tau) = \left| \int_{-\infty}^{\infty} \int_{-\infty}^{\infty} \bar{E}_{\text{sig}}(t, \Omega) \exp(-i\omega t - i\Omega\tau) dt d\Omega \right|^2 \quad (5.4)$$

Here, we see that the measured quantity, $I_{\text{FROG}}^{\text{PG}}(\omega, \tau)$, is the squared magnitude of the two-dimensional Fourier transform of $\bar{E}_{\text{sig}}(t, \Omega)$.

Yeah, you're probably saying, that may be true, but is it helpful? We just took a difficult-looking one-dimensional integral-inversion problem and turned it into an *impossible*-looking two-dimensional integral-inversion problem. And we all learned in calculus class that, in order to solve integral equations, you're supposed to *reduce* the number of integral signs, not increase it. In doing this substitution, it would seem that we've made the problem harder, rather than easier!

But looking more closely at Eq. (5.4), it's more elegant than at first glance. From it, we see that the measured FROG trace yields the magnitude, but not the phase, of the two-dimensional Fourier transform of the desired quantity $\bar{E}_{\text{sig}}(t, \Omega)$. If we had the phase, we'd be done because we'd have $\bar{E}_{\text{sig}}(t, \Omega)$ in its entirety. So the problem is then to find the phase of $\bar{E}_{\text{sig}}(t, \Omega)$.

It turns out that this inversion problem is well known. It is called, quite reasonably, the *two-dimensional phase-retrieval problem* [14].

FROG and the Two-Dimensional Phase-Retrieval Problem

Now, we discussed a close relative of the two-dimensional phase-retrieval problem in the previous chapter, the *one-dimensional* phase-retrieval problem, and we concluded that it was bad news. Almost certainly, the two-dimensional analog of a one-dimensional piece of mathematical bad news can only be worse news.

Quite unintuitively, however, the two-dimensional phase-retrieval problem has an essentially *unique solution* and is a *solved* problem when certain additional information regarding $\bar{E}_{\text{sig}}(t, \Omega)$ is available such as that it has finite support (that is, is zero outside a finite range of values of t and Ω) [14–17]. This is in stark contrast to the one-dimensional problem, where many solutions can exist, despite additional information, such as finite support. Indeed, in the one-dimensional case, *infinitely* many additional solutions typically exist, as we saw. On the other hand, the two-dimensional phase-retrieval problem, when finite support is the case, has only the usual “trivial” ambiguities. If $\bar{E}_{\text{sig}}(t, \Omega)$ is the solution, then the ambiguities are:

- 1) an absolute phase factor $\exp(i\phi_0)$ $\bar{E}_{\text{sig}}(t, \Omega)$
- 2) a translation: $\bar{E}_{\text{sig}}(t - t_0, \Omega - \Omega_0)$
- 3) inversion: $\bar{E}_{\text{sig}}^*(-t, -\Omega)$

In addition, there is an extremely small probability that another solution may exist, but this is generally not the case for a given trace. This is what is meant by *essentially unique*. We'll have more to say shortly about the meaning of this vague-sounding phrase.

Okay, so the solution isn't really totally unique, but it's good enough for practical measurements, where we don't care about the trivial ambiguities,

and we probably won't be around long enough to do enough experiments to bump into one of the highly improbable ambiguities.

Now we should mention that finite support is only one type of constraint that one could have on the function whose two-dimensional Fourier magnitude is known. The point is that a much weaker constraint suffices to yield an essentially unique solution in two-dimensional phase retrieval problems than in one-dimensional ones. In other words, the same constraint that will yield an essentially unique solution in two-dimensional problems, when modified to one dimension, won't suffice to eliminate ambiguities in one-dimensional ones.

In FROG, we actually don't have finite support because our function is $\bar{E}_{\text{sig}}(t, \Omega)$, and its extent along the t axis is essentially that of $E(t)$, and its extent along the Ω axis is essentially that of the $\tilde{E}(\omega)$. Since no function can be finite in extent in both time and frequency, $\bar{E}_{\text{sig}}(t, \Omega)$ does not have finite support.

However, we do have another, much better constraint. We know that $E_{\text{sig}}(t, \tau) = E(t)|E(t - \tau)|^2$, which is a very strong constraint on the *mathematical form* that the signal field can have. Hence we refer to this constraint as the *mathematical-form constraint*. Since it results from the nonlinear-optical process used to generate the signal field, it is often also called the *nonlinear-optical constraint*. There are other versions of FROG whose constraints are slightly different. For example, in second-harmonic-generation (SHG) FROG, $E_{\text{sig}}(t, \tau) = E(t)E(t - \tau)$.

This additional information turns out to be sufficient, and thus, the problem is solved [5]. Indeed, it is solved in a particularly robust manner, with many other advantageous features, such as feedback regarding the validity of the data [11,18,19]. And many of the remaining chapters of this book discuss additional useful features of FROG.

So we're done. Because the FROG trace is related to a quantity that yields the pulse [$\bar{E}_{\text{sig}}(t, \Omega)$] by the two-dimensional phase-retrieval problem, and we have a reasonably strong constraint on $\bar{E}_{\text{sig}}(t, \Omega)$, then the FROG trace essentially uniquely yields the pulse field, $E(t)$, that is the full pulse intensity and phase. In Chapters 8 and 21, we'll discuss the algorithms that find the solution to the two-dimensional phase-retrieval problem for ultrashort-laser-pulse measurement in detail.

The Two-Dimensional Phase-Retrieval Problem and the Fundamental Theorem of Algebra

So why does the two-dimensional phase-retrieval problem yield unique results when the one-dimensional case does not? Interestingly, it is because the *Fundamental Theorem of Algebra*, which guarantees that we can factor polynomials, holds for polynomials of one variable, but *fails* for polynomials of two variables!

We'll now sketch the proof of this fascinating fact [14].

We consider the case of a set of data, which are necessarily discrete. So suppose, first, that we have a one-dimensional problem, a sequence of numbers, $\{f_1, f_2, \dots, f_N\}$, each corresponding to a different time, which could be the complex pulse field vs. time. Suppose we measure the magnitude of the Fourier transform of this sequence, $\{|F_1|, |F_2|, \dots, |F_N|\}$, and from this measurement, we'd like to find the original sequence, $\{f_1, f_2, \dots, f_N\}$. The discrete Fourier transform relates F_k to f_m :

$$F_k = \sum_{m=1}^N f_m e^{-2\pi i m k / N} \quad (5.5)$$

where m is our time variable.

We can rewrite this expression by letting $z = e^{-2\pi i k / N}$:

$$F_k = \sum_{m=1}^N f_m z^m \quad (5.6)$$

which is just a polynomial in the variable z . The Fundamental Theorem of Algebra guarantees that we can factor this polynomial, so we can write it as the product of its factors:

$$F_k = f_N(z - z_1)(z - z_2) \cdots (z - z_N) \quad (5.7)$$

where the z_k 's are the (potentially complex) zeroes of the polynomial in Eq. (5.6). Now, recall that we measure only the magnitude of each F_k .

$$|F_k| = |f_N(z - z_1)(z - z_2) \cdots (z - z_N)| \quad (5.8)$$

We must now ask, "Are there any ambiguities? That is, are there any other functions of m (or z) that yield the same values for $|F_k|$?" And the answer is clearly, "Yes." All that we need do is to complex-conjugate one or more factors in Eq. (5.8). Because the magnitude of a product is the same if we complex-conjugate any one of its factors, $|F_k|$ does not change under complex conjugation of any of its factors. By the way, you might be concerned that the complex conjugate of the variable $z = e^{-2\pi i k / N}$ is $z^* = e^{+2\pi i k / N}$, which is not of the correct form for the Fourier transform. However, because $e^{2\pi i N / N} = 1$, we can divide z^* by this quantity and write $z^* = e^{2\pi i (k-N) / N} = e^{-2\pi i (N-k) / N}$, which is of the correct form.

So in one-dimensional phase retrieval, there are as many ambiguities as different subsets of factors we can complex-conjugate, or 2^N .

Now, suppose our data are two-dimensional $\{|F_{11}|, |F_{12}|, \dots, |F_{NN}|\}$. This will require a two-dimensional discrete Fourier transform:

$$F_{k,h} = \sum_{m,n=1}^N f_{m,n} e^{-2\pi i(mk+nh)/N} \quad (5.9)$$

which can be rewritten, letting $y = e^{-2\pi ih/N}$ and $z = e^{-2\pi ik/N}$:

$$F_{k,h} = \sum_{m,n=1}^N f_{m,n} z^m y^n \quad (5.10)$$

which is a two-dimensional polynomial.

But the Fundamental theorem of Algebra fails for polynomials of two variables, so this polynomial can't be factored. And, as a result, there won't be any ambiguities.

Actually, polynomials of two variables occasionally can be factored, and then an ambiguity results, but as N increases, such cases become increasingly rare. As a result, we typically say that the solution in two-dimensional phase retrieval is *essentially unique*.

Of course we can complex-conjugate the entire expression or multiply it by a complex exponential with a constant phase factor in it, hence the trivial ambiguities.

Also, note that we built in the finite-support constraint (or periodicity) by using a finite set of data.

Finally, as in the one-dimensional case, it's important to ask how densely distributed the ambiguities are. It can be shown that the ambiguities are quite sparse, as sparse as a continuous function of one variable in a two-dimensional plane. The probability of accidentally stumbling on one is very close to zero and decreases rapidly as N increases.

The two-dimensional phase-retrieval problem occurs frequently in imaging problems [14,16,17,20–24], where the squared magnitude of the Fourier transform of an image is often measured and where finite support is common. The two-dimensional phase-retrieval problem and its solution are the basis of an entire field, that of image recovery. If you're interested in reading more on it, please check out Henry Stark's excellent book on this subject, *Image Recovery* [14].

Finally, it should be mentioned that the above argument must be modified for the FROG constraints. This has not yet been done, so a rigorous proof of essential uniqueness for FROG does not yet exist. However, thousands of pulses, many quite complex, have been retrieved using FROG, and no such ambiguities have ever been found (except for the trivial ones and a few that we will discuss that occur in SHG FROG). So don't worry. But if you come up with a proof, please let me know.

Understanding FROG

Okay, so FROG works because the Fundamental Theorem of Algebra fails for polynomials of two variables. That's all very interesting, but it's a bit abstract. What we'd really like to know is how, in practice, FROG gets around the fundamental dilemma of ultrashort laser pulse measurement, that to measure an event in time, you need a shorter one.

Another way to look at this issue is that phase retrieval is a type of de-convolution, which extracts information that's just beyond the resolution of the device and that initially doesn't seem to be there. For example, image de-convolution techniques can de-blur a photograph, thus retrieving details smaller in size than the apparent resolution of the camera that took the picture. After all, how else can CIA spy satellites read your license plate on the ground? (Please don't quote me on that...)

Indeed, recall Fig. 5.2, in which a shorter rectangular pulse gates the unknown longer pulse. This was the allegedly required shorter pulse. At the time you first looked at that figure, you were probably thinking, "Too bad we don't have an *infinitely short* gate pulse—a delta-function in time. That'd really do a nice job of measuring the pulse."

But you'd be wrong. If it really were the case that $g(t - \tau) = \delta(t - \tau)$, it's easy to do the integral and see that the resulting spectrogram would be completely independent of frequency. In fact, we would find that $\Sigma_g^E(\omega, \tau) = I(\tau)$. Thus, in this allegedly ideal case, the spectrogram reduces to precisely the pulse intensity vs. time! All phase-vs.-time information is lost!

So it turns out that using too short a gate pulse is a bad idea. The time-frequency domain is subtle. Having time- and frequency-domain information simultaneously can be a bit unintuitive. Remember, you can't have perfect time and frequency resolution at the same time, or you'd violate the uncertainty principle. The better your time resolution the worse your frequency resolution. Choosing the gate width determines the shape of your resolution region in time-frequency space. A great deal has been written about the ideal length of the gate pulse for making spectrograms. An excellent discussion of this issue is in Cohen's wonderful book, *Time-Frequency Analysis* [2]. One answer is that, for pulses whose phase variations dominate, the ideal gate pulse width, T_g , is given by:

$$T_g \sim 1/\sqrt{2|\phi''(t)|} \quad (5.11)$$

where $\phi''(t)$ is the second derivative of the phase vs. time. In other words, you'd like to resolve the fastest variations in the phase, but if you use too short a gate pulse, you lose all phase information completely, so it must be a compromise, which is the above result.

For general pulse measurement, however, use of a pulse as short as or slightly shorter than the pulse is desirable. In SHG FROG, the gate pulse is exactly as short as the pulse to be measured. In other FROG beam geometries, we will gate the pulse with itself squared or mag-squared, which typically

shortens the gate pulse a bit. For example, squaring a Gaussian pulse shortens it by about $\sqrt{2}$. This has proven to be ideal.

You may also wonder whether gating the complex (i.e., having nonzero phase) pulse by another complex function (i.e., having nonzero phase) is a good idea. After all, the simple picture of the making of a spectrogram in Fig. 5.2 shows a real gate pulse. Use of a real gate pulse adds no phase to the signal field whose spectrum is measured, but a complex gate function can change its color. And indeed, use of a complex gate function complicates visual interpretation of the spectrogram and hence FROG trace. The polarization-gate version of the FROG technique uses the mag-squared pulse as the gate, and it yields the most intuitive traces, and the pulse-retrieval algorithm works best for it. But we find that, although the traces of other FROG techniques are a bit more complicated and difficult to interpret by themselves, the technique works about as well in all cases, whether the gate is $E(t - \tau)$, $E^2(t - \tau)$, $E^*(t - \tau)$, or $|E(t - \tau)|^2$.

What do FROG traces look like for commonly encountered pulses? Polarization-gate FROG traces look just like the spectrograms in Fig. 5.2. Figure 6.2 gives a more complete array of traces for various pulses for the various gates corresponding to the various FROG beam geometries (which will be discussed in more detail in the next chapter).

Properties of FROG

The pulse intensity and phase may be estimated simply by looking at the experimental FROG trace, or the iterative algorithm may be used to retrieve the precise intensity and phase vs. time or frequency.

There are many nice features of FROG. FROG is very accurate. Few approximations are made regarding the pulse. All that must be assumed in FROG is a nearly instantaneously responding medium, and even that assumption has been shown to be unnecessary, as the medium response can be included in the pulse-retrieval algorithm (see Chapter 18) [25]. Similarly, any known systematic error in the measurement may also be modeled in the algorithm [18,19], although this is not generally necessary, except for extremely short pulses (<10 fs) or for exotic wavelengths. And systematic error can often be removed by preprocessing the measured trace (see Chapter 10) [19]. Also, unlike other ultrashort pulse measurement methods, FROG completely determines the pulse with essentially infinite temporal resolution [8,18]. It does this by using the time domain to obtain long-time resolution and the frequency domain for short-time resolution. As a result, if the pulse spectrogram is entirely contained within the measured trace, then there can be no additional long-time pulse structure (since the spectrogram is effectively zero for off-scale delays), and there can be no additional short-time pulse structure (since the spectrogram is essentially zero for off-scale frequency offsets). Interestingly, this extremely high temporal resolution can be obtained by using delay increments that are as large as the time scale of the structure. Again, this is because

the short-time information is obtained from large frequency-offset measurements. Thus, as long as the measured FROG trace contains all the nonzero values of the pulse FROG trace, the result is rigorous. (Of course, the trace typically only falls asymptotically to zero for delays and frequency offsets of $\pm\infty$, but these low values outside the measured trace do not significantly affect the retrieved pulse.)

Another useful and important feature that's unique to FROG is the presence of feedback regarding the validity of the measurement data. FROG actually contains two different types of feedback. The first is probabilistic, rather than deterministic, but it is still very helpful. It results from the fact that the FROG trace is a time-frequency plot, that is, an $N \times N$ array of points, which are then used to determine N intensity points and N phase points, that is, $2N$ points. There is thus significant over-determination of the pulse intensity and phase—there are many more degrees of freedom in the trace than in the pulse. As a result, the likelihood of a trace composed of randomly generated points corresponding to an actual pulse is very small. Similarly, a measured trace that has been contaminated by systematic error is unlikely to correspond to an actual pulse. Thus, convergence of the FROG algorithm to a pulse whose trace agrees well with the measured trace virtually assures that the measured trace is free of systematic error. Conversely, non-convergence of the FROG algorithm (which rarely occurs for valid traces) indicates the presence of systematic error. To appreciate the utility of this feature, recall that intensity autocorrelations have only three constraints: a maximum at zero delay, zero for large delays, and even symmetry with respect to delay. These constraints do not limit the autocorrelation trace significantly, and one commonly finds that the autocorrelation trace can vary quite a bit in width during alignment while still satisfying these constraints. It should be emphasized that this argument is merely probabilistic, and that, on one occasion, we encountered a systematic-error-contaminated SHG FROG trace that yielded convergence. However, the SHG FROG trace has additional symmetry that's lacking in other FROG methods, so such an occurrence is more likely there. The other FROG methods have so far reliably revealed systematic error in this manner.

Another feedback mechanism in FROG is deterministic and has proven extremely effective in revealing systematic error in SHG FROG measurements of $\sim 10\text{-fs}$ pulses, where crystal phase-matching bandwidths are insufficient for the massive bandwidths of the pulses to be measured. It involves computing the *marginals* of the FROG trace, that is, integrals of the trace with respect to delay or frequency. The marginals can be compared to the independently measured spectrum or autocorrelation, and expressions have been derived relating these quantities. Comparison with the spectrum is especially useful. Marginals can even be used to correct an erroneous trace. For more on this topic, see Chapter 10 [11,18,19].

In practice, FROG has been shown to work very well in the IR [26,27], visible [28], and UV [29–31]. Work is underway to extend FROG to other wavelength ranges, such as the x-ray. It has been used to measure pulses from

a few fs to many ps in length. It has measured pulses from fJ to mJ in energy. And it can measure simple near-transform-limited pulses to extremely complex pulses with time-bandwidth products in excess of 1000 (see Chapters 13 and 14). It can use nearly any fast nonlinear-optical process that might be available. FROG has proven to be a marvelously general technique that works. If an autocorrelator can be constructed to measure a given pulse, then making a FROG is straightforward since measuring the spectrum of it is usually easy.

What FROG doesn't measure

We've been saying that FROG measures the complete intensity and phase vs. time or frequency. Actually, there are a few aspects of the intensity and phase that FROG does not measure (the "trivial" ambiguities). First, since FROG is a magnitude-squared quantity, it doesn't measure the absolute phase, φ_0 , in the Taylor expansion of the spectral phase. Also, because FROG involves the pulse gating itself, there is no absolute time reference, so FROG doesn't measure the pulse arrival time, which corresponds in the frequency domain to φ_1 , the first-order term coefficient in the spectral-phase Taylor series. The mathematical-form constraint removes the direction-of-time, or inversion, ambiguity in all but one FROG variation. So φ_0 and φ_1 are the only two parameters not measured in FROG, although a few versions of FROG have their own unmeasured parameters in specific situations, which we'll discuss in the next chapter.

Appendix: Other Time-Frequency Quantities

There are infinitely many different possible time-frequency-domain quantities. Examples include the Wigner Distribution [32–35], the Wavelet Transform [36,37], and the Gabor Transform [1,2]. Indeed, most are considered by theorists to be better, more elegant measures than the spectrogram. For example, integrals of the Wigner Distribution over delay or frequency (the *marginals*) yield precisely the spectrum and intensity, respectively, which is very nice. Also, the measures just mentioned have direct inversions and don't require an iterative algorithm. So why don't we use one of them instead of the klunky old spectrogram?

The answer is that what the spectrogram lacks in theoretical mathematical elegance, it more than makes up for in experimental optical elegance. It's very easy to make a spectrogram in the lab (see, for example, Chapter 12). And so far no one's figured out how to make the others, and you can bet that, if someone does, it won't be easy. For example, making a Wigner Distribution would require making a time-reversed replica of the pulse. Making a Wavelet Transform would require that the gate pulse length be rescaled as the wavelength changes, among other complexities. All would require the measurement of

negative values, which means that the signal would have to measured against a coherent background, and the measurement becomes interferometric, which adds considerable complexity. And that's assuming we could figure out how to do it in the first place. So the spectrogram is looking a lot better now, isn't it?

Indeed, the iterative algorithm used to retrieve pulses in FROG will prove to be much more versatile than any of the above direct retrieval algorithms. For example, suppose you'd like to include a potential finite response time of the nonlinear medium used to make the measurements or the group-velocity dispersion the pulse experiences in propagating through said medium. This would achieve a more precise measurement. All of a sudden, the elegance of any quantity is gone, and the "modified Wigner Transform," for example, no longer easily yields the spectrum or intensity or has a direct inversion. The FROG spectrogram inversion algorithm, however, requires only minor modifications (see, for example, Chapters 16, 18 and 20).

The bottom line is that the more complex spectrogram inversion algorithm is the investment whose payoff is a very simple apparatus and very general technique. And if you simply need to measure a pulse and don't really care how it's done, you can simply buy the FROG algorithm software for a few hundred dollars, and you're done.

There is one quantity that can be generated in the lab and is a close relative of the spectrogram: the *sonogram* [38,39]. (By the way, there's no relation between this quantity and the medical images created using ultrasound that also go by the same name.) Experimentally, a sonogram involves spectrally filtering the pulse and then gating it in time, effectively the same operations as required by the spectrogram, but in opposite order. It's given by:

$$\Psi_{\tilde{g}}^{\tilde{E}}(\omega, \tau) \equiv \left| \int_{-\infty}^{\infty} \tilde{E}(\omega') \tilde{g}(\omega - \omega') \exp(+i\omega'\tau) d\omega' \right|^2 \quad (5.12)$$

where $\tilde{g}(\omega - \omega')$ is a frequency-gate, analogous to the time-gate, $g(t - \tau)$ used in the spectrogram. If $\tilde{g}(\omega)$ is the Fourier transform of $g(t)$, then it can be shown that the sonogram is precisely equivalent to the spectrogram! (This is why the FROG trace visually yields the group delay vs. frequency, as well as the instantaneous frequency vs. time; see Fig. 13.6.)

Indeed, if a spectrogram is a musical score of the waveform, the sonogram is a musical score rotated by 90°. And if the spectrogram asks the question, "What frequencies are occurring at a given time?" the sonogram asks, "At what times does a given frequency occur?"

To make a sonogram of a pulse in the lab, it's first necessary to generate a frequency-gate. This is usually done by frequency-filtering the pulse itself using a filter with a variable center frequency. This narrower-band pulse then undergoes cross-correlation with the original pulse for a range of different filter center frequencies. The sonogram is then the output energy vs. filter center frequency and delay. While "direct" inversion algorithms exist for sonograms, they require picking the "average" delay for each filter center frequency, which

can be very tricky. Experience has shown that it's better to use the FROG algorithm, which can be done since the sonogram is mathematically equivalent to the spectrogram [39].

Experimentally, the sonogram is more complex than FROG and also less sensitive than FROG because it performs the nonlinear-optical process after filtering, which throws away valuable pulse energy before it's needed. But it lacks the direction-of-time ambiguity of SHG FROG (see Chapter 6), so it's of interest in some cases.

One final comment on the sonogram: you also can make one by simply placing a well-characterized frequency filter—with *fixed* central frequency—in one arm of an SHG FROG device [40]. So this implementation is simpler experimentally than the standard sonogram arrangement.

References

1. Cohen, L., *Time-Frequency Distributions—A Review*. Proceedings of the IEEE, 1989. **77**(7): p. 941–81.
2. Cohen, L., *Time-Frequency Analysis*. 1995, Englewood Cliffs, NJ: Prentice-Hall.
3. Altes, R.A., *Detection, Estimation, and Classification with Spectrograms*. J. Acoust. Soc. Amer., 1980. **67**(4): p. 1232–46.
4. Nawab, S.H., T.F. Quatieri, and J.S. Lim, *Signal Reconstruction from Short-Time Fourier Transform Magnitude*. IEEE Transactions on Acoustics, Speech, and Signal Processing, 1983. **ASSP-31**(4): p. 986–98.
5. Trebino, R. and D.J. Kane, *Using Phase Retrieval to Measure the Intensity and Phase of Ultrashort Pulses: Frequency-Resolved Optical Gating*. J. Opt. Soc. Amer. A, 1993. **10**(5): p. 1101–11.
6. Trebino, R. and D.J. Kane, *The Dilemma of Ultrashort-Laser-Pulse Intensity and Phase Measurement and Applications*. IEEE J. Quant. Electron., 1999. **35**(4): p. 418–20.
7. Trebino, R., et al., *Measuring Ultrashort Laser Pulses in the Time-Frequency Domain Using Frequency-Resolved Optical Gating*. Review of Scientific Instruments, 1997. **68**(9): p. 3277–95.
8. Kane, D.J. and R. Trebino, *Single-Shot Measurement of the Intensity and Phase of an Arbitrary Ultrashort Pulse By Using Frequency-Resolved Optical Gating*. Opt. Lett., 1993. **18**(10): p. 823–5.
9. Kane, D.J. and R. Trebino, *Characterization of Arbitrary Femtosecond Pulses Using Frequency Resolved Optical Gating*. IEEE Journal of Quantum Electronics, 1993. **29**(2): p. 571–9.
10. DeLong, K.W. and R. Trebino, *Improved Ultrashort Pulse-Retrieval Algorithm for Frequency-Resolved Optical Gating*. J. Opt. Soc. Amer. A, 1994. **11**(9): p. 2429–37.
11. DeLong, K.W., R. Trebino, and D.J. Kane, *Comparison of Ultrashort-Pulse Frequency-Resolved-Optical-Gating Traces for Three Common Beam Geometries*. J. Opt. Soc. Amer. B, 1994. **11**(9): p. 1595–608.
12. DeLong, K.W., et al., *Frequency-Resolved Optical Gating With the Use of Second-Harmonic Generation*. J. Opt. Soc. Amer. B, 1994. **11**(11): p. 2206–15.
13. DeLong, K.W., et al., *Pulse Retrieval in Frequency-Resolved Optical Gating Based on the Method of Generalized Projections*. Optics Letters, 1994. **19**(24): p. 2152–4.
14. Stark, H., ed. *Image Recovery: Theory and Application*. 1987, Academic Press: Orlando.
15. Kotlyar, V.V., P.G. Seraphimovich, and V.A. Soifer, *Regularized Iterative Algorithm for the Phase Retrieval*. Optik, 1993. **94**(2): p. 96–9.
16. Fienup, J.R., *Phase Retrieval Algorithms: A Comparison*. Applied Optics, 1982. **21**(15): p. 2758–69.
17. Peri, D., *Optical Implementation of a Phase Retrieval Algorithm*. Applied Optics, 1987. **26**(9): p. 1782–5.
18. DeLong, K.W., D.N. Fittinghoff, and R. Trebino, *Practical Issues in Ultrashort-Laser-Pulse Measurement Using Frequency-Resolved Optical Gating*. IEEE J. Quant. Electron., 1996. **32**(7): p. 1253–64.
19. Taft, G., et al., *Measurement of 10-fs Laser Pulses*. Selected Topics in Quantum Electronics, 1996. **2**, Special Issue on Ultrafast Phenomena(3): p. 575–85.
20. Millane, R.P., *Phase Retrieval in Crystallography and Optics*. J. Opt. Soc. Am. A, 1990. **7**(3): p. 394–411.

21. Fienup, J.R., *Reconstruction of an Object from the Modulus of its Fourier Transform*. Optics Letters, 1978. **3**(1): p. 27–9.
22. Fienup, J.R. and C.C. Wackerman, *Phase-Retrieval Stagnation Problems and Solutions*. Opt. Soc. of Am. A, 1986. **3**: p. 1897–907.
23. Fienup, J.R., *Reconstruction of a Complex-Valued Object from the Modulus of its Fourier Transform Using a Support Constraint*. J. Opt. Soc. Am. A, 1987. **4**(1): p. 118–23.
24. Fienup, J.R. and A.M. Kowalczyk, *Phase Retrieval for a Complex-Valued Object by Using a Low-Resolution Image*. J. Opt. Soc. Am. A, 1990. **7**(3): p. 450–8.
25. DeLong, K.W., et al., *Ultrashort-Pulse Measurement Using Non-instantaneous Nonlinearities: Raman Effects in Frequency-Resolved Optical Gating*. Optics Letters, 1995. **20**(5): p. 486–8.
26. Richman, B.A., M.A. Krumbügel, and R. Trebino, *Temporal Characterization of Mid-IR Free-Electron-Laser Pulses by Frequency-Resolved Optical Gating*. Opt. Lett., 1997. **22**(10): p. 721–3.
27. Kohler, B., et al., *Phase and Intensity Characterization of Femtosecond Pulses from a Chirped-Pulse Amplifier by Frequency-Resolved Optical Gating*. Optics Letters, 1994. **20**(5): p. 483–5.
28. Clement, T.S., A.J. Taylor, and D.J. Kane, *Single-shot measurement of the amplitude and phase of ultrashort laser pulses in the violet*. Opt. Lett., 1995. **20**(1): p. 70–2.
29. Kane, D.J., et al., *Single-Shot Measurement of the Intensity and Phase of Femtosecond UV Laser Pulse Using Frequency-Resolved Optical Gating*. Optics Letters, 1994. **19**(14): p. 1061–3.
30. Michelmann, K., et al., *Frequency resolved optical gating in the UV using the electronic Kerr effect*. Applied Physics B (Lasers and Optics), 1996. **B63**(5): p. 485–9.
31. Backus, S., et al., *16fs ultraviolet pulse generation in air: 1 μJ pulses at 257 nm at 1 kHz*. Optics Letters, 1996. **21**: p. 665.
32. Gase, R., *Ultrashort-pulse amplitude and phase retrieval using time-frequency distribution functions*. Experimental Technique of Physics, 1996. **42**(1): p. 25–31.
33. Gase, R., *Ultrashort-pulse measurements applying generalized time-frequency distribution functions*. Journal of the Optical Society of America B (Optical Physics), 1997. **14**(11): p. 2915–20.
34. Mukamel, S., C. Ciordas-Ciurdariu, and V. Khidekel, *Wigner spectrograms for femtosecond pulse-shaped heterodyne and autocorrelation measurements*. IEEE Journal of Quantum Electronics, 1996. **32**(8): p. 1278–88.
35. Paye, J., *The Chronocyclic Representation of Ultrashort Light Pulses*. IEEE Journal of Quantum Electronics, 1992. **28**(10): p. 2262–73.
36. Heil, C.E. and D.F. Walnut, *Continuous and Discrete Wavelet Transforms*. SIAM Review, 1989. **31**(4): p. 628–66.
37. Hirlimann, C. and J.G. Morhange, *Wavelet Analysis of Short Light Pulses*. Applied Optics, 1992. **31**(17): p. 3263–6.
38. Treacy, E.B., *Measurement and Interpretation of Dynamic Spectrograms of Picosecond Light Pulses*. J. Appl. Phys., 1971. **42**(10): p. 3848–58.
39. Wong, V. and I.A. Walmsley, *Ultrashort-pulse characterization from dynamic spectrograms by iterative phase retrieval*. Journal of the Optical Society of America B, 1997. **14**(4): p. 944–9.
40. Rhee, J.K., et al., *Real-Time Dispersion Analyzer of Femtosecond Laser Pulses with Use of a Spectrally and Temporally Resolved Upconversion Technique*. J. Opt. Soc. Am. B, 1996. **13**(8): p. 1780–5.

6. FROG Beam Geometries

Rick Trebino

Introduction

In the last chapter, we described the general concepts of FROG. And we gave examples from the polarization-gate version of FROG. But, because FROG is a spectrally resolved autocorrelation, every nonlinear-optical process that can be used to make an autocorrelator can also be used to make a FROG (see Fig. 6.1). In this chapter, we'll describe and compare the several most common FROG beam geometries and their traces, so you can choose which geometry to use for your application.

The traces are slightly different for each of these geometries, and Fig. 6.2 compares the traces of these different FROG techniques. Basically, the third-order FROG geometries, such as polarization gating, self-diffraction, and transient grating, all yield traces that can be considered musical scores of the pulse, graphically depicting the frequency vs. time. On the other hand, the second-order FROG geometry, second-harmonic generation (SHG), yields a symmetrized version of these traces and so is a bit less intuitive. Third-harmonic generation (THG) is intermediate between the two cases.

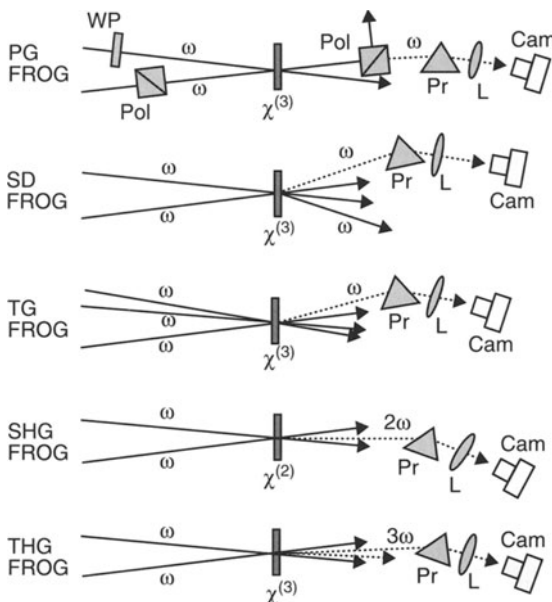


Fig. 6.1: Various beam geometries for FROG measurements of ultrashort pulses. The prism/lens combination represents a spectrometer [7].

Basically, if you have weak (i.e., nJ) pulses, use SHG FROG; it's the most sensitive geometry. If your pulses are more powerful, then you can use a third-order method. If your pulses are in the UV, you must use a third-order geometry because SHG crystals don't exist in the UV.

Polarization-Gate FROG

Polarization-gate (PG) FROG [1–6] uses the polarization-gate beam geometry, discussed in Chapter 3 and shown in Fig. 6.1 and in greater detail in Fig. 6.3. In this geometry, the pulse is split into two, with one pulse (the “probe”) then sent through crossed polarizers and the other (the “gate”) through a half-wave plate or other device in order to achieve a ± 45 degrees

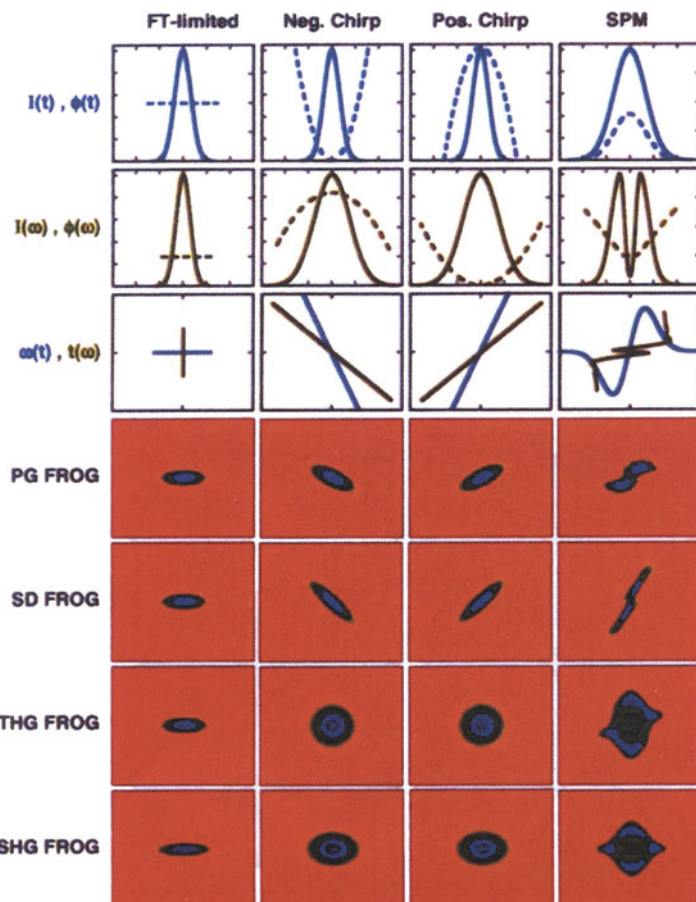


Fig. 6.2a: Comparison of traces for common ultrashort pulse distortions for the most common FROG beam geometries [7].

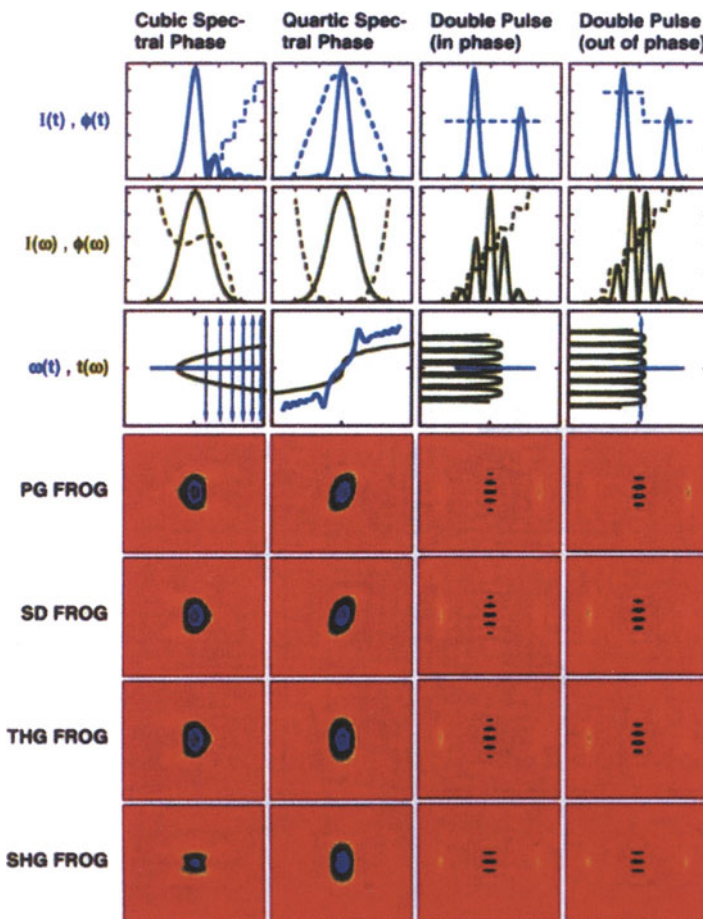


Fig. 6.2b: Comparison of traces for common ultrashort pulse distortions for the most common FROG beam geometries. Additional pulses [7].

linear polarization with respect to that of the probe pulse. The two pulses are then spatially overlapped in a piece of fused silica (or other medium with a very fast third-order susceptibility). In the fused silica, the gate pulse induces a birefringence through the electronic Kerr effect, a third-order optical nonlinearity, also known as the nonlinear refractive index. As a result, the fused silica acts as a wave plate while the gate pulse is present, rotating the probe pulse's polarization slightly, which allows some light to be transmitted through the analyzer. Because birefringence occurs only when the gate pulse is present, this geometry yields an autocorrelation measurement of the pulse if one simply measures the energy of the light transmitted through the analyzer vs. the relative delay between the two pulses. And by spectrally resolving the light transmitted by the analyzer vs. delay, a PG FROG trace is measured.

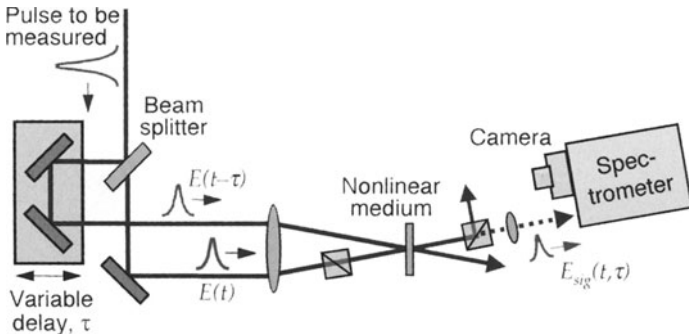


Fig. 6.3: Polarization-gate (PG) FROG apparatus.

The PG FROG trace is given by:

$$I_{\text{FROG}}^{\text{PG}}(\omega, \tau) = \left| \int_{-\infty}^{\infty} E(t) |E(t - \tau)|^2 \exp(-i\omega t) dt \right|^2 \quad (6.1)$$

Note that the gate function in PG FROG is $|E(t - \tau)|^2$, which is a real quantity and so adds no phase information to the gated slice of $E(t)$ whose spectrum is measured. As a result, PG FROG traces are quite intuitive, accurately and visually reflecting the pulse frequency vs. time. Sample PG FROG traces are shown in Fig. 6.2.

PG FROG is the most intuitive FROG variation, and it has many other desirable qualities. First, and most importantly, except for the trivial ones mentioned in the previous chapter (φ_0 and φ_1), there are no known ambiguities in PG FROG. Thus, PG FROG yields complete and unambiguous pulse intensity and phase characterization in all known cases.

This lack of ambiguities is quite useful, but it's also interesting because it's well known that the spectrogram—which is different from FROG in that it uses an independent gate function (i.e., not a gate consisting of the pulse itself, as in FROG)—has an ambiguity in the relative phase of well-separated pulses. For such an independent-gate spectrogram, the relative phase of well-separated pulses is completely undetermined. This is because, when the two pulses are separated by more than the gate width, the spectrogram splits into the sum of the two individual-pulse spectrograms, and the squared magnitudes prevent the determination of the relative phase. There are thus infinitely many different relative-phase values possible in the independent-gate spectrogram of well-separated pulses. This ambiguity doesn't occur in PG FROG because, in PG FROG (and all other versions of FROG), the gate is the pulse itself, so the pulses *cannot* be separated by more than the gate width under any circumstances.

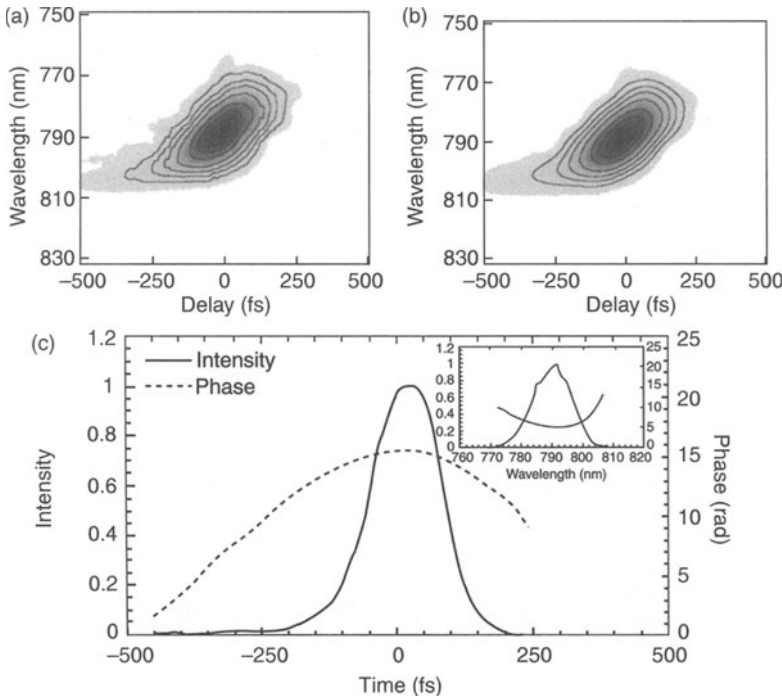


Fig. 6.4: a. Measured PG FROG trace of a linearly positively chirped pulse from a Ti : Sapphire amplifier. b. Computed PG FROG trace of the retrieved pulse. c. Retrieved intensity (solid) and phase (dashed) vs. time. Inset: retrieved spectrum and spectral phase [3].

Figure 6.4 shows an example of a PG FROG trace of a linearly chirped pulse from a regeneratively amplified Ti : Sapphire laser and taken by Kohler and co-workers [3, 7]. Note that it's customary to plot both the measured trace and the trace of the retrieved pulse, in order to compare them. They should look alike, as they do here. Also, (although not reported for this traces), it's a good idea to mention the *FROG error*, which is the rms difference between the two traces, which should be below 1%, depending on the noise level.

Another advantage of PG FROG is that the nonlinear-optical process is automatically phase-matched. This has two consequences: (1) alignment is easy; and (2) PG FROG has infinite bandwidth. So if you have a very broadband pulse, PG FROG is a good and often overlooked option.

Disadvantages of PG FROG are that it requires high-quality polarizers (an extinction coefficient of better than 10^{-5} is recommended), which can be expensive (>\$1000 for a 1-cm calcite polarizer). In addition, high-quality polarizers tend to be fairly thick, so pulses can change due to material dispersion while propagating through them. This is not as problematic as it first appears because the full pulse intensity and phase are measured at the nonlinear medium, so it is possible to theoretically back-propagate the pulse to any point before or after the point where it was measured. Nevertheless, this

is somewhat undesirable. A further disadvantage of the requirement for high-quality polarizers is that they are unavailable in spectral regions such as the deep UV ($<\sim 250$ nm). They also limit sensitivity because there is always some leakage.

These disadvantages are not severe, however, especially for amplified ultra-short pulses in the visible and the near-IR. And to date, the PG FROG technique has been used by many groups to perform multi-shot and single-shot measurements of ultrashort pulses, and a commercial PG FROG product is currently available (from Positive Light).

Typical values of the various optical elements in a multi-shot PG FROG device for measuring amplified 100-fs, 800-nm, >100 -nJ pulses from a regeneratively amplified Ti:Sapphire laser are as follows [3]. A 50% beam splitter splits the pulse to be measured into two, one of which passes through crossed calcite polarizers (extinction coefficient $<10^{-5}$; with minimal optics placed between them, to avoid depolarizing the beam), the other of which is polarization-rotated by a wave plate (or out-of-plane propagation) to a ± 45 -degree (or circular) polarization. The pulses, lightly focused using a ~ 50 -cm lens, overlap in an approximately 100- μm - to 1-mm-thick piece of fused silica. The light passing through the second polarizer is the signal pulse, and it is sent into a 1/4-meter spectrometer incorporating a ~ 1200 -line-per-mm diffraction grating. A home-made spectrometer, using a grating and a pair of lenses also works well (the focus in the fused silica can function as the entrance slit; see Chapter 11). A video or CCD camera at the output plane of the spectrometer then measures the spectrum averaged over as many pulses as desired. The delay of one of the two pulses is then varied using a delay line, and the spectrum is measured for about 100 different delays, which are a few fs apart. The above spectrometer yields more than sufficient spectral resolution for measurements of ~ 100 -fs pulses, and it may be necessary to combine adjacent spectral values to reduce the number of points per spectrum. Indeed, for the measurement of significantly shorter pulses, a prism spectrometer may be used [8,9].

Finally, recall that PG FROG utilizes a third-order nonlinearity, so the signal intensity scales as the third power of the input intensity. Consequently, pulses that are longer or weaker by a factor of two yield one eighth the output power. And an increase in the spot size by a factor of two yields one sixty-fourth the signal intensity. The same is, of course, true for other third-order FROG and autocorrelation methods.

Self-diffraction FROG

Self-diffraction (SD) [10,11] is another beam geometry that uses a third-order nonlinear-optical process for optical gating in FROG measurements (See Figs. 6.1 and 6.5). SD FROG also involves crossing two beams in a piece of fused silica (or other third-order nonlinear medium), but in SD FROG, the

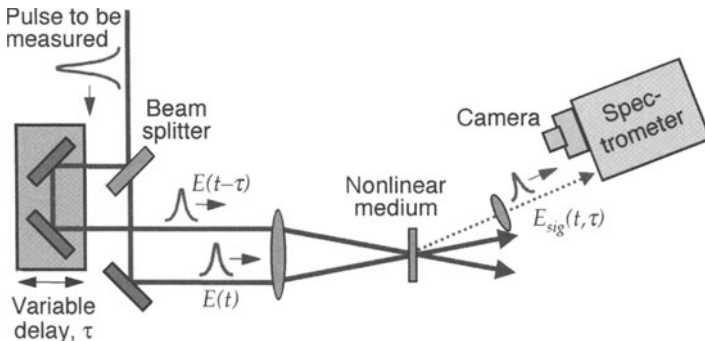


Fig. 6.5: Self-diffraction FROG.

beams can have the same polarizations. The beams generate a sinusoidal intensity pattern and hence induce a material grating, which diffracts each beam into the directions shown in Figs. 6.1 and 6.5. Spectrally resolving one of these beams as a function of delay yields a SD FROG trace, examples of which are shown in Fig. 6.2. The expression for the SD FROG trace is:

$$I_{\text{FROG}}^{\text{SD}}(\omega, \tau) = \left| \int_{-\infty}^{\infty} E(t)^2 E(t - \tau) \exp(-i\omega t) dt \right|^2 \quad (6.2)$$

SD FROG traces differ slightly from PG FROG traces [4]. For a linearly chirped pulse, the slope of the SD FROG trace is twice that of the PG FROG trace [4]. As a result, SD FROG is more sensitive to this and other even-order temporal-phase distortions. It is, however, less sensitive to odd-order temporal-phase distortions. SD FROG also uniquely determines the pulse intensity and phase (except, of course, for φ_1 and φ_2).

An advantage of SD FROG over PG FROG is that it does not require polarizers, so it can be used for deep UV pulses or pulses that are extremely short, for which high-quality polarizers are unavailable or undesirable. On the other hand, SD is not a phase-matched process. As a result, the nonlinear medium must be kept thin ($< \sim 200 \mu\text{m}$) and the angle between the beams small ($< \sim 2$ degrees) in order to minimize the phase mismatch. In addition, the phase mismatch is wavelength dependent. Consequently, if the pulse bandwidth is large, the SD process can introduce wavelength-dependent inefficiencies into the trace, resulting in distortions. These pitfalls are easily avoided for ≥ 100 -fs pulses, and Clement and coworkers have shown that SD FROG is a good method for measuring amplified ultrashort pulses in the violet on a single shot [10]. Figure 6.6 shows two very short (20 fs) violet pulses measured using SD FROG.

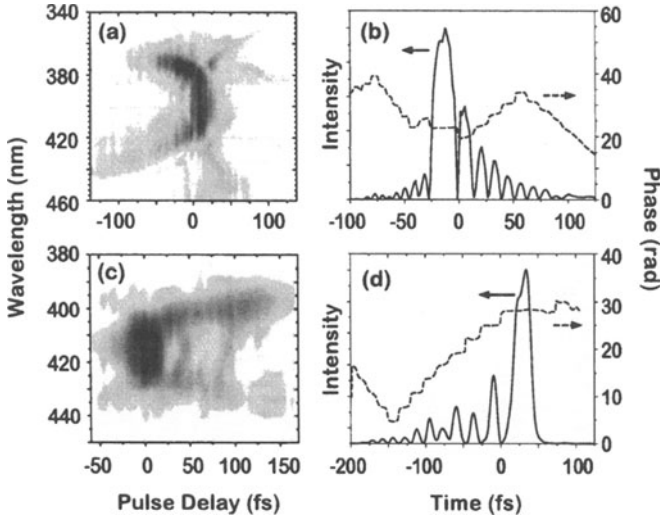


Fig. 6.6: a,c. Measured SD FROG traces of a compressed 20-fs blue broadband continuum produced in an Ar-filled hollow fiber source with pulse energies of as much as 20 mJ. b,d. Retrieved intensity (solid) and phase (dashed) vs. time. Notice the third-order spectral phase distortions [12].

Transient-Grating FROG

Ideally, one would like a beam geometry that is both phase-matched and free of large chunks of material, such as polarizers. The transient-grating (TG) beam geometry (see Figs. 6.1 and 6.7) is such a geometry, and we consider it to be the most versatile all-round beam geometry for FROG measurements of amplified ultrashort pulses [13]. Indeed, the TG geometry is very popular in nonlinear-spectroscopy measurements [14–16], also, and its advantages for such measurements are also advantages for FROG measurements [13].

The price for these advantages is added complexity. TG FROG is a three-beam geometry, requiring that the input pulse be split into three pulses. Two of the pulses are overlapped in time and space at the optical-Kerr medium, producing a refractive-index grating, just as in SD FROG. In TG, however, the third pulse is variably delayed and overlapped in the fused silica and is diffracted by the induced grating to produce the signal pulse. The four beam angles (three input and one output) in TG geometries usually take the form of what is known as the BOXCARS arrangement [17], in which all input pulses and the signal pulse are nearly collinear, but appear as spots in the corners of a rectangle on a card placed in the beams. While nonlinear spectroscopists often use an arrangement in which two beams nearly counter-propagate with the other two [18,19], all four beams should nearly co-propagate in FROG measurements in order to avoid temporal smearing effects due to large beam angles.

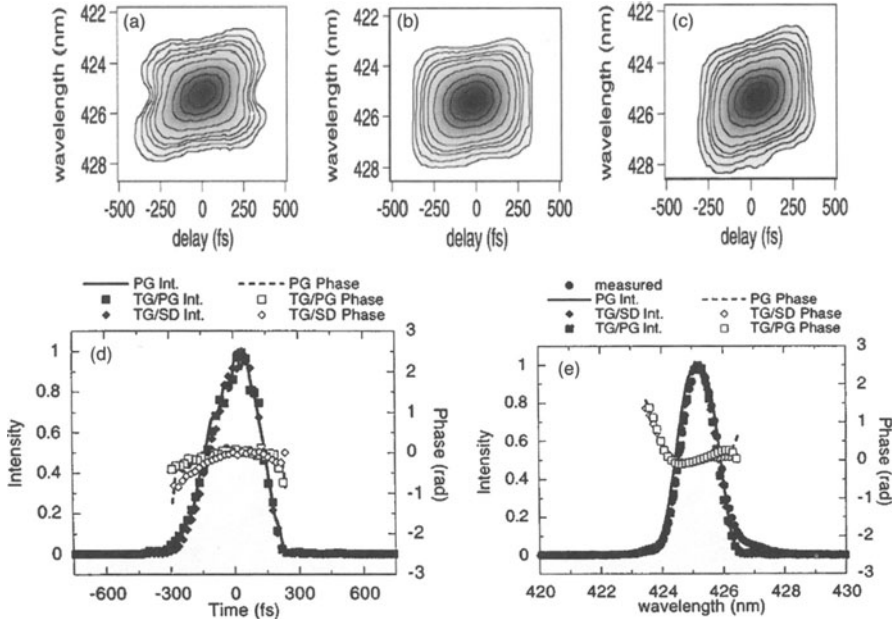


Fig. 6.7: a. Measured PG FROG trace of an asymmetrical-intensity, slightly chirped pulse. b. TG FROG trace of the same pulse using the PG mode of TG FROG. c. TG FROG trace of the same pulse using the SD mode of TG FROG. Note that the slope of the TG FROG trace is larger in the SD mode, as expected. d. Retrieved intensity (solid) and phase (dashed) vs. time. e. Retrieved spectrum (solid) and spectral phase (dashed) [13]. All FROG errors < .01.

The signal field in TG FROG is: $E_{\text{sig}}(t, \tau) = E_1(t)E_2^*(t)E_3(t)$ where $E_i(t)$ is the i th input pulse. Depending on which pulse is variably delayed (with the other two coincident in time), the TG FROG trace is mathematically equivalent to PG FROG or SD FROG. To see this, note that if pulse #2 is variably delayed, the signal pulse is given by:

$$I_{\text{FROG}}^{\text{TG2}}(\omega, \tau) = \left| \int_{-\infty}^{\infty} E_1(t) E_2^*(t - \tau) E_3(t) \exp(-i\omega t) dt \right|^2 \quad (6.3)$$

Since all pulses are identical, this becomes:

$$I_{\text{FROG}}^{\text{TG2}}(\omega, \tau) = \left| \int_{-\infty}^{\infty} E^2(t) E^*(t - \tau) \exp(-i\omega t) dt \right|^2 \quad (6.4)$$

which is just the expression for the SD FROG signal field.

An analogous argument shows that if either of the other two pulses is variably delayed, the signal field is identical to the PG FROG signal field

(with a reversed sign of the delay):

$$I_{\text{FROG}}^{\text{TG3}}(\omega, \tau) = \left| \int_{-\infty}^{\infty} E_1(t) E_2^*(t) E_3(t - \tau) \exp(-i\omega t) dt \right|^2 \quad (6.5)$$

Since all pulses are identical, this becomes:

$$I_{\text{FROG}}^{\text{TG3}}(\omega, \tau) = \left| \int_{-\infty}^{\infty} |E(t)|^2 E(t - \tau) \exp(-i\omega t) dt \right|^2 \quad (6.6)$$

Changing variables, from t to $t - \tau$, and redefining τ as $-\tau$, we have:

$$I_{\text{FROG}}^{\text{TG3}}(\omega, \tau) = \left| \int_{-\infty}^{\infty} |E(t - \tau)|^2 E(t) \exp(-i\omega t) dt \right|^2 \quad (6.7)$$

which is just the expression for the PG FROG signal field. Thus, TG FROG yields familiar traces.

TG FROG has several advantages over its two-beam cousins. Unlike PG FROG, it avoids polarizers, so it does not distort extremely short pulses, and hence can be used in the deep UV (see Chapter 13). More importantly, it is background-free. It can use all parallel polarizations, which yields greater signal strength because the diagonal element of the susceptibility tensor is a factor of three larger than the off-diagonal elements used in PG FROG. This fact, coupled with the lack of polarizer-leakage background, makes TG FROG significantly more sensitive than PG FROG. Unlike SD FROG, TG FROG is phase-matched, so long interaction lengths in the nonlinear medium may be used, enhancing signal strength due to the length-squared dependence of the signal. In addition, larger beam angles may be used than in SD FROG, reducing any scattered-light background. As a result, TG FROG is also significantly more sensitive than SD FROG. At the same time, TG FROG retains the intuitive traces and ambiguity-free operation common to these two-beam FROG methods. The only disadvantage of TG FROG is the need for three beams and to maintain good temporal overlap of the two constant-delay beams. But we have found these requirements not to be particularly inconvenient, and the advantages of this geometry far outweigh the disadvantages. For example, the large bandwidth of this entirely phase-matched geometry and the avoidance of potentially pulse-distorting polarizers make TG FROG ideal for measuring extremely short pulses (~ 20 fs) of a few tens of nJ or more. Indeed, Rundquist and coworkers have made such measurements with excellent results [20]. Figure 6.7 shows some TG FROG measurements of a regeneratively amplified Ti : Sapphire pulses [13].

Second-Harmonic-Generation FROG

SHG FROG involves spectrally resolving a standard SHG-based autocorrelator:

$$I_{\text{FROG}}^{\text{SHG}}(\omega, \tau) = \left| \int_{-\infty}^{\infty} E(t) E(t - \tau) \exp(-i\omega t) dt \right|^2 \quad (6.8)$$

The first such measurement was made by Ishida and coworkers in 1995, but they didn't attempt to extract the intensity and phase from their measurements [21–23]. Kane and Trebino pointed out that it could yield the intensity and phase, although it had ambiguities, and they compared it to other FROG beam geometries in 1993, and DeLong and Trebino later developed a reliable pulse-retrieval algorithm [2,11,24]. Others rediscovered it later, occasionally referring to it by a different name, such as “spectrally resolved autocorrelation.” [25].

Figures 6.1 and 6.8 show schematics of this method. The main advantage of SHG FROG is *sensitivity*: it involves only a second-order nonlinearity, while the previously mentioned FROG variations use third-order optical nonlinearities, which are much weaker. As a result, for a given amount of input pulse energy, SHG FROG will yield more signal pulse energy. SHG FROG is commonly used to measure unamplified pulses directly from a Ti : Sapphire oscillator, and it can measure pulses as weak as about 1 pJ; it is only slightly less sensitive than an autocorrelator.

SHG FROG also achieves the best S/N ratios because its signal beam is a different color, so scattered light is easily filtered. And SHG FROG has proven ideal for few-fs pulse measurement.

The main disadvantages of SHG FROG are that, unlike the previously mentioned third-order versions of FROG, it has a somewhat unintuitive trace that is symmetrical with respect to delay, and, as a result, it has an ambiguity

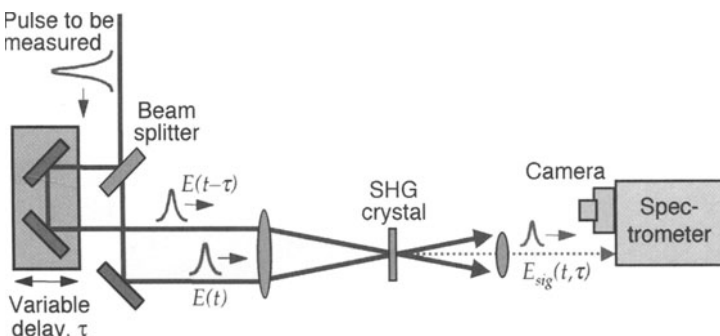


Fig. 6.8: Experimental apparatus for SHG FROG.

in the direction of time. The pulse complex amplitude, $E(t)$, and its complex-conjugated time-reversed replica, $E^*(-t)$, both yield the same SHG FROG trace. In terms of the intensity and phase, $E^*(-t)$ corresponds to $I(-t)$ and $-\phi(-t)$. In the frequency domain, because $E^*(-t)$ Fourier-transforms to $E^*(\omega)$, $E^*(-t)$ corresponds to $S(\omega)$, and $-\varphi(\omega)$. Thus, when an SHG FROG trace is measured and the phase-retrieval algorithm is run on it, it is possible that the actual pulse is the time-reversed version of the retrieved pulse.

This ambiguity can easily be removed in one of several ways. One is to make a second SHG FROG measurement of the pulse after distorting it in some known manner. The most common method is to place a piece of glass in the beam (before the beam splitter), introducing some positive dispersion and hence chirp into the pulse. Only one of the two possible pulses is consistent with both measurements. (Placing a piece of glass after the beam splitter—in only one beam—and measuring only a single SHG FROG trace is *not* sufficient to remove this ambiguity, unless traces using two different elements are made.) Another is to know in advance something about the pulse, such as that it is positively chirped. And finally, Taft [9] has found that placing a thin piece of glass in the pulse before the beam splitter so that surface reflections introduce a small trailing satellite pulse also removes the ambiguity. This method has the advantage of requiring only one SHG FROG trace measurement to determine the pulse (the time-reversed pulse in this case has a leading satellite pulse). We'll discuss this latter technique more in Chapter 11.

In addition to the direction-of-time ambiguity, there is another class of ambiguities in SHG FROG. These ambiguities rarely appear in practical measurements but are worth mentioning. If the pulse consists of two (or more) well-separated pulses, then the relative phase of the pulses has an ambiguity. Specifically, the relative phases, ψ_0 and $\psi_0 + \pi$, yield the same SHG FROG trace and hence cannot be distinguished. Note, however, that this ambiguity disappears when knowledge of the spectrum is available. This is because the spectral fringes that result have different phases (by π) for the two cases. Unfortunately, SHG FROG doesn't provide this information. This ambiguity is less severe than an ambiguity that occurs in standard spectrograms, which is complete indeterminacy of the relative phase between well-separated pulses (which also disappears when knowledge of the spectrum is available). Finally, if two well-separated pulses are symmetrical, one pulse's phase can also be time-reversed.

The single most important experimental consideration in SHG FROG is that the SHG crystal has sufficient bandwidth (i.e., be thin enough, since the bandwidth is inversely proportional to the crystal thickness) to frequency-double the entire bandwidth of the pulse to be measured (see Chapter 3 for a detailed discussion of phase-matching bandwidth). If the crystal is too thick, then the SHG FROG trace will be too narrow along the spectral axis, leading to non-convergence of the algorithm. It is important to realize that autocorrelators carry the same crystal-bandwidth requirement, but this requirement is often violated in practice because, unlike FROG, no independent check of

the autocorrelation trace exists, and a distorted autocorrelation trace results. Also, a very convenient feature of FROG is that it is possible to correct for this effect (see Chapter 10) [9]. SHG FROG is the most common FROG method in use [2,4,5,8,9,24,25]. Indeed, since most labs already have an autocorrelator and spectrometer, SHG FROG is easy to set up: it simply requires placing the spectrometer behind the autocorrelator.

Figure 6.8 shows a typical SHG FROG apparatus, consisting of a 50% beam-splitter, a delay line using two mirror pairs (or corner cubes) on translation stages to give variable delays, a 10- to 50-cm-focal-length lens or mirror to focus the pulses into the SHG crystal (usually KDP or BBO), and a 1/8- to 1/4-m spectrometer/camera. A filter blocks the fundamental-frequency light, although this is also done by the spectrometer. As in autocorrelation and other pulse-measurement methods, the crystal thickness for measuring 100-fs, 800-nm pulses should be no more than $\sim 300\text{ }\mu\text{m}$ for KDP and $\sim 100\text{ }\mu\text{m}$ for BBO. Figure 6.9 shows an experimental SHG FROG trace for a pulse with very small satellite pulses, the retrieved FROG trace, and the retrieved intensity and phase. Note the good agreement between experimental and retrieved traces [7,24], even at the $\sim 10^{-4}$ level. The retrieved pulse yields a FROG error (the rms error between experimental and retrieved traces; see Chapter 10 for

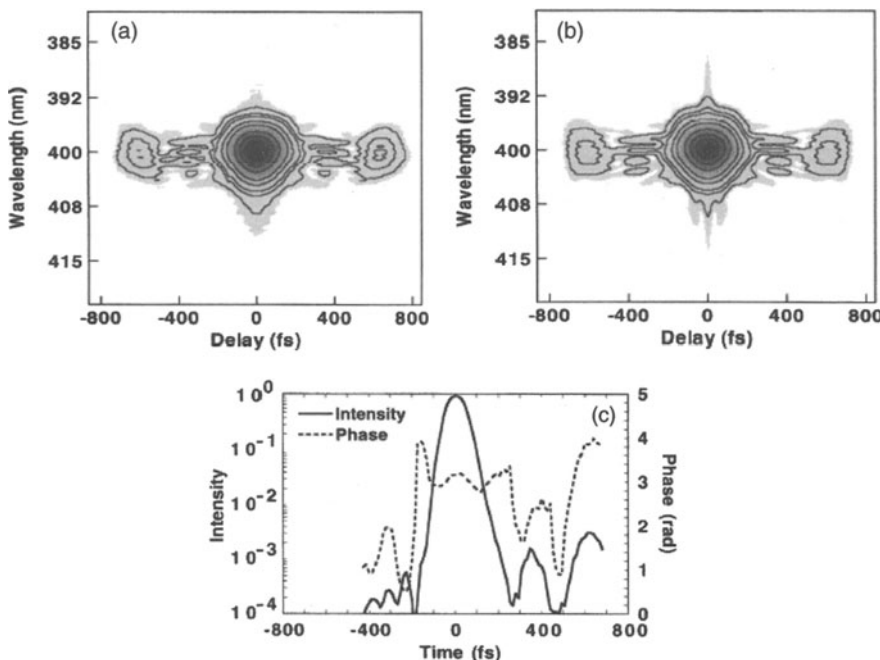


Fig. 6.9: (a) Measured SHG FROG trace of a pulse from a misaligned Ti : Sapphire oscillator. (b) Computed SHG FROG trace of the retrieved pulse. (c) Retrieved intensity (solid) and phase (dashed) vs. time [7,24]. FROG error = 0.0016.

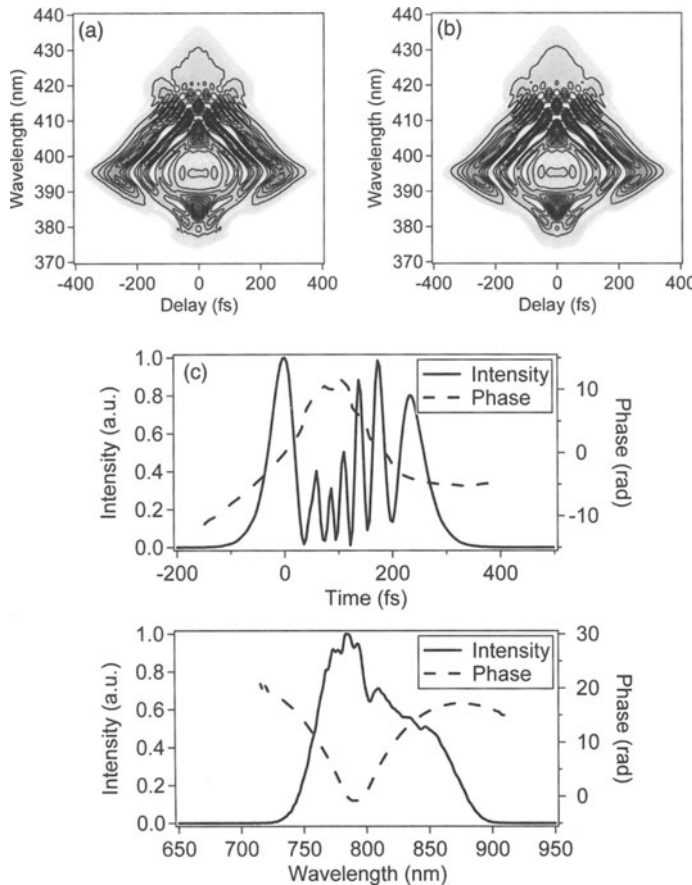


Fig. 6.10: Complex pulse and its measured and retrieved SHG FROG traces. Upper left: Measured trace. Upper right: Retrieved trace. Lower: Retrieved pulse vs. time and wavelength. FROG can easily measure complex pulses. FROG errors in these measurements: 0.01 [27].

further discussion of the FROG error) of 0.0016, indicative of a very accurate measurement. We also refer you to the excellent recent work of Dudley and coworkers (Chapter 15), who've used SHG FROG to measure complex pulses resulting from propagation through 700 m of fiber [26].

Figure 6.10 shows another nice example of an SHG FROG measurement of a pulse, generated by Erik Zeek.

Third-Harmonic-Generation FROG

It is also possible to use third-harmonic generation (THG) as the nonlinear-optical process in a FROG apparatus. This has been done by Tsang, et al., using

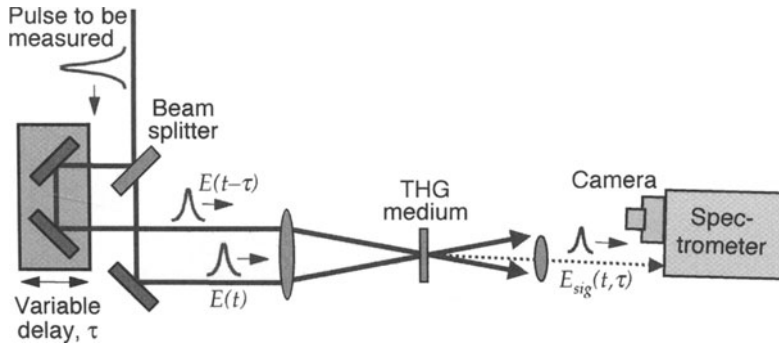


Fig. 6.11: Experimental apparatus for THG FROG.

THG [28], using highly focused beams, which has allowed the measurement of unamplified pulses from a Ti : Sapphire oscillator. Figures 6.1 and 6.11 show the arrangement for THG FROG.

The expression for the THG FROG trace is:

$$I_{\text{FROG}}^{\text{THG}}(\omega, \tau) = \left| \int_{-\infty}^{\infty} E(t - \tau)^2 E(t) \exp(-i\omega t) dt \right|^2 \quad (6.9)$$

which is similar to that of SHG FROG, except that one of the factors is squared. There are two possible signal beams that can be spectrally resolved in THG FROG measurements, and the choice of these beams determines which factor of the field, $E(t)$ or $E(t - \tau)$, is squared in the above expression. The choice is irrelevant and only serves to reflect the trace with respect to τ .

The main advantage of THG FROG is that, like the other third-order FROG methods, it removes the direction-of-time ambiguity that occurs in SHG FROG. In addition, the THG effect is sufficiently strong that THG FROG can be used to measure unamplified pulses from a Ti : Sapphire oscillator. Indeed, currently, the only third-order FROG method to achieve this measurement has been THG FROG.

In terms of its performance, THG FROG is intermediate between SHG FROG and the other third-order FROG methods. It is less sensitive than SHG FROG, but more sensitive than PG and SD FROG. Its traces are similar to SHG FROG traces—somewhat unintuitive—but they have a slight asymmetry that distinguishes them from SHG FROG traces and removes the direction-of-time ambiguity. On the other hand, THG FROG traces are not as intuitive as the other third-order FROG traces. And while THG FROG lacks the direction-of-time ambiguity of SHG FROG, it does have relative-phase ambiguities with well-separated multiple pulses, as is the case for SHG FROG, but not for the other third-order FROG methods. And, for pulses that are perfectly chirped and perfectly Gaussian in intensity, the sign of the chirp parameter is

Table 6.1: Comparison of the basic FROG geometries. Sensitivities are only approximate and assume the 800-nm 100-fs pulses focused to about 100 μm (10 μm for THG) are to be measured [7].

Geometry	PG	SD	TG	THG	SHG
Nonlinearity Sensitivity (single shot)	$\chi^{(3)}$ $\sim 1 \mu\text{J}$	$\chi^{(3)}$ $\sim 10 \mu\text{J}$	$\chi^{(3)}$ $\sim 0.1 \mu\text{J}$	$\chi^{(3)}$ $\sim 0.03 \mu\text{J}$	$\chi^{(2)}$ $\sim 0.01 \mu\text{J}$
Sensitivity (multishot)	$\sim 100 \text{nJ}$	$\sim 1000 \text{nJ}$	$\sim 10 \text{nJ}$	$\sim 3 \text{nJ}$	$\sim 0.001 \text{nJ}$
Advantages	Intuitive traces; Automatic phase matching	Intuitive traces	Bkgrnd-free; Sensitive; Intuitive traces	Sensitive; Very large bandwidth	Very sensitive
Disadvantages	Requires polarizers	Requires thin medium; not phase matched	Three beams	Unintuitive traces; Very short- λ signal	Unintuitive traces; Short- λ signal
Ambiguities	None known	None known	None known	Relative phase of multiple pulses: $\varphi, \varphi \pm 2\pi/3$	Direction of time; Rel. phase of multiple pulses: $\varphi, \varphi + \pi$

indeterminate in THG FROG (although this is extremely unlikely to occur in practice). Thus, THG FROG represents a compromise between other FROG variations and hence may best be used only in special cases, such as for the measurement of an unamplified oscillator pulse train when only one trace can be made, no additional information is available, and direction-of-time ambiguity is unacceptable.

Cascaded $\chi^{(2)}$ FROG (CC FROG)

A method that simultaneously achieves intuitive traces, completely unambiguous intensity-and-phase measurement, signal light at the fundamental wavelength, and sufficient sensitivity to measure unamplified Ti:Sapphire laser-oscillator pulses would be very useful. Such a technique is FROG using *cascaded $\chi^{(2)}$* effects for the optical nonlinearity, specifically, up-conversion (i.e., SHG) followed by down-conversion. We refer to cascaded $\chi^{(2)}$ FROG beam geometries as CC FROG [29].

Cascaded $\chi^{(2)}$ effects simulate third-order nonlinearities but are significantly stronger [30–32]. A number of applications requiring greater signal strength than is available from third-order materials have been proposed and

demonstrated using CC effects. Typically, CC effects involve SHG of one beam, followed by a down-conversion process involving the newly created second harmonic and another beam at the fundamental frequency. The signal beam is then at the fundamental frequency. The two processes are typically not simultaneously phase-matched, but can be approximately phase-matched, yielding an overall efficiency that is approximately the square of the SHG efficiency. This efficiency can be considerably greater than that available from a single $\chi^{(3)}$ effect.

Simply by inserting an SHG crystal into an SD FROG apparatus yields a cascaded $\chi^{(2)}$ self-diffraction FROG (CC SD FROG) apparatus. The CC SD process (without spectrally resolving the signal beam to make a FROG) was first studied by Danielius, et al. [30], who showed that, in a SD geometry, SHG of one beam can be followed by a down-conversion process involving that second-harmonic beam and the other input beam yielding an additional beam at the input wavelength. No induced grating occurs, as in the usual self-diffraction process, however.

CC SD FROG simply involves spectrally resolving this self-diffracted beam from a SHG crystal for a range of delays. The analogy to SD FROG is a good one: CC SD FROG traces made in this manner are mathematically identical to those made using a true third-order SD FROG beam geometry. As a result, they are quite intuitive, and, like SD FROG traces, they uniquely determine the pulse intensity and phase.

CC FROG involving a polarization-gate (PG) beam geometry, which we call CC PG FROG, simply involves replacing the usual optical-Kerr medium between the crossed polarizers in a standard PG FROG arrangement with a type II SHG crystal. All other aspects of this geometry are identical to the usual PG arrangement. Again, the analogy to polarization gating is also valid: traces produced in this manner are identical to those of PG FROG using a true third-order medium. Use of a CC process, however, produces a device that is significantly more sensitive.

Both CC SD FROG and CC PG FROG (which we collectively refer to as CC FROG) generate highly intuitive FROG spectrograms, yield unambiguous measurements, and involve detection at the input-pulse wavelength. And CC FROG is sufficiently sensitive that it can measure *unamplified* Ti : Sapphire oscillator pulses. Because CC FROG traces are mathematically identical to highly intuitive SD or PG FROG traces, the standard FROG computer algorithm works without modification for CC FROG traces. Finally, a second-harmonic beam propagating between the two input pulses is necessarily simultaneously produced in both CC FROG apparatuses, so an SHG autocorrelation or SHG FROG trace can easily be obtained if corroboration is desired or if the laser intensity drops so that additional sensitivity is required.

Consider first CC SD FROG. The second-harmonic field produced by a pulse, $E(t)$, is given by $E_{\text{SH}}(t) \propto E(t)^2$. If this field then acts in conjunction with a delayed replica of the pulse, $E(t - \tau)$, in a down-conversion process,

as Danielius, et al. have shown, the following field results:

$$E_{\text{CCSD}}(t, \tau) \propto E_{\text{SH}}(t)E^*(t - \tau) \quad (6.10)$$

Substituting for $E_{\text{SH}}(t)$, we have:

$$E_{\text{CCSD}}(t, \tau) \propto E^2(t)E^*(t - \tau) \quad (6.11)$$

This expression has the same dependence on the fields as self-diffraction, a third-order process. While the phase-matching properties of the two second-order processes involved are different, use of a small beam angle (about a degree) maintains approximate phase-matching in both processes simultaneously. Typically, a type I SHG crystal is used and therefore the polarizations of the two input beams are the same.

Now consider CC PG FROG. First, a type II SHG crystal is placed between the two polarizers with its principal axes parallel and perpendicular to those of the polarizers (and so does not introduce additional leakage despite its birefringence). As in a standard polarization-gate apparatus, the beam passing through the crossed polarizers (the “probe” beam) is horizontally polarized, and the “gate” beam has both polarizations (and, ideally, is 45-degree linearly polarized or circularly polarized). In the first second-order process, the vertical polarization component of the gate beam, $E_v(t - \tau)$, combines with the horizontally polarized probe beam, $E(t)$, to produce phase-matched type II second harmonic: $E_{\text{SH}}(t, \tau) \propto E(t)E_v(t - \tau)$. The second second-order process then involves this newly produced second harmonic, $E_{\text{SH}}(t, \tau)$, combining with the horizontally polarized component of the gate beam, $E_h(t - \tau)$, to produce vertically polarized light collinear with the probe beam and at the fundamental frequency. This vertically polarized light then passes through the polarizer and is the signal. This signal pulse field has the expression:

$$E_{\text{CCPG}}(t, \tau) \propto E_{\text{SH}}(t)E_h(t - \tau)^* \quad (6.12)$$

Substituting for $E_{\text{SH}}(t, \tau)$, we have:

$$E_{\text{CCPG}}(t, \tau) \propto E(t)E_v(t - \tau)E_h(t - \tau)^* \quad (6.13)$$

But both polarization components of the gate pulse are identical, so $E_v(t - \tau) = E_h(t - \tau) \equiv E(t - \tau)$. Thus, we have:

$$E_{\text{CCPG}}(t, \tau) \propto E(t)|E(t - \tau)|^2 \quad (6.14)$$

which is the same expression as for the usual (third-order) PG FROG.

Unlike the CC SD process described above, this CC PG process is completely phase-matched. As long as the crystal’s extraordinary polarization axis is perpendicular to the plane of the beams, both extraordinary rays have the same refractive index, and, if one process is phase-matched, the other process is also necessarily phase-matched, independent of the angle between the probe and gate beams.

We can estimate the nonlinear-optical efficiency of these processes. We first note that (assuming at least approximate phase-matching) the efficiency of the down-conversion process is about the same as that of the SHG process. So the overall cascaded $\chi^{(2)}$ process efficiency is clearly approximately the square of the SHG efficiency. Since it is straightforward to achieve few-percent SHG efficiency with \sim nJ 100-fsec pulses typical of Ti : Sapphire oscillators, we then obtain $\sim 10^{-4}$ efficiency for the cascading of the two $\chi^{(2)}$ processes. The efficiency of the overall process is thus sufficient to achieve measurements of unamplified Ti : Sapphire oscillator pulses.

A CC FROG apparatus that we've built consists of a 50/50 beam splitter, a delay line and recombining optics, a 200-mm focal-length lens, and a 1-mm thick type I BBO crystal. The beam interaction angle external to the crystal, which must be kept small to approximately phase-match both cascaded processes in CC SD FROG measurements, was 1.5° . The crystal was aligned to yield collinear SHG of each individual beam and also non-collinear SHG involving both beams, thus verifying, not only the phase-matching requirements, but also the beam overlap in time and space. This alignment then guarantees the existence of the CC SD beam, as well as the CC PG signal beam when polarizers and a type II crystal are used. The signal beam (whether SD or PG) was then apertured and recollimated. The signal efficiency was approximately 10^{-4} in CC SD FROG measurements of the Ti : Sapphire oscillator and about 10^{-3} in CC PG FROG measurements of attenuated regeneratively amplified pulses of about 100 nJ. The signal beam was spectrally resolved and detected using a 270 mm focal length, 600 line/mm grating Spex 270M imaging spectrometer and CCD camera (although we obtain similar results using a non-imaging or home-made spectrometer and inexpensive TV camera). It's important to use considerable care to suppress scattered light from the input beams, which is of the same color and at nearly the same propagation direction as the signal beam.

While CC FROG isn't well known, both CC FROG techniques appear to be ideal for measuring pulses from Ti : Sapphire lasers. While CC FROG is not quite as sensitive as SHG FROG and requires more care to set up than SHG FROG due to scattered input-beam light at the same wavelength as the signal, it is sufficiently sensitive for routine oscillator measurements that may require intuitive traces and freedom from direction-of-time ambiguity. Of the two methods, CC SD FROG is probably to be preferred for routine applications. This is because it avoids polarizers, which can distort the pulse [29].

Collinear Type II SHG FROG

All the beam geometries we've discussed so far have involved crossed beams. What if you absolutely have to use *collinear* beams? It's possible to do so and hence to perform interferometric SHG FROG or interferometric THG FROG (in analogy to interferometric autocorrelation). But, while altering

the standard FROG algorithm to retrieve the pulses from such interferometric traces is in principle straightforward, it has not seen the intensive development that other FROG geometries have enjoyed. As a result, we'll take a different and simpler approach.

But first, why bother with collinear beams? It's much harder to align collinear beams. When would we absolutely require collinear beams? Here's an example: Suppose you're focusing your beam to $< 1 \mu\text{m}$ in a biological sample, and you really need to know the pulse length at the sample. You must use the entire numerical aperture (NA) of the microscope objective, so it's not possible to cross beams.

Here we describe a collinear FROG geometry, which yields standard SHG FROG traces. It is *Type II second harmonic generation (SHG) FROG* [33,34]. Since the beams are collinear, we can use the full numerical aperture of the objective. The experimental setup for Type II SHG FROG is similar to standard non-collinear SHG FROG, except that the beams are collinear, and there is a 90° difference in polarization between the two input pulses. Type II SHG FROG also uses Type II phase-matching instead of Type I phase-matching. Figure 6.12 shows a diagram of the Type II SHG FROG device used for the measurements we'll describe. Using two half-wave plates balances the dispersion of the two input beams while providing a 90° rotation of the polarization of one beam with respect to the other.

One important consideration in Type II SHG FROG is that the two different polarizations propagate with different propagation velocities, producing a temporal walk-off between the two input pulses [35]. For a $50 \mu\text{m}$ thick Type II potassium di-hydrogen phosphate (KDP) crystal, the temporal walk-off could be as much as 8 fs depending on the orientation of the axes. For thicker crystals or other crystals such as beta barium borate (BBO), which have greater differences in the propagation velocities, the walk-off can be larger. Such large walk-offs would badly distort the FROG signal for pulses < 50 fs. So this method should be avoided for such short pulses. Also, highly focused pulses can be distorted if a non-achromatic lens is used [36,37], so care must be taken in focusing such pulses.

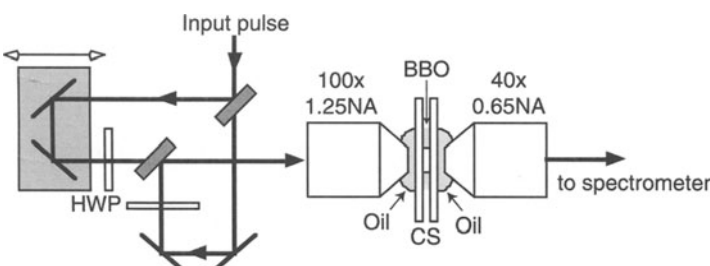


Fig. 6.12: Schematic of the collinear Type II SHG FROG used to characterize the pulses at the focus of the objective [33,34].

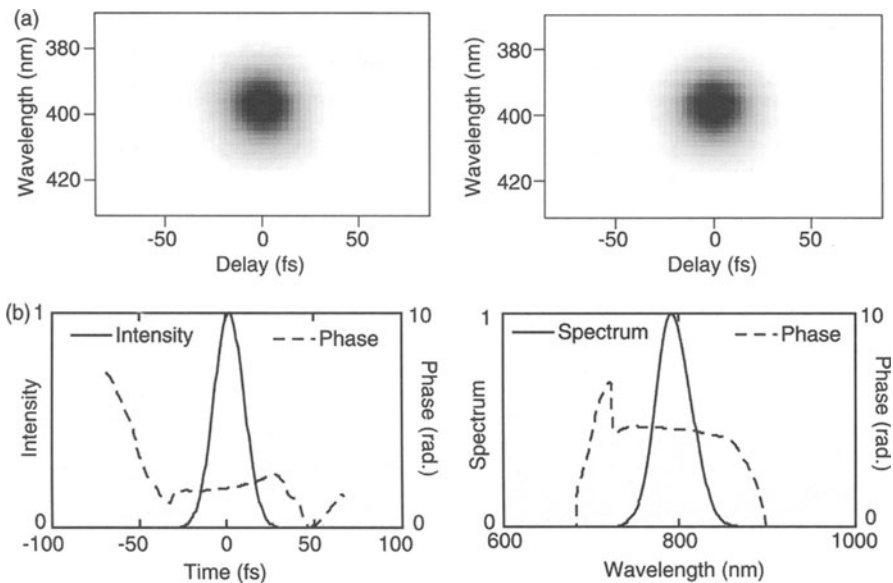


Fig. 6.13: a. The measured (symmetrized) FROG trace taken at the focus of a Zeiss CP-Achromat 100×, 1.25 NA, infinity-corrected oil objective (left). The FROG trace retrieved by the SHG FROG algorithm (right). The FROG error for the retrieval on a 128 by 128 grid was 0.0028, indicating that the retrieval is quite accurate. b. The retrieved intensity and phase at the focus vs. time (left). The temporal FWHM is 20 fs. The retrieved spectral intensity and spectral phase at the focus vs. wavelength (right). The spectral FWHM is 49 nm [33,34].

In situations where focusing is very tight, the interaction region is effectively the confocal parameter of the beam, which can be much shorter than the nonlinear medium. This reduces the temporal walk-off to negligible values when high-NA objectives are used. We note that the short interaction region also increases the effective phase-matching bandwidth. Of course, rather than using the length of the focal region to limit the effects of walk-off and the phase mismatch, one could also use a thinner crystal.

The length of the interaction region for our measurements was $\sim 1.6 \mu\text{m}$. Such a short interaction region indicates that the temporal blurring due to the walk-off in the crystal should be minimal. In addition, this interaction length is much shorter than the phase-matching length in the crystal. Thus, the walk-off and thickness of the crystal may be ignored.

Figure 6.13 shows the measured Type II SHG FROG trace when focusing with a Zeiss CP-Achromat 100×, 1.25 NA objective and the retrieved the intensity and phase of the pulse, obtained using the standard SHG FROG algorithm [7]. The FROG error for the retrieval on a 128 by 128 grid was 0.0028, and the retrieved trace is quite similar to the (symmetrized) trace.

There are many interesting issues associated with trying to measure pulses at such a tight focus, and we encourage you to have a look at the more detailed articles on the subject [33,34].

References

1. Richman, B.A., K.W. DeLong, and R. Trebino, *Temporal Characterization of the Stanford mid-IR FEL micropulses by 'FROG'*. Nuclear Instruments & Methods in Physics Research, 1995. **A 358**: p. 268–71.
2. Trebino, R. and D.J. Kane, *Using Phase Retrieval to Measure the Intensity and Phase of Ultrashort Pulses: Frequency-Resolved Optical Gating*. J. Opt. Soc. Amer. A, 1993. **10**(5): p. 1101–11.
3. Kohler, B., et al., *Phase and Intensity Characterization of Femtosecond Pulses from a Chirped-Pulse Amplifier by Frequency-Resolved Optical Gating*. Optics Letters, 1994. **20**(5): p. 483–5.
4. DeLong, K.W., R. Trebino, and D.J. Kane, *Comparison of Ultrashort-Pulse Frequency-Resolved-Optical-Gating Traces for Three Common Beam Geometries*. J. Opt. Soc. Amer. B, 1994. **11**(9): p. 1595–608.
5. Kane, D.J. and R. Trebino, *Single-Shot Measurement of the Intensity and Phase of an Arbitrary Ultrashort Pulse By Using Frequency-Resolved Optical Gating*. Opt. Lett., 1993. **18**(10): p. 823–5.
6. Kane, D.J., et al., *Single-Shot Measurement of the Intensity and Phase of Femtosecond UV Laser Pulse Using Frequency-Resolved Optical Gating*. Optics Letters, 1994. **19**(14): p. 1061–3.
7. Trebino, R., et al., *Measuring Ultrashort Laser Pulses in the Time-Frequency Domain Using Frequency-Resolved Optical Gating*. Review of Scientific Instruments, 1997. **68**(9): p. 3277–95.
8. Taft, G., et al., *Ultrashort Optical Waveform Measurements Using Frequency-Resolved Optical Gating*. Optics Letters, 1995. **20**(7): p. 743–5.
9. Taft, G., et al., *Measurement of 10-fs Laser Pulses*. Selected Topics in Quantum Electronics, 1996. **2**, Special Issue on Ultrafast Phenomena(3): p. 575–85.
10. Clement, T.S., A.J. Taylor, and D.J. Kane, *Single-shot measurement of the amplitude and phase of ultrashort laser pulses in the violet*. Optics Letters, 1995. **20**(1): p. 70–2.
11. Kane, D.J. and R. Trebino, *Characterization of Arbitrary Femtosecond Pulses Using Frequency Resolved Optical Gating*. IEEE Journal of Quantum Electronics, 1993. **29**(2): p. 571–9.
12. Nibbering, E.T.J., O. Duhr, and G. Korn, *Generation of intense tunable 20-fs pulses near 400 nm by use of a gas-filled hollow waveguide*. Optics Letters, 1997. **22**(17): p. 1335–7.
13. Sweetser, J.N., D.N. Fittinghoff, and R. Trebino, *Transient-Grating Frequency-Resolved Optical Gating*. Optics Letters, 1997. **22**(8): p. 519–21.
14. Eichler, H.J., U. Klein, and D. Langhans, *Coherence Time Measurement of Picosecond Pulses by a Light-Induced-Grating Method*. Applied Physics, 1980. **21**: p. 215–91.
15. Eichler, H.J., P. Günter, and D.W. Pohl, *Laser-Induced Dynamic Gratings*. Springer Series in Optical Sciences. 1986, Berlin: Springer-Verlag.
16. Phillion, D.W., D.J. Kuizenga, and A.E. Siegman, *Subnanosecond Relaxation Time Measurements Using a Transient Induced Grating Method*. Appl. Phys. Lett., 1975. **27**: p. 85–7.
17. Eckbreth, A.C., *BOXCARS: Crossed-Beam Phase-matched CARS Generation in Gases*. Appl. Phys. Lett., 1978. **32**(7): p. 421–3.
18. Trebino, R., C.E. Barker, and A.E. Siegman, *Tunable-Laser-Induced Gratings for the Measurement of Ultrafast Phenomena*. IEEE J. Quant. Electron., 1986. **QE-22**: p. 1413–30.
19. Trebino, R. and A.E. Siegman, *Subpicosecond-Relaxation Study of Malachite Green Using a Three-Laser Frequency-Domain Technique*. J. Chem. Phys., 1983. **79**: p. 3621.
20. Rundquist, A., et al., *Measurement of Ultrashort Optical Waveforms Using Frequency-Resolved Optical Gating*, in *Generation, Amplification, and Measurement of Ultrashort Laser Pulses II*, F.W. Wise and C.P.J. Barty, Editors. 1995, Society of Photo-Optical Instrumentation Engineers: Bellingham. p. 201–6.
21. Ishida, Y., K. Naganuma, and T. Yajima, *Self-Phase Modulation in Hybridly Mode-Locked CW Dye Lasers*. J. Quantum Electronics, 1985. **21**(1): p. 69–77.
22. Watanabe, A., et al., *Microcomputer-Based Spectrum-Resolved Second Harmonic Generation Correlator for Fast Measurement of Ultrashort Pulses*. Rev. Sci. Instrum., 1985. **56**(12): p. 2259–62.
23. Watanabe, A., et al., *Computer-Assisted Spectrum-Resolved SHG Autocorrelator for Monitoring Phase Characteristics of Femtosecond Pulses*. Optics Communications, 1987. **63**(5): p. 320–4.
24. DeLong, K.W., et al., *Frequency-Resolved Optical Gating With the Use of Second-Harmonic Generation*. J. Opt. Soc. Amer. B, 1994. **11**(11): p. 2206–15.
25. Payne, J., et al., *Measurement of the Amplitude and Phase of Ultrashort Light Pulses from Spectrally Resolved Autocorrelation*. OL, 1993. **18**(22): p. 1946–8.
26. Dudley, J.M., et al., *Direct Measurement of Pulse Distortion Near the Zero-Dispersion Wavelength in an Optical Fiber Using Frequency-Resolved Optical Gating*. Opt. Lett., 1997. **22**(7): p. 457–9.

27. Zeek, E., *Pulse-Shaping for High-Harmonic Generation*, in *Applied Physics*. 2001, University of Michigan: Ann Arbor.
28. Tsang, T., et al., *Frequency-Resolved Optical-Gating Measurements of Ultrashort Pulses Using Surface Third-Harmonic Generation*. Optics Letters, 1996. **21**(17): p. 1381–3.
29. Kwok, A., et al., *Frequency-Resolved Optical Gating Using Cascaded Second-Order Nonlinearities*. IEEE J. Quant. Electron., 1998. **4**(2): p. 271–7.
30. Danielius, R., A. Dubietis, and A. Piskarskas, *Transformation of Pulse Characteristics Via Cascaded Second-Order Effects in an Optical Parametric Amplifier*. Opt. Commun., 1997. **133**: p. 277–81.
31. Krumbügel, M.A., et al., *Ultrafast Optical Switching by Use of Fully Phase-Matched Cascaded Second-Order Nonlinearities in a Polarization-Gate Geometry*. Opt. Lett., 1997. **22**(4): p. 245–7.
32. Sweetser, J.N., M.A. Krumbügel, and R. Trebino, *Amplified Ultrafast Optical Switching by Cascaded Second-Order Nonlinearities in a Polarization-Gate Geometry*. Optics Communications, 1997. **142**: p. 269–72.
33. Fittinghoff, D.N., et al., *Collinear type II second-harmonic-generation frequency-resolved optical gating for use with high-numerical-aperture objectives*. Optics Letters, 1998. **23**(13): p. 1046–8.
34. Fittinghoff, D.N., et al., *Frequency-Resolved Optical Gating Measurement of Ultrashort Pulses Passing Through a High Numerical Aperture Objective*. IEEE J. Quant. Electron., 1999. **35**(4): p. 479–86.
35. Weiner, A.M., *Effect of Group Velocity Mismatch on the Measurement of Ultrashort Optical Pulses via Second Harmonic Generation*. IEEE J. Quant. Electronics, 1983. **QE-19**(8): p. 1276–83.
36. Kempe, M. and W. Rudolph, *Femtosecond pulses in the focal region of lenses*. Phys. Rev. A, 1993. **48**: p. 4721–9.
37. Kempe, M. and W. Rudolph, *Impact of chromatic and spherical aberration on the focusing of ultrashort light pulses by lenses*. Opt. Lett., 1993. **18**: p. 137–9.

7. Geometrical Issues: Single-shot FROG

Rick Trebino

Single-shot FROG

In all the FROG beam geometries we've just discussed, the relative delay is varied by scanning a mirror position. Because only one value of the delay can be set at a time, only one spectrum can be taken at a time. As a result, to produce a FROG trace, these methods require measuring spectra over at least as many laser pulses as the desired number of delay values. More, if we average over more than one pulse for each delay. But what if you've just amplified your pulse up to a Joule, and the rep rate is one pulse per hour, and you just don't feel like waiting around for the day or two it'll take to measure it with such a *multi-shot* method?

Here's another issue: In multi-shot measurements, an implicit assumption is that the pulse intensity and phase are the same for each pulse in the measurement. This is usually a pretty good assumption for Ti:Sapphire oscillators. But what if you're measuring pulses from, say, a free-electron laser, and they're varying like crazy from pulse to pulse, and you'd like to know the intensity and phase of just one? Or you'd like to see just how the phase vs. time varies from pulse to pulse in a kHz train of mJ pulses (you wouldn't be alone here; this is an interesting measurement waiting to be done for most ultrafast lasers; perhaps you'd like to do it for yours . . .).

It turns out that it's easy to make a *single-shot* measurement. The only condition is that the beam spatial profile is smooth (which is either true already or can be made to be true by spatial filtering). It involves *mapping delay onto transverse position*, so the relevant transverse spatial coordinate becomes the delay axis. Frequency will be the other transverse spatial coordinate, so a camera then can see the entire trace of a single pulse. Single-shot FROG techniques turn the spatial mode of the signal beam into the pulse's FROG trace for a camera to record.

All single-shot FROG techniques work like this: the pulse is split into two beams, as usual, but this time the beams are *large* (say, a few mm in diameter); a *cylindrical* lens focuses both beams to a line; and they're then crossed at a *large* angle. Figure 7.1 shows the effect of crossing two beams at a large angle. Note that, in the center, the beams overlap in time (the relative delay is zero). Toward the top of the figure, one pulse precedes the other, while, toward the bottom of the figure, the other precedes the one. Thus the delay varies transversely across the medium [1–19].

Now, if we simply image the nonlinear medium onto a camera, we'll generate a single-shot autocorrelation. To make a single-shot FROG device, we instead image the medium onto the entrance slit of an *imaging spectrometer*.

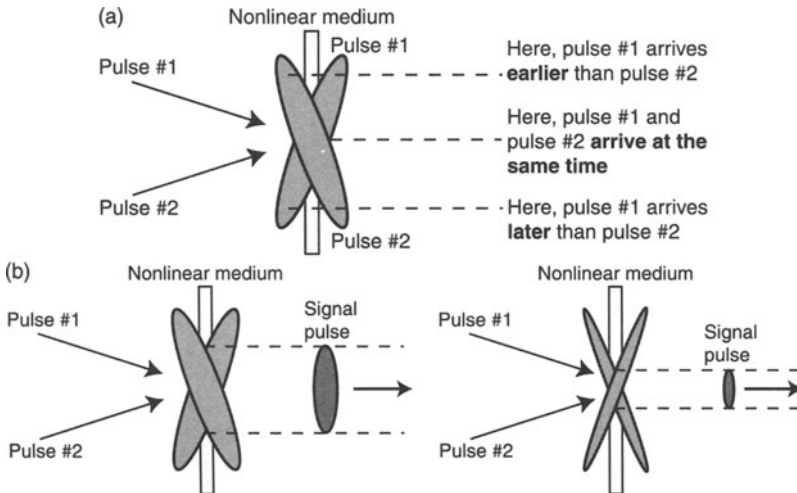


Fig. 7.1: (a) Single-shot FROG (or autocorrelation). The relative delay between two crossed input beams is zero along the center dashed line, but, above it, one beam precedes the other, and, below it, the other precedes the one. This effect allows us to achieve single-shot operation if we image the medium onto the entrance slit of a spectrometer, and then detect at the output of the spectrometer using a multi-element detector (i.e., a camera), which resolves the transverse position. (Imaging onto a camera, without the spectrometer, yields a single-shot autocorrelation.) (b) Single-shot measurement of a long pulse (left). The signal pulse has a large beam diameter, indicating the long duration of the pulse. Single-shot measurement of a short pulse (right). The signal pulse has a small beam diameter, indicating the short duration of the pulse.

The imaging spectrometer then disperses the beam in frequency in a manner that's independent of position on the entrance slit (which is required since our beam will extend along the slit). At the output of the imaging spectrometer, the delay will vary, say, vertically, and frequency will vary horizontally, yielding a FROG trace for a single pulse. Simple! Indeed, it's generally easier to set up a single-shot FROG than a multi-shot one.

To see how much delay we can create in this manner, consider that, if θ is the angle between the beams in the nonlinear medium, then the range of delays across the beam is $\Delta\tau$:

$$\boxed{\Delta\tau = 2(d/c) \tan(\theta/2) \approx d\theta/c} \quad (7.1)$$

where d is the beam diameter, and the approximate result (here and elsewhere in this chapter) will apply when θ is small (see Fig. 7.2).

The delay is a function of transverse coordinate, x . If we set the delay to be zero at the center of the beams, the delay, τ , vs. x will be:

$$\boxed{\tau(x) = 2(x/c) \sin(\theta/2) \approx x\theta/c} \quad (7.2)$$

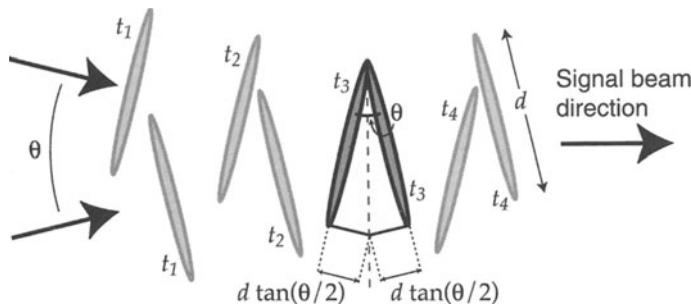


Fig. 7.2: Schematic of two ultrashort pulses of beam diameter, d , crossing at an angle, θ , for several times (t_1 , t_2 , t_3 , and t_4) as they propagate through each other. We consider the pulses at time, t_3 , when their relative delay is zero at one edge, but not zero at the other. Specifically, the upward propagating pulse precedes the other at the latter edge by $2d \tan(\theta/2)$.

The delay-range and delay-vs.-x results are slightly different for the different nonlinear-optical interactions (the precise results depend on the direction of the signal beam). The above result applies specifically to SHG, but, in the small-angle approximation, the expressions are all the same.

As an example, let's implement PG FROG in a single-shot beam geometry to measure a few-hundred-fs pulse. We begin by focusing two \sim 3-mm diameter beams with a cylindrical lens and crossing them at a fairly large angle, say, $\sim 10^\circ$. In this manner, the relative delay between the pulses varies with position at the fused silica nonlinear medium. This yields a range of delays of about 1.5 ps, which covers the possibility that the pulse may be considerably longer. The delay increment will depend on the number of pixels in the array detector used. A spherical lens (not another cylindrical one; you need to image in both dimensions) then images the line-shaped beam-overlap region at the fused silica onto the entrance slit of the spectrometer, so that delay is then mapped onto position along this slit. The optics of the spectrometer then image this delay variation onto the exit plane of the spectrometer. As a result, at the exit plane of the spectrometer (shown on its side in Fig. 7.3), delay proceeds horizontally and frequency proceeds vertically, and the entire trace is obtained on each laser shot.

It is essential, in using this type of beam geometry, to maintain excellent spatial beam quality, and spatial filtering of the beams before the FROG device is recommended unless you're really confident in your beam quality. Single-shot PG FROG experiments were first performed on visible and 308-nm UV pulses by Kane and Trebino [8,20]. And Positive Light sells a nice single-shot PG FROG device.

Also, a common use of single-shot PG FROG is to align amplifiers, when the pulse repetition rate can be low, say, 10 Hz. Check out the nice traces in Chapter 13 on high-power measurements.

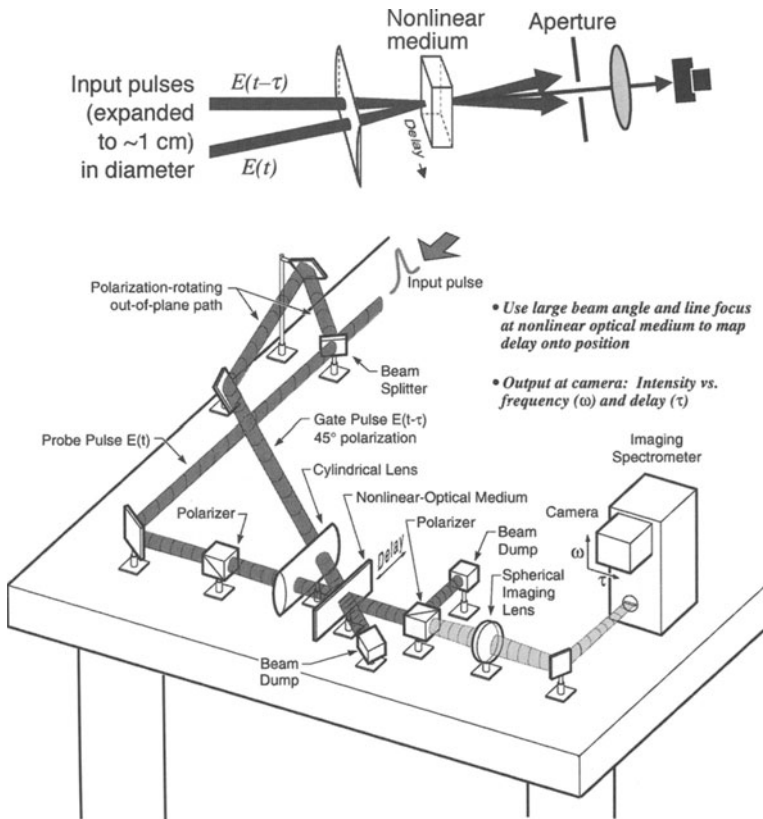


Fig. 7.3: Top: diagram of the key components of a single-shot apparatus, in which a cylindrical lens focuses the beams to lines in the nonlinear medium. Bottom: Layout of an entire single-shot PG FROG device.

By the way, just because a measurement technique is single-shot doesn't mean you can't average over many pulses. The single-shot methods we're talking about collect the entire trace on one pulse, but you can still average over many such (hopefully identical) pulses to take advantage of, not only the improved signal-to-noise-ratio achieved by averaging, but also the simpler apparatus of single-shot methods. It's considerably easier to cross line-shaped beams at a large angle than to scan a delay stage and take numerous spectra. Crossing line-focused beams in space and time involves only one sensitive alignment degree of freedom while crossing spherically focused beams in space and time involves three. Also, cameras work beautifully, are incredibly sensitive, and are inexpensive. So if a pulse's spatial mode quality is good, single-shot methods are generally preferred. Their main drawback is that the line focus has less intensity than the spherical focus, so they're an order of magnitude or three less sensitive than multi-shot methods.

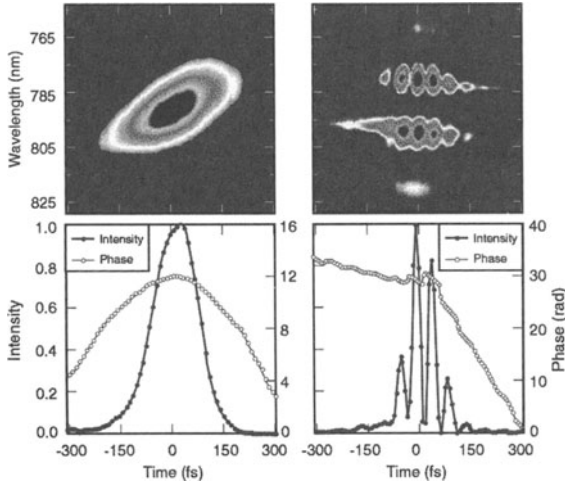


Fig. 7.4: Experimental single-shot PG FROG measurements of a simple linearly chirped pulse (left) and a complex pulse (right). Traces taken by Prof. Bern Kohler while at UCSD.

In the above example, we achieved a range of delays of about ~ 1 ps. What if the pulse to be measured is longer? How about 50 ps? While we can without too much trouble use a beam a cm or two in width and an angle up to about 20° or 30° (achieving non-collinear phase-matching could become an issue for larger angles), generating more than about 10 ps of delay using crossed beams is difficult.

Fortunately, it's also possible to tilt the pulse to achieve larger ranges of delays. This is accomplished with a dispersive optical component, such as a prism or grating (see Fig. 7.5). Physically, the prism accomplishes this because the rays that pass through the thicker region of the prism see more glass and experience the slower group-velocity of glass more than the rays that pass through air, whose group velocity is essentially that of vacuum. The near-grazing-incidence grating accomplishes this because rays that diffract off the front edge of the grating have a shorter path to travel. More mathematically, a fundamental property of dispersion is pulse tilt [21].

Single-shot operation is easily achieved with all FROG beam geometries in a similar manner. It should be emphasized that all such measurements require an imaging spectrometer, that is, a spectrometer that images the entrance slit onto a focused and untilted slit pattern at the exit plane. Because commercial spectrometers use off-axis reflections, they typically are not of this type, unless specifically designed, usually with aspherics, to be so. Interestingly, a simple “home-brew” spectrometer, discussed in Chapter 11, is, in fact, an imaging spectrometer, provided that on-axis propagation occurs at both lenses.

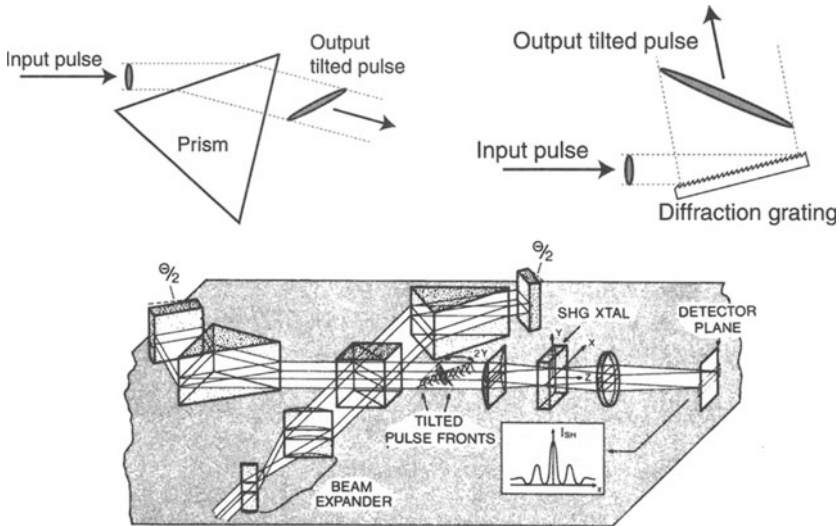


Fig. 7.5: Using dispersive elements to tilt the pulse in order to achieve larger ranges of delay. Top left: In passing through a prism, light that passes near the tip sees less material than does light that passes near the base. While the phase delay vs. transverse position results in the phase fronts remaining perpendicular to the direction of propagation, the group delay is longer and results in pulse fronts having tilt, as shown. Top right: In diffracting off a grazing-incidence grating, light takes different paths, and the pulse front tilt is clear from the drawing. Bottom: Implementation of this idea in an autocorrelator [22].

Geometrical Time-Smeearing

Single-shot measurements take advantage of the fact that the delay varies across the nonlinear medium because the beams are crossed at an angle, a desirable effect. In multi-shot versions of FROG, however, where a translation stage varies the delay, this effect still occurs and is *undesirable*; it results in the simultaneous occurrence of a range of delays rather than one single value of the delay.

In general, geometrical distortions occur in pulse measurements because, when beams are crossed at an angle, and a signal beam emerges in its own direction, the delay between the two input pulses typically varies from point to point throughout the nonlinear medium. As a result, a detector may see signal light created in spatial regions of the nonlinear medium that correspond to many different delays, rather than the single value of the delay indicated by a movable mirror's translation-stage position. This geometrical distortion or "smearing" of the delay will yield distortions in an autocorrelation, FROG, or any other pulse measurement.

There are two types of geometrical distortions: *transverse* and *longitudinal*. In the transverse case, the delay varies transversely *across* the nonlinear medium, and any detector that collects signal light from the entire transverse

extent of the medium will sample a range of delays at any given time. This is the effect that we exploit for single-shot measurements. In the longitudinal case, the delay varies longitudinally *along* the signal beam as it propagates through the nonlinear medium, and all detectors, which necessarily collect signal light from the entire longitudinal extent of the medium, will sample a range of delays along any given ray [17]. In both cases, distortions, specifically, a broadening of the measured trace in the delay direction, will occur, resulting in a longer measured pulse width than would be correct.

Now, if there's anything an ultrafast scientist really hates, it's something that claims his pulses are longer than they really are. So it's crucial, for more than just scientific reasons, to understand and eliminate these effects.

Fortunately, geometrical time-smearing is usually negligibly small in FROG, and there are many simple methods for reducing, eliminating, or avoiding these effects. Usually, it can be effectively suppressed by proper choice of beam geometry, use of small beams and small angles, or spatial filtering. In addition, we'll see that single-shot SHG FROG turns out to be immune to all geometrical smearing effects. And there's even a method for *correcting* for the typically small amounts of longitudinal distortion [17]. So no measurement should ever be adversely affected by them. Indeed, I know of no report of a measurement that was non-negligibly affected by such distortions. But that doesn't mean that you shouldn't understand them; I'm looking for an example for the next edition of this book.

Transverse Geometrical Distortions in FROG

As we mentioned, transverse variation in the delay (see Fig. 7.1) is actually the *desired* effect in single-shot autocorrelation and FROG geometries. Single-shot FROG, in fact, requires that we go to some length to increase this effect! *As a result, all single-shot pulse-measurement techniques are completely free of transverse geometrical distortions.*

In multi-shot measurements, on the other hand, when we do not spatially resolve the signal beam, transverse variations in the delay broaden the trace and hence the measured pulse, too. We've already considered single-shot FROG, where these effects are desirable, and the same discussion applies in multi-shot FROG, when they're not. So the transverse geometrical smearing time, $\Delta\tau_{\text{trans}}$, is:

$$\boxed{\Delta\tau_{\text{trans}} = 2(d/c)\tan(\theta/2) \approx d\theta/c} \quad (7.3)$$

But whereas the range of delays across the medium must be large compared to the pulse length in single-shot arrangements, in multi-shot FROG, they must be small. Specifically, the range of delays across the focused beam diameter in the medium must be kept small compared to the smallest temporal variations in the pulse, typically, the pulse coherence time, τ_c . For small angles, this

condition is simply:

$$\frac{d\theta}{c} \ll \tau_c \quad (7.4)$$

This condition is usually very easy to satisfy. We're focusing tightly anyway to obtain high intensity in the nonlinear medium, and a small angle is required for interaction-length and phase-matching considerations. But is it *always* possible to satisfy this condition? It turns out that, in the extreme case of pulses with bandwidths on the order of their average frequency, i.e., ultrabroadband pulses (such as single-cycle pulses), this condition actually turns out to be *impossible* to meet.

To see this, recall that the coherence time is $\tau_c \approx 1/\Delta\nu$, and for such broadband pulses, $\Delta\nu \approx \nu$, so, for such pulses, $\tau_c \approx 1/\nu$. Now, consider that the best we can hope to do is to propagate the two input beams parallel to each other and as close as possible to each other (i.e., one input beam diameter, d_i , apart) and then to focus and cross them with a lens of focal length, f . Which focal length and which input beam diameter to use are questions we must answer by our analysis. For Gaussian beams, the focused spot size will be approximately $d \approx f\lambda/d_i$, and the crossed-beam angle will be $\theta = d_i/f$. Substituting into Eq. (7.4), we find:

$$\frac{d\theta}{c} = (f\lambda/d_i)(d_i/f)/c = \lambda/c = 1/\nu = \tau_c \quad (7.5)$$

Amazingly, the focal length and input beam diameter cancel out! Also, the minimum geometrical smearing is one optical period! And in this ultrabroadband case, one optical period corresponds precisely to the coherence time! So $d\theta/c$ cannot be much less than τ_c , because the best we can do is to make them equal—*independent* of the input beam size and lens focal length. Thus, beams with temporal structure on the order of one optical period (that is, have a bandwidth on the order of the frequency of the pulse) will necessarily require effort to avoid distortions in multi-shot measurements.

On the other hand, in measurements of the shortest pulse ever created at the time of this writing (2.5 cycles)—where such distortions should be the most deleterious according to the above argument—they in fact proved to be negligible. This is because this record-setting pulse had a bandwidth of only about half of its frequency, order-unity factors we neglected in our rough estimate must also be considered (and they turn out to be helpful), and the smearing parameter affects the pulse measurement as the square in a Pythagorean sum (see Chapter 14). Thus, the pulse-measurement problem has to become fairly extreme before transverse geometrical smearing is an issue.

Nevertheless, people worry about this effect (someone once went so far as to announce in a conference talk that, due to this effect, FROG was “dead”). So it's worth mentioning that this distortion is easily suppressed by spatially filtering out the edges of the signal beam, as shown in Fig. 7.6. Interestingly,

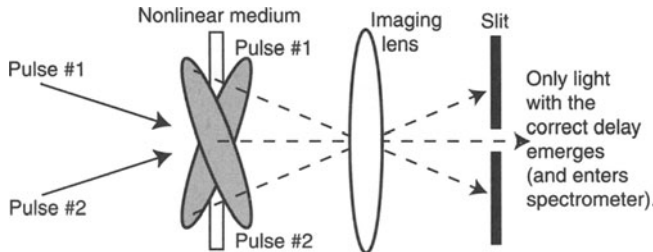


Fig. 7.6: Simple method for suppressing transverse geometrical distortions in multi-shot FROG measurements. Since the signal beam must be imaged onto a spectrometer slit, and the off-center regions of the signal beam correspond to undesired values of delay, it is simply necessary to close the slit somewhat to eliminate the undesired values of the delay.

the lens and slit are already present in most FROG apparatuses, since the next device that the beam sees is a spectrometer! So this method for removing transverse geometrical distortions is not only effective, but also free, and it takes almost no time to implement! Thus, even in the most extreme cases, transverse geometrical distortions shouldn't be a problem.

We delay a quantitative, practical analysis of transverse geometrical smearing until the chapter on the measurement of near-single-cycle pulses (Chapter 14), where it is more relevant. But we conclude that, while one must keep this effect in mind when setting up apparatus, it plays a minimal role in FROG as well as in autocorrelation. And, even in extreme cases (such as few-fs pulse measurement), when it could play a role, and extremely precise results are required, filtering removes it effectively if it isn't negligible to begin with.

Finally, our results for transverse geometrical smearing were derived specifically for SHG FROG. Transverse distortions can also broaden traces in other multi-shot versions of FROG, but the small-angle approximation to our results applies to them as well. We conclude that this effect will be equally small in these geometries. In addition, the resulting (potentially broadened) traces will not correspond to traces of actual pulses (as is the case for SHG FROG). This is because, while SHG FROG traces are necessarily symmetrical with respect to delay, the traces of these other methods are not. For example, unlike SHG FROG, where the relative widths of the trace in the delay and frequency directions indicate the chirp, it's instead the *slope* of the trace in other FROG methods that indicates the chirp. Thus, since the frequency width and slope of a non-SHG FROG trace will remain unchanged, this effect should cause even less error in these other versions of FROG. By the way, the same is true for broadening due to longitudinal distortions, as well.

So if you hear someone talking about his world's record 1-fs pulse, which he first measured to be 100 fs long, but which he then reduced in length by making massive corrections due to huge transverse geometrical smearing

effects, I hope you'll ask a very pointed question. Don't laugh; something like this has already happened, and I had laryngitis at the time.

Longitudinal Geometrical Distortions in FROG

Longitudinal distortions occur when the delay varies along the signal beam direction as it propagates through the nonlinear medium (see Fig. 7.7). Whereas transverse distortions allow us to perform single-shot measurements and hence can be useful, longitudinal geometrical distortions, on the other hand, have no known useful purpose and hence must be minimized, avoided, or removed. Fortunately, this effect is also almost always negligible, but there are extreme cases when it is not, so again, it's important to consider.

Fortunately, when an autocorrelation or FROG signal beam propagates along the *bisector* of the angle formed by the input beams (see Fig. 7.8), the relative beam delay remains the same along all rays of the signal beam for the entire length of the nonlinear medium. Consequently, methods in which the signal beam bisects the input beam angle are free from longitudinal geometrical distortions. This is case for all SHG-based methods. Thus, because they lack longitudinal geometrical distortions and use the transverse delay variations to achieve single-shot operation, *single-shot SHG autocorrelation and single-shot SHG FROG have no geometrical distortions at all*.

On the other hand, longitudinal distortions do occur in all beam geometries in which the signal beam does not propagate as the bisector of the input beams, that is, all third-order geometries and even second-order cross-correlation measurements if the two pulses are different colors.

We can calculate the amount of longitudinal geometrical smearing for a single-shot polarization-gate FROG or autocorrelation beam geometry. The geometrical distance walked by the zero-delay point, g , can be calculated by inspection of Fig. 7.9, which shows the paths of the two beams through

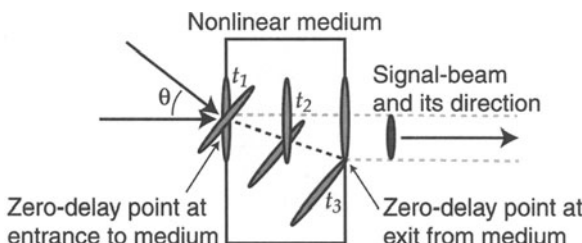


Fig. 7.7: Asymmetric beam geometry used for PG FROG, in which the signal beam propagates collinearly with one of the input beams (and not along the bisector of the input beams). The zero-delay point shifts as a function of depth in the nonlinear medium. Thus, along any path of the signal beam, a range of delays is sampled. This geometry experiences longitudinal distortion, whether used in the single- or multi-shot configuration. The signal pulse shown reveals the resulting (broadened) width of the trace in a single-shot PG FROG measurement.

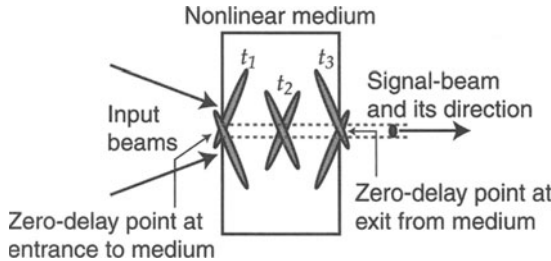


Fig. 7.8: Symmetrical beam geometry showing the two crossed beams at three distinct times as they propagate through the nonlinear medium. Here the signal beam propagates along the bisector of the input beam angle. Note that, along the dashed line (and all other lines parallel to it), the same relative beam delay occurs for the entire length of the medium. Thus, no longitudinal distortion is present when the signal beam propagates along the bisector of the two input beams. The signal pulse shown reveals the resulting (accurate) width of the trace in a single-shot SHG FROG measurement.

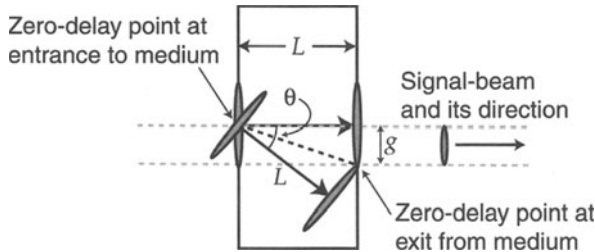


Fig. 7.9: Beam geometry for calculating the longitudinal geometrical smearing. The two black solid arrows represent the two beams. The zero-delay point drifts transversely by a distance, g . Similarly, the point of any particular delay drifts the same amount.

the nonlinear medium of length, L (over the time L/c). Note that the zero-relative-delay point drifts a distance g downward along the black dashed line. If we observe that the black dashed line (the zero-delay line) bisects the angle formed by the two beam paths, we can calculate g :

$$g = L \tan(\theta/2) \approx L\theta/2 \quad (7.6)$$

The amount of smearing, $\Delta\tau_{\text{long}}$, to which this corresponds in a single-shot geometry depends on the mapping of delay onto position. Above, we saw that the delay vs. position is $\tau(x) \approx x\theta/c$ in the small-angle approximation, so the delay per unit position will be: θ/c and the smearing will be g times this amount or $g\theta/c$:

$$\Delta\tau_{\text{long}} \approx L\theta^2/2c \quad (7.7)$$

In this result, we can see that the length of the nonlinear medium now plays the key role, rather than the beam diameter, as in the transverse case. And the angle enters as the square.

In single-shot PG FROG, for instance, when the thickness of the medium is 400 μm and the intersection angle is 8° , the longitudinal geometrical smearing is about 20 fs; this means pulse structure shorter than 20 fs will be washed out in the delay direction under these conditions. The temporal resolution can be improved by use of a thinner medium and a smaller intersection angle. This, however, is not always the optimal solution: the signal level will decrease due to the thinner medium, and scattered light will increase due to the smaller angle. As a result, the signal-to-noise ratio could decrease to unacceptable limits. In addition, a shallow angle between the beams limits the range of delays for a given beam diameter, thus limiting the length of the pulse that can be measured in single-shot measurements. Of course, a short pulse can be measured using a smaller beam angle and thus suffers from less longitudinal distortions. And, analogously, a long pulse requires a larger beam angle but will be unbothered by the somewhat larger distortions it will see. The use of an 8° angle is generally required for pulses nearly a ps long, so this is generally only an issue for complex pulses that are both picoseconds long, but also have structure on a few-fs time scale, and which we plan to measure with a medium longer than $\sim 100 \mu\text{m}$ long.

If longitudinal geometrical smearing is an issue, choosing a geometry whose signal beam propagates as close as possible to the input beam bisector (such as SHG or THG) also reduces or eliminates these distortions.

Rigorous Theory of Single-shot Geometries and Geometrical Distortions

We can treat this problem a bit more rigorously to see how single-shot FROG works and to see how both transverse and longitudinal geometrical effects occur in most FROG beam geometries. Let the signal beam propagate along the z -axis. And let the two input beams, which have k -vectors, k_1 and k_2 , propagate at angles, θ_1 and θ_2 , respectively, to the z -axis.

Without specifying a particular geometry, let the signal field be given, in the limit of parallel beams, by the product of a “probe” pulse and a “gate” pulse complex amplitudes:

$$E_{\text{sig}}(t, \tau) = P(t)G(t - \tau) \quad (7.8)$$

where $P(t) = G(t) = E(t)$ for SHG FROG. But $P(t) = E(t)$ and $G(t) = |E(t)|^2$ for PG FROG. The time co-ordinate is the usual co-moving time variable that's always zero at the pulse center. The FROG trace in this ideal limit is then:

$$I_{\text{FROG}}(\omega, \tau) = \left| \int_{-\infty}^{\infty} P(t) G(t - \tau) \exp(-i\omega t) dt \right|^2 \quad (7.9)$$

The above expression has no geometrical effects, however. Now suppose that the beams are non-collinear, with P having k -vector k_1 and G having

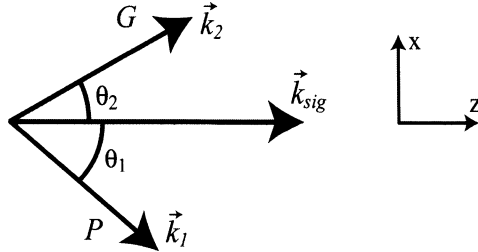


Fig. 7.10: Beam geometry for calculating the geometrical smearing in general FROG measurements. P is the probe pulse, and G is the gate pulse.

k -vector k_2 in Fig. 7.10. We can write P and G , taking into account their directions:

$$P(x, z, t') = P(t' - z \cos \theta_1/c + x \sin \theta_1/c) \quad (7.10)$$

$$G(x, z, t') = E(t' - z \cos \theta_2/c - x \sin \theta_2/c - \tau) \quad (7.11)$$

where t' is real time. Ordinarily, we assume that the FROG signal field is independent of x and z . But here, we realize that the contribution, δE_{FROG} , to the FROG signal field at the exit of the nonlinear medium is a function of x , z , t' , and a delay, τ :

$$\begin{aligned} & \delta E_{\text{FROG}}(x, z, t', \tau) \\ &= P(t' - z \cos \theta_1/c + x \sin \theta_1/c) G(t' - z \cos \theta_2/c - x \sin \theta_2/c - \tau) \end{aligned} \quad (7.12)$$

Transforming to a co-moving co-ordinate system, we can let:

$$t = t' - z \cos \theta_1/c + x \sin \theta_1/c \quad (7.13)$$

so:

$$\delta E_{\text{FROG}}(x, z, t, \tau) = P(t)G(t - \tau') \quad (7.14)$$

where the delay parameter, τ' , depends on the delay and the two spatial co-ordinates, x and z :

$\tau' = \tau'(\tau, x, z) = \tau + z[\cos \theta_1 - \cos \theta_2]/c - x[\sin \theta_1 + \sin \theta_2]/c$

(7.15)

The signal field is the integral of $\delta E_{\text{FROG}}(x, z, t, \tau)$ along its propagation direction, assumed to be the z -axis:

$$E_{\text{FROG}}(x, L, t, \tau) = \int_0^L P(t)G(t - \tau') dz \quad (7.16)$$

where we have assumed a phase-matched interaction.

Finally, the FROG trace is given by the squared magnitude of the Fourier transform of the above signal field:

$$I_{\text{FROG}}(x, L, \omega, \tau) = \left| \int_{-\infty}^{\infty} \int_0^L P(t) G(t - \tau') \exp(-i\omega t) dz dt \right|^2 \quad (7.17)$$

We can interchange orders of integration:

$$I_{\text{FROG}}(x, L, \omega, \tau) = \left| \int_0^L \left[\int_{-\infty}^{\infty} P(t) G(t - \tau') \exp(-i\omega t) dt \right] dz \right|^2 \quad (7.18)$$

This is the desired result. It yields the measured trace for arbitrary crossing angle, θ , and nonlinear-medium thickness, L . Notice that the bracketed expression contains the usual FROG trace. However, there is an additional z -integration that must be performed, and the delay, τ' , is potentially a function of x and z . Thus this expression contains both transverse and longitudinal geometrical distortions for an arbitrary two-beam FROG set-up.

Let's consider some limiting cases. First, consider that the medium is very thin. In this case, the z -integration involves simply setting $z = 0$ and multiplying by L :

$$I_{\text{FROG}}(x, L, \omega, \tau) = \left| \int_{-\infty}^{\infty} P(t) G(t - \tau') \exp(-i\omega t) dt \right|^2 L^2 \quad (7.19)$$

where:

$$\tau' = \tau'(\tau, x) = \tau - x[\sin \theta_1 + \sin \theta_2]/c \quad (7.20)$$

Thus, we obtain the usual FROG trace, but with the possible presence of transverse geometrical smearing if the FROG signal beam is integrated over all x , as in multi-shot measurements. Alternatively, if we set $\tau = 0$, and measure the signal vs. transverse position, x , we have a single-shot FROG device with delay mapped onto transverse position, given by Eq. (7.20). Note that, when the nonlinear medium is thin, there is no geometrical smearing in any single-shot FROG geometry.

Another case of interest occurs when the signal beam bisects the angle formed by the two input beams, as occurs in SHG FROG. Here, we allow the medium to potentially be very thick.

In this case, $\theta_1 = \theta_2 = \theta/2$, so the cosine terms cancel in τ' , and the z -dependence in τ' again disappears:

$$\tau' = \tau'(\tau, x) = \tau - 2x \sin(\theta/2)/c \quad (7.21)$$

Indeed, the integrand now has no z -dependence. Since the z -integration is simply over a constant, we again obtain Eq. (7.19), the standard FROG trace, but again with the possibility of transverse geometrical smearing. And again, if $\tau = 0$ and we measure the FROG signal vs. transverse position, x , we

obtain a single-shot (SHG) FROG measurement of the pulse. Significantly, notice that, in this case, there is *no geometrical distortion at all, even for a very thick medium!* This confirms the conclusion we drew based on symmetry in the previous section.

Other cases: as discussed earlier, other geometries, in which the signal beam does not bisect the angle formed by the input beams, will suffer from some geometrical smearing in both multi-shot and single-shot cases. Fortunately, these effects are typically small in most practical arrangements. For example, in multi-shot PG FROG, looking at Eq. (7.15), we see that the upper limit for longitudinal geometrical smearing is:

$$\Delta\tau_{long} \leq \frac{L}{c} [\cos(\theta_1) - \cos(\theta_2)] \quad (7.22)$$

$$\leq \frac{L}{c} \left[1 - \left(1 - \frac{\theta^2}{2} \right) \right] \quad (7.23)$$

$$\leq \frac{L\theta^2}{2c} \quad (7.24)$$

the same expression as for single-shot PG FROG. But because θ is so much smaller for multi-shot measurements, typical values of multi-shot longitudinal smearing are in the tens of attoseconds.

Before we close, if you'd like to know more about these interesting effects, Tien, et al., have considered longitudinal geometrical smearing in single-shot PG FROG using a thick medium and have shown that it can be removed from the trace by a clever mathematical manipulation [17].

Finally, there is yet another geometrical effect to be considered. In Chapter 14, we'll see that, when the input beams are very broadband and there is significant phase distortion in the pulse, the signal beam can actually *wobble* during the pulse. This means that θ_1 and θ_2 can become time-varying (or equivalently, frequency-varying) quantities. Fortunately, even in measurements of the shortest pulses generated to date, such effects are very small.

References

1. Arakelian, S.A., R.N. Gyuzalian, and S.B. Sogomonian, *Comments on the Picosecond Pulse Width Measurement By the Single-Shot Second Harmonic Beam Technique*. Optics Communications, 1982. **44**(1): p. 67–72.
2. Bourne, O.L. and A.J. Alcock, *Ultraviolet and Visible Single-Shot Autocorrelator Based on Multiphoton Ionization*. Review of Scientific Instruments, 1986. **57**(12): p. 2979–82.
3. Brun, A., et al., *Single-Shot Characterization of Ultrashort Light Pulses*. J. Phys. D., 1991. **24**: p. 1225–33.
4. Clement, T.S., A.J. Taylor, and D.J. Kane, *Single-shot measurement of the amplitude and phase of ultrashort laser pulses in the violet*. Optics Letters, 1995. **20**(1): p. 70–2.
5. Fourkas, J.T., et al., *Spatially-Encoded, Single-Shot Ultrafast Spectroscopies*. J. Opt. Soc. of Amer. B, 1995. **12**(1): p. 155–65.
6. Janszky, J. and G. Corradi, *Full Intensity Profile Analysis of Ultrashort Laser Pulses Using Four-Wave Mixing or Third Harmonic Generation*. Optics Communications, 1986. **60**(4): p. 251–6.

7. Kabelka, V. and A.V. Masalov, *Angularly resolved autocorrelation for single-shot time-frequency imaging of ultrashort light pulse*. Optics Communications, 1995. **121**(4–6): p. 141–8.
8. Kane, D.J. and R. Trebino, *Single-Shot Measurement of the Intensity and Phase of an Arbitrary Ultrashort Pulse By Using Frequency-Resolved Optical Gating*. Opt. Lett., 1993. **18**(10): p. 823–5.
9. Kane, D.J., et al., *Simultaneous measurement of two ultrashort laser pulses from a single spectrogram in a single shot*. Journal of the Optical Society of America B (Optical Physics), 1997. **14**(4): p. 935–43.
10. Le Blanc, S.P., G. Szabo, and R. Sauerbrey, *Femtosecond Single-Shot Phase-Sensitive Autocorrelator for the Ultraviolet*. Optics Letters, 1991. **16**(19): p. 1508–10.
11. Mehendale, M., et al., *Method for single-shot measurement of the carrier envelope phase of a few-cycle laser pulse*. Optics Letters, 2000. **25**(22): p. 1672–4.
12. Michelmann, K., et al., *Frequency resolved optical gating in the UV using the electronic Kerr effect*. Applied Physics B (Lasers and Optics), 1996. **B63**(5): p. 485–9.
13. Salin, F., et al., *Single-Shot Measurement of a 52-fs Pulse*. Applied Optics, 1987. **26**(21): p. 4528–31.
14. Saltiel, S.M., K.A. Stankov, and P.D. Yankov, *Realization of a Diffraction-Grating Autocorrelator for Single-Shot Measurement of Ultrashort Light Pulses Duration*. Applied Physics B, 1986. **40**: p. 25–7.
15. Sarukura, N., et al., *Single-Shot Measurement of Subpicosecond KrF Pulse Width by Three-Photon Fluorescence of the XeF Visible Transition*. Optics Letters, 1988. **13**(11): p. 996–8.
16. Szatmári, S., F.P. Schäfer, and J. Jethwa, *A Single-Shot Autocorrelator for the Ultraviolet with a Variable Time Window*. Review of Scientific Instruments, 1990. **61**(3): p. 998–1003.
17. Tien, A.C., et al., *Geometrical distortions and correction algorithm in single-shot pulse measurements: application to frequency-resolved optical gating*. Journal of the Optical Society of America B (Optical Physics), 1996. **13**(6): p. 1160–5.
18. Tünnermann, M.H.R., et al., *Single-Shot Autocorrelator for KrF Subpicosecond Pulses Based on Two-Photon Fluorescence of Cadmium Vapor at $\lambda = 508\text{ nm}$* . OL, 1991. **16**(6): p. 402–4.
19. Wyatt, R. and E.E. Marinero, *Versatile Single-Shot Background-Free Pulse Duration Measurement Technique for Pulses of Subnanosecond to Picosecond Duration*. Applied Physics, 1981. **25**: p. 297–301.
20. Kane, D.J., et al., *Single-Shot Measurement of the Intensity and Phase of Femtosecond UV Laser Pulse Using Frequency-Resolved Optical Gating*. Optics Letters, 1994. **19**(14): p. 1061–3.
21. Diels, J.C. and W. Rudolph, *Ultrashort Laser Pulse Phenomena*. 1996, San Diego: Academic Press.
22. Szabo, G., Z. Bor, and A. Muller, *Phase-Sensitive Single-Pulse Autocorrelator for Ultrashort Laser Pulses*. Optics Letters, 1988. **13**(9): p. 746–8.

8. The FROG Algorithm

Marco A. Krumbuegel and Rick Trebino

Introduction

While much qualitative information about a pulse can be gleaned from its FROG trace, we'd usually like to obtain more quantitative information, specifically, the intensity and phase vs. time or frequency. Unfortunately, no reliable closed-form solution for inversion of a spectrogram is known (especially when the pulse gates itself). We saw in Chapter 5 that retrieving the pulse from a FROG trace is equivalent to the 2D phase retrieval problem, and that algorithms exist for doing this. Indeed, almost all of the several available FROG algorithms are modified phase-retrieval algorithms.

The task of every FROG algorithm is the same: retrieve the complex electric field $E(t)$ of the pulse from its FROG trace $I_{\text{FROG}}(\omega, \tau)$. The FROG trace is a spectrogram, $\Sigma_g^E(\omega, \tau)$:

$$\Sigma_g^E(\omega, \tau) = \left| \int_{-\infty}^{\infty} E(t)g(t - \tau) \exp(-i\omega t) dt \right|^2 \quad (8.1)$$

In FROG, however, the gate function $g(t - \tau)$ is a function of the electric field $E(t)$, and it may gate, not $E(t)$ itself, but a function of $E(t)$. We thus can write the FROG trace more generally as:

$$I_{\text{FROG}}(\omega, \tau) = \left| \int_{-\infty}^{\infty} E_{\text{sig}}(t, \tau) \exp(-i\omega t) dt \right|^2 \quad (8.2)$$

where the signal field $E_{\text{sig}}(t, \tau)$ is the result of a function of the pulse's electric field $E(t - \tau)$ gating another function of the pulse's field $E(t)$. The exact mathematical form of the signal field depends on the type of the non-linear optical interaction employed in the experimental setup, a few of which are given by [1]:

$$E_{\text{sig}}(t, \tau) \propto \begin{cases} E(t) |E(t - \tau)|^2 & \text{for PG FROG} \\ E(t)^2 E^*(t - \tau) & \text{for SD FROG} \\ E(t) E(t - \tau) & \text{for SHG FROG} \\ E(t)^2 E(t - \tau) & \text{for THG FROG} \end{cases} \quad (8.3)$$

Several FROG pulse-retrieval algorithms exist, and the best possible computer program for pulse retrieval would incorporate all of them, switching from one to another if one stagnates (and the commercially available FROG code does indeed switch in this manner). A common feature of most FROG algorithms

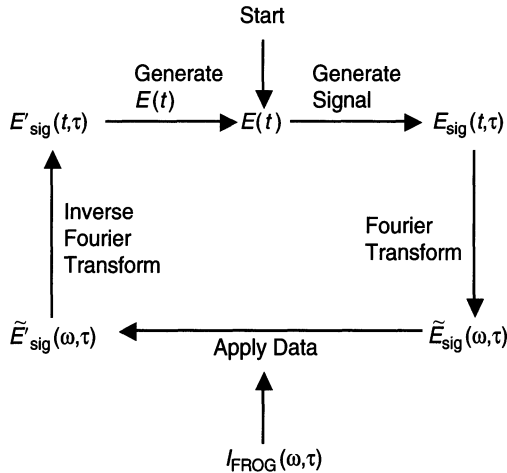


Fig. 8.1: Schematic of a generic FROG algorithm.

is that they're based on the iterative-Fourier-transform algorithm commonly used in phase retrieval [1–4] and schematically shown in Fig. 8.1.

It works like this: Starting with an initial guess for the field $E(t)$, a signal field $E_{\text{sig}}(t, \tau)$ is generated using Eq. (8.3). This field is then Fourier transformed with respect to t in order to generate the signal field $\tilde{E}_{\text{sig}}(\omega, \tau)$ in the frequency domain. The measured FROG trace $I_{\text{FROG}}(\omega, \tau)$ is then used to generate an improved signal field $\tilde{E}'_{\text{sig}}(\omega, \tau)$. Since the squared magnitude of $\tilde{E}_{\text{sig}}(\omega, \tau)$ should be equal to $I_{\text{FROG}}(\omega, \tau)$, this step nearly always involves simply replacing the magnitude of $\tilde{E}_{\text{sig}}(\omega, \tau)$ with the square root of the measured trace to generate $\tilde{E}'_{\text{sig}}(\omega, \tau)$. $\tilde{E}'_{\text{sig}}(\omega, \tau)$ is then transformed back into the time domain by applying an inverse Fourier transform. In the last step of the cycle, the modified signal field $\tilde{E}'_{\text{sig}}(t, \tau)$ is used to generate a new guess for $E(t)$. And the process is repeated. Ideally, each iteration of the algorithm generates a better guess, which eventually approaches the correct complex electric field.

In this chapter, we first summarize the basic algorithm used in the original implementation of FROG [5,6], often referred to as the *vanilla algorithm* because it's quick, simple, but not that satisfying (it doesn't always converge). We then discuss the algorithm that has made FROG a technique that can measure virtually every imaginable ultrashort laser pulse. This is the *generalized projections algorithm*, which, in the absence of noise [7,8], generally converges to the correct solution with an accuracy only limited by the host-computer system's numerical precision. It's also very versatile: it can be modified for any nonlinear-optical interaction that you may have handy to measure a pulse (see, for example, Chapters 18 and 20).

There is also something that can be done to speed up generalized-projections-based algorithms: a *short-cut* technique that not only improves the algorithm's speed, but also aids a more robust convergence in the presence of noise.

We delay discussion of a considerably faster algorithmic technique based on the idea of singular-value decomposition, called the Principal Component Generalized Projections algorithm [9,10], until Chapter 21.

Finally, we discuss a host of additional improvements to the basic algorithm [11]. Although the two generalized-projections approaches have proven superior, the improved basic algorithm is still useful as part of a composite algorithm that often proves to be more robust than any single algorithm alone. Indeed, the combination of these algorithms, as implemented in the commercially available code (from FemtoSoft and MakTech) is extremely robust, and poor convergence only results when the trace is contaminated with massive amounts of systematic error or noise or is badly cropped.

Basic (“Vanilla”) FROG Algorithm

We can consider Eqs. (8.2) and (8.3) as two constraints that the signal field $E_{\text{sig}}(t, \tau)$ must satisfy. The *mathematical-form constraint* is embodied by Eq. (8.3), and the *data constraint* is embodied by Eq. (8.2). The different iterative phase retrieval algorithms used in FROG can be distinguished by the way the constraints on the signal field $E_{\text{sig}}(t, \tau)$ are applied: (1) how the new guess for $E(t)$ in the $(k + 1)$ -th iteration is generated from the mathematical form of the signal field $E'_{\text{sig}}(t, \tau)$ of the k -th iteration, and (2) how the measured data are used.

The data constraint is the easier one. In the basic FROG algorithm [5,6], as well as in most other FROG algorithms, the data-trace is applied in the frequency domain by simply replacing the magnitude of the current guess $\tilde{E}_{\text{sig}}(\omega, \tau)$ with the square root of the intensity of the measured FROG trace $I_{\text{FROG}}(\omega, \tau)$, leaving the phase unchanged:

$$\tilde{E}'_{\text{sig}}(\omega, \tau) = \frac{\tilde{E}_{\text{sig}}(\omega, \tau)}{\left| \tilde{E}_{\text{sig}}(\omega, \tau) \right|} \sqrt{I_{\text{FROG}}(\omega, \tau)} \quad (8.4)$$

Implementation of the mathematical-form constraint is less intuitive. In the basic vanilla FROG algorithm, the new guess for $E(t)$ is generated from the signal field $E'_{\text{sig}}(t, \tau)$ by a simple integration over the delay τ :

$$E^{(k+1)}(t) = \int_{-\infty}^{\infty} E_{\text{sig}}^{(k)}(t, \tau) d\tau \quad (8.5)$$

Why do this? Well, consider, for example, the PG FROG signal field, $E(t)|E(t - \tau)|^2$. If we integrate it vs. τ , the $E(t)$ factor, which is independent of τ , factors out of the integral, which can then be seen to be independent of

time by changing integration variables from t to $t - \tau$. Thus, Eq. (8.5) generates a quantity proportional to $E(t)$, which we take to be its next iteration.

In order to quantify the progress of the retrieval, i.e., the convergence of the algorithm, we must further define a measure of the error between exact and derived pulse fields. Fortunately, even though the actual pulse field $E(t)$ is unknown in experimental situations, such an error measure is readily available from the FROG trace. We define the FROG error in the k -th iteration as

$$G^{(k)} = \sqrt{\frac{1}{N^2} \sum_{i,j=1}^N \left| I_{\text{FROG}}(\omega_i, \tau_j) - \mu I_{\text{FROG}}^{(k)}(\omega_i, \tau_j) \right|^2} \quad (8.6)$$

where μ is a real normalization constant that minimizes the error $G^{(k)}$. $I_{\text{FROG}}(\omega_i, \tau_j)$ is the measured FROG trace, $I_{\text{FROG}}^{(k)}(\omega_i, \tau_j)$ is the k -th iteration of the retrieved FROG trace, i.e., the squared magnitude of $\tilde{E}_{\text{sig}}^{(k)}(\omega, \tau)$, and ω_i and τ_j are the i -th frequency and the j -th delay vectors, respectively. The FROG error G has proven to be an effective measure for convergence, and it's not only used in the vanilla FROG algorithm discussed here, but it's also used in all other FROG algorithms.

An advantage of the vanilla algorithm is that it's extremely fast and often works surprisingly well, particularly for PG FROG. Random noise for the intensity and phase is typically used as the initial guess, but it is also possible to use a pulse closer to the correct solution, e.g., a pulse with Gaussian intensity profile and random or flat phase, as the initial guess. While this sometimes helps, especially in SHG FROG with its direction-of-time ambiguity, FROG algorithms are generally not very sensitive to the particular choice of an initial guess, and noise works surprisingly well.

Unfortunately, the vanilla algorithm tends to be unstable in the presence of noise and fails to converge for pulses with significant intensity substructure, most notably the relatively simple case of a symmetrical double pulse with two well separated Gaussian peaks and a flat phase, and more generally also for sequences of independent pulses. While the noise problem can be alleviated by proper noise filtering [7], the cause of failure in the double-pulse case is not easily discernible, and it occurs even if the algorithm is started with an almost perfect initial guess instead of random noise [11]. The problem seems to be associated to the problem of “striping” in the usual phase-retrieval problem [12], but the solutions to this problem suggested in the phase-retrieval literature are either inapplicable or ineffective when applied to the FROG algorithm [11]. Nevertheless, the vanilla algorithm is very fast, so it is usually used first, until it stagnates, and then more reliable, but slower, algorithms kick in.

Generalized Projections

Experience has shown that a single algorithmic technique is so reliable and so superior to the others that most pulses can be retrieved with it alone. This

method is called *generalized projections* [8,13–23], and it is frequently used in phase-retrieval problems, from which it was borrowed for FROG. It is also commonly used in many other problems, from x-ray crystallography to the training of artificial neural networks. Indeed, it is one of the few algorithmic methods than can be *proven* to converge when reasonable conditions are met.

The essence of the generalized projections technique is graphically displayed in Fig. 8.2. Consider Fig. 8.2 a Venn diagram in which the entire figure represents the set of all complex functions of two variables, i.e., potential signal fields, $E_{\text{sig}}(t, \tau)$. The signal fields satisfying the data constraint, Eq. (8.2), are indicated by the lower elliptical region, while those satisfying the mathematical-form constraint, Eq. (8.3), are indicated by the upper elliptical region. The signal-pulse field satisfying both constraints corresponds to the intersection of the two elliptical regions and is the solution, uniquely yielding the pulse field, $E(t)$.

The solution is found by making *projections*, which have simple geometrical analogs. We begin with an initial guess at an arbitrary point in signal-field space (usually a signal field consisting entirely of random numbers), which typically satisfies neither constraint. In the first iteration, we make a projection onto one of the constraint sets, which consists of moving to the point in that set closest to the initial guess. From this point, we then project onto the other set, moving to the point in that set closest to the first iteration. This process is continued until the solution is reached. When the two constraint sets are convex, i.e., all line segments connecting two points in each constraint set lie entirely within the set, convergence is guaranteed.

Unfortunately, the constraint sets in FROG are not convex. When a set is not convex, the projection is not necessarily unique, and a *generalized projection* must be defined. The technique is then called generalized projections (GP), and convergence cannot be guaranteed. Although it thus is conceivable that

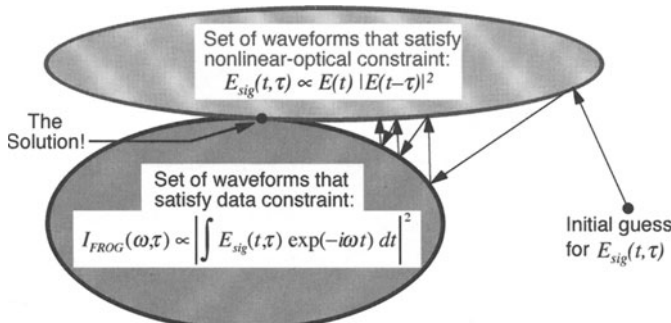


Fig. 8.2: Generalized projections applied to FROG. Two equations are considered as constraints on the function, $E_{\text{sig}}(t, \tau)$, which, when found, yield $E(t)$, the pulse field. Moving to the closest point in one constraint set and then the other yields convergence to the solution. Although the mathematical form constraint for PG-FROG is shown, other FROG geometries can be treated as easily [21].

the algorithm may stagnate at a constant value, this approach is in practice quite robust in FROG problems.

We implement the generalized-projections technique by considering the pulse field, $E^{(k)}(t_i)$, the signal field in the time-delay domain, $E_{\text{sig}}^{(k)}(t_i, \tau_j)$, and the signal field's Fourier transform with respect to time, $\tilde{E}_{\text{sig}}^{(k)}(\omega_i, \tau_j)$, where t_i, τ_i , and $\omega_i = 1, \dots, N$. The superscript (k) indicates that $E^{(k)}(t_i)$ and $E_{\text{sig}}^{(k)}(t_i, \tau_j)$ are k -th iterations of the actual quantities.

In order to perform a GP to the FROG-trace data constraint set, it is simply necessary to replace the magnitude of $\tilde{E}_{\text{sig}}^{(k)}(\omega_i, \tau_j)$ with the square root of the measured FROG trace, $I_{\text{FROG}}(\omega_i, \tau_j)$, as it is done in the basic algorithm. It is easy to show that this simple replacement yields the smallest change in the signal field that is consistent with the measured trace, and that it is therefore a GP for all FROG geometries.

It is, however, more difficult to perform a GP to the mathematical-form constraint set. The goal here is to find the signal field closest to the current iteration for the signal field, $E_{\text{sig}}^{(k)}(t_i, \tau_j)$, that has the desired mathematical form given in Eq. (8.3) for the particular version of FROG. In other words, we wish to find the new signal field, $E_{\text{sig}}^{(k+1)}(t_i, \tau_j)$, that minimizes the functional distance:

$$Z = \sum_{i,j=1}^N \left| E_{\text{sig}}^{(k)}(t_i, \tau_j) - E_{\text{sig}}^{k+1}(t_i, \tau_j) \right|^2 \quad (8.7)$$

and is of the form of Eq. (8.3). We can guarantee that both of these conditions are met by explicitly substituting Eq. (8.3) into the above distance function and solving directly for the pulse field. For the example of SHG FROG, our goal is to find the pulse field, $E^{(k+1)}(t_i)$, $t_i = 1, \dots, N$, that minimizes the functional distance

$$Z = \sum_{i,j=1}^N \left| E_{\text{sig}}^{(k)}(t_i, \tau_j) - E^{(k+1)}(t_i) E^{(k+1)}(t_i - \tau_j) \right|^2 \quad (8.8)$$

Z is now a function of the N parameters of the next iteration of the pulse field $E^{(k+1)}(t_i)$, $t_i = 1, \dots, N$. The analogous expression for PG FROG is:

$$Z = \sum_{i,j=1}^N \left| E_{\text{sig}}^{(k)}(t_i, \tau_j) - E^{(k+1)}(t_i) \left| E^{(k+1)}(t_i - \tau_j) \right|^2 \right|^2 \quad (8.9)$$

Once $E^{(k+1)}(t_i)$ is found, the corresponding signal field can be computed for this pulse field using Eq. (8.3) and will be the next iteration for the signal field, $E_{\text{sig}}^{(k+1)}(t_i, \tau_j)$. Clearly, $E_{\text{sig}}^{(k+1)}(t_i, \tau_j)$ satisfies the mathematical-form constraint exactly. And, because it also minimizes Z , the process in which $E_{\text{sig}}^{(k)}(t_i, \tau_j)$ is replaced with $E_{\text{sig}}^{(k+1)}(t_i, \tau_j)$ is a GP.

In order to perform this minimization, we compute the direction of steepest descent: the negative of the gradient of Z with respect to the field $E^{(k+1)}(t_i)$ at the current value for the field, $E^{(k)}(t_i)$. In other words, we compute the derivative of Z with respect to each time-point in the complex field. This vector consists of the N complex numbers, $-\partial Z / \partial E^{(k+1)}(t_i)$ evaluated at $E^{(k+1)}(t_i) = E^{(k)}(t_i)$. This computation is somewhat tedious, so we have compiled the expressions for these gradients in the Appendix.

In practice, we've found that it isn't necessary to find the field, $E(t_i)$, that precisely minimizes Z on each iteration. In principle, in a typical minimization procedure, we'd find the distance in the direction of the (negative of the) gradient that minimizes Z , and then would re-compute the above gradient for this new field and find the distance along this new gradient that minimizes Z , etc. In fact, it's only necessary to find the above gradient and to perform the one-dimensional minimization along this direction once. While this new field won't be the precise projection (the minimum of Z), it's approximate, and it suffices in FROG pulse retrieval. Indeed, because it's only one step in a larger procedure, later steps make up for this inaccuracy, and, as a result, this approximate procedure yields a significantly faster pulse-retrieval algorithm overall. And, because the multidimensional surface represented by Z becomes paraboloidal near the global minimum represented by the ultimate solution for the pulse, the overall algorithm is extremely accurate.

For noise-free data, the FROG error G obtained after applying generalized projections should be limited by machine error (typically, we achieve values of $\sim 10^{-7}$). The resulting FROG error for experimental traces should indicate the experimental error. Typical values for FROG errors achieved in experiments with 128×128 arrays using PG FROG are $< 1\%$ and using SHG FROG are $< 0.5\%$ (because there is less noise background in SHG FROG). Errors tend to be lower for larger arrays because, due to the Fast Fourier Transform relations between the delay and frequency axis ranges and increments, the fractional area of the trace that is nonzero is less in the larger array traces. The general result is: $G \sim (\text{TBP}/N)^{1/2} \varepsilon$, where TBP is the time-bandwidth product of the pulse, ε is the error in the trace data points where the trace is nonzero, and $N \times N$ is the array size [11]. In this calculation, we have assumed that the noise is multiplicative [7]. For additive noise, the error pervades the entire trace, so $G \sim \varepsilon$, independent of TBP and N .

In general, the generalized projections algorithm converges in a few seconds for near-transform-limited pulses measured with 128×128 trace arrays. For highly complex pulses or for traces contaminated by massive amounts of additive noise, convergence can take a minute or more.

Short-cut Generalized Projections

Generalized Projections involve alternately making projections (moving the shortest distance) from one constraint set to the other until the algorithm

converges to the correct pulse intensity and phase. The GP algorithm is quite robust and, when used in conjunction with additional algorithms, it essentially always converges to the correct result. The only drawback of the GP algorithm is its speed or, rather, its lack of it.

This section discusses a faster version of the GP algorithm, which we call *short-cut GP*. It is based on what we call taking “short cuts” through the usual GP path, and it is applicable not only to the standard GP algorithm, but also to the PCGP algorithm introduced in Chapter 21. The approach is simple, and it is easy to see how it works geometrically. In order to do so, we note in Fig. 8.2 that the GP approach involves many steps, each of which is almost perpendicular to the direction in which the solution lies. This suggests a gradient-based approach, which is done by the multidimensional minimization technique discussed in the next section. Unfortunately, computation of the gradient in the framework of multidimensional minimization is exceedingly slow. Instead of using minimizations, however, a much more computationally efficient approach to approximating a gradient can be used, and we do so *within the GP approach*. Specifically, we use the midpoints of successive projections to define a vector approximating the gradient, and then step along this direction (see Fig. 8.6). This vector points in a direction toward the solution but requires considerably less computation than an actual gradient.

We should note that researchers in the phase-retrieval community have briefly considered such an approach before in image-science phase-retrieval problems [13], but its implementation here in FROG is somewhat different because the constraint of Eq. (8.3) is different.

To implement short-cut GP, we take the average of the signal fields just before and just after making a projection to the data constraint set, $\tilde{E}_{\text{sig}}^{(k)}(\omega_i, \tau_j)$, and then again just before and just after making the next projection to the data constraint set, $\tilde{E}_{\text{sig}}^{(k+1)}(\omega_i, \tau_j)$. (Note that we must make a projection to the nonlinear-optical constraint set in between.) These two points in this $N \times N$ -dimensional complex (ω, τ) -space determine a line, which approximates the gradient pointing toward the solution, as indicated geometrically in Fig. 8.3. We then step along this direction, yielding a new signal field, $\tilde{E}_{\text{sig}}^{(m+1)'}(\omega_i, \tau_j)$, which is closer to the correct solution. The optimal step size not only depends on the particular pulse field but also varies while the algorithm progresses. We found, however, that a fixed step size of three times the distance between the midpoints works well in most cases. Of course, it would alternatively be possible to minimize along the gradient found from the midpoints using any standard minimization technique, but we found that a fixed step size overall works faster since its much higher speed more than compensates for the better accuracy that a minimization technique offers during each iteration.

After stepping along the gradient, we must return to the standard GP algorithm. To do so, we can simply implement the data constraint by replacing the signal-field magnitude with the measured trace. Or we can Fourier transform

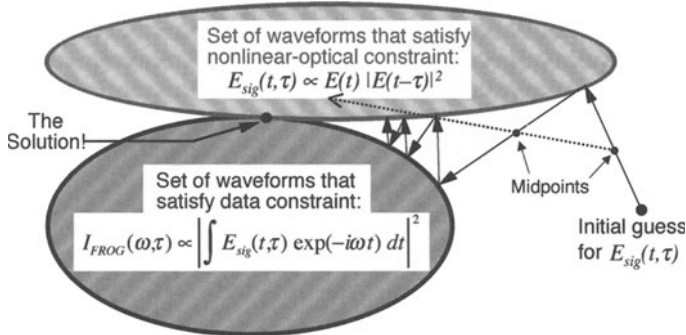


Fig. 8.3: Short-cut generalized projections. Generalized projections involves mapping the current guess to the closest point in the constraint set (solid arrows). Unfortunately, this involves mapping in directions nearly perpendicular to the direction that leads to the correct result and hence is slow. If, in addition, we include steps that involve minimizing along a line formed by midpoints of two consecutive projections (dashed arrow), we move in a direction toward the correct answer, avoiding the numerous bounces perpendicular to the optimal direction and improving the algorithm speed.

$\tilde{E}_{\text{sig}}^{(m+1)'}(\omega_i, \tau_j)$ with respect to ω to yield a signal field in the (t, τ) -space and then implement the nonlinear-optical constraint by making a generalized projection or using a step of the vanilla FROG algorithm specified in Eq. (8.5), which is simply

$$E^{(k+1)}(t_i) = \sum_{j=1}^N E_{\text{sig}}^{(k)}(t_i, \tau_j) \quad (8.10)$$

We suggest this latter approach. We have found that using Eq. (8.10) for this purpose within the short-cut GP approach combines the advantages of both Eq. (8.5) and Generalized Projections, yielding a fast and reliable algorithm.

We have tested this new algorithm with numerous pulses, both simple and highly complicated in shape, and found that it achieves a significant improvement in speed without loss of robustness. It also works well for all geometries of the FROG technique, and it always proceeds faster than the standard GP algorithm. It occasionally stagnates, but generally only in situations when the standard Generalized Projections algorithm would stagnate, too. When stagnation occurs, switching to another algorithm, such as the basic algorithm or one of the improvement versions discussed in section 8.6 nearly always yields convergence.

The final question is how often a short-cut should be taken. If short-cuts are taken too often, the GP algorithm is not allowed to settle into its rapid back-and-forth oscillations, thus producing inaccurate short-cut vectors. If, on the other hand, short-cuts are taken too infrequently, the purpose of the method is defeated. We have found empirically that every third iteration works best.

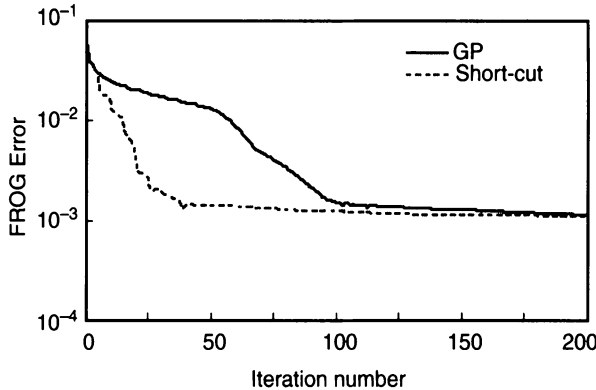


Fig. 8.4: Typical FROG error vs. iteration number with and without the short-cut method. The short-cuts were applied every third iteration. Algorithm speed improves considerably using the short-cut approach.

Figure 8.4 shows the performance of the short-cut GP algorithm on a noisy test trace for a cubic-spectral-phase pulse.

Improvements to the Basic FROG Algorithm

Three major improvements were developed shortly after the vanilla FROG algorithm was first introduced, which largely extend the useful range of the algorithm and enable it to converge for a much larger class of pulses, including the troublesome double pulse, as well as pulses with more complicated intensity and phase profiles. These improvements involve the use of an intensity constraint, an over-correction method, and a multidimensional minimization technique [11].

The failure of the vanilla FROG algorithm to converge for some pulses is apparently due to under-constraint—the constraints that are used are insufficient to force convergence to the correct field. Therefore, the use of some additional constraint can improve the performance of the algorithm.

The *intensity constraint* is formed by the use of additional information from the signal field, in this case the form of the gate, which is the intensity envelope of the pulse. The use of this additional constraint permits us to get much closer to the correct solution in cases where the vanilla FROG algorithm does not converge.

In order to generate the gate function from the signal field, we note that a generic form of Eq. (8.3), represented in the frequency domain, is

$$\tilde{E}_{\text{sig}}(\omega, \tau) = \int_{-\infty}^{\infty} P(t)g(t - \tau) \exp(-i\omega t) dt \quad (8.11)$$

where $P(t)$ is the field or a function of it; and $g(t - \tau)$ is the gate. To extract the gate function, we integrate with respect to ω to yield

$$\int_{-\infty}^{\infty} \tilde{E}_{\text{sig}}(\omega, \tau) d\omega = \int_{-\infty}^{\infty} \delta(t) P(t) g(t - \tau) dt = P(0) g(-\tau) \quad (8.12)$$

The integration of the signal field thus yields a time-reversed version of the gate function (without an inverse Fourier transform), which in the case of the polarization-gate geometry is identical to the intensity envelope of the pulse. To apply the intensity constraint, we replace the intensity of the current guess for $E(t)$ with the time-reversed intensity derived by integration of $\tilde{E}'_{\text{sig}}(\omega, \tau)$ with respect to ω , while leaving the phase unchanged.

The repeated application of the intensity constraint alone leads to large errors in the phase of the current-guess field, as well as noise in the wings of the field. One must therefore alternate between the basic FROG algorithm and the use of the intensity constraint when applying this method. It was found empirically that two iterations with the intensity constraint followed by one iteration with the vanilla algorithm generally yields the best results [11]. The error G actually gets larger during the application of the intensity constraint and is reduced with the application of the vanilla FROG algorithm, but the overall result for the error is much smaller than with the vanilla algorithm alone.

The intensity constraint has proven to be a very useful addition to the vanilla FROG algorithm in PG-FROG. Its application to other FROG geometries, however, is complicated due to the fact that the gate function is complex valued, and no practical improvement by this technique for geometries other than PG-FROG has been demonstrated.

As an alternative, the use of an independently measured spectrum as an additional intensity constraint in the frequency domain could be considered [24], but this tends to cause instabilities due to a required de-convolution, and this approach hence is generally not appropriate [20,25].

Unlike the application of the intensity constraint, the *over-correction method* is applicable to all FROG geometries. As discussed earlier, the basic FROG algorithm replaces the magnitude of the signal field $E_{\text{sig}}(\omega, \tau)$ generated by the current guess for $E(t)$ with the magnitude of the experimentally measured FROG data as described by Eq. (8.4). This replacement corrects the magnitude of $\tilde{E}_{\text{sig}}(\omega, \tau)$, i.e., increases the magnitude where it is too small and decreases it where it is too large, yielding $\tilde{E}'_{\text{sig}}(\omega, \tau)$ with a magnitude that is equal to that of the actual FROG trace.

As you might imagine, overcorrecting for the errors between $|\tilde{E}_{\text{sig}}(\omega, \tau)|^2$ and $I_{\text{FROG}}(\omega, \tau)$ can sometimes speed the convergence of the algorithm. Such an overcorrection can be accomplished by adding a term that is proportional

to the deviation between the two FROG traces to Eq. (8.4), e.g.,

$$\tilde{E}_{\text{sig}}^{(c)}(\omega, \tau) = \frac{\tilde{E}_{\text{sig}}(\omega, \tau)}{\left| \tilde{E}_{\text{sig}}(\omega, \tau) \right|} \sqrt{I_{\text{FROG}}(\omega, \tau)} \times \left[1 + \frac{I_{\text{FROG}}(\omega, \tau) - \left| \tilde{E}_{\text{sig}}(\omega, \tau) \right|^2}{\left| \tilde{E}_{\text{sig}}(\omega, \tau) \right|^2} \right] \quad (8.13)$$

Eq. (8.13) can be rewritten as

$$\tilde{E}_{\text{sig}}^{(c)}(\omega, \tau) = \tilde{E}_{\text{sig}}(\omega, \tau) \left\{ \frac{\sqrt{I_{\text{FROG}}(\omega, \tau)}}{\left| \tilde{E}_{\text{sig}}(\omega, \tau) \right|} \right\}^3 \quad (8.14)$$

This replacement step can be generalized to

$$\tilde{E}_{\text{sig}}^{(c)}(\omega, \tau) = \tilde{E}_{\text{sig}}(\omega, \tau) \left\{ \frac{\sqrt{I_{\text{FROG}}(\omega, \tau)}}{\left| \tilde{E}_{\text{sig}}(\omega, \tau) \right|} \right\}^b \quad (8.15)$$

where b is an adjustable exponent, and the GP (and vanilla) FROG algorithm is characterized by $b = 1$. An equivalent approach to over-correction has also been used in standard phase retrieval and blind de-convolution algorithms [26].

Values of b slightly larger than unity can speed the convergence of the algorithm. Values larger than about 1.5 tend to cause the algorithm to become unstable, however. The value of b at which the instability begins is dependent on the size of the FROG error G ; the smaller G is, the larger the value of b that can safely be used. It is easy to understand the reason for this instability: A field with a large error G by definition has large deviations from the correct FROG trace. When the value of b is high, a large error will lead to a large correction. If the correction is too large, this will lead to even greater errors in the field, which then lead to larger corrections and so forth. An unstable positive feedback cycle is created, and the error diverges. Larger values of b can be used, however, if the basic algorithm is permitted to reduce the error before the value of b is increased. Using such a scheme, stable convergence of the algorithm with values of b larger than 3 has been observed.

While the over-correction method is generally quite helpful in speeding convergence, and it can increase the speed and level of convergence for pulses with complicated phase profiles that only slowly converge under the vanilla FROG algorithm, this method alone is unable to overcome the vanilla algorithm's stagnation problems associated with some pulses, including the symmetrical double pulse.

The problem of the double pulse can be solved by the inclusion of *multi-dimensional minimization*. Minimization involves considering the FROG error G to be a single-valued function of $2N$ variables, where N is the linear size of a $N \times N$ pixel FROG trace. The $2N$ variables are the values of the real and imaginary parts of the electric field at each of the N sampling points of the array that hold the field.

Considerable computational effort can be saved if the gradient of the function at an arbitrary point can be calculated. Luckily, this is possible in FROG. First, a new error function is defined by

$$H = \sum_{i,j=1}^N \left[I_{\text{FROG}}(\omega_i, \tau_j) - \left| \tilde{E}_{\text{sig}}(\omega_i, \tau_j) \right|^2 \right]^2 = N^2 G^2 \quad (8.16)$$

(See Eq. (8.6); the factor that minimizes the error is neglected.) In the case of PG FROG, the signal field is defined as

$$\tilde{E}_{\text{sig}}(\omega_i, \tau_j) = \sum_{k=1}^N E(t_k) \left| \tilde{E}(t_k - \tau_j) \right|^2 \exp(i\omega_i t_k) \quad (8.17)$$

where $\omega_k = 2\pi f_k/N$ and f_k takes integer values when sums over ω_k are performed.

The task is to calculate the derivative of H for every point in the field $E(t)$; the derivative has to be calculated separately for the real and imaginary parts of $E(t)$. After some algebra, the derivatives are obtained for each t_k and t_0 :

$$\begin{aligned} \frac{dE(t_k)}{dE^r(t_0)} &= -4 \sum_{i,j=1}^N \left[I_{\text{FROG}}(\omega_i, \tau_j) - \left| \tilde{E}_{\text{sig}}(\omega_i, \tau_j) \right|^2 \right] \\ &\times \operatorname{Re} \left(\left\{ i \left| E(t_0 - \tau_j) \right|^2 \exp(i\omega_i t_0) + 2E^r(t_0)E(t_0 + \tau_j) \right. \right. \\ &\quad \left. \left. \times \exp(i\omega_i(t_0 + \tau_j)) \right\} \times E_{\text{sig}}^*(\omega_i, \tau_j) \right) \end{aligned} \quad (8.18)$$

for the real part and

$$\begin{aligned} \frac{dE(t_k)}{dE^i(t_0)} &= -4 \sum_{i,j=1}^N \left[I_{\text{FROG}}(\omega_i, \tau_j) - \left| \tilde{E}_{\text{sig}}(\omega_i, \tau_j) \right|^2 \right] \\ &\times \operatorname{Re} \left(\left\{ i \left| E(t_0 - \tau_j) \right|^2 \exp(i\omega_i t_0) + 2E^i(t_0)E(t_0 + \tau_j) \right. \right. \\ &\quad \left. \left. \times \exp(i\omega_i(t_0 + \tau_j)) \right\} \times \tilde{E}_{\text{sig}}^*(\omega_i, \tau_j) \right) \end{aligned} \quad (8.19)$$

for the imaginary part. The relations

$$\frac{dE(t_k)}{dE^r(t_0)} = \delta_{t_k, t_0} \quad \text{and} \quad \frac{dE(t_k)}{dE^i(t_0)} = i\delta_{t_k, t_0} \quad (8.20)$$

were used with $\delta_{i,j} = 1$ for $i = j$ and $\delta_{i,j} = 0$ for $i \neq j$.

With the gradient calculated according to Eqs. (8.18) and (8.19), standard minimization techniques can be used to solve the problem. For example, the Fletcher-Reeves and Polack-Ribierre methods [18], which are conjugate gradient methods, were successfully used. Both methods involve a series of one-dimensional minimizations along directions selected with the aid of the gradient, but they differ in the way these new directions are generated; see Ref. 12 for details. Although Eqs. (8.18) and (8.19) were derived for the special case of the PG FROG geometry, analogous expressions can be derived for other FROG geometries.

Contrary to the iterative Fourier-transform methods discussed before, a multidimensional minimization routine will necessarily always reduce the error. Unfortunately, it cannot distinguish between global and local minima. Worse, the multidimensional surface of $H(E)$ contains a plethora of local minima, and the minimization routine therefore needs a fairly good initial guess to ensure convergence to the global minimum.

It can be imagined that a different error function with the same global minimum might have different local minima and that using such a function might assist in convergence to the global minimum. For example, such a modified error function can be defined by

$$H_w = \sum_{i,j=1}^N \left[\frac{I_{\text{FROG}}(\omega_i, \tau_j) - |\tilde{E}_{\text{sig}}(\omega_i, \tau_j)|^2}{I_{\text{FROG}}(\omega_i, \tau_j)} \right]^2 \quad (8.21)$$

This particular new error function has the effect of emphasizing the areas of the FROG trace that are small in intensity, and it thus helps to determine the wings of the pulse more accurately. In practice, we find that sometimes switching between the error function defined by Eq. (8.16) and the error function defined by Eq. (8.21) is effective, whereas in other cases switching to the new error function does not serve to free the minimization routine from a local minimum. The use of this new error functions also presents a unique challenge since H can increase as H_w decreases.

The largest drawback of multidimensional minimization techniques remains their comparatively large numerical effort and the resulting slow convergence.

The improvements to the vanilla FROG algorithm discussed above allow the construction of composite algorithms in a variety of ways, switching from one method to the next once stagnation is detected. In its original implementation, the composite algorithm [11] starts with the vanilla FROG algorithm, and then switches to the over-correction method once stagnation is detected; the value of b in Eq. (8.15) is increased with the number of iterations k according to

$$b = (1.1)^{1+k/5} \quad (8.22)$$

If stagnation of the over-correction method is detected, the composite algorithm switches to the intensity constraint method. Note that in this method the algorithm performs two iterations with the intensity constraint, followed by one iteration with the vanilla FROG algorithm, and the error therefore fluctuates with a period of three iterations when this method is applied. It is thus important not to compare the error after each iteration as a measure of convergence, but rather to keep track of the error for a number of iterations. The same applies to the minimization techniques, which are applied after the intensity gate method stagnates. The first minimization scheme applied is the Polack-Ribierre method. If the Polack-Ribierre method stagnates, the composite algorithm switches to the new error function of Eq. (8.A28). If this method stagnates, the algorithm switches back to the original error function H but uses the Fletcher-Reeves method. Finally, if this fails, the algorithm switches back to the intensity constraint method, and the cycle begins again.

It should be noted that it was also attempted to improve the algorithm by the application of support constraints [27] and by mimicking the hybrid input-output algorithm [2,11]. While these techniques are successfully used in phase-retrieval problems, they have proven to be ineffective in FROG [11].

Conclusion

While the additional algorithms just mentioned can make the simple vanilla algorithm fairly robust, the generalized projections algorithm is usually sufficient by itself to retrieve essentially all pulses. However, the combination of all of these methods is very powerful. The commercially available FROG algorithm (Femtosoft and MakTech) uses all of these methods.

Appendix A: Expressions for the Mathematical Form-Constraint Gradient for Implementation of Generalized Projections

In the generalized-projections technique, it is necessary to minimize the functional distance Z given by Eq. (8.7). In order to do this, we compute the gradient of Z with respect to $E^{(k+1)}(t_k)$, i.e., $\partial Z / \partial E^{(k+1)}(t_k)$ for each value of $t_k = 1, \dots, N$. Each of the resulting N complex quantities is a component of the complex gradient vector. Instead of calculating the complex gradient, we in practice compute the $2N$ real quantities, $\partial Z / \text{Re}\{\partial E^{(k+1)}(t_k)\}$ and $\partial Z / \text{Im}\{\partial E^{(k+1)}(t_k)\}$. The expressions for these quantities are given below [21]. Note that the superscripts were dropped in order to simplify the complex equations. This can be done because, throughout this appendix, $E_{\text{sig}}(t, \tau)$, always indicates the k -th iteration for the signal field, and $E(t)$ always indicates the $(k + 1)$ -th iteration for the pulse field. Finally, we make use of the

following simple results:

$$\begin{aligned}
 \frac{\partial E(t_i)}{\partial \text{Re}\{E(t_k)\}} &= \delta(t_i - t_k) & \frac{\partial E(t_i - \tau_i)}{\partial \text{Re}\{E(t_k)\}} &= \delta(t_i - \tau_i - t_k) \\
 \frac{\partial E^*(t_i)}{\partial \text{Re}\{E(t_k)\}} &= \delta(t_i - t_k) & \frac{\partial E^*(t_i - \tau_i)}{\partial \text{Re}\{E(t_k)\}} &= \delta(t_i - \tau_i - t_k) \\
 \frac{\partial E(t_i)}{\partial \text{Im}\{E(t_k)\}} &= i\delta(t_i - t_k) & \frac{\partial E(t_i - \tau_i)}{\partial \text{Im}\{E(t_k)\}} &= i\delta(t_i - \tau_i - t_k) \\
 \frac{\partial E^*(t_i)}{\partial \text{Im}\{E(t_k)\}} &= -i\delta(t_i - t_k) & \frac{\partial E^*(t_i - \tau_i)}{\partial \text{Im}\{E(t_k)\}} &= -i\delta(t_i - \tau_i - t_k)
 \end{aligned} \tag{8.A1}$$

SHG FROG

We consider SHG FROG first because its equations are the simplest. In SHG FROG, the signal field is given by

$$E_{\text{sig}}^{\text{SHG}}(t, \tau) = E(t)E(t - \tau) \tag{8.A2}$$

Consequently, the distance function to be minimized is:

$$Z^{\text{SHG}} = \sum_{i,j=1}^N |E_{\text{sig}}(t_i, \tau_j) - E(t_i)E(t_i - \tau_j)|^2 \tag{8.A3}$$

The required gradient is then:

$$\frac{\partial Z^{\text{SHG}}}{\partial \text{Re}\{E(t_k)\}} = \sum_{i,j=1}^N \left(-\frac{\partial E(t_i)}{\partial \text{Re}\{E(t_k)\}} E(t_i - \tau_j) - E(t_i) \frac{\partial E(t_i - \tau_j)}{\partial \text{Re}\{E(t_k)\}} \right) \sigma^{\text{SHG}*} + c.c. \tag{8.A4}$$

where σ^{SHG} is the quantity in the absolute-value brackets in Eq. (8.A3). Using Eqs. (8.A1), we have:

$$\frac{\partial Z^{\text{SHG}}}{\partial \text{Re}\{E(t_k)\}} = \sum_{i,j=1}^N (-\delta(t_i - t_k)E(t_i - \tau_j) - E(t_i)\delta(t_i - \tau_j - t_k)) \sigma^{\text{SHG}*} + c.c. \tag{8.A5}$$

Substituting for σ^{SHG} :

$$\begin{aligned}
 \frac{\partial Z^{\text{SHG}}}{\partial \text{Re}\{E(t_k)\}} &= \sum_{j=1}^N -E_{\text{sig}}^*(t_k, \tau_j)E(t_k - \tau_j) + E^*(t_k)|E(t_k - \tau_j)|^2 \\
 &\quad - E_{\text{sig}}^*(t_k + \tau_j, \tau_j)E(t_k + \tau_j) + E^*(t_k)|E(t_k + \tau_j)|^2 + c.c.
 \end{aligned} \tag{8.A6}$$

Similarly,

$$\begin{aligned} & \frac{\partial Z^{\text{SHG}}}{\partial \text{Im}\{E(t_k)\}} \\ &= \sum_{i,j=1}^N \left(-\frac{\partial E(t_i)}{\partial \text{Im}\{E(t_k)\}} E(t_i - \tau_j) - E(t_i) \frac{\partial E(t_i - \tau_j)}{\partial \text{Im}\{E(t_k)\}} \right) \sigma^{\text{SHG}*} + c.c. \end{aligned} \quad (8.\text{A}7)$$

$$= i \sum_{i,j=1}^N (\delta(t_i - t_k) E(t_i - \tau_j) - E(t_i) \delta(t_i - \tau_j - t_k)) \sigma^{\text{SHG}*} + c.c. \quad (8.\text{A}8)$$

$$\begin{aligned} & \frac{\partial Z^{\text{SHG}}}{\partial \text{Im}\{E(t_k)\}} = i \sum_{j=1}^N -E_{\text{sig}}^*(t_k, \tau_j) E(t_k - \tau_j) + E^*(t_k) |E(t_k - \tau_j)|^2 \\ & \quad - E_{\text{sig}}^*(t_k + \tau_j, \tau_j) E(t_k + \tau_j) + E^*(t_k) |E(t_k + \tau_j)|^2 + c.c. \end{aligned} \quad (8.\text{A}9)$$

PG FROG

In PG FROG, the signal field is given by:

$$E_{\text{sig}}^{\text{PG}}(t, \tau) = E(t) |E(t - \tau)|^2 \quad (8.\text{A}10)$$

The distance function to be minimized is:

$$Z^{\text{PG}} = \sum_{i,j=1}^N |E_{\text{sig}}(t_i, \tau_j) - E(t_i) |E(t_i - \tau_j)|^2|^2 \quad (8.\text{A}11)$$

The gradient is then:

$$\begin{aligned} & \frac{\partial Z^{\text{PG}}}{\partial \text{Re}\{E(t_k)\}} \\ &= \sum_{i,j=1}^N \left(-\frac{\partial E(t_i)}{\partial \text{Re}\{E(t_k)\}} |E(t_i - \tau_j)|^2 - E(t_i) \frac{\partial E(t_i - \tau_j)}{\partial \text{Re}\{E(t_k)\}} E^*(t_i - \tau_j) \right. \\ & \quad \left. - E(t_i) E(t_i - \tau_j) \frac{\partial E^*(t_i - \tau_j)}{\partial \text{Re}\{E(t_k)\}} \right) \sigma^{\text{PG}*} + c.c. \end{aligned} \quad (8.\text{A}12)$$

where σ^{PG} is the quantity in the outer absolute-value brackets in Eq. (8.A11). Using Eqs. (8.A1), we have:

$$\frac{\partial Z^{\text{PG}}}{\partial \text{Re}\{E(t_k)\}} = \sum_{i,j=1}^N \left(-\delta(t_i - t_k) |E(t_i - \tau_j)|^2 - E(t_i) \delta(t_i - \tau_j - t_k) E^*(t_i - \tau_j) \right. \\ \left. - E(t_i) E(t_i - \tau_j) \delta(t_i - \tau_j - t_k) \right) \sigma^{\text{PG}*} + c.c. \quad (8.\text{A}13)$$

$$= \sum_{j=1}^N -E_{\text{sig}}^*(t_k, \tau_j) |E(t_k - \tau_j)|^2 + E^*(t_k) |E(t_k - \tau_j)|^4 \\ - (E(t_k) + E^*(t_k)) (E_{\text{sig}}^*(t_k + \tau_j, \tau_j) E(t_k + \tau_j) \\ - |E(t_k) E(t_k + \tau_j)|^2) + c.c. \quad (8.\text{A}14)$$

and

$$\frac{\partial Z^{\text{PG}}}{\partial \text{Im}\{E(t_k)\}} \\ = \sum_{i,j=1}^N \left(-\frac{\partial E(t_i)}{\partial \text{Im}\{E(t_k)\}} |E(t_i - \tau_j)|^2 - E(t_i) \frac{\partial E(t_i - \tau_j)}{\partial \text{Im}\{E(t_k)\}} E^*(t_i - \tau_j) \right. \\ \left. - E(t_i - \tau_j) E(t_i) \frac{\partial E^*(t_i - \tau_j)}{\partial \text{Im}\{E(t_k)\}} \right) \sigma^{\text{PG}*} + c.c. \quad (8.\text{A}15)$$

$$= i \sum_{i,j=1}^N \left(-\delta(t_i - t_k) |E(t_i - \tau_j)|^2 - E(t_i) \delta(t_i - \tau_j - t_k) E^*(t_i - \tau_j) \right. \\ \left. + E(t_i) E(t_i - \tau_j) \delta(t_i - \tau_j - t_k) \right) \sigma^{\text{PG}*} + c.c. \quad (8.\text{A}16)$$

$$= i \sum_{j=1}^N \left(-E_{\text{sig}}^*(t_k, \tau_j) |E(t_k + \tau_j)|^2 + E^*(t_k) |E(t_k - \tau_j)|^4 \right. \\ \left. - (E^*(t_k) - E(t_k)) (E_{\text{sig}}^*(t_k + \tau_j, \tau_j) E(t_k + \tau_j) \right. \\ \left. - |E(t_k) E(t_k + \tau_j)|^2) \right) + c.c. \quad (8.\text{A}17)$$

SD FROG

In SD FROG, the signal field is given by:

$$E_{\text{sig}}^{\text{SD}}(t, \tau) = E^2(t) E^*(t - \tau) \quad (8.\text{A}18)$$

So the distance function to be minimized is:

$$Z^{\text{SD}} = \sum_{i,j=1}^N |E_{\text{sig}}(t_i, \tau_j) - E^2(t_i)E^*(t_i - \tau_j)|^2 \quad (8.\text{A}19)$$

$$\begin{aligned} \frac{\partial Z^{\text{SD}}}{\partial \text{Re}\{E(t_k)\}} &= \sum_{i,j=1}^N \left(-2E(t_i) \frac{\partial E(t_i)}{\partial \text{Re}\{E(t_k)\}} E^*(t_i - \tau_j) \right. \\ &\quad \left. - E^2(t_i) \frac{\partial E^*(t_i - \tau_j)}{\partial \text{Re}\{E(t_k)\}} \right) \sigma^{\text{SD}*} + c.c. \end{aligned} \quad (8.\text{A}20)$$

where σ^{SD} is the quantity in the absolute-value brackets in Eq. (8.A20). Using Eqs. (8.A1), we have:

$$\begin{aligned} \frac{\partial Z^{\text{SD}}}{\partial \text{Re}\{E(t_k)\}} &= \sum_{i,j=1}^N (-2E(t_i) \delta(t_i - t_k) E^*(t_i - \tau_j) \\ &\quad - E^2(t_i) \delta(t_i - \tau_j - t_k)) \sigma^{\text{SD}*} + c.c. \end{aligned} \quad (8.\text{A}21)$$

$$\begin{aligned} &= \sum_{j=1}^N -2E_{\text{sig}}^*(t_k, \tau_j) E(t_k) E^*(t_k - \tau_j) + 2E^*(t_k) |E(t_k)E(t_k - \tau_j)|^2 \\ &\quad - E_{\text{sig}}^*(t_k + \tau_j, \tau_j) E^2(t_k + \tau_j) + E(t_k) |E(t_k + \tau_j)|^4 + c.c. \end{aligned} \quad (8.\text{A}22)$$

and

$$\begin{aligned} \frac{\partial Z^{\text{SD}}}{\partial \text{Im}\{E(t_k)\}} &= \sum_{i,j=1}^N \left(-2E(t_i) \frac{\partial E(t_i)}{\partial \text{Im}\{E(t_k)\}} E^*(t_i - \tau_j) - E^2(t_i) \frac{\partial E^*(t_i - \tau_j)}{\partial \text{Im}\{E(t_k)\}} \right) \sigma^{\text{SD}*} + c.c. \end{aligned} \quad (8.\text{A}23)$$

$$\begin{aligned} &= i \sum_{i,j=1}^N (-2 E(t_i) \delta(t_i - t_k) E^*(t_i - \tau_j) + E^2(t_i) \delta(t_i - \tau_j - t_k)) \sigma^{\text{SD}*} + c.c. \end{aligned} \quad (8.\text{A}24)$$

$$\begin{aligned}
&= i \sum_{j=1}^N -2E_{\text{sig}}^*(t_k, \tau_j) E(t_k) E^*(t_k - \tau_j) + 2E^*(t_k) |E(t_k) E(t_k - \tau_j)|^2 \\
&\quad + E_{\text{sig}}^*(t_k + \tau_j, \tau_j) E^2(t_k + \tau_j) - E(t_k) |E(t_k + \tau_j)|^4 + c.c. \quad (8.A25)
\end{aligned}$$

THG FROG

In THG FROG, the signal field is given by:

$$E_{\text{sig}}^{\text{THG}}(t, \tau) = E^2(t) E(t - \tau) \quad (8.A26)$$

So the distance function to be minimized is:

$$Z^{\text{THG}} = \sum_{i,j=1}^N |E_{\text{sig}}(t_i, \tau_j) - E^2(t_i) E(t_i - \tau_j)|^2 \quad (8.A27)$$

The gradient is then:

$$\begin{aligned}
\frac{\partial Z^{\text{THG}}}{\partial \text{Re}\{E(t_k)\}} &= \sum_{i,j=1}^N \left(-2E(t_i) \frac{\partial E(t_i)}{\partial \text{Re}\{E(t_k)\}} E(t_i - \tau_j) \right. \\
&\quad \left. - E^2(t_i) \frac{\partial E(t_i - \tau_j)}{\partial \text{Re}\{E(t_k)\}} \right) \sigma^{\text{THG}*} + c.c. \quad (8.A28)
\end{aligned}$$

where σ^{THG} is the quantity in the absolute-value brackets in Eq. (8.A28). Using Eqs. (8.A1), we have:

$$\begin{aligned}
\frac{\partial Z^{\text{THG}}}{\partial \text{Re}\{E(t_k)\}} &= \sum_{i,j=1}^N \left(-2E(t_i) \delta(t_i - t_k) E(t_i - \tau_j) \right. \\
&\quad \left. - E^2(t_i) \delta(t_i - \tau_j - t_k) \right) \sigma^{\text{THG}*} + c.c. \quad (8.A29)
\end{aligned}$$

$$\begin{aligned}
&= \sum_{j=1}^N -2E_{\text{sig}}^*(t_k, \tau_j) E(t_k) E(t_k - \tau_j) + 2E^*(t_k) |E(t_k) E(t_k - \tau_j)|^2 \\
&\quad - E_{\text{sig}}^*(t_k + \tau_j, \tau_j) E^2(t_k + \tau_j) + E^*(t_k) |E(t_k + \tau_j)|^4 + c.c. \quad (8.A30)
\end{aligned}$$

and

$$\begin{aligned} & \frac{\partial Z^{\text{THG}}}{\partial \text{Im}\{E(t_k)\}} \\ &= \sum_{i,j=1}^N \left(-2E(t_i) \frac{\partial E(t_i)}{\partial \text{Im}\{E(t_k)\}} E(t_i - \tau_j) \right. \\ &\quad \left. - E^2(t_i) \frac{\partial E(t_i - \tau_j)}{\partial \text{Im}\{E(t_k)\}} \right) \sigma^{\text{THG}*} + c.c \end{aligned} \quad (8.\text{A}31)$$

$$= i \sum_{i,j=1}^N \left(-2E(t_i) \delta(t_i - t_k) E(t_i - \tau_j) - E^2(t_i) \delta(t_i - \tau_j - t_k) \right) \sigma^{\text{THG}*} + c.c. \quad (8.\text{A}32)$$

$$\begin{aligned} &= i \sum_{j=1}^N -2E_{\text{sig}}^*(t_k, \tau_j) E(t_k) E(t_k - \tau_j) + 2E^*(t_k) |E(t_k) E(t_k - \tau_j)|^2 \\ &\quad - E_{\text{sig}}^*(t_k + \tau_j, \tau_j) E^2(t_k + \tau_j) + E^*(t_k) |E(t_k + \tau_j)|^4 + c.c. \end{aligned} \quad (8.\text{A}33)$$

A final comment: we provided all of these expressions in terms of the real and imaginary parts of the field because programming languages, such as C, do not always easily deal with complex numbers. But much simpler versions of these expressions can be obtained by treating the field and its complex conjugate as the independent variables.

References

1. K. W. DeLong, R. Trebino, D. J. Kane, "Comparison of ultrashort-pulse frequency-resolved-optical-gating traces for three common beam geometries," *J. Opt. Soc. Amer. B*, vol. 11, pp. 1595–1608.
2. J. R. Fienup, "Phase retrieval algorithms: a comparison," *Appl. Opt.*, vol. 21, pp. 2758–2769, 1982.
3. J. R. Fienup, A. M. Kowalczyk, "Phase retrieval for a complex-valued object by using a low-resolution image," *J. Opt. Soc. Amer. A*, vol. 7, pp. 450–458, 1990.
4. R. P. Milane, "Multidimensional phase problems," *J. Opt. Soc. Amer. A*, vol. 13, pp. 725–734, 1996.
5. R. Trebino, D. J. Kane, "Using Phase Retrieval to Measure the Intensity and Phase of Ultrashort Pulses: Frequency-Resolved Optical Gating," *J. Opt. Soc. Amer. A*, vol. 10, pp. 1101–1111, 1993.
6. D. J. Kane, R. Trebino, "Single-Shot Measurement of the Intensity and Phase of an Arbitrary Ultrashort Pulse By Using Frequency-Resolved Optical Gating," *Opt. Lett.*, vol. 18, pp. 823–825, 1993.
7. D. N. Fittinghoff, K. W. DeLong, R. Trebino, C. L. Ladera, "Noise sensitivity in frequency-resolved optical gatting measurements of ultrashort pulses," *J. Opt. Soc. Amer. B*, vol. 12, no. 10, pp. 1955–2466, 1995.
8. K. W. DeLong, D. N. Fittinghoff, R. Trebino, B. Kohler, and K. Wilson, "Pulse Retrieval in Frequency-Resolved Optical Gating Based on the Method of Generalized Projections," *Optics Letters*, vol. 19, pp. 2152–2154, 1994.
9. D. J. Kane, "Recent Progress Toward Real-Time Measurement of Ultrashort Pulses," *IEEE J. Quant. Electr.*, vol. 35, no. 4, pp. 421–431, 1999.
10. D. Kane, "Real time measurement of ultrashort laser pulses using principal component generalized projections," *IEEE J. Sel. Top. Quant. Electron.*, vol. 4, pp. 278–284, 1998.
11. K. W. DeLong, R. Trebino, "Improved Ultrashort Pulse-Retrieval Algorithm for Frequency-Resolved Optical Gating," *JOSA A*, vol. 11, pp. 2429–2437, 1994.

12. J. R. Fienup, C. C. Wackerman, "Phase-retrieval stagnation problems and solutions," *J. Opt. Soc. Amer. A*, vol. 3, pp. 1897–1907, 1986.
13. A. Levi, H. Stark, "Restoration from Phase and Magnitude by Generalized Projections," in *Image Recovery: Theory and Applications*, pp. 277–320, H. Stark, ed., Academic, San Diego, 1987.
14. E. Yudilevich, A. Levi, G. J. Haberle, H. Stark, "Restoration of signals from their signed Fourier-transform magnitude by the method of generalized projections," *J. Opt. Soc. Amer. A*, vol. 4, p. 236, 1987.
15. Y. Yang, N. P. Galatsos, H. Stark, "Projection-based blind deconvolution," *J. Opt. Soc. Amer. A*, vol. 11, pp. 2401–2409, 1994.
16. K. W. DeLong, C. L. Ladera, R. Trebino, B. Kohler, K. R. Wilson, "Ultrashort-pulse measurement using noninstantaneous nonlinearities: Raman effects in frequency-resolved optical gating," *Opt. Lett.*, vol. 20, pp. 486–488, 1995.
17. K. W. DeLong, R. Trebino, W. E. White, "Simultaneous recovery of two ultrashort laser pulses from a single spectrogram," *J. Opt. Soc. Amer. B*, vol. 12, pp. 2463–2466, 1995.
18. W. H. Press, S. A. Teukolsky, W. T. Vetterling, B. P. Flannery, *Numerical Recipes in C – The Art of Scientific Computing*, Cambridge University Press, Cambridge, 1995.
19. A. K. Jain, *Fundamentals of Digital Image Processing*, 1st ed., Prentice Hall, Englewood Cliffs, 1989.
20. K. W. DeLong, R. Trebino, J. Hunter, and W. E. White, "Frequency-Resolved Optical Gating With the Use of Second-Harmonic Generation," *JOSA B*, vol. 11, pp. 2206–2215, 1994.
21. R. Trebino, K. W. DeLong, D. N. Fittinghoff, J. N. Sweetser, M. A. Krumbügel, B. A. Richman, "Measuring ultrashort laser pulses in the time-frequency domain using frequency-resolved optical gating," *Rev. Sci. Instrum.*, vol. 68, no. 9, pp. 3277–3295, 1997.
22. H. Anton, *Elementary Linear Algebra*, 2nd ed., Wiley, New York, 1977.
23. C. W. Siders, A. J. Taylor, M. C. Downer, "Multi-pulse interferometric frequency-resolved optical gating: Real time phase-sensitive imaging of ultrafast dynamics," vol. 22, pp. 624–626, 1997.
24. J. Payne, M. Ramaswamy, J. G. Fujimoto, and E. P. Ippen, "Measurement of the Amplitude and Phase of Ultrashort Light Pulses from Spectrally Resolved Autocorrelation," *Opt. Lett.*, vol. 18, pp. 1946–1948, 1993.
25. D. J. Kane, G. Rodriguez, A. J. Taylor, and T. S. Clement, "Simultaneous Measurement of Two Ultrashort Laser Pulses from a Single Spectrogram in a Single Shot," *J. Opt. Soc. Am. B*, vol. 4, pp. 935–943, 1997.
26. J. H. Seldin, J. R. Fienup, "Iterative blind de-convolution algorithm applied to phase retrieval," *J. Opt. Soc. Am. A*, vol. 7, pp. 428–433, 1990.
27. J. R. Fienup, "Reconstruction of a complex-valued object from the modulus of its Fourier transform using a support constraint," *J. Opt. Soc. Amer. A*, vol. 4, pp. 118–123, 1987.

9. Noise: Its Effects and Suppression

David N. Fittinghoff and Michael Munroe

Introduction

In practice, noise is present in all measurements, and FROG measurements are no exception. As a result, it's important to ask several questions with regard to FROG [1]: How well does the FROG-retrieval algorithm retrieve the pulse in the presence of such noise? Does it always converge? If so, then what errors can be expected in the retrieved pulse intensity and phase versus time for a given noise level in the experimental FROG trace? What additional numerical techniques can be incorporated to improve the retrieval? Finally, can one calculate error bars on the retrieved intensity and phase for a noisy experimental FROG trace? If so, how?

It is particularly important to determine whether the algorithm has converged. Poor convergence is essentially always an indication that the trace is contaminated by too much random or nonrandom error and needs to be retaken. In the absence of noise, determining convergence is generally a straightforward task: either the error between the retrieved FROG trace and the measured trace goes to zero or it does not. Unfortunately, in the presence of noise, this task is not so straightforward. In general, the algorithm proceeds until it reaches a finite minimum error. Is the resulting inevitable error in the recovered pulse intensity and phase simply the error due to measurement error? Or is the error an indication of a lack of convergence due to excessive error in the trace? This distinction is important because, in the former case, the result is simply the best estimate of the pulse obtainable from the available data, whereas in the latter case, the resulting pulse may bear no relation to the actual pulse and hence is *meaningless*.

It is thus crucial to define the concept of convergence in the presence of noise, and we will. Using it, we will find that the algorithm essentially always converges, even for complex pulses and in the presence of massive noise. Surprisingly, in most cases the algorithm converges to a more accurate FROG trace than the original trace! In other words, using only the noisy trace as input, the algorithm retrieves a pulse whose FROG trace *better* approximates the noise-free trace than the original noisy trace. This result is due to the over-sampling and redundancy that are naturally built into the FROG trace: while the pulse has only $2N$ degrees of freedom (N intensity points and N phase points), the FROG trace has N^2 degrees of freedom. Thus the overwhelming majority of mathematically constructable two-dimensional images do not correspond to FROG traces of possible pulses. So the addition of noise produces a trace that does not correspond to a physically realizable pulse, and the algorithm must then find a trace that does and is also reasonably close to

the input trace. In so doing, it finds a somewhat “averaged,” generally more accurate, trace.

Several image-processing techniques improve the retrieval significantly. We'll discuss additive noise (due to a source such as scattered light or dark current), which provides an effective nonzero Poisson distributed background. We show that it is important to subtract off the mean of such background before running the algorithm on the trace. Even *constant* background is undesirable. This is because background at large delay implies nonzero intensity in the pulse wings, and constant background at large frequency offsets implies that this intensity has high-frequency oscillations. Constant background at both large delay and frequency offsets therefore yields pulse wings with high-frequency noise in the retrieved intensity (and phase). Spurious background, whether constant or noisy, is thus extremely undesirable. In other words, the region of nonzero values in the FROG trace must be *an island in a sea of zeroes*.

Background problems are different from the problem of cropping the FROG trace in either the delay or frequency directions; if the trace continues off the grid, information about the trace is missing. We will assume that the trace is not cropped in this manner. We will also discuss a variety of methods to ensure that any spurious background in the periphery of the trace is removed. Simply subtracting off any constant background should be the first step in the processing of every trace. *Corner-suppression*, or multiplying the trace by a function to preferentially reduce the values at the edges of the trace is also useful for suppressing the background. Another method for removing noise is simple *Fourier-low-pass filtering* of the trace, which removes high-frequency noise without significantly affecting the pulse-intensity-and-phase information present in the trace.

We will use an extended example involving a complex pulse with intensity substructure and a phase jump (chosen to be a challenge to the algorithm even in the absence of noise) and show how its retrieval is affected by the above filters and the various types and quantities of noise. We will also calculate the mean intensity and phase errors induced by the filters themselves. Such filtering, while not essential for achieving convergence, is extremely helpful for noisy traces and improves the retrieval significantly in high noise situations, and we will give a guide as to how and when to use such filtering. Note that, while we will concentrate on the intensity and phase versus time throughout the chapter, we could retrieve the spectral intensity and phase with equal accuracy. That this must be the case will be shown using a simple Parseval's Theorem argument.

Convergence of the algorithm does not necessarily mean, however, that the retrieved pulse intensity and phase will necessarily be less noisy than the trace from which they have been retrieved. This is an entirely different question, one that we will discuss in detail. To do so, we numerically simulate several types of noise for the two most commonly used FROG geometries, PG FROG and SHG FROG. Additive and multiplicative noise will contaminate

our theoretical traces at each pixel to simulate, for example, dark current and pixel-to-pixel gain variation, respectively.

We will also model the effects of quantization error on the FROG retrieval algorithm's performance and determine the price to be paid in accuracy by using a, say, 8-bit camera.

If you're in a hurry and don't want to read the whole chapter, here's what we find: The FROG algorithm performs very well. For multiplicative noise, adding a massive 10% noise in the trace results in only 1% rms error in the retrieved pulse intensity and phase. (It should be kept in mind that 10% multiplicative noise corresponds to 10% noise near the peak if the pulse, but 0% in the wings of the pulse—an rms error of about 1% for the traces used in this study.) Additive noise, on the other hand, is a much harder problem because it distorts the zero, as well as the nonzero, regions of the trace: unlike 10% multiplicative noise, 10% additive noise means 10% noise everywhere in the trace. However, using the aforementioned simple filtering techniques to remove such noise, we show that 10% additive noise also yields an impressive 1% rms error in the retrieved pulse intensity and phase. This excellent suppression of noise in the resulting intensity and phase is partly due to noise reduction due to filtering and partly due to the redundancy in the FROG trace. We will also show that an eight-bit video camera records FROG traces accurately enough to obtain 1% rms errors in the retrieved intensity and phase. Finally, we will describe the boot-strap method for determining error bars for the retrieved intensities and phases of FROG measurements. This approach to determining error bars is particularly convenient because it requires no effort on the part of the experimenter; the error bars are automatically determined by the code.

But no matter how big a hurry you're in, check out the Figs. 9.3–10, which show how filtering drastically improves the retrieved pulse.

In these studies, we use an early version of the commercial code algorithm that consists of the generalized-projections approach [2] and the additional methods described in the previous chapter, although we find that the latter methods only improve the retrieval slightly [3,4].

FROG Basics and Noise

The goal of the algorithm is to find the best solution defined as the pulse with the minimum FROG error,

$$G = \left[\frac{1}{N^2} \sum_{i=1}^N \sum_{j=1}^N (I_{\text{FROG}}^n(\omega_i, \tau_j) - \mu I_{\text{FROG}}(\omega_i, \tau_j))^2 \right]^{1/2} \quad (9.1)$$

Here I_{FROG}^n is the experimental FROG trace including any noise, I_{FROG} is the retrieved FROG trace (the FROG trace calculated from the retrieved intensity

and phase), and μ is a normalization constant that minimizes G (as discussed in the previous chapter). The summations are over the N frequency and N delay points in the FROG traces. The FROG error indicates the degree to which the retrieved FROG trace reproduces the experimental FROG trace. The use of this error definition is necessary because the actual pulse field is not available in practice. It is also reasonable because the FROG trace essentially uniquely determines the pulse, and similar traces yield similar pulses. Thus the least-squares distance from the FROG trace is a good (the best available) measure of the distance of the retrieved pulse from the actual pulse. The computer program changes to a different technique when the error has decreased by less than 0.5% of the value 10–15 iterations before. The algorithm is very cautious. To be certain that the error is the minimum obtainable, the program cycles through the different techniques twice, even though it typically produces the minimum error on the first cycle at the generalized projection step. When the algorithm stops, the program outputs the pulse with the smallest FROG error as the best estimate of the pulse that generated the FROG trace.

Simulation of Noise in FROG Traces

We will use five test pulses in this chapter, and they are shown in Fig. 9.1. These pulses are representative of many experimental pulses. The pulses are shown in order of increasing complexity from Pulse 1, a transform-limited Gaussian, in Fig. 9.1a to Pulse 5, a double pulse with phase distortions that include linear chirp, spectral cubic phase and self-phase modulation,

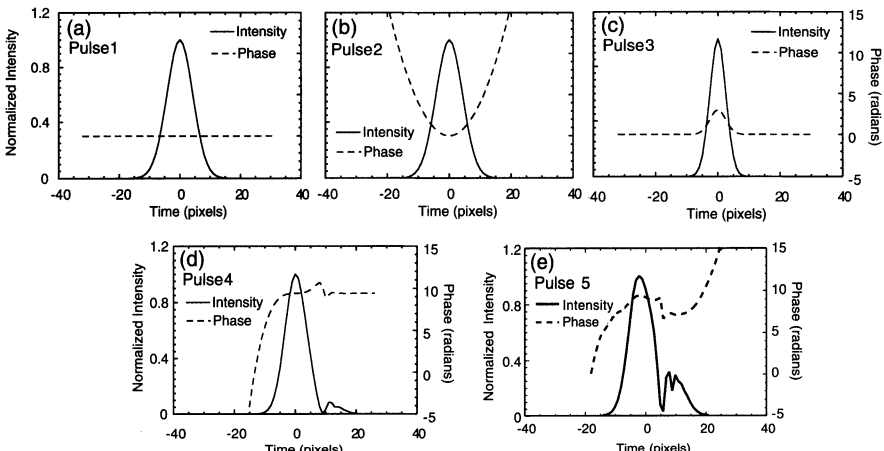


Fig. 9.1: Intensities and phases of the five pulses used in this study. (a) Pulse 1, a flat phase Gaussian. (b) Pulse 2, a linearly chirped Gaussian. (c) Pulse 3, a self-phase modulated Gaussian. (d) Pulse 4, a double pulse with spectral cubic phase. (e) Pulse 5, a double pulse with linear chirp, self-phase modulation and spectral cubic phase, which has a phase jump.

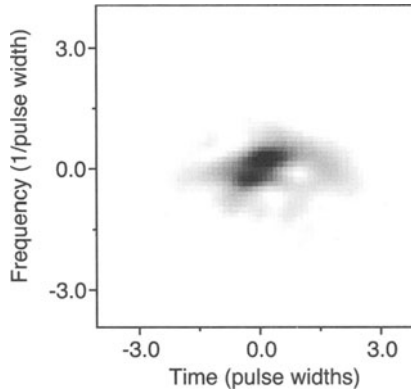


Fig. 9.2: The polarization-gate FROG trace of Pulse 5 (shown in Fig. 9.1e).

in Fig. 9.1e. As an example of a FROG trace, Fig. 9.2 shows the PG FROG trace of the pulse shown in Fig. 9.1e.

Since the FROG trace is the measured quantity, all noise occurs on the FROG trace, which, for this work, is a 64×64 array of data values representing the response of camera pixels. We will consider three types of noise that are representative of experimental noise: multiplicative noise, additive noise, and quantization error. Multiplicative noise describes pixel-to-pixel signal variations that are proportional to the intensity at the pixel. Gain variation at each pixel of the CCD camera is a common example of multiplicative noise for a single-shot experiment. We simulate multiplicative noise at each pixel by defining the value of the noisy FROG trace at frequency ω_i and time delay τ_j as:

$$I_{\text{FROG}}^n(\omega_i, \tau_j) = I_{\text{FROG}}(\omega_i, \tau_j) [1 + m_{ij}\alpha] \quad (9.2)$$

Here m_{ij} is a pseudorandom number drawn from a zero-mean, unit-variance Gaussian distribution, and α is the noise fraction. The noise fraction is a convenient measure of the amount of noise, and we use it as such throughout this work. The maximum value of the noiseless FROG trace is normalized to one. It should be remembered, however, that the rms noise in the trace contaminated by multiplicative noise is considerably less than α , generally about $\alpha/10$ for traces in this work.

Additive noise describes pixel-to-pixel signal variations independent of the FROG intensity at the pixels. A common example of additive noise is thermal noise that occurs in the charge-coupled device (CCD) cameras typically used for single-shot FROG measurements. We simulate additive noise at each pixel by defining

$$I_{\text{FROG}}^n(\omega_i, \tau_j) = I_{\text{FROG}}(\omega_i, \tau_j) + \eta_{ij}\alpha/\bar{\eta} \quad (9.3)$$

Here η_{ij} is a pseudorandom number drawn from a Poisson distribution of mean η . We use a Poisson distribution for additive noise because this distribution probably best describes thermal noise. Simulations for a uniform noise distribution and a half Gaussian noise distribution gave results similar to those for the Poisson distribution indicating, so the choice of a Poisson distribution is sufficiently general. For additive noise, unlike multiplicative noise, the rms noise in a trace contaminated by such noise is approximately α .

In this chapter, we will ignore large-scale systematic errors, such as an inadequate phase matching bandwidth. Large-scale systematic error is inherently a problem for the algorithm (as it necessarily is in any scientific measurement technique) because it represents a deviation from a physically realizable FROG trace. Observations and simulations show that such noise rapidly degrades the performance of the algorithm and removal of any large-scale systematic error is necessary to ensure accurate retrieval as it must be in any method. Many types of such noise can be removed easily. For example, stray light from the probe pulse, biases in dark current and *incoherent* polarizer leakage (in PG FROG) may both be subtracted off by blocking the gate pulse and recording the background levels, provided these levels are repeatable from shot to shot. Incoherent polarizer leakage yields a delay-independent pulse-spectrum-shaped baseline across the trace. It can be removed by sampling the few columns of data at the maximum and minimum delays, averaging these values, and subtracting the computed spectrum from the trace for all values of the delay. *Coherent* polarizer leakage yields fringes that cannot be simply subtracted. Thus, for PG FROG, using polarizers with high extinction ratios ($\geq 10^5$) is desirable. Other types of systematic error can actually be removed—often without even knowing their source—by the techniques presented in the next chapter.

Trace Preparation: Background Subtraction and Image Processing

Some preprocessing of the experimental trace is quite helpful. In this section we will describe background subtraction, multiplication of the trace by a function that is unity near the center of the trace but which falls to zero at the edges, typically a super-Gaussian (what we call “corner suppression”), and Fourier low-pass filtering.

It is important that any data used as input to the FROG algorithm contain the entire trace, that is, have zero signal intensity around the perimeter. Significant nonzero background at large delay or frequency offset tends to cause algorithm stagnation. There are several reasons for this. First, even if such background were physically valid, its failing to fall to zero would indicate a truncation of the trace. Without the full pulse data, the algorithm cannot be expected to accurately reproduce the correct pulse. Also, when it is not valid, background at large time delays in the FROG trace leads to incorrect non-zero background intensity, while noise at large frequency offsets in the FROG trace

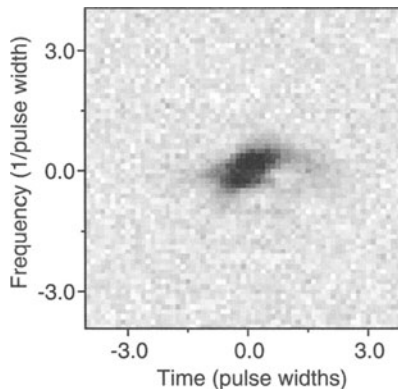


Fig. 9.3: The PG FROG trace of Pulse 5 after including 10% additive noise. The noise is Poisson distributed with $n = 5$. No image processing has been used on the trace. The noise at large time delays leads to non-zero background intensity, and the noise at large frequency offsets leads to high-frequency fluctuations in the recovered intensity and phase.

leads to incorrect high-frequency noise fluctuations in the recovered intensity and phase. Thus, a constant background everywhere in a FROG trace leads to *noisy* background everywhere in the retrieved pulse. Unfortunately, noise in the perimeter acts like background. As a result, the methods discussed in this section are aimed mainly at suppressing noise in the perimeter of the trace, although one method (Fourier low-pass filtering) also addresses the problem of noise in the central region of the trace as well.

For the purposes of illustration, let us consider the test pulse of Fig. 9.1e, whose trace is shown in Fig. 9.2, and show how these methods improve pulse retrieval. Figure 9.3 shows the FROG trace from Fig. 9.2 with additive Poisson-distributed noise added. The noise fraction shown here is quite large: 0.1 (i.e., 10% of peak FROG signal). The mean of the Poisson distribution, n , was chosen to be 5 counts, while the peak of the trace corresponds to 50 counts; thus, quantization noise is fairly large in this trace, as well. The noise does not have a zero mean, and this introduces an effective background offset with a magnitude approximately equal to the mean of the noise. Comparison of Figs. 9.2 and 9.3 indicates that the structure in the surrounding regions of the trace in Fig. 9.2 is now buried in the noise in Fig. 9.3, and even some of the main components of the trace are difficult to resolve, raising serious doubts that the algorithm can be reasonably expected to reproduce the pulse. This is a particularly challenging case.*

Traces such as that in Fig. 9.3 will yield less than satisfying results if the algorithm operates on the trace as is. As an illustration of the expected results of such a trace, see Fig. 9.4a, b, which show the actual intensity and phase

* Indeed, we don't wish to encourage you to measure pulses by making traces like this, even if the results we'll present will encourage you to do so!

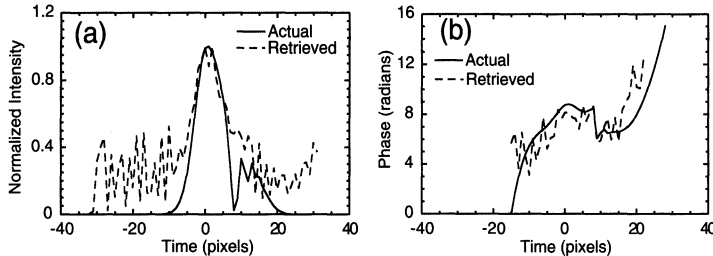


Fig. 9.4: The retrieved pulse for the FROG trace of Fig. 9.3 without mean subtraction. The retrieved intensity exhibits a large background intensity, and the secondary peak is unresolved. Both the retrieved intensity and phase exhibit high-frequency fluctuations. (a) The actual and retrieved intensities. The rms intensity error defined in Equation 9.5 is 15%. (b) The actual and retrieved phases. The rms phase error defined in Equation 9.6 is 0.65 radians.

and the retrieved phase to which the algorithm has converged for this trace. Surprisingly, the algorithm does roughly retrieve the major features of the intensity and phase. The pulse length is about right, and the general shape of the phase is correct. The retrieved phase even contains the phase jump near $t = 5$. There is, however, sufficient noise elsewhere in the phase, that it is difficult to be confident in the jump. Worse, the secondary intensity peak cannot be resolved, and there is a large background intensity with high-frequency fluctuations, as expected due to the large background in the trace.

Significantly better algorithm performance is obtained in all cases, and especially this one, simply by subtracting the background off. In particular, before running the pulse-retrieval algorithm, let us process the trace by subtracting off the mean of the noise. The mean is obtained by averaging the data in the 8×8 pixel squares in the corners of the FROG trace. Any negative points that result from the subtraction are set to zero. In practice, other methods might be preferred. For real experimental data, we prefer the following background removal techniques. In a multishot experiment, where spectra of the signal field are taken for various values of the relative delay time, we generally subtract off a background spectrum taken under dark conditions from all the measured spectra. Similarly, in a single shot experiment, we subtract the spectrum measured at large delay times to remove the contributions of incoherently scattered light.

Figure 9.5 shows the resulting FROG trace after this simple procedure for the example trace. Figures 9.6a, b show the retrieved intensity and phase for the FROG trace of Fig. 9.5. The algorithm now resolves the secondary intensity peak, and the amplitude of the high-frequency fluctuating background has been reduced by nearly an order of magnitude. The phase jump near $t = 5$ is still accurately retrieved, and the remainder of the phase behavior is much more accurately obtained, yielding more confidence in the phase jump. Significant phase deviations remain only at very low intensity values. The improvement is significant, and quite impressive, given the amount of

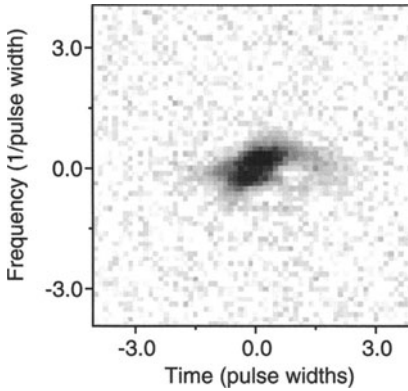


Fig. 9.5: The PG FROG trace of the test pulse with 10% additive noise in the trace after subtracting the mean of the noise. Subtracting the mean of the noise lowers the unphysical values at large time delays and frequencies, which is crucial for accurate pulse retrieval.

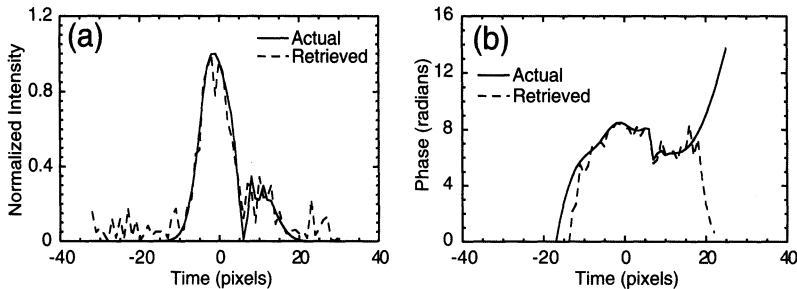


Fig. 9.6: The retrieved pulse for the FROG trace of Fig. 9.5. Subtracting the mean greatly reduces the background intensity and high-frequency fluctuations. (a) The actual and retrieved intensities. (b) The actual and retrieved phases.

noise present in the original trace. Nevertheless, even after mean subtraction, the tail of the Poisson distribution of the noise causes pixels at the edges of the trace to have non-negligible values. This leads to the residual noise in the wings of the pulse seen in Figs. 9.6a, b.

As a result, because the FROG trace is essentially a two-dimensional image, let us consider several image-processing techniques to improve the retrieval. Out-range pixel smoothing and median filtering [6] do not work well. These methods involve replacing the actual pixel values with the average or median value of the surrounding pixels. This has the effect of broadening the traces in both the time and frequency dimensions without the corresponding changes in such trace features as slope that would be expected to occur as well, thus unphysically increasing the apparent pulse time-bandwidth products. As a result, the traces no longer resemble those of physically valid pulses. This

confuses the algorithm sufficiently that clear improvements in the retrieved intensities and phases are rarely obtained.

For additive noise, the retrieval can sometimes be improved by corner suppression, that is, simply multiplying the FROG trace by a radially symmetric super-Gaussian of the form:

$$\Gamma(\omega_i, \tau_j) = \exp \left[-16 \ln(2)((\omega_i - N/2)^2 + (\tau_j - N/2)^2)/d^4 \right] \quad (9.4)$$

Here d is the full-width at half-maximum of the super-Gaussian. Fig. 9.7 shows the FROG trace of Fig. 9.3 after mean subtraction and corner suppression with $d = 45$. The corner suppression reduces the values and also the noise at the edges, and especially the corners, of the trace without significantly distorting the nonzero regions of the trace. Corner suppression is reasonable because the trace ought to be zero in these regions in the first place.

Figures 9.8a, b show the retrieved intensity and phase from the trace in Fig. 9.7. Note the significant improvement in this retrieval over Figs. 9.4a, b and 9.6a, b, especially in the wings of the intensity. They illustrate that, after mean subtraction and corner suppression, the algorithm is able to extract the pulse intensity and phase remarkably well considering the initial noise.

It should be remembered that corner suppression, while extremely useful for high-noise cases, can distort the trace somewhat, and the errors produced by the filter limit the accuracy of the retrieval. Thus, corner suppression is quite useful for noisy traces when some pulse distortion can be tolerated, but it is of less utility for clean traces. It is also more useful for traces with additive noise than for those with multiplicative noise, for which, corner suppression is generally unnecessary.

Of all the image processing techniques that have been considered, Fourier low-pass filtering of the FROG trace has proved to be the most useful. We

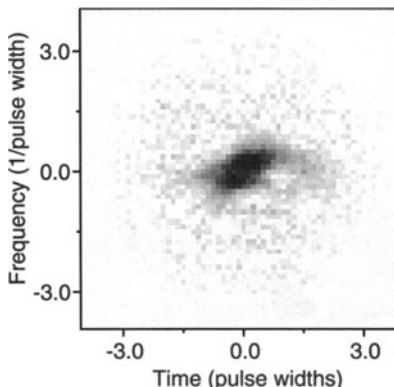


Fig. 9.7: The PG FROG trace of the test pulse with 10% additive noise after subtracting the mean of the noise and corner-suppression with $d = 45$ pixels. Super-Gaussian corner suppression forces the values at the perimeter and especially the corners to zero.

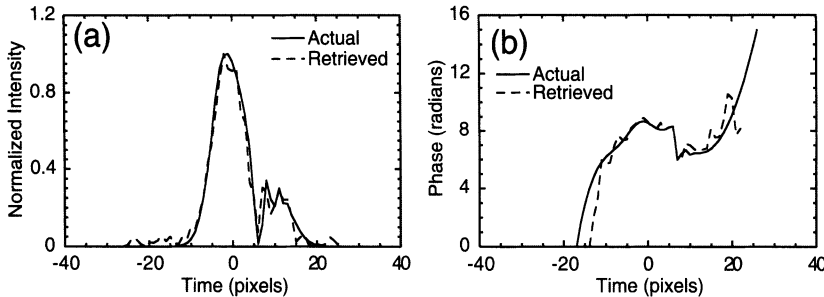


Fig. 9.8: The retrieved pulse for the FROG trace of Fig. 9.7. Note that the use of corner-suppression lowers the background intensity in the retrieved pulse. Also the reduction in the high-frequency noise allows the algorithm to resolve the two peaks of the pulse cleanly. (a) The actual and retrieved intensities. (b) The actual and retrieved phases.

implement the low-pass filter by 2-D Fourier transforming the FROG trace, multiplying the transformed trace by a top-hat function of radius, in pixels, of $\rho N/2$ (setting all values outside $\rho N/2$ equal to zero) and transforming the result back from the transform space to the image space. Note that when $\rho = 1$ the top-hat function has a diameter of N pixels and excludes only the corners of the transformed trace. The effect of low-pass filtering on the FROG trace is to remove the higher spatial frequencies and smooth through the noise, but without significantly broadening the trace. $\rho = 1$ corresponds to suppression of one half of the fluctuations between adjacent points. Values of ρ less than 1 yield suppression of lower-spatial frequency noise in the trace. Be careful, when using values of ρ less than 1, not to filter out real spatial frequencies in the trace corresponding to actual pulse fluctuations. Since the simulated noise (and noise which usually occurs in experiments) is generally at higher spatial frequencies than are contained in any reasonable FROG trace, it is generally possible to improve the retrieval by low-pass filtering with an appropriate choice of ρ .

Figure 9.9 shows the smoothing that occurs on the FROG trace of Fig. 9.7 using a low-pass filter with $\rho = 0.5$ (in addition to using background subtraction and corner suppression with $d = 45$). Figs. 9.10a, b show the improvement in the retrieval provided by the filtering. In particular, the retrieval of the phase is very good, except for slight ringing induced by the low-pass filter at the sharp phase change near $t = 5$. Also the noise-induced prepulses evident in Fig. 9.8a are reduced. Note that the retrieved pulse phase agrees beautifully with the actual phase and deviates only in regions of very low intensity, where the phase is not well defined.

The choice of how tightly to low-pass filter, that is, the choice of the value of filter radius, ρ , depends on the quantity of noise and the type of noise present. Like all other filtering operations, low-pass filtering distorts the trace and introduces errors of its own. Low-pass filtering, while critical for traces with large amounts of noise, is not as useful for low levels of noise, which yield

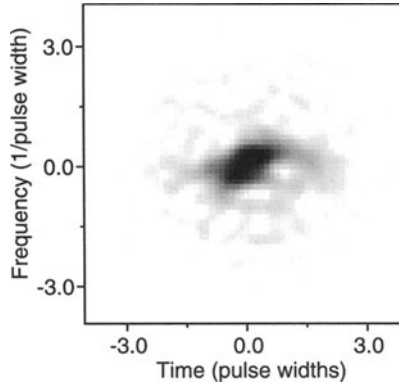


Fig. 9.9: The PG FROG trace of the test pulse with 10% additive noise after subtracting the mean of the noise, corner-suppression with $d = 45$ pixels and low-pass filtering with $\rho = 0.5$. The low-pass filtering removes the high spatial frequency noise from the entire trace. The resulting smoothing effect is apparent.

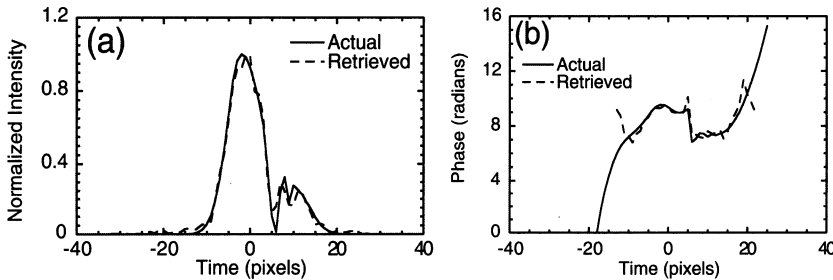


Fig. 9.10: The retrieved pulse for the FROG trace of Fig. 9.9. The retrieved intensity is very good, clearly reproducing the peaks of the pulse with minimal background or high-frequency noise. The phase is also remarkably good for such an initially high amount of noise and does not strongly deviate from the actual phase except, as expected, at times where the intensity is below 1% of the peak intensity. (a) The actual and retrieved intensities. The rms intensity error is 4% (b) The actual and retrieved phases. The rms phase error is 0.14%.

much better results anyway. To give an idea of the magnitude of the distortion involved, let us apply low-pass filtering to a noise-free trace. Fig. 9.11 shows a plot of the mean intensity and phase errors (as defined in the next section), as a function of filter radius, induced by low-pass filtering noise-free PG FROG traces of the five test pulses. Note that, as expected, as the radius of the filter decreases, the errors introduced by the low-pass filter increase. When minimal noise is present in the trace, distortions induced by the low-pass filter will be quite noticeable and hence undesirable. On the other hand, when large amounts of noise are present in the trace, the error introduced by filtering may be negligible compared to the noise reduction obtained by using it. Thus the

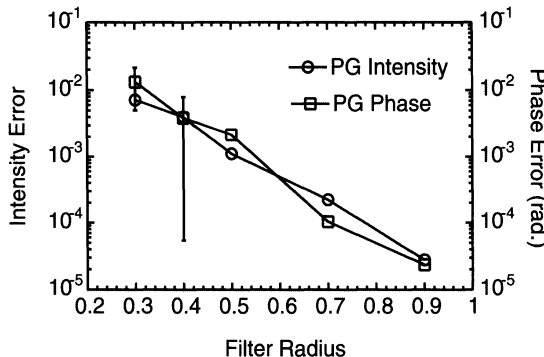


Fig. 9.11: The rms intensity and phase errors for PG FROG induced by low-pass filtering the FROG trace for the five test pulses. The data are plotted as a function of filter radius. The filter radius ρ in the transform space is given as a fraction of $N/2$ where N is the number of pixels in each of the two dimensions of the FROG trace. Error bars indicating one standard deviation from the mean error for the intensity and phase are shown at filter radii of 0.4 and 0.3, respectively.

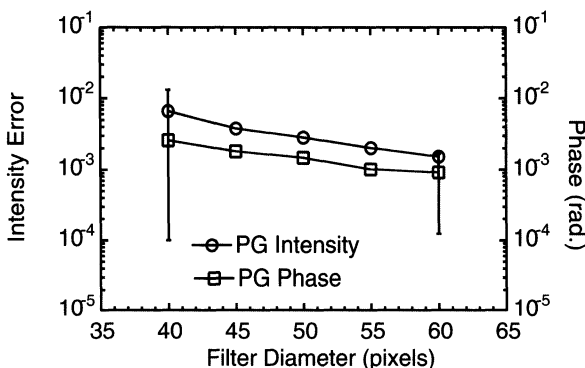


Fig. 9.12: The rms intensity and phase errors for PG FROG induced by using corner suppression on the FROG trace for the five test pulses. The data are plotted as a function of filter radius. The filter is centered on the FROG trace and has a diameter given in pixels in each of the two dimensions of the FROG trace. Error bars indicating one standard deviation from the mean error for the intensity and phase are shown at filter diameters of 40 and 60, respectively.

use of the low-pass filter will in practice depend on the type and amount of noise.

A similar noise-suppression distortion trade-off exists for corner suppression. Fig. 9.12 shows a plot of the mean intensity and phase errors induced as a function of the corner-suppression filter diameter. Just as for low-pass filtering, as the radius of the filter decreases, the errors introduced increase. In this case, however, the errors are nearly constant and moderate in magnitude even for relatively large diameters such as $d = 60$.

In view of these results, let us define the concept of *optimized filtering*, which will involve heavy filtering in high-noise cases, and weaker filtering in low-noise cases where it is less necessary and our standards for pulse distortion are higher. Section 6 will discuss the specific details of optimized filtering in a discussion of the effects of noise on the retrieval of the intensity and phase.

Before going to the next section, we note that additional, more sophisticated image-processing techniques, such as Wiener filtering [6] and, in particular Wavelet noise reduction [7–9] may eventually prove to be useful for removing noise from FROG traces.

The Intensity and Phase Errors

The performance of the algorithm can be quantitatively measured in two ways: (1) how well it retrieves the original intensity and phase, and (2) how well it retrieves the original FROG trace. In experiments, where the original intensity and phase are unknown, only the latter error is available. As a result, it plays a central role in the algorithm, as previously discussed. In this section, we will also define intensity and phase errors to give us an idea of how well the algorithm retrieves the pulse itself in simulations, rather than only its trace. All of these measures are related due to the one-to-one correspondence of pulses to possible FROG traces, but it is not a priori obvious what rms intensity and phase errors correspond to a given rms FROG trace error. We will find that the former errors will be on the order of the latter error.

To measure how closely the algorithm retrieves the original intensity let us use the rms intensity error in the obvious manner,

$$\varepsilon_I = \left[\frac{1}{N} \sum_{j=1}^N (\hat{I}(t_j) - I(t_j))^2 \right]^{1/2} \quad (9.5)$$

where I and \hat{I} are the actual and retrieved intensities, respectively. Here the peak of $I(t)$ is normalized to one, so this error is often quoted as a percentage. The summation is over the N discrete time points.

The choice of error to use as a monitor of the algorithm's ability to retrieve the phase is not as obvious. An unweighted rms phase error is inappropriate because the phase of the pulse is meaningless when the intensity is near zero. The retrieved phase can thus exhibit large—but meaningless—phase variations for low intensities that skew the rms phase error. Therefore, we would not want to include such phase points in an error calculation. A more appropriate choice of the error to use to monitor the retrieval of the phase is the *intensity-weighted* rms phase error:

$$\varepsilon_\phi = \left[\frac{1}{N} \sum_{j=1}^N I^2(t_j) (\hat{\phi}(t_j) - \phi(t_j))^2 \right]^{1/2} / \left[\frac{1}{N} \sum_{j=1}^N I^2(t_j) \right]^{1/2} \quad (9.6)$$

Here ϕ and $\hat{\phi}$ are the actual and retrieved phases, respectively. Note that ε_ϕ has units of radians.

When calculating both of these errors, it is important to minimize the errors with respect to the peak intensity, a temporal shift, and the absolute phase. This minimization accounts for the fact that the FROG trace is invariant to overall shifts in time and phase in the pulse and that the algorithm yields a pulse of no particular peak intensity. As an example of the relative magnitude of the errors, the intensity and phase errors obtained for Figs. 9.4a, b were 15% and 0.65 radians, respectively, while the intensity and phase errors obtained for Figs. 9.10a, b were only 4% and 0.14 radians, respectively.

We could also define and calculate the errors in the spectral intensity and phase rather than the temporal quantities. A simple argument, however, shows that the spectral errors contain no additional information. Consider the error in the field as a function of time, ε_t , defined by:

$$\varepsilon_t^2 = \sum_{j=1}^N \left| \hat{E}(t_j) - E(t_j) \right|^2 / \sum_{j=1}^N |E(t_j)|^2 \quad (9.7)$$

Here $E(t)$ is the reconstructed field at time t , and the summation is over the N discrete times. The error in the field as a function of frequency may be similarly defined by:

$$\varepsilon_\omega^2 = \sum_{j=1}^N \left| \hat{E}(\omega_j) - \tilde{E}(\omega_j) \right|^2 / \sum_{j=1}^N |\tilde{E}(\omega_j)|^2 \quad (9.8)$$

Here $\hat{E}(\omega)$ and $\tilde{E}(\omega)$ are the actual and reconstructed fields as a function of frequency ω , respectively, and the summation is over the N discrete frequencies. By Parseval's Theorem, $\varepsilon_t^2 = \varepsilon_\omega^2$. Thus, since the error in the field versus time equals the error in the field versus frequency, the errors in the spectral intensity and phase will be similar to those in the temporal intensity and phase.

The Effects of Additive and Multiplicative Noise on Retrieval

Let us now consider the behavior of the intensity and phase errors in the presence of additive and multiplicative noise. We will use the same noise (i.e., set of η_{ij}) in all cases and only its magnitude α changes. For additive noise, Fig. 9.13 shows the mean PG and SHG FROG retrieval errors for the five pulses versus noise fraction, α . The mean of the noise background was subtracted from the FROG traces before retrieval, but no other filtering has been performed. In general, filtering is strongly advised; this example without filtering is for the sake of illustration only. The error bars indicate one standard deviation from the mean for the five pulses. The errors for PG and SHG FROG are comparable and decrease as roughly the square root of the noise fraction.

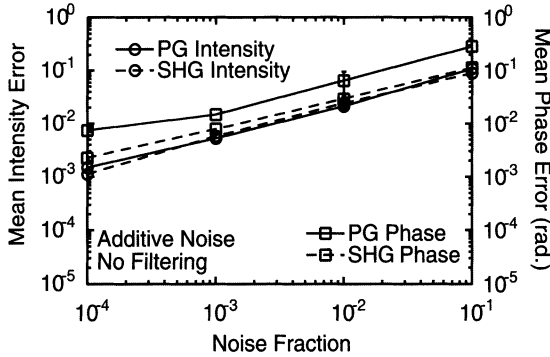


Fig. 9.13: The rms intensity and phase errors for PG and SHG FROG for additive noise with $n = 5$. The mean of the noise background was subtracted from the FROG traces before retrieval, *but no other filtering has been performed*. The data are plotted as a function of noise fraction. The errors decrease roughly as the square root of the noise. An error bar indicating one standard deviation from the mean phase error for PG FROG is shown at a noise fraction of 10^{-2} . The standard deviation for the PG intensity at a noise fraction of 10^{-3} is contained within the circular marker. These high noise levels in the retrieved intensity and phase reveal the importance of filtering (see Fig. 9.15).

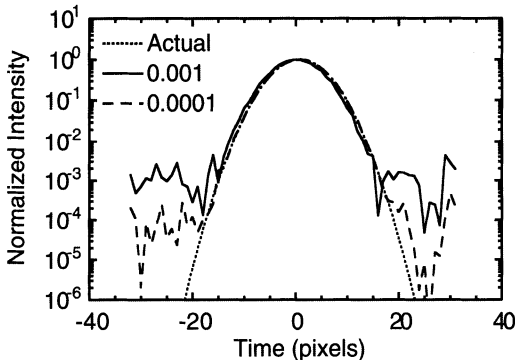


Fig. 9.14: The actual and retrieved intensities of Pulse 1 for additive noise with $\alpha = 0.001$ and $\alpha = 0.0001$ for PG FROG. The noise floor in the wings of the retrieved intensities are roughly equal to, and decrease linearly with, the amount of additive noise, α .

For 0.1% additive noise ($\alpha = 10^{-3}$), the algorithm achieves intensity and phase errors of order 1% and 0.01 radians, respectively. For 10% additive noise, the algorithm achieves intensity and phase errors of order 10% and 0.1 radians, respectively.

It is interesting to consider where in the pulse the noise resides. It occurs mainly where the intensity is highest, and is much lower in the wings of the pulse. Fig. 9.14 shows, plotted on a log scale, the actual intensity for Pulse 1 and the retrieved intensities for additive noise with $\alpha = 0.001$ and $\alpha = 0.0001$ for PG FROG without filtering. While the rms intensity errors for these noise

levels are .0071 and .00145, respectively, the background levels or noise floors of the retrieved intensities are much lower: roughly equal to the amount of noise. This result holds for all the pulses and noise levels and shows that FROG measurements can be made with dynamic range limited only by (and equal to) the level of noise. FROG thus effectively finds weak satellite pulses, but it is less adept at revealing slight distortions in the high-intensity regions of the pulse.

Significantly better results can be obtained using optimized filtering, which involves selective corner-suppression and low-pass filtering, mostly in cases when noise is large and some pulse distortion can be tolerated as the price to be paid for noise reduction. Specifically, in view of the results of Figs. 9.11 and 9.12, define optimized filtering for additive noise to include low-pass filtering and corner suppression with filter radii chosen such that the mean induced errors due to the filters themselves are at the level of error desired. The optimized filter thus uses smaller filter radii in high-noise cases, where some distortion can be tolerated, and larger radii in low-noise cases, where such distortions will be noticed. Let the desired errors be an order of magnitude lower than the mean errors obtained without filtering, which are shown in Fig. 9.13. Thus the optimized corner-suppression radii are $d = 60, 41$ and 35 for additive noise with $\alpha = 10^{-3}, 10^{-2}$ and 10^{-1} , respectively. For $\alpha = 10^{-4}$, corner suppression is not used. The optimized low-pass filter radii for additive noise are $\rho = 0.58, 0.58, 0.4$ and 0.3 for $\alpha = 10^{-4}, 10^{-3}, 10^{-2}$ and 10^{-1} , respectively.

Figure 9.15 shows the results of optimized filtering of the additive-noise-contaminated traces before running the algorithm for PG FROG. Note the significant improvement obtained, which is consistent with the extended example of the earlier section. Now, for 10% additive noise, the rms intensity

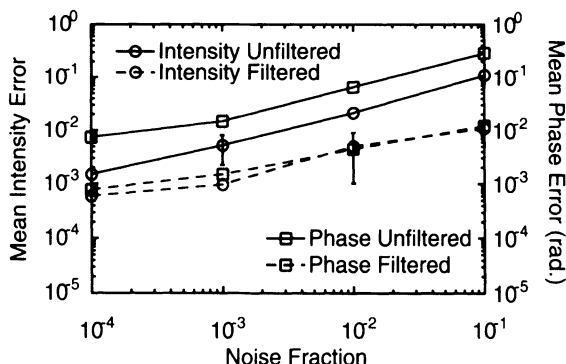


Fig. 9.15: The intensity and phase errors for PG FROG for additive noise with $n = 5$ with and without optimized filtering. Filtering lowers the retrieved errors dramatically. Error bars indicating one standard deviation from the mean intensity error for the filtered and unfiltered cases are shown at noise fractions of 10^{-2} and 10^{-3} , respectively.

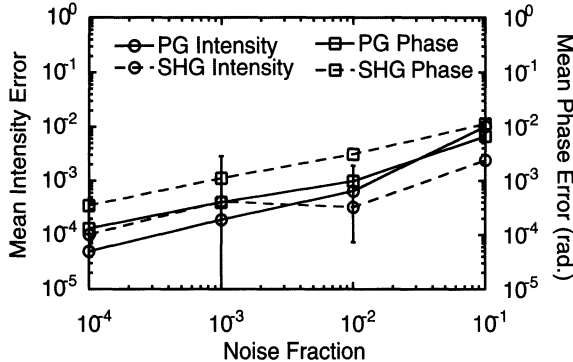


Fig. 9.16: The intensity and phase errors for PG and SHG FROG for multiplicative noise. The traces were not filtered before retrieving the pulse. The data are plotted as a function of noise fraction. Error bars indicating one standard deviation from the mean phase error for PG and SHG FROG are shown at noise fractions of 10^{-2} and 10^{-3} , respectively.

and phase errors are only on the order of 1% and 0.01 radians, respectively. The results for SHG FROG are similar. It is thus clear that filtering should play a significant role in the pulse retrieval process in FROG in the presence of additive noise. As for the unfiltered case, the noise resides mainly where the intensity is highest, and is lower in the wings of the pulse. The noise floors of the retrieved intensity for filtered traces are roughly equal to the noise that remains in the wings of the trace after filtering.

Figure 9.16 shows the PG and SHG FROG retrieval errors versus noise fraction for multiplicative noise. Multiplicative noise as high as 10% produces errors of 1%, indicating that, of course, the algorithm deals with multiplicative noise better than it deals with additive noise. This is not surprising because multiplicative noise is only significant where the signal intensity is large, so multiplicative noise leaves the perimeter of the trace unchanged. In addition, the average error in the trace for a given value of α is less for multiplicative noise than for additive noise. As happens for additive noise, the errors decrease with decreasing noise fraction. One can used optimized filtering for multiplicative noise cases, but significant improvements in the reconstructions do not occur. The errors without the filters are much smaller than for additive noise and require such large filter radii (to prevent inducing even larger errors with the filters) that the filters prove unnecessary where only multiplicative noise exists.

The Convergence Criterion

As mentioned earlier, it is important to define a convergence condition to determine whether error in the retrieved pulse is simply the noise resulting from the measurement or instead is an indication of algorithm stagnation. In

the former case, the retrieved pulse is meaningful, whereas, in the latter, it would not be.

For theoretical traces, when we know the actual pulse, we could simply consider how well the algorithm retrieves the original pulse intensity and phase. However, it isn't clear how to define a quantitative criterion because noise in the FROG trace has different units from that in the phase, for example. And noise in the intensity isn't relatable to noise in the FROG trace either, even though they have the same units, because the two quantities live in different functional spaces. Instead, let us attack this issue by asking how well the algorithm retrieves the desired (i.e., noise free) FROG trace, which is directly relatable to the noise in the noisy FROG trace. This is reasonable in view of the uniqueness of FROG traces.

Thus, we consider the algorithm to have converged to the original trace if the error between the retrieved FROG trace and the actual noise-free FROG trace is at most only slightly larger than the error between the noisy FROG trace and the actual FROG trace. Formally, convergence occurs when:

$$R = \frac{\varepsilon[\hat{I}_{\text{FROG}}(\omega_i, \tau_j), I_{\text{FROG}}(\omega_i, \tau_j)]}{\varepsilon[I_{\text{FROG}}^n(\omega_i, \tau_j), I_{\text{FROG}}(\omega_i, \tau_j)]} < 2 \quad (9.9)$$

where

$$\varepsilon[C, D] = \left[\frac{1}{N^2} \sum_{i=1}^N \sum_{j=1}^N (C_{ij} - D_{ij})^2 \right]^{1/2} / \left[\frac{1}{N^2} \sum_{i=1}^N \sum_{j=1}^N D_{ij}^2 \right]^{1/2} \quad (9.10)$$

is the rms error of FROG trace C with respect to FROG trace D . If R is less than 2, the retrieved trace is a reasonable representation of the original trace. We use 2, and not 1, because the noisy trace is in some sense displaced in function space from the original noise-free trace, and the retrieved trace is then expected to be displaced somewhat from this trace still. So a number greater than 1 is appropriate, and 2 is reasonable. If, as often happens, R is less than one, the retrieved FROG trace is a *better* representation of the correct FROG trace than the noisy trace used as input to the algorithm. The algorithm has in some sense ignored the noise and found a solution that is better than the input! This apparent ability of the algorithm to separate the noise from the true FROG trace occurs because the noise does not satisfy the mathematical constraint imposed by the nonlinear interaction on the signal field (Equation 9.2 or Equation 9.3) and because the FROG trace has built in redundancy. The FROG trace has N^2 data points while only $2N$ data points are required to describe the intensity and phase.

Figure 9.17 shows the mean convergence criterion versus noise fraction for additive and multiplicative noise for PG FROG and SHG FROG. No filters are used for these results. In all cases, R is significantly less than 2, and the algorithm converges. For the individual pulses, the algorithm gives

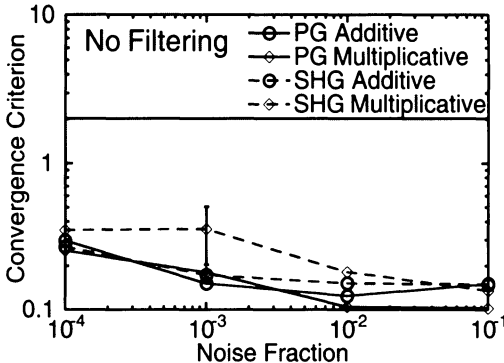


Fig. 9.17: The convergence ratio for PG and SHG FROG for additive and multiplicative noise without filtering. For additive noise $n = 5$. The solid horizontal line indicates the convergence limit where $R = 2$. The algorithm converges for all cases. Error bars indicating one standard deviation from the mean convergence ratio for multiplicative noise for PG and SHG FROG are shown at noise fractions of 10^{-2} and 10^{-3} , respectively. The upper error bar for PG FROG is contained within the diamond marker.

convergence ratios below one and in some cases the convergence ratios are lower even than 0.1. As stated above, these convergence ratios indicate that the algorithm smoothes through the noise to produce a representation of the pulse that is significantly more accurate than the original trace with noise. In addition, the results for optimized filtering are numerically even better. We conclude that the algorithm converges beautifully in the presence of noise.

Quantization Noise

Digitizing a FROG trace, as is inevitable when transferring the data to a digital computer, leads to inaccuracies in retrieval. The data assume discrete values and no longer represent the pulse accurately. A standard camera has 8 bits of resolution, and much more expensive cameras can have up to 16 bits of resolution. Let us focus here on 8-bit digitization. For PG and SHG FROG, Figs. 9.18 and 9.19 show the retrieved intensity and phase for Pulse 5 after the FROG traces were reduced to 8 bits of resolution. For PG FROG the intensity and phase errors are 1.1% and 0.0044 radians, respectively, and for SHG FROG the intensity and phase errors are 0.63% and 0.00216 radians, respectively. In both cases, the deviations of the retrieval are only apparent for intensities near 10^{-3} of the peak intensity. This is not surprising since the FROG traces have 256 levels. These traces are generally representative of the results of our quantization studies, and we conclude that a standard 8-bit camera is probably sufficient for measurements with over $\sim 10^2$ dynamic range in the intensity of the FROG signal assuming that the full eight bits are used. If an experimenter only uses four of the available bits while taking data, he will obtain poorer results. Switching to a 14-bit camera will increase

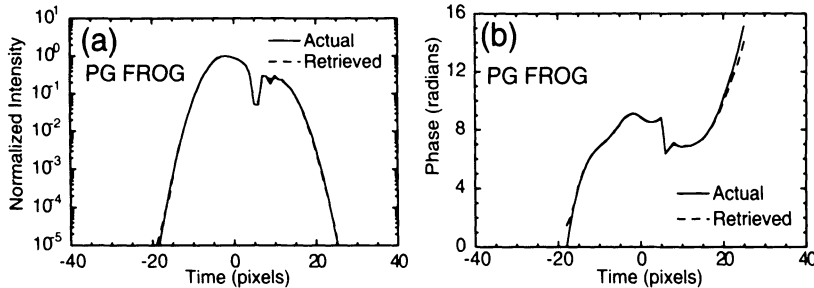


Fig. 9.18: The retrieved test pulse for PG FROG after quantization to 8 bits. The errors in the retrieved intensity and phase are small and become apparent mainly intensities below 10^{-3} of the peak intensity. a) The actual and retrieved intensities. The rms intensity error is 1.1%. b) The actual and retrieved phases. The phase error is .0044 radians.

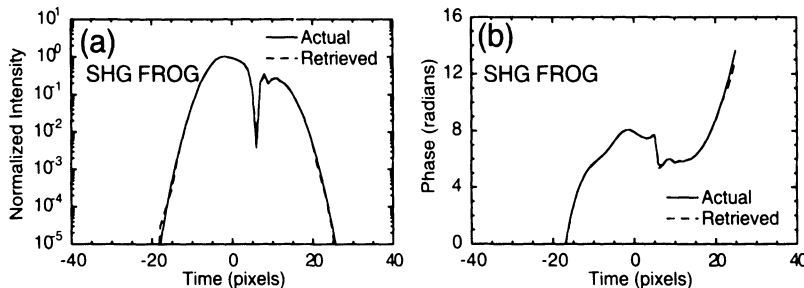


Fig. 9.19: The retrieved test pulse for SHG FROG after quantization to 8 bits. The errors in the retrieved intensity and phase are small and become apparent mainly intensities below 10^{-3} of the peak intensity. (a) The actual and retrieved intensities. The rms intensity error is 0.63%. (b) The actual and retrieved phases. The phase error is .00216 radians.

the number of quantization levels to 16384, and will give a dynamic range up to $\sim 10^4$. Making measurements with dynamic ranges of 10^5 or more will require separate calibrations of a FROG device for different intensity regimes. No filtering was used in this analysis, but optimized filtering may yield some improvement (although probably not as much as in the additive noise case).

Error Bars and Boot-Strap Methods

How accurate is a given FROG measurement of a pulse? While some indication of the measured pulse accuracy is available from the FROG error, we need a method for determining *the error in each of the retrieved intensity and phase points*. In other words, how do we place *error bars* on the intensity and phase at each time (and frequency)? In this section, we present a simple, robust, and general method for doing this. By applying this method to both theoretical and experimental FROG measurements of pulses, we will show that it gives reasonable results.

The method that we will use is called the *boot-strap* method, an established statistical method [10,11]. In this case, it involves running the FROG algorithm several times for the measured FROG trace, but each time with a random set (about half) of the data points removed, and tabulating the statistics of the retrieved intensity and phase values obtained during these runs. The statistics of these re-sampled values approximate the actual statistics of the retrieved intensity and phase values at the various times (and frequencies). In this way, we can place error bars on the intensity and phase at each time or frequency.

Figure 9.20 shows the retrieved intensity and phase of a theoretical Gaussian flat-phase pulse with error bars determined this way. To simulate experimental noise, 1% uniform, additive noise has been added to the FROG trace. The error bars represent the ± 1 standard deviation points about the mean value of each retrieved intensity or phase value for each time. The resulting intensity errors are on the order of 1% of the intensity peak, but vary with intensity. The phase noise is large in the pulse wings, as expected, because the intensity goes to zero there. Note also that about 60% of the actual points fall within the error range, which indicates that this procedure is reasonable.

Figure 9.21 shows the retrieved intensity and phase of an experimentally measured pulse using TG FROG, with error bars obtained using the boot-strap

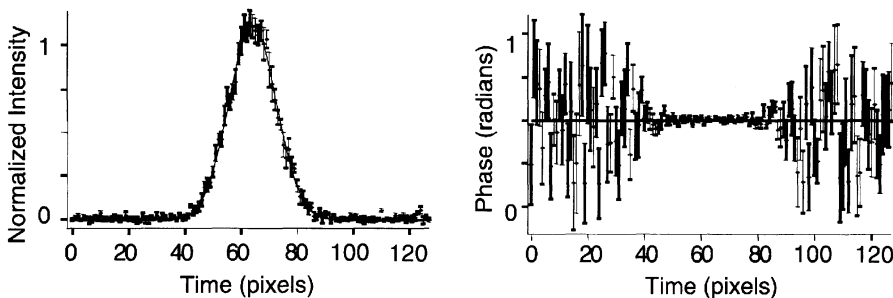


Fig. 9.20: The retrieved intensity and phase of a theoretical Gaussian flat-phase pulse with 1% additive noise in its trace with error bars determined using the boot-strap method.

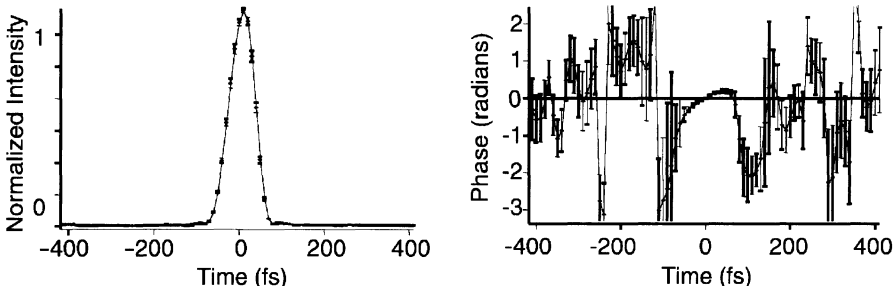


Fig. 9.21: Retrieved intensity and phase of an experimental pulse measured with a transient-grating FROG device. The error bars were obtained using the boot-strap method.

method. The experimental noise corresponded to a few percent multiplicative noise in the FROG trace. Note that the resulting errors are also a few percent but vary with intensity.

The boot-strap method is easy to implement. It may seem that, because it requires about ten runs of the algorithm, it could be quite slow. The FROG code, however, typically requires only a few seconds on a PC or Macintosh to converge, a time that is rapidly decreasing with improvements in computer speed. Also by using the retrieved intensity as an initial guess for the additional required runs, these additional runs proceed in a small fraction of the time required for the first run.

Another method for determining error bars for FROG measurements that is being developed using a Principle Components Generalized Projection Algorithm (PCGPA) [12,13]. The method relies on the fact that the FROG trace may be described as the outer product of two vectors. Since noise and systematic errors convert FROG traces into images that can no longer be described by a single outer product pair, it is possible to perform a singular value decomposition of the FROG measurement and learn about the noise and systematic errors by looking at the weights of the outer product pairs [14] (see Chapter 21).

References

1. D. N. Fittinghoff, K. W. DeLong, R. Trebino, and C. L. Ladera, "Noise sensitivity in frequency-resolved optical-gating measurements of ultrashort pulses," *Journal of the Optical Society of America B* **12**, 1955–67 (1995).
2. K. W. DeLong, D. N. Fittinghoff, R. Trebino, B. Kohler, and K. Wilson, "Pulse retrieval in frequency-resolved optical gating based on the method of generalized projections.,," *Optics Letters* **19**, 2152–4 (1994).
3. R. Trebino and D. J. Kane, "Using Phase Retrieval to Measure the Intensity and Phase of Ultrashort Pulses: Frequency-Resolved Optical Gating," *J. Opt. Soc. Amer. A* **10**, 1101–11 (1993).
4. K. W. DeLong and R. Trebino, "Improved Ultrashort-Pulse Retrieval Algorithm for Frequency-Resolved Optical Gating," *Journal of the Optical Society of America A* **11**, 2429–37 (1994).
5. H. Stark, "Image Recovery: Theory and Application," (Academic Press, Orlando, 1987).
6. Jae S. Lim, *Two-dimensional signal and image processing* (Prentice Hall, Englewood Cliff, New Jersey, 1990).
7. R. R. Coifman and D. L. Donoho, "Translation-Invariant De-Noising" in *Wavelets and Statistics*, edited by Anestis Antoniadis (Springer-Verlag Lecture Notes, 1995).
8. David L. Donoho, "Wavelet Shrinkage and W.V.D-A Ten-Minute Tour," Stanford University Tech. Rep. 416 (Stanford University, Stanford, California, January 1993).
9. M. A. Krumbügel, K. W. DeLong, D. N. Fittinghoff, J. N. Sweetser, and R. Trebino, "Wavelet noise reduction for frequency-resolved-optical-gating measurements of ultrashort laser pulses," presented at the Wavelet Applications III, Orlando, FL, USA, 1996.
10. B. Efron and Tibshirani, *Science* **253**, 390 (1991).
11. William H. Press, Saul A. Teukolsky, William T. Vetterling, and Brian P. Flannery, *Numerical Recipes in C* (University Press, Cambridge, 1992).
12. D. J. Kane, "Real-time measurement of ultrashort laser pulses using principal component generalized projections," *IEEE Journal of Selected Topics in Quantum Electronics* **4**, 278–84 (1998).
13. D. J. Kane, "Recent progress toward real-time measurement of ultrashort laser pulses," *IEEE Journal of Quantum Electronics* **35**, 421–31 (1999).
14. D. J. Kane, private communication.

10. Practical Issues, Marginals, Error Checks, and Error Correction

Greg Taft and Ken DeLong

Introduction

The usefulness of a new scientific technique is determined by the details of its implementation. Many clever techniques that are otherwise rigorous and sound fail to become useful workhorse laboratory techniques because of difficulties in experimental implementation, noise sensitivity, cumbersomeness, or other more fundamental limitations. Often these details go unreported (who wants to write a paper explaining how he failed to be able to do something?), resulting in a loss of valuable time and resources for research groups that attempt to use the technique. It's therefore incumbent upon the developers of an experimental technique to determine whether practical limitations will render the technique less than ideal.

In our experience developing and using FROG, we have found it to be extremely well-suited to its purpose and free of irritating or debilitating complications. But, as with any technique, there are practical issues involved in the everyday use of FROG. These include questions like "What limits the minimum and maximum intensities that can be used with FROG?" "How can we tell if our FROG data are valid?" "How densely should we sample the points in a FROG trace?" "Can a pulse of arbitrary complexity be represented on a FROG trace?" It's the purpose of this chapter to answer practical questions such as these.

We start with a discussion of redundancy and error detection in FROG. Then we present a simple and powerful technique to check the consistency of FROG data with an independently measured spectrum and autocorrelation of the pulse. We show how these checks can uncover systematic errors in the measurement apparatus that might otherwise go undiscovered. We also show how these checks can be used to correct faulty FROG data. We then explore some fundamental limits to the FROG technique. We explore the low-power limits to FROG and find that, in its most sensitive incarnation (SHG FROG), it just breaks the 1 pJ barrier for 100 fs pulses (the new beam geometry, called GRENOUILLE and discussed in Chapter 12, does even better). On the other end of the scale, we find that the upper limit to allowable FROG-signal efficiency is about 1%, and is limited in $\chi^{(3)}$ geometries by self- and cross-phase modulation-induced distortion. We compute the maximum time-bandwidth product for pulses that can be properly represented on a FROG trace of a given size. This maximum (rms) time-bandwidth product ranges anywhere from 3 to 20 for a FROG trace of 128×128 pixels, and varies strongly with the form of the pulse itself and the desired accuracy. More

complex pulses can be measured by using larger arrays. We also discuss the issue of how densely to sample the FROG trace. We end the chapter with a discussion of FROG error values.

Redundancy and Error Detection in FROG

We've used the FROG algorithm to retrieve thousands of pulses, both simulated and experimental, and we wish to stress that, for valid data, the algorithm has never failed to converge. In our experience, the algorithm always converges for properly taken traces. The only occasions on which it didn't were for traces that were badly undersampled (aliased), incorrectly calibrated, truncated, distorted, or excessively corrupted by random or systematic error. This is in fact a unique advantage of the FROG method: *if the algorithm doesn't converge, one can be sure that an error exists in the data collection apparatus, while, if the algorithm converges well, it nearly guarantees that the correct result has been found.* The reason for this is that an electric field sampled at N points has $2N$ degrees of freedom (N points of both magnitude and phase), but corresponds to a FROG trace with N^2 pixels. Thus, there's great redundancy in the FROG trace (it's overdetermined), meaning that there are many more possible FROG traces—configurations of N^2 pixels—than are allowed by a physically realizable electric field. Thus, a real FROG trace with some systematic or much random error added to it most likely won't correspond to a physically valid FROG trace, leading to non-convergence of the algorithm, while convergence of the algorithm nearly guarantees that the measurement was accurate and free of artifacts.

Typically, the algorithm converges to the closest physically valid FROG trace to the input trace. As shown in the previous chapter, in the presence of random noise, the algorithm often converges to a trace that is considerably closer to the noise-free trace than the original (noisy) input data [1]! In the case of systematic error, the corrupted trace is almost always quite unlike any physically valid trace, leading to non-convergence of the algorithm. Fortunately, there are ways to detect this type of systematic error, even before running the algorithm, as we shall see below.

The redundancy in the FROG trace allows for several types of checks on the accuracy of the data. When analyzing experimental FROG data, in the majority of cases we have discovered systematic errors in the data collection apparatus simply from inspection of the FROG trace and its marginals (see next section), allowing us to “debug” experiments remotely. In methods that do not provide such checks, these errors would probably have gone undiscovered. Far from being a disadvantage, the two-dimensional, redundant nature of the FROG data set gives us the powerful ability to detect and correct systematic errors in the experimental setup.

This sensitivity to systematic experimental errors is a crucial part of the diagnostic power of FROG. The FROG technique consists of a pump-probe

type process followed by the measurement of the spectrum. If one is unable to do these two experiments correctly (due to spatial chirp in the beam, incorrect calibrations, beam distortions at the focus, etc.) then it is unlikely that any other experimental results generated by the apparatus will be valid, as almost all experiments require a pump-probe and/or spectral measurement. Thus, FROG allows an extremely germane check on the performance of the experimental apparatus.

Self-consistency Checks for FROG Data: The Marginals

The fact that the FROG trace contains redundant data (i.e. it is overdetermined) allows for some fairly simple, yet powerful, checks on the consistency of the experimental data. These checks involve the *marginals*, which are the one-dimensional curves obtained by integrating the FROG trace over one of its coordinates. The marginals can be compared to quantities involving the pulse's spectrum and autocorrelation. When these easily computed quantities agree, one can be fairly sure of the consistency of the data. The more useful of the two marginals is the frequency marginal,

$$M_\omega(\omega) = \int_{-\infty}^{\infty} I_{\text{FROG}}(\omega, \tau) d\tau \quad (10.1)$$

obtained by integration of the FROG trace over the delay variable.

The form of the marginals was explored in an earlier work [2]. As an example, we consider here the case of SHG FROG, which is perhaps the easiest to understand. In this case, the frequency marginal should have a functional form identical to the autoconvolution of the pulse spectrum $S(\omega)$:

$$M_\omega^{\text{SHG}}(\omega - 2\omega_0) = S(\omega - \omega_0) * S(\omega - \omega_0) \quad (10.2)$$

where ω_0 is the carrier frequency and the asterisk denotes convolution. Therefore, by simply measuring the fundamental pulse spectrum, one can easily check the consistency of the FROG data. If the SHG FROG frequency marginal does not agree with the autoconvolution of the pulse spectrum, one can be assured that there is a systematic experimental error somewhere in the system. Some typical possibilities are incorrect wavelength or temporal calibrations of the FROG data, a spectrometer/camera response that varies with wavelength, insufficient doubling crystal bandwidth, spatial chirp, spatio-temporal distortions of the pulse at the focus, etc. Under these conditions, it is illogical to expect that the spectrum of the field retrieved by the FROG algorithm should match the experimentally measured spectrum—the failure of Eq. (10.2) indicates that the SHG FROG data are *inconsistent* with the measured pulse spectrum.

In the PG and SD FROG geometries, the same sorts of consistency checks are available. However, the exact form of the frequency marginal varies with the type of geometry. In the case of PG FROG, the frequency marginal has the form

$$M_{\omega}^{\text{PG}}(\omega - \omega_0) = S(\omega - \omega_0) * \Im\{A(\tau)\} \quad (10.3)$$

where $\Im\{\cdot\}$ indicates Fourier transform and $A(\tau)$ is the usual second-order intensity autocorrelation. Thus in PG FROG, it is possible to check the consistency of the FROG data with both the spectrum and the autocorrelation of the pulse through a simple convolution of these two quantities. In SD FROG, the frequency marginal is

$$M_{\omega}^{\text{SD}}(\omega - \omega_0) = S(-\omega + \omega_0) * S^{\text{SH}}(\omega - 2\omega_0) \quad (10.4)$$

where $S^{\text{SH}}(\omega)$ is the spectrum of the second harmonic of the pulse. When using the marginals as a check on the data consistency, it is important to remember to center all spectra on the same carrier frequency ω_0 and to interpolate laboratory spectra to a constant frequency spacing. In the case of extremely broadband light, in addition to merely changing the abscissa of the data, this also involves a nonlinear scaling factor

$$S_{\omega}(\omega) = \frac{\lambda^2}{2\pi c} S_{\lambda}(\lambda) \Big|_{\lambda=\frac{2\pi c}{\omega}} \quad (10.5)$$

to change from a spectrum sampled on a constant wavelength interval (as most spectrometers yield) to one sampled on a constant frequency interval (as needed for an FFT).

In addition, the delay marginal is the integral of the trace over all frequencies. Because it un-spectrally resolves the trace, it's obviously equal to the autocorrelation, which can also yield a useful check on the data.

Removing Systematic Error from FROG Traces

The marginals are extremely useful for detecting the systematic errors mentioned above. With SHG FROG, the marginals also can be used to *correct* the FROG trace for these systematic errors by *simply multiplying the trace by the ratio of the fundamental spectrum autoconvolution and the frequency marginal, thus enforcing agreement of these two quantities*. Remarkably, this correction procedure corrects, not only for all known frequency-dependent effects, but for *unknown* effects, as well. In other words, even if you haven't measured the spectral response of the diffraction grating in your spectrometer, any wavelength-dependence of this element will be compensated by this correction procedure. Of course, this procedure only works if no zeroes (or very low values) occur in the various wavelength-dependent responsivity, reflection, transmission, or efficiency curves.

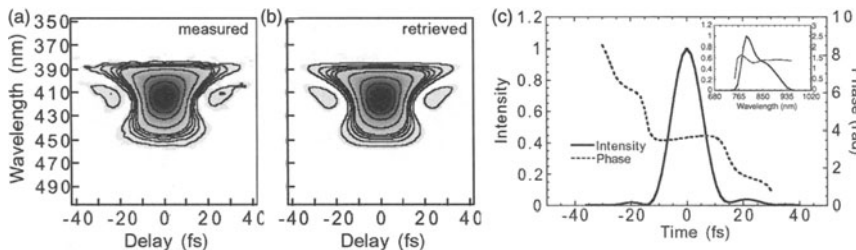


Fig. 10.1: FROG measurements using insufficient phase-matching bandwidth. (a) The experimentally measured SHG FROG trace for a 12-fs pulse with a double-peaked spectrum; (b) retrieved FROG trace; (c) retrieved intensity and phase. In Figs. 10.1 and 10.3 the traces are shown as density plots with overlaid contour lines at the following intensity values: 2%, 4%, 6%, 8%, 10%, 20%, 40%, 60%, and 80%.

We will now demonstrate the use of this procedure for the measurement of a 12-fs, 150-nm-bandwidth pulse from a low-dispersion self-modelocked Ti:Sapphire laser [3,4] whose experimental SHG FROG trace is shown in Fig. 10.1a. Fig. 10.1b shows the retrieved SHG FROG trace of this pulse, and Fig. 10.1c shows the retrieved intensity and phase in both domains. Note that convergence has occurred (the FROG error for this 128×128 trace is 0.00273, approximately equal to the noise in the trace), and the retrieved SHG FROG trace agrees well with the experimental trace. Unfortunately, uniform phase-matching of the entire bandwidth of this pulse has not occurred, as shown by the comparison of the pulse autoconvolution with the FROG-trace frequency marginal in Fig. 10.2. Clearly, for the particular angle of the SHG crystal used in the measurement, the crystal phase-matching efficiency is greater for the short wavelengths than for long ones. (Further evidence for this conclusion is that, for different SHG crystal angles, different spectral regions were underrepresented in the trace.) As a result, the retrieved pulse is suspect, despite the good convergence of the algorithm. Indeed, we have found that, while algorithm convergence is a very good indicator of a correct pulse measurement in other versions of FROG, convergence is usually, but not always, such an indicator in SHG FROG, mainly due to the additional symmetry and time ambiguity of SHG FROG traces. Consequently, additional care must be used in SHG FROG measurements.

We can, however, use the knowledge of the spectrum autoconvolution to correct the FROG trace by multiplying the measured trace by the ratio of the spectrum auto-convolution and the trace frequency marginal. Since the frequency marginal of the corrected trace now necessarily agrees with the spectrum autoconvolution, systematic errors associated with inadequate phase-matching bandwidth and potential wavelength-dependences of other components no longer corrupt the data. Figure 10.3a shows the corrected FROG trace using this procedure; Fig. 10.3b shows the retrieved FROG trace; and Fig. 10.3c shows the retrieved intensity and phase. The FROG error for

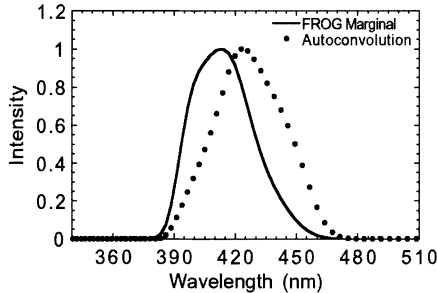


Fig. 10.2: Comparison of the autoconvolution and frequency marginal of the pulse whose trace is shown in the previous figure. Note the attenuated frequency marginal at long wavelengths compared to the autoconvolution of the spectrum, indicating poor phase-matching efficiency for those wavelengths.

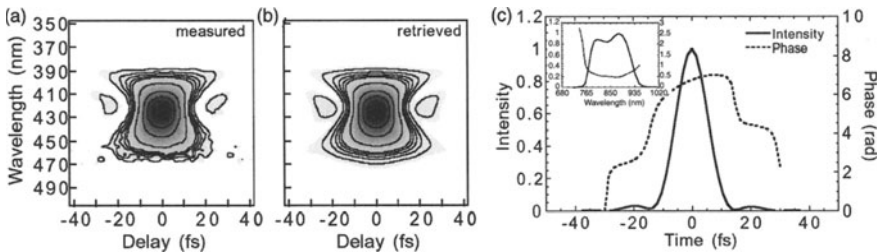


Fig. 10.3: Corrected FROG trace using the measured frequency marginal and spectrum auto-convolution. (a) The corrected experimental SHG FROG trace for a 12 fs pulse with a double peaked spectrum; (b) retrieved FROG trace; (c) retrieved intensity and phase. Note the double-humped spectrum that was missing in the retrieved spectrum shown in Fig. 10.1c.

this trace and its retrieved twin is 0.003 31, which is again approximately the experimental error (note that the error has increased slightly after using the correction procedure, because it has augmented regions of the trace that were formerly of low intensity, thus amplifying the noise somewhat, as can be seen in the corrected trace). Notice that the long-wavelength component of the double-peaked spectrum associated with this particular low-dispersion laser is much more evident in this retrieved pulse than in the previous retrieval using the uncorrected trace. Indeed, this measured spectrum agrees well with the independently measured pulse spectrum and theoretical simulations of the laser. As a result, this correction procedure has improved the pulse measurement considerably. Although this correction procedure is limited to SHG FROG, the marginals still can be used as an effective diagnostic tool with other FROG geometries.

This correction procedure is important and, as a result, is now commonplace in measurements of broadband pulses (see Chapters 14 and 17). It is especially helpful and reliable because, while the SHG FROG trace is measured at the

SH (often in the UV), where wavelength-dependent systematic error is more likely, the spectrum is measured at the fundamental wavelength, where such errors are less likely, or at least different, and are more easily corrected. It is also currently unique to FROG.

Limitations to the FROG Technique

In this section we'll explore some experimental limitations to FROG. Because FROG uses a nonlinear process to generate the signal field, there's a limit to the lowest intensity pulse that can be measured with a given medium. We'll quantify some of these limits. Also, we'll discuss the maximum allowable diffraction efficiency in the $\chi^{(3)}$ techniques and the maximum obtainable time-bandwidth products available for a FROG trace of fixed size. Finally, we discuss the appropriate sampling rates for FROG traces.

Low-power Limits

Because a nonlinear process generates the FROG signal field, FROG requires a minimum pulse power, which varies from version to version of FROG. The single-shot versions of FROG, for example, require more power than the multi-shot versions because, in single-shot versions, the pulse is focused to a line, instead of a point as in the multi-shot version. For a pulse of given power, this results in a higher intensity at the nonlinear medium for the multi-shot case. Also, the minimum pulse power necessary to generate a usable FROG trace will vary with the geometry used. Second-order effects (SHG) require lower intensities at the nonlinear medium than third-order effects (PG and SD), so SHG FROG can function with lower pulse powers.

Multi-shot SHG FROG is the most sensitive of the FROG geometries. In one of our experiments, we used a KDP crystal as the nonlinear medium. Pulses from a Ti:Sapphire oscillator operating at 860 nm with 80 fs FWHM were split into two beams by a beam splitter and focused with a 200 mm focal length spherical lens onto a 300 micron thick KDP sample. The non-collinear SHG signal beam was collected and recollimated with another spherical lens, dispersed by a grating, and focused onto a CCD camera. We were able to record SHG FROG traces at a 40:1 peak signal-to-dark-current-noise ratio with our setup for peak pulse powers as low as 190 W (15 pJ for our pulses) in each of the two beams. The 96 MHz pulse train was averaged over the camera read-out time of 16 ms. The spectrum covered approximately 50 pixels on the camera.

The apparatus was not optimized, and further gains in sensitivity could have been realized through the use of a crystal with a higher nonlinearity (e.g. BBO), tighter focusing, or using a more sensitive or less noisy camera (our camera produced about 5 counts of dark current per pixel over a measurement period). With these improvements, multi-shot SHG FROG traces could be

Table 10.1: Practical low-power limits for various FROG geometries. (Multi-shot and signal-averaged single-shot geometries assume a 96 MHz pulse repetition rate and a 16 ms camera averaging time. Energies in parentheses are for an 80 fs long pulse. An asterisk indicates values extrapolated from other entries in the table.) Longer camera averaging times, tighter focusing, and use of BBO (instead of KDP) would yield better sensitivities.

FROG geometry	Multi-shot	Avg. single-shot	True single-shot
SHG	190 W (15 pJ)	25 kW (2 nJ)	3 MW* (240 nJ)
PG	6 MW (480 nJ)	–	45 MW (3.6 μ J)

made for pulses in the femtojoule range when the pulse length is 100 fs or shorter.

In the single-shot SHG FROG configuration, we were able to record FROG traces for input pulse powers as low as 25 kW (2 nJ for our pulses) when using signal averaging of the 96 MHz pulse train over the 16 ms camera read-out time. From these numbers, we anticipate that true single-shot operation should be available for pulse powers of 3 MW.

In a multi-shot PG FROG geometry, using 1 mm of UV-grade fused silica as the nonlinear medium produced acceptable signals for a total input power of 300 nJ for 45 fs pulses (6 MW peak power). This experimental setup used a 150 cm focal length lens to focus the beams into the sample. Single-shot PG FROG results are taken from ref. [5].

Our results for the low-power limits to FROG are given in Table 1.

Signal-efficiency Limit

In PG and SD FROG, the signal efficiency of the process used to generate the FROG signal field cannot be made arbitrarily high, even if the pulse energy is high, because the same fundamental mechanism that is responsible for generating the signal field is also responsible for self- and cross-phase modulation, which distort the pulse spectrum and hence the FROG trace. Here, we make a simple estimate (ignoring propagation effects) of the maximum signal efficiency available without significant distortion of the pulse being measured. We calculate the FROG signal efficiency as a function of the maximum gate-beam-induced phase change $\Delta\phi$ of the probe beam. We then calculate the amount of pulse distortion for a given amount of cross-phase modulation, which is also measured by $\Delta\phi$. In this way we can place an upper limit to the FROG signal efficiency.

In PG FROG, the signal efficiency is easily found to be $\eta = (\Delta\phi)^2/4$, where $\Delta\phi = k_0 n_2 I L$, and k_0 is the vacuum wavevector, n_2 is the nonlinear refractive index, I is the intensity of the gate pulse and L is the length of the medium. To estimate the effects of cross-phase modulation for a given

Table 10.2: High-signal efficiency limits in third-order FROG. The induced phase change and its corresponding efficiency and spectral broadening.

$\Delta\phi$	Peak signal efficiency	Spectral broadening	
		rms	FWHM
0.2 rad	1%	1.5%	0.16%
0.6 rad	9%	13%	1.4%

value of $\Delta\phi$, we examine a Gaussian pulse with a time-dependent phase of $\Phi(t) = \Delta\phi I(t)$, where $I(t)$ is the intensity of the pulse normalized to a peak of unity. The results of numerical calculations are summarized in Table 2. Because the time-domain intensity profile is unaffected, the amount of spectral broadening is equal to the increase in the time-bandwidth product.

We see that, to limit the rms spectral broadening to $<1.5\%$, $\Delta\phi$ must be <0.2 radians, corresponding to a peak signal efficiency of $(0.2)^2/4$ or 1%. In SD FROG, the argument is essentially identical. The limits to maximum signal efficiency in SHG FROG (again, about 1%) stem from pump-depletion considerations, and were discussed in ref. [6].

Maximum Time-bandwidth Product

In all FROG measurements, it's essential to measure the *entire* trace and not to crop it: after all, we wish to measure the entire pulse, not just a piece of it! *The trace should be an island in a sea of zeros.* That no cropping of the trace should occur may seem obvious, but cropped traces are the most common cause of poor pulse measurements for new users of FROG. In fairness to new FROG users, however, this issue is a bit more subtle than we're implying here. Since a function can't have finite extent in both time and frequency, the FROG trace, which is a function of time in one direction and frequency in the other, must extend from $-\infty$ to $+\infty$ in at least one direction. If we were to require that *all* nonzero values of the trace be measured, then we'd have to scan infinitely far in at least one direction, thus delaying quite unacceptably the relevant graduate student's graduation date. So there's no way to avoid some cropping of the trace, but everyone agrees that it's important that the trace decrease to a fraction of a per cent of its maximum value at its edges. If you desire greater accuracy, then you may wish to scan a bit further.

A consequence of this is that a given FROG trace of $N \times N$ pixels cannot represent a pulse with an arbitrarily large time-bandwidth product (TBP). For pulses with too large a TBP, the trace will have significant intensity off the edge of the numerical array, and the pulse will be aliased in the time and/or frequency domains (this issue will be more fully discussed in the next section). Therefore there is an upper limit to the TBP of a pulse that can be properly represented on a FROG trace of a given size (number of pixels). We have

Table 10.3: The maximum TBP's representable on a FROG trace of 128×128 pixels. The products are computed as rms values (with FWHM values in parentheses) for which the FROG trace is truncated to $<10^{-4}$ of the peak. These values scale roughly with the size N of the FROG trace.

Pulse type	PG	SD	SHG
Linear chirp	8.8 (7.8)	4.9 (4.3)	5.1 (4.5)
Self-phase mod.	20 (20)	7.5 (7.6)	8.8 (9.0)
Spectral cubic phase	3.4 (0.89)	3.0 (0.86)	3.3 (0.87)

numerically determined these upper limits for FROG traces of several sizes. (In making this calculation, we continue with our convention of generating an $N \times N$ FROG trace from a field N elements long.)

The TBP's we report use the full-width at half maximum (FWHM) measured in cycles and the root-mean-square (rms) measured in radians. In Chapter 2, we saw that, in the respective units, a transform-limited Gaussian has a TBP_{FWHM} of 0.441 (cycles) and a TBP_{rms} of 0.5 (rad). It should be noted that an rms TBP of 0.5 is an absolute minimum for all waveforms, while the FWHM TBP can range quite low (a transform-limited Lorentzian has a FWHM time-bandwidth product of 0.221, while its rms TBP is 2.47!).

We found that the upper limit for the TBP varies strongly with the form of the pulse. Therefore, we used pulses with linear chirp, self-phase modulation, and spectral cubic phase. The results for a 128×128 FROG trace are seen in Table 3 for the three main FROG geometries. The criterion chosen was that the intensity at the edge of the FROG trace grid was 10^{-4} or less of the peak intensity. For an $N \times N$ FROG trace we found that the maximum available TBP scales roughly with N , except for the case of self-phase modulated pulses, where it appears to scale roughly like $1.2N$. The algorithm was able to retrieve all of the pulses with maximum TBP. However, it should be noted that these were noise-free, simulated pulses, and the presence of noise may make these pulses more difficult to retrieve (the amount of redundancy is minimal for data that fills the FROG trace grid). Therefore, with experimental data, it is probably best to use a larger array when the TBP of the pulse approaches the maximum value.

Sampling Rate

The issue of sampling in a time-frequency technique such as FROG is a subtle issue. Before we directly address this issue, there are some basic terms and concepts that must be established.

As noted in the previous section, the FROG trace is considered properly sampled when the data aren't truncated; i.e., all non-zero FROG data lie within

the FROG trace grid. Of course, in a strict mathematical sense, FROG trace data never go to zero: the FROG trace of a Gaussian pulse, for example, decays like a Gaussian in all directions. As a practical criterion, we'll consider FROG trace data to be properly sampled when the intensity of the data points at the perimeter of the FROG trace grid are 10^{-4} or less of the peak of the trace. A data set that satisfies this criterion is said to satisfy the *FROG sampling rate (FSR)*. A FROG trace that satisfies the FSR completely determines the intensity and phase of the pulse that created it, as we shall show.

A similar criterion that arises in signal processing is the Nyquist criterion [7]. A band-limited function is properly sampled if the sampling rate is at least as high as the so-called Nyquist rate, where the highest frequency occurring in the signal is sampled at least twice per period. In this case, the discrete samples of the signal contain *all* the information about the signal: sampling at a higher rate, noise considerations aside, gains nothing. Note that a signal sampled at the Nyquist rate is not necessarily pretty: a sine wave sampled twice per period looks like a sawtooth, while a Nyquist-sampled Gaussian has only one point above the half-maximum and only 5 points larger than 1% of the peak! (Note that a Gaussian can never be a band-limited function, as it has infinite extent in both time and frequency. However, in analogy with the FROG trace, we can consider the 10^{-4} points of the spectrum as the “band limit.”) Nevertheless, despite their jagged appearance, these sampled signals completely determine the original waveform.

The FSR is a stricter criterion than the Nyquist rate. A pulse sampled at the Nyquist rate will have FROG trace data that are truncated at significant energies: the data won't be fully contained on the FROG trace grid, and thus the FSR won't be satisfied. In order to get all of the data on the grid and satisfy the FSR, the pulse must be sampled at a higher rate than the Nyquist rate. This means that any FROG trace data that satisfy the FSR automatically contain all the information about the pulse. No new information is gained (except perhaps noise immunity) by sampling at higher rates.

The FSR actually comprises two limits to the sampling of the data. First, the data must be sampled with a small enough temporal step $\delta\tau$ so that the data do not extend off the FROG trace grid in the frequency direction.* For a Gaussian spectrum and PG FROG, this occurs when

$$\delta\tau \leq \frac{1}{6.3\Delta\nu_p^{\text{FWHM}}} \approx \frac{\lambda_0^2}{6.3c\Delta\lambda_p^{\text{FWHM}}} \quad (10.6)$$

* Fundamentally, the delay coordinate and the frequency coordinate are not constrained by the fast Fourier-transform (FFT); the FFT relates the *temporal* coordinate t to the frequency coordinate ω . In principle, one could use a different step size when sampling the delay τ than when sampling the time t . However, this will lead to many practical difficulties in the programming of the algorithm, so that, for the sake of convenience, the step size in both delay τ and time t are usually taken to be identical. This leads to an effective coupling, through the FFT, of the delay and frequency axes. We assume this convention throughout this book.

where λ_0 is the central wavelength and $\Delta\lambda_p^{\text{FWHM}}$ ($\Delta\nu_p^{\text{FWHM}}$) is the spectral width FWHM in wavelength (frequency). If the pulse is transform limited, this becomes $\Delta\tau_p^{\text{FWHM}}/\delta\tau \geq 2.78$, where $\Delta\tau_p^{\text{FWHM}}$ is the pulse length (FWHM in intensity). The second limit inherent in the FSR is that the temporal sampling step size be large enough that the FROG trace data do not extend off the grid in the time delay direction. For a Gaussian pulse in time and for PG FROG, this evaluates to:

$$\delta\tau \geq \frac{4.5\tau_p^{\text{FWHM}}}{N} \quad (10.7)$$

In general, then, the procedure for selecting the sampling rate and grid size for an arbitrary pulse is: First, the upper limit for the temporal step size is set by Eq. (10.7). The minimum grid size N is then selected so that the extent of the FROG trace grid in the delay direction contains all of the non-zero FROG trace data. If the pulse is complex enough that both limits cannot be satisfied simultaneously, the grid size N must be increased. The numerical factors in Eqs. (10.6) and (10.7) were calculated for Gaussian pulses; other pulse and spectral shapes will have slightly different FSR limits. Differing FROG geometries will also have slightly different FSRs.

Sampling a pulse close to both limits of the FSR, so that the data nearly fill the FROG trace grid, allows one to use a very small size FROG trace grid. (The FSR can be satisfied for a transform-limited pulse in PG FROG on a 16×16 pixel trace!) Using a smaller number of pixels is of great advantage in retrieving the pulse: the FROG algorithm slows down as $N^2 \ln(N)$. However, the resulting retrieved pulse will look jagged and decidedly un-Gaussian in both the time and frequency domain.

One way to avoid the jaggedness in the output field is to sample faster than the FSR. This necessarily involves a larger grid size for the FROG trace. If the temporal sampling rate is kept constant while moving to a larger grid, the spectrum of the pulse will be sampled at a higher rate (because the frequency increment is the reciprocal of the temporal range). If the temporal sampling rate is increased commensurate with the increase in the size of the FROG trace, then the sampling in the frequency domain will remain constant (while the temporal rate increases). However, this method of increasing the grid size extracts its toll in the slowing down of the FROG algorithm.

A better solution to this problem is to sample the pulse at a rate near the FSR: use a FROG trace grid that is small enough that the FROG trace data nearly fill the grid. Pulse retrieval using the algorithm will be swift on a small grid, but the output fields will look jagged. The jaggedness of the retrieved field can be eliminated, however, by taking advantage of the completeness of a Nyquist-sampled field. Specifically, in order to get a higher point density in the frequency domain, pad the $E(t)$ returned by the algorithm with zeroes on the left and right and put it into a larger array before Fourier transforming to obtain $\tilde{E}(\omega)$. A high point density in the time domain can be achieved by similarly padding the field in the frequency domain before inverse Fourier

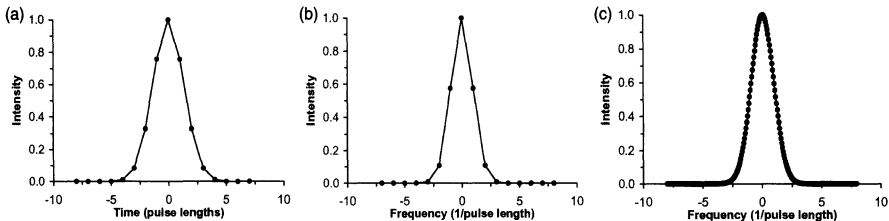


Fig. 10.4: The intensity vs. (a) time and (b) frequency for a transform-limited Gaussian pulse sampled near the FROG sampling rate limit. The pulse had a FWHM of 3.16 pixels in the time domain on a 16×16 pixel grid. In both the time and frequency domain the pulse profile is jagged and not aesthetically pleasing. (c) The time-domain field in (a) was padded with zeroes to fit in a 256 element-array, and then Fourier transformed to give this spectrum. The spectrum is now densely sampled and looks quite Gaussian. Although the field in (a) and (b) looks undersampled, the information content is equivalent to that in (c).

transforming to the time domain. This is a valid procedure, at least to the order of the approximations that we made for band-limited functions above (i.e., truncation at or below the 10^{-4} level). Thus, it is straightforward to obtain as many data points as desired in each domain.

This procedure is illustrated in Fig. 10.4. Figure 10.4a shows a Gaussian transform-limited pulse sampled so that its intensity FWHM is 3.16 pixels. This pulse satisfies the FSR for a 16×16 pixel grid. Both the temporal and spectral intensity (Fig. 10.4b) are quite jagged, yet sampled at a higher rate than the Nyquist rate. Figure 10.4c shows the spectrum of the exact same field, where the field in the time domain was padded out to 256 pixels before the Fourier transform to obtain $\tilde{E}(\omega)$. We see the spectrum is now extremely smooth and densely sampled. Figures 10.4b, c display the same waveform and the same information, but have a quite different appearance.

One particularly pleasing sampling rate for FROG data is one that makes the sampling rates roughly equal in both domains. Equal sampling in both the time and frequency domains could be defined as having the ratio of the delay step size to the temporal FWHM of the pulse be the same as the ratio of the frequency step size to the spectral FWHM of the pulse. Therefore, equal sampling in both the time and frequency domains is satisfied when the delay step size is $\delta\tau = \Delta\tau_p^{\text{FWHM}}/M$ and the wavelength step size $\delta\lambda = \Delta\lambda_p^{\text{FWHM}}/M$. On a FROG trace of $N \times N$ pixels, the frequency step size is set to $\delta\nu = 1/(N\delta\tau)$ by the fast Fourier transform [8]. A simple calculation yields

$$M = \sqrt{\Delta\tau_p^{\text{FWHM}} \Delta\nu_p^{\text{FWHM}} N} \approx \sqrt{\frac{\Delta\tau_p^{\text{FWHM}} \Delta\lambda_p^{\text{FWHM}} N c}{\lambda_0^2}} \quad (10.8)$$

For a transform-limited Gaussian pulse, the spectral width FWHM is defined in terms of the pulse length FWHM $\Delta\tau_p^{\text{FWHM}}$ as $\Delta\nu_p^{\text{FWHM}} = 2 \ln(2)\pi \Delta\tau_p^{\text{FWHM}}$,

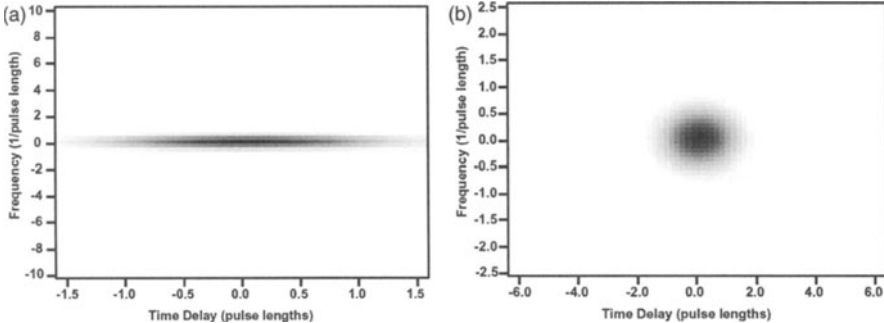


Fig. 10.5: Two SHG FROG traces (64×64) of the same transform-limited Gaussian pulse. The field in (a) was sampled at 20 points per temporal FWHM, while the field in (b) was sampled at the optimum 5.3 points per temporal FWHM. Although the two traces contain equivalent information, the trace in (a) extends over only a few pixels in the frequency direction, while in (b) there's a more even distribution between time and frequency.

so that $M = \sqrt{2N \ln(2)/\pi}$. Note that for this sampling, the SHG FROG trace contours describe perfect circles. For pulses farther from the transform limit, the delay step size can be decreased while still maintaining a reasonable frequency domain sampling rate.

Figure 10.5 demonstrates this effect. In Fig. 10.5a, we see the (64×64) PG FROG trace of a Gaussian transform-limited pulse sampled in time at a rate of $\delta\tau = \Delta\tau_p^{\text{FWHM}}/20$. The trace extends over only a few pixels in frequency. In Fig. 10.5b we see the same pulse sampled at the optimum rate of $\delta\tau = \Delta\tau_p^{\text{FWHM}}/5.3$. In this case the trace (and hence the resulting fields) are sampled evenly in both time and frequency.

It should be stressed that as long as the pulse satisfies the FSR, the FROG trace contains equivalent (and complete) information regardless of the sampling rate. It is only the visual appeal of the trace and the resulting fields that is affected by the choice of sampling rates. Also, intuitively we expect that a trace of the form of Fig. 10.5b will have a more robust retrieval in the algorithm than a trace like that in Fig. 10.5a.

A Note on the FROG Error

The FROG error G is an important quantity, as it is used in the algorithm to guide and monitor the retrieval and also to measure the quality of the retrieved FROG trace. The FROG error is computed as an rms average across the entire trace

$$G = \sqrt{\frac{1}{N^2} \sum_{i,j=1}^N \left| I_{\text{FROG}}(\omega_i, \tau_j) - \mu I_{\text{FROG}}^{(k)}(\omega_i, \tau_j) \right|^2} \quad (10.9)$$

of the difference between the experimental FROG trace I_{FROG} and the retrieved or reconstructed FROG trace $I_{\text{FROG}}^{(k)}$. I_{FROG} is always normalized to a peak of unity. In the case of numerically generated data (i.e., noise free), the scaling parameter μ is also selected so that $I_{\text{FROG}}^{(k)}$ is also normalized to a peak of unity. In the case of experimental data, this is not appropriate. The reason is that if the highest intensity pixel in I_{FROG} is corrupted by noise, the normalization of I_{FROG} will be skewed, thus biasing the calculation of G and leading to incorrectly retrieved pulses.

For experimental data, we use the following procedure. The experimental data I_{FROG} are, as usual, normalized to a peak of unity. On each iteration (labeled by k), the algorithm calculates a new estimate for the retrieved FROG trace $I_{\text{FROG}}^{(k)}$. When calculating the error G , the normalization of the retrieved trace $I_{\text{FROG}}^{(k)}$ is allowed to vary to a value that gives the minimum value for the error G . In other words, G is minimized with respect to μ on each iteration. This procedure reduces the sensitivity of the algorithm to the effects of noise-distorted normalization in experimental data. Although the calculation of the error on each iteration takes slightly longer than before (due to the minimization), we find that the algorithm generally converges in fewer steps, so that the amount of real time taken is less.

As noted above, G provides the only quantitative measure of the convergence of the FROG algorithm. Therefore, whenever experimental FROG results are given, the value of G should always be quoted. In our experience, errors of 0.005 or less result from accurate retrieval of low-noise data (128×128 pixel trace). In SHG FROG, errors of 0.002 are readily obtainable. A visual comparison of the experimental and retrieved traces is also enlightening, and should be considered essential: noise in experimental data will always raise the value of G , even if the experimental and retrieved traces are exactly the same shape.

The size of the FROG trace grid should also be reported along with the error. Due to the varying number of pixels in the trace, we find that the magnitude of the FROG error G scales as $N^{-1/2}$ for an $N \times N$ trace. Thus, if the error between two traces generated by a pair of distinct pulses is 0.01 on a 64×64 trace, it becomes an error of 0.00707 on a 128×128 trace. Thus care must be taken when comparing errors between traces of varying sizes.

Additional Experimental Issues

It should also be mentioned that fused silica isn't the only material available for third-order FROG measurements of ultrashort laser pulses. Any strongly nonlinear fast-responding material can be used. Luther-Davies, et al. [8] have used the thin-film polymer, PPV, which offers excellent signal strength in a very thin (few micron) thickness. Heavy-metal-doped glasses also appear promising. We urge you to try new materials, as this has not been explored yet, and you could write some easy, but highly appreciated, papers.

Other nonlinear-optical processes can also be used. Parametric up- or down-conversion may also be used. Any other fast nonlinear-optical process can produce an autocorrelation measurement, and hence a FROG measurement, as well. Indeed, almost any process that yields a signal field that's a function of the input pulse, time, and delay will work. It's simply necessary to modify the algorithm to account for the change in the expression for the signal field, as will be discussed in Chapter 18.

References

1. D. N. Fittinghoff, K. W. DeLong, R. Trebino, and C. L. Ladera, "Noise Sensitivity in Frequency-Resolved-Optical-Gating Measurements of Ultrashort Pulses," *JOSAB*, vol. 12, pp. 1955–67, 1995.
2. K. W. DeLong, R. Trebino, and D. J. Kane, "Comparison of Ultrashort-Pulse Frequency-Resolved-Optical-Gating Traces for Three Common Beam Geometries," *J. Opt. Soc. Amer. B*, vol. 11, pp. 1595–608, 1994.
3. G. Taft, A. Rundquist, M. M. Murnane, H. C. Kapteyn, K. DeLong, R. Trebino, and I. P. Christov, "Ultrafast optical waveform measurements using frequency-resolved optical gating," *Opt. Lett.*, vol. 20, pp. 733–5, 1995.
4. G. Taft, A. Rundquist, M. M. Murnane, I. P. Christov, H. C. Kapteyn, K. W. DeLong, D. N. Fittinghoff, M. A. Krumbügle, J. N. Sweetser, and R. Trebino, "Measurement of 10-fs Laser Pulses," *IEEE J. Sel. Top. Quant. Electron.*, vol. 2, no. 3, pp. 575–85, 1996.
5. D. J. Kane and R. Trebino, "Single-Shot Measurement of the Intensity and Phase of an Arbitrary Ultrashort Pulse By Using Frequency-Resolved Optical Gating," *Opt. Lett.*, vol. 18, pp. 823–5, 1993.
6. K. W. DeLong, R. Trebino, J. Hunter, and W. E. White, "Frequency-Resolved Optical Gating With the Use of Second-Harmonic Generation," *JOSA B*, vol. 11, pp. 2206–15, 1994.
7. W. H. Press, W. T. Vetterling, and S. A. Teukolsky, *Numerical Recipes in C: Second Edition* (Cambridge University Press, Cambridge, 1992).
8. Luther-Davies, B., et al., *Diagnostics of Femtosecond Laser Pulses Using Films of Poly(p-phenylenevinylene)*. Optics Communications, 1996. 131: p. 301–6.

11. *Improvisation in FROG*

Rick Trebino

Introduction

If you're building a FROG, you'd like to build the simplest and most cost-effective device possible.

Consider the spectrometer, for example. Can we simplify it? Well, it turns out that FROG already has built into it the front half of a spectrometer (the slit and collimating optic). This allows us to attach a simple home-made spectrometer back-end to any FROG. Not only does this reduce cost and size, but it's actually a lot simpler to use and align than a commercial device. And it's in this chapter.

Speaking of simplifying things, if you're doing an ultrafast spectroscopy experiment, and you need to measure your pulse at the sample medium, you're in luck. It also turns out that almost any ultrafast spectroscopy apparatus can be turned into a FROG that measures the pulse at the sample medium by doing little more than adding to the apparatus the above home-made spectrometer! This is a very nice feature of FROG (and autocorrelation), and it's in this chapter, too.

Finally, we'll give a simple method for automatically calibrating any FROG and removing the ambiguity in the direction of time in SHG FROG.

A Simple Home-brew Imaging Spectrometer for all FROG Measurements

It's amazingly easy to make your own imaging spectrometer for a FROG. Recall that a spectrometer requires an entrance slit, a collimating lens, a grating, and a focusing lens. No output slit is required in FROG because the camera at the output plane records all wavelengths. So how do we build such a complex-sounding device from spare parts on hand?

Well, first realize that the entrance slit has as its purpose simply to confine the beam to a tiny region in space. But, hey, so does focusing the beam into the nonlinear-optical medium! Indeed, the focus in the nonlinear medium can act as the entrance slit of a spectrometer. So all we then have to do is to collimate the beam with a lens or curved mirror, diffract the beam off a grating, and then focus it. If both lenses are used on axis (and there's no reason not to), then we're done. See Fig. 11.1.

This device is much less expensive than a spectrometer. Another advantage of this device is that it removes several sensitive alignment parameters from the apparatus—you no longer have to worry about coupling the beam into a spectrometer.

This design is so elegant and simple that I can't think of a reason not to use it in any FROG that you may decide to build.

Getting Most of a FROG for Free in Ultrafast Laser Spectroscopy

Most ultrafast laser experiments involve exciting a medium with one pulse and probing it a variable delay later with another, usually a replica of the excitation pulse (see Fig. 11.2). Sound familiar?

It should, as this is basically the greater part of a FROG set-up! What this means is that you can make a simple modification to your apparatus to make it measure a pulse! Figure 11.2 shows such an apparatus. So you only have

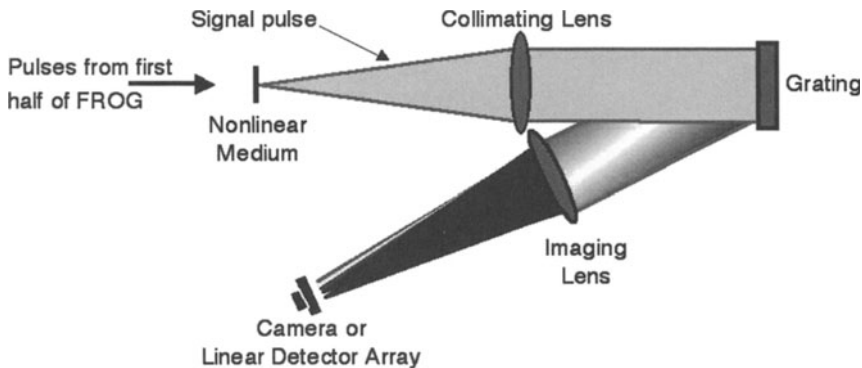


Fig. 11.1: Simple home-brew imaging spectrometer for all FROG devices. This device uses the beam focus in the nonlinear medium as the entrance slit.

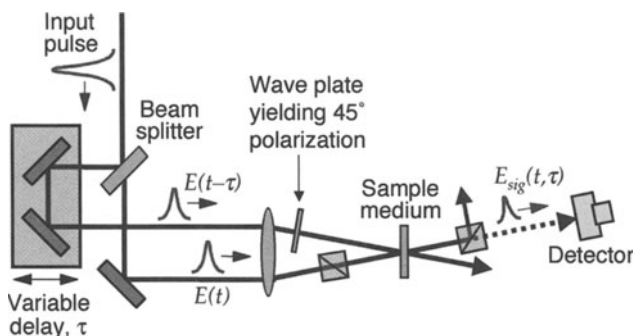


Fig. 11.2: A typical polarization-spectroscopy ultrafast-spectroscopy experiment for measuring material lifetimes and dynamics of a sample. Note the beam splitter, delay line, and beam-recombing optics, reminiscent of the front end of a FROG. About the only difference between such an experiment and a PG FROG is the use of a sample medium and the lack of a spectrometer (although the signal pulse is often spectrally resolved, too!).

to build one apparatus to measure both relevant quantities. Talk about getting something for nothing!

And an additional very nice feature of this set up is that it'll measure the pulse *at the sample medium*. This is very important, especially when the pulses are very short, as any medium that the pulse passes through can distort it. The alternative is that the pulse would pass through one set of optics on the way to the sample in the experiment and a completely different set of optics on the way to the pulse-measurement device, with the result that the measured pulse may differ from the pulse used in the experiment considerably. So simply replacing the sample with an SHG crystal enables, for example, an SHG FROG measurement of the pulse exactly where you need to know it.

And you can use the simple home-brew spectrometer, too.

What if the two pulses used in such an experiment are potentially different? Maybe even different colors? Now we need to measure two independent pulses. Amazingly, this can also be done. But we've saved this for Chapter 20. And if you thought the phase-retrieval math that we did to show how FROG works was cool, there's some even more amazing mathematics behind this!

Procedure for Objectively Learning the Kalibration and Direction of Time (POLKADOT FROG)

FROG is quite simple to implement, but, as with any technique, we'd like to eliminate the most arduous features, which also represent potential sources of error. One such task is the calibration of the relevant axes, which is arduous in almost any technique and always can yield errors. FROG measurements are made as functions of both delay and frequency, whose increments of delay per pixel and wavelength per pixel, respectively, must be determined. Mis-calibration of one or both axes can yield high retrieval error and/or incorrect results.

Another task—in the second-harmonic-generation (SHG) version of FROG—is the removal of the ambiguity in the direction of time. While most versions of FROG uniquely determine the pulse, the pulse and its mirror image yield the same trace in SHG FROG, so one must perform additional measurements or have *a priori* information to determine which pulse field is the correct one. While FROG contains checks and balances on all measurements, a very desirable development would be a method for automatic calibration and the removal of this ambiguity.

This section describes a simple and elegant method for simultaneously solving both of these problems, which we call the Procedure for Objectively Learning the Kalibration And Direction Of Time (POLKADOT) FROG [1].

Consider the calibration problem first. The solution is inspired by the FROG trace of a double pulse, shown in Fig. 11.3. This trace contains three islands of intensity, each separated by the pulse separation, τ_{sep} , just as in an autocorrelation of a double pulse, shown as the delay marginal. However, in FROG,

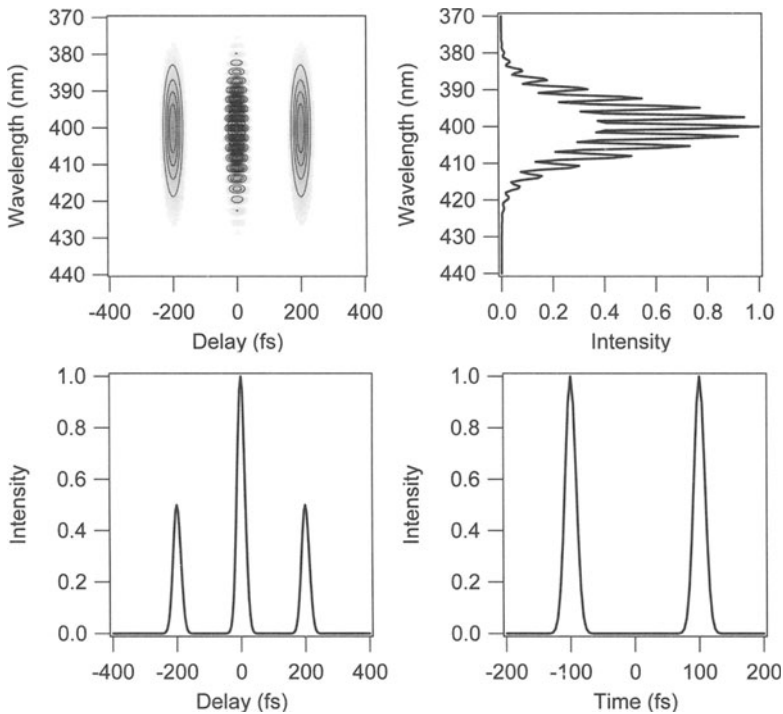


Fig. 11.3: FROG trace (upper left) of a double pulse (lower right). Note the islands in both delay and frequency. The frequency marginal (upper right) and delay marginal (lower left) show the frequency and delay fringes, which depend only on the pulse separation.

the islands are also frequency resolved. Moreover, in FROG the central island has fringes in frequency with a separation of $1/\tau_{\text{sep}}$ as illustrated in the frequency marginal. Thus, the pulse separation determines the spacing of the main structure of the double-pulse FROG trace in both delay and frequency. So propagating a double pulse with known pulse spacing into a FROG automatically yields the increments of both delay and frequency per pixel and hence calibrates the FROG device. This method works even when the pulse has structure to begin with, provided that the separation of the double pulse is greater than that of the individual pulses.

Accordingly, the solution involves making a double pulse and identifying these islands and their separation in the resulting trace. This can easily be done by simply placing an etalon with known optical thickness in the beam before the FROG device. Of course, an etalon produces an infinite train of pulses, but using a sufficiently low etalon reflectivity yields essentially one additional pulse—all that is needed.

While the above solution is quite simple, a more elegant solution is to replace the usual beam splitter in the FROG device with an etalon

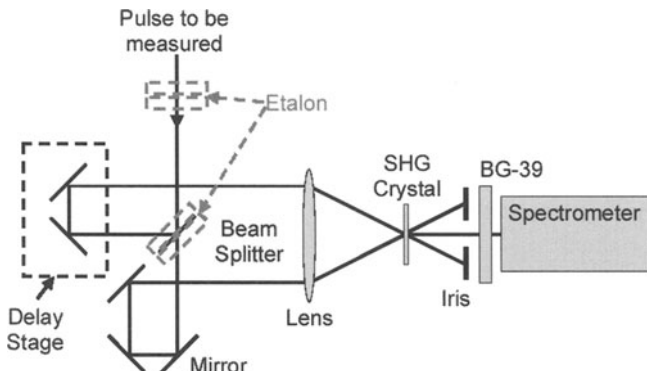


Fig. 11.4: Implementation of POLKADOT in an SHG FROG apparatus. The etalon can be placed in the beam before the FROG or, even better, it can replace the beam-splitter.

(see Fig. 11.4). The etalon's front and back reflectivities must be carefully chosen in order to yield identically shaped pulses in both arms of the FROG device, so that the usual pulse-retrieval algorithm will operate effectively, as it assumes that the shapes of the two pulses are identical (the pulse energies may, however, be different). Specifically, the ratio of the first and second pulse energies in each pulse train should be the same. It is easy to show (the proof is left to the student!) that this ratio will be the same for both arms as long as the front surface has a 50% reflectivity. Interestingly, the back-surface reflectivity cancels out of this result and hence is arbitrary! So we have chosen a back-surface reflectivity of about 10% for our experiments, yielding a second pulse with 5% of the energy of the first pulse, to minimize the additional pulses in the train and also to minimize the wasted energy in such pulses.

Note that, despite the weakness of the second pulse, the frequency fringes remain strong: their relative amplitude is given by the geometric mean of the first and second pulse energies, which is 45% in the above example. Finally, for these values of the reflectivities, the third pulse has an energy of 0.25% of the first pulse and hence is negligible (although it does introduce slight fringes in the outer islands, which can in fact be used to check the calibration or simply ignored with no adverse consequences).

This replacement also solves the direction-of-time ambiguity in SHG FROG. The second pulse is necessarily weaker than the first, so it is impossible to confuse the retrieved pulse with its weaker trailing pulse from its mirror image whose weaker pulse leads the stronger one. The use of an etalon to determine the direction of time has been implemented previously [2], but not with the etalon as beam splitter or in conjunction with an auto-calibration scheme.

POLKADOT FROG requires no change in the FROG pulse-retrieval algorithm. It only requires a somewhat larger delay scan range (to see the extra

islands) and slightly better spectral resolution (to resolve the spectral fringes). This increase in range/resolution is not significant, as it is not necessary to accurately acquire the details in the wings of the additional islands or in the spectral fringes, but instead only to find their separations.

For the purpose of automatic calibration, some simple code suffices to find the peaks in the trace. This code does not require the use of the entire FROG trace, and instead simply involves computing the frequency and delay marginals. It then uses a simple peak-finding routine to get an initial guess of the peak locations and then curve fits the marginals to a sum of Gaussians. The functional form of the equations is:

$$FIT = a + b\tau + c_{\text{back}} \exp \left[-\left(\frac{\tau - x_{\text{back}}}{w_{\text{back}}} \right)^2 \right] + \sum_{j=0}^n c_j \exp \left[-\left(\frac{\tau - x_j}{w_j} \right)^2 \right] \quad (11.1)$$

where $a + b\tau$ accounts for a constant background with perhaps some slope, c_j is the amplitude of a Gaussian peak, x_j is the center of the peak, and w_j is the width of a peak. Also included is a background Gaussian peak, with the c_{back} , x_{back} , and w_{back} parameters. This Gaussian takes into account possible pulse-shape variations and insufficient resolution. This is especially important for the frequency marginal, which has small peaks on top of a large peak. The important information in this equation is contained in the x_j parameters. These parameters define the centers of the peaks, and contain the information needed to calibrate the FROG trace. Of course, only one such peak is necessary in each direction, but two or even four or more yield statistical data, which can be fit for even better results.

Given the peak centers, it's a simple matter to calculate the calibrations of the FROG trace. The delay spacing, $d\tau$, is simply:

$$d\tau = \frac{\tau_{\text{sep}}}{S_\tau} \quad (11.2)$$

where τ_{sep} is the peak-to-peak separation in time, and S_τ is the peak-to-peak separation in pixels. The wavelength spacing, $d\lambda$, is slightly more complicated:

$$d\lambda = \frac{\lambda_0^2}{\tau_{\text{sep}} S_\lambda c} \quad (11.3)$$

where λ_0 is the center wavelength of the delay marginal, S_λ is the peak separation, and c is the speed of light. The S_λ used in these experiments is the average separation. For very broadband pulses, this is not an exact solution; the separation is constant in frequency, not wavelength. When the bandwidth is small, this effect is not significant. The center wavelength, λ_0 , must be determined by an independent method, although halving the fundamental's center wavelength is probably sufficient for most purposes.

We illustrate POLKADOT FROG using an SHG FROG device in which we replaced the usual beam splitter with a 26.8-μm etalon having a 50%

first surface reflectivity and a 10% second-surface reflectivity, as mentioned. The etalon was air spaced, and the two windows were each 5 mm thick. (It is interesting to note that the etalon beam splitter balances the dispersion of both arms. Since the reflective surface is at the center of the beam splitter, all pulses traverse the same amount of glass, and there is no need for a compensation plate in either arm.) This etalon yielded pulses separated by 179 fs. The etalon spacing is itself easily calibrated by measuring the spectrum of light transmitted through it and using the same formula as above for the fringe spacing. To measure this we used a commercial spectrophotometer, a Varian Cary 500 Scan, and fit the peaks using a simple LabVIEW code.

We used a distorted pulse whose FROG trace was obtained using POLKA-DOT FROG and is shown in Fig. 11.5. It clearly shows one pair of additional islands. The marginals for the FROG trace are also shown in Fig. 11.5. Fitting Eq. (11.1) to each set of marginals, we determined the peak locations. For both marginals, we obtained more than one set of additional peaks. Using a

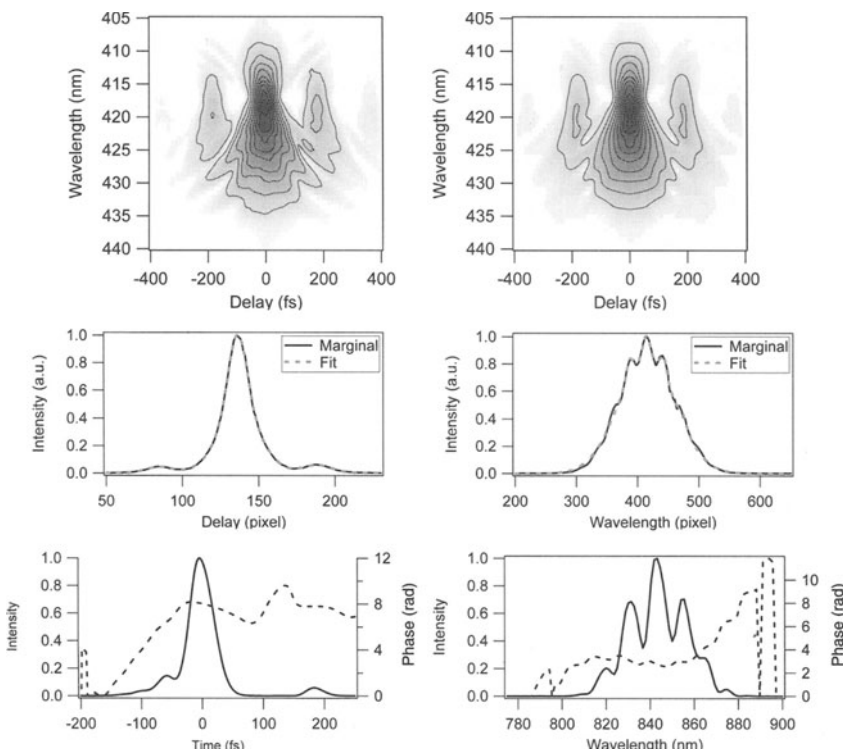


Fig. 11.5: Experimental and retrieved POLKADOT FROG traces (top row), delay and frequency marginals (second row), and retrieved pulse vs. time and frequency (bottom row). Note the POLKADOT satellite pulse at about 190 fs in the retrieved pulse intensity and the fringes in the retrieved spectrum.

simple linear fit, we determined the average spacing between the peaks. For the delay marginal, the spacing was 51.6 ± 0.2 pixels and for the frequency marginal the spacing was 28.9 ± 0.5 pixels. This yields a temporal calibration of 3.47 ± 0.01 fs/pixel and a frequency calibration of 0.106 ± 0.002 nm/pixel, using 405 nm as the center wavelength. Both axes were also calibrated through more traditional means. The delay calibration was read directly from the encoder on the translation stage. The step size was $0.518 \mu\text{m}$, which yields a temporal spacing of 3.46 fs/pixel. The spectrometer was calibrated using a Hg vapor lamp. By fitting several spectral lines, the spacing was found to be 0.1067 fs/pixel. The etalon calibration values are easily within experimental error of the independently determined values.

Now you might think that this trick might not work as well with a complex pulse. But that's not the case. We've also simulated the performance of POLKADOT FROG on a complex pulse with a Gaussian spectrum and spectral quadratic and cubic phase. In this case, the pulse has structure that could, in principle, confuse the fitting procedure. However, the FROG trace and the resulting marginals smooth out this structure, leaving only the desired structure. And POLKADOT worked well in this case, also.

It must be admitted that pathological cases in which the pulse is in fact a double pulse separated by approximately the etalon round-trip time could, perhaps, confuse this procedure. The solution to this problem is simply not to use such pathological pulses in the calibration stage.

The POLKADOT option can be used in all FROG variations. Also, it is easy to imagine many other methods for fitting the peaks. You could, for example, force the peaks to be equally spaced, thus allowing only one peak separation parameter. Alternatively, one could incorporate a multiple-pulse formula into the FROG algorithm.

POLKADOT FROG also simultaneously removes the direction-of-time ambiguity from an SHG FROG trace. Ordinarily, the retrieved pulse in an SHG FROG measurement would be ambiguous: both the pulse obtained by the algorithm and its mirror image yield the same FROG trace (that is, the measured one) and so it is not possible to determine which is correct. However, when dealing with such a double pulse created using an etalon, we know that the second pulse is much weaker than the first, and we know when it occurs. In the pulse shown in Fig. 11.5, the secondary pulse must occur at, and is clearly evident at, about +180 fs, and hence is easily identified as the second pulse in the train. Thus, the POLKADOT FROG geometry also eliminates the direction-of-time ambiguity in SHG FROG.

It should also be mentioned that, if the pulse has a symmetrical intensity, the pulse and its satellite should overlap somewhat, or an obscure ambiguity (in SHG FROG only) in which only the phase is time-reversed, could defeat this technique.

Finally, when we measure a pulse, we wish to obtain that pulse, not a version of it with a weak second pulse trailing behind it. Fortunately, removal of the second pulse is amazingly easy. Note that, more precisely, an infinite train

of additional pulses follows behind the first pulse, each delayed by τ_{sep} and reduced by a factor of, say, ε . Thus POLKADOT FROG yields a measured field, $E_{\text{meas}}(t)$, with additional delayed replicas of the pulse field:

$$E_{\text{meas}}(t) = E(t) + \varepsilon E(t - \tau_{\text{sep}}) + \varepsilon^2 E(t - 2\tau_{\text{sep}}) + \dots \quad (11.4)$$

where $E(t)$ is the actual pulse, which we desire. To obtain $E(t)$, it is simply necessary to subtract off the measured field reduced in magnitude by ε and displaced by τ_{sep} : that is, by subtracting off the quantity: $\varepsilon E_{\text{meas}}(t - \tau_{\text{sep}})$. This yields a new quantity:

$$E'_{\text{meas}}(t) = E_{\text{meas}}(t) - \varepsilon E_{\text{meas}}(t - \tau_{\text{sep}}) \quad (11.5)$$

Substitution of $E_{\text{meas}}(t)$ into this expression, followed by some simple arithmetic yields:

$$E'_{\text{meas}}(t) = E(t) \quad (11.6)$$

Thus it is trivial to obtain $E(t)$ from the measured field. The pulse shown in Fig. 11.6 is the pulse from Fig. 11.5 with this simple procedure applied and shows remarkably good removal of the secondary pulse.

Interestingly, it's possible to set up a version of this technique in which you can simply convert from standard FROG to POLKADOT FROG. It involves using an etalon at Brewster's angle with no coating on the second surface. As a result, the back surface will have a reflectivity of about 10% for the s-polarization and 0% for the p-polarization. The etalon should also be designed to have a 50% reflectivity for the s-polarization, and any reflectivity between about 25% and 75% for the p-polarization. As a result, an input pulse with s-polarization will be transformed to a train of pulses and hence will experience the POLKADOT effect, while a pulse with p-polarization will not and hence will experience a standard FROG measurement. Since it's easy to rotate the polarization of a pulse before the FROG device (with a half-wave plate), this POLKADOT arrangement could be very convenient.

Finally, a minor practical issue: Of course, the relatively thick (off-the-shelf) optical elements of the etalon used in the above demonstration distorted

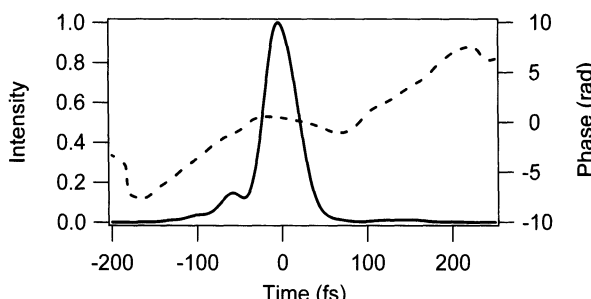


Fig. 11.6: Retrieved experimental pulse, after subtraction of the satellites.

our pulse and would seriously distort extremely short pulses. Obviously, the thinner the elements used the less distortion will be present, and it is possible to construct etalons from such elements. For extremely short pulses, one could use an ultra-thin piece of glass as the etalon.

References

1. Zeek, E., et al., *Simultaneous Automatic Calibration and Direction-of-Time Removal in Frequency-Resolved Optical Gating*. *Appl. Phys. B*, in press. 2002.
2. Taft, G., et al., *Measurement of 10-fs Laser Pulses*. Selected Topics in Quantum Electronics, 1996. **2**, Special Issue on Ultrafast Phenomena(3): p. 575–585.

12. Very Simple FROG Apparatus: GRENOUILLE

Rick Trebino, Patrick O'Shea, Mark Kimmel, and Xun Gu

Complexity in Pulse Measurement

The first goal in developing a measurement technique is to make it work. Once that's done, the next step is to make it simple.

The FROG apparatus comprises an autocorrelation followed by a spectrometer. Unfortunately, autocorrelation is actually a fairly *difficult* measurement to make. It requires splitting the pulse into two replicas and then focusing and recombining them in, for example, an SHG crystal. This involves overlapping them in both space and time, that is, carefully aligning three sensitive degrees of freedom (two spatial and one temporal). It is also necessary to maintain this alignment while scanning the delay. Worse, the phase-matching-bandwidth condition mandates a thin SHG crystal, yielding a very weak signal and poor measurement sensitivity. This latter problem compounds alignment difficulties. As a result, an autocorrelator is a time-consuming and high-maintenance undertaking; it requires significant table space; and commercial devices cost $\sim \$15,000$ or more.

In the past decade, the development of FROG has yielded much more information than has been available from autocorrelators, in particular, the full intensity and phase of the pulse vs. time and frequency.

But simplicity has never been the goal.

Indeed, FROG adds a spectrometer to an autocorrelator. A simple grating-lens home-made spectrometer that introduces no additional sensitive alignment degrees of freedom can be appended to an autocorrelator to make an excellent FROG (See Chapter 11), but FROG still inherits the autocorrelator's complexity, size, cost, maintenance, and alignment issues. An alternative or two to FROG have recently been introduced, but they are, unfortunately, considerably more complex. They involve two beams propagating collinearly with a precisely given delay, which by itself introduces no less than *five* sensitive alignment degrees of freedom (four spatial and one temporal). Furthermore, alternative devices contain numerous additional components, such as frequency filters, additional dispersive or non-dispersive delay lines, and even interferometers within interferometers(!), yielding as many as a dozen or more sensitive alignment degrees of freedom and increasing significantly the complexity, size, cost, maintenance, and potential for systematic error. And they lack much-needed feedback as to measurement accuracy.

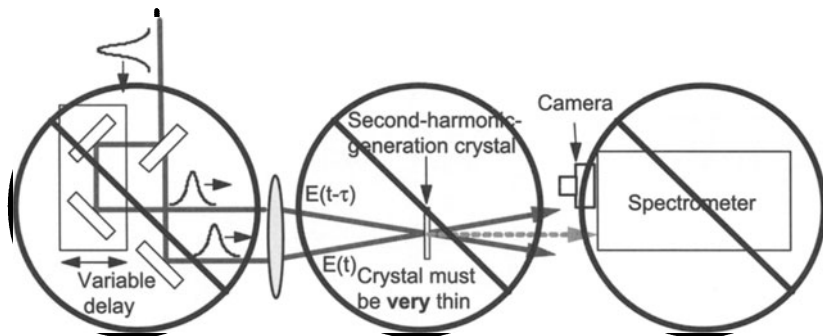


Fig. 12.1: SHG FROG device. While SHG FROG is the simplest intensity-and-phase ultra-short-pulse-measurement device, there are a few components of it that we'd like to eliminate to simplify its operation if we could.

Simplifying FROG measurements

Figure 12.1 shows an SHG FROG device and some of its components that we might like to remove in order to simplify it.

Okay, if we removed all these components, there'd be nothing left! But, surprisingly, we can almost accomplish this feat [2]!

It works like this (see Figs. 12.2 and 12.3). We first replace the beam splitter, delay line, *and* beam combining optics with a *single* simple element, a Fresnel biprism [3], which accomplishes all these tasks by itself. Second, in seemingly blatant violation of the phase-matching-bandwidth requirement, we replace the thin SHG crystal with a *thick* SHG crystal, which not only gives considerably more signal (signal strength scales as the approximate square of the thickness), but also simultaneously replaces the spectrometer! The resulting device, like its other relatives in the FROG family of techniques, has a frivolous name: GRating-Eliminated No-nonsense Observation of Ultrafast Incident Laser Light E-fields (GRENOUILLE, which is the French word for “frog”).

GRENOUILLE

How does it work? Let's consider the Fresnel biprism [3] first. It's a prism with an apex angle close to 180° and is a device usually used in classrooms to illustrate interference (I learned about it when I began teaching and actually had to read the textbook for the undergraduate optics class...). When a Fresnel biprism is illuminated with a wide beam, it splits the beam into two beamlets and crosses them at an angle, making intensity fringes (although we don't care about the fringes here). Crossing beamlets at an angle is also exactly what is required in conventional single-shot autocorrelator and FROG beam geometries (see the section on single-shot FROG in Chapter 7), in which the relative beam delay is mapped onto horizontal position at the crystal.

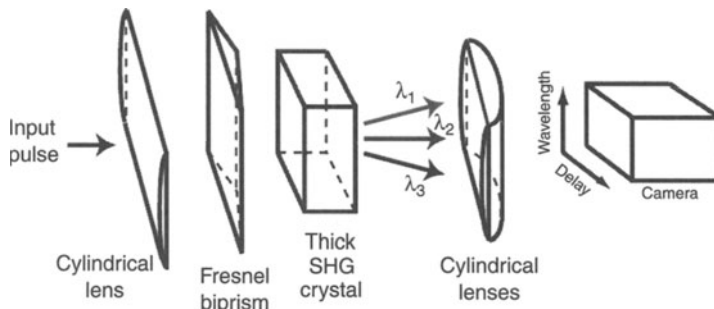


Fig. 12.2: GRENOUILLE uses a Fresnel biprism to replace the beam splitter, delay line, and beam-recombinining optics. It maps delay to position at the crystal. GRENOUILLE also utilizes a thick SHG crystal acting as both the nonlinear-optical time-gating element and the spectrometer. A complete single-shot SHG FROG trace results. Most importantly, however, GRENOUILLE has zero sensitive alignment parameters.

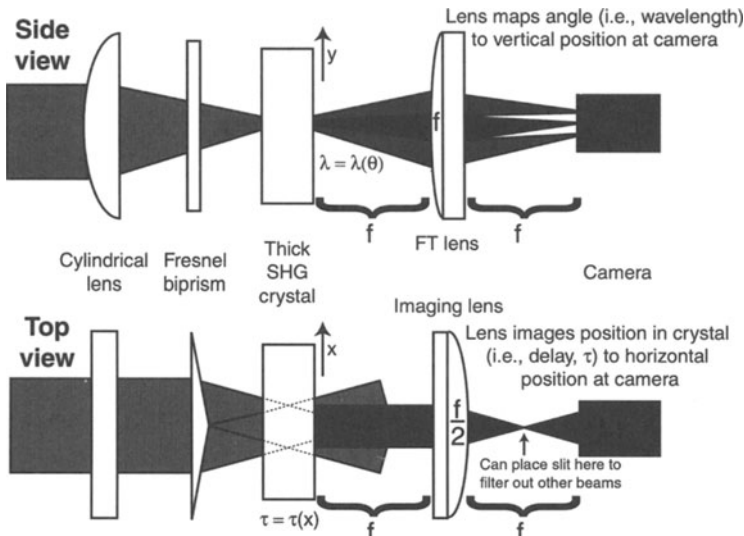


Fig. 12.3: Side and top views of the GRENOUILLE beam geometry of Fig. 12.2. Here, convenient focal lengths are shown for the two final cylindrical lenses (f and $f/2$). Note that the beam becomes a vertical line just before the camera, a convenient place for a slit to filter out any extraneous beams, ensuring good signal-to-noise ratio.

But, unlike conventional single-shot geometries, beams that are split and crossed by a Fresnel biprism are *automatically aligned* in space and in time, a significant simplification! Then, as in standard single-shot geometries, the crystal is imaged onto a camera, where the signal is detected vs. position (i.e., delay) in, say, the horizontal direction.

FROG also involves spectrally resolving a pulse that has been time-gated by itself. GRENOUILLE combines both of these operations in a single *thick* SHG crystal. As usual, the SHG crystal performs the self-gating process: the two pulses cross in the crystal with variable delay. But, in addition, the thick crystal has a relatively small phase-matching bandwidth, so the phase-matched wavelength produced by it varies with angle (see Fig. 12.4). Thus, the thick crystal also acts as a *spectrometer*. The ability of a thick nonlinear-optical medium to act as a low-resolution spectrometer was realized many years ago [4,5], but pulses then were longer and more narrowband, so its rediscovery for use in pulse measurement had to wait until pulse bandwidths increased and pulse lengths significantly decreased.

Two additional cylindrical lenses complete the device. The first cylindrical lens must focus the beam into the thick crystal tightly enough to yield a range of crystal incidence (and hence exit) angles large enough to include the entire spectrum of the pulse. After the crystal, a cylindrical lens then maps the crystal exit angle onto position at the camera, with wavelength a near-linear function of (vertical) position.

GRENOMUILLE has many advantages. It has few elements and so is inexpensive and compact. It operates single-shot. And it is considerably more sensitive than other pulse-measurement devices. Furthermore, since GRENOMUILLE produces (in real-time, directly on a camera) traces identical to those of SHG FROG, it yields the full pulse intensity and phase (except the direction of time). In addition, several feedback mechanisms on the measurement accuracy that are already present in the FROG technique work with

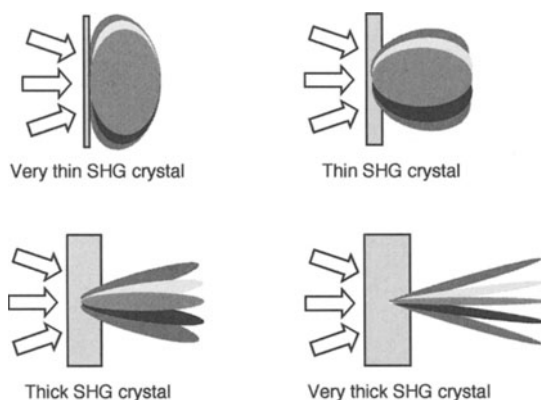


Fig. 12.4: Thin and thick SHG crystals illuminated by converging broadband light and polar plots of the generated colors vs. crystal exit angle. Different shades of gray indicate different colors. Note that the very thin crystal (ordinarily required in pulse-measurement techniques) generates the second harmonic of all colors in the forward direction. The very thick crystal, on the other hand, does not and, in fact, acts like a spectrometer. Note also that the thick crystal generates considerably more SH in the relevant directions.

GRENOMUILLE, allowing confirmation of—and confidence in—the measurement. But best of all, GRENOMUILLE is extremely simple to set up and align: it involves no beam-splitting, no beam-recombing, and no scanning of the delay, and so has *zero* sensitive alignment degrees of freedom!

The use of a thick crystal as a frequency filter in SHG FROG was simultaneously demonstrated by O’Shea, Kimmel, Gu, and Trebino [2] and by Radzewicz, Wasylczyk, and Krasinski [6].

Theory of GRENOMUILLE

The key issue in GRENOMUILLE is the crystal thickness. Ordinarily, achieving sufficient phase-matching bandwidth requires *minimizing* the group-velocity mismatch, GVM: the fundamental and the second harmonic must overlap for the entire SHG crystal length, L . If τ_p is the pulse length, $\text{GVM} \equiv 1/v_g(\lambda_0/2) - 1/v_g(\lambda_0)$, $v_g(\lambda)$ is the group velocity at wavelength λ , and λ_0 is the fundamental wavelength, this condition is: $\text{GVM} \cdot L \ll \tau_p$.

In GRENOMUILLE, however, the opposite is true; to resolve the spectrum, the phase-matching bandwidth must be *much less than* that of the pulse:

$$\text{GVM} \cdot L \gg \tau_p \quad (12.1)$$

which ensures that the fundamental and the second harmonic *cease* to overlap well before exiting the crystal, which then acts as a frequency filter. Interestingly, in contrast to all other pulse-measurement devices, GRENOMUILLE operates best with a highly dispersive crystal.

On the other hand, the crystal must not be too thick, or group-velocity dispersion (GVD) will cause the pulse to spread in time, distorting it:

$$\text{GVD} \cdot L \ll \tau_c \quad (12.2)$$

where $\text{GVD} \equiv 1/v_g(\lambda_0 - \delta\lambda/2) - 1/v_g(\lambda_0 + \delta\lambda/2)$, $\delta\lambda$ is the pulse bandwidth, and τ_c is the pulse coherence time (\sim the reciprocal bandwidth, $1/\Delta\nu$), a measure of the smallest temporal feature of the pulse. Since $\text{GVD} < \text{GVM}$, this condition is ordinarily already satisfied by the usual GVM condition. But here it is not necessarily satisfied, so it must be considered.

Combining these two constraints, we have:

$$\text{GVD}(\tau_p/\tau_c) \ll \tau_p/L \ll \text{GVM} \quad (12.3)$$

There exists a crystal length L that satisfies these conditions simultaneously if:

$\text{GVM}/\text{GVD} \gg \text{TBP}$

(12.4)

where the time-bandwidth product (TBP) of the pulse is τ_p/τ_c . Equation (12.4) is the *fundamental equation of GRENOMUILLE*, and it’s easy to remember because it’s somewhat poetic.

For a near-transform-limited pulse ($TBP \sim 1$), this condition is easily met because $GVM \gg GVD$ for all but near-single-cycle pulses. Consider typical near-transform-limited Ti:Sapphire oscillator pulses of $\sim 100\text{-fs}$ duration, where $\lambda_0 \sim 800\text{-nm}$, and $\delta\lambda \sim 10\text{-nm}$. Also, consider a 5-mm BBO crystal—about 30 times thicker than is ordinarily appropriate. In this case, Eq. (12.3) is satisfied: $20\text{ fs/cm} \ll 100\text{ fs}/0.5\text{ cm} = 200\text{ fs/cm} \ll 2000\text{ fs/cm}$. Note that, for GVD considerations, shorter pulses require a thinner, less dispersive crystal, but shorter pulses also generally have broader spectra, so the same crystal will provide sufficient spectral resolution. For a given crystal, simply focusing near its front face yields an effectively shorter crystal, allowing a change of lens or a more expanded beam to “tune” the device for shorter, broader-band pulses. Less dispersive crystals, such as KDP, minimize GVD, providing enough temporal resolution to accurately measure pulses as short as 50 fs. Conversely, more dispersive crystals, such as LiIO_3 , maximize GVM, allowing for sufficient spectral resolution to measure pulses as narrowband as 4.5 nm ($\sim 200\text{-fs}$ transform-limited pulse length at 800 nm). Still longer or shorter pulses will also be measurable, but with less accuracy (although the FROG algorithm can incorporate these effects and extend GRENOUILLE’s range). Note that geometrical temporal-blurring effects (see Chapter 7) aren’t found in GRENOUILLE because it is a single-shot SHG FROG method.

Measurements using GRENOUILLE

Typical GRENOUILLE parameters are a beam expanded to $w = 11\text{ mm}$, focused into a 5-mm-thick BBO crystal using a 200-mm focal-length cylindrical lens. The effective confocal parameter of $\sim 2\text{-mm}$ results in a $\sim 2.8\text{-nm}$ (FWHM) phase-matching bandwidth at a given angle (potentially insufficient spectral resolution can be deconvolved easily) and a spectral range of 50 nm across the range of exit angles. Other components include a Fresnel biprism with an apex angle of 168° and 100-mm and 50-mm focal-length cylindrical lenses—the precise extremely simple geometry of Fig. 12.1. A Sony XC-77 CCD camera and a Spiricon LBA PC-100 capture-card record traces. We obtained the calibrations using the POLKADOT technique (see Chapter 11). A nearly perfectly linear 5.1 nm/mm calibration resulted.

Using GRENOUILLE, we measured a simple chirped pulse and compared the measured GRENOUILLE trace with that of a calibrated multi-shot FROG. Femtosoft Technologies’ FROG code retrieved both pulses. Figure 12.5 (a-f) shows these measurements and the good agreement obtained. All traces were 128 by 128 pixels, and the FROG errors were 0.010 and 0.009 for the GRENOUILLE and FROG measurements respectively. The GRENOUILLE signal strength was ~ 1000 times greater than that of a single-shot FROG and also much greater than that of an equivalent autocorrelator.

Figure 12.5 also shows measured traces of a “double-chirped pulse:” two strongly chirped pulses separated by about one pulse width. With structure in

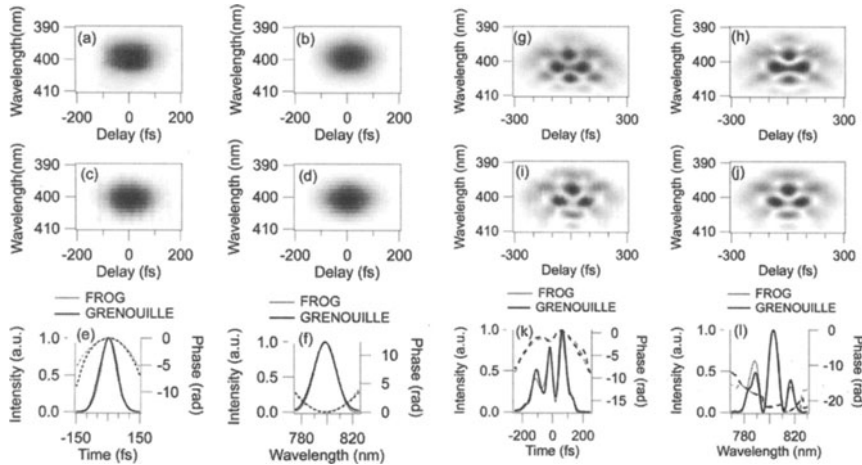


Fig. 12.5: Comparison between GRENOUILLE and (multi-shot) FROG measurements of test pulses. (a), (b): measured and retrieved GRENOUILLE traces, respectively, for a linearly chirped pulse; (c), (d): measured and retrieved FROG traces for the same linearly chirped pulse; (e), (f): retrieved intensities (solid lines) and phases (dashed lines) for the time and frequency domains, respectively; (g)–(l): same as (a)–(f), but for a much more complicated pulse consisting of two highly chirped pulses separated by one pulse width.

both delay and frequency, it puts GRENOUILLE to the test; if the GVM is too small, frequency resolution will be inadequate; if the GVD is too large, the pulse will spread, and the temporal structure will be lost. Furthermore, if the depth of field of the imaging optics is less than the crystal width, trace structure will also wash out. Fig. 12.5 (g–l) shows that GRENOUILLE accurately retrieves the intensity and phase of this complicated pulse. The FROG errors for the 128×128 traces were 0.031 and 0.013 for the GRENOUILLE and FROG measurements, respectively.

Other issues in GRENOUILLE: As with other single-shot techniques, a clean beam profile with minimal spatial chirp is required. Extremely short pulses will lengthen in the biprism and first lens, but simple theoretical back-propagation of the pulse through these elements remedies this. Alternately, an all-reflective GRENOUILLE can be built, using a “Fresnel bi-mirror.”

Thus GRENOUILLE combines full-information pulse measurement with much-needed experimental simplicity. Only a few simple optical elements are required, and no sensitive alignment is required. It is also extremely compact and more sensitive than other pulse diagnostics, including even those that don’t yield the full intensity and phase. Variations under consideration promise to increase its sensitivity even more. While its range of applicability is a bit limited at present (40 to 300 fs if high accuracy is required), measurements outside this range that require less accuracy are possible, and future work incorporating GVD and GVM in the FROG algorithm (see Chapter 18 for the approach)

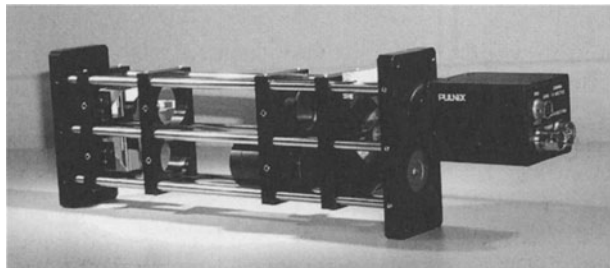


Fig. 12.6: Commercial GRENOUILLE without its cover. The entire device is $37 \times 7 \times 5$ cm, weighs less than 2 kg, and measures the beam spatial profile, too. Except for crystal-angle adjustment for the relevant wavelength, the device has no knobs. And two 45° mirrors can be switched into the beam to bypass the GRENOUILLE, allowing the beam to propagate directly into the camera for spatial-profile measurement.

should extend this range considerably. In the meantime, GRENOUILLE's operating range nicely matches that of most ultrafast Ti:Sapphire lasers and amplifiers, and it proves ideal for everyday diagnostics. And it is available commercially and inexpensively from Swamp Optics (see Fig. 12.6).

References

1. R. Trebino, K. W. DeLong, D. N. Fittinghoff, J. N. Sweetser, M. A. Krumbügel, and D. J. Kane, Rev. Sci. Instrum., **68**, 3277–3295 (1997).
2. P. O’Shea, M. Kimmel, X. Gu, and R. Trebino, Opt. Lett., **26**, 932 (2001).
3. E. Hecht, in *Optics*, 3rd edition (Addison Wesley, Reading, Massachusetts), 391 (1998).
4. A. G. Akmanov, A. I. Kovrigin, N. K. Podolskaya, Radio Engineering and Electron Physics, **14**, 1315 (1969).
5. D. H. Auston, Opt. Commun., **3**, 272, (1971).
6. C. Radzewicz, P. Wasylczyk, J. S. Krasinski, Opt. Commun. **76**, 329–333 (2000).

13. Ultraviolet and High-Power Pulse Measurement

Sterling Backus and Charles Durfee

The Issues in UV and High-power Pulse Measurement

So far, we've discussed the general ideas behind FROG and an array of tricks for simplifying FROG measurements. And because nearly every ultrafast lab's workhorse laser is an infrared low-power Ti : Sapphire oscillator, our discussion revolved around SHG FROG, which is ideal for measuring such pulses. Consequently, in this chapter, we consider quite different problems: the measurement of ultraviolet and high-power pulses. These are interesting—and important—problems that are often neglected in discussions of measurement techniques.

Indeed, many researchers believe it's not possible to measure UV pulses because SHG crystals don't exist in this wavelength range. While such crystals don't, in fact, currently exist, *third-order* FROG methods work beautifully in the UV, where third-order nonlinearities yield signal pulses at the same wavelength as the input pulse. Also, third-order nonlinearities are stronger in the UV, so even relatively weak pulses are measurable.

On the other hand, many researchers believe that high-power pulse measurement is trivial; after all, there's plenty of intensity—which means that any nonlinearity will yield plenty of signal—so what's the problem? The problem is that high-power pulses have their own unique problems that seriously complicate their measurement. For a variety of reasons, not the least of which is the high complexity of amplifier systems that produce them, they tend to have poor spatial quality. Worse, they suffer from *spatio-temporal distortions*, such as spatial chirp, in which the intensity and phase vary from point to point across the beam. Such distortions violate the assumption made by essentially all pulse measurement techniques that the intensity and phase vs. time are the same throughout the beam. We'll discuss measuring the intensity and phase vs. time *and space* later, but for now, we'll see that FROG's ability to check the accuracy of a measurement will be crucial for such measurements. And to further complicate the problem of measuring high-power pulses, their temporal distortions can also be quite severe. And at the same time, our standards for them can be higher. For example, they can have satellite pulses several orders of magnitude less intense. Weaker satellites would be of no significance in low-power pulses, but, in high-power pulses, they can be intense enough to do some damage, so we really need to know about them. Finally, high-power pulses also tend to have significant fluctuations from shot to shot, necessitating single-shot methods. Interestingly, third-order FROG methods

will also turn out to be ideal for high-power measurements (although SHG FROG works well, too).

UV Pulse Measurement

Ultrashort-pulse light sources in the ultraviolet (UV) [1–5] have many applications, including time-resolved studies of atoms, molecules, solids, and biological systems [6,7]. Their generation typically involves frequency-up-conversion from wavelengths near 800 nm, where generation, amplification, and compression techniques are well established [8–12]. While frequency conversion into the UV using nonlinear crystals experiences difficulties due to severe group velocity walk-off and poor phase-matching bandwidths [1], gaseous media circumvent these problems. In either case, however, temporal distortions in the resulting pulses are common, and informative pulse-measurement techniques are essential, both for understanding the generation process and for using the resulting pulses in any application.

Using a simple focused-beam gas-phase geometry, Backus, et al. have generated 16-fs, 1- μ J pulses by frequency-tripling 1-mJ, 22-fs pulses at 800 nm [2]. In more recent work, Durfee and coworkers [3] demonstrated very efficient generation of UV through optical parametric amplification of pulses confined in gas-filled capillary wave-guides. Phase-matching was obtained by tuning the gas pressure to achieve a balance between the gas and modal dispersion of the waveguide. The difference-frequency-mixing process ($3\omega = 2 \times 2\omega - \omega$) produced a single-spatial-mode beam with a conversion efficiency $> 40\%$. In addition to this nonlinear process, other simultaneously occurring desirable nonlinear-optical processes—self- and cross-phase modulation—can broaden the UV output spectrum [3,13], yielding nearly transform-limited 8-fs pulses at 270 nm after compression [14].

How were UV pulses measured in the past? Before Ti:Sapphire, excimer lasers were the rule, emitting subpicosecond UV pulses, which were auto-correlated using such nonlinear processes as two-photon absorption or two-photon fluorescence. Nishioka, et al. employed two-photon absorption in water, using the photo-acoustic effect to detect the signal. Their detector had spatial resolution, allowing a single-shot autocorrelation measurement [15]. Two-photon absorption in semiconductors [16] and two- and three-photon fluorescence have also been used. More recently, two-photon conductivity has been used for autocorrelation of UV pulses [17]. An advantage of these methods is that a two-photon-absorption process is often present as part of an experiment, and measurement of the autocorrelation in this way allows for an *in situ* check of the pulse duration. However, these two-photon processes must be examined carefully to ensure that the spectral response is sufficiently wide and flat to avoid distortion of the autocorrelation trace, especially for short pulse-width, wide-bandwidth pulses. The dependence of the signal strength on the incident intensity also has to be examined to ensure that the power-dependence of the response is constant over the intensity range of the test.

These problems are compounded by the fact that autocorrelation lacks sufficient independent checks to be sure that a measurement is in fact correct. And it cannot be corrected when these problems occur. Worse, the high dispersion of materials in the UV means that the measurement device can itself introduce potentially severe pulse distortions. And, as we've seen, even when it's correct, an autocorrelation measurement barely yields the pulse length, never mind the intensity structure and the phase.

Clearly, FROG is in order. Full characterization of short-wavelength pulses using FROG simply requires spectrally resolving a nonlinear signal. Unfortunately, the above processes can't be spectrally resolved. Thus the challenge will be to find an appropriate nonlinear-optical process.

Pushing SHG to its Limits

Of course, second-harmonic generation, which can be spectrally resolved, is not an option, as it's limited to wavelengths above 410 nm. Nevertheless, let's consider the limits of SHG, in case you have a borderline situation, such as a blue pulse, which can, in fact, be measured using SHG. Several problems begin to occur, however, at these wavelengths:

- 1) The SHG crystal may not be able to phase-match the relevant SHG process. The shortest wavelengths that can be phase-matched for type-I SHG in KDP and BBO are 532 nm and 410 nm, respectively. While new UV SHG crystals are under development, fs pulses with wavelengths below 410 nm must currently be measured using a nonlinearity other than SHG in a crystal.
- 2) If phase-matching is possible, the phase-matching *bandwidth* may be inadequate. Figure 13.1a shows the phase-matching bandwidth for an input pulse at a wavelength of 410 nm using a 10- μm -thick BBO crystal. Without compensation for the limited phase-matching bandwidth (19 nm FWHM),

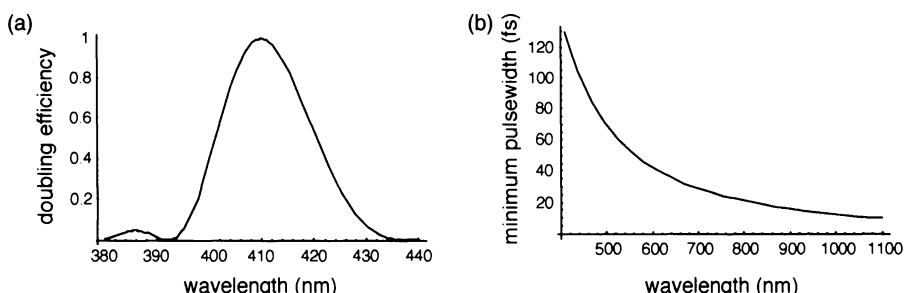


Fig. 13.1: (a) Efficiency envelope for frequency doubling a pulse in 100 μm BBO at the phase-matching angle appropriate for 410 nm. The FWHM of the curve corresponds to a bandwidth of 14 fs. (b) Minimum pulse duration that can be frequency-doubled with a 100- μm -thick type-I BBO crystal.

the shortest pulse that could be characterized is on the order of 13 fs [18]. Figure 13.1b shows the minimum pulse duration that can be measured in a 100- μm BBO crystal as a function of fundamental wavelength. Note that, while fairly short pulses can be measured in the IR, dispersion limits a 100- μm BBO crystal to the measurement of blue pulses longer than 100 fs.

- 3) The crystal may absorb the VUV second harmonic. BBO begins to absorb heavily at 190 nm. Surface SHG [19] is an option because its effective interaction length is less than a wavelength (so phase-matching is irrelevant), and the signal does not propagate through the crystal. However, if the fundamental wavelength of the pulse to be measured is below \sim 380 nm, the SH signal is in the vacuum UV, where it's absorbed by oxygen. The device, including the spectrometer, must therefore either be purged with another gas or evacuated. It's not called the *vacuum* UV for nothing!
- 4) A VUV detector is required.

It's clearly much more convenient to operate with a signal that does not require vacuum or special detectors. If another—not necessarily shorter—pulse is available, such as the 800-nm pulse used to create the UV pulse, the $\chi^{(2)}$ nonlinearity can then be used in a *down-conversion* process to generate a signal pulse in the visible or IR. Spectral resolution of this signal then allows the retrieval of the intensity and phase (see Chapter 16). This method works well if one pulse is known. If not, it's still in principle possible to retrieve the intensity and phase of *both* pulses, but the details of FROG methods for measuring two unknown pulses simultaneously are just now being developed (see Chapter 20).

Third-order FROG Methods for UV Measurements

Given sufficient pulse energy, the best option for FROG measurements of ultraviolet pulses, however, is the $\chi^{(3)}$ nonlinearity. The aforementioned non-spectrally-resolvable effects, two-photon absorption and two-photon fluorescence, are $\chi^{(3)}$ effects. But third-order autocorrelations have been also been generated using induced-grating four-wave-mixing effects, which do produce a spectrally resolvable signal beam. In these third-order methods (with the exception of THG, which, after all we've just said, we'd have to be crazy to try here!), the signal beam has the same wavelength as the input pulse ($\omega_{\text{sig}} = \omega - \omega + \omega$). Another advantage of third-order FROG methods is the ambiguity-free determination of the pulse. Also, the resulting FROG traces are much more intuitive: for example, the sign and approximate magnitude of any chirp can be directly inferred from the FROG trace without inversion. Thus, third-order wave-mixing-type FROG methods are the best options for UV pulse measurement.

There are several such third-order options: polarization-gate (PG), self-diffraction (SD), and transient-grating (TG) FROG. While we've discussed

these geometries in earlier chapters, it's useful to review them in the context of measurements in the ultraviolet.

First, let's consider PG FROG. In this geometry, two replicas of a pulse cross in a thin nonlinear medium (e.g., fused silica or sapphire). Both pulses are linearly polarized, but one polarization is rotated 45° with respect to the other (see Fig. 6.3). To preserve polarization purity, this can be accomplished by a polarization-rotating out-of-plane path (see Fig. 7.3) [20]. The latter beam serves as the gate: a part of the probe beam experiences a rotation of polarization that's detected by transmission through a polarizer that's crossed relative to the input. The background signal is determined by the contrast-ratio of the polarizer and the purity of polarization of the input. An input polarizer can be used to ensure that the input polarization is sufficiently pure, minimizing the background in the FROG trace. The principal disadvantage in PG FROG for UV use is the added dispersion introduced by this polarizer. In principle, this polarizer could be eliminated if the harmonic process generating the UV light resulted in a pure linear polarization. High-contrast, low-dispersion thin-film polarizers have been used at 800 nm, but these are costly and not readily available for UV wavelengths. Like other FROG geometries, the PG geometry can be used in single-shot mode by using a cylindrical optic to focus the beams in one direction and crossing them in the other direction. As in all single-shot geometries, care must be taken that the portions of the beam that form the interaction must have a smooth and flat intensity profile.

SD FROG is experimentally the simplest geometry of the three. Here, two beams are simply focused and crossed in a thin material (see Fig. 6.5). The intensity fringes that result from the interference between the crossed beams induce a refractive index grating owing to the nonlinear refractive index in the material. Light from the pulses diffracts from this grating, and the first-order diffraction is used as the signal. Note that it's irrelevant which pulse acts as the probe. Since the signal propagates in a different direction from the input beams, the main source of background is scattered light from the nonlinear medium, which can be reduced by aperturing the signal beam well. The SD geometry has also been implemented in single-shot mode [21]. The principle disadvantage of the SD geometry is that it's not actually phase-matched. The phase-mismatch can be reduced to acceptable levels by using a small crossing angle and a thin nonlinear medium. We'll discuss this issue in more detail below.

A third variation, TG FROG [22], can achieve good phase-matching and good signal separation simultaneously. TG requires three input beams, which all cross at their focus in the nonlinear medium. The three beams are arranged so that on a card they appear to be on three corners of a square. As in self-diffraction, two beams form an index grating in the nonlinear medium, and the third beam probes it. The diffracted signal beam appears after the nonlinear medium in the position of the missing corner of the square (open circle in Fig. 13.2). Aligned correctly, the phase-mismatch is zero, independent of the input wavelength. As a result, a thicker medium can be used than in SD

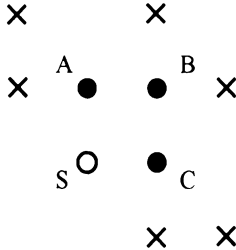


Fig. 13.2: Location of the input beams and signal beams for transient grating FROG. Filled circles are the input beams, the open circle is the TG signal beam, X's mark the location of the first-order SD signals.

FROG. This results in a stronger signal than in SD. Interestingly, in the TG setup, first-order SD signals appear (in the position of the X's in Fig. 13.2), and experimentally are seen to be much weaker. In general, the TG geometry is much more sensitive than the SD geometry [23]. The disadvantage of TG is the alignment of the additional beam. While TG-FROG has been used principally for near-IR pulses [10,22,24], it has also been used to characterize 400 nm second-harmonic pulses from an amplified Ti : Sapphire system.

To understand the differences between the geometries, let us consider the phase-matching issues. Fig. 13.3 shows the k -vectors for the three geometries. PG (Fig 13.3a) is perfectly phase-matched: the k -vectors form the sides of a parallelogram. The gate k -vectors are on opposite sides of the parallelogram. One of the gate arrows is reversed because one of the factors of the gate E-field in the FROG signal is complex-conjugated: $E^*(t) E(t)$. Even if the probe and gate pulses are at different wavelengths (Fig. 13.3b), the PG process remains phase-matched.

In contrast, self-diffraction is inherently non-phase-matched. The phase-mismatch is given by $\Delta kL = 2kLn(1 - \cos\theta_{int}) \approx kL\theta^2/n$, where L and n are the length and the refractive index of the material, and θ_{int} is the full *internal* crossing angle and θ is the full external crossing angle (see Fig. 13.3c). While phase-mismatch reduces the signal strength, by itself, it's not intrinsically a problem; it is the *variation* of phase-matching efficiency across the bandwidth that can distort the signal. The phase-matching efficiency varies (see Chapter 3) as $\text{sinc}^2(\Delta kL/2)$, which is proportional to θ^4 for small angles. Thus, achieving a small ΔkL requires a small crossing angle and a thin medium (small L), the latter of which reduces the signal strength. Both of these requirements hurt the signal-to-noise ratio because, experimentally, the small crossing angle tends to increase the background level because the beams are closer together.

The phase-matching diagram for transient-grating FROG is similar to that for polarization-gate FROG. For TG, however, the parallelogram is bent out-of-plane as shown schematically in Fig. 13.3d. The correspondence between the k -vectors in the diagram and the input beams in Fig. 13.2 are indicated

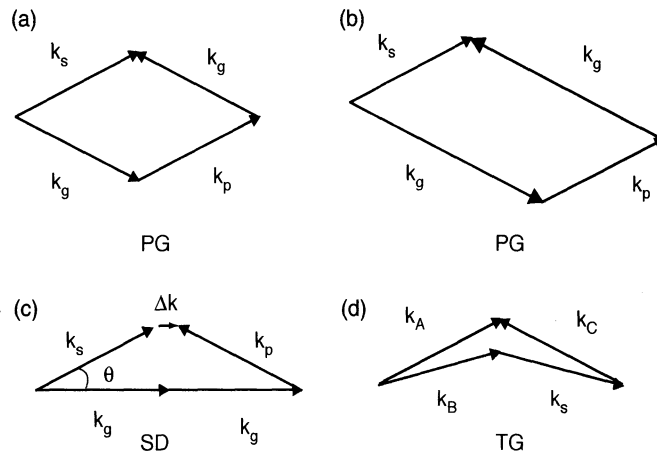


Fig. 13.3: k -vector diagrams for the three third-order FROG geometries. (a) Polarization-gate; (b) polarization-gate with different gate and probe wavelengths; (c) self-diffraction; (d) transient-grating (perspective intended to show the parallelogram as in PG is bent out-of-plane). The subscripts for the k -vectors in (d) correspond to the beam positions shown in Fig. 13.2. In this figure, the signal k -vector is given by k_s .

by the labels. If beam B is delayed, the nonlinearity acts as $E^2(t)$, i.e. like self-diffraction. Delaying beams A or C yields a nonlinearity $E^*(t)E(t)$, as in the polarization-gate geometry. In the transient-grating geometry, as in the PG geometry, all k -vectors line up, and the process is phase-matched independent of the input wavelength. Unlike PG, however, if, for some value of the delay, the three pulses aren't at the same wavelength (as would be found for strongly chirped pulses and a large delay), there is a small phase-mismatch that increases with crossing angle and medium thickness. Another reason to use a thin substrate is to minimize dispersive broadening of the pulses within the interaction region.

There are several convenient optical layouts for SD and TG FROG devices (see Fig. 13.4). The distinguishing features are the methods for splitting and recombining the beam and the number of reflective surfaces (which are lossy at short wavelengths and hence should be minimized). In the first demonstrations of SD-FROG [21,25,26] and TG-FROG [10,22,27] the input pulse was split into replicas with a partially reflective beam-splitter. Although a dielectric-coated beam-splitter is the most efficient, its use may limit the bandwidth. Also it can constrain the use of the device to a particular wavelength range. Partially reflective inconel coatings operate over a wide wavelength range, although they are very lossy. Note that using approximately equal intensities in each beam is important only for efficiency: there is no distortion in the signal resulting from such a mismatch since the signal is linear in each of the input intensities.

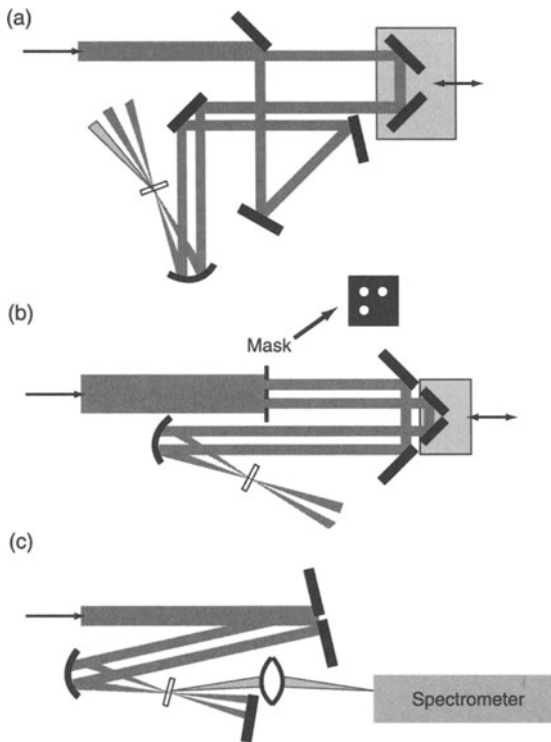


Fig. 13.4: Three zero-dispersion layout options for SD and TG FROG, which all avoid any transmitting optics before the nonlinear medium. a. A mirror picks off half of the beam. This can be done twice for TG FROG. b. A mask with two or three holes in it generates two or three parallel beams, guaranteed to be, not only parallel, but also synchronous in time. c. Two nearby mirrors, slightly titled with respect to each other generate two approximately time-synchronous beams. Note that dispersion is irrelevant after the nonlinear medium, so a lens can be used there.

The use of a beam splitter also introduces dispersion: as in other FROG geometries, the beam that reflects from the beam-splitter must also pass through a compensation plate to ensure that the pulses interacting in the nonlinear medium are identical. This added dispersion is an especially important consideration for characterizing short-wavelength pulses. Consider the use of a beam-splitter involving a 1-mm thick fused silica substrate in two different cases: measuring 1) a 20-fs 800-nm pulse and 2) a 12-fs 267-nm pulse. After two passes through the substrate (at 45°), a transform-limited 20-fs pulse centered at 800 nm broadens to only ~23 fs. Not only is this small, but a small pre-chirp introduced by a grating adjustment in the amplifier system compressor would correct for this dispersion without introducing a significant amount of higher-order phase. For the shorter pulse at the shorter wavelength, the broadening is much more severe: the 12-fs pulse centered at 267 nm will broaden to 103 fs. If the pulse is generated through harmonic conversion, as is

usually the case, a secondary compressor is not always available to give a short pulse at the nonlinear medium. While the material within the apparatus may be accounted to determine the input pulse shape, this pulse broadening can reduce the signal level too much for low energy pulses. In this example, the signal would be reduced by almost a factor of 10^3 . Even when an additional compressor is part of the system, full compensation for the pulse stretching introduced by the beam-splitter would require compensation of higher-order phase—not an easy task!

The good news, however, is that, *after* the nonlinear medium, dispersion is irrelevant! Once the nonlinear interaction takes place, FROG's interest lies only in the signal beam spectrum. The signal beam can propagate through a kilometer of high-dispersion glass, and it wouldn't matter.

It is clear, then, that a FROG device for the UV is much more useful if it is dispersion free before the nonlinear medium. If sufficient pulse energy is available, this can be accomplished by simply *spatially* selecting different portions of the input beam and recombining them in the nonlinear medium. In the characterization of 16-fs pulses at 266 nm, Backus, et al. used the edge of a mirror to split half of the beam (see Fig. 13.4a). Each portion of the beam traveled a different path before being focused by a mirror into the nonlinear medium. An alternative method, demonstrated for TG-FROG at 800 nm [28] is to place a mask with openings at the input to generate the three separate beams required for that geometry (see Fig. 13.4b). This technique is particularly advantageous for the TG geometry because it allows a single mirror to be used for the two reference pulses, ensuring that there is zero time-delay between them.

On the other hand, separation of the beams into two paths makes the identification of the time-zero difficult. To obtain any signal, the individual pulses must be focused into the nonlinear medium, they must spatially overlap, and they must temporally overlap. (We'll discuss alignment techniques shortly.) Recently, a much simpler SD FROG setup was demonstrated in which a split mirror is used to form two beams (see Fig. 13.4c). The beams travel directly to a focusing mirror, and from there into the nonlinear medium. The identification of the time-zero can be approximated to within 20–50 μm by simple visual inspection of the adjacent mirrors. This is in contrast to the arrangements in which the two beams travel separate paths, where measurement puts the time-zero to within $\sim 1 \text{ mm}$. The split mirror arrangement can be converted to the PG or TG setup by introducing a mask on the split mirror. Since the split mirror does not direct the beams backwards, the delayed beam experiences a slight lateral translation during the delay scan. For parallel beams, however, this changes only the crossing angle slightly and does not change the beam overlap at the focus of the mirror. Furthermore, for fs pulses, the total range of the scan is very small.

While both SD and TG FROG give a background-free signal because the signal propagates in a different direction from the incident beams, stray light is still an issue that must be addressed. The signal wavelength is the same as

that of the incident beams, so wavelength filtering (which works so well for SHG FROG) is not applicable. One source of stray light is scatter from the nonlinear medium. Super-polished substrates of high optical quality are best.

A second source of stray light is the edge of each incident beam. The location for a mask after the interaction can be chosen such that the stray light from this source is minimized. To better define the outer edge of the beam, place an iris around the beam somewhere before the focusing optic. If a partially reflecting beam-splitter is used, place the iris before the beam-splitter. If the beam is clipped, the iris should be very close to the point where the beams are clipped. To isolate the signal beam, place the output mask in a position after the focus where the input iris has a relayed image. The mask at this position must be as large as possible without passing the incident beams: the signal, having passed through the induced grating, is spatially chirped at this position, and there is a risk of clipping the spectrum.

Alignment

PG, TG, and SD geometries all have similar alignment considerations. The pulses must overlap spatially and temporally to see a signal. Aligning the beams to be parallel first and then simultaneously crossing and focusing them with a lens or curved mirror ensures that the pulses cross precisely where they focus. The parallelism is also important for correct phase-matching in the TG geometry. It's best to check the parallelism first by propagating the beams some distance. Then place the nonlinear medium at the measured focal point of the mirror, and inspect the beam overlap by viewing the scatter from a thin plate (<0.25 mm) with a CCD camera. Some materials (e.g., sapphire excited by fs 266-nm pulses) exhibit two-photon fluorescence in the visible, and this can be used as a diagnostic for beam overlap. The temporal overlap may be found by using near-IR input and looking for the sum-frequency signal from a nonlinear crystal, then by looking for the self-diffraction signal. In the TG geometry, each individual pair will show an SD signal if the medium is thin enough (at the location of the X's in Fig. 13.2). Optimization of the spatial overlap by inspecting the signal itself can be misleading with short input pulses, since that adjustment also affects the timing. For TG, optimization of the timing can be accomplished by alternating scans of the two delay stages and setting the zero point at the position of maximum signal. Because this alignment becomes more critical with short input pulses, it must be checked with the shortest pulses available. This extra degree of freedom in the alignment can be avoided by using the same mirror for two of the input beams, since in this case, they automatically arrive at the same time. Also note that if the intensity is too high, higher-order diffraction spots will appear. You probably shouldn't operate at such a strong input level, as this implies that the depletion regime is near (in which additional nonlinear-optical processes can occur), and distortions in the FROG trace can occur.

After the signal beam is isolated, it is directed to the spectrometer. Whether operating single- or multi-shot, the interaction region should be imaged onto the spectrometer entrance slit to ensure the full spectrum enters the spectrometer. Alternatively, the simple home-brew spectrometer can be used (see Chapter 11). Note that if this image is formed with magnification, the temporal blurring that results from the finite crossing angle can be reduced, although this effect shouldn't be important in the first place. Finally, the spectrometer must be well calibrated, and its spectral response should be measured.

Measured UV Pulses

We give a couple of examples of UV-pulse measurement from our work with frequency-converted pulses from a \sim 20-fs Ti : Sapphire kilohertz amplifier. Backus, et al [2] found that mJ, 22-fs, 800-nm pulses could be conveniently converted directly to the third-harmonic with 0.1% efficiency by focusing them *in air*. The duration (without pre-compression) of the pulses was measured to be 16 fs using SD FROG. The experimental arrangement is shown in Fig. 13.4a. Figure 13.5 show the measured SD FROG trace and intensity and phase.

In later work, Durfee, et al., developed a more efficient method for generating light at the third harmonic of Ti : Sapphire [3]. The fundamental (ω_1) and the second harmonic (ω_2) were injected into an Ar-filled capillary (150 mm ID \times 70 cm) and mixed in a $\chi^{(3)}$ process to produce light near 267 nm ($\omega_3 = 2\omega_2 - \omega_1$). The output pulses are positively chirped owing to the propagation through the cell window and air. Moreover, cross-phase modulation from the intense pulses can yield very strong spectral broadening, which adds to the chirp. A simple grating compressor (300 l/mm) was used to compress the pulses, which were measured with SD FROG in the simplified configuration shown in Fig. 13.4c. Since the grating reflectivity was only 75%, a single-pass of the grating pair was used to minimize losses. This left the beam spatially chirped: the direction of chirp was chosen to be vertical so that when the beam

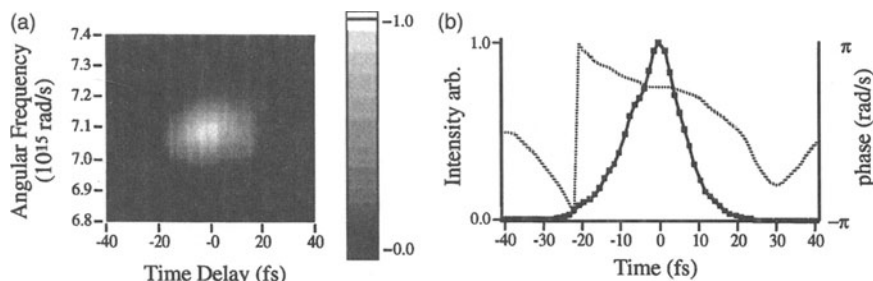


Fig. 13.5: Measurement of a 16-fs 267-nm pulse. (a) Measured SD FROG trace. (b) Retrieved intensity and phase [2].

was clipped, each half would contain the full spectrum. In this configuration, it was important that the nonlinear medium was exactly in the focus, where there was no spatial chirp. The compressed pulses were measured to be 8 fs, the shortest measured in that wavelength region. SD FROG has also been successfully used to characterize compressed pulses at 400 nm [29].

High-intensity-pulse Issues

High-power ultrafast laser systems [30,31] are achieving incredible average powers, peak powers, and peak intensities and are allowing previously unimagined phenomena to be observed. As ultrafast laser oscillators tend to yield mere nJ pulses [8], achieving such powers requires significant amplification, typically involving many stages. Due to the large dispersion present in amplifier systems, an amplified laser pulse very often has a complicated and non-ideal intensity and phase vs. time. Just as an aberrated beam brought to a focus will not achieve high intensity, significant temporal structure or too long a pulse length can also limit the achieved intensity.

Thus it is crucial to measure such pulses' complete temporal behavior. With this knowledge, the laser system can be optimized, and the experimenter can know the actual pulse intensity that is achieved. Furthermore, the dynamics of the laser system itself can be much better understood.

There are, however, several important issues in the characterization of pulses from high power systems. Measurements of amplified pulses are susceptible to a myriad of problems, many unique to such systems, which, if not considered, can give rise to a poor measurement [23].

First, in addition to having considerably different pulse energies, amplified systems and oscillators also differ in the amount of dispersion to which the pulses are subject. Chirped-pulse amplification is the rule for amplified pulses, which are typically first stretched by a factor of 10,000 and then recompressed by a similar factor—without significant distortion [10]. This involves ensuring that the optical path through ~25 m in the system is equal for all wavelengths to within ~2.5 μm ! In addition, there are a plethora of potentially imperfect optics and coatings, which can yield considerable phase distortion.

Typically the spectral phase of the laser system can be described by:

$$\varphi(\omega) = \varphi_s(\omega) + \varphi_c(\omega) + \varphi_o(\omega) + \varphi_m(\omega) + \varphi_g(\omega) \quad (13.1)$$

where $\varphi(\omega)$ is the total system spectral phase, $\varphi_s(\omega)$ is the stretcher phase, $\varphi_c(\omega)$ is the compressor phase, $\varphi_o(\omega)$ is the refractive-optics phase, $\varphi_m(\omega)$ is the material phase, and $\varphi_g(\omega)$ is the gain-dispersion phase. All these components conspire (or at least it seems that way) to destroy the flat phase that's typically desired for high intensity. Thus, it is important for our measurement technique to be capable of measuring potentially very complex pulses.

Another amplifier-induced distortion is spectral modulation, which corresponds to the presence of satellite pulses surrounding the main pulse.

In most situations, satellite pulses are very undesirable, as they can themselves be intense enough to do serious damage. Also, in attempts to generate x-rays or produce laser fusion, leading satellite pulses many orders of magnitude weaker can significantly disturb the medium, effectively preventing the desired process. It is thus important for the measurement to have a dynamic range of as many as eight orders of magnitude to see these pulses.

Although pulse characterization techniques all rely on nonlinear effects, such as SHG or PG, with high-power pulses, the nonlinearities can easily get out of control. For example, PG depends on a third-order process, so the FROG signal is the product of three fields. But self-phase modulation and cross-phase modulation are also third-order, and if the intensity where the beams cross is too high, the pulses you're trying to measure are actually being changed by the process. With SHG FROG, beam depletion can also occur, also resulting in distortions in the measured trace. As mentioned above, if the input power for SD, TG, or even PG FROG is too high, higher diffraction orders appear. The diffracted power into these higher orders has a different (higher-order) signal field expression than the nonlinearity that produces the desired signal. Thus, it's important to avoid accidentally using one of them for the signal beam, or you could be performing, say, a seventh-order FROG measurement. Also, when such beams occur, the correct signal beam is itself probably on the verge of distortions due to depletion.

Another issue is the tendency of high-power pulses to fluctuate from shot to shot. Because amplified pulses involve pulsed flash-lamps, the resulting pulse energy stability is many orders of magnitude poorer than that of unamplified pulse trains. Not only can the pulse energy fluctuate wildly from shot to shot, but, since many distortions result from nonlinear self-action effects in the various media through which the pulse passes, so can their *intensity and phase*. It is thus essential to perform measurements of high-power pulses on a single shot.

An issue for extremely intense pulses is that too much power can damage the nonlinear medium (or other optics) in a FROG device. Thus, it is necessary to attenuate the input beam into the apparatus without distorting the pulse or beam. There are many ways to do this. One is to use an iris to radially clip the beam to lower the total power into the FROG device. Another is to use the surface reflection from a glass plate that is either thick, wedged, or frosted on the back side (to avoid a second pulse). However the beam is attenuated, it is important to do it in a way that is largely independent of polarization. Say you have a beam that is polarized 1000:1. If you attenuate the beam using a polarizer or by taking reflections off a glass plate at Brewster's angle, what you are actually measuring is the s-polarized component of the pulse. Why is this a problem? The s-component of polarization sees different dispersion in the system (due to birefringent materials such as calcite and sapphire), and also has a different spectrum, since the reflectivity of the compressor gratings is quite different for s- vs. p-polarization.

A final issue that arises in measurements of high-power pulses is that, even with attenuation, the beam may still be intense enough that focusing it is out of the question. If a large beam is used at the nonlinear medium in the FROG, geometrical distortions can arise (see Chapter 7).

High-power FROG

The high-power effects mentioned above are significantly reduced by using single-shot FROG, which completely removes all transverse geometrical distortions, as was discussed in Chapter 7. Conveniently, single-shot FROG requires a large beam and thus can reduce the need to focus or attenuate the input beam. Single-shot FROG has the additional advantage that it yields the intensity and phase for a single pulse in real time—required so that pulse intensity-and-phase fluctuations can be seen.

Single-shot PG and SD FROG are particularly convenient methods for measuring amplified pulses. They are higher-order than SHG, so beam depletion is not an issue (other third-order effects, such as SPM can generally be kept to a minimum and typically do not represent a problem, especially when a weak line focus is used). They yield very intuitive traces, graphically illustrating the frequency vs. time or group delay vs. frequency, which is very useful for aligning systems without the need to retrieve the intensity and phase. Indeed, Fig. 13.6 shows typical distortions in amplifier systems, beautifully illustrated by single-shot PG FROG measurements.

When the system is compensated properly, residual fourth-order (Fig. 13.6c), and in some cases fifth-order phase (Fig. 13.6d), can be seen directly from a FROG trace. This useful tool aids in the construction and

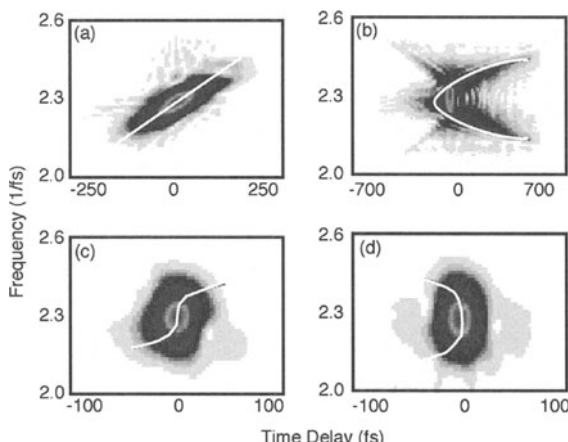


Fig. 13.6: (a) Second, (b) Third, (c) Fourth, and (d) Fifth orders of spectral phase, which can be read directly from the PG FROG trace, which graphically display the group delay vs. frequency (the derivative of the spectral phase).

alignment of femtosecond high power laser systems by allowing a qualitative picture of the phase aberrations of the system. In many instances, bad or non-optimal optics can be identified by this method, which almost certainly would not be the case when using a simple autocorrelation or FRAC.

Many researchers use single-shot PG FROG to align pulse compressors, which require careful adjustment of the separation of a grating pair. Because the wrong separation yields chirp with a sign proportional to the deviation from the ideal spacing, PG FROG is ideal for this application. Figure 13.7 shows such traces for different grating separations in a pulse compressor. The feedback provided by this measure makes this otherwise difficult alignment problem almost trivial.

One of the biggest advantages of FROG for complicated systems, such as amplifiers, is the ability to detect spatio-temporal problems in the pulse.

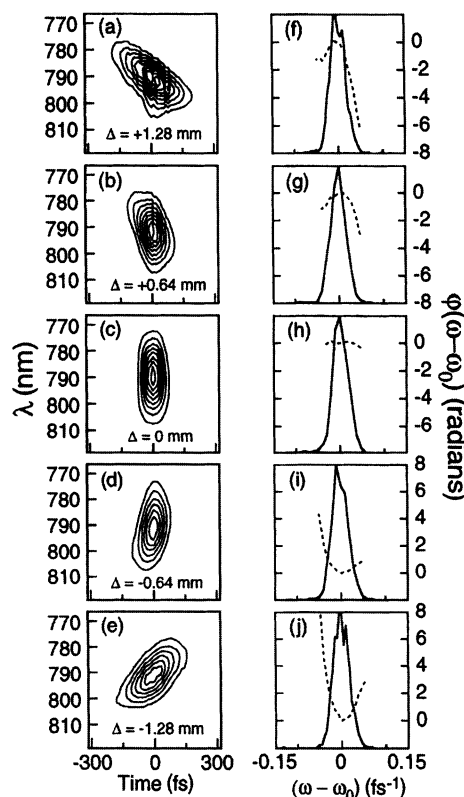


Fig. 13.7: Experimental PG FROG measurements of pulses from a chirped-pulse amplified Ti : Sapphire laser. a–e: PG FROG traces of pulses corresponding to different pulse-compressor diffraction-grating separations. The change in distance, Δ , from the optimal grating separation of 510 mm is shown for each measurement. f–j: Retrieved spectrum (solid) and spectral phase (dashed) vs. frequency offset for the various traces in a–e. The spectrum remains constant, while the spectral phase varies with grating spacing. The grating spacing is optimal in h, which corresponds to a pulse length of 77 fs [38].

This is done by the use of the frequency (and, to a lesser extent, delay) marginals, which act as a check on the validity of the data taken using the FROG technique. The main concerns are spatial chirp (caused mostly by grating misalignment in the compressor or stretcher), and spectral clipping (often due to the use of too thick a nonlinear medium, which has too small a phase-matching bandwidth). These types of errors yield an error in the frequency marginal indicating that the pulse has one of these errors. The use of marginals was described in detail in Chapter 10, so we say no more on this subject here, except to say that they are crucial for measuring amplified pulses, which frequently suffer from spatial effects, which are detected and even corrected using the marginals.

High-dynamic-range FROG measurements are also possible. CCD cameras used for FROG measurements have as many as 16 bits, corresponding to a pulse dynamic range of better than 10^4 , and such measurements are routine (see Fig. 6.9, for example). It is not difficult to make two measurements, one with an ND4 filter and the other without one, allowing the center of the trace to saturate (or, better, blocking it to avoid scattering in the camera). The full trace can then be constructed from the two traces with better than 10^8 dynamic range. Since we have found that the FROG algorithm determines the intensity with the same dynamic range as that of the trace, this allows the measurement of relatively weak satellite pulses.

A question that often arises is: "If a pulse has a weak satellite pulse, how weak does it appear in a third-order FROG trace, such as PG FROG?" In other words, would a satellite pulse of relative intensity 10^{-4} correspond to a peak in the third-order FROG trace with a height of only 10^{-12} ? The answer is that the peak in the FROG trace corresponding to the satellite pulse will always have the same relative height as in the intensity, independent of the order of the nonlinearity. This can be seen by observing that it is the main pulse that mostly gates each pulse. Thus, for example, a satellite pulse that is 10^{-4} of the main pulse will yield a satellite pulse in the trace for all versions FROG that is also 10^{-4} of the main peak in the trace, independent of the order of the nonlinearity. Even better, a weak satellite pulse will also yield frequency fringes in the main peak in the FROG trace with amplitude of twice the square root of the satellite pulse relative height, or about 2% for a satellite with relative height of 10^{-4} . *Thus, even with insufficient dynamic range to see the additional peaks due to the satellite pulse, the frequency fringes reveal it unambiguously.* And the FROG algorithm is very good at retrieving it.

A slight drawback to third-order FROG measurements is a Raman ringing effect that can slightly distort a pulse measurement for pulses between ~ 15 and ~ 40 fs (see Chapter 18, where we show that distortions of up to a few per cent are possible due to this effect). As a result, when it is convenient to attenuate the beam sufficiently, people have also used SHG FROG for highly accurate high-power pulse measurement, especially to measure pulses under 50 fs. To date the shortest pulse measured directly from an amplifier system, 15 fs [32], was measured using SHG FROG. With the advent of the

hollow core fiber pulse compression scheme, pulses as short as 4.5 fs have been measured with SHG FROG [33].

SHG FROG can also be used to characterize and align the phase of an amplifier system: by sending the unamplified seed pulses through the system. This has the advantage that the spectrum is wider than it will be after amplification (i.e., not gain-narrowed), and it's easier to see farther out in the spectral wings, where most of the higher-order spectral distortions are.

Recently, pulse shapers have allowed arbitrary phase compensation, eliminating the need for perfect phase compensation by the stretcher and compressor [34]. FROG measurements play an important role in calibrating the pulse shaper, so the effects of adjusting each channel of the shaper can be determined. Since most pulse shapers are linear, this calibration procedure allows a desired pulse shape to be dialed in without a feedback loop.

With pulse-shapers, very complicated waveforms can be generated. Thus, we require a sophisticated way of retrieving the amplitude and phase of the pulse, which must have the sensitivity to resolve fine detail in the intensity and phase of the shaped, amplified pulse. Figure 13.8 shows a pulse train generated by an acousto-optic modulator called a DAZZLER, from Fastlite Inc. [35]. This pulse was generated by placing a sinusoidal phase function on a transform-limited pulse to generate a complex pulse.

The SHG FROG retrieval clearly shows the multiple pulse structure of the pulse. Other types of pulse shapers include deformable mirrors and spatial light modulators (SLM). SLM's are LCD crystal displays, which can modulate the intensity and phase of a pulse, and are capable of imparting π phase jumps. Deformable mirrors are phase-only devices and are limited to

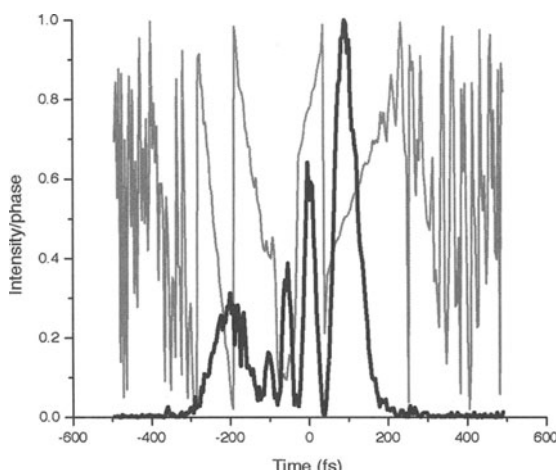


Fig. 13.8: SHG FROG measurement of a sinusoidal phase function applied to an 18 fs pulse. The intensity is shown in black, and the phase is shown in gray.

smooth phase functions. Such pulse-shaping techniques are revolutionizing high-power experiments, such as high harmonic generation (HHG) [36]. And FROG has been used in these experiments to characterize the complex shaped pulses. Indeed, FROG is the *only* technique that has been shown to be capable of measuring such complex pulses. And it can do so very accurately. In these experiments, small changes in the phase of the driving pulse were detected by the use of FROG. This led to discoveries of new physics and allowed the quantum control of high order processes.

Finally, in very high-power situations, we should mention a method demonstrated by Mysyrowicz and coworkers. A relative of FROG, it involves splitting off a fraction of the beam and allowing the more intense pulse to cross-phase-modulate the weaker one in a third-order medium [37]. This broadens and, at very high power, also significantly complicates the weaker pulse's spectrum. Measuring the weaker pulse's spectrum vs. delay yields the pulse intensity and phase. The algorithm requires solving the nonlinear Shrodinger equation for propagation through the non-linear medium (see Chapters 18–20 for analogous problems), but it works.

So FROG is an excellent method for determining phase distortions in both UV and high-power situations. Indeed, it has already become an important tool for investigating new physics and phenomena in these exciting new regimes.

References

1. J. Ringling, O. Kittelmann, F. Noack, G. Korn, and J. Squier, "Tunable femtosecond pulses in the near vacuum ultraviolet generated by frequency conversion of amplified Ti:sapphire laser pulses," *Optics Letters* **18**, 2035 (1993).
2. S. Backus, J. Peatross, E. Zeek, A. Rundquist, G. Taft, M. M. Murnane, and H. C. Kapteyn, "16-fs, 1-mJ ultraviolet pulses generated by third-harmonic conversion in air," *Optics Letters* **21**, 665 (1996).
3. C. G. Durfee, S. Backus, M. M. Murnane, and H. C. Kapteyn, "Ultrabroadband phase-matched optical parametric generation in the ultraviolet by use of guided waves," *Optics Letters* **22**, 1565 (1997).
4. D. C. Edelstein, E. S. Wachman, L. K. Cheng, W. R. Bosenberg, and C. L. Tang, "Femtosecond ultraviolet pulse generation in $b\text{-BaB}_2\text{O}_4$," *Applied Physics Letters* **52**, 2211 (1988).
5. L. D. Ziegler, J. Morais, Y. Zhou, S. Constantine, M. K. Reed, M. K. Steiner-Shepard, and D. Lommel, "Tunable 50-fs pulse generation in the 250–310-nm range," *IEEE Journal of Quantum Electronics* **34**, 1758 (1998).
6. R. M. Bowman, J. J. Gerdy, G. Roberts, and A. H. Zewail, "Femtosecond real-time probing of reactions. 6 A joint experimental and theoretical study of Bl_2 dissociation," *Journal of Physical Chemistry* **95**, 4635 (1991).
7. S. Pullen, L. A. Walker II, B. Donovan, and R. J. Sension, "Femtosecond transient absorption study of the ring-opening reaction of 1,3-cyclohexadiene," *Chemical Physics Letters* **242**, 415 (1995).
8. M. T. Asaki, C. P. Huang, D. Garvey, J. Zhou, H. C. Kapteyn, and M. M. Murnane, "Generation of 11-fs pulses from a modelocked Ti:sapphire laser," *Optics Letters* **18**, 977 (1993).
9. S. Backus, C. Durfee, G. Mourou, H. C. Kapteyn, and M. M. Murnane, "0.2 Terawatt laser system at 1 kHz," *Optics Letters* **22**, 1256 (1997).
10. S. Backus, C. Durfee, M. M. Murnane, and H. C. Kapteyn, "High power ultrafast lasers," *Review of Scientific Instruments* **69**, 1207 (1998).
11. M. Nisoli, S. De Silvestri, and O. Svelto, "Generation of High-Energy 10fs pulses by a new pulse compression technique," *Applied Physics Letters* **68**, 2793 (1996).
12. M. Nisoli, S. De Silvestri, O. Svelto, R. Szipoocs, K. Ferencz, Ch. Spielmann, S. Sartania, and F. Krausz, "Compression of High Energy Pulses below 5fs," *Optics Letters* **22**, 522 (1997).
13. N. I. Koroteev and A. M. Zheltikov, "Chirp control in third-harmonic generation due to cross-phase modulation," *Applied Physics B* **67**, 53 (1998).

14. C. G. Durfee, S. Backus, H. C. Kapteyn, and M. M. Murnane, "Intense 8fs pulse generation in the deep ultraviolet," *Optics Letters* **24**, 697 (1999).
15. H. Nishioka, M. Ishiguro, T. Kawasumi, K. Ueda, and H. Takuma, "Single-Shot UV Autocorrelator that Uses a Two-Photon-Induced Photoacoustic Signal in Water," *Optics Letters* **18**, 45 (1993).
16. S. P. LeBlanc, G. Szabo, and R. Sauerbrey, "Femtosecond single-shot phase-sensitive autocorrelator for the ultraviolet," *Optics Letters* **16**, 1508 (1991).
17. A. M. Streltsov, J. K. Ranka, and A. L. Gaeta, "Femtosecond ultraviolet autocorrelation measurements based on two-photon conductivity in fused silica," *Optics Letters* **23**, 798 (1998).
18. S. Backus, M. T. Asaki, C. Shi, H. C. Kapteyn, and M. M. Murnane, "Intracavity frequency doubling in Ti:sapphire: generation of 14fs pulses at 416 nm," *Optics Letters* **19**, 399 (1994).
19. E. J. Canto-Said, P. Simon, C. Jordan, and G. Marowsky, "Surface second-harmonic generation in Si(111) for autocorrelation measurements of 248-nm femtosecond pulses," *Optics Letters* **18** (1993).
20. D. J. Kane, and R. Trebino, "Single-shot measurement of the intensity and phase of an arbitrary ultrashort pulse by using frequency-resolved optical gating," *Optics Letters* **18**, 823 (1993).
21. T. S. Clement, A. J. Taylor, and D. J. Kane, "Single-shot measurement of the amplitude and phase of ultrashort laser pulses in the violet," *Optics Letters* **20**, 70 (1995).
22. J. Sweetser, D. Fittinghoff, and R. Trebino, "Transient-Grating Frequency-Resolved Optical Gating," *Optics Letters* **22**, 519 (1997).
23. R. Trebino, K. W. DeLong, D. N. Fittinghoff, J. N. Sweetser, M. A. Krumbiegel, B. A. Richman, and D. J. Kane, "Measuring ultrashort laser pulses in the time-frequency domain using frequency-resolved optical gating," *Review of Scientific Instruments* **68**, 3277 (1997).
24. C. G. Durfee, S. Backus, H. C. Kapteyn, and M. M. Murnane, in *Applications of High Field and Short Wavelength Sources VII*, edited by L. DiMauro, M. Murnane and A. L'Huillier (Optical Society of America, Washington DC, Santa Fe, NM, 1997), Vol. 7, p. 251.
25. D. J. Kane, and R. Trebino, *IEEE Journal of Quantum Electronics* **29**, 571 (1993).
26. D. J. Kane, A. J. Taylor, R. Trebino, and K. W. DeLong, "Single-shot measurement of the intensity and phase of a femtosecond UV laser pulse with frequency-resolved optical gating," *Optics Letters* **19**, 1061 (1994).
27. C. G. Durfee, S. Backus, M. M. Murnane, and H. C. Kapteyn, "Design and implementation of a TW-class kilohertz amplifier system," *IEEE Journal of Selected Topics in Quantum Electronics* **4**, 395 (1998).
28. M. Li, J. P. Nibarger, C. Guo, and G. N. Gibson, "Dispersion-free transient-grating frequency-resolved optical gating," *Applied Optics* **38**, 5250 (1999).
29. O. Dühr, E. T. J. Nibbering, G. Korn, G. Tempea, and F. Krausz, "Generation of intense 8-fs pulses at 400 nm," *Optics Letters* **24**, 34 (1999).
30. V. Bagnoud, and F. Salin, "Amplifying laser pulses to the terawatt level at a 1-kilohertz repetition rate", *App. Phys. B* **70**, S165–70, Suppl. 2000.
31. K. Yamakawa, S. Matsuoka, M. Aoyama, T. Kase, Y. Akahane, H. Takuma, and C. Barty, "Design and performance of a 100 TW, sub-20 fs Ti: sapphire laser system", *X-Ray lasers 1998* **159**, 645–8 (1999).
32. E. Zeek, R. Bartels, M. M. Murnane, H. C. Kapteyn, S. Backus, and G. Vdovin, *Optics Letters*, vol. 25, p. 587, (2000).
33. A. Baltuska, M. Pshenichnikov, and D. Wiersma, "Second-harmonic generation frequency-resolved optical gating in the single-cycle regime", *IEEE JQE* **35**(4), 459–78 (1999).
34. E. Zeek, K. Maginnis, S. Backus, U. Russek, M. Murnane, G. Mourou, H. Kapteyn, and G. Vdovin, "Pulse compression by use of deformable mirrors", *Optics Letters* **24**(7), 493–5, (1999).
35. F. Verlucose, V. Laude, Z. Cheng, C. Spielmann, and P. Tournois, "Amplitude and phase control of ultrashort pulses by use of an acousto-optic programmable dispersive filter: pulse compression and shaping", *Optics Letters* **25**(8), 575–7, (2000).
36. R. Bartels, S. Backus, E. Zeek, L. Misoguti, G. Vdovin, I. Christov, M. Murnane, and H. Kapteyn, "Shaped-pulse optimization of coherent emission of high-harmonic soft X-rays," *Nature* **406**(6792), 164–6, (2000).
37. J. M. Schins, P. Breger, P. Agostini, R. C. Constantinescu, H. G. Muller, A. Bouhal, G. Grillon, A. Antonetti, A. Mysyrowicz, "Cross-correlation Measurements of Femtosecond Extreme-Ultraviolet High-Order Harmonics," *Journal of the Optical Society of America B* **13**(1), 197, (1996).
38. B. Kohler, et al., Phase and Intensity Characterization of Femtosecond Pulses from a Chirped-Pulse Amplifier by Frequency-Resolved Optical Gating, *Optics Letters* **20**(5), p. 483–5, (1994).

14. FROG in the Single-Cycle Regime

***Andrius Baltuska, Maxim S. Pshenichnikov,
and Douwe A. Wiersma***

Introduction

Extremely short (~ 10 fs or less) pulse are now available in several labs and have a wide range of applications. You might think that such extremely short pulses couldn't possibly be distorted and still be so short, but that's absolutely not the case. Indeed, intensity and phase distortions not only exist in such incredibly short pulses, but they play decisive—and even useful—roles in many phenomena. For instance, pulses with identical spectra but different spectral phases yield wildly different efficiency in high-harmonic-generation processes [1]. The spectral phase also heavily affects wave-packet motion in organic molecules [2,3], population inversion in liquid [4] and gas [5] phases, and even the direction of a chemical reaction [6]. Moreover, a totally automated search for the best shaped pulse to optimize a pre-selected reaction channel was recently demonstrated [7–9]. Measuring the phase and amplitude of the excitation pulses in such experiments then allows a back-reconstruction of potential surfaces of the parent molecule.

The complete determination of the electric field of femtosecond pulses also uncovers the physics behind their generation, as has been demonstrated in the case of fs Ti:Sapphire lasers [10,11]. Such information is invaluable in determining, not only the methods for their generation, but also the ultimate limits to further pulse shortening. Due to the great complexity of the broadband phase correction required to produce transform-limited pulses with duration shorter than 5 fs [12–15], such measurements are as difficult as they are important. And, because the broader the pulse spectrum, the shorter the pulse can potentially be, it is important to develop methods for measuring very broadband pulses, such as the continuum generated by self-phase modulation and other nonlinear-optical processes at high intensity and long path lengths.

A breakthrough in the full characterization of ultrashort pulses occurred recently with the introduction of frequency-resolved optical gating (FROG) [16,17,18]. Notably, no *a priori* information about the pulse shape is necessary to reconstruct the pulse from the experimental FROG trace.

In general, FROG is quite accurate and rigorous [19]. Also, the large number of data points in the two-dimensional FROG trace and the resulting over-determination of the pulse make it much less sensitive to noise than pulse diagnostics based on one-dimensional measurements, such as the ordinary autocorrelation and interferometric methods. Last but not least, FROG offers data self-consistency checks that are unavailable in other pulse measuring techniques. This feedback mechanism involves computing the temporal and

spectral marginals that are the integrals of the FROG trace along the delay and frequency axes (see Chapter 10). The comparison of the marginals with the independently measured fundamental spectrum and autocorrelation verifies the validity of the measured FROG trace [11,20,21]. To date, FROG methods have been applied to measure a vast variety of pulses with different duration, wavelength and complexity [22].

A number of outstanding features make FROG especially valuable for the measurement of sub-10-fs pulses.

First, because FROG uses a type of excite-probe geometry, common for most nonlinear optical experiments, it's ideally suited to measure pulses used in spectroscopy experiments. Unlike other pulse diagnostics [23–32], FROG does not require splitting of auxiliary laser beams and pre-fabrication of reference pulses. This fact is a great practical advantage, since the set-up complexity in many spectroscopic experiments is already quite high [33–39]. FROG directly offers pulse characterization precisely at the position of the sample by simply interchanging the sample with a nonlinear medium for optical gating (see Chapter 11). The last point is essential for ~10-fs pulses [12–15,40] currently used in spectroscopy. The dispersive lengthening that such pulses experience even due to propagation through air precludes the use of a separate diagnostic device. Although an alternative technique, Spectral Phase Interferometry for Direct Electric-field Reconstruction (SPIDER), [25,29–32] can also measure sub-6-fs pulses [28], it, however, requires a cumbersome additional set-up, which can lead to errors in measurement. In this respect, the simplicity of FROG and its compatibility with nonlinear spectroscopy provides an undisputed advantage by both saving experimental effort and ensuring that the “right pulse at the right location” is being measured. Thus, FROG is the ideal way to measure and optimize pulses on target prior to carrying out a spectroscopic experiment.

Second, it's possible to correctly measure sub-10-fs pulses by FROG *even in presence of massive systematic error*. Several types of such errors will inevitably appear in any measurement of pulses whose spectra span a hundred nanometers or more. And FROG is unique in its ability to deal with such distortions (see Chapter 10). For example, a FROG trace affected by wavelength-dependent detector sensitivity and wavelength-dependent frequency conversion efficiency can be corrected and validated via its consistency checks [11]. In contrast, an autocorrelation or SPIDER trace measured under identical conditions may be corrupted irreparably, and it would be difficult to know.

Third, the temporal resolution of a FROG measurement isn't limited by the sampling increment in the time domain. Assuming that the whole time-frequency spectrogram of the pulse is contained within the measured FROG trace, short-time information is also provided by large-scale variations in frequency. The broadest feature in the frequency domain determines the shortest feature in the time domain. Therefore, no fine temporal pulse structure can be overlooked [22], even if the delay increment used to collect the FROG trace

is larger than the duration of such structure. Thus, reliability of the FROG data depends simply on the proper delay axis calibration rather than on the very fine sampling in time, which might otherwise be troublesome, since the pulse itself extends only a few microns in space.

Choosing the appropriate FROG geometry [20,22] requires carefully considering possible distortions due to the beam geometry (see Chapter 7) and the physics of the nonlinear medium. Consequently, not every FROG geometry can be straightforwardly applied to measure pulses shorter than 10 fs. In particular, in some $\chi^{(3)}$ -based techniques (for instance, polarization-grating, transient grating etc.), the finite response time due to the Raman contribution to the nonlinearity can play a role in the measurement of \sim 20-fs pulses [41] (see Chapter 18). Thus, SHG FROG in transparent crystals [42–44] and third-harmonic-generation FROG near a surface [45], which both have essentially instantaneous nonlinearities, are the best choices for the measurement of the shortest pulses available to date.

Another important experimental issue is sensitivity. Among the FROG geometries, SHG FROG is most appropriate for low-energy pulses because it [42] is second-order, rather than third order. The signal pulse's different color and polarization allow effective suppression of scattered input light, adding to the suppression provided by the geometry. The low-order nonlinearity, combined with this background suppression, gives SHG FROG a higher dynamic range than any other FROG geometry or other technique.

In general, the FROG pulse retrieval doesn't depend on pulse duration since the FROG traces simply scale in the time-frequency domain. Because the pulse gates itself, the shorter the pulse to be measured, the shorter the gate pulse that is automatically available to measure it. However, with the decrease of the pulse length and the accompanying increase in bandwidth, the measured trace begins to deviate significantly from the mathematically defined ideal FROG trace. Besides the obvious problems such as the pulse lengthening during its propagation before and inside the nonlinear medium due to group velocity dispersion, there are also more fundamental issues.

For example, the conventional description of nonlinear optics (see Chapter 3) applicable to multi-cycle pulses fails for near-single-cycle pulses. Clearly, for such extremely short pulses, the conventional slowly varying envelope approximation [46–48], which assumes that the pulse amplitude varies negligibly over one optical cycle, fails. Furthermore, the phase-matching bandwidth [49]—which is finite due to dispersion in the nonlinear medium—rapidly becomes problematic as the pulse spectrum broadens [10,11]. Another concern is the frequency-dependent variation in the reflectivity of the optics and gratings and the sensitivity of the photo-detector used to detect the signal light generated in the nonlinear process. These effects all potentially distort the signal pulse spectrum and hence are collectively known as the *spectral-filter* effect [49–51]. Also, geometrical distortions due to the multi-shot non-collinear geometry employed in spectroscopic experiments [11,51,52]

can potentially artificially lengthen the measured pulse (see Chapter 7). If a portion of the signal field is accidentally spectrally filtered out or if the signal is artificially “blurred” in time this could crucially influence the measured trace [53] and subsequently lead to erroneous measurements.

In this chapter we give a detailed description of FROG’s performance for ultrabroadband pulses, which would correspond to pulses 3 fs in length if the spectral phase were flat. Starting with Maxwell’s equations, we derive a complete expression for the SHG FROG signal that is valid even in the single-cycle pulse regime. It includes phase-matching in the crystal, beam-geometry effects, dispersive pulse-broadening inside the crystal, and dispersion of the second-order nonlinearity. Subsequently, we describe a simplified—but still quite accurate—expression that decomposes the SHG FROG signal into a simple product of the ideal SHG FROG trace and a spectral filter. Remarkably, this simplification allows the commercial FROG code that retrieves longer pulses to be used for even single-cycle pulses, provided that the trace is first divided by the spectral-filter correction factor. Then we describe numerical simulations, which convincingly show that the approximations made in the derivation of the simplified expression are well justified. We also show that, despite all these potential sources of error, accurate measurements of single-cycle pulses are possible.

We then discuss the performance of $\chi^{(3)}$ -based FROG techniques—transient grating (TG) and self-diffraction (SD)—in the single-cycle regime and numerically analyze the effects of geometrical distortions and spectral filtering in these geometries.

Next, we discuss the practical implementation of these ideas in the FROG measurement of near-single-cycle and very broadband pulses. Finally, we present experimental results of SHG FROG characterization of white light continuum and pulses <5 fs long.

Theory

The ideal FROG signal is a simple mag-squared Fourier transform of a time- and delay-dependent signal field [22]. This formalism describes the case of an ideal nonlinear medium, which has zero-thickness and an infinitely fast nonlinear response. This, of course, never occurs in reality. In this section, we present a comprehensive theoretical analysis, thoroughly re-examining the formalism describing the FROG signal. We derive complete expressions valid even for single-cycle pulses. Among other results, we show that the slowly varying envelope approximation, with its rejection of derivatives of the time-domain electric field, is *unnecessary*. We also show that geometrical delay smearing does not introduce a significant distortion of the observed traces, even for near-single-cycle pulses, provided that the geometry is carefully optimized.

SHG FROG in the Single-Cycle Regime

We consider first the case of $\chi^{(2)}$ -based FROG and derive a general formalism for pulses of arbitrarily broad bandwidth, allowing us to carry out a scrupulous numerical analysis of the performance of SHG FROG in various experimental situations.

General Formalism

In this section, we derive the complete equation that describes SHG FROG for pulses as short as one optical cycle. We include such effects as the phase-matching condition, time-smearing effects due to a non-collinear geometry, spectral filtering of the second harmonic radiation, and dispersion of the second-order nonlinearity.

We consider the case of a non-collinear geometry in which the fundamental beams intersect at a small angle (Fig. 14.1). As has been pointed out [49], pulse broadening due to crystal bulk dispersion is negligibly small compared to the group-velocity mismatch. This means that the appropriate crystal thickness is mostly be determined from the phase-matching condition. For instance, in a 10- μm BBO crystal the bulk dispersion broadens a single-cycle pulse by only by ~ 0.1 fs, while the group-velocity mismatch between the fundamental and second-harmonic pulses is as much as 0.9 fs.

We assume that the confocal parameter and the longitudinal beam overlap of the fundamental beams are considerably longer than the crystal length. For instance, for an ideal Gaussian beam of ~ 2 -mm diameter focused by a 10-cm achromatic lens, the confocal parameter, that is, the longitudinal extent of the focal region, is ~ 1.2 mm. This is considerably longer than the nonlinear crystal. Under such conditions, all wavefronts inside the crystal are practically flat. Therefore, second harmonic generation will be a function of the longitudinal coordinate only and include the transversal coordinates only at the last step to account for the spatial beam profile. Note that the

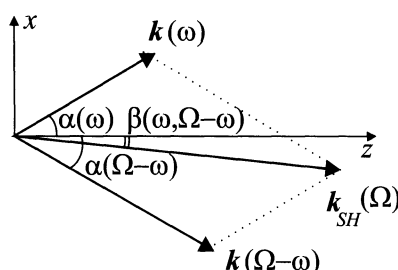


Fig. 14.1: Non-collinear phase matching for three-wave interaction. $k(\omega)$ and $k(\Omega - \omega)$ are the wave-vectors of the fundamental fields that form an angle α with z axis. $k_{SH}(\Omega)$ is the wave-vector of the second-harmonic that intersects z axis at an angle β .

constraint on focusing isn't necessarily always fulfilled. For example, very tight focusing using a 1-cm lens in the situation described above reduces the length of the focal region to only 12 μm, and, in this case, it would be impossible to disregard the dependence on transverse coordinates.

We assume that the second-harmonic field is not absorbed in the nonlinear crystal, which is well justified even for single-cycle pulses. Absorption bands of the crystals that are transparent in the visible occur below ~200 nm. If the central wavelength of a single-cycle pulse is 800 nm, the field of the SH components around 200 nm will be more than 1000 times smaller than the SH peak at 400 nm and can be safely ignored. We also require the SHG efficiency to be low enough to neglect depletion of the fundamental beams, so the system of two coupled equations describing the nonlinear interaction [54] will simplify to one. The equation that governs propagation of the second harmonic wave in the +z direction inside the crystal can be obtained directly from Maxwell's equations [55]:

$$\frac{\partial^2}{\partial z^2} \mathcal{E}_{\text{SH}}(z, t) - \varepsilon_0 \mu_0 \frac{\partial^2}{\partial t^2} \int_{-\infty}^t \varepsilon(t-t') \mathcal{E}_{\text{SH}}(z, t') dt' = \mu_0 \frac{\partial^2}{\partial t^2} \mathcal{P}^{(2)}(z, t) \quad (14.1)$$

where $\mathcal{E}_{\text{SH}}(z, t)$ is the second harmonic field, $\mu_0 \varepsilon_0 = 1/c^2$, ε is the relative permittivity, and $\mathcal{P}^{(2)}(z, t)$ is the induced second-order dielectric polarization. In our analysis, we do *not* write $\mathcal{E}_{\text{SH}}(z, t)$ as the product of a slowly varying $E(t)$ and $\exp(i\omega t)$, as we have elsewhere. Instead we Fourier-transform both $\mathcal{E}_{\text{SH}}(z, t)$ and $\mathcal{P}^{(2)}(z, t)$, obtaining a result equivalent of Eq. (14.1) in the frequency (Ω) domain:

$$\frac{\partial^2}{\partial z^2} \tilde{\mathcal{E}}_{\text{SH}}(z, \Omega) + k_{\text{SH}}^2(\Omega) \tilde{\mathcal{E}}_{\text{SH}}(z, \Omega) = -\mu_0 \Omega^2 \tilde{\mathcal{P}}^{(2)}(z, \Omega) \quad (14.2)$$

where $\tilde{\mathcal{E}}_{\text{SH}}(z, \Omega)$ and $\tilde{\mathcal{P}}^{(2)}(z, \Omega)$ are Fourier transforms of $\mathcal{E}_{\text{SH}}(z, t)$ and $\mathcal{P}^{(2)}(z, t)$, respectively, Ω is the frequency and $k_{\text{SH}}(\Omega)$ is the wave-vector of the second harmonic field: $k_{\text{SH}}^2(\Omega) = \Omega^2 \varepsilon_0 \mu_0 \tilde{\varepsilon}(\Omega)$, with $\tilde{\varepsilon}(\Omega)$ being the Fourier-transform of the relative permittivity $\varepsilon(t)$.

In order to simplify the left part of Eq. (14.2), we write the second harmonic field as a plane wave propagating along z axis (and ignore the complex conjugate):

$$\tilde{\mathcal{E}}_{\text{SH}}(z, \Omega) = \tilde{E}_{\text{SH}}(z, \Omega) \exp(i k_{\text{SH}}(\Omega) z) \quad (14.3)$$

Note that we've used a different font for the E in $\tilde{E}_{\text{SH}}(z, \Omega)$ to distinguish this complex spatio-temporal envelope of $\mathcal{E}_{\text{SH}}(z, t)$ from its complex temporal envelope, $E(t)$, used elsewhere in this book. Substituting $\tilde{E}_{\text{SH}}(z, \Omega)$ into Eq. (14.2) yields:

$$\begin{aligned} 2ik_{\text{SH}}(\Omega) \frac{\partial}{\partial z} \tilde{E}_{\text{SH}}(z, \Omega) + \frac{\partial^2}{\partial z^2} \tilde{E}_{\text{SH}}(z, \Omega) \\ = -\mu_0 \Omega^2 \tilde{\mathcal{P}}^{(2)}(z, \Omega) \exp(-ik_{\text{SH}}(\Omega) z) \end{aligned} \quad (14.4)$$

So far we've made no simplifications concerning the pulse duration. Now we apply the slowly-varying amplitude approximation [55], i.e.

$$\left| \frac{\partial}{\partial z} \tilde{E}_{\text{SH}}(z, \Omega) \right| \ll \left| 2k_{\text{SH}}(\Omega) \tilde{E}_{\text{SH}}(z, \Omega) \right| \quad (14.5)$$

in order to omit the term $\partial^2 \tilde{E}_{\text{SH}}(z, \Omega)/\partial z^2$.

Note that the standard time-domain description of the signal wave propagation results in a second-order differential equation, similar in its structure to our Eq. (14.4). Unlike Eq. (14.4), however, simplification of the time-domain expression requires a rejection of the second-order *temporal* derivative of the envelope, i.e.,

$$\left| \frac{\partial^2}{\partial t^2} E(t) \right| \ll \left| \frac{4\pi}{T_{\text{per}}} \frac{\partial}{\partial t} E(t) \right| \quad (14.6)$$

where T_{per} is the characteristic period of light oscillation. Such an approach implies the assumption of slow envelope variation vs. time. This condition is *not* fulfilled for pulses only a few cycles long, since the change of the envelope in one optical period is comparable to the magnitude of the envelope itself. Brabec and Krausz [56], who explored the time-domain approach for the propagation of near-single-cycle pulses, found that rejection of the second-order derivative term is warranted when the phase and the group velocities of light are close to each other. On this point, we note that application of condition (14.5) to the frequency-domain Eq. (14.4) requires no assumptions on the change of the temporal envelope altogether. Therefore, condition (14.5) is safe for even single-cycle pulses, provided linear absorption is negligible on lengths comparable to the wavelength. The only remaining concern is the lowest frequencies, for which k_{SH} becomes close to zero. However, the amplitude of the low-energy spectral wing is negligible even for single-cycle optical pulses and therefore can be disregarded. Consequently, Eq. (14.4) can be readily solved by integration over the crystal length L :

$$\tilde{E}(L, \Omega) = i \frac{c \mu_0 \Omega}{2n_{\text{SH}}(\Omega)} \int_0^L \tilde{\mathcal{P}}^{(2)}(z, \Omega) \exp(-k_{\text{SH}}(\Omega)z) dz \quad (14.7)$$

where $n_{\text{SH}}(\Omega) = \sqrt{\tilde{\varepsilon}(\Omega)}$ is the refractive index of the second harmonic.

Now we calculate the second-order polarization $\tilde{\mathcal{P}}^{(2)}(z, \Omega)$. We assume that two fundamental fields cross in the xz plane at a small angle θ (Fig. 14.1). Each beam's angle with the z -axis inside the crystal is then $\alpha(\omega) = \arcsin[n(\omega) \sin \theta/2] \approx n(\omega)\theta/2$. The relative delay between the pulses is τ . An additional delay for off-axis components of the beam due to the geometry can be expressed for a plane wave as $\tau'(x) = xn(\omega) \sin \alpha(\omega)/c = x \sin \alpha_0/c \approx x\alpha_0/c$ for the beam propagating in $+x$ direction, and $\tau'(x) \approx -x\alpha_0/c$ for the beam in $-x$ direction. The electric fields in the frequency

domain are the Fourier transforms:

$$\begin{aligned}\tilde{E}_1(\omega) &= \tilde{E}(\omega) \exp(i\omega(x\alpha_0/c)) \\ \tilde{E}_2(\omega) &= \tilde{E}(\omega) \exp(i\omega(-x\alpha_0/c - \tau))\end{aligned}\quad (14.8)$$

In order to calculate the second-order dielectric polarization induced at frequency Ω by the two fundamental fields, we must sum over all possible permutations of fundamental frequencies:

$$\begin{aligned}\tilde{P}^{(2)}(z, \Omega) &\int \tilde{\chi}^{(2)}(\Omega, \omega, \Omega - \omega) \tilde{E}_1(\omega) \tilde{E}_2(\Omega - \omega) d\omega \\ &= \exp(i\Omega(\tau + x\alpha_0/c)) \int \tilde{\chi}^{(2)}(\Omega, \omega, \Omega - \omega) \tilde{E}(\omega) \tilde{E}(\Omega - \omega) \times \\ &\quad \times \exp[i(k_z(\omega)z + k_z(\Omega - \omega)z + \omega(\tau + 2x\alpha_0/c))] d\omega\end{aligned}\quad (14.9)$$

In Eq. (14.9) we've included the frequency-dependence of the nonlinear susceptibility $\tilde{\chi}^{(2)}(\Omega, \omega, \Omega - \omega)$, and we've represented the fundamental field analogously to Eq. (14.3). The electric field of the second harmonic therefore becomes:

$$\begin{aligned}\tilde{E}_{\text{SH}}(L, \Omega) &= i \frac{c\mu_0\Omega L}{2n(\Omega)} \exp(i\Omega(\tau + x\alpha_0/c)) \int \tilde{\chi}^{(2)}(\Omega, \omega, \Omega - \omega) \tilde{E}(\Omega - \omega) \tilde{E}(\omega) \\ &\quad \times \exp\left(i\frac{\Delta k(\omega, \Omega - \omega)L}{2} + i\omega\left(\tau + \frac{2x\alpha_0}{c}\right)\right) \text{sinc}\left(\frac{\Delta k(\omega, \Omega - \omega)L}{2}\right) d\omega\end{aligned}\quad (14.10)$$

where $\Delta k(\omega, \Omega - \omega)$ is the phase mismatch given by the equation:

$$\begin{aligned}\Delta k(\omega, \Omega - \omega) &= k(\omega) \cos(\alpha_0 n_1(\omega)) + k(\Omega - \omega) \cos(\alpha_0 n_2(\Omega - \omega)) \\ &\quad - k_{\text{SH}}(\Omega) \cos \beta(\omega, \Omega - \omega)\end{aligned}\quad (14.11)$$

with n_1 and n_2 being the refractive indices of the fundamental waves, and $\beta(\omega, \Omega - \omega)$ being the angle between $\mathbf{k}_{\text{SH}}(\Omega)$ and the z axis inside the crystal. The appearance of this angle can be easily understood from Fig. 14.1. The momentum conservation law determines the direction of emitted second harmonic field:

$$\mathbf{k}(\omega) + \mathbf{k}(\Omega - \omega) = \mathbf{k}_{\text{SH}}(\Omega)\quad (14.12)$$

where $\mathbf{k}(\omega)$ and $\mathbf{k}(\Omega - \omega)$ are the wave-vectors of the incident fundamental waves. In the case $\mathbf{k}(\omega) \neq \mathbf{k}(\Omega - \omega)$, β is non-zero and can be found from

the following equation:^{*}

$$\sin \beta(\omega, \Omega - \omega) = \sin \alpha_0 \frac{k(\omega)n_1(\omega) - k(\Omega - \omega)n_2(\Omega - \omega)}{k_{\text{SH}}(\Omega)} \quad (14.13)$$

Since β is of the same order as the intersection angle, the correction $\cos \beta(\omega, \Omega - \omega)$ is required only in the Δk expression (Eq. (14.11)). Elsewhere this correction can be dropped.

The values of the wave-vectors and refractive indices in Eqs. (14.11) and (14.13) depend on the actual polarization of the three interacting waves. For Type I we obtain:

$$\begin{aligned} \Delta k(\omega, \Omega - \omega) &= k_O(\omega) \cos(\alpha_0 n_O(\omega)) + k_O(\Omega - \omega) \cos(\alpha_0 n_O(\Omega - \omega)) \\ &\quad - k_E(\Omega) \cos \beta(\omega, \Omega - \omega) \end{aligned} \quad (14.14)$$

and for Type II:

$$\begin{aligned} \Delta k(\omega, \Omega - \omega) &= k_E(\omega) \cos(\alpha_0 n_E(\omega)) + k_O(\Omega - \omega) \cos(\alpha_0 n_O(\Omega - \omega)) \\ &\quad - k_E(\Omega) \cos \beta(\omega, \Omega - \omega) \end{aligned} \quad (14.15)$$

Indices O and E indicate ordinary and extraordinary waves, respectively.

To calculate the total FROG signal, we integrate the signal intensity:

$$S_{\text{SHG}}(L, \Omega) = \varepsilon_0 \frac{n_{\text{SH}}(\Omega)}{c} \left| \tilde{\mathbf{E}}_{\text{SH}}(L, \Omega) \right|^2 \quad (14.16)$$

over the transverse coordinates x and y . Hence, for the second-harmonic signal detected in FROG we obtain:

$$\begin{aligned} I_{\text{meas}}(\Omega, \tau, L) &= \frac{\Omega^2 L^2 Q(\Omega)}{2c^3 \varepsilon_0 n_{\text{SH}}(\Omega)} [\ln 2]^{3/2} \int \exp \left(-4 \ln 2 \left(\frac{x}{d_0} \right)^2 \right) \\ &\quad \times \left| \int_0^\Omega \tilde{\chi}^{(2)}(\Omega, \omega, \Omega - \omega) \tilde{\mathbf{E}}(\Omega - \omega) \tilde{\mathbf{E}}(\omega) \right. \\ &\quad \times \exp \left(i \frac{\Delta k(\omega, \Omega - \omega)L}{2} + i\omega \left(\tau + \frac{2x\alpha_0}{c} \right) \right) \\ &\quad \left. \times \text{sinc} \left(\frac{\Delta k(\omega, \Omega - \omega)L}{2} \right) d\omega \right|^2 dx \end{aligned} \quad (14.17)$$

In Eq. (14.17), $Q(\Omega)$ is the spectral sensitivity of the photo-detector, and the transverse beam profile is assumed Gaussian with the FWHM diameter of d_0 .

^{*} In fact, if the second harmonic is an extraordinary wave, the magnitude of $k_{\text{SH}}(\Omega)$ in Eq. (14.13) is a function of $\beta(\omega, \Omega - \omega)$. The problem of finding the exact values of both $k_{\text{SH}}(\Omega)$ and $\beta(\omega, \Omega - \omega)$ could be easily solved by employing the relations of crystal optics and Eq. (14.13). However, Eq. (14.13) alone gives an excellent approximation for $\beta(\omega, \Omega - \omega)$ if one chooses $k_{\text{SH}}(\Omega)|_{\beta=0}$.

We've limited our discussion to the case of low-efficiency SHG, i.e. when the depletion of the fundamental waves can be disregarded—and where useful pulse measurements must be performed. In the high conversion efficiency regime, additional effects play an important role, distorting the trace in both Type I [57] and Type II crystals [58,59].

Another important example of undesirable distortions in the high-conversion-efficiency regime is nonlinear (two-photon) absorption of the frequency-doubled radiation inside the SHG crystal [60]. Fortunately, at the minuscule crystal thicknesses necessary for measuring such short pulses, these effects are not usually a problem.

To conclude this section, we wish to emphasize the many advantages of the frequency-domain—vs. the time-domain—approach to the wave equation Eq. (14.1) in the single-cycle regime. The frequency representation allows us to *automatically* include dispersive broadening of both fundamental and second-harmonic pulses, as well as their group-velocity mismatch, frequency-dependence of the nonlinear susceptibility, frequency-dependent spatial profiles of the beams, and the blue shift of the second-harmonic spectrum (analogous to self-steepening in fibers [61]). Also, we've only had to make a single approximation (Eq. (14.5)), which itself is easily avoidable in computer simulations. A similar frequency-domain approach to ultrashort-pulse propagation in optical fibers [62] helped solve a long-standing question of the magnitude of the shock term [61,63].

Ultimate Temporal Resolution of SHG FROG

For arbitrary pulses, the complete expression for the SHG FROG signal (Eq. (14.17)) must be computed numerically. However, for linearly-chirped Gaussian pulses, Eq. (14.17) can be evaluated analytically.

With such a result, we can study such effects as geometrical delay smearing, as discussed in Chapter 7. Recall that this distortion occurs because, with crossed beams, the relative delay varies across the beam. As discussed in Chapter 7, this transverse geometrical smearing effect allows single-shot measurement [64]. Indeed, in Chapter 7, we saw that performing a single-shot SHG FROG measurement actually took advantage of this effect and effectively removed all geometrical smearing from the FROG trace—even when a pulse has near-single-cycle length. However, as multi-shot measurements of such pulses are common, we restrict our attention to the multi-shot case, where geometrical smearing can, in principle, be an issue.

As can be seen from Eq. (14.17) the dependence on the transverse coordinate x yields a range of delays across the beam simultaneously, which broadens the FROG trace along its delay axis. As in Taft, et al. [11], we assume Gaussian-intensity pulses and, under perfect phase-matching conditions, we find that geometrical smearing yields an SHG FROG trace that's temporally wider than

it should be. We find that the measured pulse duration τ_{meas} is longer:

$$\tau_{\text{meas}}^2 = \tau_p^2 + \Delta\tau^2 \quad (14.18)$$

where τ_p is the true pulse width, and $\Delta\tau$ is the delay smear parameter:

$$\Delta\tau = \theta d/2c \quad (14.19)$$

where d is the beam diameter in the crystal, and θ the intersection angle of the fundamental beams. Notice that $\Delta\tau$ is actually a factor of 2 smaller than the result we obtained in Chapter 7 using a simple, but approximate, approach, neglecting order-unity factors.

We consider the best-case scenario of the two input Gaussian beams separated by their input diameter d_i on the focusing optic. In this case the intersection angle $\theta = d_i/f$, and the beam diameter in the focal plane $d = f\lambda/\pi d_i$, where f is the focal length of the focusing optic. Thus, at $\lambda = 800$ nm, the resulting delay smearing amounts to only $\Delta\tau = \lambda 2\pi c = 0.4$ fs. This value represents the ultimate resolution of pulse measurement in a non-collinear geometry, and it is quite good, allowing the accurate measurement of even a single-cycle pulse. Recall from chapter 7 that, furthermore, this result is independent of the focusing optic, angle, and beam diameters. The temporal resolution deteriorates, however, if the beams are other than Gaussian: for beams with a rectangular spatial profile, the resulting temporal resolution worsens to 0.7 fs.

The temporal resolution can be improved further by filtering out signal light of the wrong delay with a narrow slit behind the nonlinear medium, or, better, by imaging the nonlinear medium onto a slit (like the entrance slit of a spectrometer in a FROG), as discussed in Chapter 7 [65]. It's also possible to use a collinear geometry [66–69]. Still better, single-shot SHG FROG avoids this effect entirely.

Approximate Expression for the SHG FROG Signal

In this section, we obtain a simplified expression for SHG FROG accurate even for single-cycle pulses. We show that, remarkably, the measured signal can be simply described by an ideal, i.e. perfectly phase-matched, SHG FROG trace multiplied by a spectral filter. In other words, the measured SHG FROG trace can simply be divided by this spectral filter, and the standard SHG FROG algorithm will yield the pulse field.

In order to simplify Eq. (14.17), we make several reasonable approximations. First, as was shown in the previous Section, using a carefully chosen beam geometry (with a small crossing angle), the effect of geometrical smearing is negligibly small. For instance, it causes only a 10% error in the duration measurement of a 3-fs pulse and hence can be safely neglected for all pulses that have been created at the time of this writing. With such an approximation, the integral along x in Eq. (14.17) can be performed analytically. Second, we

expand $k_O(\omega)$ and $k_O(\Omega - \omega)$ in a Taylor series around $\omega = \Omega/2$ and keep the terms that are linear with frequency.* Hence, for Type I phase-matching we write:

$$\begin{aligned}\Delta k(\omega, \Omega - \omega) &\approx 2k_O(\Omega/2) \cos(\theta/2n_O(\Omega/2)) - k_E(\Omega) \\ &= \Delta k(\Omega/2, \Omega/2)\end{aligned}\quad (14.20)$$

Third, we estimate the dispersion of the second harmonic and calculate the second-order susceptibility $\tilde{\chi}^{(2)}(\Omega, \omega, \Omega - \omega)$ using the dispersion of the refractive index. For a classical inharmonic oscillator model [54], $\tilde{\chi}^{(2)}(\Omega, \omega, \Omega - \omega) \propto \tilde{\chi}^{(1)}(\Omega)\tilde{\chi}^{(1)}(\omega)\tilde{\chi}^{(1)}(\Omega - \omega)$, where the first-order susceptibility, $\tilde{\chi}^{(1)}(\Omega) = n^2(\Omega) - 1$. Equation (14.17) can now be decomposed into a product of the spectral filter $R(\Omega)$, which originates from the finite conversion bandwidth of the second harmonic crystal and varying detector sensitivity, and an ideal FROG signal $I_{\text{FROG}}^{\text{SHG}}(\Omega, \tau)$:

$$I_{\text{meas}}(\Omega, \tau, L) \propto R(\Omega) I_{\text{FROG}}^{\text{SHG}}(\Omega, \tau) \quad (14.21)$$

where

$$I_{\text{FROG}}^{\text{SHG}}(\Omega, \tau) = \left| \int \tilde{\mathbf{E}}(\Omega - \omega) \tilde{\mathbf{E}}(\omega) \exp(i\omega\tau) d\omega \right|^2 \quad (14.22)$$

and

$R(\Omega)$

$$= Q(\Omega) \frac{\Omega^2}{n_E(\Omega)} [(n_E^2(\Omega) - 1)(n_O^2(\Omega/2) - 1)^2]^2 \text{sinc}^2\left(\frac{\Delta k(\Omega/2, \Omega/2)L}{2}\right) \quad (14.23)$$

In Eqs. (14.21–14.23) we've kept only terms that are Ω -dependent.

The FROG signal given by Eq. (14.22) is the well-known definition of SHG FROG [16,20,42] written in the frequency domain (see Chapter 5). The same formula is also used in existing FROG retrieval algorithms. Note that, alternatively, the complete Eq. (14.17) can be readily implemented in the algorithm based on the method of generalized projections [71]. However, relation (14.21) is better numerically because the integral Eq. (14.22) takes the form of an autoconvolution in the time domain and can be rapidly computed via a Fast Fourier Transform [72]. It is also important that the use of Eq. (14.21) permits a direct check of FROG marginals to validate experimental data (see Chapter 10).

* Alternatively, one can perform a Taylor expansion around the central frequency of the fundamental pulse $\omega = \omega_0$ [24,49,70]. However, in this case, the first derivative terms don't cancel each other and must be retained. Our simulations also prove that the expansion around $\omega = \Omega/2$ provides a better approximation for broadband pulses.

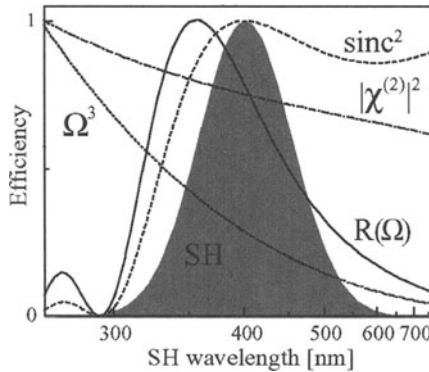


Fig. 14.2: Constituent terms of the spectral filter $R(\Omega)$, given by Eq. (14.23): the Ω^3 dependence (dotted line), estimated squared magnitude of second-order susceptibility $\chi^{(2)}$ (dash-dotted line), the crystal phase-matching curve for a Type I 10- μm BBO crystal cut at $\Theta = 29^\circ$ (dashed line), and their product (solid curve). The second-harmonic spectrum of a 3-fs Gaussian pulse is shown for comparison (shaded contour).

The spectral filter $R(\Omega)$, given by Eq. (14.23), is a product of several factors (Fig. 14.2). The Ω^2 -dependence follows directly from Maxwell's equations. The meaning of this factor is that higher frequency components are more efficiently generated than lower frequency ones. It has been shown that in some cases it's appropriate to include an additional Ω -dependence that accounts for the difference in the efficiency of generation of various SH components as a result of spatial overlap of the fundamental spectral components [51,73]. In other words, this extra Ω -term originates from a frequency-dependent beam waist as a consequence of pulse propagation and focusing into the SH crystal. The combined dependence of the FROG signal on the signal frequency in such a case is Ω^3 . This situation is applicable, for instance, for relatively short (several mm or less) pieces of a single-mode fiber [51,73]. In other cases, such as the output of a hollow fiber [70,74] or of a Kerr-lens mode-locked laser [75], where the distribution of the beam waist size of the fundamental beam in the SH crystal does not change appreciably with wavelength, the additional Ω -term can be disregarded. To bring our theoretical considerations into accordance with the experimental results of the fiber-compressed-pulse FROG characterization, which will be presented later, we include the effect the spatial overlap in our numerical calculations and use the combined Ω^3 dependence. As can be seen from Fig. 14.2, the Ω^3 -term (dotted curve) leads to a substantial distortion of the second-harmonic spectrum of ultrabroadband pulses. For instance, due to this factor alone, the up-conversion efficiency of a spectral component at 600 nm is 4.5 times higher than of a 1000-nm one.

The variation of the second-order susceptibility with frequency (dash-dotted curve), expressed in Eq. (14.23) as the dependence on the refractive indices, plays a much smaller role than the Ω^3 factor (dotted curve). For example, for a BBO crystal, the squared magnitude of $\tilde{\chi}^{(2)}$ for the 600-nm

component of the fundamental wave is only 1.3 times larger than for the 1000-nm component. Such a virtually flat second-order response over such an immense bandwidth is a good indication of the almost instantaneous nature of $\tilde{\chi}^{(2)}$ in transparent crystals. Nonetheless, the contribution of the $\tilde{\chi}^{(2)}$ dispersion would affect the measurement of pulses with spectra that are hundreds of nanometers wide.

The last factor contributing to $R(\Omega)$ is the phase-matching curve of the SHG crystal (Fig. 14.2, dashed line). The shape and the bandwidth of this curve depend on the thickness, orientation, and type of the crystal.

Numerical Simulations

In this section we verify the approximations we used to derive Eqs. (14.21–14.23). In order to do so, we numerically generate FROG traces of various pulses using the complete expression, Eq. (14.17), and compare them with the ideal FROG traces calculated according to Eq. (14.22). To examine contributions of different factors to pulse retrieval, we compare FROG inversion results with the input pulses.

We consider two types of pulses with central wavelength 800 nm: (1) a bandwidth-limited 3-fs Gaussian pulse, and (2) a pulse with the same bandwidth that is linearly chirped to 26 fs. We assume that the fundamental beam diameter in the focus is $d = 20 \mu\text{m}$ and the beams intersect at $\theta = 2^\circ$. Therefore, the geometrical delay smearing that was defined in section 2.2 (Eq. 14.19)) amounts to $\Delta\tau = 1.2 \text{ fs}$. The thickness of the Type I BBO is $L = 10 \mu\text{m}$. As we pointed out earlier, such a short crystal lengthens the pulse $<0.1 \text{ fs}$, and, therefore, dispersive pulse broadening inside the crystal can be disregarded. The crystal is oriented for the peak conversion efficiency at 700 nm*. The spectral sensitivity of the light detector $Q(\Omega)$ is set to unity.

The results of FROG simulations for each type of pulse are shown in Figs. 14.3 and 14.4. The ideal traces, calculated according to Eq. (14.22), are shown in Figs. 14.3a and 14.4a, while the traces computed using Eq. (14.17) are displayed in Figs. 14.3b and 14.4b. The FROG trace of the 3-fs pulse is noticeably extended along the delay axis due to geometrical smearing from the choice of an excessively large beam angle. For the 26-fs pulse, however, this effect is negligible because this pulse is so much longer. The spectral filtering occurring in the crystal becomes apparent from the comparison of the spectral marginals that are depicted in Figs. 14.3d and 14.4d. Calculated marginals are asymmetric and substantially shifted toward shorter wavelengths.

* The phase-matching angle is slightly affected by the non-collinear geometry. Due to the fact that the fundamental beams intersect at an angle θ , the equivalent phase-matching angle is different from that in the case of collinear SHG: $\Theta = \Theta_{\text{collinear}} + \theta/2n$, where n is the refractive index of the fundamental wave at the phase-matching wavelength. For instance, the 800-nm phase-matched cut of a BBO crystal for $\theta = 2^\circ$ becomes $\Theta = 29.6^\circ$ instead of $\Theta_{\text{collinear}} = 29^\circ$ for collinear SHG. This fact should be kept in mind because the phase-matching curve is quite sensitive to the precise orientation of the crystal.

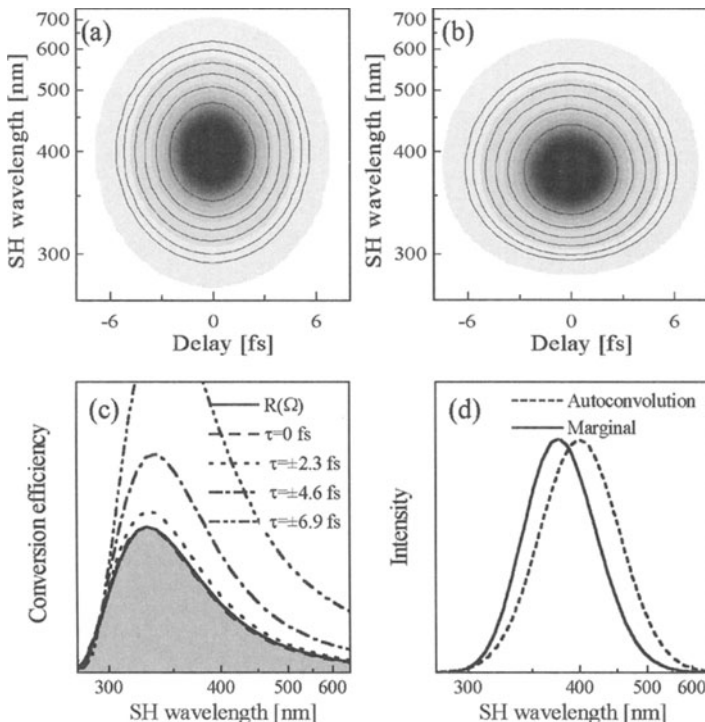


Fig. 14.3: Simulations of the SHG FROG trace for an ideal 3-fs Gaussian pulse for Type I phase-matching. (a) ideal FROG trace, as given by Eq. (14.22). (b) complete FROG trace as given by Eq. (14.17). (c) spectral filter curve $R(\Omega)$ computed according to Eq. (14.23) (shaded contour) and the ratio of FROG traces given in (b) and (a) at several delays (broken curves). (d) spectral marginal of the traces shown in (b) (solid curve) and autoconvolution of the fundamental spectrum (dashed curve). The FROG traces here and further on are shown as density plots with overlaid contour lines at the values 0.01, 0.02, 0.05, 0.1, 0.2, 0.4, and 0.8 of the peak second harmonic intensity.

By computing the ratio of the FROG signals given by Eq. (14.22) and Eq. (14.17) we obtain delay-dependent conversion efficiency, as shown in Figs. 14.3c and 14.4c. The spectral filter $R(\Omega)$, calculated according to Eq. (14.23), is shown as shaded contours. Clearly, at the small delays, the conversion efficiency is almost exactly described by $R(\Omega)$. As the delay increases, the approximation given by Eq. (14.23) worsens, as both the conversion peak position and the magnitude change. The rapid ratio scaling at non-zero delays for the 3-fs pulse (broken curves in Fig. 14.3c) is mostly determined by geometrical smearing rather than by phase matching, as in the case of the chirped pulse (Fig. 14.4c). On the other hand, the deviations from $R(\Omega)$ at longer delays become unimportant because the signal decreases for large delays.

To estimate the significance of the spectral correction in distorted FROG traces and to determine the feasibility of performing it in the case of extreme

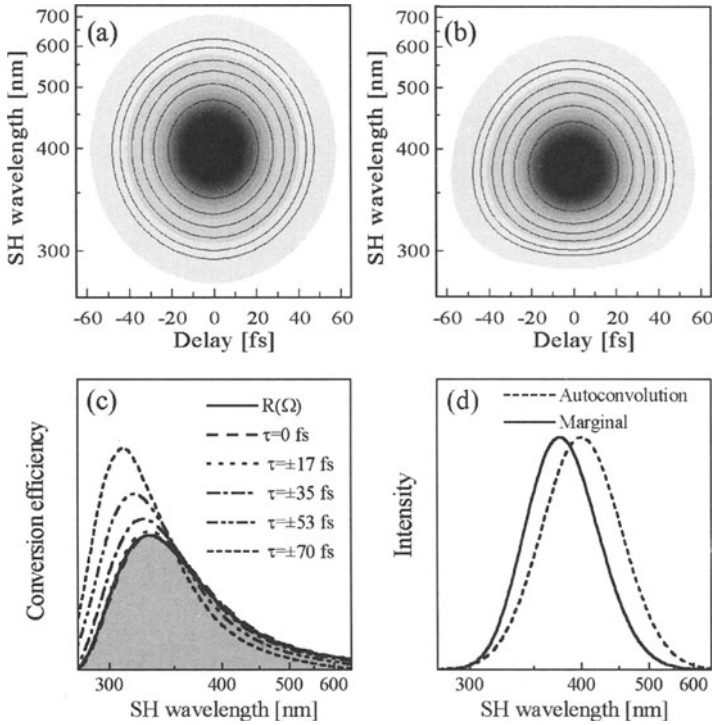


Fig. 14.4: Simulation of the SHG FROG trace for a linearly-chirped 26-fs Gaussian pulse. The conditions are the same as in Fig. 14.3. (a) ideal FROG trace, as given by Eq. (14.22). (b) complete FROG trace as given by Eq. (14.17). (c) spectral filter curve $R(\Omega)$ computed according to Eq. (14.23) (shaded contour) and the ratio of FROG traces given in (b) and (a) at several delays (broken curves). (d) spectral marginal of the traces shown in (b) (solid curve) and autoconvolution of the fundamental spectrum (dashed curve).

bandwidths, we examined FROG inversion results of the numerically generated traces using the commercially available program from Femtosoft Technologies. We considered four different cases for each type of pulse: (a) ideal phase-matching (zero-thickness crystal); (b) a 10- μm BBO crystal with the parameters defined above; (c) the trace generated in case (b) but corrected by $R(\Omega)$; and, last, (d) the trace generated in case (c), but with geometrical smearing included as well. The results of the FROG inversion of the cases (a)–(d) are shown in Fig. 14.5.

In case (a), the Ω^3 dependence is exclusively responsible for the spectral filtering that substantially shifts the whole FROG trace along the frequency axis. Both the bandwidth-limited and the chirped Gaussian pulses converged excellently to their input fields, but around a blue-shifted central frequency. In (b), where the phase-matching of a 10- μm BBO crystal is taken into account as well, the central wavelength is even more blue-shifted due to spectral filtering in the crystal. A small phase distortion is obtained for both types of pulses.

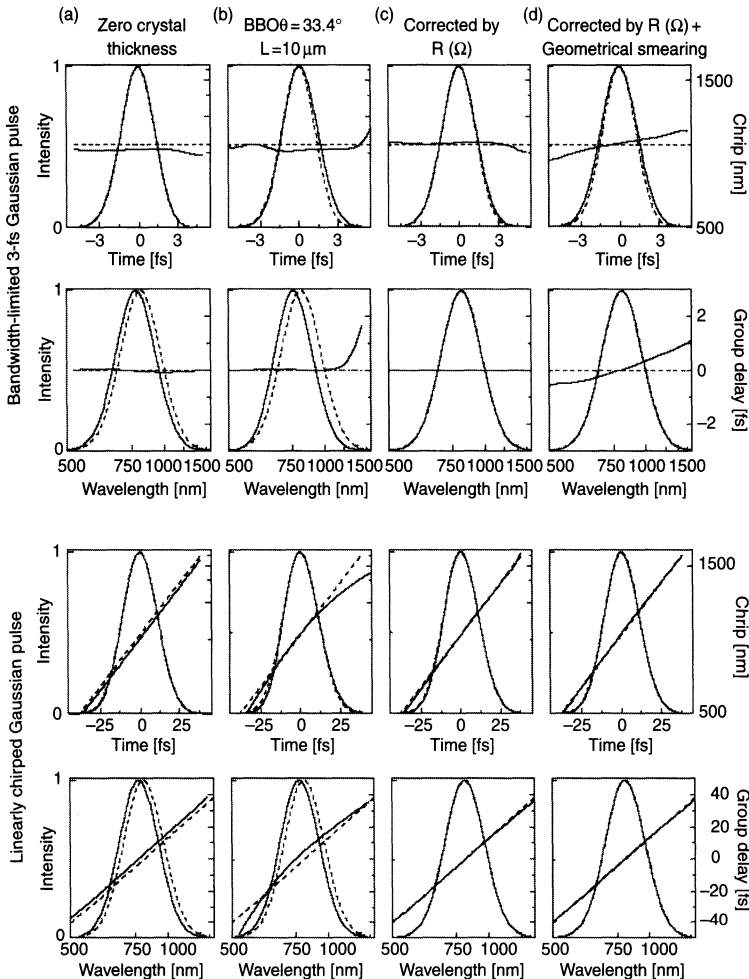


Fig. 14.5: Retrieved pulse parameters in the time and frequency domains for various simulated FROG traces. (a) perfectly phase-matched crystal, no geometrical smearing. (b) Type I 10- μm BBO crystal cut at $\Theta = 33.4^\circ$, no geometrical smearing. (c) same as in (b), the FROG trace is corrected according to Eq. (14.23). (d) same as in (c) but with the geometrical smearing included. Dashed curves correspond to initial fields, while solid curves are obtained by FROG retrieval.

The retrieved 3-fs pulse is also artificially lengthened to ~ 3.4 fs to match the bandwidth narrowed by the spectral filtering in the crystal. The results of FROG retrieval of the same trace upon the correction by $R(\Omega)$ (case (c)) indicate an excellent recovery of both the bandwidth-limited and the chirped pulses.

Finally, in case (d) the geometrical smearing had a negligible effect on the 26-fs pulse. However, the FROG retrieval of the shorter pulse converged to a linearly chirped 3.3-fs Gaussian pulse. This should be expected, since

the FROG trace broadens in time and remains Gaussian, while the spectral bandwidth is not affected. In principle, like the spectral correction $R(\Omega)$, correction for the temporal smearing should also be feasible. It can be implemented directly in the FROG inversion algorithm by temporal averaging of the guessed trace, produced in every iteration, prior to computing the FROG error.

Several important conclusions can be drawn from these simulations. First, they confirm the correctness of approximations used to obtain Eqs. (14.21–14.23). Therefore, the spectral correction given by $R(\Omega)$ is satisfactory even in the case of single-cycle pulses, provided the crystal length and orientation permits maintaining a certain, though not necessarily high, level of conversion over the entire bandwidth of the pulse. Second, geometrical time-smearing does not greatly affect the retrieved pulses if the experimental geometry is carefully chosen. Third, the unmodified version of the FROG algorithm can be readily applied even to the shortest pulses. Fourth, it is often possible to closely reproduce the pulse parameters by FROG-inversion of a spectrally filtered trace without any spectral correction [70]. However, such traces rather correspond to similar pulses shifted in frequency than to the original pulses for which they were obtained.

In order to quantify the distortions that are introduced into the SHG FROG traces by the phase-matching and the non-collinear geometry and that cannot be removed by the $R(\Omega)$ -correction, we compute the systematic error as rms average of the difference between the actual corrected FROG trace and the ideal trace. Given the form of the FROG error [21], the systematic error can be defined as follows:

$$G = \frac{1}{N} \sqrt{\sum_{i,j=1}^N \left| I_{\text{FROG}}^{\text{SHG}}(\Omega_i, \tau_j) - \mu \frac{I(\Omega_i, \tau_j, L)}{R(\Omega)} \right|^2} \quad (14.24)$$

where $I_{\text{FROG}}^{\text{SHG}}(\Omega, \tau)$ and $R(\Omega)$ are given by Eq. (14.22) and Eq. (14.23), and $I(\Omega, \tau, L)$ is computed according to Eq. (14.17). The parameter μ is a scaling factor necessary to obtain the lowest value of G . The dependence of G on the duration of a bandwidth-limited pulse for the 128×128 FROG matrix that has optimal sampling along the delay and frequency axes is presented in Fig. 14.6. As can be seen, the systematic error for $\sim 5\text{-fs}$ pulses becomes comparable with the typical achievable experimental SHG FROG error. It also should be noted, that the contribution of geometrical smearing is about equal to or higher than that due to the spectral distortions remaining after the spectral correction.

The systematic error should not be confused with the ultimate error achievable by the FROG inversion algorithm. Frequently, as, for instance, in the case of linearly-chirped Gaussian pulses measured in the presence of geometrical smearing, it means that the FROG trace continues to exactly correspond to a pulse, but to a different one. However, for an arbitrary pulse of $\sim 3\text{ fs}$

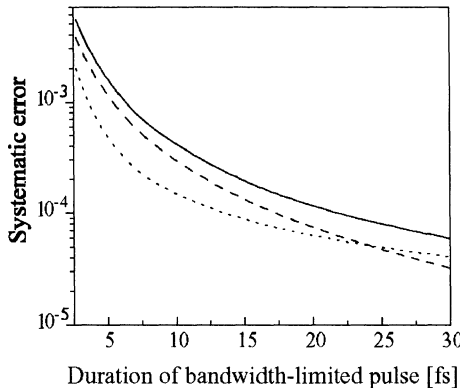


Fig. 14.6: Dependence of the systematic FROG trace error on the pulse duration. FROG matrix size is 128×128 . The dotted curve corresponds to the trace after the spectral correction given by Eq. (14.23). The error due to geometrical smearing of a perfectly phase-matched trace is shown as a dashed curve, while the error of a spectrally corrected and geometrically smeared FROG is given by the solid curve. The parameters of the crystal and of the geometrical smearing are the same as above. The central wavelength of the pulse is kept at 800 nm.

in duration it is likely that the FROG retrieval error will increase due to the systematic error.

Type II Phase Matching

So far, we've limited our consideration to Type I phase-matching. In this section we briefly discuss the use of Type II phase-matching to the measurement of ultrashort laser pulses.

In Type II the two fundamental wave polarizations are orthogonal, i.e. one ordinary and one extraordinary. This allows use of a collinear SHG FROG geometry, which is free of geometrical smearing [67,68]. The FROG traces generated in this arrangement don't contain optical fringes associated with the fringe-resolved autocorrelation (FRAC) and, therefore, can be processed using the existing SHG FROG algorithms.

However, the group velocities of the two fundamental pulses in a Type II crystal are typically quite different, a fact that has several important implications. First, the second-harmonic signal is no longer a symmetric function of the time delay [49]. Second, because the faster traveling fundamental pulse can catch up and pass the slower one, some broadening of the second-harmonic signal along the delay axis can occur [49].

In order to check the applicability of collinear Type II SHG FROG for conditions comparable to those discussed above for Type I phase matching, we describe numerical simulations identical to those in the previous section. The same pulses were used, i.e., the bandwidth-limited 3-fs pulse at 800 nm and the pulse with the same bandwidth stretched to 26 fs. The thickness of the

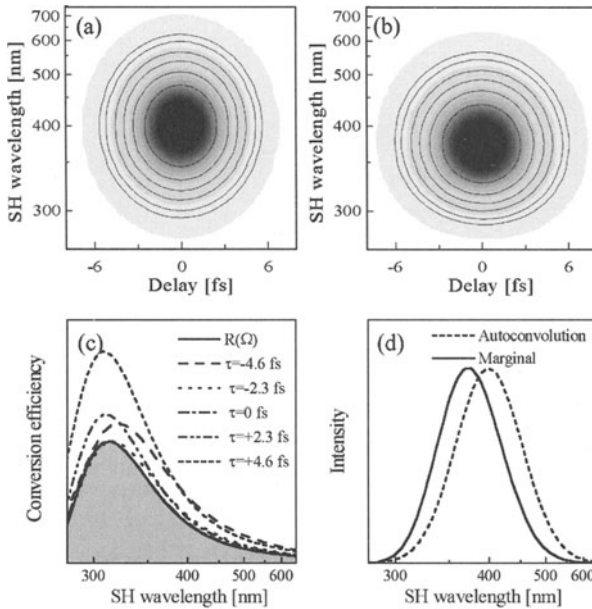


Fig. 14.7: Simulation of SHG FROG traces for an ideal 3-fs Gaussian pulse for Type II phase-matching. (a) ideal FROG trace, as given by Eq. (14.22). (b) complete FROG trace as given by Eq. (14.17). (c) spectral filter curve $R(\Omega)$ computed according to Eq. (14.23) (shaded contour) and the ratio of FROG traces given in (b) and (a) at several delays (broken curves). (d) spectral marginal of the traces shown in (b) (solid curve) and autoconvolution of the fundamental spectrum (dashed curve).

Type II BBO is $L = 10 \mu\text{m}$, and the crystal is oriented for peak conversion efficiency at 700 nm ($\Theta = 45^\circ$). The expression for the spectral filter, adapted for Type II, is given by:

$$R(\Omega) = Q(\Omega) \frac{\Omega^3}{n_E(\Omega)} \left[(n_E^2(\Omega) - 1) \left(n_O^2 \left(\frac{\Omega}{2} \right) - 1 \right) \left(n_E^2 \left(\frac{\Omega}{2} \right) - 1 \right) \right]^2 \times \text{sinc}^2 \left(\frac{\Delta k \left(\frac{\Omega}{2}, \frac{\Omega}{2} \right) L}{2} \right) \quad (14.25)$$

where the phase mismatch* is

$$\Delta k \left(\frac{\Omega}{2}, \frac{\Omega}{2} \right) = k_O \left(\frac{\Omega}{2} \right) + k_E \left(\frac{\Omega}{2} \right) - k_E(\Omega) \quad (14.26)$$

FROG simulations are shown in Figs. 14.7 and 14.8. The FROG trace of the 3-fs pulse (Fig. 14.7b) is practically symmetrical along the delay axis.

* Unlike in the case of Type I phase-matching, the first derivative terms do not cancel each other but they have been disregarded anyway.

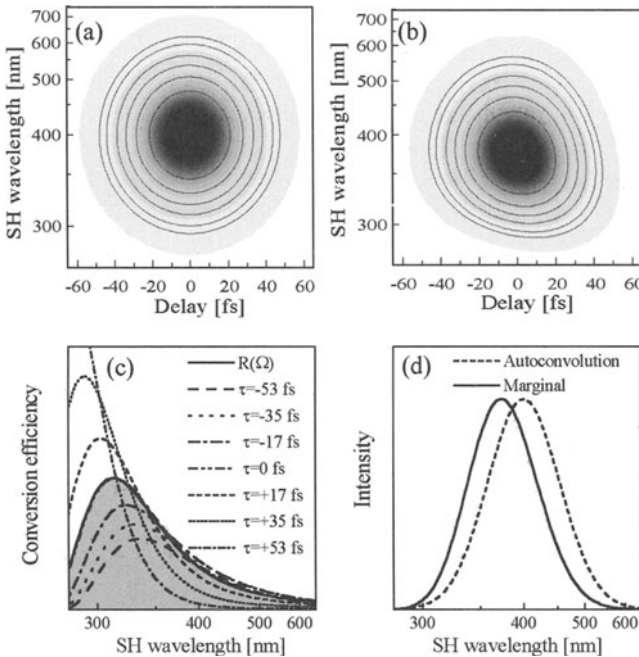


Fig. 14.8: Simulation of SHG FROG traces for a linearly-chirped 26-fs Gaussian pulse. The conditions are the same as in Fig. 14.7. (a) ideal FROG trace, as given by Eq. (14.22). (b) complete FROG trace as given by Eq. (14.17). (c) spectral filter curve $R(\Omega)$ computed according to Eq. (14.23) (shaded contour) and the ratio of FROG traces given in (b) and (a) at several delays (broken curves). (d) spectral marginal of the traces shown in (b) (solid curve) and autoconvolution of the fundamental spectrum (dashed curve). Note the skewness of the FROG trace in (b).

However, despite the lack of geometrical smearing, temporal walk-off has broadened it along the delay axis. Consequently, the FROG inversion of this trace after the spectral correction yields a longer ~ 3.3 -fs pulse.

The magnitude of this temporal distortion is similar to the geometrical smearing discussed in the previous section. The trace of the chirped pulse, produced under the same conditions (Fig. 14.7), is more severely distorted than that of the bandwidth-limited pulse. The straightforward use of this trace is not possible due to its strong asymmetry.

As in Type I, the conversion efficiency, obtained as a ratio of the ideal and simulated FROG traces, continues to correspond nicely the spectral filter $R(\Omega)$ (Figs. 14.7c and 14.8c, shaded contours) at near-zero delays. Conversion efficiency at other delays, however, sharply depends on the sign of the delay τ . Similar to Type I phase-matching, the frequency marginals (Figs. 14.7d and 14.8d) are substantially blue-shifted. It is also apparent from Figs. 14.7c and 14.8c that the phase-matching bandwidth in this case is somewhat broader than in the analogous Type I crystal.

We conclude that Type II SHG FROG offers no enhancement in temporal resolution and is actually less versatile than non-collinear Type I phase-matching for pulse measurement. Also, collinear Type II SHG FROG is experimentally more complex than Type I SHG FROG. However, for some applications such as confocal microscopy, where the implementation of a non-collinear geometry isn't practical due to the high numerical aperture of the focusing optics, the use of Type-II-based FROG is quite promising [67,68]. Recently, it has been demonstrated that Type II SHG FROG can successfully measure even sub-10-fs pulses, provided a relatively low-dispersion crystal (such as ADP) is used [69].

Spatial Filtering of the Second-Harmonic Beam

Earlier, we mentioned that transverse geometrical smearing in multi-shot FROG, although typically small already, can be further suppressed by placing a slit at the nonlinear medium or, better, by imaging the nonlinear medium onto a slit, such as the entrance slit of the spectrometer that the signal beam must enter anyway. It's easy to see that proper imaging of the signal beam from the nonlinear medium to the spectrometer entrance slit accomplishes two desirable feats simultaneously. First, it maps delay at the nonlinear medium, which varies transversely across the medium, to the plane of the slit with delay now varying across the slit. Closing down the slit thus removes the signal light from the outer regions (i.e., those with the smallest and largest delays and hence that deviate the most from the desired delay value), yielding a detected signal with a smaller range of delays and hence less geometrical smearing. Second, as is always true in imaging, *all signal beam angles* are collected at the slit.

These observations are important because another effect that occurs for very broadband and chirped pulses is that the signal beam angle can vary *during* the pulse for some values of the delay (see Fig. 14.9). If the red component of one beam coincides with the blue component of the other, the signal beam will tilt away from its mean direction. Fortunately, this in no way distorts the FROG trace if imaging onto a slit occurs. Indeed, this angular variation could be allowed to occur perpendicular to the dispersion plane of the spectrometer to avoid any slightly erroneous spectral measurements due to the varying spectrometer input beam angle.

If, due to poor experimental design, some cropping of the signal beam angle range occurs, distortions could occur. However, it should be emphasized that this should not occur in most geometries. And it is easy to actually see whether the signal beam is being cropped in practice.

Alternatively, use of a single-shot SHG FROG geometry, which uses the transverse geometrical delay variation to achieve single-shot performance and inherently involves such imaging, also nicely solves this problem. Indeed, single-shot SHG FROG also naturally restricts all angular variations in the

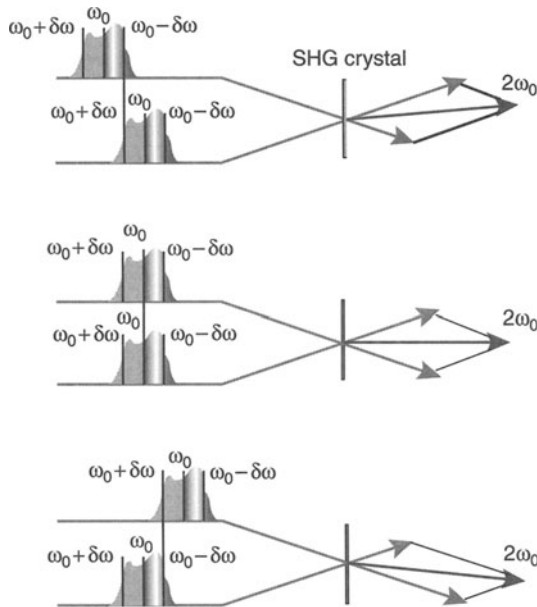


Fig. 14.9: Delay-dependent change of the second-harmonic direction in the case of a chirped pulse.

signal beam to the plane perpendicular to the spectrometer's resolution, conveniently avoiding potential errors in the required spectral measurements.

Third-Order FROG Characterization of Near-Single-Cycle Pulses

In this section, we'll analyze the class of FROG techniques that use third-order optical nonlinearities. We'll consider the same issues that we did for SHG FROG. However, the extra of input field in a $\chi^{(3)}$ -based FROG measurement inevitably involves greater complexity of the formalism and a greater number of experimental parameters, so careful optimization is necessary.

The Formalism

We consider a non-collinear geometry in which three beams $E_i(z, t)$ ($i = 1 - 3$) intersect at small angles in a nonlinear medium (Fig. 14.10). The corresponding geometries for two third-order geometries are shown in Figs. 14.10b and 14.10c. The self-diffraction (SD, Fig. 14.10b) and transient grating (TG, Fig. 14.10c) signals are equivalent to the two- and three-pulse stimulated photon-echo signals originating from the systems with phase memory—common spectroscopic experiments that would potentially be modified to

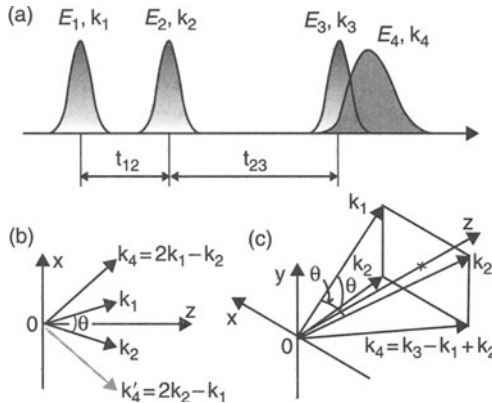


Fig. 14.10: (a) Schematic representation of the pulse sequence in a three-pulse nonlinear spectroscopic experiment. $E_{1,2,3}$ are the input fields, and E_4 is the signal due to the third-order nonlinear process. t_{12} and t_{23} are the delay between pulses $E_1 - E_2$ and $E_2 - E_3$, respectively. (b) Self-diffraction (two-pulse photon echo) configuration. Two conjugated signal are emitted in the directions k_4 and k'_4 . (c) Transient grating in a “box” geometry.

yield FROG apparatuses that measure the pulse at the sample medium, as discussed in Chapter 11.

As before, the focusing conditions of the beams are chosen with the confocal parameter [54] and the longitudinal beam overlap considerably longer than the interaction length. We also neglect absorption in the nonlinear medium and assume a purely third-order nonlinear response. The input beams then induce a third-order nonlinear polarization $P^{(3)}(z, t)$ that serves as a source for the signal field $E_4(z, t)$. The approach used here is similar to our treatment of the second-order nonlinear polarization (see Eqs. 14.2–14.9). Analogously to the derivation of Eqs. 14.7 and 14.9, for both $P^{(3)}(z, t)$ and $E_4(z, t)$ written as a Fourier superposition of monochromatic waves, we obtain:

$$\tilde{E}_4(L, \Omega) = i \frac{c\mu_0\Omega}{2n_4(\Omega)} \int_0^L \tilde{\mathcal{P}}^{(3)}(z, \Omega) \exp(-ik_{4z}(\Omega)z) dz \quad (14.27)$$

where $n_4(\Omega)$ is the refractive index for the signal wave and L is the thickness of the nonlinear medium.

In order to calculate the third-order dielectric polarization induced at frequency Ω by the fundamental fields, we must sum over all possible permutations of fundamental frequencies weighted according to the third-order

susceptibility [78]:

$$\begin{aligned} \tilde{P}^{(3)}(z, \Omega) = & \iint d\omega' d\omega'' \tilde{\chi}^{(3)}(\omega_{eg} - \omega', \omega' - \omega'', -\omega_{eg} + \Omega) \tilde{E}_1^*(z, \omega') \\ & \times \tilde{E}_2(z, \omega'') \tilde{E}_3(z, \Omega - \omega'' + \omega') \\ & \times \exp[i(-k_{1z}(\omega') + k_{2z}(\omega'') + k_{3z}(\Omega - \omega'' + \omega'))z] \\ & \times \exp[-i\omega''t_{12} - i(\Omega - \omega'' + \omega')(t_{12} + t_{23})] \end{aligned} \quad (14.28)$$

where $\tilde{E}_i(z, \omega')$ is the Fourier transform of $E_i(z, t)$. Analogously to Eq. (14.3), the phase accumulated as the result of linear propagation is separated into a separate oscillating term. In Eq. (14.28), t_{12} and t_{23} are the delays between pulses E_1 and E_2 , and between E_2 and E_3 , respectively. In the SD case (Fig. 14.10b) t_{23} is set to zero, and t_{12} is scanned, while in the TG experiment (Fig. 14.10c) $t_{12} = 0$ and t_{23} is scanned. Representation of the frequency-dependent third-order nonlinear susceptibility, $\tilde{\chi}^{(3)}(\omega_{eg} - \omega', \omega' - \omega'', -\omega_{eg} + \Omega)$, is based on the interaction of the input fields with an electronic transition with the frequency ω_{eg} . The inclusion of the third-order susceptibility due to Raman and two-photon processes is also straightforward.

To calculate the signal field, one should integrate the signal intensity over the longitudinal coordinate z according to Eq. (14.27). This can be performed analytically in the case of a nonlinear process with a low efficiency ($E_{1,2,3} = \text{const}$):

$$\begin{aligned} \tilde{E}_4(\Omega, t_{12}, t_{23}) = & i \frac{c\mu_0\Omega L}{2n_4(\Omega)} \iint d\omega' d\omega'' \tilde{\chi}^{(3)}(\omega_{eg} - \omega', \omega' - \omega'', -\omega_{eg} + \Omega) \\ & \times \tilde{E}_1^*(\omega') \tilde{E}_2(\omega'') \tilde{E}_3(\Omega - \omega'' + \omega') \operatorname{sinc}\left(\Delta k_z(\Omega, \omega', \omega'') \frac{L}{2}\right) \\ & \times \exp\left[i\Delta k_z(\Omega, \omega', \omega'') \frac{L}{2} - i\omega''t_{12} - i(\Omega - \omega'' + \omega')(t_{12} + t_{23})\right] \end{aligned} \quad (14.29)$$

The phase mismatch

$$\Delta k_z(\Omega, \omega', \omega'') = -k_{1z}(\omega') + k_{2z}(\omega'') + k_{3z}(\Omega - \omega'' + \omega') - k_{4z}(\Omega) \quad (14.30)$$

must be calculated for each geometry in Fig. 14.10b and c.

The FROG trace registered by a quadratic detector is written as

$$I_{\text{FROG}}^{(3)}(\Omega, t_{12}, t_{23}) = \varepsilon_0 \frac{n_4(\Omega)\mathcal{Q}(\Omega)}{c} \left| \tilde{E}_4(\Omega, t_{12}, t_{23}) \right|^2 \quad (14.31)$$

where $Q(\Omega)$ is the spectral sensitivity of the monochromator–detector combination. To obtain a FROG trace, one of the two delay arguments in Eq. (14.31) should be set to zero. $t_{12} = 0$ corresponds to a PG FROG trace, and $t_{23} = 0$ to an SD FROG trace.

Equation (14.29), which constitutes the basis of the numerical simulations presented below, is the master equation, valid even for single-cycle optical pulses. Analogously to the case of SHG FROG (see Eq. (14.17)), the frequency representation allows us to include in a self-consistent way dispersive broadening of interacting pulses and the frequency-dependence of the nonlinear susceptibility. In addition, we avoid the introduction of the carrier frequency [79] the definition of which actually becomes confusing for a few-cycle pulses! We also draw attention to the Ω term in front of the integral, which follows directly from Maxwell's equations and reflects the fact that higher frequencies are generated more efficiently. It is this term that is responsible for the effect of self-steepening of the pulses propagating in optical fibers [61].

Ultimate Temporal Resolution of SD and TG Experiments

In this section, we address transverse geometrical delay smearing in third-order FROG geometries. As in our previous treatment of this effect for multi-shot SHG FROG, we evaluate the role of transverse geometrical smearing on the widths of SD and TG FROG traces.

We should point out that *single-shot* third-order FROG geometries, like single-shot SHG FROG, deliberately use a large beam angle and spatially resolve the signal beam vs. the transverse co-ordinate, x , and hence turn geometrical delay smearing into a beneficial technique. Thus, as discussed in Chapter 7, single-shot third-order geometries also are immune to transverse geometrical smearing. They are, however, potentially prone to *longitudinal* geometrical smearing, in which the delay varies *along* the signal beam (the z -direction) because the signal beam propagates along a direction other than the bisector of the input beams. Fortunately, for the extremely thin samples considered for single-cycle pulses, this effect is also negligible. Recalling that the longitudinal geometrical smearing time (see Chapter 7) is given by $\Delta\tau_{\text{long}} \approx L\theta^2/2c$, which for $\theta = 1^\circ$ and $L = 10\mu\text{m}$, is only 4 attoseconds. Thus, as in single-shot SHG FROG, all geometrical-smearing effects in single-shot third-order FROG measurements are negligible or non-existent. However, since multi-shot third-order measurements are common, we consider the transverse geometrical smearing.

For arbitrary pulses and beam profiles, the shapes of the resulting traces should be computed numerically by integrating Eq. (14.31) over each transverse component of the beam. For linearly chirped Gaussian pulses with a Gaussian spatial profile, however, these traces can be calculated analytically. Assuming that the nonlinear response of the medium is instantaneous (i.e. $\tilde{\chi}^{(3)} = \text{const}$) and $\Delta k = 0$, we can obtain the width of the ideal SD or TG

traces from the conventional expression [22]:

$$I_{\text{FROG}}^{(3)\text{ideal}}(\Omega, t_{12}, t_{23}) = \left| \iint d\omega' d\omega'' \tilde{\mathbf{E}}_1^*(z, \omega') \tilde{\mathbf{E}}_2(z, \omega'') \tilde{\mathbf{E}}_3(z, \Omega - \omega'' + \omega') \right. \\ \times \exp(-i\omega''t_{12} + i(\omega'' - \omega')(t_{12} + t_{23})) \left. \right|^2 \quad (14.32)$$

For a Gaussian pulse, the SD or TG FROG trace given by Eq. (14.32) also has a Gaussian intensity profile in time, whose width, τ_0 , is a factor of $\sqrt{3}/2$ broader than the pulse duration. Similarly to Eq. (14.18), the width of the actual signal, τ_{meas} , which has been stretched by geometrical smearing, can be expressed by

$$\tau_{\text{meas}}^2 = \tau_0^2 + \beta \Delta\tau^2 \quad (14.33)$$

where β is a scaling constant dependent on the employed beam geometry, and $\Delta\tau$ is the effective delay smearing given by Eq. 14.19.

As we found for SHG FROG, the lowest value of $\Delta\tau$ occurs for Gaussian pulses and beams, where it amounts to 0.4 fs if the central wavelength of the pulse is 800 nm and increases for the beam profiles other than Gaussian.

For SD FROG, $\beta = 4/3$, while for TG FROG in the “box” beam arrangement $\beta \approx 5/3$. The influence of geometrical smearing on the width of the trace observed in these two measurement configurations is illustrated in Fig. 14.11. Note that the temporal resolution of SD FROG is somewhat higher than that of TG FROG. This is explained by the fact that the smearing in the case of TG FROG takes place in the xz and yz planes (Fig. 14.10c) simultaneously. In any case, for intersection angles smaller than 10° , the lengthening of the detected signal is less than 10%.

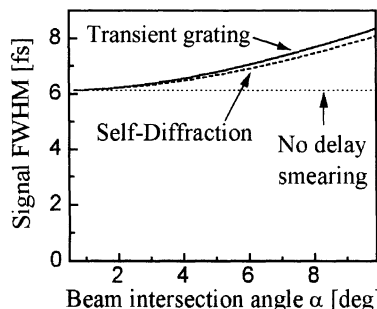


Fig. 14.11: Geometrical smearing of transient grating and self-diffraction traces as a function of beam intersection angle. The temporal widths of the observed signals are shown by solid and dashed curves for transient grating and self-diffraction FROG, respectively. The duration of the assumed ideal Gaussian pulse is 5 fs and the nonlinear response is assumed instantaneous. The focal length of the focusing optics is 125 mm and the FWHM of the input collimated Gaussian beams is 2 mm.

Therefore, the effect of geometrical smearing on the generated signals is insignificant even for experiments with pulses as short as 5 fs, provided the intersection angle is kept sufficiently small and the beams are properly focused.

Calculation of the Spectral Filter for SD and TG

We now demonstrate the practical value of our formalism to the calculation of the spectral filter and optimization of the SD and TG experimental parameters. As a model situation, we consider the measurement of a 5-fs pulse around 800 nm using a *thin jet of water*. The conditions are taken to simulate our recent photon-echo experiments on the hydrated electron [52]. Since the electronic hyper-polarizability [80–82] heavily dominates the overall water response [83,84], it is reasonable to treat the nonlinearity as nearly instantaneous on the time scale of 5-fs pulses. This amounts to treating $\tilde{\chi}^{(3)}$ as a constant. To further simulate the experimental conditions, we include in the calculation of the complete SD and TG traces the dispersive properties of a 100- μm layer of water [85,86] and the impact of the non-collinear beam geometry on the phase-mismatch given by Eq. (14.30). The small thickness of the medium is crucial to prevent dispersive broadening of the pulse inside the jet. The lengthening of a 5-fs 800-nm pulse caused by a 100- μm layer of water is less than 0.1 fs and, therefore, is negligible.

The ideal frequency-resolved traces were calculated according to Eq. (14.32), while the complete TG and SD traces were produced by using Eqs. (14.29–14.31). The comparison of the respective complete and ideal signals provides us with information on the spectral filter effect, that is, a combined influence of the spectral variations in the generation efficiency of the signal field and in its detection. The spectral filters for the SD and TG cases, obtained as the ratios of the respective complete vs. ideal signals, are presented in Fig. 14.12. The dashed and dotted curves correspond to TG and SD, respectively, for the case of a flat spectral response of the detector ($Q(\Omega) = \text{const}$). Apparently, both spectral filters are dominated by the Ω^2 -dependence that originates from the Ω -term in Eq. (14.29). The curve representing the SD filter is somewhat steeper compared with the one in the TG case. This reflects the fact that the phase mismatch for SD is greater since SD is intrinsically a non-phase-matched geometry [22].

Taking into account a typical real spectral sensitivity of a silicon photodiode, $Q(\Omega)$ (dash-dotted curve in Fig. 14.12) results in the overall spectral filter for TG FROG depicted by the solid curve. Interestingly, the overall spectral filtering effect is nearly frequency-independent throughout most of the spectrum of a 5-fs pulse (shaded contour in Fig. 14.12) because the photo-detector sensitivity balances off the Ω^2 -dependence. Therefore, we can disregard the effect of spectral filtering when it's counterweighed by the proper choice of the spectral response of the detector. This is an important conclusion for the

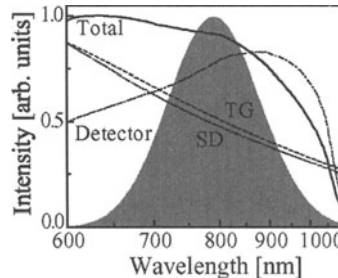


Fig. 14.12: Spectral filters for two configurations of photon-echo experiment in water. The shaded contour represents the spectrum of ideal 5-fs pulses. The spectral filter calculated for self-diffraction FROG is shown by a dotted line, and that for transient-grating FROG is shown by a dashed line. The dash-dotted line depicts the typical spectral sensitivity of a silicon light detector, $Q(\lambda)$. The spectral filter for transient grating FROG corrected by $Q(\lambda)$ is given by a solid curve. The thickness of the water layer is taken to be 100 μm , and the intersection angles of the beams are 4°. Note that the solid curve (the overall spectral filter in the TG case) is nearly flat in the wavelength region up to 900 nm because the photo-detector sensitivity balances off the more efficient generation of the nonlinear signal at higher frequencies.

practical purpose of nonlinear spectroscopy with 5-fs pulses because it allows the use of spectrally uncorrected TG and SD FROG signals.

Case study: Blue Pulse Characterization by Third-order FROG

Here we put the above results to work by addressing the problem of SD and TG FROG measurements of a blue pulse around 400 nm with an \sim 10-fs duration. This precise problem has recently been confronted experimentally in attempts to characterize tunable pulses around this wavelength generated in gas-filled hollow fibers [87,88]. The severity of the spectral filtering in this wavelength region is aggravated by the steeply rising bulk dispersion in both crystals and glasses because of the proximity of the resonance absorption lying in the UV. The spectral filter calculated for SD and TG measurement configurations in a BBO crystal and quartz (fused silica) is depicted in Fig. 14.13.

Here the frequency-dependant conversion efficiency is shown against the spectral content of the pulse. Compared with SD FROG, TG FROG (the dotted line) provides a much wider spectral window that is determined mainly by the self-steepening effect, i.e. more effective generation of blue spectral components. The broadening of the spectral window is a direct consequence of the “box” geometry used in TG FROG [22]. In the SD FROG case, the central frequency components are substantially suppressed while the wings are enhanced. The resulting broader spectrum corresponds to a shorter pulse. To illustrate this effect, Fig. 14.14 depicts an ideal SD FROG trace of an 11-fs pulse, calculated using conventional expression [22], and the full SD FROG trace calculated according to Eq. (14.29–14.31).

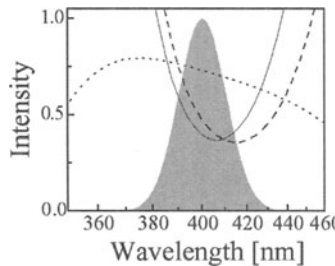


Fig. 14.13: Spectral filtering effect in SD and TG FROG techniques. As a nonlinear medium, a 100- μm thick slab of BBO (solid curve, SD) or fused silica (dashed curve, SD, and dotted curve, TG) is used. Angles between interacting beams are set at 4° . A spectrum of a 10-fs spectral-limited pulse is shown as a shaded contour for a comparison.

The ideal trace is tilted, indicating that the pulse is slightly chirped. However, the full SD FROG trace doesn't show this tilt. Moreover, the pulse retrieved from the full trace (Fig. 14.14c, solid curve) is noticeably shorter than its counterpart (Fig. 14.14c, dashed curve) recovered from the ideal trace. The same applies to SD autocorrelation traces (not shown), i.e. temporal marginals of the SD traces that would be measured without spectral resolution. This artificial temporal narrowing is mostly the result of phase-matching: signal spectral components with the same frequency, but generated from different frequency combinations of fundamental waves have different phase shifts and therefore can interfere constructively or destructively.

Thus, strong spectral filtering in a SD FROG measurement can distort the pulse shape and duration retrieved from the FROG trace. It is important to

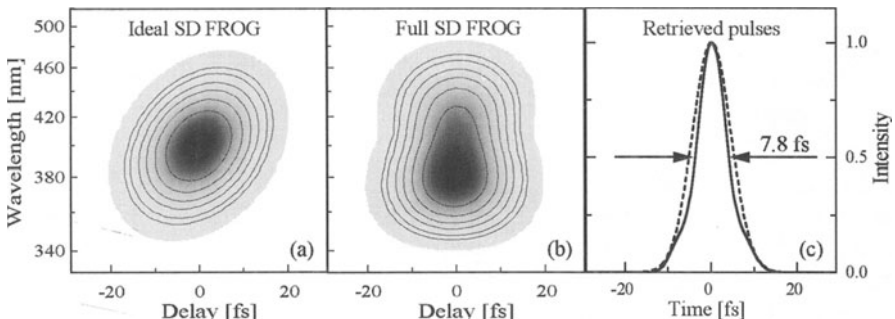


Fig. 14.14: (a) Ideal SD FROG trace of a slightly-chirped 11-fs pulse centered around 400 nm. (b): SD FROG trace of the same pulse calculated according to Eq. (14.28–14.30). (c): Temporal pulse intensities retrieved from ideal (dotted curve) and calculated (solid curve) SD FROG data, i.e. (a) and (b), respectively. A 100- μm BBO crystal is employed as a nonlinear medium. Angles between interacting beams are set at 4° . Note that the trace in (b) appears to belong to a chirp-free pulse.

take spectral-filtering into account by simply dividing the measured trace by this curve prior to running the FROG algorithm.

SHG FROG Characterization of Fiber-Compressed Pulses

In this section we put to work experimentally the various ideas we've discussed regarding the SHG FROG pulse characterization. We demonstrate the practical application of SHG FROG to strongly chirped ultrabroadband pulses and compressed 4.5-fs pulses from a cavity-dumped-laser-based white-light generator. Several practical implications for dealing with these extraordinarily broad bandwidths will be considered here. The basic experimental requirements for a broadband SHG FROG apparatus are adequate phase-matching bandwidth of the SHG crystal and low overall dispersion of the optical elements. Also, the device should be able to create two replicas of the pulse that do not differ from each other in their spectral content or phase.

In particular, the practical details of the SHG crystal in a FROG measurement are important. One reason is the usual SHG crystal conflict: a thick crystal is more efficient, but a thin crystal has greater phase-matching bandwidth. Another issue is the angular orientation of the crystal or the wavelength it's cut for. The difficulty here comes from the fact that a "red" crystal cut (a crystal cut for preferentially phase-matching the red wavelengths of the pulse) typically provides nearly flat frequency conversion efficiency over the most of the bandwidth of an ultrabroadband pulse. Such an orientation, however, dispenses with the blue-shifted wing of the spectrum where the conversion efficiency dramatically falls. On the other hand, use of a "blue" crystal-cut significantly lowers the frequency-conversion efficiency in the red wing of the spectrum. To find a reasonable balance that satisfies the demands of various pulses, we develop a useful criterion on crystal selection in this section. Finally, we compare the merits of the two most commonly used SHG crystals for FROG measurements, BBO and KDP.

We next focus our attention on details of the FROG apparatus and the peculiarities of the measurement of strongly chirped and nearly fully compressed laser pulses by this technique. The spectral phase of a white light pulse measured before and after a pulse compressor permits a good verification of the ray-tracing routine employed to design it. We then present valuable observations on how extra information about the level of pulse compression can be gained from a simple examination of the SHG FROG trace, which is normally considered quite unintuitive.

The Choice of the SHG Crystal

In this section, we provide several guidelines for selecting the correct SHG crystal for a FROG measurement. We use a simple criterion to determine the required crystal thickness: the conversion efficiency calculated according

to Eq. (14.23) must be $>50\%$ of the peak conversion efficiency over the entire FWHM of the FROG spectral marginal. For pulses that are Gaussian in frequency, the ideal spectral marginal (the autoconvolution of the fundamental spectrum) is $\sqrt{2}$ times broader than the pulse bandwidth. Using this criterion, we evaluated BBO and KDP crystals. For each crystal, we consider two different angle cuts: one for Type I phase-matching at the wavelength of 800 nm and the other for 600 nm. Figure 14.15 depicts the appropriate crystal thickness of the BBO (solid curve) and KDP (dashed curve) as a function of duration of a bandwidth-limited Gaussian pulse.

As can be seen from Fig. 14.15, an approximately 10- μm BBO should be used to measure 5-fs pulses at 800 nm. The thickness of the KDP crystal is approximately 2.5 times larger due to its lower dispersion. However, while clearly providing an advantage in thickness, the KDP crystal has a disadvantage in the SHG efficiency. The signal level that can be obtained with a 2.5 times thinner BBO crystal is still approximately a factor of 6 larger than in KDP due to the higher nonlinear coefficient and lower phase-matching angle in the BBO crystal [89]. Therefore, BBO is a more suitable choice for characterization of weak-intensity pulses. For high-intensity pulses, where the low level of the second-harmonic signal is not really the issue, KDP presents a better choice [70].

Once the phase-matching bandwidth is sufficiently flat, the Ω^3 dependence (see Eq. (14.23)) begins to dominate the conversion efficiency. This dependence blue-shifts the second-harmonic spectrum. If the phase-matching bandwidth of the SHG crystal exceeds that required by the pulse bandwidth, angle-tuning the crystal to the red can effectively counteract such a blue shift [70]. To illustrate the point, we consider a 10- μm BBO crystal for the purpose of measuring 8-fs Gaussian pulses at 800 nm. Figure 14.16a shows the blue-shift of the FROG spectral marginal (filled circles) with respect to the autoconvolution (solid curve) if the crystal is perfectly phase-matched at 800 nm, i.e. $\Theta = 29^\circ$. However, after adjusting the phase-matching angle

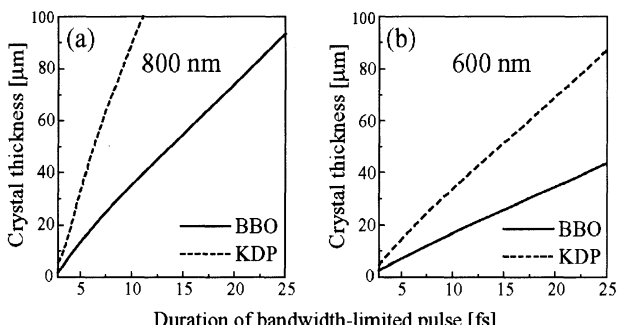


Fig. 14.15: Type I crystal thickness required for SHG FROG measurement as a function of the pulse duration at the central wavelength of 800 nm (a) and 600 nm (b). The crystals are cut at $\Theta = 29^\circ$ for BBO (solid line) and $\Theta = 44^\circ$ for KDP (dashed line).

to $\Theta = 24.4^\circ$ that now corresponds to the central wavelength of 970 nm (Fig. 14.16b), the phase-matching curve of the crystal (dashed curve) nearly perfectly balances the Ω^3 dependence (dotted curve). The overall conversion efficiency becomes almost flat, and no spectral correction of the FROG trace is required. Experimentally, Taft *et al.* [11] demonstrated the effectiveness of the angular adjustment that enabled them to yield correct FROG data.

The mutual compensation of the Ω^3 and phase-matching terms is only possible for relatively long (~ 10 fs) pulses. As a thinner crystal is chosen to measure shorter pulses, the high-frequency slope of the phase-matching curve grows steeper than the low-frequency one (Fig. 14.16c,d). This is to be expected, since crystal dispersion is low in the infrared but is high in the UV, near the UV absorption band. Tuning the central wavelength of the crystal from 800 nm (Fig. 14.16c) to 970 nm (Fig. 14.16d) substantially narrows the SH spectrum in the blue due to crystal phase-matching. Even worse, it becomes difficult to correct the FROG trace for the spectral filter because the conversion efficiency falls so low in the blue wing (Fig. 14.16d). This should be in contrast to the 800-nm-cut case when correction is still possible (see Fig. 14.5). Thus, to extend the phase matching-bandwidth in the blue, one should consider

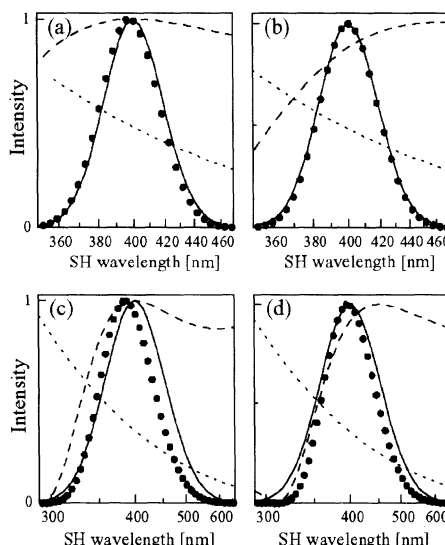


Fig. 14.16: Correction of frequency conversion efficiency by crystal orientation for 8-fs (a,b) and 3-fs (c,d) bandwidth-limited Gaussian pulses. A Type I 10- μm BBO crystal is oriented for the phase-matched wavelength of 800 nm (a,c) and 970 nm (b,d). The phase-matching curve and the Ω^3 dependence are shown as the dashed and dotted lines, respectively. The solid curves depict the autoconvolution of the fundamental spectra, while spectral margins of FROG traces are given by filled circles. In (b), no spectral correction of the FROG trace is required for an 8-fs pulse because of the red-shifted phase-matched wavelength. In contrast, the use of the 970-nm phase-matched crystal irreparably corrupts the second-harmonic spectrum in the case of a shorter 3-fs pulse (d). Note different horizontal scales in (a), (b) and (c), (d).

using a crystal with the phase-matching wavelength blue-shifted with respect to the central frequency of the pulse. For example, a $L = 10 \mu\text{m}$ BBO crystal oriented for peak conversion efficiency at 700 nm is more suitable for the measurement of sub-5-fs pulses centered at 800 nm than the same crystal tuned to 970 nm. Although the 700-nm-cut crystal has poorer conversion efficiency in the infrared, it, nonetheless, allows the extension to phase matching below 600 nm. Consequently, this crystal has an appreciable SHG efficiency over the entire spectrum of a 5-fs pulse and, therefore, spectral correction can yield an adequate FROG trace. In contrast, information about the blue spectral wing is lost if a crystal cut for 970 nm is used. We'll show how a poor choice of SHG crystal can affect the FROG recovery of a sub-5-fs pulse in the next section.

Before closing this section, we mention an interesting property of very thin crystals, i.e. those that have a thickness in order of a few microns. In such thin crystals the differentiation between the Type I (oo-e interaction) and Type II (eo-e interaction) becomes less strict. For instance, if we speak about a Type I 800-nm-cut crystal this means that the phase mismatch, Δk , for this wavelength is zero. However, if the thickness of the crystal, L , is very small then the product $\Delta k_{EO-E}L$, albeit never reaching a zero value, becomes comparable to the magnitude of $\Delta k_{OO-E}L$ for the wavelengths detuned from the phase-matching frequency. Therefore, we can no longer neglect the contribution to the SH signal produced by Type II interaction. Additionally, even for fundamental waves with a perfect linear polarization, the second harmonic beam, obtained in this case, becomes somewhat depolarized. This situation reciprocates for thin Type II crystals where the mixture of the oo-e contribution adds up to the total signal. This has far-reaching consequences. For instance, this means that in collinear Type II FROG experiments some fringes that are due to the interference of the SH waves, produced by each interacting fundamental wave, will always be present, no matter how perfectly orthogonal the polarizations of fundamental beams are kept. This property is considerably stronger for BBO than for KDP, for which no such effect occurs for the crystal thickness we've considered. Finally, we point out that the need to account for both Type I and Type II contributions applies only to sub-10- μm BBO crystals.

SHG FROG Apparatus

In our experiments, we used pulses from a self-mode-locked cavity-dumped Ti:Sapphire oscillator, which were then compressed after undergoing self-phase modulation in a single-mode fused silica fiber. We measured the amplitude and phase of the white-light continuum (WLC) directly at the fiber output and, again, upon the their compression [13].

Figure 14.17 shows a photograph of the all-solid-state sub-5-fs laser and the SHG FROG device. Unlike a conventional Ti:Sapphire oscillator, this cavity-dumped version incorporates an additional mirror fold around an acousto-optic modulator. In this way the intracavity pulse energy is stored in a relatively

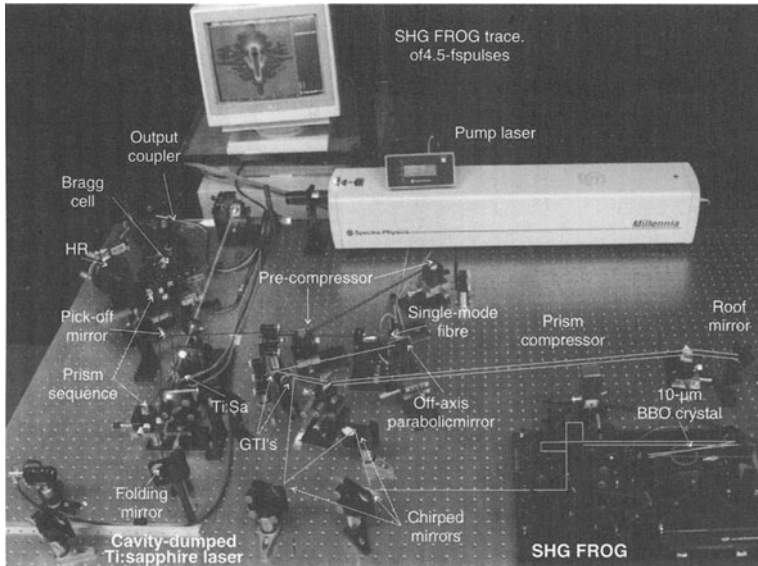


Fig. 14.17: The measurement of the 4.5-fs pulses by SHG FROG. Photo: Foppe de Haan.

high-Q cavity, which can be switched out of the resonator at any desired repetition rate. The maximal pulse energy of a cavity-dumped Ti:Sapphire laser is typically of factor of 10 higher than that of its non-cavity-dumped counterpart. A careful cavity design ensures that the Kerr-lens self-mode-locking is not disturbed by the extra fold and by the added dispersion due to the Bragg cell [90].

With ~ 4 W of the pump power (Spectra Physics Millennia), the cavity-dumped laser routinely produced ~ 13 fs, 40-nJ pulses at a 1-MHz repetition rate. Pre-compressed, these pulses had ~ 75 nm spectral bandwidth around 790 nm. They were launched into an ~ 2 -mm long piece of a single-mode polarization-preserving fiber (Newport, 2.75 μm core diameter) through an 18/0.35 microscope objective. The fiber output was collected by an off-axis paraboloidal mirror, which ensured achromatic beam recollimation. The optimal pulse energy for injection into the fiber was found to be ~ 35 nJ, as judged by the quality of the generated continuum. The continuum pulse energy measured after recollimation was about 18 nJ. The continuum was compressed by a prism-chirped-mirror Gires-Tournois-interferometer (GTI) pulse compressor. The overall size of the sub-5-fs laser system was $1\text{ m} \times 1.5\text{ m}$, which made it extremely robust and ensures excellent stability over time.

The SHG FROG apparatus (Fig. 14.18) was based on a phase and amplitude balanced multi-shot autocorrelator designed for sub-5-fs short pulses [13]. The input beam was split and recombined in such a way that each of the beams traveled once through an identical 50% beam splitter with both

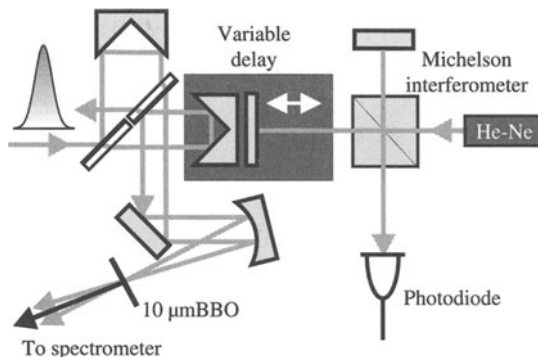


Fig. 14.18: Schematic of the SHG FROG apparatus. Spectrometer and its coupling optics are not shown.

reflections occurring on the same coating-air interfaces*. To match the beam splitters, the initial horizontal polarization of the laser beam was rotated by a periscope. The moving arm of the autocorrelator was driven by a piezo transducer (Physik Instrumente), which was controlled by a computer via a digital-analog converter and a high voltage amplifier. Because such short delay increments (~ 0.1 fs) were necessary, the precise time calibration was provided by an auxiliary Michelson interferometer. The photo-diode monitored the interference fringes that served as time calibration marks.

Fundamental pulses were focused in the nonlinear crystal with a spherical mirror (radius of curvature = -25 cm) at near-normal incidence to minimize astigmatism. Due to the low curvature of the mirrors, delay variations within each beam were less than 0.1 fs. To achieve up-conversion of the entire fundamental bandwidth, we used a $10\text{-}\mu\text{m}$ -thick BBO crystal cut for a central wavelength of 700 nm (EKSMA Inc.). Dispersive lengthening of a 5-fs pulse by such a crystal is less than 0.02 fs. The blue-shifted central wavelength permitted us to extend the phase-matching bandwidth below 600 nm as shown in Fig. 14.3c. The crystal cut angle was verified with a tunable 100-fs laser. Retro-reflection of the beams from the crystal surface provided exact reference for the crystal orientation. This enabled us to accurately calculate $R(\Omega)$ required for data correction according to Eq. (14.23). A visible-IR PC1000 (Ocean Optics) spectrometer was used to detect the fundamental spectra.

We used two different second-harmonic detection systems in these measurements of the compressed and uncompressed pulses. For the compressed pulses, we used a well-characterized UV-Vis PC1000 (Ocean Optics) spectrometer. Thus, the FROG traces could be readily corrected by $R(\Omega)$, as described above.

* For shorter pulses, one should use lower-reflectivity beam splitters that have a broader reflectivity range and flatter spectral phase.

For the strongly chirped pulses, a combination of a scanning monochromator and a photo-multiplier tube provided the dynamic range necessary to measure the spectral wings (see the next section). The reason for this was that the dynamic range of the measurement in a CCD-based spectrometer is determined not only by the spectral sensitivity, which is adequately high, but also by the charge spreading all over the array due to overload of some channels. To further extend the dynamic range, a lock-in amplifier was used to detect the second-harmonic signal. Because of the unknown spectral sensitivity $Q(\Omega)$, the spectral correction of the FROG traces in this case was performed according to the method suggested in Taft *et al.* [11], i.e., by using the ratio of the autoconvoluted fundamental spectrum and the spectral marginal (see Chapter 10).

SHG FROG of White-Light Continuum

Knowledge of the group delay, i.e., the spectral phase, of the chirped WLC is the key to its compression. The spectral-phase measurement of the pulses leaving the fiber allows us to assess the feasibility of pulse compression in general. The spectral phase must be sufficiently smooth to allow compensation by existing dispersion-control methods. A measurement of the spectral intensity, on the other hand, provides only a limited insight and reveals the minimum duration of the would-be compressed pulse. As an example of virtually uncompressible pulses, one might consider the case of spectral broadening due to a pure self-phase modulation. Furthermore, the task of building an appropriate pulse compressor is substantially simplified if the phase distortion of the pulse is measured beforehand. This becomes increasingly important with the growth of the pulse spectral bandwidth, which puts severe limitations on tunability of the pulse compressor. Therefore, it is desirable to replace most of the “trial and error” work by measuring the phase distortion and computing the settings of the pulse compressor.

Somewhat counter-intuitively, the FROG measurement of a strongly chirped pulse is considerably more complicated than that of a bandwidth-limited pulse with the identical spectrum. First, the up-conversion signals are weaker due to the lower peak power. This is evident, since the second harmonic intensity of a pulse that is stretched to the ten times its initial duration drops by a factor of 100.

Second, a higher dynamic range is required due to the pulse structure in the spectral wings. This occurs due to the high-order material dispersion. To explain this, we consider two spectral components with frequencies separated by 1000 cm^{-1} . The group delay accumulated between them after passing 1 mm of quartz amounts to 4 fs if these components are situated around 1000 nm and exceeds 11 fs in the case of 600 nm. So, roughly speaking, the corresponding elements of the FROG trace scale ~ 7 times in intensity. In our experiments, the bandwidth of the WLC that needs to be captured in the FROG trace is

broader than $10,000\text{ cm}^{-1}$, and, therefore, the signal intensity varies very strongly across the resultant FROG traces.

The third complication is purely numerical, since FROG inversion demands greater matrix sizes to provide the adequate sampling in both the time and frequency domains. For the sake of speed, the FROG inversion algorithms employ Fast Fourier Transform (FFT) routines [72]. To avoid the loss of information in the change from the time to the frequency domain and vice versa, the FFT requires an equal number of points N in both domains. Therefore, if the FROG matrix covers the total delay of $N\delta\tau$ in the time domain, where $\delta\tau$ is the delay step, the spectral range of the trace is $1/\delta\tau$. Compared with bandwidth-limited pulses, the pulses stretched in time require a larger $\delta\tau$ to contain the whole time information of the FROG trace in the matrix used in the FROG inversion algorithm. This narrows the spectral window covered by the matrix if N remains constant. Consequently, the number of points N , which in an FFT should be a power of two, must be increased to fully represent the FROG trace in the matrix used by the algorithm. This has an appreciable effect on the calculation speed. The change of N from 2^n to 2^{n+1} , where n is an integer number, slows the FROG retrieval by a factor of $4(1+n^{-1})$. In other words, by replacing a 128×128 matrix with a 256×256 one increases the calculation time by a factor of ~ 4.5 .

The SHG FROG traces of the chirped WLC in our experiments were recorded in 2.5-fs delay steps and converted into 256×256 matrices for processing. To reveal the conditions best suited for the compression of the WLC we varied the parameters of the pulses entering the fiber, by changing of the settings of the prism precompressor. The intensity and the chirp of the input pulses, derived by SHG FROG, are shown in Fig. 14.19a. The measured and retrieved FROG traces of the WLC are depicted in Figs. 14.19c and d, and the retrieved WLC spectra and the group delay are shown in Fig. 14.20b. The combined action of self-phase modulation and dispersion leads to a nearly linear group delay over most of the spectrum (Fig. 14.19b, solid curves).

The departure of the overall group delay from a linear asymptote can be partly explained by the bulk dispersion of the fiber, air, and the beam-splitters in the FROG apparatus. For instance, while the optimal fiber length was estimated to be 1 mm [12], we used a longer piece for practical convenience and to improve the exiting mode structure.

The WLC spectrum changes dramatically with the change of the input pulses (Fig. 14.19b, shaded contours). The widest and least modulated spectrum corresponds to the almost chirp-free input pulse (Fig. 14.19b, the third from the top panel). Positive as well as negative chirping leads to a substantial narrowing of the WLC spectrum. In contrast, the overall behavior of the group delays shown as solid lines in Fig. 14.19b, remains virtually unaffected. This ensures efficient pulse compression under different experimental conditions.

Group delay measurements of the generated continuum served as a target function for the design of the three-stage, high throughput compressor

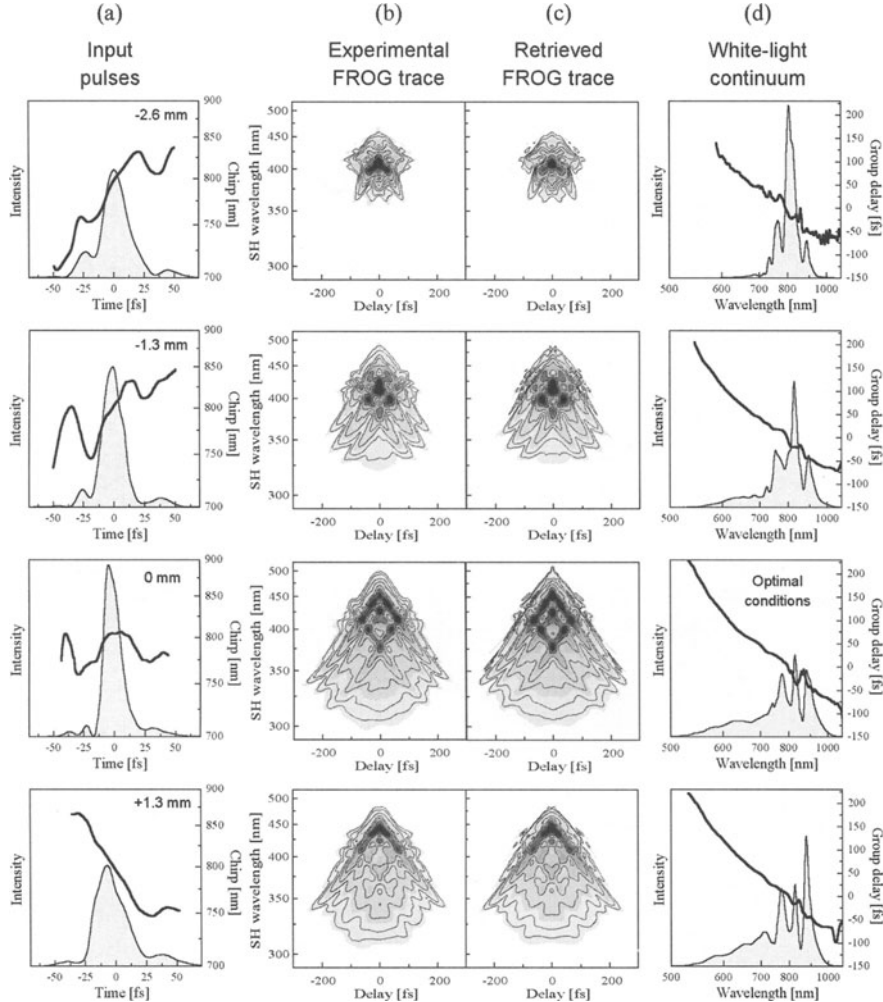


Fig. 14.19: Experimental results of FROG measurements of the strongly chirped white-light continuum (WLC). (a) temporal intensity (shaded contours) and chirp (solid curves) of the pulses entering a single-mode fused-silica fiber. (b) measured and (c) retrieved SHG FROG traces of the WLC. (d) retrieved spectral intensity (shaded contours) and the group delay of the WLC (solid curves) (solid curves). The amount of bulk material (fused silica) used to pre-chirp the input pulses is indicated in right top corners of (a). Note that the input pulse energy is kept constant, while the respective scaling of the WLC spectra in (d) is preserved.

(Fig. 14.17), consisting of a quartz 45°-prism pair, broadband chirped mirrors and thin-film Gires-Tournois dielectric interferometers [13]. The spectral bandwidth of the compressor was 590–1100 nm, which was limited by the reflectivity of the chirped mirrors involved [91]. The phase characteristics of the compressor were analyzed using dispersive ray tracing and were mapped

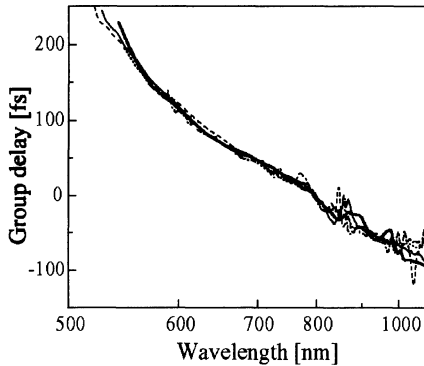


Fig. 14.20: Group delay of the designed pulse compressor. Solid curve was calculated by dispersive ray-tracing and is depicted reversed in time. Broken curves are the measured group delay of the WLC reproduced from panels in Fig. 14.19d.

onto the measured group delay of the continuum. Figure 14.20 depicts the measured group delay for different pulses, entering the fiber (shown as broken curves), which were reproduced from Fig. 14.19d and the calculated group delay of the pulse compressor (solid line). As you can see, our design compensates the group delay of the white light everywhere across the compressor bandwidth. Adjusting the length of material of the prism-pair (by translating a prism into or out of the beam) allows final fine-tuning of the compressor dispersion, as judged from the FROG trace of the compressed pulses.

SHG FROG of Compressed Pulses

FROG traces of the compressed pulses were recorded by scanning the delay between the arms in steps of 0.5 fs. The acquired two-dimensional arrays of points were converted into a 128×128 FROG matrix. The experimental and retrieved FROG traces of compressed pulses are depicted in Figs. 14.21a and b. The FROG error amounted to 0.004 and is mainly caused by the noise in the spectral wings, which increased when the spectral correction of the FROG trace was performed.

The delay marginal of the measured FROG trace nicely corresponds to the independently measured intensity autocorrelation (Fig. 14.21c) obtained by detecting the un-spectrally-resolved second-harmonic signal beam. This suggests that no spatial filtering of the second-harmonic beam has taken place. Comparison of the FROG frequency marginal and the autoconvolution of the fundamental spectrum (Fig. 14.21d) indicates that no loss of spectral information has occurred and that the spectral-filter correction was correct.

Figure 14.22 shows the retrieved intensity and phase in the time and frequency domains. To remove the time direction ambiguity in the measurement of the compressed pulses, we performed an additional FROG measurement introducing a known amount of dispersion (a thin fused silica plate) in front of

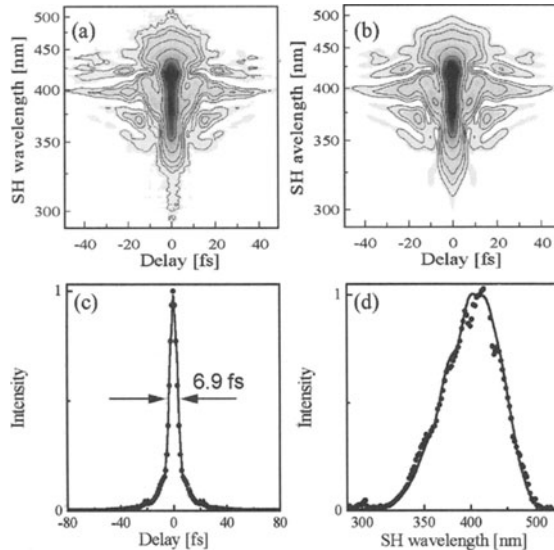


Fig. 14.21: The results of SHG FROG characterization of compressed pulses. (a) experimental and (b) retrieved traces. (c) temporal marginal (filled circles) and independently measured autocorrelation of 4.5-fs pulses (solid curve). (d) frequency marginal (filled circles) and autoconvolution of the fundamental spectrum (solid curve).

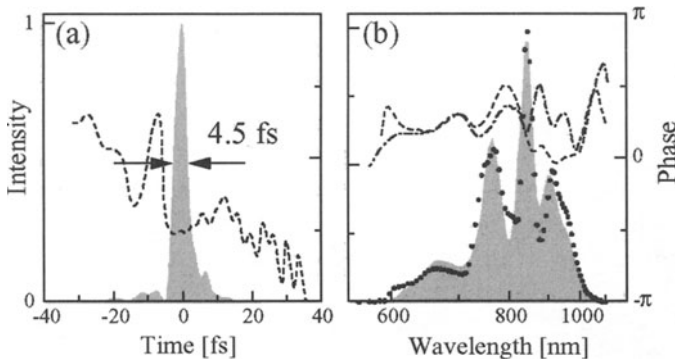


Fig. 14.22: Retrieved intensity and phase of 4.5-fs pulses in the time (a) and frequency (b) domains. The FROG-retrieved intensity and phase are shown as shaded contours and dashed curves, respectively. Independently measured spectrum (filled circles) and computed residual phase of the pulse compressor (dash-dotted curve) are given in (b) for comparison.

the FROG apparatus. The resulting pulse duration is 4.5 fs. Variations of the spectral phase (dashed line in Fig. 14.22b) are less than $\pm\pi/4$ across the whole bandwidth. These results fully confirm our previous analysis using the interferometric autocorrelation (which could not yield the pulse shape or phase) [13].

To additionally verify both the self-consistency of our compressor calculations and the accuracy of the FROG retrieval, we compare the retrieved spectral phase of the 4.5-fs pulse (Fig. 14.22b, dashed curve) with the predicted residual phase of the pulse compressor (Fig. 14.22b, dash-dotted curve). The close similarity of the two reassures us of the correctness of all the procedures we used, including the measurement of the chirped WLC, knowledge of the dispersion of compressor constituent parts, the numerical routines employed for the ray tracing analysis, and, finally, the characterization of the compressed pulses.

SHG FROG traces are generally considered unintuitive due to their symmetry along the delay axis [20,22,42]. We found that for nearly bandwidth-limited pulses, we can significantly increase the amount of information available from mere visual inspection of the trace. To do so, consider every constant-frequency slice of the trace (each of which is a function of delay only). Now normalize each slice to unity at its peak. Effectively, the SHG FROG trace has become a series of normalized autocorrelations. For a pulse with an arbitrary spectrum and flat spectral phase, such a representation of the SHG FROG trace would give a streak of uniform thickness around zero delay. The result of such an operation applied to the FROG trace of the 4.5-fs pulse is presented in Fig. 14.23a. The variation of the thickness, that is, the width of autocorrelation at a given second-harmonic wavelength,* which can be seen in Fig. 14.24a, visually indicates any imperfect pulse compression without the need to run the FROG inversion algorithm.

Figure 14.23b shows two autocorrelation traces derived from the spectrogram in Fig. 14.23a at two separate wavelengths. The FWHM of the autocorrelation at 350 nm is merely 6 fs, indicative of a \sim 4-fs pulse duration. However, the autocorrelation at 470 nm is three times broader. Such a difference clearly illustrates the effect of the spectral filtering in the nonlinear crystal, as well as the detection of the autocorrelation width. This also underscores the importance of pulse characterization by frequency-resolved (e.g., FROG) rather than non-frequency-resolved (e.g., intensity autocorrelation) methods for such broadband pulses.

Finally, we note that the width of the autocorrelation traces, such as the ones shown in Fig. 14.23a, can be directly related to the instrument response of a spectroscopic experiment. For instance, the temporal resolution of a kinetic trace in a frequency-resolved pump-probe experiment [92,93] detected at 950 nm will be \sim 12 fs, albeit the weighted average pulse duration is 4.5 fs [94,95]. Therefore, the frequency-resolved measurement (as FROG) brings invaluable information even if the correct estimation of the pulse width could be achieved by other, simpler means, such as the autocorrelation measurement.

* Here we apply the term “autocorrelation” to a slice of a frequency-resolved autocorrelation of the pulse intensity purely for the sake of convenience. In an arbitrary case, such a slice in itself is not necessarily an autocorrelation function of any real non-negative distribution.

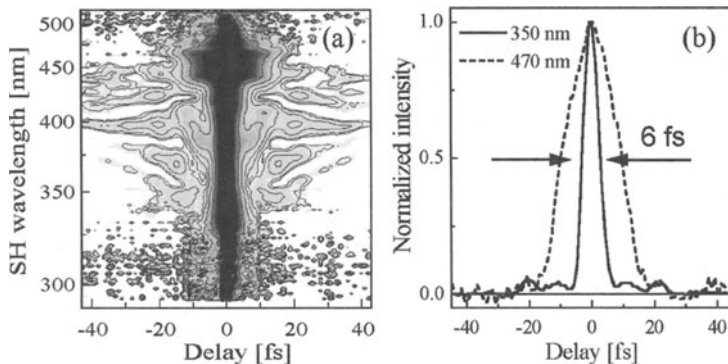


Fig. 14.23: Normalized FROG data of the 4.5-fs pulses. (a) SHG FROG trace of compressed pulses normalized along the delay axis as described in the text. (b) autocorrelation traces derived from the FROG trace at the second-harmonic wavelength of 350 nm (solid curve) and 470 (dashed curve). Note that because of spectral selection the pulse duration estimated from the autocorrelation width can be both lower and higher than the real one and differ by as much as a factor of 3.

Conclusions

FROG is a powerful and accurate pulse diagnostic, ideally suited for the measurement of a vast variety of pulses. In particular, the essentially instantaneous nonlinearity, high sensitivity, and broadband response allow the measurement of the shortest pulses available to date. FROG is currently probably the only available means to measure the parameters and the temporal resolution of pulses shorter than 5 fs in a nonlinear-spectroscopic experiment, i.e., in a useful application.

In this chapter, we've developed the theory of FROG in this regime and applied it to the SHG FROG measurement of 2.5-optical-cycle pulses with a central wavelength around 800 nm. To the best of our knowledge, these are the shortest pulses that have been completely characterized to date. We have also successfully measured uncompressed strongly non-transform-limited weak-intensity pulses. These two key measurements, which were required to design, test, and optimize the pulse compressor, were both performed without a single change in the SHG FROG apparatus. No other pulse measurement technique known allows such versatility.

References

1. J. Zhou, J. Peatross, M.M. Murnane, H.C. Kapteyn, and I.P. Christov, *Enhanced High-Harmonic Generation Using 25 fs Laser Pulses*, Phys. Rev. Lett. **76**(5), p. 752 (1996).
2. C.J. Bardeen, Q. Wang, and C.V. Shank, *Selective Excitation of Vibrational Wavepacket Motion Using Chirped Pulses*, Phys. Rev. Lett. **75**(19), p. 3410 (1995).
3. B. Kohler, V.V. Yakovlev, J. Che, J.L. Krause, M. Messina, K.R. Wilson, N. Schwentner, R.M. Whinnell, and Y. Yan, *Quantum Control of Wave Packet Evolution with Tailored Femtosecond Pulses*, Phys. Rev. Lett. **74**(17), p. 3360 (1995).

4. V.V. Yakovlev, C.J. Bardeen, J. Che, J. Cao, and K.R. Wilson, *Chirped pulse enhancement of multiphoton absorption in molecular iodine*, J. Chem. Phys. **108**(6), p. 2309 (1998).
5. M. Fetterman, D. Goswami, D. Keusters, J.-K. Rhee, X.-J. Zhang, and W.S. Warren, *Generation of amplified shaped pulses for highly adiabatic excitation*, in *XIth International Conference on Ultrafast Phenomena*. 1998. Garmisch-Parenkirchen, Germany, July 12–17: paper MoA3.
6. C.J. Bardeen, J. Che, K.R. Wilson, V.V. Yakovlev, P. Cong, B. Kohler, J.L. Krause, and M. Messina, *Quantum Control of Nal Photodissociation Reaction Product States by Ultrafast Tailored Light Pulses*, J. Phys. Chem. **101**(20), p. 3815 (1997).
7. A. Assion, T. Baumert, M. Bergt, T. Brixner, B. Kiefer, V. Seyfried, M. Strehle, and G. Gerber, *Control of Chemical Reactions by Feedback-Optimized Phase-Shaped Femtosecond Laser Pulses*, Science **282**, p. 919 (1998).
8. A. Assion, T. Baumert, M. Bergt, T. Brixner, B. Kiefer, V. Seyfried, M. Strehle, and G. Gerber, *Automated coherent control of chemical reactions and pulse compression by an evolutionary algorithm with feedback*, in *XIth International Conference on Ultrafast Phenomena*. 1998. Garmisch-Parenkirchen, Germany, July 12–17: postdeadline paper ThD9.
9. M. Bergt, T. Brixner, B. Kiefer, M. Strehle, and G. Gerber, *Controlling the Femtochemistry of Fe(CO)5*, J. Chem. Phys. **103**(49), p. 10381 (1999).
10. G. Taft, A. Rundquist, M.M. Murnane, and H.C. Kapteyn, *Ultrashort optical waveform measurement using frequency-resolved optical gating*, Opt. Lett. **20**(7), p. 743 (1995).
11. G. Taft, A. Rundquist, M.M. Murnane, I.P. Christov, H.C. Kapteyn, K.W. DeLong, D.N. Fittinghoff, M.A. Krumbügel, J. Sweetser, and R. Trebino, *Measurement of 10-fs pulses*, IEEE J. Select. Topics in Quantum Electron. **2**(3), p. 575 (1996).
12. A. Baltuška, Z. Wei, M.S. Pshenichnikov, and D.A. Wiersma, *Optical pulse compression to 5 fs at a 1-MHz repetition rate*, Opt. Lett. **22**(2), p. 102 (1997).
13. A. Baltuška, Z. Wei, M.S. Pshenichnikov, D.A. Wiersma, and R. Szipočs, *All-solid-state cavity-dumped sub-5-fs laser*, Appl. Phys. B **65**(2), p. 175 (1997).
14. M. Nisoli, S.D. Silvestri, R. Szipočs, K. Ferencz, C. Spielmann, S. Sartania, and F. Krausz, *Compression of high-energy laser pulses below 5 fs*, Opt. Lett. **22**(8), p. 522 (1997).
15. M. Nisoli, S. Stagira, S.D. Silvestri, O. Svelto, S. Sartania, Z. Cheng, M. Lenzner, C. Spielmann, and F. Krausz, *A novel-high energy pulse compression system: Generation of multigigawatt sub-5-fs pulses*, Appl. Phys. B **65**, p. 189 (1997).
16. D.J. Kane and R. Trebino, *Characterization of arbitrary femtosecond pulses using frequency-resolved optical gating*, IEEE J. Quantum Electron. **29**(2), p. 571 (1993).
17. R. Trebino and D.J. Kane, *Using phase-retrieval to measure the intensity and phase of ultrashort pulses: frequency-resolved optical gating*, J. Opt. Soc. Am. **10**(5), p. 1101 (1993).
18. E.B. Treacy, *Measurement and interpretation of dynamic spectrograms of picosecond light pulses*, J. Appl. Phys. **42**(10), p. 3848 (1971).
19. D.N. Fittinghoff, K.W. DeLong, R. Trebino, and C.L. Ladera, *Noise sensitivity in frequency-resolved optical-gating measurements of ultrashort pulses*, J. Opt. Soc. Am. B **12**(10), p. 1955 (1995).
20. K.W. DeLong, R. Trebino, and D.J. Kane, *Comparison of ultrashort-pulse frequency-resolved-optical-gating traces for three common beam geometries*, J. Opt. Soc. Am. B **11**(9), p. 1595 (1994).
21. K.W. DeLong, D.N. Fittinghoff, and R. Trebino, *Practical Issues in Ultrashort-Laser-Pulse Measurement Using Frequency-Resolved Optical Gating*, IEEE J. Quantum Electron **32**(7), p. 1253 (1996).
22. R. Trebino, K.W. DeLong, D.N. Fittinghoff, J. Sweetser, M.A. Krumbügel, B. Richman, and D.J. Kane, *Measuring ultrashort laser pulses in the time-frequency domain using frequency-resolved optical gating*, Rev. Sci. Instrum. **68**(9), p. 3277 (1997).
23. J.-K. Rhee, T.S. Sosnowski, A.-C. Tien, and T.B. Norris, *Real-time dispersion analyzer of femtosecond laser pulses with use of a spectrally and temporally resolved up-conversion technique*, J. Opt. Soc. Am. **13**(8), p. 1780 (1996).
24. J.-P. Foing, J.-P. Likforman, M. Joffre, and A. Migus, *Femtosecond pulse phase measurement by spectrally resolved up-conversion: application to continuum compression*, IEEE J. Quantum. Electron. **QE-28**(10), p. 2285 (1992).
25. C. Iaconis and I.A. Walmsley, *Spectral phase interferometry for direct electric-field reconstruction of ultrashort optical pulses*, Opt. Lett. **23**(10), p. 792 (1998).
26. I.A. Walmsley and V. Wong, *Characterization of the electric field of ultrashort optical pulses*, J. Opt. Soc. Am. B **13**(11), p. 2453 (1996).
27. V. Wong and I.A. Walmsley, *Ultrashort-pulse characterization from dynamic spectrograms by iterative phase retrieval*, J. Opt. Soc. Am. **14**(4), p. 944 (1997).

28. L. Gallmann, D.H. Sutter, N. Matuschek, G. Steinmeyer, and U. Keller, *Characterization of sub-6-fs pulses with spectral phase interferometry for direct electric-field reconstruction*, Opt. Lett. **24**(18), p. 1314 (1999).
29. C. Dorrer, *Influence of the calibration of the detector on spectral interferometry*, J. Opt. Soc. Am B **16**(7), p. 1160 (1999).
30. C. Dorrer, B.d. Beauvoir, C.L. Blanc, S. Ranc, J.-P. Rousseau, P. Rousseau, J.-P. Chambaret, and F. Salin, *Single-shot real-time characterization of chirped-pulse amplification systems by spectral phase interferometry for direct electric-field reconstruction*, Opt. Lett. **24**(22), p. 1644 (1999).
31. C. Dorrer, *Implementation of spectral phase interferometry for direct electric-field reconstruction with a simultaneously recorded reference interferogram*, Opt. Lett. **24**(21), p. 1532 (1999).
32. C. Iaconis and I.A. Walmsley, *Self-referencing spectral interferometry for measuring ultrashort optical pulses*, IEEE J. Quantum. Elec. **35**(4), p. 501 (1999).
33. M.S. Pshenichnikov, K. Duppen, and D.A. Wiersma, *Time-resolved femtosecond photon echo probes bimodal solvent dynamics*, Phys. Rev. Lett. **74**(5), p. 674 (1995).
34. P. Vöhringer, D.C. Arnett, T.-S. Yang, and N.F. Scherer, *Time-gated photon echo spectroscopy in liquids*, Chem. Phys. Lett. **237**(5–6), p. 387 (1995).
35. T. Steffen and K. Duppen, *Time resolved four- and six-wave mixing in liquids. II. Experiments*, J. Chem. Phys. **106**(10), p. 3854 (1997).
36. A. Tokmakoff and G.R. Fleming, *Two-dimensional Raman spectroscopy of the intermolecular modes of liquid CS₂*, J. Chem. Phys. **106**(7), p. 2569 (1997).
37. A. Tokmakoff, M.J. Lang, D.S. Larsen, G.R. Fleming, V. Chernyak, and S. Mukamel, *Two-Dimensional Raman Spectroscopy of Vibrational Interactions in Liquids*, Phys. Rev. Lett. **79**(14), p. 2702 (1997).
38. K. Tominaga and K. Yoshihara, *Fifth Order Optical Response of Liquid CS₂ Observed by Ultrafast Nonresonant Six-Wave Mixing*, Phys. Rev. Lett. **74**(15), p. 3061 (1995).
39. W.P.d. Boeij, M.S. Pshenichnikov, and D.A. Wiersma, *Ultrafast solvation dynamics explored by femtosecond photon echo spectroscopies*, in *Ann. Rev. Phys. Chem.* 1998, p. 99.
40. A. Shirakawa, I. Sakane, and T. Kobayashi, *Sub-5-fs pulse generation by pulse-front-matched optical parametric amplification*, in *XIth International Conference on Ultrafast Phenomena*. 1998. Garmisch-Partenkirchen, Germany, July 12–17, 1998: post-deadline paper ThD2.
41. K.W. DeLong, C.L. Ladera, R. Trebino, B. Kohler, and K.R. Wilson, *Ultrashort-pulse measurement using non-instantaneous nonlinearities: Raman effects in frequency-resolved optical gating*, Opt. Lett. **20**(5), p. 486 (1995).
42. K.W. DeLong, R. Trebino, J. Hunter, and W.E. White, *Frequency-resolved optical gating with the use of second-harmonic generation*, J. Opt. Soc. Am. B **11**(11), p. 2206 (1994).
43. J. Payne, M. Ramaswamy, J.G. Fujimoto, and E.P. Ippen, *Measurement of the amplitude and phase of ultrashort light pulses from spectrally resolved autocorrelation*, Opt. Lett. **18**(22), p. 1946 (1993).
44. J. Payne, *How to Measure the Amplitude and Phase of an Ultrashort Light Pulse with an Autocorrelator and a Spectrometer*, IEEE J. Quantum Electron. **30**(11), p. 2693 (1994).
45. T. Tsang, M.A. Krumbügel, K.W. DeLong, D.N. Fittinghoff, and R. Trebino, *Frequency-resolved optical gating measurements of ultrashort pulses using surface third-harmonic generation*, Opt. Lett. **21**(17), p. 1381 (1996).
46. K. Shimoda, *Introduction to laser physics*. 2nd ed. Optical Sciences, ed. A.L.S. D.L. MacAdam, K. Shimoda, A.E. Siegman, T. Tamir. 1991, Berlin: Springer-Verlag.
47. L. Allen and J.H. Eberly, *Optical resonance and two-level atoms*. 1987, New York: Dover Publications, Inc.
48. P.N. Butcher and D. Cotter, *The elements of nonlinear optics*. 1990, Cambridge: Cambridge University Press.
49. A.M. Weiner, *Effect of group velocity mismatch on the measurement of ultrashort optical pulses via second harmonic generation*, IEEE J. Quantum Electron. **QE-19**(8), p. 1276 (1983).
50. G. Taft, A. Rundquist, M.M. Murnane, I.P. Christov, H.C. Kapteyn, K.W. DeLong, D.F. Fittinghoff, M.A. Krumbügel, J.N. Sweetser, and R. Trebino, *Measurement of 10-fs Laser Pulses*, IEEE J. Select. Topics Quantum Electr. **2**(3), p. 575 (1996).
51. A. Baltuška, M.S. Pshenichnikov, and D.A. Wiersma, *Second-Harmonic Generation Frequency-Resolved Optical Gating in the Single-Cycle Regime*, IEEE J. Quantum Electron. **35**(4), p. 459 (1999).
52. A. Baltuška, M.F. Emde, M.S. Pshenichnikov, and D.A. Wiersma, *Early-time dynamics of the photo-excited hydrated electron*, J. Phys. Chem. A **103**, p. 10065 (1999).

53. M.S. Pshenichnikov, A. Baltuska, R. Szipocs, and D.A. Wiersma, *Sub-5-fs pulses: generation, characterisation, and experiments*, in *Ultrafast Phenomena XI*, T. Elsaesser, et al., Editors. 1998, Springer: Berlin.
54. R.W. Boyd, *Nonlinear optics*. 1992, San Diego: Academic Press.
55. Y.R. Shen, *The principles of nonlinear optics*. 1984, New York: Wiley.
56. T. Brabec and F. Krausz, *Nonlinear optical pulse propagation in the single-cycle regime*, Phys. Rev. Lett. **78**(17), p. 3282 (1997).
57. N. Bloembergen, *Nonlinear Optics*. 1965, New York: Benjamin, Inc.
58. Y. Wang and R. Dragila, *Efficient conversion of picosecond laser pulses into second-harmonic frequency using group-velocity dispersion*, Phys. Rev. A **41**(10), p. 5645 (1990).
59. A. Umbrasas, J.-C. Diels, J. Jacob, G. Valiulis, and A. Piskarskas, *Generation of femtosecond pulses through second-harmonic compression of the output of a Nd:YAG laser*, Opt. Lett. **20**(21), p. 2228 (1995).
60. A.M. Weiner, A.M. Kan'an, and D.E. Leaird, *High-efficiency blue generation by frequency doubling of femtosecond pulses in a thick nonlinear crystal*, Opt. Lett. **23**(18), p. 1441 (1998).
61. G.P. Agrawal, *Nonlinear fiber optics*. 2nd ed. 1995, San Diego, CA: Academic Press, Inc.
62. P.V. Mamyshev and S.V. Chernikov, *Ultrashort-pulse propagation in optical fibers*, Opt. Lett. **15**(19), p. 1076 (1990).
63. J.T. Manassah, M.A. Mustafa, R.R. Alfano, and P.P. Ho, *Spectral extent and pulse shape of the supercontinuum for ultrashort laser pulse*, IEEE J. Quantum Electron. **22**(1), p. 197 (1986).
64. G.R. Fleming, *Chemical Applications of Ultrafast Spectroscopy*. The international series of monographs on chemistry, ed. J.E. Baldwin. 1986, New York: Oxford University Press.
65. R. Trebino, private communication (1997).
66. J.A. Squier, D.N. Fittinghoff, C.P.J. Barty, K.R. Wilson, M. Müller, and G.J. Brakenhoff, *Characterization of femtosecond pulses focussed with high numerical aperture optics using interferometric surface-third-harmonic generation*, Opt. Commun. **147**, p. 153 (1998).
67. D.N. Fittinghoff, J.A. Squier, C.P.J. Barty, J. Sweetser, R. Trebino, and M. Müller, *Collinear Type II second-harmonic-generation frequency-resolved optical gating for use with high-numerical aperture objectives*, Opt. Lett. **23**(13), p. 1046 (1998).
68. D.N. Fittinghoff, A.C. Millard, J.A. Squier, and M. Müller, *Frequency-resolved optical gating measurement of ultrashort pulses passing through a high numerical aperture objective*, IEEE J. Quantum Electron. **35**(40), p. 479 (1999).
69. L. Gallmann, G. Steymeyer, D.H. Sutter, N. Matuschek, and U. Keller, *Collinear type II second-harmonic-generation frequency-resolved optical gating for the characterization of sub-10-fs optical pulses*, Opt. Lett. **25**(4), p. 269 (2000).
70. Z. Cheng, A. Fürbach, S. Sartania, M. Lenzner, C. Spielmann, and F. Krausz, *Amplitude and chirp characterization of high-power laser pulses in the 5-fs regime*, Opt. Lett. **24**(4), p. 247 (1999).
71. K.W. DeLong, D.N. Fittinghoff, R. Trebino, B. Kohler, and K. Wilson, *Pulse retrieval in frequency-resolved optical gating based on the method of generalized projections*, Opt. Lett. **19**(15), p. 2152 (1994).
72. W.H. Press, S.A. Teukolsky, W.T. Vetterling, and B.P. Flannery, *Numerical recipes in C*. 1996, New York: Cambridge University Press.
73. A. Baltuška, M.S. Pshenichnikov, and D.A. Wiersma, *Amplitude and phase characterization of 4.5-fs pulses by frequency-resolved optical gating*, Opt. Lett. **23**(18), p. 1474 (1998).
74. F. Krausz, Private communication, 1998.
75. L. Gallmann, D.H. Sutter, N. Matuschek, G. Steymeyer, and U. Keller. *Techniques for the characterization of sub-10-fs pulses: A comparison*. in *Ultrafast Optics*. 1999. Monte-Verita, Switzerland, July 11–16: paper Th12.
76. V. Kabelka and A.V. Masalov, *Angularly resolved autocorrelation for single-shot time-frequency imaging of ultrashort light pulse*, Opt. Commun. **121**(4–6), p. 141 (1995).
77. V. Kabelka and A.V. Masalov, *Time-frequency imaging of a single ultrashort light pulse from angularly resolved autocorrelation*, Opt. Lett. **20**(11), p. 1301 (1995).
78. M. Schubert and B. Wilhelmi, *Nonlinear optics and quantum electronics*. 1986, New York: John Wiley.
79. S.A. Akhmanov, V.A. Vysloukh, and A.S. Chirkin, *Optics of femtosecond laser pulses*. 1992, New York: American Institute of Physics.
80. D. McMorrow, W.T. Lotshaw, and G.A. Kenney-Wallace, *Femtosecond Optical Kerr Studies on the Origin of the Nonlinear Responses in Simple Liquids*, IEEE J. Quantum Electron. **24**(2), p. 443 (1988).
81. D. McMorrow and W.T. Lotshaw, *The frequency response of condensed-phase media to femtosecond optical pulses: spectral-filter effects*, Chem. Phys. Lett. **174**(1), p. 85 (1990).

82. D. McMorrow, *Separation of nuclear and electronic contributions to femtosecond four-wave mixing data*, Opt. Commun. **86**, p. 236 (1991).
83. E.W. Castner, Y.J. Chang, Y.C. Chu, and G.E. Walrafen, *The intermolecular dynamics of liquid water*, J. Chem. Phys. **102**(2), p. 653 (1994).
84. S. Palese, L. Schilling, R.J.D. Miller, P.R. Staver, and W.T. Lotshaw, *Femtosecond Optical Kerr Effect Studies of Water*, J. Phys. Chem. **98**, p. 6308 (1994).
85. *Release on the Refractive Index of Ordinary Water Substance as a Function of Wavelength, Temperature and Pressure*. 1997, Erlangen, Germany: The International Association for the Properties of Water and Steam. 1.
86. A.H. Harvey, J.S. Gallagher, and J.M.L. Sengers, *Revised formulation for the refractive index of water and steam as a function of wavelength, temperature and density*, J. Phys. Chem. Ref. Data **27**(4), p. 761 (1998).
87. O. Duhr, E.T.H. Nibbering, G. Korn, G. Tempea, and F. Krausz, *Generation of intense 8-fs pulses at 400 nm*, Opt. Lett. **24**(1), p. 34 (1999).
88. E.T.H. Nibbering, O. Duhr, and G. Korn, *Generation of intense tunable 20-fs pulses near 400 nm by use of a gas-filled hollow fiber*, Opt. Lett. **22**(17), p. 1335 (1997).
89. V.G. Dmitriev, G.G. Gurzadyan, and D.N. Nikogosyan, *Handbook of non-linear optical crystals*. 1991, Berlin: Springer-Verlag.
90. M.S. Pshenichnikov, W.P.d. Boeij, and D.A. Wiersma, *Generation of 13-fs pulses from a cavity-dumped Ti:sapphire laser*, Opt. Lett. **19**, p. 572 (1994).
91. E.J. Mayer, J. Möbius, A. Euteneuer, W.W. Rühle, and R. Szipöcs, *Ultrabroadband chirped mirrors for femtosecond lasers*, Opt. Lett. **22**(8), p. 528 (1997).
92. C. Rullière, ed. *Femtosecond laser pulses*. 1998, Springer-Verlag: Berlin. 310.
93. C.H.B. Cruz, R.L. Fork, W.H. Knox, and C.V. Shank, *Spectral hole burning in large molecules probed with 10 fs optical pulses*, Chem. Phys. Lett. **132**(4–5), p. 341 (1986).
94. A. Kummrow, M.F. Emde, A. Baltu_ka, D.A. Wiersma, and M.S. Pshenichnikov, *Hydrated Electron Dynamics at a Five Femtosecond Time Scale*, Zeitschrift für Physikalische Chemie **212**, 153–160 (1999).
95. M.F. Emde, A. Baltuška, A. Kummrow, M.S. Pshenichnikov, and D.A. Wiersma, *Hydrated electron dynamics on a 5-fs time scale*, in *Ultrafast Phenomena XI*, T. Elsaesser, et al., Editors. 1998, Springer: Berlin. p. 586.

15. FROG Characterization of Pulses with Complex Intensity and Phase Substructure

John M. Dudley

The widespread use of FROG has contributed significantly to the development of optimized ultrafast lasers producing transform-limited pulses of near single-cycle duration. However, although the characterization of optimized ultrafast sources is certainly one of its most important applications, a significant number of experiments have also used FROG to characterize pulses very far from the transform limit. The pulses being studied in these experiments have possessed very complex intensity and/or phase distortions, but FROG has still been successfully used for complete characterization. This chapter will review these previous experiments and discuss, where relevant, important experimental issues necessary for accurate results to be obtained.

Pulse Propagation in Optical Fibers

One of the important early uses of FROG to measure complex pulse profiles was the characterization of near zero-dispersion wavelength (ZDW) propagation in optical fibers. Because of its importance in high capacity optical communications systems, such propagation had been extensively studied using numerical simulations, with the results showing that an incident pulse could develop rapid temporal oscillations accompanied by the appearance of characteristic peaks in the pulse spectrum [1]. Some experiments were also carried out, but it was noted that although the expected spectral splitting was well-reproduced in the experiments, the severe temporal pulse distortion was only weakly manifested in the measurements of the pulse autocorrelation function.

For example, Fig. 15.1 shows autocorrelation and spectral measurements before and after transform-limited 2 ps pulses at 1534 nm have propagated through 700 m of commercially available dispersion-shifted fiber [2]. It is clear that there is significant temporal and spectral distortion, and a small region of ultrafast temporal modulation is observed near zero delay. The measured FROG-trace in Fig. 15.2(a), however, illustrates the temporal modulation more clearly and, furthermore, allows the relationship between the temporal and spectral structure to be seen directly. In particular, the FROG trace is seen to contain significant structure in three distinct spectral bands, referred to the corresponding structure in the fundamental pulse spectrum, shown alongside. It is clear that the components at the SHG wavelengths around 768 nm and 778 nm are associated with the two main peaks in the

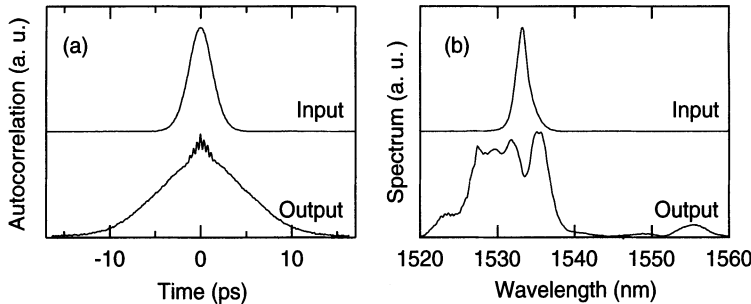


Fig. 15.1: (a) Autocorrelation functions and (b) spectra of picosecond pulses before and after propagation in 700 m of dispersion-shifted fiber.

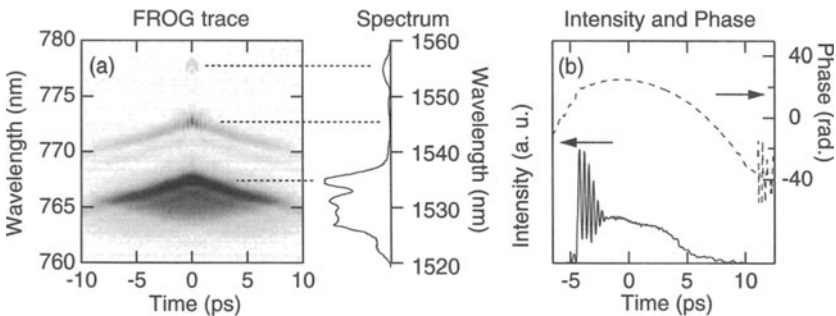


Fig. 15.2: (a) Measured FROG trace (referred to pulse spectrum on the right) and (b) retrieved intensity and phase.

fundamental spectrum, but of particular interest is the temporally-modulated component around 773 nm (the second harmonic of the ZDW) where there is no appreciable corresponding signal in the fundamental spectrum. This component is generated from the mixing of the two main components of the pulse spectrum on either side of the ZDW, clearly illustrating the physical origin of the temporal modulation on the pulse as arising from the beating between these two components.

It is appropriate now to discuss several issues relating to the measurement of such a complex FROG trace. Firstly, because of the broadband nature of the pulse spectrum after propagation, accurate measurement of the FROG trace requires both careful choice of SHG crystal used, and minimization of any effect due to spatial filtering of the generated SHG signal. These issues have been extensively considered in the context of single-cycle FROG in Chapter 14 and reference [3]. In addition, the need to simultaneously characterize both the slowly varying 10 ps pulse envelope and the sub-ps modulation constrains the temporal sampling increment and thus the minimum grid size. For these results, the FROG trace was obtained on a 256×256 grid, and the minimum

retrieval error obtained was $G = 0.009$. The retrieved intensity and phase are shown in Fig. 15.2(b).

Although the retrieval error obtained here may seem to be relatively large for an SHG-FROG trace on such a large grid, we note that when comparing retrieval errors for pulses with different types of distortion and measured on different grid sizes, it is important to consider the fractional area of the FROG trace containing “significant non-zero data.” This is given indirectly via the *rms* time-bandwidth product (in this case ≈ 15) but we have found it convenient to define it more directly as the fraction of data having an intensity greater than 1% of the trace maximum. Typically, SHG-FROG traces which are “well-gridded” (with a significant region of zeros surrounding the central region of data) have only around 5% of the data satisfying this criterion, and in this case, retrieval errors of $G < 0.005$ are routine. However, for complex pulses the fraction of significant non-zero data is typically much larger. For the trace in Fig. 15.2(a), for example, this fraction is around 25%, so that the retrieval error of $G = 0.009$ in this case can be considered acceptably low.

CW THz Pulse Trains

Interestingly, as well as being used to characterize the development of ultrafast oscillations developed on the envelope of an injected ultrashort pulse, FROG can also be used to characterize ultrafast THz pulse trains generated from the injection of a high power *continuous wave* (CW) field. Although this may seem surprising, it is a consequence of the fact that such pulse trains are necessarily periodic, and the Fourier transform operations used in the FROG generalized projections (GP) algorithm apply equally well for periodic functions as for ultrashort pulses with compact support. Existing GP algorithms can be straightforwardly adapted for the retrieval of periodic functions by introducing a cyclic time window to ensure that any temporal structure that leaves one edge of the computation window re-enters at the other edge. This preserves any periodicity present in the FROG trace, allowing the successful retrieval of periodic intensity and phase structure in the underlying electric field. With these modifications, retrieval is possible both with the standard approach to GP described in [4] as well as the recently-developed vector-based principal component generalized projections (PCGP) algorithm described in [5] and [6]. Experiments to date have been carried out using only SHG-FROG [7,8] but, in principle, any of the existing FROG geometries can be used for this purpose.

Using conventional characterization techniques, CW pulse train formation is manifested in the frequency domain by the appearance of discrete spectral sidebands, and in the time domain by an associated modulation in the auto-correlation function. These characteristics are coupled together in the FROG trace shown in Fig. 15.3(a) which presents experimental data corresponding to the formation of a 2.5 THz dark soliton train. The FROG trace here consists of a series of periodically modulated spectral bands at SHG frequencies

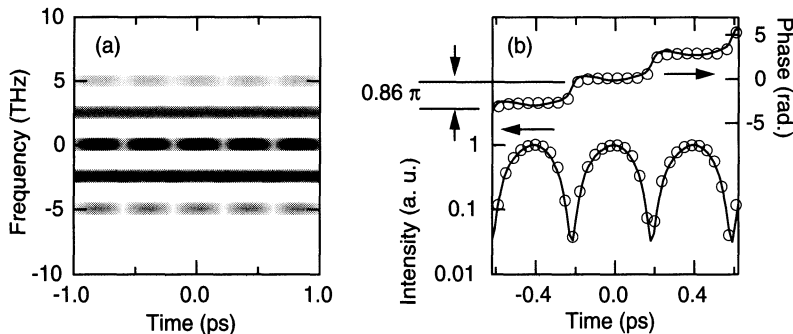


Fig. 15.3: (a) Measured FROG trace and (b) retrieved intensity and phase (lines) for a 2.5 THz dark soliton train. The circles show the expected results from simulations.

corresponding to each component in the fundamental spectrum, as well as at frequencies due to the sum-frequency mixing between these components. The trace is thus extremely sensitive to the exact intensity and phase characteristics of the incident pulse train, containing sufficient information to recover the original pulse train intensity and phase.

Applying the PCGP algorithm to these data gives a retrieval error of $G = 0.002$ with a significant non-zero data fraction of 5%. The corresponding retrieved intensity and phase are shown as the lines in Fig. 15.3(b) and, to stress the dynamic range of the measurement, the intensity is plotted on a logarithmic scale. Theory predicts that genuine dark solitons exhibit 100% intensity modulation [1], but the results here show only a reduced modulation depth of 96% and therefore must be interpreted as “gray” rather than “black.” Interestingly, this reduced modulation depth is also manifested in the characteristics of the phase shift observed across the soliton center. For 100% modulated black solitons, an abrupt phase jump of π is expected, but gray solitons are expected to be associated with a continuously varying phase shift of reduced magnitude [1]. The retrieved phase in Fig. 15.3(b) confirms this expected behavior, showing a phase shift of 0.86π across the soliton center. The results of numerical simulations of the soliton train formation are also shown in the figure (circles), and are in good agreement with the measured results, particularly with respect to the 96% modulation depth and the 0.86π phase shift. These results clearly demonstrate that an adapted FROG technique can accurately retrieve the intensity and phase of periodic ultrafast optical pulse trains.

Pulse Distortions in a Modelocked Ti:Sapphire laser

As well as its use to study dispersive and nonlinear interactions in optical fibers, FROG has also been used in many experiments which have studied how these effects affect the steady-state pulse characteristics in self-modellocked lasers. One study in particular used a real-time SHG FROG setup to study

how the pulse characteristics varied as the intracavity group-delay dispersion (GDD) in a Ti:Sapphire laser was varied from negative to positive values [9]. Although this regime had been previously studied using spectral and autocorrelation analysis [10,11], the use of FROG provided direct insight into the pulse distortions observed near zero-GDD operation and, indeed, revealed a previously unreported operating regime.

When configured to have a large negative GDD, the self modelocked Ti:Sapphire laser produces transform-limited pulses via a soliton-like pulse shaping mechanism. As the GDD is decreased, however, the effects of higher order dispersion leads to the formation of a dispersive-wave sideband on the pulse spectrum, associated with a weak pedestal pulse co-propagating with the main pulse. Although some previous experiments had studied the presence of this dispersive wave pedestal indirectly using high contrast autocorrelation [12], the results in [9] showed that it could, in fact, be directly measured using FROG.

Figure 15.4(a) shows the FROG trace for these results, compared with the fundamental spectrum shown alongside. The FROG trace here clearly shows two components; an isolated ultrashort pulse associated with the main spectral peak around 790 nm, and a longer co-propagating pulse associated with the narrow-bandwidth dispersive wave peak around 823 nm. Retrieval from this FROG trace was associated with an error of $G = 0.004$ on a 128×128 grid, with the retrieved intensity profile in Fig. 15.4(b) clearly showing the simultaneous characterization of the main pulse and the co-propagating dispersive wave pedestal. We note that the low power pedestal component of dispersive waves can always be measured with FROG, despite the nonlinearity involved in FROG; this is because the efficiency of a component in the FROG trace is determined by the strongest component of the pulse, which probes all the structure of the potentially complex pulse. Thus even weak components in either time or frequency are frequency doubled with the same efficiency as the main pulse and hence contribute to the FROG trace with the same

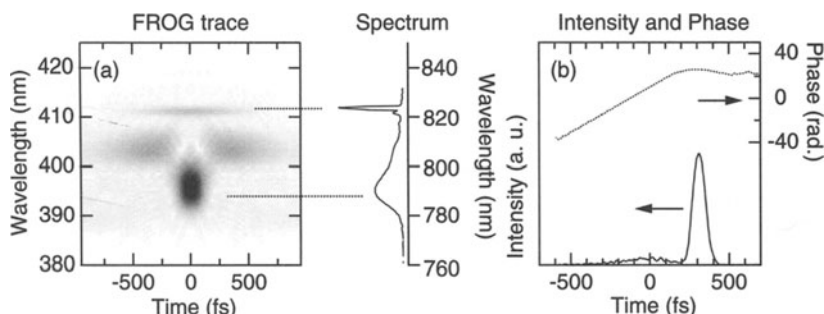


Fig. 15.4: (a) Measured FROG trace (referred to pulse spectrum on the right) and (b) retrieved intensity and phase, showing dispersive wave formation in a self-modelocked Ti : Sapphire.

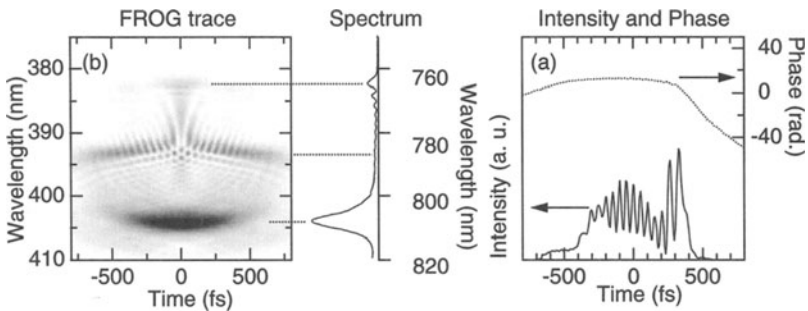


Fig. 15.5: (a) Measured FROG trace (referred to pulse spectrum on the right) and (b) retrieved intensity and phase for pulses in a self-modelocked Ti:Sapphire laser undergoing intracavity FWM.

dynamic range as in the pulse itself. This is in contrast to a statement made in reference[12].

Decreasing the intracavity GDD even further leads to more complex pulse behavior where the pulse spectrum splits about the intracavity ZDW of 785 nm. This is shown in Fig. 15.5. The retrieval error here was $G = 0.010$ on a 256×256 grid with a non-zero data fraction in the FROG trace of 30%. The *rms* time-bandwidth product here is ≈ 14 . The most notable feature of these results is the striking similarity between this FROG trace and that shown in Fig. 15.2 associated with FWM about the ZDW in an optical fiber [13]. Indeed, it was this visual similarity between the pulses in the time-frequency domain which first suggested that the underlying physics in the Ti:Sapphire laser and that in the optical fiber was the same; this interpretation was later confirmed by a phase-matching argument taking into account the magnitude of the intracavity GDD and nonlinearity [9].

Parabolic Pulses in Optical Fiber Amplifiers

Finally in this chapter, we consider an important recent application of FROG to verify the generation of highly-chirped pulses with parabolic intensity profiles in high gain optical fiber amplifiers with normal dispersion. In these amplifiers, theory predicts that any arbitrary input pulse evolves asymptotically into a linearly-chirped parabolic pulse, which propagates self-similarly as it evolves in the amplifier. Taking advantage of the current availability of high gain fiber amplifiers and the complete pulse characterization afforded by FROG, experiments have indeed been able to verify these predictions and provide the first experimental evidence for self-similar pulse propagation in optics [14].

Unlike the more complex pulses considered above, the FROG trace of a parabolic pulse has a relatively simple structure. For example, Fig. 15.6(a) shows the FROG trace for a parabolic pulse at 1060 nm generated from a

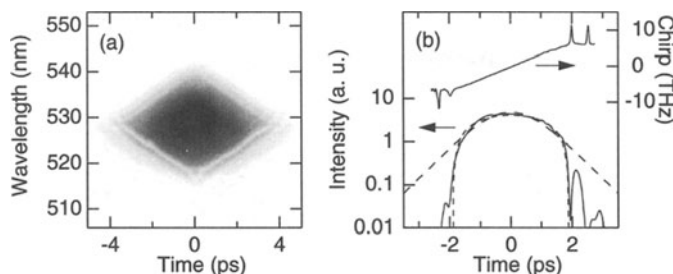


Fig. 15.6: (a) Measured FROG trace (b) retrieved intensity and phase for parabolic pulses.

Yb:doped fiber amplifier. Because of the large chirp on the pulse, a grid size of 1024×1024 is necessary for accurate retrieval, and a multigrid approach to retrieval is required to avoid impractical computation times [15]. The retrieval error of $G = 0.007$ is very low given that the non-zero data fraction is 30%, and the retrieved pulse characteristics are shown in Fig. 15.6(b). The distinction between a parabolic and the more common gaussian or sech^2 intensity profiles is most evident in the pulse wings, so the retrieved intensity (solid line) is plotted on a logarithmic scale and compared with both sech^2 (long dashes) and parabolic (short dashes) fits. There is agreement with the parabolic pulse profile over 2 orders of magnitude and we plot the chirp in this figure to emphasize its linearity as expected from theory.

Conclusions

The complete intensity and phase characterization afforded by FROG allows complex intensity and phase distortions to be directly observed and compared quantitatively with theoretical predictions. The widespread use of FROG has also reminded workers in ultrafast optics of the power of the time-frequency domain to aid the analysis and interpretation of experimental data. In this regard, the reader's attention is drawn in particular to FROG measurements of modelocked semiconductor lasers [16] where it has been shown that the laser dynamics can still be inferred in situations where intensity and phase retrieval is not possible.

In addition to FROG there are, of course, numerous other techniques currently available for the characterisation of ultrashort pulses. However, whilst some of these may be very well suited for particular experimental applications, no other technique has yet proven comparable versatility for measuring such a wide range of pulses of different durations and complexity.

Acknowledgements

The author is indebted to L. P. Barry, M. Fermann J. D. Harvey, R. Leonhardt and G. Millot for their permission to reproduce results which have been obtained from many fruitful and enjoyable collaborations.

References

1. G. P. Agrawal, *Nonlinear fiber optics*, 2nd ed. (Academic, New York, 1995).
2. J. M. Dudley, L. P. Barry, P. G. Bolland, J. D. Harvey, R. Leonhardt, P. D. Drummond: Direct measurement of pulse distortion near the zero-dispersion wavelength in an optical fiber by frequency-resolved optical gating, *Opt. Lett.* **22**, 457–9 (1997).
3. A. Baltuska, M. S. Pshenichnikov, D. A. Wiersma: Second-harmonic generation frequency-resolved optical gating in the single-cycle regime, *IEEE J. Q. Electron.* **35**, 459–78 (1999).
4. K. W. DeLong, R. Trebino: Improved ultrashort phase-retrieval algorithm for frequency-resolved optical gating, *J. Opt. Soc. Amer. A*, **11**, 2429–37 (1994).
5. D. J. Kane, G. Rodriguez, A. J. Taylor, T. Sharp Clement: Simultaneous measurement of two ultrashort laser pulses from a single spectrogram in a single shot, *J. Opt. Soc. Amer. B*, **14**, 935–43 (1997).
6. D. J. Kane: Recent progress toward real-time measurement of ultrashort laser pulses, *IEEE J. Quantum Electron.*, **35**, 421–31 (1999).
7. F. Gutty, S. Pitois, P. Grelu, G. Millot, M. D. Thomson, J. M. Dudley: Generation and characterization of 0.6–THz polarization domain-wall trains in an ultralow-birefringence spun fiber, *Opt. Lett.*, **24**, 1389–91 (1999).
8. J. M. Dudley, M. D. Thomson, F. Gutty, S. Pitois, P. Grelu, G. Millot: Complete intensity and phase characterization of optical pulse trains at terahertz repetition rates, *Electron. Lett.*, **35**, 2042–4 (1999).
9. J. M. Dudley, S. M. Boussen, D. M. J. Cameron, J. D. Harvey: Complete Characterization of a Self-Modelocked Ti:Sapphire Laser in the vicinity of zero group-delay dispersion, *Appl. Opt.* **38**, 3308–15 (1999).
10. P. F. Curley, Ch. Spielmann, T. Brabec, F. Krausz, E. Wintner, A. J. Schmidt, Operation of a femtosecond Ti:Sapphire solitary laser in the vicinity of zero group-delay dispersion, *Opt. Lett.* **18**, 54–6 (1993).
11. B. Proctor, E. Westwig, F. Wise, Characterization of a Kerr-lens modellocked Ti:Sapphire laser with positive group velocity dispersion, *Opt. Lett.* **18**, 1654–6 (1993).
12. A. Kasper and K. J. Witte, Contrast and phase of ultrashort laser pulses fro Ti:Sapphire ring and Fabry-Perot resonators based on chirped mirrors, *J. Opt. Soc. Am. B* **15**, 2490–5 (1998).
13. To emphasize this, the wavelength direction in Fig. 5 has been reversed compared to that in Fig. 2. The opposite symmetry in the structure of the FROG traces is attributed to the different signs of the third order dispersion.
14. M. E. Fermann, V. I. Kruglov, B. C. Thomsen, J. M. Dudley, J. D. Harvey: Self-Similar Propagation and Amplification of Parabolic Pulses in Optical Fibers, *Phys. Rev. Lett.* **84**, 6010–13 (2000).
15. C. W. Siders, J. L. W. Siders, F. G. Omenetto, A. J. Taylor: Multipulse interferometric frequency-resolved optical gating, *IEEE J. Quant. Electron.* **35**, 432–40 (1999).
16. P. J. Delfyett, H. Shi, S. Gee, I. Nitta, J. C. Connolly, G. A. Alphonse: Joint time-frequency measurements of mode-locked semiconductor diode lasers and dynamics using frequency-resolved optical gating, *IEEE J. Quant. Electron.* **35** 487–500 (1999).

16. XFROG—Cross-correlation Frequency-resolved Optical Gating

Stefan Linden, Jürgen Kuhl, and Harald Giessen

Introduction

FROG [1–4] allows us to measure an ultrashort laser pulse without a shorter reference pulse. But often a shorter reference pulse that has already been measured is available. In this case, it's usually preferable to use this pulse to measure the unknown pulse. In fact, even if the reference pulse isn't shorter, it's still usually preferable to use it to measure the unknown pulse. If the reference pulse is intense, then it yields higher efficiency in any nonlinear-optical process. This is especially helpful when the unknown pulse is weak enough that it doesn't yield sufficient signal strength using even the most sensitive FROG geometry (SHG FROG). For example, UV pulses with energies of less than about a nJ are too weak to be measured using a third-order FROG technique, and SHG FROG isn't available because SHG crystals absorb at the SH of such a pulse (i.e., below 190 nm). Also, when measuring a very complex pulse of any energy, gating it with a reference pulse that happens to be smooth will generate a trace that is easier to interpret.

Gating the unknown pulse with a known pulse and spectrally resolving the resulting signal pulse—a spectrally resolved cross-correlation—is called *cross-correlation frequency resolved optical gating (XFROG)* [5,6], and it yields a trace that's a true spectrogram. Researchers have in the past gated an unknown pulse with another pulse (usually uncharacterized, but usually thought to be Fourier-transform-limited) and then spectrally resolved the cross-correlation signal pulse. This gave a measure of the pulse color vs. time, but no attempt was made to extract rigorous quantitative information from this plot. It is the application of the FROG algorithm that makes these methods quantitative. And that is what makes XFROG—which does exactly that—a useful tool.

If the unknown pulse spectrum is contained within that of the reference pulse, an alternative approach is spectral interferometry (or TADPOLE) (See Chapter 22) [7], which does not involve a nonlinear-optical interaction and hence is very sensitive. XFROG, on the other hand, is much more versatile and usually easier to perform. XFROG requires no spectral overlap between the reference and unknown pulses. And depending on the relative frequencies of the pulses, sum frequency generation (SFG), difference frequency generation (DFG), or a host of third-order processes can be used to create the cross-correlation signal. Unlike spectral interferometry, which, like other types of interferometry, has extremely stringent coherence and mode-matching

requirements, XFROG does not require satisfying these experimentally difficult constraints. Also, XFROG doesn't require interferometric alignment accuracy, and it can be used for low-quality beams. The need for a fairly strong reference pulse doesn't represent much of a limitation because such a pulse is in principle always available even when working with extremely weak pulses. Indeed, in most cases, weak pulses are the result of a linear or nonlinear-optical process, which involves at least one input pulse that is much stronger and therefore can be characterized by a standard FROG technique. For example, blue or UV ultrashort pulses are often weak, but they're normally generated by frequency doubling or tripling of pulses in the near IR. And ultrafast fluorescence is usually weak, difficult to collimate, and incoherent, but again, the pulse that excites it is usually generated by near-IR pulses from a Ti:Sapphire laser. Thus, in both cases, the near-IR pulses are available to serve as a reference pulse, and XFROG can measure these otherwise difficult-to-measure pulses.

General Properties

The electric field of the XFROG signal beam has the form

$$E_{\text{Sig}}^{\text{SFG}}(t, \tau) = E(t)E_{\text{Ref}}(t - \tau) \quad (16.1)$$

for sum frequency generation and

$$E_{\text{Sig}}^{\text{DFG}}(t, \tau) = E(t)E_{\text{Ref}}^*(t - \tau) \quad (16.2)$$

for difference frequency generation if the unknown pulse has a higher carrier frequency than the reference pulse. The corresponding carrier frequency of the correlation signal is $\omega_0^{\text{SFG}} = \omega + \omega_{\text{Ref}}$ and $\omega_0^{\text{DFG}} = \omega - \omega_{\text{Ref}}$, respectively. In the following, we'll only consider the equations for SFG XFROG. The corresponding equations for DFG XFROG can be simply obtained by replacing $E_{\text{Ref}}(t - \tau)$ by $E_{\text{Ref}}^*(t - \tau)$. Also, it is easy to extrapolate to third-order XFROG processes in a similar manner. The squared magnitude of the spectrum of the cross-correlation signal recorded as a function of delay τ between the two pulses yields the XFROG trace or spectrogram:

$$I_{\text{XFROG}}^{\text{SFG}}(\omega, \tau) = \left| \int_{-\infty}^{\infty} E(t)E_{\text{Ref}}(t - \tau)e^{-i\omega t} dt \right|^2. \quad (16.3)$$

XFROG is able to characterize weak pulses because, according to Eq. (16.1), the XFROG signal field is proportional to the field of the reference pulse.

While XFROG has the usual trivial absolute-phase ambiguity, it lacks the translation ambiguity because the independent gate pulse acts as the time reference. XFROG also lacks the direction-of-time ambiguity because the trace is not necessarily symmetrical with respect to the delay τ . On the other hand,

some attention has to be paid when using SHG FROG for the characterization of the reference pulse due to its possible time ambiguity. However, the direction of time for the reference pulses characterized by SHG FROG can normally be determined by the methods described in Chapter 11 [2,8]. Additionally, inserting the time-reversed reference pulse in Eq. (16.1) yields a signal field that typically doesn't match the experimental trace and hence leads to a large error in the XFROG algorithm. Finally, XFROG has the ambiguities of the spectrogram: the relative phase of well-separated pulses is indeterminate.

XFROG is related to another version of FROG that uses two different pulses to make a trace, but in which neither pulse is known [9]. This more difficult method is the subject of Chapter 20.

The temporal resolution of XFROG is not limited by the pulse width of the reference pulse. This is because the XFROG trace simultaneously contains temporal and spectral information about the reference and unknown pulse. A reference pulse that is short compared to the unknown pulse yields good resolution in the delay direction of the spectrogram but conceals details in the frequency direction due to the broad spectrum of the reference pulse. On the other hand, a reference pulse with a narrow spectrum provides good spectral resolution but poor temporal delay resolution. While both cases can yield an adequate measurement of the pulse, it is best to distribute the information evenly in both domains. To distribute the information evenly in the time and frequency direction, the pulse width of the reference pulse should be comparable to the pulse width of the unknown pulse. Notice that this is in contrast to the desired conditions for a standard cross-correlation to determine the pulse intensity, in which the pulse should be as short as possible. The influence of the reference pulse on the shape of the XFROG trace is shown in Fig. 16.1. The unknown pulse is a Gaussian pulse with a cubic temporal phase. The reference pulses are Fourier-transform-limited Gaussian pulses with a pulse width of (a) 40%, (b) 100% and (c) 160% of the pulse width of the Gaussian unknown pulse. The short pulse with a large spectral width yields

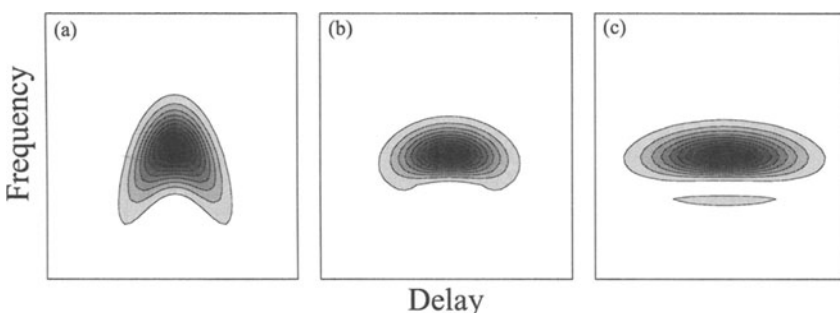


Fig. 16.1: Influence of the reference pulse on the shape of the XFROG trace. The reference pulses are Fourier-limited Gaussian pulses with a pulse width of (a) 40%, (b) 100% and (c) 160% of the pulse width of the Gaussian unknown pulse.

a XFROG trace (Fig. 16.1a) with a large spectral extent, while a long pulse produces a trace (Fig. 16.1c) dispersed in the temporal direction. Despite the different distribution of the signal in the time/frequency plane, the XFROG algorithm converges in all three cases and retrieves the correct unknown pulse.

Algorithm and Numerical Simulations

For retrieving the unknown pulse, we use an iterative Fourier-transform algorithm with generalized projections [10]. A flow chart of the algorithm is shown in Fig. 16.2. The XFROG algorithm needs the experimentally measured XFROG trace $I_{\text{XFROG}}(\omega_i, \tau_j)$ and the retrieved electric field of the reference pulse $E_{\text{Ref}}(t_i - \tau_j)$ as input data. While this is probably not essential, we nevertheless assume that all data are uniformly sampled in both the time and frequency domains. We begin with an initial guess for the electrical field of the unknown pulse $E(t_i)$ and then calculate the corresponding signal field $E_{\text{Sig}}(t_i, \tau_j)$ with Eq. (16.1) and the known electrical field of the reference pulse $E_{\text{Ref}}(t_i - \tau_j)$. Since the XFROG trace is a function of ω_i and τ_j , we Fourier transform $E_{\text{Sig}}(t_i, \tau_j)$ with respect to t_i to obtain $\tilde{E}_{\text{Sig}}(\omega_i, \tau_j)$. The first generalized projection is accomplished by replacing the magnitude of the guessed signal field $\tilde{E}_{\text{Sig}}(\omega_i, \tau_j)$ by the square root of the intensity $I_{\text{XFROG}}(\omega_i, \tau_j)$. This yields a modified field $\tilde{E}'_{\text{Sig}}(\omega_i, \tau_j)$ that's transformed back to the time domain. For the second generalized projection, we define a distance metric

$$Z = \sum_{i,j=1}^N \left| E'_{\text{Sig}}(t_i, \tau_j) - E(t_i)E_{\text{Ref}}(t_i - \tau_j) \right|^2 \quad (16.4)$$

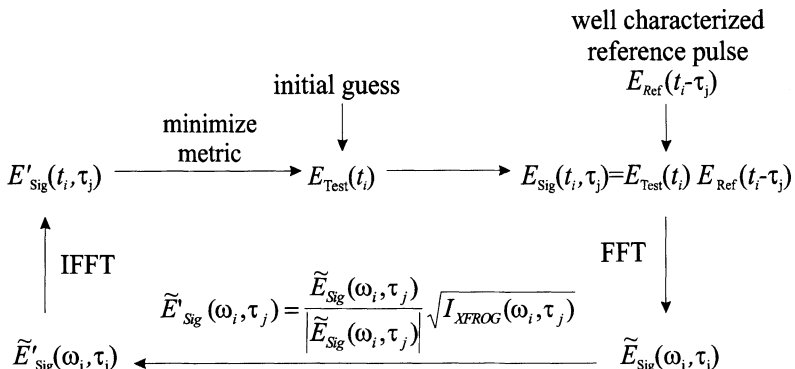


Fig. 16.2: Schematic of the XFROG algorithm.

Table 16.1: Influence of incorrect reference pulse parameters on the retrieved unknown pulse.

Reference pulse		Unknown pulse	
Pulse width [pixel]	Quadratic Phase [rad·pixel ⁻²]	Pulse width [pixel]	Quadratic Phase [rad·pixel ⁻²]
20.0	0.0	24.0	0.001
18.0 (-10 %)	0.0	26.1 (8.8 %)	0.00084
22.0 (+10 %)	0.0	22.0 (-8.3 %)	0.0012
20.0	0.001	23.9 (-0.4 %)	0.0003
20.0	-0.001	25.3 (+5.4 %)	0.0014
20.0	0.002	25.0 (+4.2 %)	-0.0002

and minimize Z with respect to $E(t)$. The reference pulse remains unchanged during the second generalized projection (and later projections also). In order to measure the progress of the algorithm, we use the FROG error G [1] also used by other FROG geometries.

The XFROG algorithm performs well in numerical simulations with several types of unknown pulses, including Fourier-transform-limited pulses, linearly chirped pulses, pulses with cubic temporal phase, self-phase modulated pulses, double-pulses with phase-substructure and variable intensity ratios. We've also used different reference pulses, chosen to be Fourier-transform-limited or linearly chirped. In simulations, the XFROG algorithm faithfully reproduced all unknown pulses with a typical value of $G = 5.0 \cdot 10^{-7}$ for a 64×64 pixel trace. An important feature of the XFROG algorithm is its tolerance of potential errors in the measurement of the electrical field of the reference pulse. To check this tolerance, we performed numerical simulations with reference pulses that had known deviations from the correct pulse width and phase (see Table 16.1). We found, for example, that increasing the pulse length of a Fourier-transform-limited Gaussian reference pulse by 10.0% yields a retrieved pulse 91.7% as long as the original linearly chirped Gaussian unknown pulse. Fortunately, the phase remains almost unchanged and the pulse shape remains Gaussian. Adding some incorrect linear chirp to the reference pulse results in a retrieved unknown pulse with nearly correct pulse width but with an increased quadratic phase. In all cases, deviations of the reference pulse from the correct field yield uncertainties in the measured pulse that are of the same order as the input error.

Experimental measurements

In the following, we describe applications of both SFG XFROG and DFG XFROG to retrieve weak pulses from experimental data.

SFG XFROG

Propagation through BK7 glass provides an example of SFG XFROG in operation. For this purpose, a beam from a Coherent MIRA 900 Ti:Sapphire laser oscillator operating at $\lambda_0 = 800$ nm was first characterized using SHG FROG. Its pulse was split in two, generating a reference and unknown pulse. The unknown pulse was passed through a variable time delay and additionally 2.5 cm (and, later, 5 cm) of BK7 glass. Then the two pulses were focused by a 120 mm lens onto a 300 μm BBO crystal, and the spectrum of the cross-correlation signal was recorded as a function of the delay between the two pulses. The measured traces are shown in Fig. 16.2. Since the two pulses are different, the XFROG traces clearly display a tilt due to linear chirp acquired in the glass, while the corresponding SHG FROG trace would show no tilt. The XFROG algorithm used a 64×64 pixel trace and yielded the unknown pulses with an error $G = 0.0029$ for 2.5 cm and $G = 0.0035$ for 5 cm of BK7 glass. The error in the SHG FROG measurement of the reference pulse was $G = 0.0027$. The effect of the additional chirp created when the pulse travels through more glass on the spectral phase of the retrieved pulses can be seen in Fig. 16.3(d). Assuming that the glass with refractive index n keeps the spectrum of the pulse unchanged and neglecting dispersion terms of higher order, the electric field of the pulse after a propagation length z can be written as

$$E(\omega, z) = E(\omega, 0) e^{i \frac{b}{2} (\omega - \omega_0)^2 z} \quad (16.5)$$

with

$$b = \left. \frac{\lambda_0^3}{2\pi c^2} \frac{d^2 n}{d\lambda^2} \right|_{\lambda_0} . \quad (16.6)$$

By calculating the difference between the quadratic fit of the spectral phase of independent measurements and averaging, we obtain a value of the chirp parameter $b = (466 \pm 23)(\text{fs}^2/\text{cm})$, in excellent agreement with $b = 450(\text{fs}^2/\text{cm})$ calculated from the Sellmeier equation.

In another example, illustrating XFROG's ability to measure a beam with potentially poor quality, a 34 mm lens was used to tightly focus the pulse of a Coherent RegA 9000 Ti:Sapphire regenerative amplifier into a thin plate of sapphire. As a result of the high-intensity due to the tight focusing, the medium spectrally broadened and reshaped the pulse due to high-intensity induced self-phase modulation and other higher-order nonlinear processes in the sapphire crystal. Since the beam had also become spatially inhomogeneous, only a small part in the middle of the beam was selected with a pinhole to be characterized by XFROG. The MIRA pulse from the previous experiment was taken as the reference pulse. Comparing the SHG FROG trace (Fig. 16.3a) of the reference pulse with the XFROG trace (Fig. 16.4a) of both pulses, it can be seen that the unknown pulse contains frequency components not present in the reference pulse. But the XFROG algorithm still retrieves

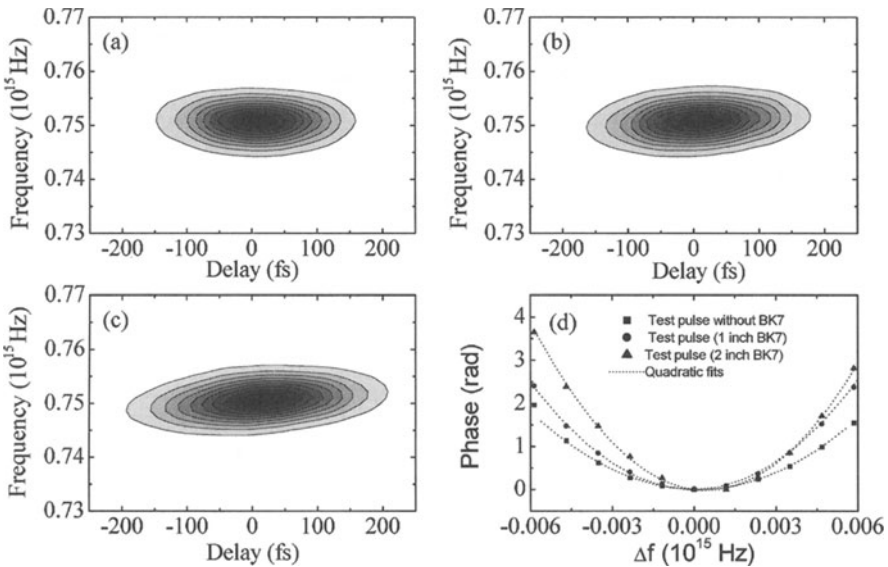


Fig. 16.3: (a) SHG FROG trace of reference pulse, (b) XFROG trace with one inch BK7, (c) XFROG trace with two inches BK7, (d) Spectral phase of the retrieved pulses as a function of frequency deviation from the carrier frequency.

the unknown pulse (Fig. 16.4c,d) with an error $G = 0.0082$. The good agreement between the experimentally measured (Fig. 16.4a) and the calculated spectrogram (Fig. 16.4b) indicates that the unknown pulse has been retrieved correctly.

DFG XFROG

As we mentioned earlier, DFG XFROG is ideal for measuring UV and blue pulses, whose SH wavelength is absorbed by SHG crystals. Here we give an example of DFG XFROG for measuring two different blue fs pulses around 400 nm that were either unchirped or intentionally chirped. In these experiments, a beam from a Coherent MIRA 900 Ti:sapphire laser oscillator operating at $\lambda_0 = 800$ nm was first characterized with standard SHG FROG. In order to create the blue unknown pulse, the main part of the beam was doubled in a 0.9-mm-thick BBO crystal using type I phase-matching. The pulse energies of the blue pulses were in the 60 pJ range. We chirped the pulses by propagating them through 2.5 cm of BK7 glass. The second part of the 800-nm Ti:sapphire laser beam was used as the reference pulse and so was passed through a variable time delay. The blue unknown pulse and the reference pulse were focused by a 120 mm focusing lens at a small angle into a 300 μm BBO crystal. The difference frequency signal was generated using type II phase-matching [11] and imaged with a focusing lens on the entrance

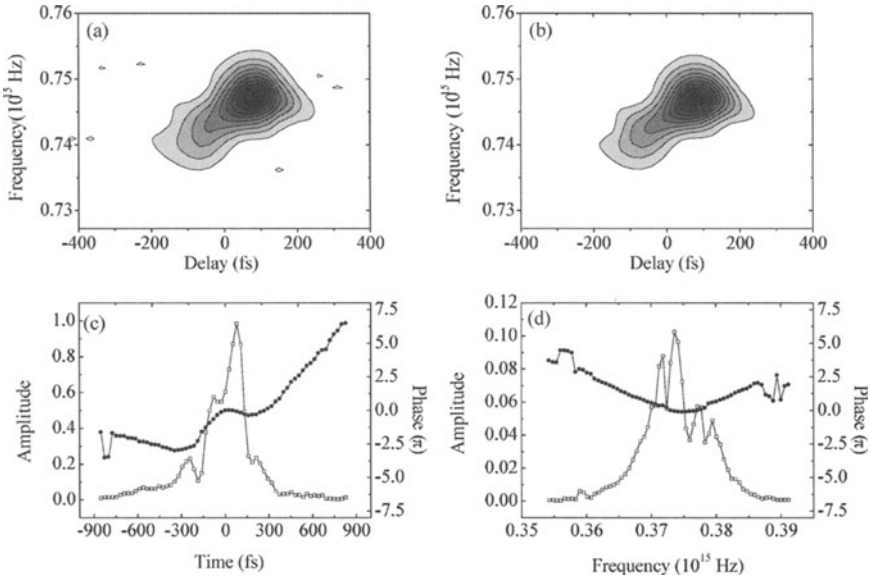


Fig. 16.4: (a) Experimental XFROG trace of a self-phase modulated pulse, (b) reconstructed spectrogram using the amplitude and phase data of Fig. 16.4c, (c) amplitude and phase of retrieved pulse as a function of time, (d) retrieved pulse in the frequency domain.

slit of the spectrometer. An OG 590 Schott filter was used to block stray light from the blue unknown pulse, which would otherwise be superimposed in second order onto the spectrogram. Subtraction of a constant background eliminated the stray light contribution by the reference pulse.

The reference pulse used in the DFG XFROG algorithm was characterized by SHG-FROG. It was well retrieved with a FROG error of 0.0023 for a 128×128 pixel trace. The FWHM of its intensity is $\tau_p = 168$ fs and the FWHM of the spectrum is $\Delta\nu = 3.1$ THz. The corresponding pulse TBP of 0.52 was due to higher-order residual distortions, which were not compensated.

Running the DFG XFROG algorithm on the experimental spectrograms of both blue pulses, we found final FROG errors for the 128×128 pixel traces were $G = 0.0036$ for the unchirped pulse and $G = 0.0057$ for the intentionally chirped pulse. Figure 16.5a shows the retrieved temporal intensity and phase of the pulses. Due to the influence of the glass, the pulse width broadened from $\tau_p = 211$ fs to $\tau_p = 239$ fs. Figure 16.5b shows the measured and retrieved spectra of the blue pulses. The agreement between experiment and calculation is quite good. The retrieved bandwidth for both pulses is $\Delta\nu = 2.2$ THz in comparison to a measured bandwidth of $\Delta\nu = 2.7$ THz. The difference is probably due to group velocity mismatch [13] between the fundamental and the second harmonic pulse in the nonlinear crystal, which

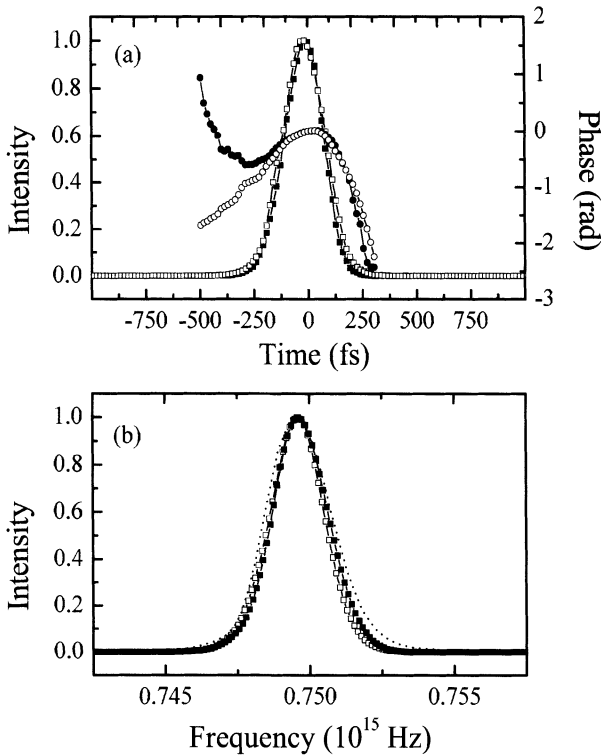


Fig. 16.5: (a) Intensity (unchirped pulse: ■, intentionally chirped pulse: □) and phase (unchirped pulse: ●, intentionally chirped pulse: ○) of the retrieved blue unknown pulses as a function of time. (b) Experimentally measured (· · ·) and calculated (unchirped pulse: ■, intentionally chirped pulse: □) spectra of the blue unknown pulse.

acts like a spectral filter and hence leads to a spectral width of the retrieved pulse which is too small.

For even shorter pulses, a thinner crystal is required for difference frequency generation to reduce the influence of group velocity mismatch. In this case, we suggest rotating the polarization of the reference pulse by 90° in order to use Type-I phase-matching for DFG, which is broader-band. This will also make it possible to remove stray light from the reference pulse with a polarizer, yielding a better signal-to-noise ratio, which is important for weak DFG signals.

Conclusion

XFROG is a powerful extension of the normal FROG technique for amplitude and phase characterization of weak, UV, or complex pulses. Or any pulse, really. It uses the spectrally resolved cross-correlation signal of the weak pulse with a fully characterized reference pulse to generate a spectrogram, which

is analyzed by an iterative algorithm. No spectral overlap between unknown and reference pulse is needed, which makes this method very flexible. It's versatile and reliable, as has been demonstrated by numerical simulations and experiments.

References

1. R. Trebino, and D. J. Kane, *J. Opt. Soc. Am. A* **10**, 1101 (1993).
2. K. W. DeLong, R. Trebino, J. Hunter, and W. E. White, *J. Opt. Soc. Am. B* **11**, 2206 (1994).
3. K. W. DeLong, R. Trebino, and D. J. Kane, *J. Opt. Soc. Am. B* **11**, 1596 (1994).
4. T. Tsang, M. A. Krumbügel, K. W. DeLong, D. N. Fittinghoff, and R. Trebino, *Opt. Lett.* **21**, 1381 (1996).
5. S. Linden, H. Giessen, and J. Kuhl, *Phys. Stat. Sol. (B)* **206**, 119 (1998).
6. S. Linden, J. Kuhl, and H. Giessen, *Opt. Lett.* **24**, 569 (1999).
7. D. N. Fittinghoff, J. L. Bowie, J. N. Sweetser, R. T. Jennings, M. A. Krumbügel, K. W. DeLong, R. Trebino, and I. A. Walmsley, *Opt. Lett.* **21**, 884 (1996).
8. R. Trebino, K. W. DeLong, D. N. Fittinghoff, J. N. Sweetser, M. A. Krumbügel, B. A. Richman, and D. J. Kane, *Rev. Sci. Instrum.* **68**, 3277 (1997).
9. K. W. DeLong, R. Trebino, and W. E. White, *J. Opt. Soc. Am. B* **12**, 2463 (1995).
10. K. W. DeLong, D. N. Fittinghoff, R. Trebino, B. Kohler and K. Wilson, *Opt. Lett.* **19**, 2153 (1994).
11. We use the definition according to Ref. [12], assuming the two *input* beams have perpendicular linear polarizations.
12. R. L. Sutherland, *Handbook of Nonlinear Optics* (Marcel Dekker, Inc., New York, 1996).
13. A. W. Weiner, *IEEE J. Quantum Electron.* **QE 19**, 1276 (1984).

17. Measuring Extremely Complex Pulses

Rick Trebino, Xun Gu, Erik Zeek, and Mark Kimmel

How Complex is Really Complex?

In Chapters 14 and 15, we saw that it's possible to measure complex pulses using FROG. But what about really complex pulses? Just how far can we go? How far can we push the FROG technique before it begins to croak?

It has recently become possible, using microstructure optical fiber, to generate *ultrabroadband continuum*, whose spectrum was measured to be smooth and which extends from 400 to \sim 1600 nm [1]. Because it's generated in a very small core (< 2 microns in diameter), this light has excellent spatial quality. And it is considered so stable that it has been used for ultra-stable metrology applications [2]. And it's been used for high-spatial-resolution optical coherence tomography [3]. Generating it involves simply allowing sub-nanojoule 800-nm pulses to propagate through a short length of newly developed microstructure optical fiber, which can be nearly dispersion-free in the visible. As numerous far-reaching applications are envisioned for this light, it is crucial to measure the continuum as well as possible, especially its intensity and phase vs. time.

Such a measurement involves many complications, however. First, a multi-shot measurement requires that all the continuum pulses in the train be identical. Second, the nonlinear-optical process used to make the measurement must have a massive phase-matching bandwidth, exceeding that of the continuum. Third, the time-bandwidth product (TBP) of the continuum is very large (\sim 1000), making it the most complex ultrashort laser pulse ever generated. The most complex pulses ever measured previously [4,5] had a TBP of about 10 and were described in Chapters 14 and 15.

Ultrabroadband XFROG

Okay, so what do we have to worry about in trying to measure such a complex pulse? First, what is its peak power? The answer is \sim 1 nJ/1 ps, which is not sufficient for a third-order nonlinearity, so we must use SHG FROG or SHG XFROG. Second, is there a SHG crystal that can accommodate the enormous bandwidth (1200 nm, which corresponds to 550 THz)? The answer is a resounding, "No!" (Surface SHG might be able to do this, but its strength is poor, so we don't consider it.) Figure 17.1 shows the phase-matching efficiency vs. wavelength for an ultra-thin 10- μ m thick BBO crystal for different cut angles. Note that no angle yields sufficient spectral coverage. It would appear that we're stuck.

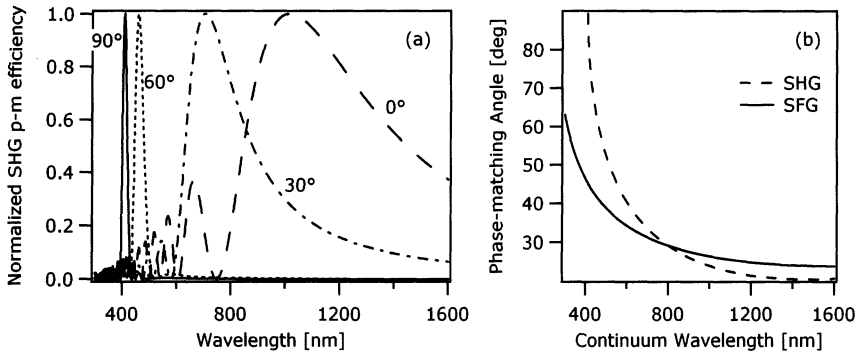


Fig. 17.1: (a) Normalized SHG phase-matching efficiency of a 10- μm -thick BBO for angles ranging from 0° to 90°; (b) phase-matching angle tuning curve for SHG and SFG with an 800-nm gate pulse.

However, there are some tricks that we can take advantage of. First, notice that light whose spectrum extends from 400 to 1600 nm generates SH from 200 to 800 nm. The main reason that it is impossible to achieve sufficient phase-matching bandwidth is that all crystals are very dispersive at 200 nm. But what if we instead perform an *XFROG* measurement and gate with a narrower-band pulse at, say, 800 nm? This will produce sum frequencies extending over the much shorter spectral range of 267 to 567 nm. While still a very large range, this is getting closer to something that's possible.

To achieve phase-matching over this still large bandwidth, we must re-examine some of our unwittingly incorrect assumptions. Specifically, it has long been assumed that, in a multi-shot pulse measurement, the phase-matching bandwidth must exceed the pulse bandwidth for *every pulse*. It is important to realize that, in multi-shot pulse measurements, this assumption is overly restrictive. In fact, only the phase-matching bandwidth *integrated over the measurement period* need exceed the pulse bandwidth. As a result, only a fraction of the pulse spectrum need be phase-matched on each shot, as long as the remaining portion of the pulse spectrum achieves phase-matching on other shots during the measurement. Because the range of wavelengths that achieve phase-matching depends sensitively on angle, we can *angle-dither* a SHG crystal that is otherwise too narrowband (that is, too thick) to yield a significantly increased effective phase-matching bandwidth for a given crystal thickness [6]. Because the SHG efficiency scales as the square of the crystal thickness, angle-dithering has the additional advantage that it allows us to use a thicker crystal (the thickness no longer matters for phase-matching) and hence also yields significantly greater signal strength.

Using an angle-dithered 1-mm-thick BBO crystal, it's possible to achieve enough bandwidth to easily make *XFROG* measurements of the continuum. These measurements require taking delay steps, $\delta\tau$, as small as a few fs (the coherence time corresponding to a bandwidth of several hundred THz) but

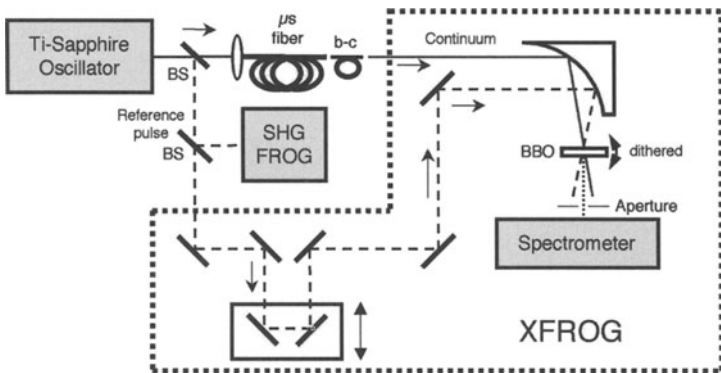


Fig. 17.2: Schematic diagram of the multi-shot XFROG measurement apparatus. BS: beam-splitter; μ s: microstructure fiber; b-c: butt-coupling fiber.

scanning over a delay range, $\Delta\tau$, of several ps (the pulse length of the continuum). They also require spectral resolution, $\delta\omega$, corresponding to wavelength resolution of less than 1 nm, but a sum-frequency spectral range, $\Delta\omega$, of > 267 to 567 nm. This means taking a trace extending over an approximately 3000×1000 array. Worse, in order to satisfy the Fourier-transform relations for the trace ($\delta\tau = 1/\Delta\omega$ and $\delta\omega = 1/\Delta\tau$), the array has to be expanded to 8192×8192 in order to run the FROG retrieval algorithm. Retrievals require several hours on a personal computer.

But the measurement is possible!

Simple observation of the measured XFROG trace (see Fig. 17.3) reveals a quadratic group delay of the pulse vs. wavelength, consistent with the observation that the group-delay dispersion (GDD) is linear, so the group delay vs. wavelength (the integral of the GDD) is quadratic.

However, the retrieved spectrum from the XFROG measurements has an incredible amount of structure, much more than the directly measured spectrum. Also, we observe fine-scale structure in the retrieved trace that is not seen in the measured trace, a clear indication that something is amiss. Usually, such poor agreement indicates that the more difficult measurement—the XFROG measurement—is contaminated with systematic error. But this time, the XFROG measurement will come out on top.

What's Going On?

A good indication that much spectral structure exists in the continuum comes from theoretical simulations of continuum generation, which predict deep and fine structure, especially when the continuum broadens as the input pulse energy increases [3]. With a continuum extending from 400 to 1400 nm (see Fig. 17.4), the oscillations in the spectrum occur on a sub-nanometer

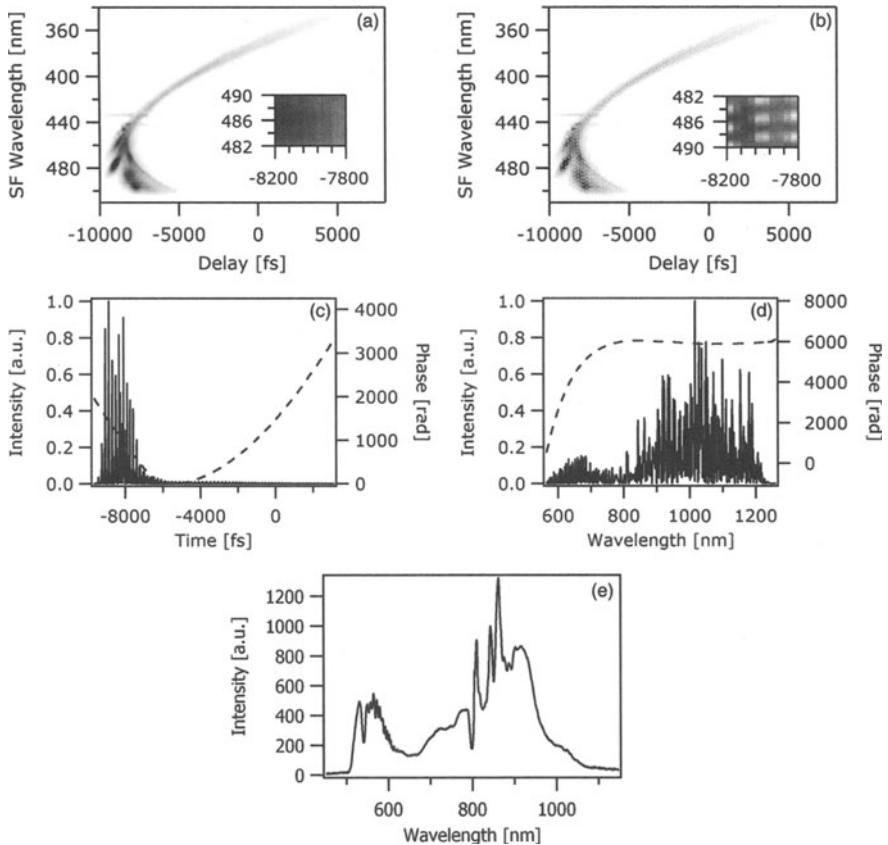


Fig. 17.3: XFROG measurement of the microstructure-fiber continuum with an 800-nm 30-fs pre-characterized reference pulse: (a) measured trace, (b) retrieved trace, (c) retrieved temporal intensity (solid) and phase (dashed), (d) retrieved spectral intensity (solid) and phase (dashed), and (e) independently measured spectrum. The insets in plots (a) and (b) are higher-resolution sections in the traces. The retrieved trace contains a very fine-scale polkadot pattern that is not in the measured trace, and the retrieved spectrum has very fine and deep oscillations.

scale, and the positions of ripples shift when very small fractional input power changes occur, in agreement with our XFROG measurements.

In work measuring ultrafast semiconductor laser sources [7], retrieved FROG traces have shown structure not present in measured traces, and later measurements with improved resolution have revealed the structure.

A possible explanation for these observations is that variations in the continuum pulse from shot-to-shot, as predicted by theory [8], are washing out the structure in directly measured spectra and in measured XFROG traces. That the structure information somehow remains in the multi-shot XFROG trace—even though it was measured over $\sim 10^{11}$ pulses—is possible because some

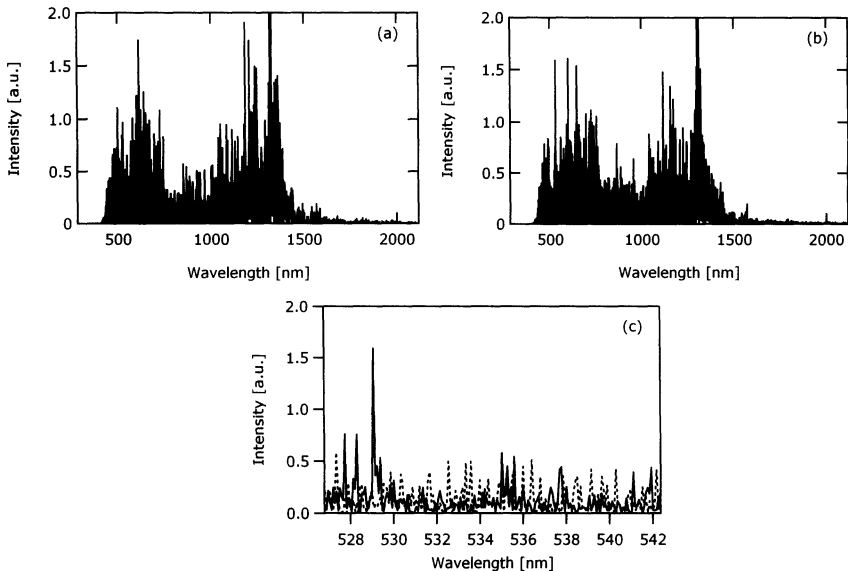


Fig. 17.4: Theoretically predicted spectra for conditions similar to those of experiments in which continuum generation occurs. Plots (a) and (b) correspond to identical conditions except that in plot (b) the input pulse energy is 0.1% higher. Plot (c) shows a high-resolution window of the two spectra [8].

single-shot information is preserved in the XFROG trace, as FROG traces contain substantial redundancy, and information washed out in one domain may remain in the other. Specifically, *fine-scale frequency information is also present in the trace in the form of slow oscillations in delay, which are less likely to be washed out*.

Verification of this hypothesis requires single-shot spectral measurements of the microstructure-fiber continuum. Figure 17.5 shows such measurements. Figures 17.5b–e show a 120-nm section of the continuum from 490 to 610 nm, with resolution of about 1 nm. Notice that, as the number of shots decreases, there appear to be more complex structures in the spectrum. Finally, in a single shot, the spectrum exhibits very deep and fine oscillations, and each single-shot spectrum is different. If we numerically average single-shot spectra (see Fig. 17.5e), the oscillations decrease significantly, and the spectrum becomes smooth, similar to those in an average over many shots.

Theoretical XFROG simulations also confirm this hypothesis and the ability of multi-shot XFROG to see fine-scale spectral structure that otherwise cancels out (see Fig. 17.6). Using a cubic spectral phase and a smooth super-Gaussian spectrum, we generate a smooth parabolic XFROG trace (Fig. 17.6a–c). Imposing 100% multiplicative noise on the spectrum, however, yields a pulse with much structure in its trace (Fig. 17.6d–h). The XFROG algorithm retrieves both the smooth and noisy spectra from their respective

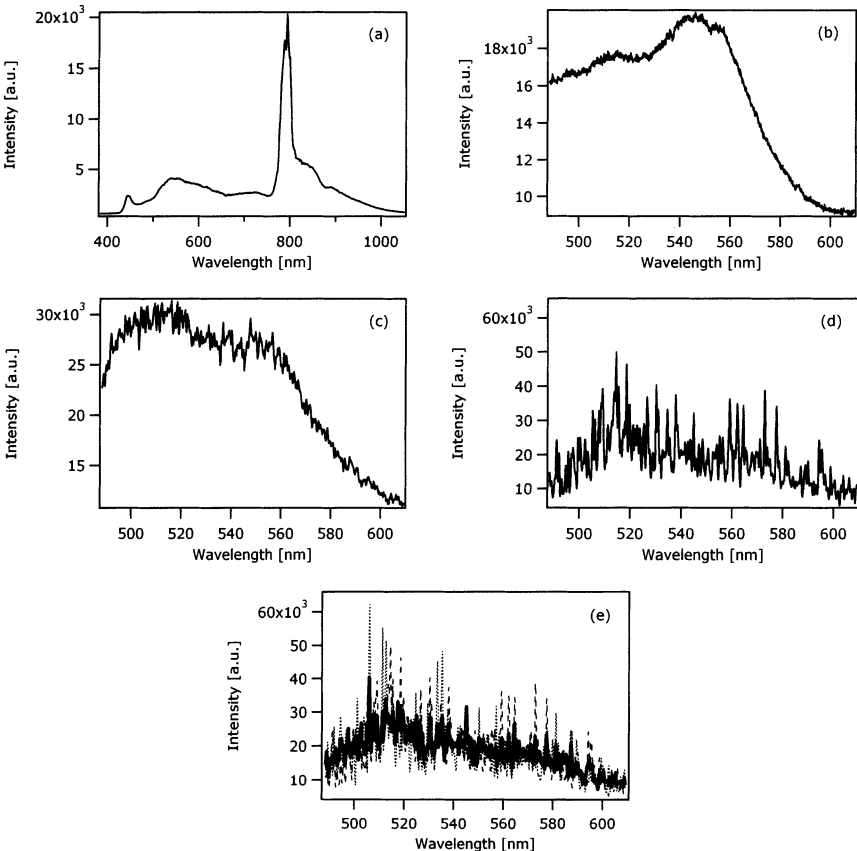


Fig. 17.5: (a) Entire range of the seemingly flat continuum (averaged over 10,000 pulses), (b) a spectral section of the continuum exposed for 10,000 shots, (c) exposed for 100 shots, (d) exposed for a single shot, (e) manual average of single-shot measurements taken successively, where the dashed and dotted lines are two single-shot spectra taken seconds apart, and the solid line is the average of four single-shot spectra.

traces. Averaging 100 of such noisy traces washes out the structure and generates a seemingly smooth trace, similar to what we measure in a multi-shot experiment (Fig. 17.6i,l). Retrieval on the smoothed-out trace not only preserves its gross shape, but also places the fine structure back into the spectrum and the trace (Fig. 17.6j,k,m). Also interesting to note is that the spectral phase is very well retrieved, whether we start from a smooth, noisy or artificially smoothed trace. This simulation imitates the real experiment and strongly supports our hypothesis.

These measurements show, incredibly, that it's possible to measure pulses as complex as the microstructure-fiber continuum, with its time-bandwidth product of >1000 . Of course, a multi-shot measurement inherently assumes that each pulse in the train is identical, and this is most assuredly not the

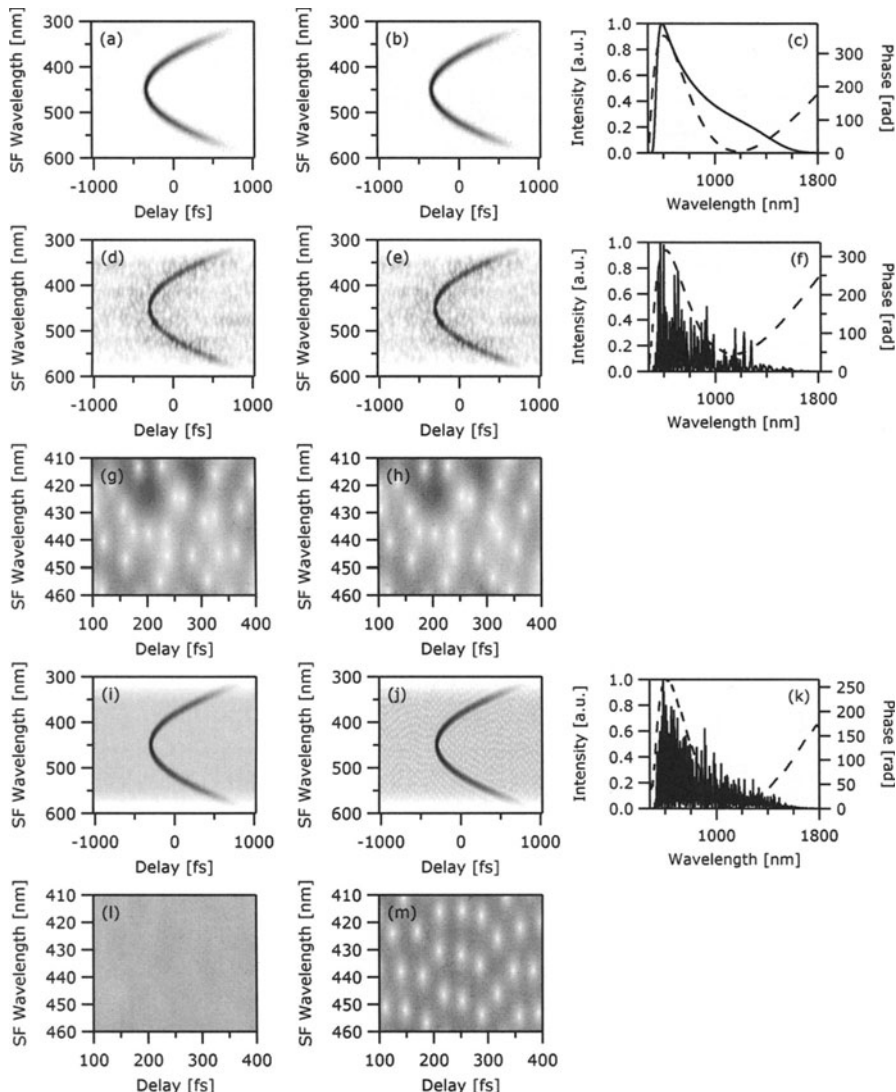


Fig. 17.6: Simulations: (a) theoretically generated, (b) retrieved XFROG traces and (c) retrieved spectral intensity and phase of a pulse of a smooth super-Gaussian spectrum and cubic spectral phase; (d) theoretically generated, (e) retrieved XFROG traces and (f) retrieved spectral intensity and phase of a pulse with a very noisy spectrum and cubic spectral phase; (i) average of 100 such noisy traces, (j) retrieved XFROG trace and (k) retrieved spectral intensity and phase from trace (i). Plots (g), (h), (l) and (m) are higher-resolution sections in traces (d), (e), (i) and (j) respectively.

case here. So any such measurement is necessarily non-quantitative. But the XFROG measurement much more accurately represented the actual pulse spectral structure than the simple averaged spectrum resulted and provided the clue that the spectrum was complex.

Work is now underway to make a single-shot measurement of the continuum. Do you think it can be done?

References

1. Ranka, J.K., R.S. Windeler, and A.J. Stentz, *Visible continuum generation in air-silica microstructure optical fibers with anomalous dispersion at 800 nm*. Opt. Lett., 1999. **25**(1): p. 25–7.
2. Diddams, S.A., et al., *Femtosecond-laser-based optical clockwork with instability $<6.3 \times 10^{-16}$ in 1 s*. Optics Letters, 2002. **27**(1): p. 58–60.
3. Hartl, I., et al., *Ultrahigh-resolution optical coherence tomography using continuum generation in an air-silica microstructure optical fiber*. Opt. Lett., 2001. **26**(9): p. 608–10.
4. Dudley, J.M., et al., *Complete Characterization of Ultrashort Pulse Sources at 1550 nm*. IEEE J. Quant. Electron., 1999. **35**(4): p. 441–450.
5. Baltuska, A., M.S. Pshenichnikov, and D.A. Wiersma, *Second-Harmonic Generation Frequency-Resolved Optical Gating in the Single-Cycle Regime*. IEEE J. Quant. Electron., 1999. **35**(4): p. 459–478.
6. O'Shea, P., et al., *Increased bandwidth in ultrashort-pulse measurement using an angle-dithered nonlinear-optical crystal*. Opt. Expr., 2001. **7**(10).
7. Delfyett, P.J., et al., *Joint Time-Frequency Measurements of Mode-Locked Semiconductor Diode Lasers and Dynamics Using Frequency-Resolved Optical Gating*. IEEE J. Quant. Electron., 1999. **35**(4): p. 487–500.
8. A. Gaeta, *Opt. Lett.*, in press.

18. Non-instantaneous Nonlinearities

Rick Trebino

The Real Shorter Event

It's time for a confession.

All along, we've been writing the induced polarization of the medium as, for example, $E_{\text{sig}}(t, \tau) \propto E(t)E(t - \tau)$, which results in a gate function, $g(t - \tau) = E(t - \tau)$. In reality, the gate function should be some sort of a convolution of $E(t - \tau)$ with some finite medium response time. In writing the above simpler expression, we've been tacitly assuming that the nonlinear-optical medium responds *instantaneously*. So when I said we could measure pulses without a shorter event, I was really cheating because the medium's response really is a shorter event.

By the way, we're not alone in assuming an instantaneous medium. Indeed, all ultrashort-pulse-measurement techniques require nonlinear-optical media with an essentially instantaneous response.* For example, autocorrelation measurements use SHG, multi-photon absorption, multi-photon ionization, or the electronic Kerr effect. These processes all occur on slightly subfemtosecond time scales and so are effectively instantaneous and hence sufficient for most pulse measurements.

Nevertheless, there are good practical reasons for developing measurement methods for use with slowly responding media. First, such nearly instantaneous effects tend to be weak, so deliberate use of a slower, but stronger, medium could extend the use of a technique to lower pulse energies if we could figure out how to make measurements using it. In general, it would be nice to have a greater choice of materials. In addition, the above "instantaneous" processes are often accompanied by non-instantaneous processes, such as Raman ringing, which can occur on a many-fs time scale. Also, when extremely broadband pulses are to be measured, it can be difficult to avoid encountering a single- or multi-photon resonance for some wavelength, which introduces slower responses than desired. Finally, subfemtosecond pulses have recently been generated, so a slightly subfemtosecond response doesn't look so fast anymore. And, of course, I don't want you to think I lied to you.

It turns out that FROG naturally accommodates a medium with a non-instantaneous response. FROG's iterative pulse-retrieval algorithm is in

* The term "instantaneous" actually caused the US Patent Office patent reviewer to reject the first FROG patent, since, as he pointed out, instantaneous media don't exist. We appealed, lost, got dumped into a mode called, "final rejection," appealed to a higher authority, and eventually won. The process dragged on for close to five years, nicely explaining the patent reviewer's skepticism of anything "instantaneous."

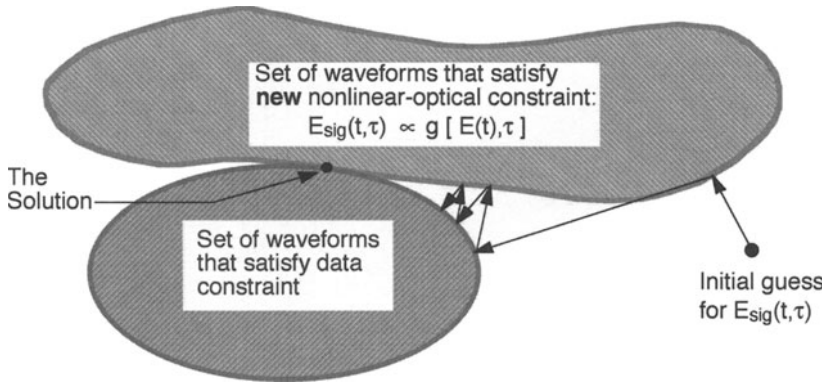


Fig. 18.1: Graphical picture of generalized projections in FROG when the medium's response is not instantaneous. Effectively, the shape of the set changes, but the basic idea is the same.

essence a deconvolution method. Recall that FROG involves only two expressions, one relating the signal field to the data and another relating the signal field to the pulse electric field. When a non-instantaneous medium is used, the latter expression would become a convolution of some sort (see Fig. 18.1). Who's to stop us from using the convolution and simply modifying the FROG algorithm to accommodate the more complex expression?

No one. The FROG algorithm simply involves computing derivatives that occur in various minimizations, and, while the expressions will be more complex, it's still straightforward to compute the relevant derivatives, and it's not hard for a computer to implement them [1].

Raman Effects in Third-order FROG

Here, we consider the Raman effect, which necessarily accompanies the electronic-Kerr effect in FROG using the polarization-gate (PG) geometry. For fused silica, it provides slight ringing on a ~ 30 -fs time scale in the induced polarization and hence distorts experimental polarization-gate (PG) FROG traces. Unaccounted for, it can lead to retrieved pulses as much as 8% too long for the worst case of 25-fs pulses. Fortunately, it's not difficult to construct a modified algorithm, based on the method of generalized projections, that accounts for the ringing—or, in principle, any other non-instantaneous effect—and accurately retrieves the correct pulse in all cases. In an experimental trace obtained for a 45-fs pulse, the modified algorithm achieved lower rms error and a shorter pulse length than previous FROG algorithms, which assumed an instantaneous response.

Using the Raman response of fused silica from Stolen and coworkers [2,3] and the formalism developed by Hellwarth [4], we can write an expression

for the PG FROG signal field including the Raman effect [1]:

$$\begin{aligned} E_{\text{sig}}^{\text{PG}}(t, \tau) = & E(t)|E(t - \tau)|^2 + E(t) \int_{-\infty}^t dt' b(t - t') |E(t' - \tau)|^2 \\ & + E(t - \tau) \int_{-\infty}^t dt' [2a(t - t') + b(t - t')] E(t) E^*(t - \tau) \end{aligned} \quad (18.1)$$

where the first term is the usual FROG signal field (attributed to the electronic Kerr effect), and the second and third terms are due to the slow response and correspond to the induced-birefringence and induced-grating terms, respectively. The response functions, $a(t)$ and $b(t)$ can be approximated [1,5]:

$$a(t) \approx \frac{43}{342} \frac{\tau_1^2 + \tau_2^2}{\tau_1 \tau_2^2} \exp(-t/\tau_2) \sin(t/\tau_1) \quad (18.2)$$

and $b(t) = 14 a(t)/43$, $\tau_1 = 12.2$ fs, and $\tau_2 = 32$ fs.

The full FROG signal field, Eq. (18.1), when Fourier transformed and magnitude squared becomes the FROG trace. In Fig. 18.2, we see the PG FROG trace created using the signal field of Eq. (18.2) and the response of Eq. (18.2) for a Gaussian, transform-limited pulse with a full-width at half-maximum (FWHM) of 25 fs. The small tails seen extending to negative delay times are a result of the slow Raman response of fused silica. Without the slow response, this FROG trace is a perfect ellipse, without any such tails.

The standard FROG pulse-retrieval algorithm, which explicitly assumes an instantaneous response, would attempt to fit the Raman-induced features of the trace by modifying the pulse. As a result, it doesn't retrieve the correct pulse

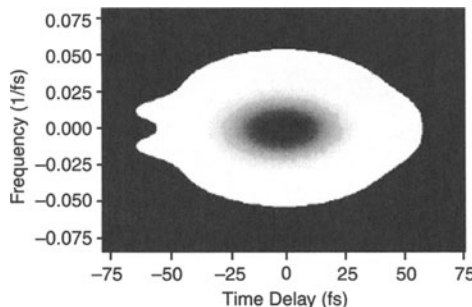


Fig. 18.2: The PG FROG trace of a transform-limited Gaussian pulse with a FWHM of 25 fs. The material response function of fused silica, including the effects of the slow Raman terms, is used to generate the trace. The small features extending to negative delay times are the result of the Raman terms. If the material response were truly instantaneous, the trace would be a perfect ellipse. The trace background is set to black wherever the intensity is less than 10^{-4} of the peak in order to accentuate the slight distortion of the trace.

when a non-negligible slow component of the response exists. Using Gaussian, transform-limited pulses with a FWHM of 10 elements on a 64-element array as input, we found that the standard algorithm retrieved pulses slightly longer than the actual pulses, and slightly asymmetric. The amount of broadening is largest for pulses of 25 fs FWHM, as seen in Fig. 18.3. Longer pulses are not affected, because the slow response is short compared to the pulse length. Extremely short pulses are not affected as strongly because the ratio of energy to intensity decreases with pulse length, so that the contribution from the integrals in Eq. (18.2) decreases relative to that of the fast term.

The effects on a 25-fs pulse retrieved with the standard FROG algorithm are shown in Fig. 18.4. We see that the time-domain pulse intensity is slightly distorted, while the frequency-domain phase has acquired a cubic character. These results are typical of the effect of the Raman terms on the retrieved pulse.

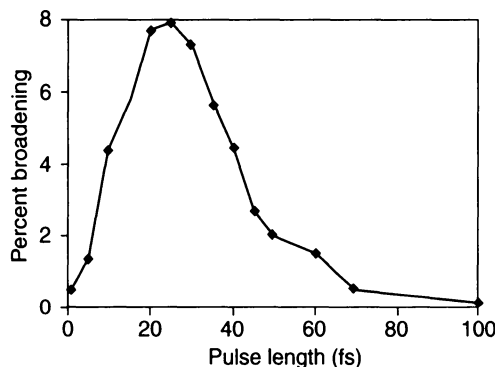


Fig. 18.3: The amount of temporal broadening in the pulse retrieved with the standard FROG algorithm due to the non-instantaneous Raman response of fused silica.

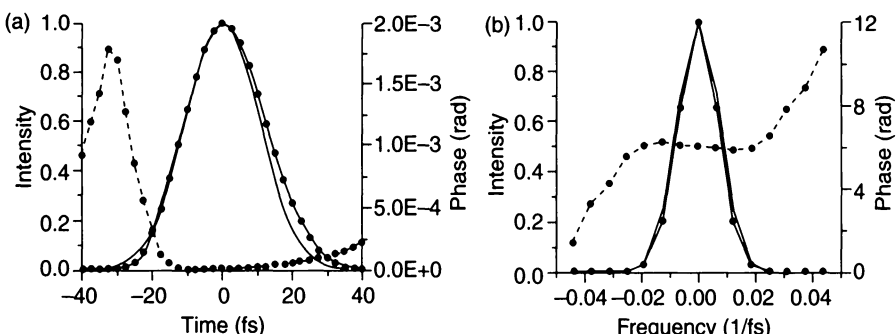


Fig. 18.4: The intensity and phase in the time domain (a) and the frequency domain (b) of the pulse retrieved by the standard FROG algorithm from a FROG trace (Fig. 18.1) distorted by the Raman response of fused silica. The original pulse was a 25 fs FWHM transform-limited Gaussian pulse. The standard FROG algorithm retrieves a pulse that is 8% longer in its temporal FWHM, and that has acquired some spectral cubic phase.

To improve the accuracy of PG FROG for 10- to 60-fs pulses, we can include Raman effects completely in a modified pulse-retrieval algorithm. The use of generalized projections allows us to use an arbitrary response function in the FROG algorithm. In this case, the time-domain error function that is now minimized in the algorithm is

$$Z = \sum_{i,j=1}^N \left| E'_{\text{sig}}(t_i, \tau_j) - E_{\text{sig}}^{\text{PG}}(t_i, \tau_j) \right|^2 \quad (18.3)$$

Here, $E'_{\text{sig}}(t, \tau)$ is the signal field after magnitude replacement by the experimental data and inverse Fourier transforming, $E_{\text{sig}}^{\text{PG}}(t, \tau)$ is from Eq. (18.2), and the summation runs over all the N^2 points in the signal field array. This modified algorithm, in principle, exactly retrieves pulses even in the presence of Raman effects. We tested this modified algorithm on several types of pulses, including pulses with complicated intensity and phase structure, and have found that in practice all of these pulses are retrieved exactly. The price to be paid for this increased accuracy, however, is speed. The modified algorithm runs much more slowly with the non-instantaneous terms: the number of calculations scales like N^3 rather than N^2 as in the purely instantaneous case.

We have also tested this modified algorithm on experimental data. The inset of Fig. 18.5 shows the PG FROG trace, made using fused silica as the nonlinear medium, of a pulse from an optical parametric generator pumped

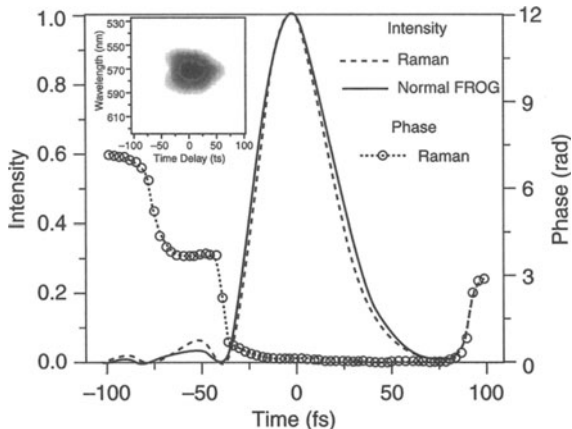


Fig. 18.5: Comparison of the pulse intensities derived by the normal instantaneous-response-based FROG algorithm and the algorithm modified to include the Raman response of fused silica. The Raman-aware algorithm achieved a lower error (0.00622 vs. 0.00733) and a shorter pulse (42.4 fs vs. 43.9 fs). The pulse phase is also shown. Inset: the PG FROG trace of the pulse. The tails seen on this trace are mostly due to residual third-order phase in the grating compressor, not to the Raman effect.

by an amplified Ti:Sapphire laser. When using the standard instantaneous-response-based FROG algorithm to invert this trace, we obtained a pulse with a 43.9 fs FWHM and a residual rms error per pixel of 0.00733. With the modified algorithm, including the Raman response, the FWHM of the retrieved pulse is 42.4 fs, and the error drops to 0.00622, indicating better convergence using the modified algorithm.

Experimental noise sets a lower limit on the obtainable error. The intensities derived by the two algorithms are compared in Fig. 18.5. Although the theory predicts only a 2.7% broadening for this pulse length, rather than the 3.5% broadening observed here, this discrepancy is probably due to experimental noise. We observed a similar reduction of retrieved pulse width for two other experimental traces of 42 and 34 fs FWHM.

This approach is very general; any response can be modeled. We're currently incorporating distortions induced by dispersion in the nonlinear medium, and we're considering exotic effects for measuring attosecond pulses.

The pulses discussed in this chapter have the same time scale as the Raman response; yet they could be retrieved using the knowledge of the response. Of course, if the medium response is much longer than the pulse, this approach will probably fail. But you may be surprised to find that in that case, it still could work if the response has, say, a fast *rise* time even if it has a very slow fall.

The same concepts discussed here could also, in principle, be used for the converse problem: to extract the response of a medium using the knowledge of the pulse field. In other words, if fully characterized pulses are used in an experiment, an algorithm such as that described here may perhaps deconvolve out the ultrafast response of a medium, even though it is on the order of, or even shorter than, the pulses used to measure it.

References

1. DeLong, K.W., Ladera, C.L., Trebino, R., Kohler, B., Wilson, K.R., Opt. Lett., **20**, 486 (1995).
2. R. H. Stolen, J. P. Gordon, W. J. Tomlinson, and H. A. Haus, J. Opt. Soc. Am. B **6**, 1159 (1989).
3. R. H. Stolen and W. J. Tomlinson, J. Opt. Soc. Am. B **9**, 565 (1992).
4. R. W. Hellwarth, Prog. Quantum Electron. **5**, 1 (1977).
5. K. J. Blow and D. Wood, IEEE J. Quantum Electron. **25**, 2665 (1989).
6. R. Hellwarth, J. Cherlow, and T.-T. Yang, Phys. Rev. B **11**, 964 (1975).

19. Fiber-FROG

John M. Dudley, John D. Harvey, and Mark D. Thomson

A wide range of FROG geometries have been used for ultrashort pulse characterisation, based on $\chi^{(2)}$ nonlinearities such as second-harmonic generation (SHG), and $\chi^{(3)}$ nonlinearities such as polarisation rotation, self-diffraction, and third harmonic generation (THG) [1]. The most sensitive technique is SHG-FROG, currently able to characterize pulses with pJ energy, but it does possess a fundamental ambiguity in the direction-of-time of the retrieved pulse. In this Chapter we describe the Fiber-FROG geometry [2], which is based on the $\chi^{(3)}$ (Kerr) nonlinearity in an optical fiber. Using a fiber waveguide increases the interaction length so that a $\chi^{(3)}$ -based geometry gives a sensitivity comparable to SHG-FROG, but without any direction-of-time ambiguity.

The Fiber-FROG Geometry

Pulse propagation in optical fibers generally depends on the combined effects of nonlinearity and dispersion. However, depending on the incident pulse characteristics and the particular fiber used, pulses can propagate such that only nonlinear effects are significant and dispersion is negligible [3]. In this case, the nonlinear pulse evolution in the fiber can be used in a FROG geometry as shown in Fig. 19.1. Here, incident pulses are split into two replicas with orthogonal linear polarisations (LP) using a polarizing beamsplitter (PBS), before being recombined with a variable delay. A half-wave plate ($\lambda/2$) at the input ensures that the output reference pulse $E(t)$ and the delayed replica $E(t - \tau)$ have equal amplitudes. A quarter-wave plate ($\lambda/4$) converts

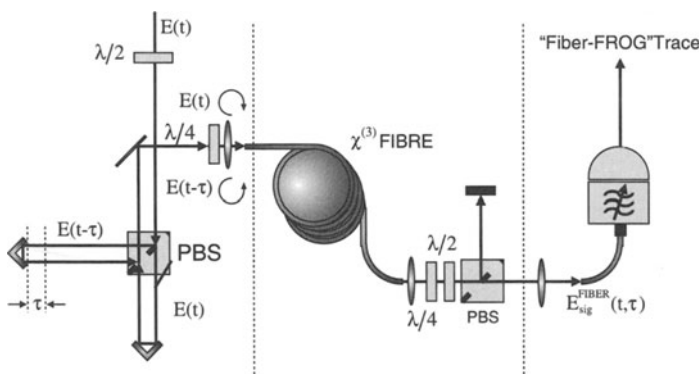


Fig. 19.1: Experimental setup for Fiber-FROG.

these LP-fields into counter-rotating circular-polarized (CP) fields, which are coupled into a length of fiber, where each pulse experiences a nonlinear phase shift due to the effects of self-phase modulation (SPM), and cross-phase modulation (XPM) from the co-propagating pulse with the opposite CP state. Note that the use of CP waves in this way increases the effect of XPM by a factor of 2 relative to LP fields and allows residual linear fiber birefringence to be neglected. A $(\lambda/4)$ plate at the fiber output converts these CP fields back into orthogonal LP fields, one of which is selected with a $\lambda/2$ plate and PBS to generate an output signal:

$$E_{\text{sig}}^{\text{FIBER}}(t, \tau) = E(t) \exp \left(i\gamma L \left[\frac{2}{3} |E(t)|^2 + \frac{4}{3} |E(t - \tau)|^2 \right] \right), \quad (19.1)$$

where γ is the fiber Kerr nonlinearity coefficient, and L is the fiber length.

It is clear that the evolution in the fiber generates a nonlinear phase transformation on the reference pulse $E(t)$. In the frequency domain, this leads to a constant amount of spectral broadening due to SPM, and a delay-dependent nonlinear frequency shift due to XPM. Although XPM in bulk media has previously been used for complete pulse characterization of mJ energy pulses [4], the use of a collinear geometry in an optical waveguide with Fiber-FROG greatly increases the sensitivity. A measurement of the spectrum of the output pulse as a function of delay thus yields the Fiber-FROG trace given by:

$$I_{\text{sig}}^{\text{FIBER}}(\omega, \tau) = \left| \int_{-\infty}^{\infty} E_{\text{sig}}^{\text{FIBER}}(t, \tau) \exp(i\omega t) dt \right|^2 \quad (19.2)$$

from which the pulse $E(t)$ is retrieved using the generalized projections (GP) algorithm. The algorithm does, however, require some modification for the Fiber-FROG geometry since the XPM phase-gating depends on the absolute pulse peak power in the fiber, and thus arbitrary normalization of the Fiber-FROG trace is not possible. In our algorithm, the Fiber-FROG trace is normalised such that the measured spectrum for each value of delay contains the same (experimentally determined) energy. In addition, efficient implementation of the algorithm requires analytic computation of the gradients of the functional distance Z giving the misfit between successive guesses for the signal field $E_{\text{sig}}^{\text{FIBER}}(t, \tau)$. For completeness, these expressions are given in the Appendix.

Experimental Design

The Fiber-FROG geometry is based on phase-gating, so that there is no harmonic frequency conversion and thus no explicit phasematching requirement to be met. This simplifies the experimental setup. The most important experimental factor in Fiber-FROG is, of course, the choice and length of optical fiber used. In particular, the fiber must be sufficiently long so that the XPM

frequency shift developed can be measured with adequate signal to noise ratio, yet sufficiently short so that dispersion is negligible and propagation remains well-described by Eq. (19.1). These constraints depend both on the properties of the incident pulses, as well as the particular fiber used, but numerical simulations of the non-linear Schrödinger equation (NLSE) have been carried out to determine accurate guidelines for experimental design. These guidelines can be quoted in terms of the nonlinear and dispersive lengths, the characteristic length scales usually used to describe pulse propagation in optical fibers. The nonlinear length depends on the pulse peak power P_0 and the Kerr nonlinearity coefficient γ and is defined as: $L_{NL} = (\gamma P_0)^{-1}$. The dispersion length usually depends on the group-velocity dispersion (GVD) parameter β_2 although for large-bandwidth pulses or near the fiber zero dispersion wavelength (ZDW), the effects of the third-order dispersion (TOD) parameter β_3 must also be considered. For an input pulse with *rms* pulse bandwidth $\Delta\omega$, the GVD and TOD dispersion lengths are defined as: $L_D = 1/(|\beta_2|\Delta\omega^2)$ and $L'_D = 1/(|\beta_3|\Delta\omega^3)$. Simulation results show that Fiber-FROG can be successfully used for pulse characterization provided that the fiber length L satisfies $L > 0.1L_{NL}$ and $L < 0.05 \min\{L_D, L'_D\}$. Note that the use of the *rms* bandwidth $\Delta\omega$ in these expressions permits their use even with non transform limited pulses. These two constraints together determine the domain of applicability of Fiber-FROG.

Results at 1.5 μm using DSF

Given the considerations in the preceding section, it is clear that Fiber-FROG is ideally-suited for pulse characterisation at wavelengths where the intrinsic fiber dispersion is minimized, around 1.3 μm in standard silica fiber, or around 1.5 μm using dispersion-shifted fiber (DSF). In our experiments we have used Fiber-FROG to characterize pulses from an erbium-doped fiber laser (EDFL) operating at 1534 nm, producing pulses of 1-2 ps FWHM at a repetition rate of 4.2 MHz. These pulses are typical of those which would be used in a high-capacity soliton or dispersion-managed RZ communications system, and thus provide an important test of the practical applicability of the technique. The experimental set-up was as in Fig. 19.1 where we used 20 m of commercially-available DSF (Corning SMF-DS) which had parameters: $\beta_2 = 9.5 \times 10^{-4} \text{ ps}^2 \text{ m}^{-1}$, $\beta_3 = 1.17 \times 10^{-4} \text{ ps}^3 \text{ m}^{-1}$, and $\gamma = 1.8 \times 10^{-3} \text{ W}^{-1} \text{ m}^{-1}$ at 1534 nm. Applying the guidelines above, such a fiber can be successfully used to characterize pulses with an *rms* bandwidth of $\Delta\omega < 1.6 \text{ Trad s}^{-1}$ (corresponding to a transform limited pulse duration (FWHM) $> 0.6 \text{ ps}$) with peak power $P_0 > 4 \text{ W}$. Taking coupling losses into account, this required a minimum incident peak power of $P_0 = 12 \text{ W}$ on our experimental set-up.

Figure 19.2 shows experimental results for EDFL pulses with an average power of 100 μW . Figure 19.2(a) shows the measured Fiber-FROG trace, centred about the fundamental wavelength, and containing spectral information

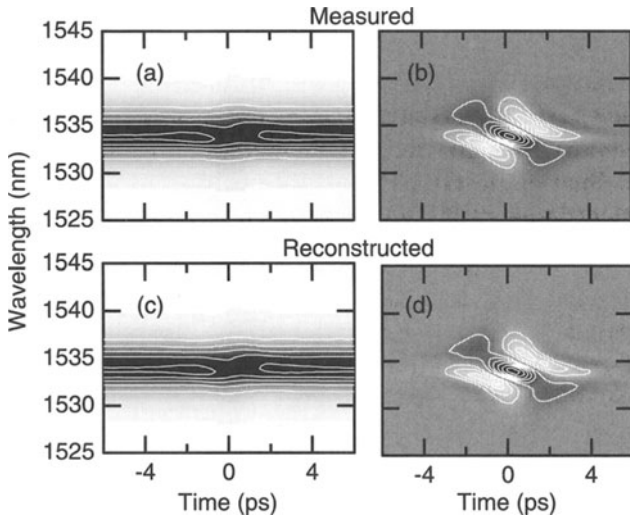


Fig. 19.2: Experimental results at $1.5 \mu\text{m}$. (a) and (c) show the measured and retrieved Fiber-FROG traces and (b) and (d) show the corresponding results after subtraction of the SPM background.

for all values of delay. For large delays the Fiber-FROG trace shows simply the self-phase modulated input pulse spectrum after propagation through the DSF, but near zero-delay, a delay-dependent nonlinear frequency shift from XPM is observed. This can be seen more clearly by subtracting the SPM component to obtain a “background-free” trace as in Fig. 19.2(b). Applying the GP algorithm to the data in Fig. 19.2(a) yields the reconstructed trace in Fig. 19.2(c), with corresponding background-free trace in Fig. 19.2(d).

The intensity and phase obtained from this retrieval are shown as the lines in Fig. 19.3(a). To confirm the accuracy of the Fiber-FROG technique, experiments using standard SHG FROG were also carried out. The SHG-FROG temporal ambiguity was removed by an additional propagation experiment, and the retrieved intensity and phase from these measurements are shown as the circles in Fig. 19.3(a). The retrieval errors were $G = 0.0024$ for the Fiber-FROG trace and $G = 0.0012$ for the SHG-FROG trace. As with other FROG geometries, there exist marginals that can be calculated from the measured trace to provide an independent check on the data quality [1]. The most useful Fiber-FROG marginal is the delay marginal obtained by calculating the mean spectral component of the Fiber-FROG trace as a function of delay [4]. This is linearly-related to the derivative of the intensity autocorrelation function, and can therefore be used to compute the autocorrelation function for comparison with that directly measured. Figure 19.3(b) shows the good agreement between this computed autocorrelation function (dotted line) and that measured (solid line). In addition, a final check on the data quality is to compare the measured autocorrelation and spectrum with those derived from

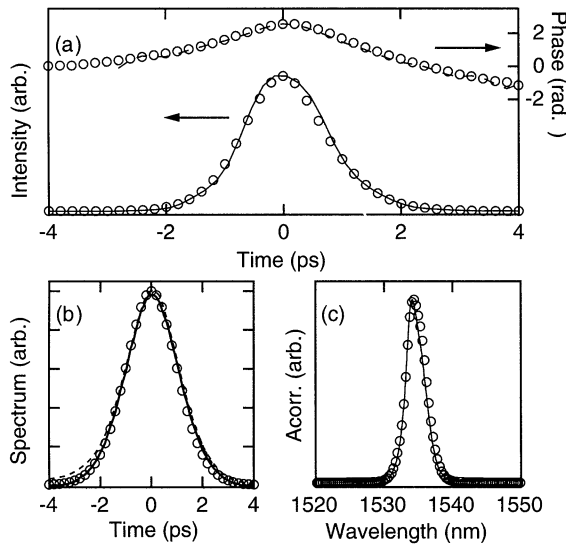


Fig. 19.3: (a) Retrieved intensity (left axis) and phase (right axis). (b) Measured autocorrelation (solid), that obtained from delay marginal (dashed) and from retrieved pulse (circles). (c) Measured spectrum (solid) and that from retrieved pulse (circles).

the retrieved pulse. These results are shown in Fig. 19.3(b) and (c) respectively (open circles), and there is clearly very good agreement. The intensity FWHM of the retrieved pulses was 1.6 ps, corresponding to an incident peak power of 15 W and an incident pulse energy of 24 pJ.

Conclusions and Future Opportunities

Fiber-FROG is a convenient technique for ultrashort pulse characterization, particularly at communications wavelengths. Experiments at $1.5\text{ }\mu\text{m}$ have demonstrated the pJ sensitivity associated with SHG-FROG, yet with no temporal ambiguity in the retrieved pulse. Experiments to date have used commercial DSF, but the use of recently-developed high-nonlinearity DSF [5], will allow the technique to be used over a much wider range of input pulse parameters. For example, considering DSF with $\gamma = 20.5 \times 10^{-3}\text{W}^{-1}\text{m}^{-1}$ [5], we can examine two ways in which the Fiber-FROG technique could be improved. Firstly, replacing the 20 m segment of commercial DSF in the experiment above with the same length of highly-nonlinear DSF, the measurement sensitivity would increase by an order of magnitude. A second application would be to use short lengths of highly-nonlinear DSF to allow Fiber-FROG to be used with broadband pulses. For example, a 5 cm length of this highly-nonlinear DSF would allow the complete characterization of 30 fs pulses with only 3 pJ energy, again yielding performance comparable to SHG-FROG but with unambiguous retrieval.

Appendix

The GP algorithm requires the minimisation of a functional distance metric relating the signal fields for two successive iterations:

$$Z = \sum_{k,j=1}^N \left| E_{\text{sig}}(t_k, \tau_j) - E'_{\text{sig}}(t_k, \tau_j) \right|^2 \quad (19.3)$$

where $E'_{\text{sig}}(t_k, \tau_j)$ is the signal array from the previous projection and $E_{\text{sig}}(t_k, \tau_j)$ is the new guess of the Fiber-FROG signal. To do this efficiently, we require the analytic derivatives of Z with respect to $\text{Re}[E(t_k)]$ and $\text{Im}[E(t_k)]$ [1], and here we give the appropriate expressions for Fiber-FROG. First we define:

$$\sigma(t_k, \tau_j) = E_{\text{sig}}(t_k, \tau_j) - E'_{\text{sig}}(t_k, \tau_j), \quad (19.4)$$

$$\varsigma(t_k, \tau_j) = \exp \left[i\gamma L \left(\frac{2}{3} |E(t_k)|^2 + \frac{4}{3} |E(t_k - \tau_j)|^2 \right) \right] \quad (19.5)$$

The expressions for the relevant derivatives are then given as follows:

$$\begin{aligned} & \frac{\partial Z}{\partial \text{Re}[E(t_k)]} \\ &= \sum_{j=1}^N 2\text{Re} \left\{ \sigma^*(t_k, \tau_j) \varsigma(t_k, \tau_j) \left(1 + \frac{4}{3} i\gamma L E(t_k) \text{Re}[E(t_k)] \right) \right\} \\ &+ \sum_{j=1}^N 2\text{Re} \left\{ \sigma^*(t_k + \tau_j, \tau_j) \varsigma(t_k + \tau_j, \tau_j) \frac{8}{3} i\gamma L E(t_k + \tau_j) \text{Re}[E(t_k)] \right\}, \end{aligned} \quad (19.6)$$

$$\begin{aligned} & \frac{\partial Z}{\partial \text{Im}[E(t_k)]} \\ &= \sum_{j=1}^N 2\text{Re} \left\{ \sigma^*(t_k, \tau_j) \varsigma(t_k, \tau_j) \left(i + \frac{4}{3} i\gamma L E(t_k) \text{Im}[E(t_k)] \right) \right\} \\ &+ \sum_{j=1}^N 2\text{Re} \left\{ \sigma^*(t_k + \tau_j, \tau_j) \varsigma(t_k + \tau_j, \tau_j) \frac{8}{3} i\gamma L E(t_k + \tau_j) \text{Im}[E(t_k)] \right\} \end{aligned} \quad (19.7)$$

We note that Z can also be minimized with respect to the nonlinearity coefficient itself, removing the need for *a priori* knowledge of this parameter.

The result in this case is:

$$\begin{aligned} \frac{\partial Z}{\partial \gamma} = & \sum_{j,k=1}^N 2\text{Re} \left\{ \sigma^*(t_k, \tau_j) E_{\text{sig}}(t_k, \tau_j) \left(\frac{2}{3} iL |E(t_k)|^2 \right) \right\} \\ & + \sum_{j,k=1}^N 2\text{Re} \left\{ \sigma^*(t_k, \tau_j) E_{\text{sig}}(t_k, \tau_j) \left(\frac{4}{3} iL |E(t_k - \tau_j)|^2 \right) \right\} \end{aligned} \quad (19.8)$$

References

1. R. Trebino, K. W. DeLong, D. N. Fittinghoff, J. N. Sweetser, M. A. Krumbügel and B. A. Richman: Rev. Sci. Instrum. **68**, 3277 (1997).
2. M. D. Thomson, J. M. Dudley, L. P. Barry, J. D. Harvey: Complete pulse characterisation using cross-phase modulation in optical fibers: Opt. Lett. **23**, 1582–1584 (1998).
3. G. P. Agrawal, *Nonlinear fiber optics*, 2nd ed. (Academic, New York, 1995).
4. M. A. Franco, H. R. Lange, J.-F. Ripoche, B. S. Prade and A. Mysyrowicz: Characterisation of ultrashort pulses by cross-phase modulation, Opt. Commun. **140**, 331–340 (1997).
5. T. Okuno, M. Onishi, T. Kashiwada, S. Ishikawa and M. Nishimura, Silica-based functional fibers with enhanced nonlinearity and their applications, IEEE J. Sel. Top. Quant. Electron. **5** 1385–1391 (1999).

20. Measuring Two Pulses Simultaneously: Blind FROG

Rick Trebino

Why One is Not Enough

It's not sufficient to be able to measure one ultrashort laser pulse; generally, one would like to be able to simultaneously measure *two* such pulses. For all ultrafast-spectroscopy experiments involve at least one ultrashort pulse to excite a medium and another to probe it, the measurement of both being necessary to characterize the experiment.

In addition, as shorter and shorter pulses are used to determine shorter and shorter material events in ultrafast nonlinear-spectroscopy experiments, more and more pulse distortions occur in propagating through optics from the laser to the sample under study. Since pulse measurements are still typically performed at the output of the laser—and not at the sample medium, which is where the pulse's parameters must be known—this source of error is becoming more and more significant. Thus, it's important to be able to measure the two pulses *at the sample medium*. In other words, the pulse-measurement device must be *incorporated into the experimental apparatus*.

So pulse-measurement techniques must be able to characterize two or more different pulses and do so at the sample medium. And, of course, such a technique should be as simple as possible. Is that asking too much?

Fortunately, it's not. Consider that a standard experiment in many labs involves exciting a medium under study with one pulse and then probing it a variable delay later with another pulse, often of a different color (see Figs 20.1 and 20.2). This type of experiment looks familiar. It involves overlapping two different pulses in time and space, varying the delay between them, and measuring something—often the spectrum!—as a function of delay. Indeed, we've already discussed turning a single-color spectroscopy experiment into a FROG (Chapters 11 and 14). Now we'd like to measure two different pulses at the sample medium by simply replacing the sample medium with, say, an SHG crystal.

In this chapter, we describe such a method. It is essentially XFROG (see Fig. 20.3), but with *two* unknown pulses, rather than with one unknown and one known. Like XFROG, it involves performing a spectrally resolved cross-correlation, in which one pulse gates another pulse [0]:

$$E_{\text{sig}}(t, \tau) = P(t)G(t - \tau) \quad (20.1)$$

The nonlinear interaction can be any fast nonlinearity. For example, using a polarization-gate beam geometry, $P(t) = E_1(t)$ and $G(t) = |E_2(t)|^2$, where $E_1(t)$ and $E_2(t)$ are the two unknown pulse electric fields. In this section,

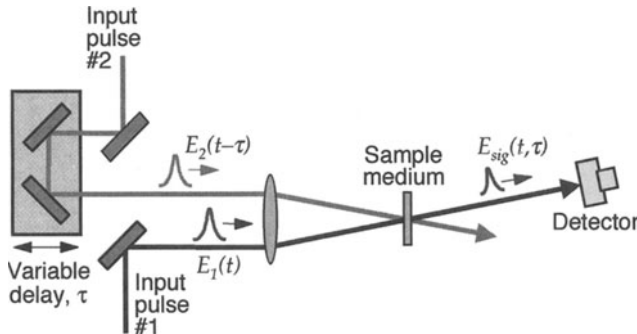


Fig. 20.1: A typical nonlinear-spectroscopy experiment, the *pump-probe* or *excite-probe* technique, in which pulse #2 (the pump pulse) excites the medium and pulse #1 (the probe pulse) probes it. The signal pulse is the change in the intensity of the probe pulse light, measured vs. delay. This set up is easily modified to yield a FROG or XFROG device.

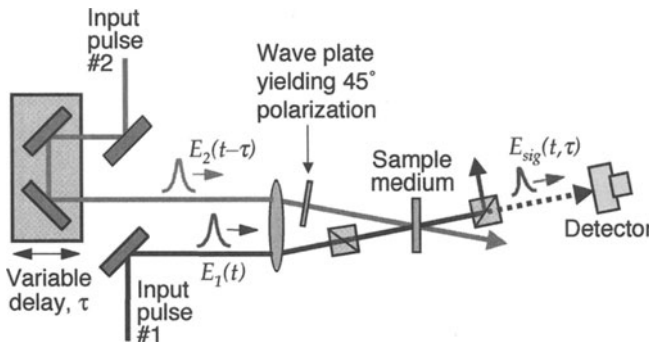


Fig. 20.2: Another typical nonlinear-spectroscopy experiment, *polarization spectroscopy*, in which pulse #2 (the excite pulse) excites the medium and pulse #1 (the probe pulse) probes it. The signal pulse is the light leaking through the polarizer. Typically, the signal pulse energy is measured vs. delay. This set-up is easily modified to yield a polarization-gate (PG) FROG.

as in XFROG, we'll use sum-frequency-generation (SFG) FROG, for which $P(t) = E_1(t)$ and $G(t) = E_2(t)$. As in XFROG, the trace is the spectrum of the signal field:

$$I_{\text{BlindFROG}}(\omega, \tau) = \left| \int_{-\infty}^{\infty} E_{\text{sig}}(t, \tau) \exp(-i\omega t) dt \right|^2 \quad (20.2)$$

but now we know *neither* of the fields and must find them *both*.

The pulse retrieval problem now is much more difficult than in XFROG, and it perhaps would not appear that such a trace contains sufficient information to determine both pulses. We'll take advantage of the fact that the mathematics that we'll encounter in this two-pulse extraction problem is equivalent to

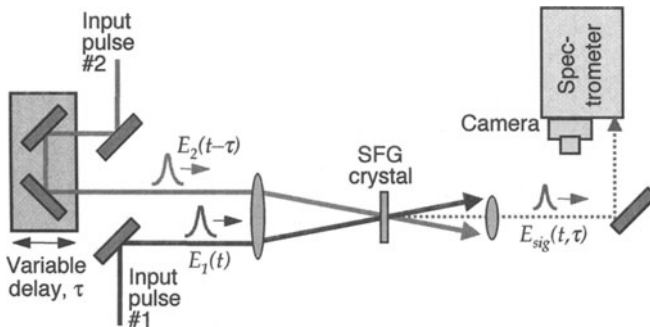


Fig. 20.3: Experimental arrangement for SFG Blind FROG, involving generating the sum frequency of the two pulses.

a remarkable problem, called *two-dimensional blind deconvolution* [1], a technique from image science that quite counter-intuitively allows one to extract *both* the image *and* an *unknown* blurring function from a blurred image. As a result, we'll call this two-pulse measurement technique *Blind FROG*. It's also been referred to as Twin Recovery of E-field Envelopes FROG, or TREE FROG. Figure 20.3 illustrates the geometry.

Blind Deconvolution

I hope you're skeptical because this is quite surprising. Consider that the convolution of two functions can be written:

$$h(t) = \int_{-\infty}^{\infty} f(t')g^*(t-t') dt' \quad (20.3)$$

This expression describes a wide range of phenomena, including the measurement of a pulse intensity with a detector that's too slow to resolve it. Much work has been devoted to the problem of obtaining $f(t)$ when $g(t)$ and $h(t)$ are known, and this problem is called *deconvolution*. It's a well developed field, and sophisticated iterative algorithms are available to do it.

Now imagine that we know $h(t)$, but *both* $f(t)$ and $g(t)$ are unknown to us. Kind of depressing, eh? Yes, this problem is impossible to solve. There are typically infinitely many pairs of functions, f and g , that yield a given h . This problem is called blind deconvolution for obvious reasons.

We can relate one-dimensional blind deconvolution to a familiar problem when $f = g$. Taking the Fourier transform of Eq. (20.3), we have in this case:

$$H(\omega) = |F(\omega)|^2 \quad (20.4)$$

If we know h , then, of course, we know H , which is the mag-squared Fourier transform of F . Thus, when $f = g$, one-dimensional blind-deconvolution reduces to our old nemesis, the *one-dimensional phase-retrieval problem!*

So one-dimensional blind-deconvolution is actually more difficult than one-dimensional phase retrieval because we typically can't even assume that $f = g$!

Of course, if you've been paying attention, you know that the trick is to consider the two-dimensional version of the problem:

$$h(x, y) = \int_{-\infty}^{\infty} \int_{-\infty}^{\infty} f(x', y') g^*(x - x', y - y') dx' dy' \quad (20.5)$$

where $h(x, y)$ is now the two-dimensional convolution of $f(x, y)$ and $g(x, y)$.

Again, if we know $h(x, y)$ and $g(x, y)$, then it's easy to find $f(x, y)$ using the same deconvolution techniques as in the one-dimensional problem.

Now, what about *two-dimensional blind deconvolution*, in which we know neither $f(x, y)$ nor $g(x, y)$?

Amazingly, it has, in fact, been shown that, while the one-dimensional blind-deconvolution problem has many ambiguities, the *two-dimensional* version of this problem surprisingly yields essentially unique results, provided that a simple constraint, such as finite support or non-negativity, exists [2]. And the special case of two-dimensional blind deconvolution when $f(x, y) = g(x, y)$ is equivalent to the two-dimensional phase-retrieval problem.

Blind FROG

The problem of retrieving two pulses from a spectrally resolved cross-correlation is equivalent to two-dimensional blind deconvolution! We can rewrite the expression for the Blind FROG trace in terms of the Wigner Distribution for each pulse field:

$$I_{\text{BlindFROG}}(\omega, \tau) = \int_{-\infty}^{\infty} \int_{-\infty}^{\infty} W_P(\omega_0, t) W_G(\omega_0 - \omega, t - \tau) dt d\omega_0 \quad (20.6)$$

where the Wigner Distribution for a function, $E(t)$, is given by:

$$W_E(\omega, \tau) \equiv \int_{-\infty}^{\infty} E\left(\tau + \frac{t}{2}\right) E^*\left(\tau - \frac{t}{2}\right) \exp[-i\omega t] dt \quad (20.7)$$

Specifically, the Blind FROG trace is the two-dimensional convolution of the Wigner distributions of the two (unknown) pulses.

In Fig. 20.4, we see the way that information about both the probe pulse $P(t)$ and gate pulse $G(t)$ is contained in the Blind FROG trace. It shows Blind FROG traces generated by a Gaussian probe pulse with temporal cubic phase and an unchirped gate pulse of various widths. Short gate pulses, which have a large spectral width, produce Blind FROG traces that are narrow in the delay direction and wide in the frequency direction, while longer gate pulses, which have a narrow spectrum, have the opposite effect.

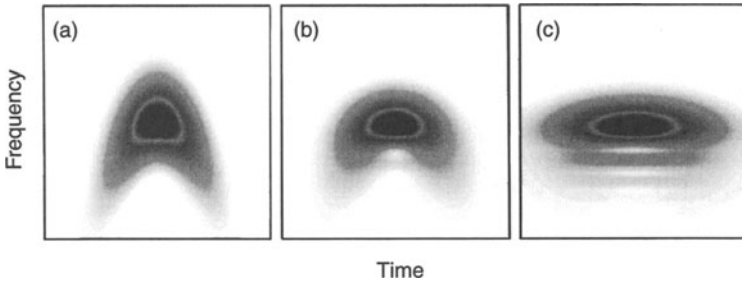


Fig. 20.4: SFG Blind FROG traces generated by a probe with temporal cubic phase and an unchirped gate. Both pulses have a Gaussian intensity profile, and were calculated on a 64-element array. The probe has a full-width at half maximum of 10, while the gate has a width of (a) 4, (b) 8, and (c) 16. As the gate gets smaller, its spectral content increases, so that the Blind FROG trace gets wider in the spectral dimension. The longer gate pulse (c), with its narrow spectrum, resolves spectral oscillations that are washed out in the traces made with shorter gate pulses.

Thus, it's clear that much information of both pulses is contained in the Blind FROG trace. Unfortunately, it's also easy to see that Blind FROG doesn't work as well as FROG. There are many ambiguities. For example, the Blind FROG trace generated by two independent linearly chirped Gaussians is a tilted ellipse, which is defined by only three parameters and hence only determines three of the required four parameters of the two pulses.

Why? Because we have no additional constraint, such as a mathematical form constraint that worked so well in FROG or even finite support. All we know about the Wigner distributions is that they're real.

Nevertheless, we can ask how well the technique works and try to fix it. Indeed, it's remarkable that any information is available at all.

The Blind FROG Algorithm

The task of the pulse retrieval algorithm is to find both $P(t)$ and $G(t)$ from $I_{\text{BlindFROG}}(\omega, \tau)$. Fortunately, we can borrow two-dimensional blind deconvolution algorithms [2,3]. The Blind FROG algorithm that we use is a modification of one such algorithm. And it is also a minor modification of the standard generalized-projections XFROG algorithm.

We begin with guesses for the fields $P(t)$ and $G(t)$, and use these guesses to generate $\tilde{E}_{\text{sig}}(\omega, \tau)$ via a Fourier transform of Eq. (20.1) with respect to t . On each iteration, we replace the magnitude of $\tilde{E}_{\text{sig}}(\omega, \tau)$ with the square root of the experimentally measured Blind FROG trace intensity, but leave the phase unchanged, to yield a modified signal field $\tilde{E}'_{\text{sig}}(\omega, \tau)$. An inverse Fourier transform with respect to ω generates $E'_{\text{sig}}(t, \tau)$. We then use the method of generalized projections [4,5] to generate new guesses for the fields.

Specifically, we formulate an error function Z , as

$$Z = \sum_{t,\tau=1}^N \left| E'_{\text{sig}}(t, \tau) - P(t)G(t - \tau) \right|^2 \quad (20.8)$$

The implementation of generalized projections proceeds by holding one of the fields fixed and modifying the other field on a given iteration [3]. On even iterations we hold $G(t)$ fixed and generate a new guess for $P(t)$ by minimizing Z with respect to $P(t)$, while on odd iterations we hold $P(t)$ fixed and generate a new guess for $G(t)$ by minimizing Z with respect to $G(t)$. This algorithm is effectively two XFROG algorithms, proceeding alternately. The algorithm continues until the resulting Blind FROG trace matches the experimental trace (or until the error between these two reaches a minimum).

In view of the ambiguities, we've found that using the spectra of the fields (easily measured quantities) as additional constraints improved the convergence of the Blind FROG algorithm considerably. On iterations where one field is modified through the use of generalized projections, we also replace the spectrum of the other field with its measured spectrum just prior to the application of the generalized projection [the minimization of Eq. (20.8)]. Including spectral constraints in this manner removes potential ambiguities and appears to make the Blind FROG algorithm quite robust. Measurement of the spectra can be achieved easily using the same spectrometer and camera that records the Blind FROG trace and hence doesn't complicate the apparatus significantly. We also emphasize here that we make no assumptions regarding the pulses; the above algorithm is completely general.

Demonstration of Blind FROG

We've demonstrated Blind FROG experimentally using SHG as the nonlinearity in a multi-shot configuration (although a single-shot arrangement should be straightforward). The experimental set-up is diagrammed in Fig. 20.3. A beam from a Spectra-Physics Tsunami Ti:Sapphire laser oscillator operating at 757 nm was split into two beams, a probe and a gate. The gate beam was passed through a variable time delay and a 6.5 cm length of BK7 glass. The two beams were then focused into a KDP frequency-doubling crystal, and the sum-frequency light was frequency resolved by a spectrometer. Recording this spectrum for all relevant delays between the two beams resulted in the Blind FROG trace seen in Fig. 20.5. Unlike SHG FROG, the SHG Blind FROG trace acquires a tilt from chirp, since the probe and gate fields are different.

We were able to retrieve the time-dependent intensity and phase of both the gate and probe fields using the Blind FROG algorithm described above. As propagation through BK7 glass leaves the spectrum of this pulse unchanged, we used the same spectrum to constrain both the probe and gate fields. Also,

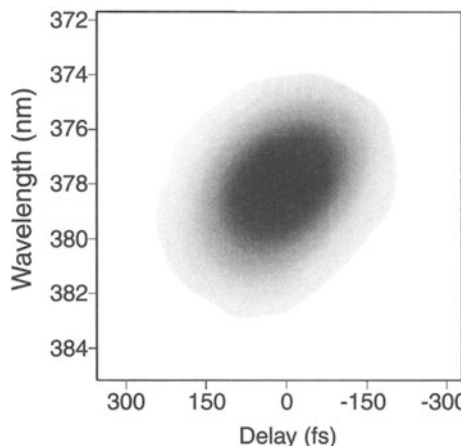


Fig. 20.5: The experimentally measured Blind FROG trace.

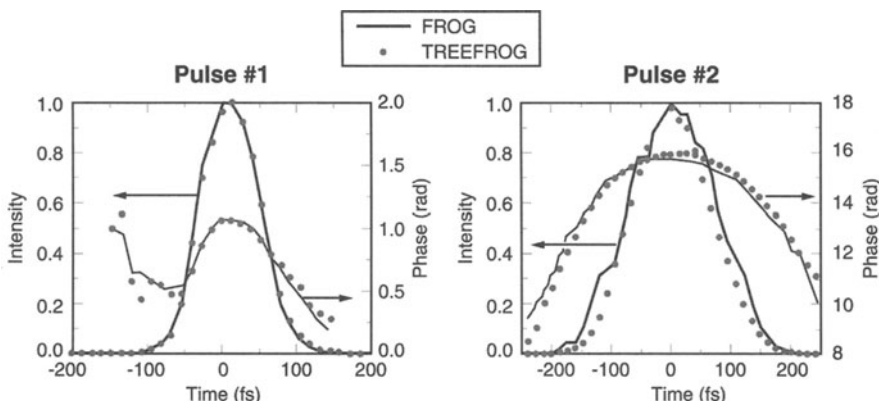


Fig. 20.6: The fields of the (a) probe and (b) gate retrieved using Blind FROG, compared to the fields retrieved using standard SHG FROG. The agreement is quite good.

because inevitable noise in the measured spectrum caused the spectrum-constraining process to introduce excess noise into the fields, after the algorithm reached what appeared to be its lowest obtainable error (after 100 iterations) we performed six additional iterations of the algorithm *without* the spectral constraint. This served to reduce the noise in the retrieved fields. The final error G was 0.00194 (on a 128×128 pixel trace).

The retrieved fields are shown in Fig. 20.6. In order to verify the fields, we independently made SHG FROG traces of the oscillator beam with and without the BK7 present in order to determine the intensity and phase of each field separately for comparison with the Blind FROG result. Figure 20.6 also shows the probe and gate fields, respectively, each measured with Blind FROG

and independently with FROG. The quite remarkable agreement between the fields retrieved with Blind FROG and the fields derived with SHG FROG indicates that the Blind FROG algorithm was quite successful at retrieving the intensity and phase of both the probe and gate fields.

Blind FROG can operate with all FROG geometries (of course, PG Blind FROG only measures the intensity of the gate pulse) and should have a variety of applications in experiments that require full characterization of both input and output pulses, even when one of the pulses is relatively weak.

Two-trace Blind FROG

While the above implementation of Blind FROG was interesting, Blind FROG unfortunately doesn't always uniquely determine the pulses unless individual pulse spectra are added as constraints. And the algorithms that have been developed for Blind FROG tend to stagnate. As a result, Blind FROG finds little use, and I frequently recommend against using it.

Nevertheless, the Blind FROG beam geometry remains compellingly convenient for spectroscopy applications. The ability to simply replace the experimental sample with a nonlinear medium and to measure two experimental input pulses at the sample would be extremely useful in many research efforts. As a result, it is important to improve Blind FROG. This can be done by noticing that most nonlinear-optical processes generate two or more signal beams (or the nonlinear medium can be forced to generate two signal beams), which have different signal beam expressions, and so taking *two* different Blind FROG traces simultaneously is possible. The second trace thus acts as the constraint we otherwise lack.

For example, we'll consider using *sum- and difference-frequency generation*, simultaneously [6]. This can be done using sandwiched sum- and difference-frequency-generation crystals. It results in an elegant setup in which both traces are taken on the same camera trace:

$$I_{\text{BlindFROG}}^{\text{SFG}}(\omega, \tau) \propto \left| \int_{-\infty}^{\infty} E_1(t) E_2(t - \tau) \exp(i\omega t) dt \right|^2 \quad (20.9)$$

$$I_{\text{BlindFROG}}^{\text{DFG}}(\omega, \tau) \propto \left| \int_{-\infty}^{\infty} E_1(t) E_2^*(t - \tau) \exp(i\omega t) dt \right|^2 \quad (20.10)$$

In order to recover the pulses from these traces, we must modify the FROG algorithm to accommodate both traces and both pulses. This is easily done and it simply involves considering the problem as two XFROG problems and alternating between treating one pulse as known and the other as unknown and vice versa. Preliminary computations have indicated that, using both traces, the pulses are fully determined by the data and the retrieval is much more reliable. This is because the frequency vs. time contributed by $E_2(t - \tau)$

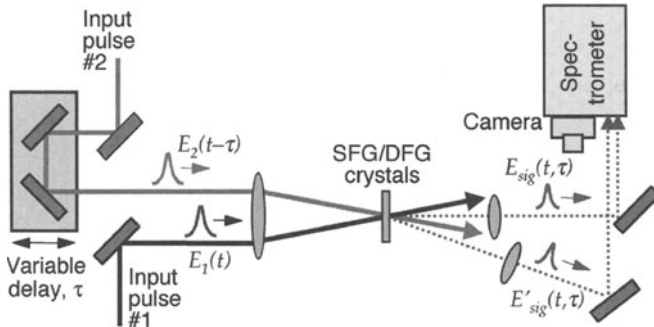


Fig. 20.7: Modified excite-probe apparatus for measuring both pulses at the sample medium. The sample medium is replaced with crystals that allow both sum- and difference-frequency generation, so each pulse acts to gate the other, but with different formulas for the signal beam for the different nonlinearities. Two signal fields are then spectrally resolved vs. delay. Only the crystals, beam-steering optics, a spectrometer, and a camera need to be added to the original excite-probe apparatus to realize this device.

is time-reversed in the two Blind FROG traces (due to the complex conjugate), so, very roughly speaking, each pulse's frequency vs. time can then be obtained by adding and subtracting the respective average frequencies vs. delay estimated from the two traces.

We have coded several versions of this new algorithm, and we have found it to be extremely robust, and convergence occurs rapidly (although this work is in progress). We have found no ambiguities, and it is unlikely that any occur, given the similarities to standard FROG, which is very robust. We have even found that the two pulses do not necessarily have to be the same length (although, in practice, they usually are), but pulses of very different lengths probably cannot be measured accurately in this manner.

Since researchers use, not only the excite-probe geometry, but other geometries such as polarization spectroscopy and induced-grating arrangements, it's possible to use analogous simple Blind FROG variations for these cases as well. Figure 20.8 shows a PG Blind FROG set-up. In this experiment, the probe pulse (pulse #2) passes through a typically isotropic sample medium placed between crossed polarizers. In the absence of an excite pulse, all probe light is rejected by the second polarizer. The excite pulse (pulse #1), polarized at 45° to the probe polarization, can, however, induce some birefringence in the sample medium, which may persist until the arrival of the probe pulse. This birefringence will then rotate the probe polarization somewhat, producing light that passes through the second polarizer. When the transmitted pulse is measured in some way vs. delay (or wavelength), this is a polarization spectroscopy experiment revealing useful information about the sample. When a piece of fused silica or other known instantaneously responding medium is the sample, and the transmitted pulse spectrum is measured vs. delay, a PG FROG

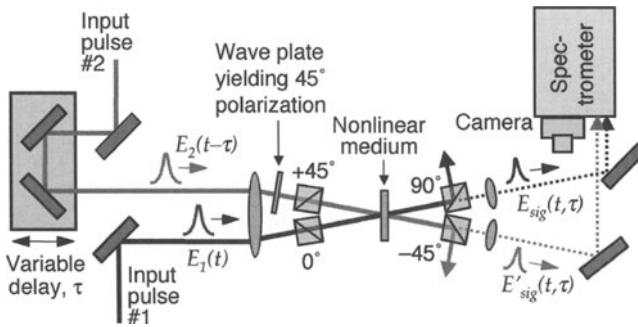


Fig. 20.8: Modified polarization-spectroscopy apparatus for measuring both pulses at the sample medium. Note that each pulse is polarized at 45° with respect to the other in the nonlinear-optical medium, so each acts to gate the other. Two signal fields are spectrally resolved vs. delay. Only another polarizer, beam-steering optics, a spectrometer, and a camera need to be added to the original polarization spectroscopy apparatus for this device.

trace is produced. Finally, when both possible signal beams are measured, it's two-trace PG Blind FROG.

Thus, the polarization spectroscopist, who would like to measure both pulses in his/her experiment, can simply replace the sample medium with a piece of fused silica and allow the excite pulse [with field, $E_2(t)$] to gate the probe pulse [with field, $E_1(t)$] achieving the signal field given by:

$$E_{\text{sig}}(t, \tau) \propto E_1(t) |E_2(t - \tau)|^2 \quad (20.11)$$

If the excite pulse is also surrounded by crossed polarizers—oriented at +45° and -45°—then it can be said that the probe pulse is also gating the excite pulse. This will then yield a signal field given by:

$$E'_{\text{sig}}(t, \tau) \propto E_2(t) |E_1(t - \tau)|^2 \quad (20.12)$$

We can also consider self-diffraction (SD) experiments, which are also common (see Fig. 20.9). In this case, the sample medium can be replaced with a piece of fused silica, and two self-diffracted pulses can be seen and spectrally resolved.

In SD Blind FROG, the two expressions for the signal fields are:

$$E_{\text{sig}}(t, \tau) \propto E_1(t)^2 E_2^*(t - \tau) \quad (20.13)$$

$$E'_{\text{sig}}(t, \tau) \propto E_2(t)^2 E_1^*(t - \tau) \quad (20.14)$$

Again, the standard FROG algorithm can be modified for these traces.

SD Blind FROG can also be used in standard two-beam excite-probe experiments if enough pulse energy is available. It is convenient because the two self-diffracted beams propagate directions that are different from the two-beam-excite-probe signal pulse and so the optics do not need to be rearranged to perform an experiment.

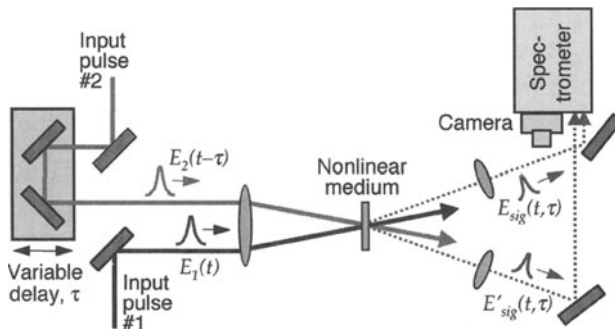


Fig. 20.9: Self-diffraction (SD) (or excite-probe) experimental apparatus in which both the excite, $E_1(t)$, and probe, $E_2(t - \tau)$, pulses are determined by simultaneous SD Blind FROG measurements. The two signal beams have the directions determined by $2\mathbf{k}_1 - \mathbf{k}_2$ and $2\mathbf{k}_2 - \mathbf{k}_1$, where \mathbf{k}_1 and \mathbf{k}_2 are the two input beam k-vectors. As before, the two signal fields are spectrally resolved vs. delay.

Finally, induced-grating, or transient-grating, experiments are also common. These experiments could in principle have three different pulses to be measured simultaneously. Using a thin piece of fused silica, three different self-diffracted beams can be generated, involving all three pairs of pulses. A similar algorithm can be imagined, but involving perhaps three traces.

Because most of the apparatus required for these measurements already exists in the ultrafast spectroscopy apparatus already present, the addition of the required optics to perform these measurements is relatively easy—much easier than it looks. And these methods should simplify and improve the accuracy of the pulse measurement task in most ultrafast spectroscopy experiments.

Finally, it's important to mention that the simple home-brew spectrometer discussed at the end of Chapter 11 may be implemented here as well, producing an apparatus that's considerably simpler.

References

0. K. W. DeLong, R. Trebino, and W. E. White, "Simultaneous recovery of two ultrashort laser pulses from a single spectrogram," *J. Opt. Soc. Am. B* **12**, 2463 (1995).
1. B. C. McCallum and J. M. Rodenburg, "Simultaneous reconstruction of object and aperture functions from multiple far-field intensity measurements," *J. Opt. Soc. Am. A* **10**, 231–239 (1993).
2. G. R. Ayers and J. C. Dainty, "Iterative blind deconvolution method and its applications," *Opt. Lett.* **13**, 547–549 (1988).
3. J. H. Seldin and J. R. Fienup, "Iterative blind deconvolution algorithm applied to phase retrieval," *J. Opt. Soc. Am. A* **7**, 428–433 (1990).
4. A. Levi and H. Stark, *Image Recovery: Theory and Applications*, H. Stark, ed. (Academic, San Diego, 1987), pp. 277–320.
5. Y. Yang, N. P. Galatsanos, and H. Stark, "Projection-based blind deconvolution," *J. Opt. Soc. Am. A* **11**, 2401–2409 (1994).
6. Erik Nibbering, private communication.

21. Principal Component Generalized Projections FROG Algorithm

Daniel J. Kane

The Need for Speed

Some pulse-measurement applications, such as pulse-shaping, require rapid computation of the intensity and phase. Unfortunately, as discussed in Chapter 8, the generalized projections algorithm can take a few seconds to converge or longer for very large arrays. This is largely due to the minimization step that's required in the standard formulation of generalized projections.

Under some circumstances, however, a different version of the generalized projections algorithm can be used that does not require the minimization step. This version [1,2], called *Principal Components Generalized Projections*, converts the generalized projections algorithm to an eigenvector problem. It works for FROG, and, it turns out, even better for Blind FROG [3,4].

To accomplish this, we borrow ideas from an analysis called *Principal Component Analysis* [5,6], commonly used in analytical chemistry and mass spectrometry. First, to make the derivation easier, we'll assume that the probe and the gate pulses are completely independent, i.e., Blind FROG. We'll add a method later to include the functional dependence between the probe and the gate to complete the derivation of the PCGP algorithm for FROG-trace inversion. The end result will be a robust, fast and easy-to-program inversion algorithm.

The derivation of the PCGP algorithm requires two important ideas. First, a FROG trace can be constructed from the outer product of two vectors (recall that the outer product of two vectors produces a 2-D matrix). One vector represents the probe and the other vector represents the gate. Second, a one-to-one transformation exists between the outer product matrix and the FROG trace, which allows us to convert from the outer product matrix to the FROG trace and back to the outer product matrix again indefinitely.

We'll start with a brief outline of the PCGP algorithm. (For a more detailed approach, please refer to the Appendix.) After the outline of the PCGP algorithm complete, we will show how to make the algorithm fast and how to convert it to a FROG algorithm for PG and SHG FROG.

Principal-Components Generalized Projections for Blind FROG

A Blind-FROG spectrogram, $I_{\text{FROG}}(\omega, \tau)$, is given by

$$I_{\text{FROG}}(\omega, \tau) = \left| \int_{-\infty}^{\infty} P(t)G(t - \tau) \exp(-i\omega t) dt \right|^2 \quad (21.1)$$

where the gate is represented as $G(t - \tau)$ and the probe as $P(t)$, with P and G having different associations with the fields, depending on the beam geometry, as described in the previous chapter.

Suppose $P(t)$ and $G(t)$ are sampled at given values of t with a constant spacing of δt . Then $P(t)$ and $G(t - \tau)$ can be thought of as vectors of length N whose elements sample P and G at discrete times. These vectors can be written as

$$\begin{aligned} \mathbf{P} &= [P(t_1), P(t_2), P(t_3), \dots, P(t_N)] \\ \mathbf{G} &= [G(t_1), G(t_2), G(t_3), \dots, G(t_N)] \end{aligned} \quad (21.2)$$

Figure 21.1 below illustrates the steps involved in producing the FROG trace from the probe and gate vectors. First, an outer product of the probe and gate vectors is taken (upper left). Then, the row number minus one shifts each row left (upper right). The columns are rearranged to form the time-domain FROG trace, $E_{\text{sig}}(t, \tau)$. Fourier transforming the columns produces the FROG trace. Once the FROG trace is calculated, the steps to generate the FROG trace can be reversed to produce the outer product matrix again.

Like all of the FROG inversion algorithms, the PCGP algorithm (Fig. 21.2) is usually started using Gaussian pulses with random phase for the initial guess for $P(t)$. The initial gate pulse is derived from $P(t)$ according to the FROG geometry used. A spectrogram is constructed, and its magnitude is

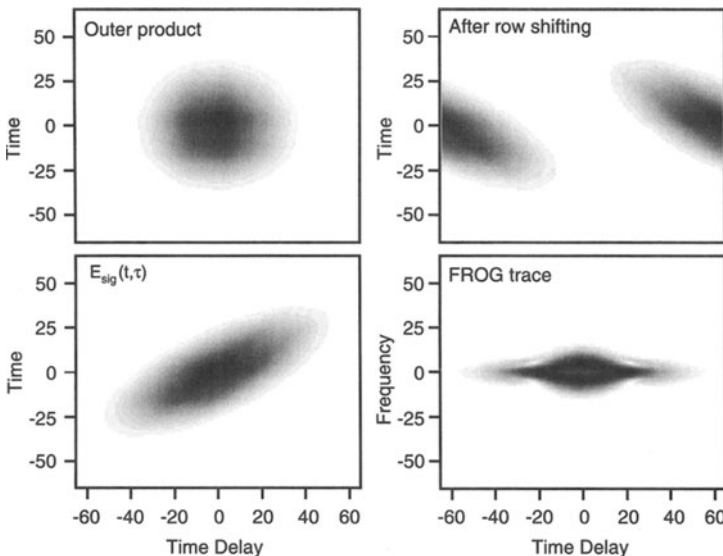


Fig. 21.1: Illustration of the steps in the PCGP algorithm for an SHG-FROG trace. The upper left image is the outer product. The upper right image shows the outer product after it has been row shifted. By rearranging the columns, $E_{\text{sig}}(t, \tau)$ can be constructed (lower left). Fourier transforming the columns produces the FROG trace (lower right).

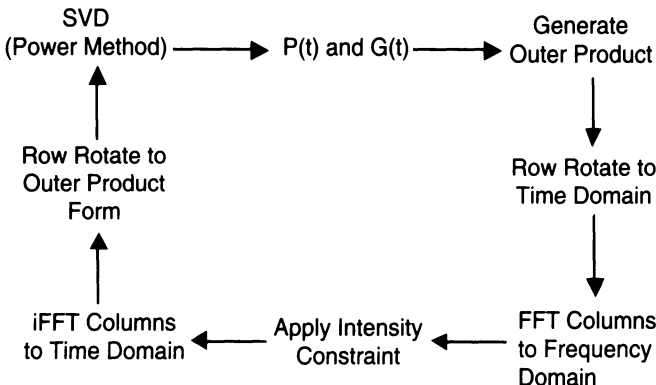


Fig. 21.2: Schematic of the PCGP algorithm.

replaced by the square root of the magnitude of the experimentally obtained spectrogram. The resulting signal field vs. frequency and delay is transformed to the time-domain using an inverse Fourier transform by column. Next, the time-domain signal field is converted to the outer product form (Eq. 21.A3) by reversing the steps used to construct the time domain spectrogram. If the intensity and phase of the spectrogram are correct, this outer product form matrix is a true outer product and has a rank of one. That is, it would have one and *only one* non-zero eigenvalue and one *right* eigenvector and one *left* eigenvector. The *right* eigenvector, the probe, spans the range of the outer product matrix. The complex conjugate of the eigenvector of the transpose of the outer product matrix, i.e., the *left* eigenvector, is the gate [5].

The outer product form matrix produced by the initial guess, however, is not of rank one and will have N left and right eigenvectors for an $N \times N$ FROG trace. Instead of describing a single line in N space, the outer product form matrix represents an ellipsoid in N space. The next guess may actually be a superposition of two or more different, but linearly independent eigenvectors, requiring an optimization such as a minimization of the FROG trace error to find the correct superposition.

Fortunately, a time consuming minimization is not required. Suppose we decompose the outer product form matrix, \mathbf{O} , into three matrices such that

$$\mathbf{O} = \mathbf{U} \times \mathbf{W} \times \mathbf{V}^T \quad (21.3)$$

where \mathbf{U} and \mathbf{V}^T are orthogonal square matrices and \mathbf{W} is a square diagonal matrix. Thus, the matrix \mathbf{O} is decomposed into a superposition of outer products between “probe” vectors (columns of \mathbf{U}) and “gate” vectors (rows of \mathbf{V}^T). Only the diagonal values of \mathbf{W} are non-zero and determine the relative weights of each outer product, and, therefore, how much each outer product contributes to the outer product form \mathbf{O} . If we only keep the outer product pair with the largest weight, or *principal component*, for the next iteration of

the algorithm, we minimize the function

$$\varepsilon^2 = \sum_{i,j=1}^N |O_{ij} - P_i G_j|^2 \quad (21.4)$$

where ε is the error [6]. Note that this is the definition of a projection and is similar but not identical to the projection in the GP algorithm discussed earlier [3,7,8].

One elegant, but computationally expensive, means to find the principal vector pair is to use a *singular value decomposition* (SVD) to decompose \mathbf{O} into \mathbf{U} , \mathbf{W} , and \mathbf{V} directly [18,19]. This approach is convenient because many commercially available mathematical libraries contain routines to compute SVD's. Another way to find the principal vector pair with much less computational effort than an SVD is to reduce the SVD step to simple, low overhead, and fast matrix-vector multiples [9], which is the best approach for real-time applications [2]. To find the next guess for the pulse ($P^{(k+1)}$) and gate ($G^{(k+1)}$), we only need to convert $P^{(k)}$ and $G^{(k)}$ to $P^{(k+1)}$ and $G^{(k+1)}$ using the following equations:

$$\begin{aligned} \mathbf{O}\mathbf{O}^T P^{(k)} &= P^{(k+1)} \\ \mathbf{O}^T \mathbf{O} G^{(k)} &= G^{(k+1)} \end{aligned} \quad (21.5)$$

where \mathbf{O} is the outer product form matrix and the superscript T denotes the transpose operator. (For a complete derivation of equation 21.5, see Appendix A.)

This implementation of the PCGP algorithm is called the *power method* implementation and is very fast and quite robust; it can loop at nearly 20 iterations/second on a 60 MFLOPS digital signal processor or nearly 80 iterations/second on a 450 MHz Pentium II (for a 64×64 pixel FROG trace). Good approximations for the pulse usually occur in about 40 iterations [2] from an initial guess.

Conversion from Blind-FROG to FROG

The PCGP algorithm, as discussed so far, is a Blind-FROG algorithm; the probe and gate are independent. The only non-linear interaction assumed is the multiplication of the probe by a gate. How the gate is constructed is of no concern. As a result, some ambiguities can occur, which, even though they are usually minor, can produce erroneous results if ignored [4]. Spectral constraints can facilitate inversion of FROG spectrograms using the PCGP algorithm. This method has been used extensively to invert experimental FROG traces and Blind-FROG traces [10]; see the MI-FROG chapter. Often, however, a spectrum is not available, and it would, therefore, be desirable if a spectrum were not required to invert the pulse's spectrogram.

The conversion of the PCGP algorithm to a FROG algorithm is accomplished by summing the outer product of the probe and the gate with the outer product of the probe constructed from the gate and the gate constructed from the probe [2]. How the gate is constructed from the probe and *vice versa* is determined from the nonlinear interaction. In the case of SHG-FROG, for example, the probe is equal to the gate; thus the outer product becomes

$$O_{ij}^{(k)} = P_i^{(k)} G_j^{(k)} + G_i^{(k)} P_j^{(k)} \quad (21.6)$$

forming the FROG trace from the sum of two outer products. Because only the principal outer product pair is used for the next estimate of the electric field, the two outer products are forced to be equal. The only way the outer products can be equal is if the probe and gate are equal.

This PCGP algorithm works very well for SHG FROG, and it has shown that it generally converges faster than the standard GP algorithm [1,2]. SHG FROG is a special case, however, because Eq. (21.6) is valid only for SHG FROG and must be modified for other FROG geometries. To do so, we note that $E_{\text{sig}}(t, \tau)$ can be written in more general form as

$$E_{\text{sig}}(t, \tau) = P(t) \Gamma[P(t - \tau)] \quad (21.7)$$

where Γ is the function that produces the gate from the probe, $E(t)$; its inverse, Γ^{-1} , produces the probe from the gate. Rather than using only the outer product of P and G to produce the next time-domain FROG trace, the sum of the outer products $P_i G_j$ and $\Gamma^{-1}(P_i) \Gamma(G_j)$ is used so that the outer product on the next iteration is given by

$$O_{ij}^{(k)} = P_i^{(k)} G_j^{(k)} + \Gamma^{-1}[G_i^{(k)}] \Gamma[P_j^{(k)}] \quad (21.8)$$

where $\mathbf{O}^{(k)}$ is the sum of the two outer products for the k -th iteration.

Equation (21.8) allows the PCGP algorithm to be used with any FROG geometry where Γ^{-1} exists. In PG-FROG, however, the inverse of the gate function does not exist. As a result, a pseudo-inverse must be constructed from the square root of the gate intensity and the phase of the pulse. Because the square root can cause small fluctuations in the wings of the gate, producing artifacts in the next guess for the pulse, instabilities may occur in the algorithm. This can be remedied by applying the square root to only well defined portions of the gate. Where the gate is not well defined, i.e., where the intensity is near zero, the intensity and phase of the pulse is used. To increase the robustness of the PCGP algorithm, the pseudo-inverse constraint is applied on alternate iterations. This pseudo-inverse method has shown to work well for PG-FROG [1], but it does not appear to work well for the self-diffraction geometry.

Real-time Inversion of FROG Traces

The PCGP algorithm is fast, easy to program and easy to optimize; it can facilitate the inversion of FROG traces in real time if the data acquisition

is integrated with the inversion algorithm. Initial work on building such a “Femtosecond Oscilloscope” used two commercially available digital signal processing (DSP) boards in a 166 MHz Pentium host PC. One DSP board was used for data acquisition while the other DSP board inverted the FROG trace. By using this system, 64×64 pixel SHG-FROG traces could be inverted at a rate of 1.25 Hz and 32×32 pixels traces at a rate of 2.3 Hz [1,2].

Because of improvements in processor technology, later versions of the femtosecond oscilloscope do not require DSP boards. By using a video camera and a frame grabber for the data acquisition, 20 Hz inversion rates for 64×64 FROG traces using a dual 550 MHz Pentium III workstation have been demonstrated. Even faster rates will be possible as camera and computer technology improves.

Appendix A: Derivation of the Principal Components Generalized Projections Algorithm

Construction of the FROG trace from the pulse and gate vectors

Suppose $P(t)$ and $G(t)$ are sampled at given values of t with a constant spacing of Δt . Then $P(t)$ and $P(t - \tau)$ can be thought of as vectors of length N whose elements sample P and G at discrete times:

$$\begin{aligned} P &= [P(-\frac{N}{2}\Delta t), P(-(\frac{N}{2}-1)\Delta t), P(-(\frac{N}{2}-2)\Delta t), \dots, P(\frac{N}{2}\Delta t)] \\ G &= [G(-\frac{N}{2}\Delta t), G(-(\frac{N}{2}-1)\Delta t), G(-(\frac{N}{2}-2)\Delta t), \dots, G(\frac{N}{2}\Delta t)] \end{aligned} \quad (21.A1)$$

For simplicity, these vectors can be written as

$$\begin{aligned} P &= [P(t_1), P(t_2), P(t_3), \dots, P(t_N)] \\ G &= [G(t_1), G(t_2), G(t_3), \dots, G(t_N)] \end{aligned} \quad (21.A2)$$

The outer product of P and G is then

$$\mathbf{O} = \begin{bmatrix} P(t_1)G(t_1) & P(t_1)G(t_2) & P(t_1)G(t_3) & \dots & P(t_1)G(t_N) \\ P(t_2)G(t_1) & P(t_2)G(t_2) & P(t_2)G(t_3) & \dots & P(t_2)G(t_N) \\ P(t_3)G(t_1) & P(t_3)G(t_2) & P(t_3)G(t_3) & \dots & P(t_3)G(t_N) \\ \vdots & \vdots & \vdots & \ddots & \vdots \\ P(t_N)G(t_1) & P(t_N)G(t_2) & P(t_N)G(t_3) & \dots & P(t_N)G(t_N) \end{bmatrix} \quad (21.A3)$$

The outer product is a rank one matrix that contains all of the points required to construct the time domain FROG trace because it contains all of the interactions between the pulse and gate for the discrete delay times. Consequently,

a simple rearrangement of the elements of the outer product can transform the outer product into the time domain FROG trace. This invertible, one-to-one mapping is the key to the *Principal Component Generalized Projections* (PCGP) algorithm allowing transformations to be made from the outer product form to the time domain FROG trace and vice versa. This transformation can be accomplished by rotating the elements of the rows in the outer product form to the left by the row number minus one. Applying this transformation, we obtain:

$$\mathbf{O} = \begin{bmatrix} P(t_1)G(t_1) & P(t_1)G(t_2) & P(t_1)G(t_3) & \dots & P(t_1)G(t_{N-1}) & P(t_1)G(t_N) \\ P(t_2)G(t_1) & P(t_2)G(t_3) & P(t_2)G(t_4) & \dots & P(t_2)G(t_N) & P(t_2)G(t_1) \\ P(t_3)G(t_3) & P(t_3)G(t_4) & P(t_3)G(t_5) & \dots & P(t_3)G(t_1) & P(t_3)G(t_2) \\ \vdots & \vdots & \vdots & \ddots & \vdots & \vdots \\ P(t_N)G(t_N) & P(t_N)G(t_1) & P(t_N)G(t_2) & \dots & P(t_N)G(t_{N-2}) & P(t_N)G(t_{N-1}) \end{bmatrix}$$

$$\tau = 0 \quad \tau = -\Delta t \quad \tau = -2\Delta t \quad \dots \quad \tau = 2\Delta t \quad \tau = \Delta t \quad (21.A4)$$

where \mathbf{O}' is the transformed outer product matrix \mathbf{O} . The first column of Eq. (21.A4) is the $\tau = 0$ column; i.e., a point-by-point multiplication of probe and gate with no time shift between them. The next column is the $\tau = -\Delta t$ column where the gate is delayed relative to the probe by one resolution element, Δt . The gate appears to be shifted “up” by one resolution element with the first element wrapped around to the other end of the vector. Column manipulation places the most negative τ on the left and the most positive on the right. Thus, Eq. (21.A4) is the time-domain of the spectrogram formed by the multiplication of the probe and gate functions; a discrete version of the product $P(t)G(t - \tau)$. The columns are constant in delay τ while the rows are constant in time t . This gives exactly the same result as calculating the time domain FROG trace directly by shifting the gate in time and multiplying the shifted gate by the probe. All that is done here is insuring that there is a reversible way to move between the outer product and the time domain FROG trace. By Fourier transforming each column of \mathbf{O}' , the Fourier transform of $P(t)G(t - \tau)$ is obtained as a function of t . The final step of taking the magnitude of the complex result produces the FROG trace.

Obtaining the Next Guess

Once the FROG trace is obtained, the intensity constraint is applied, and the steps producing the FROG trace are reversed. The columns are inverse Fourier transformed. The inverse of the outer-product-to-time-domain-FROG-trace inversion is then applied. We call the resulting matrix the outer product form matrix because it may not be a true outer product. Only when the algorithm is fully converged will the outer product form matrix be a true, rank 1, outer product matrix. When inverting experimental FROG traces, however, the outer product form matrix is never a rank 1 outer product; the outer product from

matrix is rank N (for an $N \times N$ pixel FROG trace). The next guess for the probe and the gate is obtained by determining the best rank 1 approximation for the outer product form matrix.

Suppose we decompose the outer product form matrix, \mathbf{O} , into three matrices such that

$$\mathbf{O} = \mathbf{U} \times \mathbf{W} \times \mathbf{V}^T \quad (21.A5)$$

where \mathbf{U} and \mathbf{V}^T are orthogonal square matrices and \mathbf{W} is a square diagonal matrix. Thus, the matrix \mathbf{O} is decomposed into a superposition of outer products between “pulse” vectors (columns of \mathbf{U}) and “gate” vectors (rows of \mathbf{V}^T). Only the diagonal elements of \mathbf{W} are non-zero and determine the relative weights of each outer product and, therefore, how much each outer product contributes to the outer product form \mathbf{O} . If we only keep the outer product pair with the largest weighting factor, or *principal component*, for the next iteration of the algorithm, we minimize the function

$$\varepsilon^2 = \sum_{i,j=1}^N |O_{ij} - P_i G_j|^2 \quad (21.A6)$$

where ε is the error [6]. Note that this is the definition of a projection and is similar but not identical to the projection in the GP algorithm discussed earlier [3,20,21].

One elegant but computationally expensive means to find the principal vector pair is to use a singular value decomposition (SVD) to decompose \mathbf{O} into \mathbf{U} , \mathbf{W} , and \mathbf{V} directly [5,6]. This approach is convenient because many commercially available mathematical libraries contain routines to compute SVD’s. Another way to find the principal vector pair with much less computational effort than an SVD is to reduce the SVD step to simple, low overhead, and fast matrix-vector multiples [9], which is the best approach for real-time applications [2].

Rather than finding the eigenvectors of \mathbf{O} and constructing an ortho-normal basis from these vectors, an SVD finds the eigenvectors of $\mathbf{O}\mathbf{O}^T$ (columns of \mathbf{U}) and $\mathbf{O}^T\mathbf{O}$ (columns of \mathbf{V}) which are ortho-normal [5,6]. If the columns of \mathbf{U} are written as \mathbf{U}_i and the columns of \mathbf{V} are written as \mathbf{V}_i , then they satisfy the equations

$$\begin{aligned} \mathbf{O}\mathbf{O}^T\mathbf{U}_i &= \lambda_i \mathbf{U}_i \\ \mathbf{O}^T\mathbf{O}\mathbf{V}_i &= \lambda_i \mathbf{V}_i \end{aligned} \quad (21.A7)$$

where λ_i are the eigenvalues, or “weights,” and the superscript T denotes the transpose operator. \mathbf{O} can be constructed by

$$\mathbf{O} = \sum_{i=1}^N \sqrt{\lambda_i} \mathbf{U}_i \mathbf{V}_i^T \quad (21.A8)$$

where all λ_i , U_i , and V_i are provided by the SVD, but we only need the U_i and V_i corresponding to the largest $|\lambda_i|$, or the principal eigenvectors. (We shall denote the principal eigenvectors as U_l and V_l corresponding to the largest eigenvector, λ_l .) Suppose we multiply an arbitrary nonzero vector x_0 by $\mathbf{O}\mathbf{O}^T$. Then

$$\mathbf{O}\mathbf{O}^T x_0 = \sum_{i=1}^N \kappa_i \lambda_i U_i \quad (21.A9)$$

where U_i are the eigenvectors of $\mathbf{O}\mathbf{O}^T$, λ_i the eigenvalues, and κ_i a set of constants. $\mathbf{O}\mathbf{O}^T$ can be thought of as an operator that maps x_0 onto a superposition of eigenvectors. The process can be repeated, resulting in

$$\mathbf{O}\mathbf{O}^T \kappa_i \lambda_i U_i = \kappa_i \lambda_i^2 U_i \quad (21.A10)$$

Multiplying equation 21.B9 by $(\mathbf{O}\mathbf{O}^T)^{p-1}$ gives

$$(\mathbf{O}\mathbf{O}^T)^p x_0 = \sum_{i=1}^N \kappa_i \lambda_i^p U_i \quad (21.A11)$$

As p becomes large, the largest eigenvalue, λ_l , dominates the sum so that

$$(\mathbf{O}\mathbf{O}^T)^p x_0 \approx \kappa_l \lambda_l^p U_l \quad (21.A12)$$

This method is called the *power method* [9]. After a few iterations, a very close approximation to the principal eigenvector, U_l (the eigenvector with the greatest eigenvalue), is obtained. This eigenvector is used as the next guess for the pulse vector, P (or P_i , when the vector P is written as a set of scalars). Consequently, the next guess for the pulse can be obtained by multiplying the previous guess for the pulse by $\mathbf{O}\mathbf{O}^T$. The next guess for the gate can be obtained by multiplying the previous guess for the gate by $\mathbf{O}^T\mathbf{O}$. (For polarization-gate FROG, the absolute value of the result for the gate is taken.) While better approximations for the eigenvectors may be obtained by using these operators several times per iteration, once per iteration is adequate in practice [2].

References

1. D. J. Kane, "Recent Progress Toward Real-Time Measurement of Ultrashort Pulses," *IEEE J. Quant. Electr.*, vol. 35, no. 4, pp. 421–431, 1999.
2. D. Kane, "Real time measurement of ultrashort laser pulses using principal component generalized projections," *IEEE J. Select. Topics Quantum Electron.*, vol. 4, pp. 278–284, 1998.
3. K. W. DeLong, D. N. Fittinghoff, R. Trebino, B. Kohler, and K. Wilson, "Pulse Retrieval in Frequency-Resolved Optical Gating Based on the Method of Generalized Projections," *Optics Letters*, vol. 19, pp. 2152–2154, 1994.
4. K. W. DeLong, R. Trebino, and W. E. White, "Simultaneous recovery of two ultrashort laser pulses from a single spectrogram," *J. Opt. Soc. Amer. B.*, vol. 12, pp. 2463–2466, 1995.

5. W. H. Press, S. A. Teukolsky, W. T. Vetterling, and B. P. Flannery, *Numerical Recipes in C – The Art of Scientific Computing*, 2nd Edition, Cambridge University Press, Cambridge, 1995.
6. A. K. Jain, *Fundamentals of Digital Image Processing*, 1st ed., Prentice Hall, Englewood Cliffs, 1989.
7. K. W. DeLong, R. Trebino, J. Hunter, and W. E. White, “Frequency-Resolved Optical Gating With the Use of Second-Harmonic Generation,” *JOSA B*, vol. 11, pp. 2206–2215, 1994.
8. R. Trebino, K. W. DeLong, D. N. Fittinghoff, J. N. Sweetser, M. A. Krumbügel, and B. A. Richman, “Measuring ultrashort laser pulses in the time-frequency domain using frequency-resolved optical gating,” *Rev. Sci. Instrum.*, vol. 68, no. 9, pp. 3277–3295, 1997.
9. H. Anton, *Elementary Linear Algebra*, 2nd ed., Wiley, New York, 1977.
10. C. W. Siders, A. J. Taylor, and M. C. Downer, “Multi-pulse interferometric frequency-resolved optical gating: Real time phase-sensitive imaging of ultrafast dynamics,” vol. 22, pp. 624–626, 1997.
11. J. Paye, M. Ramaswamy, J. G. Fujimoto, and E. P. Ippen, “Measurement of the Amplitude and Phase of Ultrashort Light Pulses from Spectrally Resolved Autocorrelation,” *Opt. Lett.*, vol. 18, pp. 1946–1948, 1993.
12. D. J. Kane, G. Rodriguez, A. J. Taylor, and T. S. Clement, “Simultaneous Measurement of Two Ultrashort Laser Pulses from a Single Spectrogram in a Single Shot,” *J. Opt. Soc. Am. B.*, vol. 4, pp. 935–943, 1997.
13. J. H. Seldin, and J. R. Fienup, “Iterative blind deconvolution algorithm applied to phase retrieval,” *J. Opt. Soc. Am. A.*, vol. 7, pp. 428–433, 1990.
14. J. R. Fienup, “Reconstruction of a complex-valued object from the modulus of its Fourier transform using a support constraint,” *J. Opt. Soc. Amer. A*, vol. 4, pp. 118–123, 1987.

22. Measuring Ultraweak Pulses: TADPOLE

David N. Fittinghoff

Introduction

While FROG, and especially GRENOUILLE, can measure pulses with picojoule and potentially 10- to 100-femtojoule energies, many experiments generate even weaker pulses. The difficulty in trying to measure weaker pulses with FROG, and indeed in with any potential method for measuring an isolated pulse, is the need for the nonlinear-optical process [1,2].

Fortunately, ultraweak ultrashort pulses don't exist "in a vacuum." The processes that create them generally involve a much stronger pulse as input. Indeed, the intracavity processes that produce ultrashort laser pulses are nonlinear and necessarily yield only fairly intense pulses, which are easily measurable using FROG. *Thus, a well-characterized reference pulse is available in most cases.*

With a well-characterized reference pulse, it's possible to measure the intensity and phase using a *linear* technique, and hence with great sensitivity. The method I'll describe is simply the combination of two well-known techniques, FROG and *spectral interferometry* (SI). FROG characterizes the reference pulse directly from the laser, yielding, in particular, its spectral phase, $\varphi_{\text{ref}}(\omega)$. Then SI, which simply involves measuring the spectrum of the sum of two pulses (and hence is very sensitive), measures the spectral phase *difference* between the unknown and the reference pulses: $\Delta\phi(\omega) = \varphi_{\text{ref}}(\omega) - \varphi(\omega)$, where $\varphi(\omega)$ is the phase of the ultraweak unknown pulse spectral phase and $\varphi_{\text{ref}}(\omega)$ is the phase of the reference pulse. Knowledge of $\varphi_{\text{ref}}(\omega)$ from the FROG measurement will then yield $\varphi(\omega)$, and because the unknown pulse spectrum is easily measured (using the same SI apparatus), the FROG and SI measurements together yield the full intensity and phase of the unknown ultraweak pulse.

The combination of FROG and SI, often called *Temporal Analysis by Dispersing a Pair Of Light E-fields* (TADPOLE), has been used to measure trains of pulses as weak as 42 zepto joules, or 42×10^{-21} joules per pulse. This measurement represents an eight-order-of-magnitude improvement in sensitivity, in intensity-and-phase measurement, over pulse measurements involving nonlinear processes. TADPOLE also has the advantage that it can be implemented to measure the intensity and phase as functions of position along a line as well as functions of time (or frequency).

Spectral Interferometry

Spectral interferometry, also called frequency-domain interferometry or Fourier-transform spectral interferometry, was first introduced by Froehly and coworkers [3,4], and it has been used for several applications [5,6]. SI involves simply directing a signal and a reference pulse with electric fields $E(t)$ and $E_{\text{ref}}(t)$, respectively, collinearly into a spectrometer (see Fig. 22.1) with a time delay T between them. The measured SI spectrum is:

$$\begin{aligned}
 S_{SI}(\omega) &= |\mathcal{F}\{E_{\text{ref}}(t) + E(t - T)\}|^2 \\
 &= \left| \tilde{E}_{\text{ref}}(\omega) + \tilde{E}(\omega)e^{-i\omega T} \right|^2 \\
 &= \left| \sqrt{S_{\text{ref}}(\omega)}e^{i\varphi_{\text{ref}}(\omega)} + \sqrt{S(\omega)}e^{i\varphi(\omega)-i\omega T} \right|^2 \\
 &= S_{\text{ref}}(\omega) + S(\omega) + \sqrt{S(\omega)}\sqrt{S_{\text{ref}}(\omega)} [e^{i\varphi_{\text{ref}}(\omega)-i\varphi(\omega)+i\omega T} + c.c.] \\
 &= S_{\text{ref}}(\omega) + S(\omega) + 2\sqrt{S(\omega)}\sqrt{S_{\text{ref}}(\omega)} \cos(\varphi_{\text{ref}}(\omega) - \varphi(\omega) + \omega T)
 \end{aligned} \tag{22.1}$$

Here $S_{\text{ref}}(\omega)$ and $S(\omega)$ are the spectra of the reference and signal pulses, respectively, and the negative frequency component is ignored. Thus the spectral interferometry signal is the sum of the two individual spectra plus an interference term, which has fringes determined by T and the desired phase difference, $\Delta\phi(\omega) = \varphi_{\text{ref}}(\omega) - \varphi(\omega)$.

An advantage of SI is that it is a heterodyne technique and amplifies the weak pulse. Choosing the reference pulse to be M times more intense than the unknown pulse produces fringes that are $4M^{1/2}$ times as intense as the spectrum of the unknown pulse. The only requirement of SI is that the spectrum of the unknown pulse lies within that of the reference pulse.

The main drawback to SI for ultrashort pulse measurement is that it cannot by itself be used to measure the intensity and phase of an unknown pulse unless the reference pulse is assumed to have a constant phase. If the pulse is used to measure itself in SI, its spectral phase cancels out.

Another issue in SI is the need for perfect beam collinearity and excellent spatial coherence, or the fringes also cancel out.

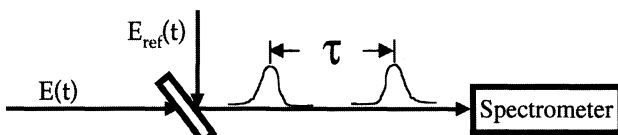


Fig. 22.1: Apparatus for Spectral Interferometry measurements of the frequency-domain phase difference between two pulses.

Finally, SI requires that the spectrum of the reference pulse contain the entire spectrum of the unknown pulse.

Data Analysis in Spectral Interferometry

Several well-known fringe-inversion techniques can extract $\Delta\phi(\omega)$ from $S_{\text{SI}}[7-9]$. All begin by recognizing that a spectrometer measures points evenly spaced in wavelength, λ , and not in frequency, ω , so the measurement scale must be converted from wavelength to frequency.

Dual-Quadrature Spectral Interferometry

Dual-Quadrature Spectral Interferometry involves measuring not only the cosine (as in Eq. 22.1), but also sine. This is accomplished by inserting a $\pi/2$ phase shift (e.g., a wave plate) in one arm of the spectral interferometer [7]. This yields an additional SI spectrum with a phase-shifted reference beam:

$$\begin{aligned} S_{\text{SI}}^y(\omega) &= \left| i\tilde{E}_{\text{ref}}(\omega) + \tilde{E}(\omega)e^{-i\omega T} \right|^2 \\ &= S_{\text{ref}}(\omega) + S(\omega) + 2\sqrt{S(\omega)}\sqrt{S_{\text{ref}}(\omega)} \sin(\varphi_{\text{ref}}(\omega) - \varphi(\omega) + \omega T) \end{aligned} \quad (22.2)$$

Both cosine and sine results can be measured simultaneously at the outputs of a polarizer. By measuring $S_{\text{ref}}(\omega)$ and $S(\omega)$ separately, it's possible to remove the non-interferometric part of the signals leaving only the sine and cosine parts of the signal. Knowing both quadratures, it's then possible to determine $\varphi_{\text{ref}}(\omega) - \varphi(\omega) + \omega T$. By either setting $T = 0$ before the experiment or by extracting the linear term ωT from the phase, the desired phase difference $\Delta\phi(\omega)$ emerges.

While DQSI provides a sensitive and elegant measure of the phase, it's rarely used due to its more complex experimental configuration.

Fourier-Transform Spectral Interferometry

The most commonly used form of SI is *Fourier-Transform Spectral Interferometry (FTSI)* and its variants [7–10]. In this approach, the phase difference is extracted by Fourier-transforming the spectrum, filtering out the negative and zero-frequency components, frequency-shifting the positive-frequency component to dc (to remove the delay term), and inverse-Fourier-transforming back to the frequency domain. The phase of the resulting spectrum is then the phase difference between the reference and unknown. $S_{\text{ref}}(\omega) + S(\omega)$ may be subtracted from $S_{\text{SI}}(\omega)$ before the Fourier transform and must definitely be subtracted whenever the individual spectra have variations on the order of the interference fringes. Otherwise, it isn't possible to separate the spectra and interference in the Fourier domain.

The magnitude of the relative delay also emerges from the analysis (it's the linear term associated with the frequency-shift to dc) and hence doesn't need to be independently measured except to determine its sign and avoid an ambiguity in the sign of the cosine argument. In fact, $\sqrt{S_{\text{ref}}(\omega)} / \sqrt{S(\omega)}$ may also be extracted from the analysis, so there's no need to measure the spectrum of the unknown pulse as long as the spectrum of the reference is known precisely.

TADPOLE: Combining Spectral Interferometry and FROG

To demonstrate TADPOLE for measuring ultraweak ultrashort pulses, we used SHG FROG to measure a train of linearly chirped 145 fs reference pulses directly from a Ti:Sapphire oscillator [9]. Figure 22.2 shows the SHG FROG trace and retrieved spectrum and phase of the reference pulses and the measured spectrum for comparison.

The train of pulses was then passed through neutral density filters and 16 cm of fused silica, lengthening the pulse to 250 fs to simulate the performance of a material-characterization experiment (see Fig. 22.3). The weak 250 fs pulse was then combined with an attenuated piece of the reference pulse in a spectrometer. A delay was chosen that yielded approximately twelve fringes across the spectrum. A thermo-electrically cooled CCD camera then recorded the SI spectrum for a 0.5 second exposure. Even though the experiment is interferometric, there was no need to stabilize the interferometer over this time scale. It was possible to make a clean measurement for average powers of 4 pW and 36.4 pW (168 nW and 2.61 μ W peak powers) in the unknown and reference arms of the experiment, respectively. Thus the average energy per unknown pulse was only 42 zJ or 1/5 of a photon. Such sensitivity is partly due to the high repetition rate, but is also due to the high sensitivity of cooled

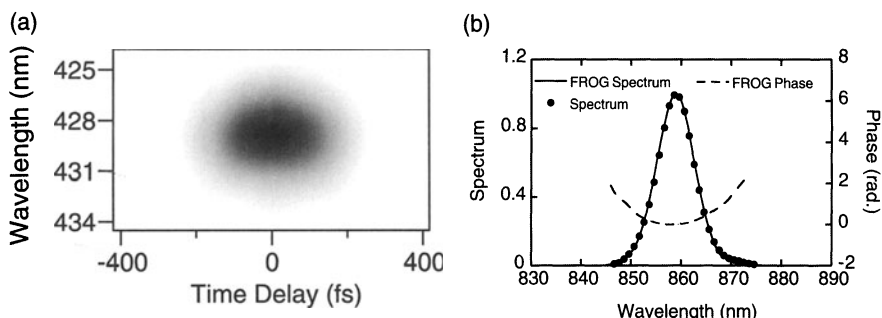


Fig. 22.2: (a) The FROG trace of the reference pulse used in TADPOLE experiments. (b) The reference-pulse measured spectrum (solid circles) and the retrieved spectrum and spectral phase from the FROG trace. Using a 128×128 grid for the FROG trace, the FROG algorithm produced a FROG error of 0.0038.

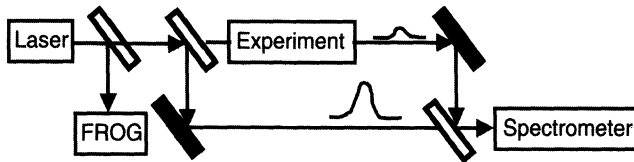


Fig. 22.3: The apparatus for TADPOLE measurements of ultraweak pulses generated in an experiment. In this work, the “experiment” consists of 16 cm of fused silica to stretch and chirp the pulse and attenuation by a factor of 10^9 .

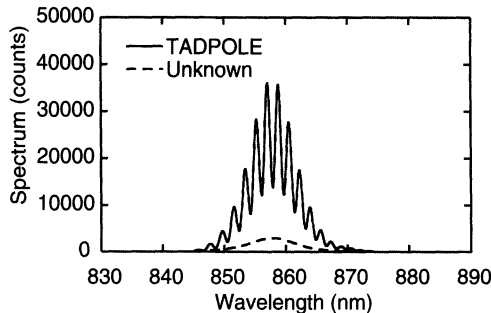


Fig. 22.4: The Spectral Interferometry spectrum (solid line) and the unknown pulse spectrum (dashed line).

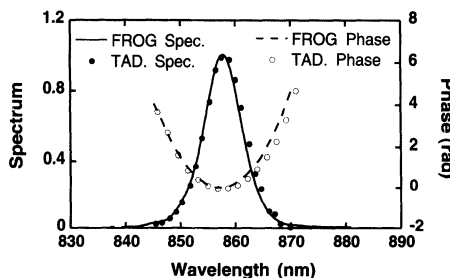


Fig. 22.5: The spectrum and phase of the unknown ultraweak pulse train measured using TADPOLE (solid and open circles, respectively), and using FROG (solid and dashed lines, respectively). The calculated phase predicted by adding the phase change due to the known dispersion of quartz to the reference phase (solid diamonds).

CCD cameras, the linear lossless nature of the technique, and the heterodyne effect discussed above.

Figure 22.4 shows the SI spectrum and unknown pulse spectrum obtained by blocking the reference beam. The unknown pulse’s spectrum and the phase obtained using FTSI are shown in Fig. 22.5. For comparison, the figure shows the independently measured spectrum and phase obtained by using FROG on the unattenuated pulses. It also shows the phase calculated from the dispersion of quartz and the phase of the reference phase. Figure 22.6 shows the unknown

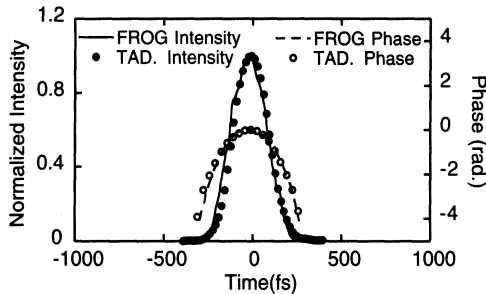


Fig. 22.6: The temporal intensity and the phase of the unknown ultraweak pulse train measured using TADPOLE (solid and open circles, respectively), and using FROG (solid and dashed lines, respectively).

pulse's intensity and phase versus time using TADPOLE and FROG. The FROG and TADPOLE measurements agree, and the change in the phase is also consistent with the known dispersion of quartz. Since the reference pulse is appreciably chirped, a measurement assuming a transform-limited pulse would have been inaccurate.

Conclusions

The ultimate sensitivity of TADPOLE is extremely high: the measurement of zJ pulses, shown above, still involved ~ 5000 counts per pixel. Additional attenuation by ~ 100 would therefore have been possible, yielding sensitivity for pulse trains in the yoctojoule (10^{-24} J) range, or a small fraction of a photon per pulse. Single-shot measurement of an individual pulse in the sub-femtojoule range should also be possible.

TADPOLE also appears to be an excellent method for measuring shaped ultrashort pulses [11]. Because they are often spread out in time, such pulses can be too weak to yield sufficient signal in a FROG measurement. Shaped pulses can also be so complex that they would require an inconveniently large number of data points in a FROG trace. The SI spectrum, on the other hand, has the advantage (for this purpose) of being one-dimensional, thus requiring significantly fewer data points for a given level of pulse complexity than FROG. Since the shaped pulse is usually constructed from a nearly transform-limited pulse, the latter pulse provides an ideal reference pulse, easily measured using FROG.

Thus, TADPOLE—the combination of FROG and SI—extends the sensitivity of rigorous full characterization of ultrashort laser pulses by many orders of magnitude, which should be useful for many applications when highly coherent beams are available. As a final note, the experimental arrangement is similar to the homodyne detection used to characterize quantum fields [12]. Indeed, in a slightly modified form, this technique can in principle be used to measure quantum field statistics of pulsed fields.

References

1. V. Wong and I. A. Walmsley, "Linear filter analysis of methods for ultrashort-pulse-shape measurements," *J. Opt. Soc. Am. B* **12**, 1491–9 (1995).
2. I. A. Walmsley and V. Wong, "Characterization of the electric field of ultrashort optical pulses," *J. Opt. Soc. Am. B* **13**, 2453–63 (1996).
3. Cl. Froehly, A. Lacourt, and J.Ch. Vienot, "Time impulse response and time frequency response of optical pupils. Experimental confirmations and applications," *Nouvelle Revue d'Optique* **4**, 183–96 (1973).
4. J. Piasecki, B. Colombeau, M. Vampouille, C. Froehly, and J.A. Arnaud, "A new technique for measuring the impulse response of optical fibres," *Appl. Opt.* **19**, 3749–55 (1980).
5. F. Reynaud, F. Salin, and A. Barthelemy, "Measurement of phase shifts introduced by nonlinear optical phenomena on subpicosecond pulses," *Opt. Lett.* **14**, 275–7 (1989).
6. L. Lepetit, G. Cheriaux, and M. Joffre, "Linear techniques of phase measurement by femtosecond spectral interferometry for applications in spectroscopy," *J. Opt. Soc. Am. B* **12**, 2467–74 (1995).
7. L. Lepetit and M. Joffre, "Two-dimensional nonlinear optics using Fourier-transform spectral interferometry," *Optics Letters* **21**, 564–6 (1996).
8. M. Kujawinski, *Interferogram Analysis* (Institute of Physics Publishing, Bristol, 1993).
9. D. N. Fittinghoff, J. L. Bowie, J. N. Sweetser, R. T. Jennings, M. A. Krumbügel, K. W. DeLong, R. Trebino, and I. A. Walmsley, "Measurement of the intensity and phase of ultraweak, ultrashort laser pulses," *Opt. Lett.* **21**, 884–6 (1996).
10. C. Dorrr, "Influence of the calibration of the detector on spectral interferometry," *J. Opt. Soc. Am. B* **16**, 1160–8 (1999).
11. A.M. Weiner, J.P. Heritage, and R.N. Thurston, "Synthesis of phase-coherent, picosecond optical square pulses," *Opt. Lett.* **11**, 153–5 (1986).
12. D. T. Smithey, M. Beck, J. Cooper, M. G. Raymer, and A. Faridani, "Complete experimental characterization of the quantum state of a light mode via the Wigner function and the density matrix: application to quantum phase distributions of vacuum and squeezed-vacuum states.," *Physica Scripta* **T48**, 2650–3 (1993).

23. Measuring Ultrafast Polarization Dynamics: POLLIWOG

Arthur L. Smirl

Introduction

It is well appreciated that by studying the phase and the amplitude of coherent ultrashort signals that are transmitted, reflected or emitted from materials during linear and nonlinear optical experiments one can obtain valuable information about the optical interactions and the fundamental processes in those material systems. Many of the signals of interest (e.g., those from four wave mixing (FWM) experiments) are very weak and require very sensitive measurement techniques. As described in previous chapters, characterization techniques [1–3] that provide both the amplitude and phase of an ultrashort pulse have been developed over the last decade, but each requires a nonlinear process. Consequently, both for practical and for fundamental reasons, they are of no use for very weak signals. Recently, in partial response to this need, a method of completely measuring the intensity and phase of an almost arbitrarily weak coherent signal has been demonstrated by performing spectral interferometry (SI) [4–9] with a well-characterized reference pulse [8,9]. The latter technique has been given the acronym TADPOLE by Fittinghoff et al. [9] and is described in some detail in the previous chapter. As described in Chapter 22, however, TADPOLE (and similar) techniques are scalar in nature. That is, they characterize the amplitude and phase of only a single polarization component.

However, much useful additional information is often carried in the temporal dynamics of the polarization state. For example, when a linearly-polarized ultrashort pulse traverses an anisotropic nonlinear material, the emerging light is both elliptically polarized and the polarization is rotated. Moreover, the polarization state changes in time from the front to the back of the pulse. In such a case, measurement of the polarization state (i.e., the ellipticity and the orientation of the ellipse) allows the simultaneous determination of both the nonlinear birefringence and the dichroism, which yields information about the anisotropy in the real and imaginary parts of the nonlinear susceptibilities [10]. As another example, it has been shown [11–13] that the polarization state of the ultrafast coherent FWM emission from semiconductors varies continuously in time and that these dynamics provide useful new information about coherent processes and exciton-exciton interactions in these materials.

In this chapter, we demonstrate that a dual-beam version of the SI techniques [8,9] discussed in Chapter 22 can be used to measure the vectorial dynamics of extremely weak signals by determining both the amplitudes and the phases of two orthogonal components of the signal. We begin with a

description of the technique. Then we illustrate the use of this technique to measure the vectorial dynamics of coherent emission from semiconductor multiple quantum wells (MQWs) and to demonstrate that the polarization dynamics can be sensitive to many-body and to quantum interference effects. Finally, we compare the present technique to earlier attempts to time-resolve the polarization state.

POLLIWOG

The dual-beam geometry that we use to perform spectral interferometric measurements on both the x and y -components of an optical signal is shown in Fig. 23.1. For purposes of illustration, the signal is shown coming from a FWM experiment, but it could be generated by any linear or nonlinear experiment. Moreover, the signal can have x and y components with independent and arbitrary temporally-varying amplitudes and phases. The reference pulse is linearly polarized at 45° , so that it has equal x and y -components. A single fixed time delay τ is introduced between the reference pulse and the FWM signal, and the amplitude and the phase of the reference are carefully measured. Any one of several techniques that have been discussed (or referenced) in previous chapters can be used to provide a fully characterized reference pulse (e.g., [1–3]). In our case, we chose to use second harmonic frequency resolved optical gating (SHG-FROG) [14]. A spectral interferometric (TADPOLE)

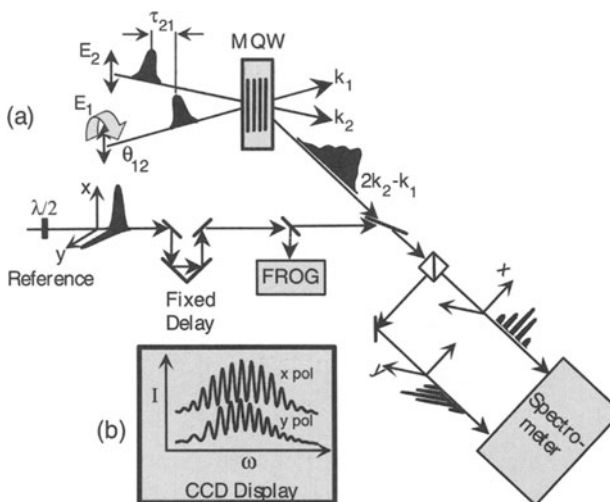


Fig. 23.1: (a) Spectral interferometric geometry for the dual-channel (POLLIWOG) measurement of the amplitude, phase, and polarization state of a FWM signal; (b) schematic of spectral interferograms for the x and y components as displayed on the CCD array attached to the spectrometer. FROG denotes the setup for the characterization of the reference pulse by Frequency Resolved Optical Gating.

measurement is then separately performed on the x and y components of the signal by combining the reference and the signal collinearly, by separating the combined reference and signal into x and y components, and by separately dispersing the x and y components with a spectrometer.

Typical spectral interferograms for the x and y components as recorded on a CCD array are shown in Fig. 23.1(b), and each has the form

$$S_{\text{SI}}^i(\omega) = S_{\text{sig}}^i(\omega) + S_{\text{ref}}^i(\omega) + 2\sqrt{S_{\text{sig}}^i(\omega)}\sqrt{S_{\text{ref}}^i(\omega)} \cos(\varphi_{\text{sig}}^i(\omega) - \varphi_{\text{ref}}^i(\omega) - \omega\tau) \quad (23.1)$$

where $S_{\text{sig}}^i(\omega)$ and $S_{\text{ref}}^i(\omega)$ are the spectral intensities; $\varphi_{\text{sig}}^i(\omega)$ and $\varphi_{\text{ref}}^i(\omega)$ are the spectral phases of the signal and reference pulses, respectively, and where i takes on the values x and y for the two polarization directions. The delay τ (typically a few ps) is chosen to yield fringes of a convenient spacing. Since the spectral intensity and spectral phase of the x component (y component) of the reference pulse are fully known (in this case, from the FROG characterization) and since the spectral intensity of the x component (y component) of the FWM signal can be separately measured by blocking the reference and measuring it with the spectrometer, then the amplitude and phase of the x component (y component) of the signal and the delay τ can be retrieved from the corresponding spectral interferograms using one of several fringe inversion techniques [8,9,15] that have been discussed previously. The temporal intensities and phases are then obtained by inverse Fourier transformation.

The technique described here [16] can be readily recognized as an extension of the dual-quadrature spectral interferometry discussed by Lepetit et al. [8], except that in [8] the reference pulse was circularly polarized, rather than linearly polarized as it is here, and the orthogonal components of the reference were used to obtain quadrature in the spectral interferograms to improve signal-to-noise rather than to measure the polarization state. Our technique should also be readily recognized as a dual beam version of the TADPOLE (acronym for Temporal Analysis by Dispersing a Pair Of Light E-fields) technique described in the previous chapter (and in [9]), with FROG providing the fully characterized reference pulse. Consequently, in the spirit that led to the acronyms FROG and TADPOLE, it has been suggested that we refer to this technique as POLLIWOG for POLarization Labeled Interference versus Wavelength of Only a Glint, and we often find it convenient to do so. While it has been suggested that spectral interferometry (SI) might be used to determine the polarization state of the unknown signal pulse (see footnote 22 of [8]), to our knowledge, this is the first actual use of SI for this purpose.

Complete Characterization of the Coherent Emission from the Heavy-Hole Exciton

In this section, we illustrate the use of this technique, and we demonstrate that the time-resolved polarization state of the coherent FWM emission from

MQW's is sensitive to many-body effects and contains essential information about them that would be difficult to obtain in any other way. The FWM geometry that we use also is shown in Fig. 23.1. Each ~ 100 fs pulse from our mode-locked Ti:sapphire laser (not shown) is divided into three parts. Two of the pulses, with wavevectors \mathbf{k}_1 and \mathbf{k}_2 , are used to generate the FWM signal in the $2\mathbf{k}_2 - \mathbf{k}_1$ direction, as shown. The third part serves as the reference. In this demonstration, we will focus on measurements that can be most easily understood and interpreted. That is, we will focus on a single set of FWM experiments in a single MQW sample in which we excite only the heavy-hole (hh) transitions, thus, eliminating the need to consider hh-light-hole (hh-lh) beating phenomena. Furthermore, we will concentrate on a single polarization scheme for the incident radiation. Namely, we will measure the amplitude, phase and polarization state of the FWM emission as the linearly polarized field \mathbf{E}_1 of the \mathbf{k}_1 -pulse is rotated through an angle θ_{12} with respect to the fixed linearly polarized field \mathbf{E}_2 of the \mathbf{k}_2 -pulse, as indicated in Fig. 23.1 and in the inset of Fig. 23.2. And, finally, we will fix the time delay between the two pump pulses at $\tau_{21} = +300$ fs. We have performed an extensive set of such measurements (at both positive and negative delays) both using POLLIWOG [17–20] and using the direct time-resolved ellipsometric (TRE) techniques [12,13] to be described later.

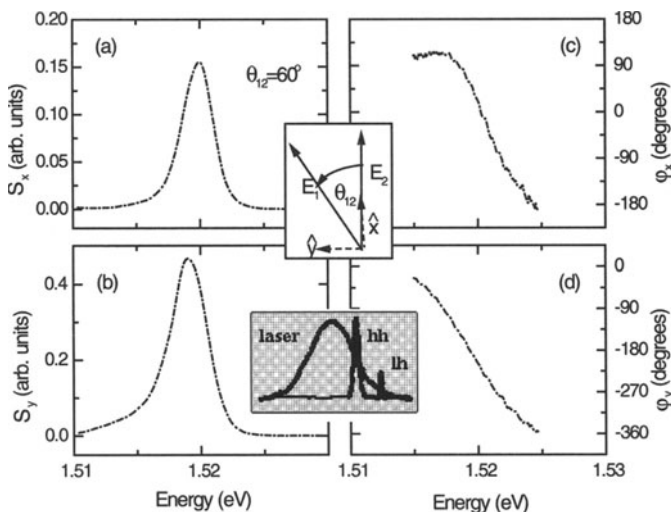


Fig. 23.2: Measured spectral intensities, (a) $S_x(\omega)$ and (b) $S_y(\omega)$, and spectral phases, (c) $\varphi_x(\omega)$ and (d) $\varphi_y(\omega)$, for the x component and the y component, respectively, of the FWM signal for an angle between the two linear input polarizations of $\theta_{12} = 60^\circ$ and for a time delay $\tau_{21} = +300$ fs. The top inset schematically shows the geometry and the nomenclature used for the two input polarizations: The linear s -polarization of E_2 was fixed along the x direction, and the linear E_1 -polarization was rotated counter-clockwise. The bottom inset shows the positions of the heavy-hole (hh) and the light-hole (lh) emission spectra with respect to the laser spectrum.

The measurements of the hh emission to be described here were performed on a sample consisting of 10 periods of 14-nm-wide GaAs wells separated by 17-nm-wide $\text{Al}_{0.3}\text{Ga}_{0.7}\text{As}$ barriers. The sample was processed by mounting it onto a glass flat, by removing the GaAs substrate with a selective etch to permit transmission measurements, and by applying an antireflection coating to the exposed semiconductor-air interface to reduce Fabry-Perot effects. The measurements were performed at 80 K to ensure that the hh exciton was homogeneously broadened. At this temperature, the hh exciton has a linewidth of ~ 1.3 meV. The splitting between the heavy-hole (hh) and light-hole (lh) excitons is ~ 12 meV. The peak absorption coefficient at the hh peak is $\sim 9 \times 10^4 \text{ cm}^{-1}$, corresponding to a peak absorbance of ~ 1.3 .

To reduce the number of lh and free carriers that were generated, the bandwidth of the two pump pulses was restricted to ~ 12 meV, which resulted in a measured pulselwidth of 150 fs, and the laser was tuned ~ 6 meV below the hh exciton, as shown schematically in the inset of Fig. 23.2. With this bandwidth and this detuning, we estimate the initial lh exciton and free-carrier populations to be less than 5% of the hh population, and at the fluence reported here ($\sim 1 \mu\text{J}/\text{cm}^2$), we estimate the hh areal density to be $\sim 4 \times 10^9 \text{ cm}^{-2}$ (corresponding to $\sim 3 \times 10^{15} \text{ cm}^{-3}$).

Typical spectral intensities and spectral phases for both the x and y components of the FWM signal (which are extracted from the corresponding spectral interferograms) are shown in Fig. 23.2 for an angle between the two input polarizations of $\theta_{12} = 60^\circ$. Notice that the x and y responses are very different. It is not sufficient to measure a single component or to perform a scalar measurement that integrates over all polarization directions. The vectorial nature is important! Specifically, notice that the emission for the y component is different in magnitude from the x component, that it is spectrally broader, and that it is slightly red-shifted with respect to the x component. In fact, this shift (~ 1.5 meV) is comparable to the expected biexcitonic binding energy. In addition, φ_x and φ_y are similar in shape; however, they are dramatically different in absolute magnitude and their phase difference ($\varphi_x - \varphi_y$) varies with wavelength. The second major point is the importance of measuring the spectral phases as well as the amplitudes. This phase information is not provided by conventional techniques. If we had failed to measure the spectral phases, then the spectral amplitudes shown in Fig. 23.2 could correspond to any number of temporal responses, depending on the shape and magnitude assumed for the spectral phases.

The corresponding temporal responses that are obtained by inverse Fourier transformation of the data in Fig. 23.2—including the measured spectral phases, $\varphi_x(\omega)$ and $\varphi_y(\omega)$,—are shown in Fig. 23.3. The time origin is taken to coincide with the center of the E_2 -pulse ($t_2 \equiv 0$). In order to simplify the presentation, we avoid the complications associated with the finite width of our pump pulses by plotting only the data for times $t > 300$ fs. In this way, we ensure that all emission shown occurs after both pulses have completely exited the sample. As in the spectral domain (see Fig. 23.2), notice that the x

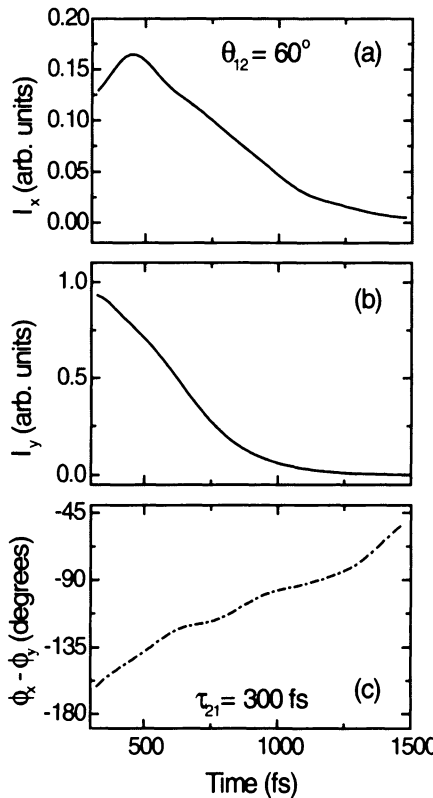


Fig. 23.3: Measurements of (a) the x component of the intensity $I_x(t)$, (b) the y component of the intensity $I_y(t)$, and (c) the difference between the temporal phases $\phi_x(t) - \phi_y(t)$ for an angle of $\theta_{12} = 60^\circ$ between the two linear input polarizations and for a time delay $\tau_{21} = +300$ fs. The data are obtained by inverse Fourier transformation of the spectral data of Fig. 23.2.

component of the emitted field has a distinctly different temporal behavior than the y component and that the difference in their temporal phases $\phi_x(t) - \phi_y(t)$ varies dramatically in time. In particular, $I_x(t)$ continues to grow long after the two pump pulses have exited the sample. This behavior is a consequence of many body effects, and it suggests that such effects must, in general, be included. By comparison, $I_y(t)$ decays more or less monotonically once the pump pulses have exited the sample. I want to emphasize that if we had performed a single scalar measurement then we would have simply obtained the total intensity, I_0 , and the information about the differences in the x and y amplitudes and phases would have been lost. Finally, of course, time-varying differences in the amplitudes and phases imply that the polarization state of the emitted radiation is varying in time.

The dynamics of the polarization state perhaps are more evident if the data are displayed in terms of the parameters that directly define the polarization ellipse, as shown in Fig. 23.4. The nomenclature that we use for the

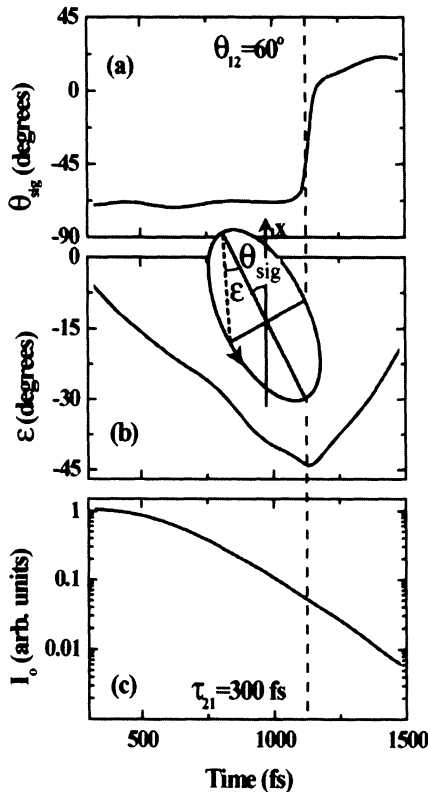


Fig. 23.4: Measurements of (a) the azimuthal angle $\theta_{\text{sig}}(t)$, (b) the ellipticity angle $\varepsilon(t)$, and the total intensity $I_0(t)$ for an angle of $\theta_{12} = 60^\circ$ between the two input polarizations. The time delay was fixed at $\tau_{21} = +300 \text{ fs}$. The notation used for the polarization ellipse is shown in the inset. The dashed vertical line indicates the time at which θ_{sig} undergoes a $\pm 90^\circ$ discontinuity in orientation and the light is roughly circularly polarized ($|\varepsilon| \sim 45^\circ$).

polarization ellipse is shown in the inset. Here, θ_{sig} denotes the azimuthal angle that determines the orientation of the polarization ellipse; ε represents the ellipticity angle, which is determined by the ratio of the minor to major axes of the ellipse; and I_0 is the total intensity. The orientation of the polarization ellipse θ_{sig} , the degree of ellipticity ε , and the total intensity I_0 are related to the intensities and phases of the x and y components of the field by the following expressions:

$$\tan(2\theta_{\text{sig}}) = \frac{2\sqrt{I_x I_y}}{I_x - I_y} \cos(\phi_x - \phi_y) \quad (23.2)$$

$$\sin(2\varepsilon) = \frac{2\sqrt{I_x I_y}}{I_x + I_y} \sin(\phi_x - \phi_y) \quad (23.3)$$

$$I_0 = I_y + I_x \quad (23.4)$$

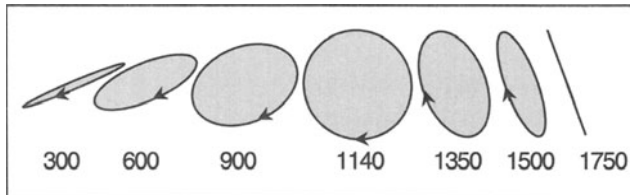


Fig. 23.5: Schematic drawings of the polarization ellipses corresponding to the data in Fig. 23.4 for selected time delays.

Clearly, both the orientation and the ellipticity of the emitted FWM signal vary dramatically and systematically with time.

The evolution of the resulting polarization ellipse is qualitatively sketched in Fig. 23.5. In this figure, we have sketched the ellipses corresponding to the data in Fig. 23.4 for $\theta_{12} = 60^\circ$ for selected times. Notice that at $t = 300$ fs the ellipse oriented with its major axis at $\theta_{\text{sig}} \sim -70^\circ$, and the ellipticity is small. As time progresses, the orientation of the ellipse remains roughly constant, but the ellipticity increases, until at $t \sim 1140$ fs, the ellipse is approximately circularly polarized. At this moment, the orientation is clearly undefined. A moment later, the major axis has become the minor axis, and the ellipse has abruptly flipped its orientation by 90° . For times longer than 1140 fs, the ellipticity begins to gradually decrease, but the orientation of the major axis remains at $\theta_{\text{sig}} \sim 20^\circ$. Eventually, the polarization approaches linear, but the orientation remains orthogonal to the initial orientation. It should be emphasized that all of these dynamics occur during a single FWM emission.

A more complete set of measurements of the time-resolved polarization state of the FWM emission is shown in Fig. 23.6. The orientation of the polarization ellipse and its ellipticity are shown for several selected angles between the two input polarizations. This figure illustrates the rich variety and complexity of the information that can be obtained. We have discussed the features shown in this figure in detail elsewhere [19,20]. The point that I want to make here is that without exciton-exciton interactions (i.e., many-body effects) the polarization state of the coherent emission from the hh exciton is expected to be linear ($\varepsilon = 0$), and the orientation and ellipticity are expected to be independent of time. Consequently, the observation of a time-varying orientation and a time-varying ellipticity are definitive signatures of many-body effects, such as local field corrections and excitation-induced-dephasing and biexcitonic effects.

Heavy-Light Hole Quantum Beats in the Polarization State

Previously, our experiments were limited to investigations of the coherent emission from the heavy hole. That is, the laser was purposefully tuned sufficiently below the hh exciton to ensure that we excited as few lh excitons

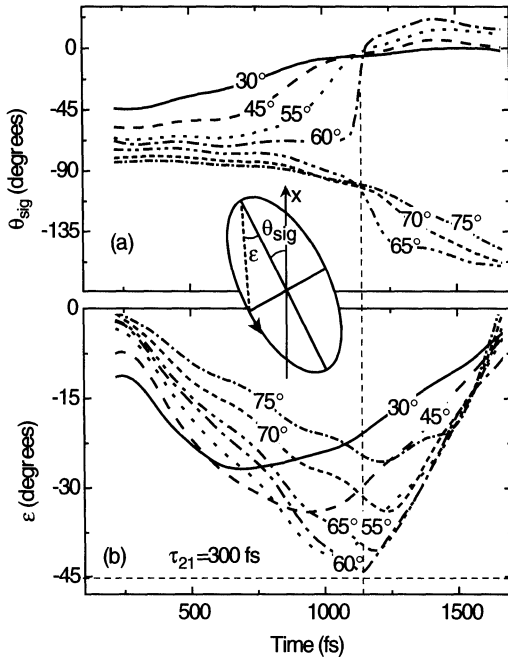


Fig. 23.6: Measurements of (a) the azimuthal angle $\theta_{\text{sig}}(t)$ and (b) the ellipticity angle $\epsilon(t)$ for selected angles θ_{12} between the two input polarizations. The time delay was fixed at $\tau_{21} = +300$ fs. The notation used for the polarization ellipse is shown in the inset. As in Fig. 23.4, the dashed vertical line indicates the time at which θ_{sig} undergoes a $\pm 90^\circ$ discontinuity in orientation and the light is roughly circularly polarized ($|\epsilon| \sim 45^\circ$) for $\theta_{12} \sim 60^\circ$.

as possible and to avoid the complication of quantum beating between the lh and hh excitons. In this section, we illustrate measurements of the dynamics of the amplitude, phase and polarization state of the emission from the same GaAs-AlGaAs MQW when the excitation spectrum is tuned so that both hh and lh excitons are excited and strong quantum beats are observed. Oscillations in both the time-integrated [21–24] and time-resolved [25] FWM signals have been studied previously when both hh and lh excitonic transitions are excited. For example, both the spectral behavior of the time-integrated signal [26] and the temporal behavior of the time-resolved signal [25] have been used to distinguish quantum beating (which is associated with two coupled oscillators that share a common level) from polarization interference (which is associated with two independent oscillators).

In addition, there have been several studies of quantum beating that have addressed the dependence of the FWM signal (or its spectrum) on the input polarization. For example, it has been demonstrated that the amplitudes of quantum beats produced by incident pulses with parallel polarizations are exactly out of phase with the beats produced by orthogonally polarized pulses [27,28]. However, conventional techniques were used for these

measurements, and the polarization state of the emitted FWM signal was not measured. In fact, to the best of our knowledge, there has been only one previous study [29] which monitored the polarization state of the emitted FWM radiation in semiconductors in the quantum beat regime. This study [29] measured the time-integrated orientation of the polarization ellipse associated with the emitted FWM signal in ZnSe epilayers, but the degree to which the FWM signal was elliptically polarized was not measured and the polarization state was not time resolved.

Here, we present an example of measurements [30,31] in which the laser was tuned onto the lh exciton so that both the hh and lh were strongly excited. Figure 23.7 shows the dynamics of the polarization state for an angle between the two input polarizations of $\theta_{12} = 60^\circ$. The data are displayed explicitly in terms of the parameters that directly define the polarization ellipse. Clearly, each of these parameters oscillates at the hh-lh beat frequency. The corresponding temporal behavior of the polarization ellipse is sketched in Fig. 23.8 for approximately one beat period (~ 377 fs). Notice that the orientation of the ellipse rotates through a full 180° in one beat period. The ellipticity goes from linear to highly elliptical and then back to linear twice per beat period. And, finally, the sense of rotation changes from clockwise (left circular) to counter clockwise (right circular) each period. We emphasize that these dramatic changes in the polarization state occur over and over again at the hh-lh beat frequency during a single emission. Moreover, it can be readily shown [20,30,31] that the qualitative features in the quantum beating shown in Fig. 23.7 and Fig. 23.8 can be reproduced without invoking many

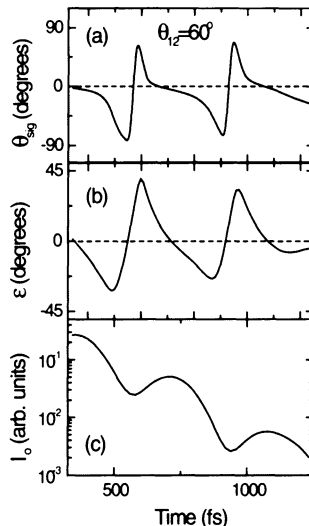


Fig. 23.7: The measured temporal evolution of (a) the azimuthal angle $\theta_{\text{sig}}(t)$, (b) the ellipticity angle $\varepsilon(t)$, and (c) the total intensity $I_0(t)$ of the FWM emission for an angle $\theta_{12} = 60^\circ$ between the two input polarizations in the strong quantum beat regime.

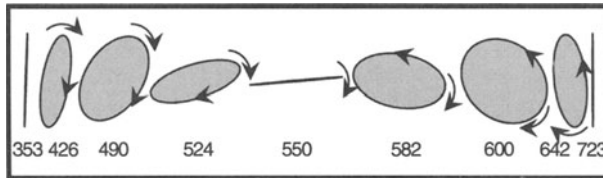


Fig. 23.8: Schematic drawings of the polarization ellipses corresponding to the data in Fig. 23.7 for selected time delays during one beat period.

body effects. Consequently, these measurement demonstrate that the polarization state also can be sensitive to quantum interference effects, in this case hh-lh quantum beating.

Femtosecond Time-Resolved Ellipsometry

The reader should be aware that there have been previous time-resolved measurements [12,13] of the polarization state of ultrafast coherent signals before the POLLIWOG measurements described here. These measurements were performed by incorporating a quarter-wave ($\lambda/4$) plate, a half-wave ($\lambda/2$) plate, and an analyzing polarizer (P) into the FWM setup shown in Fig. 23.1, as indicated in Fig. 23.9. The complete polarization state in the direction $2k_2 - k_1$ can then be determined by performing measurements using the following (or similar) procedure. With the quarter-wave plate removed, the analyzer is oriented to pass *s*-polarized light. With the analyzer held stationary, the half-wave plate then is rotated through angles ranging from 0° to 90° , and for each orientation of the half-wave plate, the FWM signal transmitted by these components is time-resolved by cross correlating it with a reference pulse in a second harmonic generation (SHG) crystal. The quarter-wave plate is then inserted and is oriented with its fast axis along the *x* direction (parallel to the incident *s*-polarized E_2 field). With the quarter-wave plate and analyzer held stationary, the half-wave plate is again rotated through angles ranging from 0° to 90° , and for each angle, the signal is again cross correlated with the reference pulse. This entire procedure is necessary for obtaining the time-resolved polarization state for a single FWM configuration. It must be repeated for each change in input polarization state, time delay, or excitation fluence.

One can readily show that the intensity transmitted by the analyzer without I_{wo} and with I_w the quarter wave-plate present is given by

$$I_{wo}(\varphi_{HWP}) = \frac{1}{2} [S_0 + S_1 \cos(4\varphi_{HWP}) + S_2 \sin(4\varphi_{HWP})] \quad (23.5)$$

and

$$I_w(\varphi_{HWP}) = \frac{1}{2} [S_0 + S_1 \cos(4\varphi_{HWP}) - S_3 \sin(4\varphi_{HWP})], \quad (23.6)$$

respectively, where φ_{HWP} is the angle between the *x* axis and the fast axis of the half-wave plate and where the S_i represent the four Stokes parameters that are

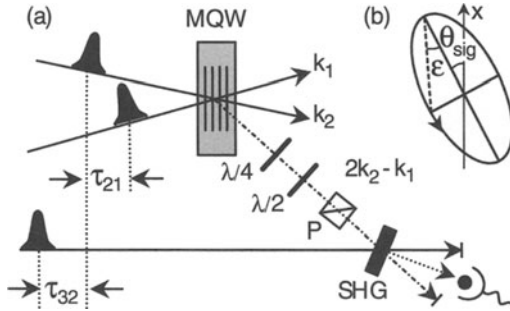


Fig. 23.9: (a) Schematic of the time-resolved ellipsometric (TRE) apparatus for directly time resolving the polarization state of the emitted FWM signal, where $\lambda/4$ denotes a quarter-wave plate; $\lambda/2$, a half-wave plate; P, a polarizer; and SHG, a second-harmonic-generation crystal. (b) The nomenclature and conventions used to define the polarization ellipse.

sufficient to completely determine the degree and state of polarization of the FWM signal [32]. These Stokes parameters are conventionally defined as: [32] $S_0 = I_x + I_y = I_{+45} + I_{-45} = I_+ + I_-$, $S_1 = I_x - I_y$, $S_2 = I_{+45} - I_{-45}$, and $S_3 = I_+ - I_-$, where I_x , I_y , I_{+45} , and I_{-45} denote the four linear components of the intensity along the x axis, y axis, and at $\pm 45^\circ$ with respect to the x axis, respectively, and where I_+ and I_- denote the right and left circularly polarized components.

Inspection of Eqs. (23.5) and (23.6) indicates that all four Stokes parameters can be determined from measurements of the FWM signal for four orientations of the half-wave plate [e.g., $I_{wo}(0^\circ)$, $I_{wo}(22.5^\circ)$, $I_{wo}(45^\circ)$, and $I_w(-22.5^\circ)$]. To check internal consistency, however, we always make six measurements as a function of reference delay τ_{32} : $I_{wo}(0^\circ)$, $I_{wo}(45^\circ)$, $I_{wo}(\pm 22.5^\circ)$, and $I_w(\pm 22.5^\circ)$, and we check that the intensities $S_0 = I_{wo}(0^\circ) + I_{wo}(45^\circ) = I_{wo}(22.5^\circ) + I_{wo}(-22.5^\circ) = I_w(22.5^\circ) + I_w(-22.5^\circ)$ give identical results in both magnitude and time dependence.

Once the Stokes parameters are extracted, the extent to which the FWM signal has a well determined polarization state is determined by calculating the degree of polarization P from the expression [32]:

$$P = \frac{1}{S_0} (S_1^2 + S_2^2 + S_3^2)^{\frac{1}{2}} \quad (23.7)$$

For the polarized component of the signal, the parameters that determine the polarization ellipse can also be directly determined from the Stokes parameters:

$$\tan(2\theta_{sig}) = S_2/S_1 \quad (23.8)$$

and

$$\sin(2\epsilon) = S_3/(S_1^2 + S_2^2 + S_3^2)^{\frac{1}{2}} \quad (23.9)$$

The roles of the various optical components shown in Fig. 23.9 are now more readily apparent. On the one hand, a high-contrast linear polarizer is needed that is capable of selecting the various polarization components that determine the Stokes parameters. On the other, the transmitted FWM signal is required to have a constant linear polarization because of the phase matching requirements of the nonlinear up-conversion process used for time-resolution. The combination of the half-wave plate and polarizer satisfies both requirements. The half-wave plate rotates the desired linear polarization component into coincidence with the pass axis of the polarizer, which is stationary and always oriented to provide the appropriate polarization for SHG. The insertion of the quarter wave plate effectively converts the components of circular polarization to linear so that they can then be passed by the combination of the half-wave plate and the analyzer.

Discussion: Comparison of POLLIWOG and TRE

While POLLIWOG is a straightforward extension of existing SI techniques, it is nevertheless a useful one, which has many advantages over previously used techniques for determining the polarization state. As we discussed earlier, the temporal amplitudes, phases and polarization state of FWM signals can also be measured by using the time-resolved ellipsometric (TRE) techniques described there. TRE has the advantage of directly measuring the temporal amplitudes and phase differences, rather than indirectly obtaining them by inverse Fourier transformation of the spectral amplitudes and phases as required by POLLIWOG. TRE does not require interferometric stability. It also relaxes the requirements for characterizing the reference pulse, since it is usually sufficient to characterize it with an autocorrelation trace. Because of the use of lock-in techniques and because of the temporal gating associated with the cross correlation process, TRE has excellent discrimination against scattered light, and it requires very little data reduction. However, TRE is labor intensive, requiring the tedious manipulation of waveplates to isolate the various components of the field that determine the polarization state and the scanning of delay stages to perform the cross correlations necessary for obtaining the time resolution. Most importantly, these cross correlations require the use of a nonlinear process (e.g., upconversion) which limits the sensitivity, making them unsuitable for measuring extremely weak FWM signals. This limited sensitivity of TRE has, for example, previously restricted the investigations of coherent effects in semiconductors to relatively large carrier densities.

By comparison, SI directly measures the spectral amplitudes and phases. The temporal amplitudes and phases are obtained indirectly by inverse transformation. In this sense, POLLIWOG and TRE techniques are complementary. In general, POLLIWOG requires more complete characterization of the reference pulse and short-term interferometric stability, but POLLIWOG

is simpler in the sense that it does not require the tedious scanning of delay stages or the manipulation of waveplates. Consequently, it requires less effort in the laboratory; however, POLLIWOG requires more processing of the data once it is acquired. Fortunately, this processing can be easily automated. In addition, POLLIWOG provides additional information not provided by TRE. From TRE measurements, one can directly extract the temporal evolution of the total intensity, $I_x(t) + I_y(t)$, and the state of polarization, i.e., the azimuthal angle $\theta_{\text{sig}}(t)$ and the ellipticity angle $\varepsilon(t)$. Put another way, TRE directly provides the individual intensities, $I_x(t)$ and $I_y(t)$, and the phase difference $\phi_x(t) - \phi_y(t)$; but the individual phases, $\phi_x(t)$ and $\phi_y(t)$, are not obtained.

Notice that a single, simpler linear POLLIWOG measurement provides *all* of this information with a sensitivity that has been shown to extend into the zeptojooule (10^{-21} J) regime! [33]. In fact, this sensitivity is arguably the most important advantage of POLLIWOG. To date, the minimum usable SI signal levels in our FWM experiments have been limited to ~ 1 aJ because of the randomly scattered coherent light from the semiconductor surface and the dewar windows and because of the background photoluminescence from the sample. The latter level is still more than an order of magnitude better than we have achieved using time-resolved cross correlation techniques. This (~ 1 aJ) should not be regarded as a fundamental limit, but is merely a reflection of the limitations of our current apparatus.

References

1. K. W. DeLong, R. Trebino, and D. J. Kane, *J. Opt. Soc. Am. B* **11**, 1595 (1994) and references therein.
2. J. L. A. Chilla and O. E. Martinez, *Opt. Lett.* **16**, 39 (1991).
3. K. C. Chu, J. Heritage, R. S. Grant, K. X. Liu, A. Dienes, W. E. White, and A. Sullivan, *Opt. Lett.* **16**, 39 (1991).
4. C. Froehly, A. Lacourt, and J. C. Vienot, *J. Opt. (Paris)* **4**, 183 (1973); J. Piasecki, B. Colombeau, M. Vampouille, C. Froehly, and J. A. Arnaud, *Appl. Opt.* **19**, 3749 (1980).
5. F. Reynaud, F. Salin, and A. Barthelemy, *Opt. Lett.* **14**, 275 (1989).
6. E. Tokunaga, A. Terasaki, and T. Kobayashi, *Opt. Lett.* **17**, 1131 (1992).
7. J. P. Geindre, P. Audebert, A. Rousse, F. Fallières, J. C. Gauthier, A. Mysrowicz, A. Dos Santos, G. Hamoniaux, and A. Anonetti, *Opt. Lett.* **19**, 1997 (1994).
8. L. Lepetit, G. Chériaux and M. Joffre, *J. Opt. Soc. Am. B* **12**, 2467 (1995).
9. D. N. Fittinghoff, J. L. Bowie, J. N. Sweetser, R. T. Jennings, M. A. Krumbügel, K. W. DeLong, R. Trebino, I. A. Walmsley, *Opt. Lett.* **21**, 884 (1996).
10. W. A. Schroeder, D. S. McCallum, D. R. Harken, M. D. Dvorak, D. R. Andersen, A. L. Smirl, B. S. Wherrett, *J. Opt. Soc. Am. B* **12**, 402 (1995).
11. S. Patkar, A. E. Paul, W. Sha, J. A. Bolger, A. L. Smirl, *Phys. Rev. B* **51**, 10,789 (1995).
12. A. E. Paul, J. A. Bolger, A. L. Smirl, J. G. Pelligrino: *J. Opt. Soc. Am. B* **13**, 1016 (1996).
13. J. A. Bolger, A. E. Paul, A. L. Smirl: *Phys. Rev. B* **54**, 11666 (1996).
14. K. W. DeLong, R. Trebino, J. Hunter, and W. E. White, *J. Opt. Am. B* **11**, 2206 (1994) and references therein.
15. M. Kujawinska, in *Interferogram Analysis*, D. W. Robinson and G. T. Reid, eds. (Institute of Physics, Bristol, UK, 1993), pp.141–193.
16. W. J. Walecki, D. N. Fittinghoff, A. L. Smirl, R. Trebino: *Opt. Lett.* **22**, 81 (1997).
17. X. Chen, W. J. Walecki, O. Buccafusca, D. N. Fittinghoff, A. L. Smirl: *Phys. Rev. B* **56**, 9738 (1997).
18. O. Buccafusca, X. Chen, W. J. Walecki, A. L. Smirl: *J. Opt. Soc. Am. B* **15**, 1218 (1998).

19. A. L. Smirl: In *Semiconductor Quantum Optoelectronics: From Quantum Physics to Smart Devices*, edited by A. Miller, M. Ebrahimzadeh and D. M. Finlayson (Institute of Physics Publishing, London, 1999), pp. 25–94.
20. A. L. Smirl: In *Ultrafast Phenomena in Semiconductors*, edited by K-T Tsen (Springer Verlag, New York, 2000) pp.
21. K. Leo, E. O. Göbel, T. C. Damen, J. Shah, S. Schmitt-Rink, W. Schäfer, J. F. Müller, K. Köhler, P. Ganser: *Phys. Rev. B* **44**, 5726 (1991).
22. K. Leo, T. C. Damen, J. Shah, E. O. Göbel, K. Köhler: *Appl. Phys. Lett.* **57**, 19 (1990).
23. K. Leo, T. C. Damen, J. Shah, K. Köhler: *Phys. Rev. B* **42**, 11359 (1990).
24. E. O. Göbel, K. Leo, J. Damen, J. Shah, S. Schmitt-Rink, W. Schäfer, J. F. Muller, K. Köhler: *Phys. Rev. Lett.* **64**, 1801 (1990).
25. M. Koch, J. Feldmann, G. von Plessen, E. O. Göbel, P. Thomas, K. Köhler: *Phys. Rev. Lett.* **69**, 3631 (1992).
26. V. G. Lyssenko, J. Erland, I. Balslev, K.-H. Pantke, B. S. Razbirin, J. M. Hvam: *Phys. Rev. B* **48**, 5720 (1993).
27. S. Schmitt-Rink, D. Bennhardt, V. Heuckeroth, P. Thomas, P. Haring, G. Maidorn, H. Bakker, K. Leo, D. S. Kim, J. Shah, K. Köhler: *Phys. Rev. B* **46**, 10460 (1992).
28. J. Kuhl, E. J. Mayer, G. Smith, R. Eccleston, D. Bennhardt, P. Thomas, K. Bott, O. Heller: In *Coherent Optical Interactions in Semiconductors*, edited by R. T. Phillips (Plenum, New York, 1994), pp. 1–31, and references therein.
29. A. Tookey, D. J. Bain, I. J. Blewett, I. Galbraith, A. K. Kar, B. S. Wherrett, B. Vögele, K. A. Prior, B. C. Cavenett: *J. Opt. Soc. Am. B* **15**, 64 (1998).
30. A. L. Smirl, X. Chen, O. Buccafusca: *Opt. Lett.* **23**, 1120 (1998).
31. A. L. Smirl, X. Chen, O. Buccafusca, *IEEE J. Quantum Electron.* **35**, 523 (1999).
32. R. M. A. Azzam, N. M. Bashara: *Ellipsometry and Polarized Light* (North-Holland, Amsterdam, 1988).
33. D. N. Fittinghoff, J. L. Bowie, J. N. Sweetser, R. T. Jennings, M. A. Krumbügel, K. W. DeLong, R. Trebino, I. A. Walmsley: *Opt. Lett.* **21**, 884 (1996).

24. Multi-pulse Interferometric FROG

Craig W. Siders and Antoinette J. Taylor

By now you're well aware that in just ten years the measurement of ultrashort light pulses has advanced from practically impossible to nearly indispensable. FROG and related techniques see daily use in labs around the world. Moreover, FROG's self-consistency checks have firmly established it as the gold standard of pulse measurement. In addition, a rarely touted feature of FROG is that it is a type of ultrafast BOXCAR integrator, gating only the pulse and not undesired cw backgrounds. Indeed, if your goal is to characterize a pulse, FROG is undoubtedly the right choice.

However, if your aim is to characterize the *interaction* of a light pulse with something else, e.g., in a pump-probe experiment where you want to time-resolve the optical properties of a laser-excited material, then FROG (or any other self-gating technique) may actually be a *poor choice*. For example, imagine placing in a beam a 1-cm thick piece of fused silica, which only negligibly distorts a 30-fs 800-nm pulse. As a result, the FROG trace of this pulse will be unaltered. However, relative to propagation in air, the pulse is delayed by some 15 ps in time and nearly 6000 wavelengths in phase! Because FROG doesn't measure the zeroth- and first-order spectral phase terms, it doesn't see these effects. Usually this is desirable, but occasionally it isn't. Spectral interferometry (SI) does see these terms, but SI signals are often obscured due to SI's inability to gate a weak signal out from a cw background. As we shall show in this chapter, one can combine the advantages of both FROG and SI by using what we call *Multi-pulse Interferometric FROG, or MI-FROG*.

Before delving into the details of MI-FROG, let's first look at some of the available techniques for materials studies, namely the inter-related techniques of spectral blue-shifting [1], spectral interferometry (SI [2–4]), and FROG [5], and its variants TREEFROG [6] and TADPOLE [7]). Each of these has been successfully used to extract from spectral power density measurements details of ultrafast phase distortions. The first two of these techniques, being linear-optical effects, are powerful tools for measuring constant (or "DC") and slowly varying time-domain phase distortions with extremely high, milliradian, sensitivity. On the other hand, the optically nonlinear FROG accurately recovers only nonlinear variations in spectral phase of an optical pulse and is oblivious to DC and slowly varying terms. Thus FROG provides a complementary diagnostic, yielding only the higher-order phase distortions. One way to combine the advantages of FROG and SI, called TADPOLE [7] and discussed in the previous two chapters, utilizes the time-domain intensity and phase extracted from a standard FROG apparatus to fully deconvolve the frequency-domain

fringes obtained in a basic SI experiment [3]. TADPOLE is especially useful for measuring the phase distortion impressed upon an extremely weak, clean probe pulse. This phase distortion is encoded in the SI data in the form of a frequency-domain hologram [3], so interpretation of TADPOLE data is dependent upon post-processing and does not present an immediate or visually intuitive measurement. Moreover, as we shall show, it is not well suited for intense short-pulse pump, weak probe experiments.

MI-FROG [8,9] was developed as an alternative combination of standard FROG with multi-pulse spectral interferometry, which is uniquely suited for pump-probe coherent spectroscopy using amplified short-pulse systems and/or emissive targets. As a demonstrated new technique with an “ultrafast boxcar” advantage, MI-FROG has proven to be a powerful diagnostic of ultrafast dynamics: a femtosecond phase-sensitive oscilloscope if you will.

In this chapter, we present a review of the analytical theory behind MI-FROG. Next we present a detailed discussion of the data reduction process, including the multi-grid method, the Principle Components Generalized Projections (PCGP) based iterative phase recovery (IPR) analysis, and the “power method” approximation used to dramatically improve the real-time convergence of our algorithm. We also include demonstrative data of cross-phase modulation (XPM) in fused silica, studied using MI-FROG, and we show how MI-FROG is used to study ultrafast ionization in noble gases and homonuclear diatomic gases. Finally, we summarize and conclude.

Theory

FROG is a specific application of a spectrogram [10,11]. For a given complex-valued function $P(t)$, termed here the “probe”, the real-valued spectrogram intensity $\Sigma_G^P(\omega, \tau)$ is defined as the magnitude of the Fourier Transform of a variable-delay gated probe:

$$\Sigma_G^P(\omega, \tau) = \left| \int_{-\infty}^{\infty} P(t) G(t - \tau) e^{i\omega t} \right|^2 \quad (24.1)$$

$$= |\sigma_G^P(\omega, \tau)|^2 \quad (24.2)$$

where $G(t - \tau)$ is a complex-valued variable-delay gate function and $\sigma_G^P(\omega, \tau)$ is a complex-valued “spectrogram field”. In all implementations of FROG to date, an optical nonlinearity has been used to generate the gate. Given two optical fields $E_1(t)$ and $E_2(t)$, expressions for the $P(t)$ and $G(t)$ for the most commonly used FROG geometries are presented in Table 24.1.

In the standard terminology of the field, “FROG” refers to the case when $E_1(t) = E_2(t)$ (e.g. $E_1(t)$ and $E_2(t)$ are produced using a beam splitter) while “TREEFROG” or “blindFROG” refers to the case when $E_1(t)$ and $E_2(t)$ are two different pulses, both unknown.

Table 24.1: $P(t)$ and $G(t)$ for common FROG geometries.

Geometry	$P(t)$	$G(t)$
Polarization Gate (PG)	$E_1(t)$	$ E_2(t) ^2$
Self-Diffraction (SD)	$E_1(t)^2$	$E_2(t)^*$
Second Harmonic (SHG)	$E_1(t)$	$E_2(t)$
Third Harmonic (THG)	$E_1(t)^2$	$E_2(t)$

When the two pulses are different, the spectrogram remains unaffected by:
a) a pulse delay, provided that both pulses are so delayed, $t \rightarrow t + \tau$ and
b) a phase shift, so that either or both $E_1(t)$ and $E_2(t)$ can be multiplied by a constant phase factor, $e^{i\phi_0}$. These are the well-known “trivial ambiguities” of FROG pointed out by Trebino and Kane in their original papers [5,12] and correspond to the constant and linear terms in the frequency-dependent phase of $\tilde{E}(\omega) = A(\omega)e^{i\varphi(\omega)}$. These two ambiguities are indeed completely unimportant when characterizing a single pulse. In other words, an optical pulse $\tilde{E}(\omega)$ is uniquely determined by $A(\omega)$ and $(\partial^2\varphi/\partial\omega^2)$. However, if we are interested in *changes* to an optical pulse as it propagates through different optical materials or optical systems, these two ambiguities, a delay of the pulse in time and a shift of the electric field oscillations with respect to the intensity envelope, are the lowest-order and dominant effects.

To demonstrate this effectively, we can define a characteristic length of material $L_\varphi = \pi c / n\omega_o$, where c is the speed of light, n the refractive index, and ω_o the pulse’s center frequency, as that length which produces a phase change of π . Similarly, $L_\tau \sim ct_p/n$, where t_p is the pulse’s temporal width, is that length of material that produces a temporal delay on the order of a pulse width. Finally, $L_{t_p} = t_p^2/k_2$, where k_2 is the material’s group velocity dispersion, is the characteristic length to broaden the pulselength by a factor of $\sqrt{2}$. For a 100-fs Ti:Sapphire pulse in fused silica ($n = 1.45$, $k_2 = 36.1 \text{ fs}^2/\text{mm}$), the ratios $L_\varphi : L_\tau : L_{t_p}$ are approximately $1 : 10^2 : 10^6$. Clearly then, when looking for changes to a pulse when interacting with material, sensitivity to the trivial ambiguities is desired and necessary.

Spectral Interferometry (SI, [2,13,14]) is a well-known technique for measuring differences in both the zeroth (i.e. a constant) and first order (i.e. time delay) terms of the spectral phase — exactly those terms we’d like to be sensitive to. It has been profitably used to, among other things [15–19], time resolve Langmuir oscillations in plasmas [3,4] and measure expansion velocities of laser-excited surfaces [20]. A heterodyne technique, SI uses two temporally separated pulses collinearly input to a spectrometer so that they will interfere

in the frequency domain:

$$S(\omega) = |\tilde{E}_{\text{ref}}(\omega) + \tilde{E}_{\text{sig}}(\omega)|^2 \quad (24.3)$$

$$= |\tilde{E}_{\text{ref}}(\omega)|^2 + |\tilde{E}_{\text{sig}}(\omega)|^2 + 2|\tilde{E}_{\text{ref}}(\omega)||\tilde{E}_{\text{sig}}(\omega)| \cos(\Delta\varphi(\omega)) \quad (24.4)$$

The cross term yields the phase difference $\Delta\varphi(\omega) = \varphi_{\text{sig}}(\omega) - \varphi_{\text{ref}}(\omega)$ between the signal and reference fields. SI is, strictly speaking, a Leith-Upatnieks [3,21] hologram recording a time-domain object in a frequency-domain hologram. As such, it may be accurately read out, yielding $\phi(t)$, if the original reference wave is available. In the case of spectral interferometry, the reference pulse can be characterized, up to the two trivial ambiguities, using standard FROG techniques. This combination of spectral interferometry and FROG, termed TADPOLE [7], is particularly well suited for clean trains of low-power pulses. It requires prior knowledge of the fact that the measured interferogram and power spectra correspond *solely* to the reference and signal pulses. In the case of pulses with significant structure in the wing, pre- or post-pulses, and significantly emissive targets, this is not true and the use of TADPOLE and SI for time-resolved applications becomes difficult or impossible. Unfortunately, amplified short-pulse lasers more often than not fall into this category, with as much as 10% of the measured output energy residing not in the main pulse but in a combination of amplified spontaneous emission, pre- and post-pulses, and wing. As this extraneous output has similar or nearly identical power spectra with the main pulse, agreement of the reference pulse FROG marginals with the measured power spectrum is still quite good. In any SI experiment, the temporally offset signal and reference pulses are derived from the same original input pulse—hence all components of the pulse (ASE, wing, pre- and post-pulses) will produce high-contrast fringes with identical fringe spacing. However, when a small time-domain phase shift is impressed only upon the main pulse, the corresponding SI interferogram is a complicated admixture of shifted and unshifted fringes.

Most significantly, FROG utilizes an ultrafast optical gate and long-time-scale integration (e.g. the multi-ms diode array or CCD integration time) and hence is a form of ultrafast boxcar, or gated integrator, detection. It effectively eliminates extraneous long-time-scale contributions to the measured spectra. What is required, then, is a different combination of FROG and SI which retains the key ingredient in FROG: the ultrafast optical gate. Using multi-pulse assemblies for the probe and gate in a modified FROG apparatus, this can be attained.

Returning to the expression for a spectrogram (Eq. (24.1)), we consider the situation where both the probe $P(t)$ and gate $G(t)$ are two-pulse assemblies, formed from an initial single short optical pulse after passage through a Michelson or Mach-Zehnder interferometer: $P(t) \rightarrow Q(t - \tau_\Delta) + P(t)$, $G(t) \rightarrow G_o(t) + G_o(t - \tau_\Delta)$. Here we've assumed that the delay τ_Δ between the two pulses is sufficiently large that the two pulses do not overlap in time

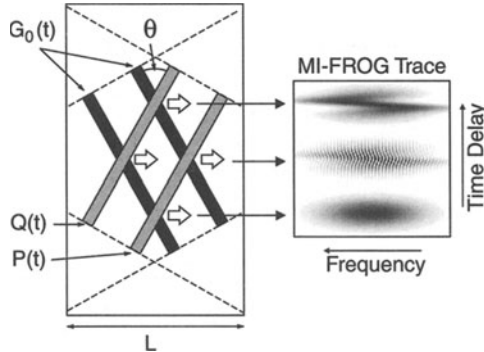


Fig. 24.1: Schematic of single-shot MI-FROG geometry. Two double-pulse assemblies, moving from left to right, are shown crossing in a nonlinear medium of length L at an angle θ , thereby mapping time delay along the vertical axis in the figure. Where the pulses overlap, leakage (for PG MI-FROG) or upconverted light (e.g. for SHG MI-FROG) is generated via the nonlinear optical gate. For simplicity, this light is shown propagating along the perpendicular bisector. After relay imaging and frequency dispersion in a spectrometer, these four crossing regions produce three distinct features in the MI-FROG trace. The gating of P by the trailing G_0 produces the lower feature, while the gating of Q by the leading G_0 produces the upper feature. The other two crossing regions, being temporally separated, interfere in the frequency domain to produce the central, interferometric, feature.

and hence any cross terms, which may exist to a degree depending on the nonlinearity used, are negligible. Note that the two temporally separated pulses $G_0(t)$ and $G_0(t - \tau_\Delta)$ which make up the gate are identical, while the two pulses $P(t)$ and $Q(t - \tau_\Delta)$ which make up the probe, though initially identical, will be different due to the effect of an intense pump pulse, other nonlinearity, or modification. Additionally, since the simultaneous gating and frequency dispersion yields a differential phase shift, the gate pulse could be shortened using nonlinear pulse compression techniques while the probe pulse can be broadened from an initially short pulse by linear dispersion or spectral narrowing. After substitution, we have for the MI-FROG trace

$$I_{\text{MI-FROG}}(\tau, \omega) = \Sigma_{G_0}^P(\omega, \tau - \tau_\Delta) + \Sigma_{G_0}^Q(\omega, \tau + \tau_\Delta) + \Sigma_{G_0}^{Q+P} e^{i\omega\tau_\Delta}(\omega, \tau). \quad (24.5)$$

An illustrative plot of $I_{\text{MI-FROG}}$ is presented in Fig. 24.2. The two side features, given by the first two terms in $I_{\text{MI-FROG}}$, are spectrogram traces of the $Q(t)$ and $P(t)$ individually, offset along the delay axis by $\pm\tau_\Delta$. The central feature, given by the last term in $I_{\text{MI-FROG}}$, is formed by the interference of the two complex-valued spectrogram fields.

When, as in Fig. 24.2, the gate pulse is significantly shorter than the probe, the interference term simplifies to

$$|P(\tau)|^2 + |Q(\tau)|^2 + 2|P(\tau)Q(\tau)| \cos(\omega\tau_\Delta + \phi(\tau)). \quad (24.6)$$

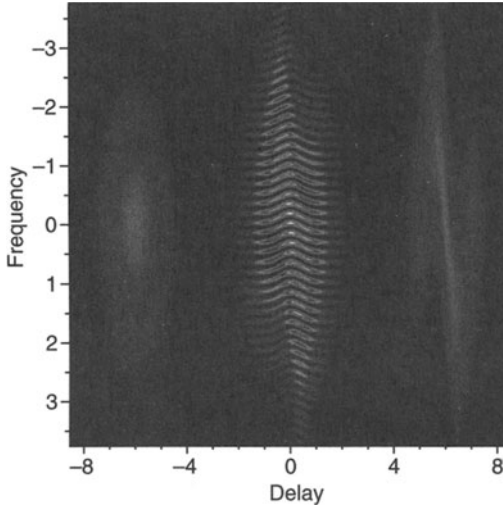


Fig. 24.2: Illustrative calculation of MI-FROG trace. Time is in units of pump pulse widths with the probe two units wide, the gate 0.33 units wide, and $\tau_\Delta = 6$. A cross-phase modulation from a co-propagating pump pulse exists between the two individual probe pulses, resulting in a redshift/blueshift on the leading/trailing edge the second pulse.

For pure phase modulations, i.e. $Q(\tau) = P(\tau)e^{i\phi(\tau)}$, this simplifies further to $2|P(\tau)|^2[1 + \cos(\omega\tau_\Delta + \phi(\tau))]$. Hence for a non-zero phase shift, the time-resolved frequency-domain fringe pattern deforms from the perfectly straight null-phase condition to directly follow $\phi(\tau)$, as shown. More generally, it is straightforward to show that Fourier Transformation of Eq. (24.5) along the ω axis yields peaks about zero and $\pm\tau_\Delta$. Masking of the peaks at zero and $-\tau_\Delta$ followed by an inverse transform yields the complex product of the two spectrogram fields: $\sigma_{G_0}^Q(\omega, \tau)\sigma_{G_0}^{P*}(\omega, \tau)$. As the magnitudes of the individual spectrogram traces are known, we have a full characterization of the amplitude and phase shift between the two spectrogram fields. Once the results of iterative phase recovery [6,22] on either of the traces are in hand, the other spectrogram field and hence $P(t)$, $Q(t)$, and $G_o(t)$ can be fully and simply determined.

The unique abilities of MI-FROG center around its inherently differential nature: ultrafast changes in the time-domain phase of a laser pulse are measured, unlike standard FROG, to all orders while shot-to-shot fluctuations in the pulse structure are discriminated against. Additionally, a time-domain phase shift $\Delta\phi(t)$ can be measured, unlike SI, *in a single shot* over a time-scale much longer than the pump pulse which induces it. Unlike TADPOLE [7], the ultrafast boxcar advantage of FROG is retained in MI-FROG: the sub-picosecond optical gating essentially eliminates amplifier leakage, ASE, satellite pulses, and target emission. The real-time nature of MI-FROG allows immediate and direct observation of pump-pulse time scale dynamics *without*

computational analysis, a significant advantage over traditional single-pulse FROG. Finally, iterative computational techniques [22] similar to those used in standard FROG can elucidate femtosecond time-scale detail from the MI-FROG trace. In fact, it is possible to recover the time-domain intensity and phase of not only the two pulses $P(t)$ and $Q(t)$ which make up the probe, but, in the case of SHG MI-FROG, $G_o(t)$ as well (in PG MI-FROG only $|G_o(t)|^2$ is recovered). That is to say, with MI-FROG, the intensity and phase of *three* pulses can be measured in a single shot.

MI-FROG Data Reduction

In this section, we will discuss the data reduction procedures used in this work. While some of these procedures may be specific to our experiment geometry, many of them, such as the multi-grid technique, are applicable to any FROG or iterative phase recovery algorithm. The Power Method approximation can similarly be used in any PCGP algorithm. As our experiments required the analysis of many thousands of spectrogram traces, a high priority was placed upon execution speed and complete automation of the data reduction.

For convenience, in this Section we will work with normalized time and frequency units, defined by requiring a Gaussian pulse to have unit FWHM temporal width and therefore a frequency-domain FWHM of $\kappa \approx 0.441$.

Multi-grid FROG Matrices

The spectrogram is a time-frequency distribution which must, in the course of iterative phase recovery, be Fourier Transformed repeatedly along the $\nu = \omega/2\pi$ axis. For the sake of computational efficiency, the Fast Fourier Transform (FFT) on 2^n -length arrays is used. We therefore choose to discretize our (τ, ν) spectrogram intensities and fields using matrices which have the special property that a ν -FFT of each column produces an array which matches in sampling interval, $\delta\tau$, and extent, $N\delta\tau$, that of the τ axis. From the properties of the FFT, this implies that we must use $N \times N$ matrices, where $N = 2^n$, with sampling intervals along the τ and ν axes which are related via

$$\delta\tau = \frac{1}{\delta\nu N}. \quad (24.7)$$

A second requirement of these matrices is that, in order to equally sample the FROG trace of a transform-limited Gaussian pulse along both the ν and τ directions, we require

$$\frac{1}{\delta\tau} = \frac{\kappa}{\delta\nu}, \quad (24.8)$$

Table 24.2: FROG Matrices.

N	$\delta\tau$	$\delta\nu$	N_{fwhm}	$N\delta\tau$
2	1.065	0.470	0.94	2.13
4	0.753	0.332	1.33	3.01
8	0.532	0.235	1.88	4.26
16	0.377	0.166	2.66	6.02
32	0.266	0.117	3.76	8.52
64	0.188	0.083	5.31	12.05
128	0.133	0.059	7.51	17.04
256	0.094	0.042	10.63	24.09
512	0.067	0.029	15.03	34.07
1024	0.047	0.021	21.25	48.19
2048	0.033	0.015	30.05	68.15
4096	0.024	0.010	42.50	96.37
8192	0.017	0.007	60.11	136.3
16384	0.012	0.005	85.00	192.8
32768	0.008	0.004	120.2	272.6
65536	0.006	0.003	170.0	385.5

where $\kappa \approx 0.441$ is the minimum time-bandwidth product for a Gaussian pulse. Together, these two requirements give us

$$\delta\nu = \sqrt{\kappa/N} \quad (24.9)$$

$$\delta\tau = 1/\sqrt{\kappa N}. \quad (24.10)$$

Table 24.2 presents $\delta\nu$ and $\delta\tau$, in normalized units. Also included are the number of points sampled in the FWHM of a Gaussian pulse and the total extent of the matrix along the τ axis. Several points should be noted about these “FROG matrices”. First and foremost is that the size N^2 of the matrix increases quite rapidly as the sampling interval decreases: $N^2 \sim (\delta\nu)^{-4}$. Even with a very modest spectrometer, experimental FROG traces have ≥ 100 points across the FWHM. The FROG matrix with equivalent sampling would be Giga- to Tera-elements in size, requiring Giga- to Tera-bytes of memory—clearly an impractical calculation. In order to use modest- N matrices ($N = 512$, 1024, or 2048), we may take advantage of a particular nicety of the FROG Matrices. One can verify that halving the sampling interval of a $N \times N$ FROG matrix produces a $4N \times 4N$ matrix with twice the extent, with the points of the $N \times N$ matrix coinciding with alternating elements of the new matrix. This leads to a particularly efficient multi-grid algorithm, applicable to any IPR method. We start by casting our experimental data on a fine grid (e.g. 512×512 in our case). Any smaller multi-grid matrix may be picked out of this matrix simply by lookup—no interpolation is needed. Iterative phase recovery is started on a small grid, say 32×32 , with very fast iteration rates.

After convergence, the best-fit fields are interpolated with half the sampling interval and zero padded on the ends, producing 128×128 FROG matrices. Iteration rates on this level are slower, but as it was seeded with the results of the prior multi-grid level, convergence is prompt. Finally, a handful of iterations at 512×512 provides high-resolution results at a much reduced total calculation time.

Data Preparation

In Chapters 8 and 10, we saw how to prepare raw FROG data for input to the iterative phase retrieval algorithm, and we will briefly describe the similar procedures used for MI-FROG.

First, both temporal and spectral calibrations are performed. Two TREE-FROG traces with a known delay are used for the former, while a standard Argon spectral lamp is used for the latter. Each column of the 512×512 CCD array is independently calibrated, therefore removing any effects from spectral-line curvature. As the spectrometer output is not linear in frequency, all measured MI-FROG and TREEFROG traces are cast onto a regularly spaced frequency axis which spans the same range as the initial data.

Next, all traces are background subtracted and digitally filtered to remove any CCD artifacts. The experimental TREEFROG traces are then cast via spline interpolation onto 512×512 FROG matrices, with a corresponding order-of-magnitude loss of resolution.

MI-FROG Interferogram Analysis

As the MI-FROG traces are not subject to iterative phase recovery, they are not cast into FROG matrices. Instead, they are first Fourier transformed along the ν -axis, masked to exclude the lower half plane and zero, and inverse transformed. This procedure gives $\sigma_{G_0}^Q(\omega, \tau)\sigma_{G_0}^{P*}(\omega, \tau)$ for both the pumped and unpumped conditions. The unpumped data are used as a null-phase reference, thereby providing the full phase difference between the pumped and unpumped spectrogram fields—with the full experimentally available resolution. Finally, this phase difference is cast into a FROG matrix for later use.

Iterative Phase Recovery

Iterative phase retrieval was performed only on “unpumped” spectrogram traces. As these pulses are nearly transform limited, convergence of the IPR algorithm was always quickly and easily achieved using a modified Principle Components Generalized Projects (PCGP) algorithm. The Generalized Projections (GP) IPR algorithm was first implemented by DeLong and coworkers [23] by numerically minimizing the least-square FROG error with respect to $E(t)$. Kane [22] later showed that, in fact, this minimization step

was analytically solvable, greatly speeding up the GP algorithm. We will discuss briefly here our implementation of the multi-grid PCGP algorithm itself, as well as the Power Method [24] shortcut which further reduces real-time convergence times.

We start by initializing $P(t)$ and $G(t)$ with Gaussian-envelope modulated random noise and calculating what Kane [22] has termed the time-domain TREEFROG trace, $P(t)G(t - \tau)$, or in discrete form $P(t_i)G(t_{1+(i+j-1 \bmod N)})$. From the general expression for the spectrogram field, Eq. 24.2, we can calculate $\sigma_{G_0}^P(\omega, \tau)$. We replace the magnitude of $\sigma_{G_0}^P(\omega, \tau)$ with the measured TREEFROG trace and calculate a new time-domain TREEFROG trace. The key insight of Ref. [22] is that by a straightforward row rotation, the time-domain TREEFROG trace can be converted to an outer product form $A_{ij} = P(t_i)G(t_j)$. More generally, bidirectional conversion of A_{ij} from the TREEFROG form to the outer product form is accomplished via $A_{ij} = A_{ik}$, where k is given by

$$k = 1 + \left[\left(\left[\frac{N}{2} + i \bmod N \right] + (N - j) \right) \bmod N \right]. \quad (24.11)$$

Thus we are faced with the problem of determining which two complex-valued vectors P and G best approximate A_{ij} . Fortunately, any square matrix can be decomposed into a weighted sum of outer products,

$$A_{ij} = \sum_{k=1}^N w_k U_{ik} V_{kj}^* \quad (24.12)$$

via Singular Value Decomposition (SVD). The two vectors which best approximate A_{ij} in a least-squares sense are those two with the largest weighting factor w_k , i.e. the principle components of the decomposition.

In practice, most SVD algorithms are rather time consuming—primarily because for an $N \times N$ matrix, they return N weighting factors and outer product pairs. Luckily, a simple approximation, the Power Method, can be used to estimate the principle components. Given two estimates for the principle components, e_i and g_i , and A_{ij} , we can obtain two better estimates, \check{e}_i and \check{g}_i via

$$\check{e}_i = \sum_{k=1}^N \sum_{j=1}^N A_{ij} A_{kj}^* e_k = \sum_{k=1}^N \sum_{j=1}^N P(t_i)G(t_j)P^*(t_k)G^*(t_j)e_k \quad (24.13)$$

$$\check{g}_i = \sum_{k=1}^N \sum_{j=1}^N A_{ji} A_{jk}^* g_k = \sum_{k=1}^N \sum_{j=1}^N P(t_j)G(t_i)P^*(t_j)G^*(t_k)g_k. \quad (24.14)$$

The reader can verify that substitution of $e_k = P(t_k)$ and $g_k = G(t_k)$ results in $\check{e}_i = P(t_i)$ and $\check{g}_i = G(t_i)$. Starting with our initial guesses for P_i and G_i , iteration of Eqs. 24.13 and 24.14 proceeds until little change is seen from

one iteration to the next. By this means, new guesses for $P(t_i)$ and $G(t_i)$ are obtained and the whole process repeats. Convergence is determined when the FROG error drops below a preset level.

Once convergence is achieved on a coarse multi-grid level (e.g. 32×32), $P(t_i)$ and $G(t_i)$ are transferred to the next (finer) multi-grid level using simple linear interpolation. In this manner, rapid convergence on high-resolution (512×512 or 1024×1024) grids. In our experience, for 512×512 grids, multi-grid convergence times are approximately an order of magnitude faster than using 512×512 throughout.

Finally, having obtained the full phase difference between the pumped and unpumped spectrogram fields via the MI-FROG interferograms, the magnitude of the pumped spectrogram field, and the IPR-obtained unpumped spectrogram field, we can calculate the full pumped spectrogram field, A'_{ij} . Since the same gate is used in both spectrograms, we can simply project the pumped probe pulse via $Q(t_i) = \sum_{j=1}^N A'_{ij} G(t_j)$.

Demonstrative MI-FROG Experiments

Two examples of MI-FROG-based experiments are presented here. Both were done in the polarization-gate geometry. The first, cross-phase modulation (XPM) in materials demonstrates the key features of MI-FROG, while the second utilizes MI-FROG to observe previously unseen phenomena in ultrafast ionization in gases.

XPM in Materials

MI-FROG can also be used to measure fast (femtosecond) or slow (picosecond) time-scale changes in refractive index caused by atomic or molecular response to a co-propagating pump pulse. The former also acts as a simple demonstration of this new technique.

A standard chirped pulse amplified laser system was used to provide 1 mJ, 175 fs, 802 nm pulses at one kHz. Twenty percent of this pulse was used to generate, in a Michelson interferometer, the multi-pulse probe and gate sequences while the remainder was frequency doubled in a $300 \mu\text{m}$ BBO crystal, providing a 30 μJ , 401 nm pump pulse (see Fig. 24.3). After dumping the residual IR, the UV pump and attenuated IR probes, all of the same linear polarization, were collinearly focused in a 10 cm focal length telescope. Overlap of the pump with the trailing probe was established via sum frequency generation in a $500 \mu\text{m}$ KDP crystal. The gate pulses traveled a separate path to a modified FROG apparatus while the probes were dichroically separated from the pump and entered the same FROG apparatus. A $500 \mu\text{m}$ fused silica plate, thinner than the $650 \mu\text{m}$ walkoff length, was translated axially near the focus to induce an adjustable amount of cross-phase modulation (XPM). In addition to recording MI-FROG traces, TREEFROG traces of the leading or trailing

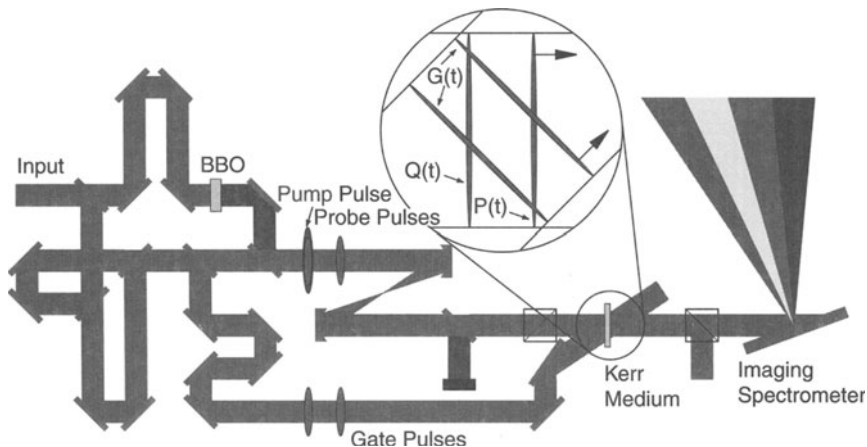


Fig. 24.3: Schematic representation of MI-FROG apparatus used to study cross-phase modulation in materials and ionization fronts.

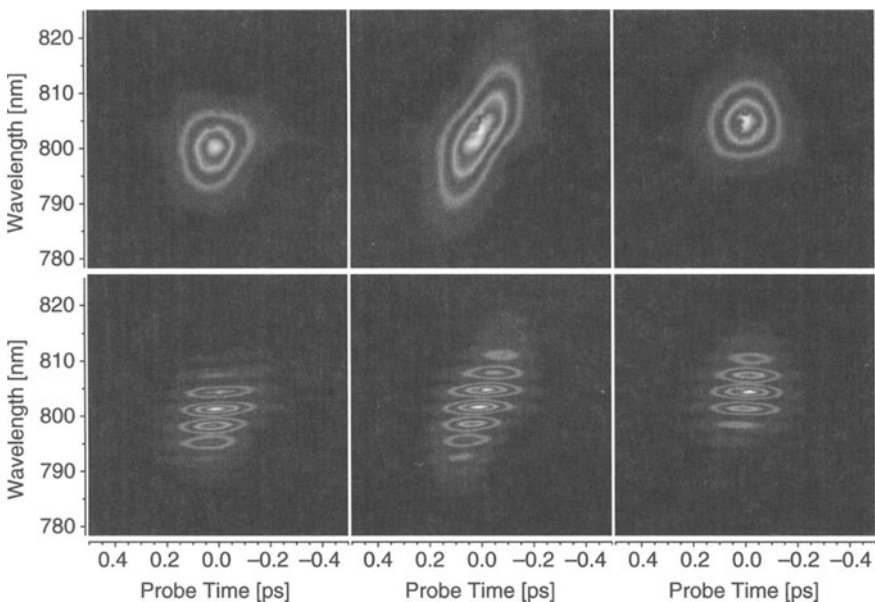


Fig. 24.4: MI-FROG (bottom) and trailing-pulse TREEFROG (top) traces measured in the case of cross-phase modulation in fused silica for +100 fs (left column), 0 fs (center column), and -100 fs (right column) pump-probe delay.

probe pulses could be measured by blocking individual arms in the Michelson. Three sets of TREEFROG/MI-FROG traces were recorded both with and without the pump pulse: one each for 0 fs, and ± 100 fs delay between the pump and trailing probe pulse (see Fig. 24.4). As expected, the spectrogram

traces of the leading pulse did not differ from the unpumped traces, while the corresponding traces of the trailing pulse show characteristic blue/red shifts [1] for the delayed cases and a symmetric broadening for the overlapped case, with shifts of ± 2.5 nm. When the probe rides the leading/trailing edge of the pump, the probe is red/blue-shifted, as expected from the $n_2 I(t)$ nature of the XPM [1]. The MI-FROG traces, all of which have straight fringe patterns with the pump blocked, display a characteristic fringe tilt, indicative of the clean blue/red shift seen in the TREEFROG trace, while the coincident case evidences a downward curvature. That is to say, the fringe pattern follows the time-domain phase shift $\phi(t) = -n_2 I(t)\omega_o z/c$. Indeed, the $\sim\pi/2$ per 200 fs phase ramp in the ± 100 fs delay cases corresponds to a shift [1] of $\Delta\lambda = (\lambda^2/2\pi c)(0.5\pi/200\text{fs}) = 2.7$ nm, in excellent agreement with the TREEFROG traces.

The MI-FROG traces were analyzed to extract the amplitude and phase difference between the pumped and unpumped TREEFROG traces while the unpumped trailing-pulse TREEFROG trace was analyzed via iterative phase recovery based upon Principle Components Generalized Projections [22]. The power spectrum of the initial pulse, obtained in the same CCD frame as the TREEFROG and MI-FROG traces, was used as a constraint. Typical FROG trace errors [6] for *both* recovered traces were 0.4% (128×128 grid). In each of three cases (see Fig. 24.5), the relative phase difference extends from zero in the wings to a negative peak, as expected, whose magnitude is consistent with visual inspection of the MI-FROG traces as well as the observed frequency shifts. Also present is a significant change in the intensity profiles of the probe pulse near the peak of the pump, which is attributable to the lens-like transverse profile of the XPM. It should be stressed that both the DC component of the phase shift as well as the relative temporal offset between the pulses are obtained from the MI-FROG data with interferometric accuracy and no adjustable parameters are used.

Ultrafast Ionization in Gases

The detailed dynamics of an atom in a laser field with strength comparable to the barrier suppression field is rich in both interesting physics and potential applications. The source of both high-harmonic UV-VUV-XUV radiation [25] and ionization-based sources of tunable radiation [1,26,27], “mode-locking” of ultrafast ionization is the route to attosecond pulses [28].

The effect upon a short optical pulse co-propagating a distance z with an ionization front can be viewed [1,29] in the frame of the pulse as a simple time-dependent phase shift,

$$\phi(t) = \frac{z\omega_o}{c} \sqrt{1 - \frac{n_e}{n_{cr}}} \approx \frac{z\omega_o}{c} \left(1 - \frac{n_e}{2n_{cr}}\right), \quad (24.15)$$

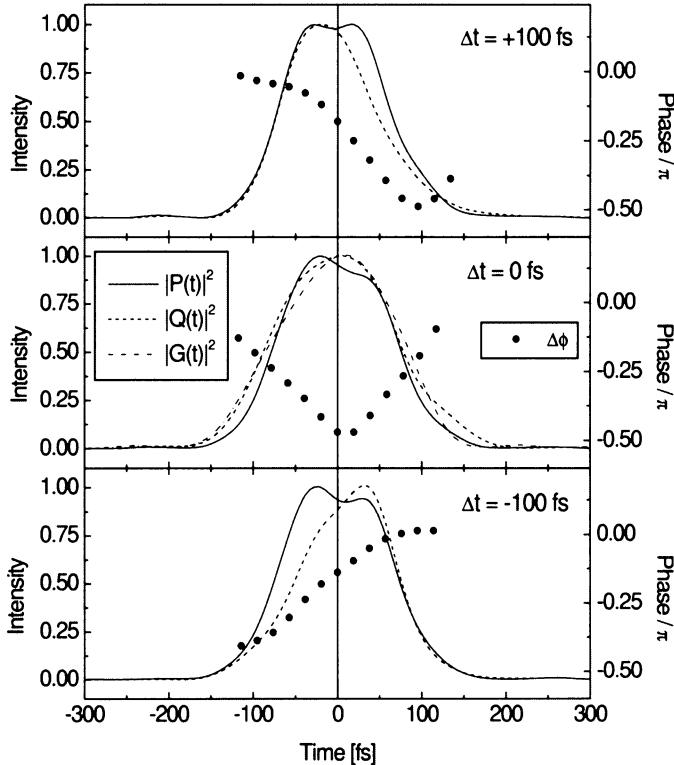


Fig. 24.5: Results of MI-FROG interferogram analysis and iterative phase recovery. For each time delay, the intensity profiles of the unpumped, $|P(t)|^2$, and pumped, $|Q(t)|^2$, probe pulses are plotted, along with their relative phase difference, $-\Delta\phi(t)$. The intensity profile of the gate pulse, $|G(t)|^2$, is, for clarity, shown only for the zero delay case. Intensity profiles are unit normalized and the centroid of $|P(t)|^2$ is used to define $t = 0$.

where $n_e(t)$ is the electron density of the plasma, $n_{cr} = \pi r_e \lambda_o^2$ is the critical density of the plasma, r_e is the classical electron radius, and λ_o is the center wavelength of the pulse. Since the instantaneous frequency of the pulse is proportional to the derivative of the phase, the pulse will experience an ultrafast time-dependent frequency shift

$$\Delta\nu(t) = \frac{-1}{2\pi} \frac{\partial\phi(t)}{\partial t} \approx \frac{zr_e\lambda_o}{2\pi} \frac{\partial n_e(t)}{\partial t}. \quad (24.16)$$

Since the plasma density scales linearly with the ambient gas density ρ and laser wavelength, we can normalize this shift by $\rho\lambda_o$. We can also include the effects of cross-phase modulation in the gas by adding a term proportional to a per-molecule nonlinearity γ_a ,

$$\frac{\Delta\nu(t)}{r_e\lambda_o\rho} = z_g \frac{\partial(\gamma_a I(t))}{\partial t} - z_p \frac{\partial N_a(t)}{\partial t} \quad (24.17)$$

where $I(t)$ is the pump-pulse intensity, $N_a(t)$ is the per-molecule ionization fraction, and z_p and z_g are interaction lengths for the plasma and gas respectively. We can see from Eq. (24.17) that an increasing electron density results in a frequency shift to the blue, while for $\gamma_a > 0$, cross-phase modulation produces a frequency shift towards the red on the leading edge ($\partial I/\partial t > 0$) of the pump and a blueshift on the trailing edge ($\partial I/\partial t < 0$).

Previous studies [1,26,27] of ultrafast ionization have relied on spectral power density measurements using 100 fs pulses. As the detailed structure of the ionization-front blue-shifted spectra depends on a complicated interplay of the input pulse structure (i.e. its temporal phase), the ionization dynamics [30], and cross-phase modulation in the neutral gas, the conclusions made from these experiments have been at best well-thought-out and limited inferences.

To surpass these limitations and achieve a quantitative time-domain measure of the ionization rate independent of probe structure, we have utilized an experiment configuration which, by utilizing three power-spectra channels and one optically gated frequency-resolved channel (see Fig. 24.6) per each of four CCD images (pumped and unpumped cases with one or two probe pulses), provides simultaneous and self-consistent dual-channel power spectra and frequency domain interferograms, MI-FROG, and FROG data. TADPOLE analysis performed upon the raw data yielded results inconsistent

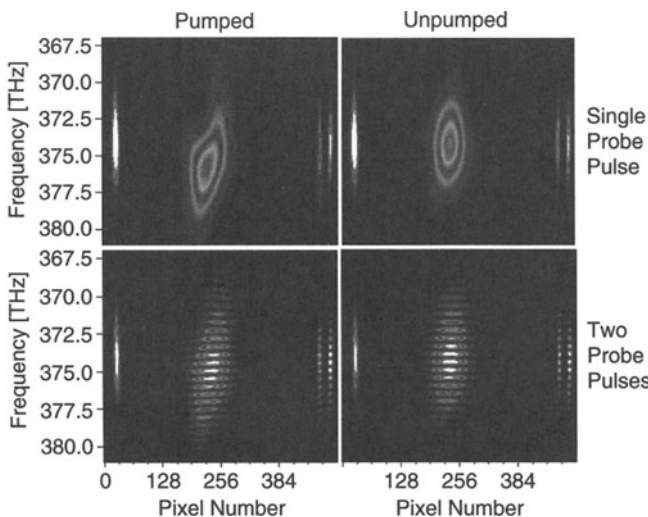


Fig. 24.6: Example CCD Data. MI-FROG (bottom) and TREEFROG (top) traces for pumped (left) and unpumped (right) conditions. The three power spectra channels are the incident pulse from the amplifier (left), the single or double pulse sequence entering (right) and exiting the interaction region. Note the strong blueshift and corresponding fringe rotation. The pseudo-color map is the same as in Fig. 24.7b.

with the FROG and MI-FROG analyses, a result of interferogram corruption by residual pump leakage at 800 nm. It is important to note that as MI-FROG is a temporally gated spectroscopy it was not similarly affected.

Using an experimental setup similar to that described earlier (see Fig. 24.3), with the addition of a backfilled gas cell with low-nonlinearity CaF₂ windows, data was taken with various gas densities of He, Ne, Ar, Kr, Xe, H₂, N₂, O₂, and Air at pump-probe increments of 12 fs. The polarization of the 124 fs, 400 nm pump was oriented either parallel or orthogonal to that of the weak 800 nm, 175 fs, multi-pulse probe. Temporal overlap in the focal region was determined using sum-frequency generation ($\omega_{\text{pump}} + \omega_{\text{probe}} = 3\omega_{\text{probe}}$) in the gases themselves while spatial overlap was ensured using focal plane imaging onto a CCD camera. Completely automated, one data set consisting of 51 delay points and 255 CCD images could be acquired in ~ 30 minutes.

The power spectra channels in Fig. 24.6 allow both centroid-based power spectrum analysis and interferogram analysis, which provide a pulse-width averaged measure of frequency and phase shift, respectively. They can depend sensitively [1,30] on the detailed temporal and frequency-domain structure of the probe pulse. As MI-FROG recovers, to all orders, the phase *difference* between the pumped and unpumped probe pulses, we can utilize it to a) verify the intensity and phase structure of the probe pulse and b) recover the sub-pulsewidth time-resolved phase and frequency shifts impressed upon the probe by the pump pulse and ionization front, *independently* of the probe pulse structure.

Figure 24.7a illustrates the doubly time-resolved probe pulse frequency shift in the case of above-threshold ionization of Xenon. The upper, red-shifted, diagonal corresponds to $n_2 I$ cross-phase modulation via the neutral gas and is strongest for early pump delays. This asymmetry suggests defocusing is significant, a hypothesis supported by independent probe spectral data. The lower, blueshifted, diagonal is predominately due to the ultrafast ionization front, though comparison of the *p* and *s*-polarized cases indicates that neutral gas contributions are not always negligible. Figure 24.7b similarly illustrates the corresponding probe pulse intensity profile versus time. It should be stressed that by using MI-FROG a zero of time is well defined and the apparent motion of the pulse profile is genuine.

Modeling [31,32] of the data in Fig. 24.7 and similar cases reveal frequency mixing via the transverse plasma current [33] on such a large scale that ultrafast depletion of the probe pulse occurs within the ionization front. Though this mixing is clearly accompanied by 2D effects not included in the model, the observed ultrafast depletion, as it occurs only *within* the ionization front and for *both* polarizations, cannot be due to defocusing or neutral gas effects. This work (published in [34]) represents the first direct, ultrafast-time-resolved observation of this phenomena. MI-FROG has also been used to study ultrafast ionization in molecular gases [35].

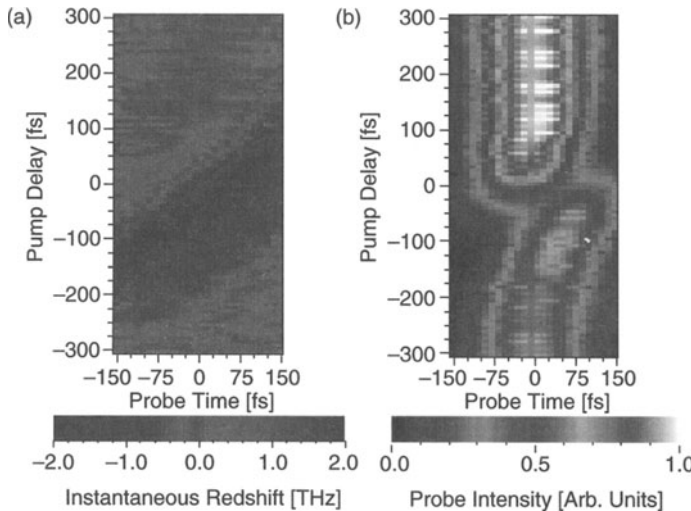


Fig. 24.7: (a) Doubly time-resolved frequency shift (left) in 600 T Xenon, with pump and probe orthogonally polarized. The large dark diagonal corresponds to a strong blueshift, while the upper, lighter diagonal corresponds to a weak redshift. (b) Time-resolved probe intensity profile (right).

Summary and Conclusions

We have provided a detailed review of Multi-pulse Interferometric Frequency Resolved Optical Gating, including the multi-grid Power Method PCGP algorithm used for iterative phase recovery, as we have used it to study ultrafast cross-phase modulation in materials and plasmas. Being a sensitive direct-reading “oscilloscope” of ultrafast time-domain phase shifts, MI-FROG has proven itself a powerful new tool for ultrafast science. By retaining the “ultrafast boxcar” advantage of FROG, MI-FROG is uniquely suited for pump-probe coherent spectroscopy using amplified visible and near-IR short-pulse systems and/or emissive targets.

Two example uses of MI-FROG were shown. The first, cross-phase modulation in fused silica, illustrated the unique ability of MI-FROG to observe both the all-order phase shift and the apparent pulse motion in time due to the nonlinear interaction. In the second, the study ultrafast ionization in gases, MI-FROG allowed the clear identification and differentiation among pump depletion from ionization losses, pump and probe defocusing from the plasma, and the hitherto unseen probe depletion within the ionization front itself. This latter effect might provide an interesting new route to nonlinear pulse shaping via rapid time-domain modulation.

References

1. Wm. M. Wood, C. W. Siders, and M. C. Downer: Measurement of Femtosecond Ionization Dynamics of Atmospheric Density Gases by Spectral Blueshifting, *Phys. Rev. Lett.* **67**, 3523–3526 (1991).

2. C. Froehly, A. Lacourt, J. C. Vienot: *J. Opt. (Paris)* **4**, 183 (1973).
3. C. W. Siders, S. P. Le Blanc, A. Babine, A. Stepanov, A. Sergeev, T. Tajima, and M. C. Downer: Plasma-Based Accelerator Diagnostics Based upon Longitudinal Interferometry with Ultrashort Optical Pulses, *IEEE Trans. Plasma Sci.* **24**, 301–315 (1996).
4. C. W. Siders, S. P. Le Blanc, D. Fisher, T. Tajima, M. C. Downer, A. Babine, A. Stepanov, and A. Sergeev: Laser Wakefield Excitation and Measurement by Femtosecond Longitudinal Interferometry, *Phys. Rev. Lett.* **76**, 3570–3573 (1996).
5. D. J. Kane and R. Trebino: Single-shot measurement of the intensity and phase of an arbitrary ultrashort pulse by using frequency-resolved optical gating, *Opt. Lett.* **18**, 823–825 (1993).
6. K. W. DeLong, R. Trebino, and W. E. White: Simultaneous recovery of two ultrashort laser pulses from a single spectrogram, *J. Opt. Soc. Am. B* **12**, 2463–2466 (1995).
7. D. N. Fittinghoff, J. L. Bowie, J. N. Sweetser, R. T. Jennings, M. A. Krumbügel, K. W. DeLong, R. Trebino, and I. A. Walmsley: Measurement of the intensity and phase of ultraweak, ultrashort laser pulses, *Opt. Lett.* **21**, 884–886 (1996).
8. C. W. Siders, A. J. Taylor, and M. C. Downer: Multipulse interferometric frequency-resolved optical gating: real-time phase-sensitive imaging of ultrafast dynamics, *Opt. Lett.* **22**, 624–626 (1997).
9. C. W. Siders, J. L. W. Siders, F. G. Omenetto, and A. J. Taylor: Multi-pulse Interferometric Frequency Resolved Optical Gating, *IEEE J. Quantum Electron.* **35**, 432–440 (1999).
10. R. A. Altes: Detection, estimation, and classification with spectrograms, *J. Acoust. Soc. Am.* **67**, 1232–1246 (1980).
11. R. Trebino, K. W. DeLong, D. N. Fittinghoff, J. N. Sweetser, M. A. Krumbügel, B. A. Richman, and D. J. Kane: Measuring ultrashort laser pulses in the time-frequency domain using frequency-resolved optical gating, *Rev. Sci. Instrum.* **68**, 3277–3295 (1997).
12. R. Trebino and D. J. Kane: Using phase retrieval to measure the intensity and phase of ultrashort pulses: frequency-resolved optical gating, *J. Opt. Soc. Am. B* **10**, 1101–1111 (1993).
13. J. Piasecki, B. Colombeau, M. Vampouille, C. Froehly, and J. A. Arnaud: Nouvelle méthode de mesure de la réponse impulsionale des fibres optiques, *App. Opt.* **19**, 3749–3755 (1980).
14. C. Froehly, B. Colombeau, and M. Vampouille: Shaping and analysis of picosecond light pulses, in *Progress in Optics XX*, (North-Holland Pub. Co., Amsterdam 1983).
15. F. Reynaud, F. Salin, A. Barthélémy: Measurement of phase shifts introduced by nonlinear optical phenomena on subpicosecond pulses, *Opt. Lett.* **14**, 275–277 (1989).
16. E. Tokunaga, A. Terasaki, T. Kobayashi: Femtosecond phase spectroscopy by use of frequency-domain interference, *J. Opt. Soc. Am. B* **12**, 753–771 (1995).
17. E. Tokunaga, A. Terasaki, and T. Kobayashi: Frequency-domain interferometer for femtosecond time-resolved phase spectroscopy, *Opt. Lett.* **17**, 1131–1133 (1992).
18. X. D. Cao, L. Zheng, and D. D. Meyerhofer: Measurement of group-velocity walk-off of short pulses in nonlinear crystals: a novel method, *Opt. Lett.* **20**, 392–394 (1995).
19. X. D. Cao and D. D. Meyerhofer: Frequency-domain interferometer for measurement of the polarization mode dispersion in single-mode optical fibers, *Opt. Lett.* **19**, 1837–1839 (1994).
20. J. P. Geindre, P. Audebert, A. Rousse, F. Fallies, J. C. Gauthier, A. Mysyrowicz, A. Dos Santos, G. Hamoniaux, and A. Antonetti: Frequency-domain interferometer for measuring the phase and amplitude of a femtosecond pulse probing a laser-produced plasma, *Opt. Lett.* **19**, 1997–1999 (1994).
21. E. N. Leith and J. Upatnieks: Reconstructed Wavefronts and Communication Theory, *J. Opt. Soc. Am.* **52**, 1123–1130 (1962).
22. D. J. Kane, G. Rodriguez, A. J. Taylor, and T. Sharp Clement: Simultaneous measurement of two ultrashort laser pulses from a single spectrogram in a single shot, *J. Opt. Soc. Am. B* **14**, 935–943 (1997).
23. K. W. DeLong, D. N. Fittinghoff, R. Trebino, B. Kohler and K. Wilson: Pulse retrieval in frequency-resolved optical gating based on the method of generalized projections, *Opt. Lett.* **19**, 2152–2154 (1994).
24. D. J. Kane: Recent progress toward real-time measurement of ultrashort laser pulses, *IEEE J. Quantum Elec.* **35**, 421–431 (1999).
25. M. Gavrila (Ed.): *Atoms in Intense Laser Fields* (Academic Press, Boston 1992).
26. C. W. Siders, N. C. Turner III, M. C. Downer, A. Babine, A. Stepanov, and A. M. Sergeev: Blue-shifted third-harmonic generation and correlated self-guiding during ultrafast barrier suppression ionization of subatmospheric density noble gases, *J. Opt. Soc. Am. B* **13**, 330–335 (1996).
27. S. Backus, J. Peatross, E. Zeek, A. Rundquist, G. Taft, M. M. Murnane, H. C. Kapteyn: Femtosecond 1 μ J ultraviolet pulses generated by third-harmonic conversion in air, *Opt. Lett.* **21**, 665–667 (1996).
28. I. P. Christov, M. M. Murnane, and H. C. Kapteyn: High-Harmonic Generation of Attosecond Pulses in the “Single-Cycle” Regime, *Phys. Rev. Lett.* **78**, 1251–1254 (1997).

29. Wm. M. Wood, C. W. Siders, and M. C. Downer: Femtosecond growth dynamics of an underdense ionization front measured by spectral blueshifting, *IEEE Trans. Plasma Sci.* **21**, 20–33 (1993).
30. B. Rau, C. W. Siders, S. P. Le Blanc, D. L. Fisher, M. C. Downer, and T. Tajima: Spectroscopy of short, intense laser pulses due to gas ionization effects, *J. Opt. Soc. Am. B* **14**, 643–649 (1997).
31. B. M. Penetrante, J. N. Bardsley, W. M. Wood, C. W. Siders, and M. C. Downer: Ionization-induced frequency shifts in intense femtosecond laser pulses, *J. Opt. Soc. Am. B* **9**, 2032–2041 (1992).
32. C. W. Siders, J. L. W. Siders, and A. J. Taylor: Femtosecond Coherent Spectroscopy at 800 nm: MI-FROG Measures High-Field Ionization Rates in Gases, in *Ultrafast Phenomena XI*, (Springer, Berlin, Heidelberg 1998) pp. 438–440.
33. F. Brunel: Harmonic generation due to plasma effects in a gas undergoing multiphoton ionization in the high-intensity limit, *J. Opt. Soc. Am. B* **7**, 521–526 (1990).
34. C. W. Siders, G. Rodriguez, J. L. W. Siders, F. G. Omenetto, and A. J. Taylor: Measurement of Ultrafast Ionization Dynamics of Gases by Multi-pulse Interferometric Frequency Resolved Optical Gating, *Phys. Rev. Lett.* **87**, 263002 (2001).
35. G. Rodriguez, C. W. Siders, C. Guo, and A. J. Taylor: Coherent Ultrafast MI-FROG Spectroscopy of Optical Field Ionization in Molecular H₂, N₂, and O₂, *IEEE J. Sel. Top. Quantum. Electron.* **7**, 579 (2001).

25. The Future of Pulse Measurement: New Dilemmas

Rick Trebino

Successes

So the fundamental dilemma of pulse measurement is resolved. We've learned to avoid one-dimensional phase retrieval and embrace its two-dimensional cousin, and people have been busy taking advantage of the solution. FROG has allowed measurements undreamt of a mere ten years ago.

In this book, we've described techniques for measuring a wide range of pulses, from the IR to the UV, from a few fs to many ps, from simple to the most complex ultrashort pulses ever generated. We've even shown how to make these measurements easily and with confidence. But to keep this book a reasonable size, we neglected the applications of these methods.

There have been many. For example, FROG has played a pivotal role in determining the phase distortions in Ti:Sapphire oscillators and in their breaking the 10-fs barrier and in the approach to a single cycle [1,2].

FROG is now routinely used in the generation of extremely high-power pulses [3–5] and is rapidly becoming the method of choice for pulses at exotic wavelengths. Several groups are now even working on x-ray FROG and x-ray XFROG (would that be XXFROG? One more X and we might have to take a different approach to acronyms...).

FROG measurements of chirped, spectrally broadened pulses have been crucial for the generation of ever-shorter pulses via external compression. The direct phase measurement of the output of glass fibers (as discussed in Chapter 14), hollow wave-guides, and parametric amplification [6–8] provides a rigorous target function for the pulse compressor design.

FROG measurements of shaped pulses for coherent control applications have helped to accelerate progress this exciting field [9–15].

FROG has provided exciting advances in materials characterization in all phases of matter, especially in understanding nonlinear-optical phenomena [16–25].

With FROG, aligning lasers and amplifiers has never been simpler [26]. And general diagnostics of ultrafast laser devices and amplifiers is also an important application of FROG [27–30].

New versions of FROG for specialized applications seem to appear every month. Versions of FROG using heterodyning for greater sensitivity and faster algorithmic performance have been demonstrated [31,32]. Two-photon absorption is turning out to be a useful process for broadband weak pulses [33]. New materials for FROG measurements in new wavelength ranges are proving helpful [34]. Even when a pulse is too complex to consider deterministically,

and statistical methods are required, there's a clever FROG method available [35]. In fact, things have evolved to the point where use of FROG in a research effort no longer seems to require a reference to a FROG paper, which makes it difficult to assess its full impact.

And occasionally, FROG is suggested for some very wild applications, such as astronomy. That one might be a few years off, however.

FROG's versatility coupled with the importance of the intensity and phase in science virtually guarantee future applications not yet dreamt of.

Measurement of Attosecond Pulses

Recently, researchers have, not only theoretically modeled, but have actually experimentally broken the *attosecond barrier*, both generating—and measuring—pulses of light a few hundred *attoseconds* long [36–53]. These results—in particular, the experimental demonstrations by Hentschel, et al., and Paul, et al.—represent impressive accomplishments.

The next step, of course, will be to better understand and refine these pulses. Measurement of their intensity and phase will undoubtedly provide the key to both. Fortunately, the time-frequency domain is well suited to this regime. Indeed, the methods used to measure these unimaginably short events were both time-frequency methods! One [46] involved frequency-filtering the pulse and measuring the resulting slower temporal response—a sonogram (see Chapter 5). The other [53] involved gating the pulse with a longer reference pulse field and spectrally resolving the signal (which happened to be photo-electrons, but no matter)—a spectrogram or XFROG trace (see Chapter 16). While Hentschel, et al., didn't, they probably could have written a modified XFROG algorithm using a model for the photo-electron spectrum and retrieved the intensity and phase of their attosecond pulse.

Other advantages of FROG for the attosecond regime: it's self-referencing, so the “shorter event”—a particularly difficult quantity in this regime!—is, of course, unnecessary. And, since physical processes in this regime are unlikely to be effectively instantaneous (a required assumption in all other measurement techniques), FROG's ability to operate with an arbitrary non-instantaneous effect (Chapter 18) will be very useful. Also, FROG's generality, allowing it to potentially operate in any wavelength or temporal range, will also be crucial. Any delay-dependent effect that can be spectrally resolved in some manner will yield a FROG.

Measurement of the Absolute Phase

There is one thing FROG definitely cannot currently do, however. In fact, *no* currently existing pulse-characterization technique can measure the *absolute phase*, ϕ_0 , of a pulse. We discussed the effect of ϕ_0 on the pulse structure in

Chapter 2. Recall that the absolute phase is the relative phase of the optical carrier wave with respect to the pulse envelope. It's illustrated in Fig. 25.1 for the 4.5-fs pulse generated and measured by Bathuska, et al. [2,54]. It becomes an important parameter when the envelope approaches a single cycle, and the 4.5-fs pulse consists of only ~ 2.5 optical cycles. As a result, the two different absolute phases shown in Fig. 25.1 correspond to physically different electric fields, but they can't be distinguished with available pulse-measurement techniques.

Knowledge of the absolute phase becomes essential in strong-field optics of pulses that contain only a few optical cycles [37,55–61]. The understanding of the importance of the absolute phase has come about only in the last few years, as several-optical-cycle pulses have become available due to the rapid progress in their generation and amplification. For example, it's been suggested that large fluctuations observed in the X-ray intensity were directly related to the variation of the absolute phase that could not have been stabilized [55].

To complicate matters, because the round-trip phase and group delays typically differ, conventional Ti:Sapphire oscillators produce pulses with an absolute phase that drifts from pulse to pulse [62]. Scenarios have been suggested and implemented for absolute-phase stabilization [51,58,59,63–68], but this is only the first step towards its measurement.

Presumably, pulses with stabilized absolute phase will subsequently be amplified and used in various high-intensity applications that depend on the precise value of the absolute phase [59,63,64]. And using any one of these processes, a FROG could almost certainly be designed. After all, FROG is not so much a technique, as a *concept*. While the usual versions of FROG cannot measure the absolute phase, simply provide such a nonlinear-optical process that depends on the quantity to be measured (in this case the absolute phase), vary the delay between two or more input beams, and measure a spectrum vs. delay; you now have a FROG that can measure the absolute phase.

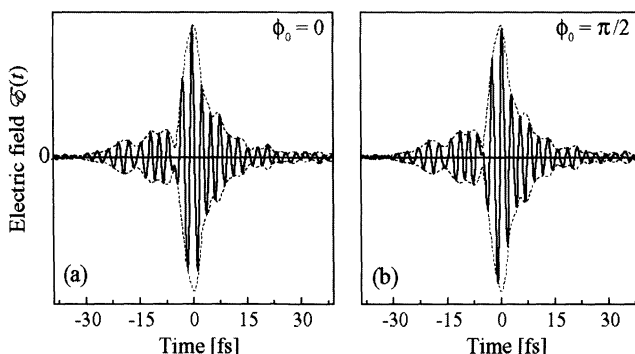


Fig. 25.1: Two possible electric fields of the 4.5-fs pulses described in Chapter 14 for different absolute phases. (a) $\phi_0 = 0$ and (b) $\phi_0 = \pi/2$.

Practical Pulse Measurement

While measurement of the absolute phase is an exotic problem, whose solution would impact exotic fields such as ultrafast high-harmonic generation, it's always the more mundane unsolved problem that would actually have the highest impact. (Which has had greater impact in human history: the zero-G pen astronauts use or the simple ordinary pencil?)

And ultrashort laser-pulse measurement techniques have tended to focus on the exotic, while neglecting the mundane. (For example, while well-developed techniques make it easy to measure a 50-fs pulse, it's actually still quite difficult to measure one a thousand times longer.) Indeed, ultrashort laser pulses are themselves, by definition, exotic, which in part explains the interest—and progress—in measuring them.

However, there are innumerable sources found *in nature* whose emission is broadband and hence ultrafast. The light illuminating this page, for example. And nearly any weak fluorescence. When excited by an ultrashort laser pulse, essentially all solids and liquids emit ultrashort light pulses. To complicate the issue, however, not only are all of these light pulses spatially incoherent, but the shorter the fluorescent pulse, the weaker it is. Broadband fluorescence is typically ultrafast because other ultrafast processes compete for the energy. In fact, it's molecules whose excitation energy is rapidly converted into a useful function that emit ultrashort pulses. For example, rapid electron or proton transfer or photo-isomerization reduces the fluorescence lifetime to the picosecond or subpicosecond time scale with an accompanying several-order-of-magnitude reduction of the fluorescence yield. It's these other (typically energy utilization) processes that make ultrafast processes interesting from a biological or chemical point of view, and the measurement of the intensity and phase of the fluorescence in these cases is an important window into these processes.

Much work has been performed studying ground-state effects (i.e., transient absorption) through the use of excite-probe methods. And time- and frequency-resolved spectrogram-like studies are now yielding important information [69–76]. The lack of specificity in the transient absorbance spectrum, however, can become a problem when the features are broad and overlapping, as is often the case for biological molecules. As a result, a few researchers are looking directly at ultrafast emission or fluorescence [77–79]. The emitted luminescence (in particular, its intensity and phase vs. time) of a chromophore is sensitive to its electronic state, its conformation, and its surrounding environment. All these factors determine its potential energy surfaces, thereby providing a spectroscopic handle for probing its chemical dynamics. This is the general problem described in Chapter 1 and illustrated in Fig. 1.2 as an example of why ultrashort pulse measurement is important.

This problem is unsolved.

Thus, an important pulse-measurement problem is *the development of a sensitive technique for measuring ultraweak luminescence from molecules of interest in biology, chemistry, and engineering.*

In Chapters 22 and 23, we discussed spectral interferometry (SI) and showed that it could measure trains of pulses with less than a photon each. Could SI solve this problem?

In a word, *no*. Why not? First, fluorescence has random—and, for this purpose, *uninteresting*—absolute phase from shot to shot. As a result, if we were to make a multi-shot SI measurement of fluorescence, the SI fringes would completely wash out. Thus, SI with fluorescence is limited to *single-shot* measurements, which reduces its sensitivity by many orders of magnitude. Second, fluorescence has poor spatial coherence, so measurements of it are limited by the van Cittert-Zernike Theorem [80], which severely limits the size of the fluorescing region, and hence the intensity of the fluorescence that can be measured without losing spatial coherence. This double-whammy essentially eliminates SI from consideration. And then there's the practical problem of generating a well-characterized, time-synchronized source at the fluorescence wavelength, which is necessarily different from that of the excitation source.

Okay, so what about FROG? The good news, ironically, is that FROG *doesn't* measure the absolute phase. This is quite advantageous when the absolute phase varies randomly and uninterestingly: the variation of fluorescence's absolute phase from shot to shot produces no cancellations in a FROG measurement. For the same reason, FROG also has a high tolerance of spatial incoherence. The bad news, however, is FROG's requirement of a nonlinear-optical process, which limits its efficiency. Use of XFROG with a relatively intense gate pulse helps. Nevertheless, weak fluorescence cannot be measured sufficiently sensitively.

An extremely sensitive technique for measuring the intensity and phase of weak fluorescence would allow breakthroughs in many fields. In biology alone, processes such as vision, photosynthesis, and protein folding, for example, would benefit greatly. Such a development would make ultrashort-pulse-measurement techniques practical devices of great utility in many fields. With such a development, instead of describing these techniques as measuring ultrashort *laser* pulses, we could perhaps say, much more generally, that they measure ultrashort *light* pulses.

Conclusion

The field of ultrashort-light-pulse measurement had its origins in the early days of the development of sub-nanosecond laser pulses, when it was first realized that light pulses were faster than light detectors. But some 30 years later, it is a livelier field than ever, with the continued discovery of techniques

that can uncover ever more information about an individual fs pulse or a whole train of them. We hope that this book has provided an introduction to the subject of ultrashort-light-pulse measurement that'll be useful to someone just beginning the study of ultrafast phenomena. But, at the same time, we've tried to create a useful source for the experienced scientist requiring a detailed description of the FROG technique, its implementation and inversion algorithms, and its subtleties.

Finally, we also hope this book has inspired some of you to take advantage of these recent developments, apply them to your work, and to make your own contributions using them. Or maybe develop some new pulse-measurement methods. Perhaps even solve the above problems or discover new ones to be solved. As in other fields of scientific endeavor, the unproven axiom of research seems to hold: the more we know, the more there appears that we need to know. But the field of ultrashort pulse measurement, on the other hand, would seem to have a definite end: once we possess techniques that characterize a pulse completely in all relevant regimes, are we not then done? We suspect that the need to be able to measure pulses in new wavelength ranges, such as the x-ray; in new temporal regimes, such as the attosecond; in new regimes of complexity, such as trains of non-identical pulses; with ever-increasing sensitivity; and in *space* as well as time, will keep us busy for a long time to come. But who knows? This is a new dilemma that we leave to future generations.

References

1. Taft, G., et al., *Ultrashort Optical Waveform Measurements Using Frequency-Resolved Optical Gating*. Optics Letters, 1995. **20**(7): p. 743–5.
2. Baltuska, A., M.S. Pshenichnikov, and D. Wiersma, *Amplitude and Phase Characterization of 4.5 fs Pulses by Frequency-Resolved Optical Gating*. Opt. Lett., 1998. **23**(18): p. 1474–6.
3. Bonlie, J.D., et al., *Production of >10¹² W/cm² from a large-aperture Ti:sapphire laser*. Applied Physics B, 2000. **B70**(suppl.issue): p. S155–60.
4. Hong, K.H., et al., *Temporal characterization of a femtosecond terawatt Ti:sapphire laser using frequency-resolved optical gating*. Journal of the Korean Physical Society, 1998. **33**(3): p. 315–19.
5. Cheng, Z., et al., *Amplitude and Chirp Characterization of High-Power Laser Pulses in the 5-fs Regime*. Opt. Lett., 1999. **24**(4): p. 247–9.
6. Shirakawa, A., et al. *Visible sub-5-fs Pulse Generation by Pulse-Front-Matched Optical Parametric Amplification*. In *Conference on Lasers and Electro-Optics*. 1999. Baltimore: Optical Society of America.
7. Cerullo, G., et al., *Sub-8-fs pulses from an ultrabroadband optical parametric amplifier in the visible*. Opt. Lett., 1998. **23**(16): p. 1283.
8. Wilhelm, T., J. Piel, and E. Riedle, *Sub-20-fs pulses tunable across the visible from a blue-pumped single-pass noncollinear parametric converter*. Opt. Lett., 1997. **22**(19): p. 1494–6.
9. Baumert, T. and G. Gerber, *Molecules in Intense Femtosecond Laser Fields*. Physica Scripta, 1996. **T72**.
10. Bartels, R., et al., *Shaped-pulse optimization of coherent emission of high-harmonic soft X-rays*. Nature, 2000. **406**(6792): p. 164–6.
11. Bartels, R., et al., *Attosecond time-scale feedback control of coherent X-ray generation*. Chemical Physics, 2001. **267**(1–3): p. 277–89.
12. Feurer, T., et al., *Control of the photodissociation process of CsCl using a feedback-controlled self-learning fs-laser system*. Chemical Physics, 2001. **267**(1–3): p. 223–9.

13. Hornung, T., et al., *Coherent control of the molecular four-wave-mixing response by phase and amplitude shaped pulses*. Chemical Physics, 2001. **267**(1–3): p. 261–76.
14. Tesch, C., K. Kompa, and R. de Vivie-Riedle, *Design of optical infrared femtosecond laser pulses for the overtone excitation in acetylene*. Chemical Physics, 2001. **267**(1–3): p. 173–185.
15. Kleiman, V.D., et al., *Controlling condensed-phase vibrational excitation with tailored infrared pulses*. Chemical Physics, 1998. **233**(2–3): p. 207–16.
16. Diddams, S.A., et al., *Characterizing the nonlinear propagation of femtosecond pulses in bulk media*. IEEE Journal of Selected Topics in Quantum Electronics, 1998. **4**(2): p. 306–16.
17. Eaton, H.K., et al., *Investigating Nonlinear Femtosecond Pulse Propagation with Frequency-Resolved Optical Gating*. IEEE J. Quant. Electron., 1999. **35**(4): p. 451–8.
18. Taylor, A.J., G. Rodriguez, and T.S. Clement, *Determination of n_2 by Direct Measurement of the Optical Phase*. Opt. Lett., 1996. **21**(22): p. 1812–14.
19. Barry, L.P., et al., *Complete characterisation of pulse propagation in optical fibres using frequency-resolved optical gating*. Electronics Letters, 1996. **32**(25): p. 2339–40.
20. Bollond, P.G., et al., *Characterization of nonlinear switching in a figure-of-eight fiber laser using frequency-resolved optical gating*. IEEE Photonics Technology Letters, 1998. **10**(3): p. 343–5.
21. Yabushita, A., T. Fuji, and T. Kobayashi, *SHG FROG and XFROG methods for phase/intensity characterization of pulses propagated through an absorptive optical medium*. Optics Communications, 2001. **198**(1–3): p. 227–32.
22. Nikitin, S.P., et al., *Guiding of Intense Femtosecond Pulses in Preformed Plasma Channels*. Opt. Lett., 1997. **22**(23): p. 1787–9.
23. Nikitin, S.P., et al., *Ionization-induced pulse shortening and retardation of high intensity femtosecond laser pulses*. Optics Communications, 1998. **157**(1–6): p. 139–44.
24. Young, P.E. and P.R. Bolton, *Propagation of subpicosecond laser pulses through a fully ionized plasma*. Physical Review Letters, 1996. **77**(22): p. 4556–9.
25. Bolton, P.R., et al., *Propagation of intense, ultrashort laser pulses through metal vapor: refraction-limited behavior for single pulses*. Journal of the Optical Society of America B (Optical Physics), 1996. **13**(2): p. 336–46.
26. Kohler, B., et al., *Phase and Intensity Characterization of Femtosecond Pulses from a Chirped-Pulse Amplifier by Frequency-Resolved Optical Gating*. Optics Letters, 1994. **20**(5): p. 483–5.
27. Kasper, A. and K.J. Witte, *Contrast and phase of ultrashort laser pulses from Ti:sapphire ring and Fabry-Perot resonators based on chirped mirrors*. Journal of the Optical Society of America B, 1998. **15**(9): p. 2490–5.
28. Weigand, R., M. Wittmann, and J.M. Guerra, *Generation of femtosecond pulses by two-photon pumping supercontinuum-seeded collinear traveling wave amplification in a dye solution*. Applied Physics B, 2001. **B73**(3): p. 201–3.
29. Reid, D.T., et al., *Amplitude and phase measurement of mid-infrared femtosecond pulses by using cross-correlation frequency-resolved optical gating*. Optics Letters, 2000. **25**(19): p. 1478–80.
30. Efimov, E., et al., *Minimization of dispersion in an ultrafast chirped pulse amplifier using adaptive learning*. Applied Physics B, 2000. **70**(Suppl.): p. S133–44.
31. Gardecki, J.A., et al., *Optical heterodyne detected spectrograms of ultrafast nonresonant electronic*. Journal of the Optical Society of America B, 2000. **17**(4): p. 652–62.
32. Yeremenko, S., et al., *Frequency-resolved pump-probe characterization of femtosecond IR pulses*. Opt. Lett., 2002.
33. Ogawa, K. and M.D. Pelusi, *High-sensitivity pulse spectrogram measurement using two-photon absorption in a semiconductor at 1.5- μ m wavelength*. Optics Express, 2000. **7**(3).
34. Taira, K. and K. Kikuchi, *Highly sensitive frequency-resolved optical gating in 1.55 μ m region using organic nonlinear optical crystal for second-harmonic generation*. Electronics Letters, 2000. **36**(20): p. 1719–20.
35. Stimson, M.J., et al., *Noisy-light correlation functions by frequency resolved optical gating*. Journal of the Optical Society of America B (Optical Physics), 1998. **15**(2): p. 505–14.
36. Branning, D., A.L. Migdall, and A.V. Sergienko, *Simultaneous measurement of group and phase delay between two photons*. Physical Review A, 2000. **62**(6): p. 063808/1–12.
37. Christov, I.P., M.M. Murnane, and H.C. Kapteyn, *High-Harmonic Generation of Attosecond Pulses in the "Single-Cycle" Regime*. Physical Review Letters, 1997. **78**(7): p. 1251.
38. Christov, I.P., M.M. Murnane, and H.C. Kapteyn, *Attosecond Pulse Generation in the Single Cycle Regime*. Physical Review Letters, 1997. **78**: p. 1251.
39. Christov, I.P., M.M. Murnane, and H.C. Kapteyn, *Generation and Propagation of Attosecond X-Ray Pulses in Gaseous Media*. Physical Review A Rapid Communications, 1998. **57**: p. R2285.

40. Christov, I.P., H.C. Kapteyn, and M.M. Murnane, *Quasi-phase matching of high-harmonics and attosecond pulses in modulated*. Optics Express, 2000. **7**(11).
41. Christov, I.P., *Control of high harmonic and attosecond pulse generation in aperiodic modulated waveguides*. Journal of the Optical Society of America B, 2001. **18**(12): p. 1877–81.
42. Christov, I.P., et al., *Attosecond time-scale intra-atomic phase matching of high harmonic generation*. Physical Review Letters, 2001. **86**(24): p. 5458–61.
43. Geissler, M., A. Scrinzi, and T. Brabec, *Attosecond cross-correlation technique*. Physical Review Letters, 2001. **86**(3): p. 412–5.
44. Lappas, D.G. and A. L'Huillier, *Generation of attosecond xuv pulses in strong laser-atom interactions*. Physical Review A, 1998. **58**(5): p. 4140–6.
45. Milosevic, D.B., et al., *High-harmonic generation by a bichromatic bicircular laser field*. Laser Physics, 2001. **11**(2): p. 165–8.
46. Paul, P.M., et al., *Observation of a train of attosecond pulses from high-order harmonic generation*. Science, 2001. **292**(5522): p. 1689–92.
47. Roos, L., M.B. Gaarde, and A. L'Huillier, *Tailoring harmonic radiation to different applications using a genetic algorithm*. Journal of Physics B, 2001. **34**(24): p. 5041–54.
48. Saari, P., *Evolution of subcycle pulses in nonparaxial Gaussian beams*. Optics Express, 2001. **8**(11).
49. Scrinzi, A., M. Geissler, and T. Brabec, *Attosecond cross correlation technique*. Physical Review Letters, 2001. **86**(3): p. 412–15.
50. Scrinzi, A., M. Geissler, and T. Brabec, *Techniques for attosecond pulse detection and the observation of electronic quantum motion*. Laser Physics, 2001. **11**(2): p. 169–73.
51. Telle, H.R., et al., *Carrier-envelope offset phase control: a novel concept for absolute optical frequency measurement and ultrashort pulse generation*. Applied Physics B, 1999. **B69**(4): p. 327–32.
52. Tempea, G., et al., *Comment on "Observation of attosecond light localization in higher order harmonic generation" [and reply]*. Physical Review Letters, 2001. **87**(10): p. 109401/1–2/2.
53. Hentschel, M., et al., *Attosecond Metrology*. Nature, 2001. **414**: p. 509–13.
54. Baltuska, A., M.S. Pshenichnikov, and D.A. Wiersma, *Second-Harmonic Generation Frequency-Resolved Optical Gating in the Single-Cycle Regime*. IEEE J. Quant. Electron., 1999. **35**(4): p. 459–78.
55. Spielmann, C. and a.e. al, *Generation of Coherent X-ray Pulses in the Water Window using 5fs Laser Pulses*, in *Science*. 1997. p. 661.
56. Chang, Z., et al., *Generation of Coherent Soft-X-Rays at 2.7nm using High Harmonics*. Physical Review Letters, 1997. **79**: p. 2967.
57. Krausz, F., et al., *Extreme Nonlinear Optics: Exposing Matter to a Few Periods of Light*. Opt. Phot. News, 1998. **9**(7): p. 46.
58. Bohan, A.D., et al., *Phase-Dependent Harmonic Emission with Ultrashort Laser Pulses*. Phys. Rev. Lett., 1998. **81**(9): p. 1837.
59. Tempea, G., M. Geissler, and T. Brabec, *Phase sensitivity of high-order harmonic generation with few-cycle laser pulses*. J. Opt. Soc. Am. B, 1999. **16**(4): p. 669.
60. Schnürer, M., et al., *Absorption-Limited Generation of Coherent Ul-trashort Soft-X-Ray Pulses*. Phys. Rev. Lett., 1999. **83**(4): p. 722.
61. Rundquist, A., et al., *Phase Matching of Soft-X-Ray Harmonic Emission in Hollow-Core Fibers*, in *Science*. 1998. p. 1412.
62. Xu, L., et al., *Route to Phase Control of Ultrashort Light Pulses*. Opt. Lett., 1996. **21**(24): p. 2008–10.
63. Christov, I.P., *Phase-dependent loss due to nonadiabatic ionization by sub-10-fs pulses*. Opt. Lett., 1999. **24**: p. 1425.
64. Dietrich, P., F. Krausz, and P.B. Corkum, *Determining the absolute carrier phase of a few-cycle laser pulse*. Opt. Lett., 2000. **25**: p. 16.
65. Apolonski, A., et al., *Controlling the phase evolution of few-cycle light pulses*. Physical Review Letters, 2000. **85**(4): p. 740–3.
66. Jones, D.J., et al., *Carrier-envelope phase control of femtosecond modelocked lasers and direct optical frequency synthesis*. Science, 2000. **288**(5466): p. 635.
67. Jones, D.J., et al. *Long-term locking of the carrier-envelope phase in a 15-fs Ti:S laser using a self-referencing frequency domain technique*. in *Conf. on Lasers and Electro-Optics*. 2000. San Francisco.
68. Pshenichnikov, M.S. and D.A. Wiersma, *Absolute-phase control of femtosecond pulses*. 2000.
69. Nakamura, K., et al., *Picosecond time-resolved X-ray diffraction from a silicon crystal under laser-induced breakdown*, in *Ultrafast Phenomena XII*, T. Elsaesser, et al., Editors. 2001, Springer. p. 284–6.
70. Lenchenkov, V., et al., *Femtosecond Study of Electron Photodetachment from Complex Anions: Fe(CN) (sub 6 exp -4-) and CuBr (sub 2 exp -) in H (sub 2) O*, in *Ultrafast Phenomena XII*, T. Elsaesser, et al., Editors. 2001, Springer. p. 476–8.

71. Vauthhey, E., *Investigation of the Ultrafast Dynamics of Charge Recombination of Ion Pairs Using Multiplex Transient Grating Spectroscopy*, in *Ultrafast Phenomena XII*, T. Elsaesser, et al., Editors. 2001, Springer. p. 485–7.
72. Son, D., et al., *Femtosecond multicolor pump-probe investigation of ultrafast electron transfer of (NH₂sub 3)sub5 Ru (exp III) NCRu (exp II) (CN) sub 5 exp - in solution*, in *Ultrafast Phenomena XII*, T. Elsaesser, et al., Editors. 2001, Springer. p. 491–3.
73. Kobayashi, T., *Vibrational Dynamics in Molecules and Polymers Revealed by Sub-5-fs Real-time Spectroscopy*, in *Ultrafast Phenomena XII*, T. Elsaesser, et al., Editors. 2001, Springer. p. 575–9.
74. Brabec, C., et al., *Direct observation of the ultrafast electron transfer process in a polymer/fullerene blend*, in *Ultrafast Phenomena XII*, T. Elsaesser, et al., Editors. 2001, Springer. p. 589–91.
75. Riedle, E., et al., *Does the proton move during ultrafast excited state intramolecular proton transfer?*, in *Ultrafast Phenomena XII*, T. Elsaesser, et al., Editors. 2001, Springer. p. 645–7.
76. Kumazaki, S., et al., *Ultrafast charge separation in the plant photosystem I reaction center*, in *Ultrafast Phenomena XII*, T. Elsaesser, et al., Editors. 2001, Springer. p. 665–7.
77. Nagahara, T., Y. Kanematsu, and T. Okada, *Femtosecond Time-Resolved Fluorescence Spectroscopy Utilizing Optical Kerr Shutter: Direct Observation of a Temporal Fluorescence Band Shape*, in *Ultrafast Phenomena XII*, T. Elsaesser, et al., Editors. 2001, Springer. p. 192–4.
78. Gruetzmacher, J. and N. Scherer, *Time and frequency-gated FID: a new approach to study the vibrational dephasing of water*, in *Ultrafast Phenomena XII*, T. Elsaesser, et al., Editors. 2001, Springer. p. 530–2.
79. Shibata, Y., et al., *Femtosecond fluorescence dynamics of porphyrins; internal conversion, energy relaxation, and quantum beats*, in *Ultrafast Phenomena XII*, T. Elsaesser, et al., Editors. 2001, Springer. p. 689–91.
80. Goodman, J., *Statistical Optics*. 1985: Wiley.

Index

- absolute phase 19–20, 412–14
absolute-phase shift 63, 67, 105
absolute-phase stabilization 19, 412–14
acousto-optic modulator
 dazzler 253
additive noise 183–7, 193–7, 200
 poisson distribution for 184
additive-noise-contaminated traces
 optimized filtering of 195
alignment 246
ambiguities 63–87, 100, 105, 108, 112, 128,
 131, 132, 349
 (see also trivial ambiguities)
asymmetry in autocorrelation 93
attosecond pulse measurement 412
autocorrelation 67–74, 84–5, 90, 92–3,
 96–7, 206, 229, 239, 286, 296–7,
 305, 331
 background-free 84–5
 electronic Kerr effect 77–9, 331
 fringe-resolved 84–7
 interferometric 84–8
 multi-photo absorption 331
 numerically equivalent 70
 of complex pulses 71
 of noisy pulse trains 73
 polarization gate 77–8
 phase-sensitive 84–8
 SHG 65–76, 331
 self-diffraction 77–9
 single-shot 96
 spectrally resolved 93
 systematic error 90
 systematic error in measurements 92
 third-harmonic generation 78–9
autocorrelator 292
bandwidth-limited pulse 32–3, 274, 277
basic FROG algorithm
 improvements 166–71
Blaschke products 64
Blind FROG (see also TREE FROG) 350, 392
 algorithm 352, 360
 beam geometry 352
 traces 348–50, 353
 spectrogram 357
boot-strap methods 199–201
carrier wave $\exp(i\omega_0 t)$ 12
cascaded $\chi^{(2)}$ FROG (CC FROG) 132–5
chirped pulse 2, 271, 277–8, 293
 amplification 248
coherence artifact 71–2
coherence spike 71–2
 a measure of the pulse spectrum 72
collinear FROG geometry 136
common spectroscopic experiments 279
complex gate function 110
complex intensity 305, 311
complex pulses 145, 323
compressed pulses 296
compressor phase 248
conjugate gradient methods
 Fletcher-Reeves 170
 Polack-Ribierre 170
continuum 325, 330
 spectral structure 325
convergence criterion 196
corner-suppression 180, 188, 191
cross-correlation, $C^{(2)}(\tau)$ 88
cross-correlation frequency resolved optical
 gating (XFROG) 313–14, 321–2,
 346, 415
 amplitude 321
 ultrabroadband 323
cross-phase modulation (XPM) 247, 249,
 338, 392, 401, 404, 406
crystal phase-matching bandwidth 53–7, 93,
 323–4
cubic-spectral-phase 23–4, 250, 325–6
CW THz pulse trains 307
data constraint 159, 164
deconvolution 347
delay-dependent conversion efficiency 271
delta-function pulse 89
DFG XFROG 314, 317, 319–20
difference-frequency generation (DFG) 41,
 313
differential phase shift 395
dispersion-shifted fiber (DSF) 339
Dual-Quadrature Spectral Interferometry
 369
dynamic range 194, 252

- efficiencies
spectrally non-uniform 91
- electric field oscillations 393
- erbium-doped fiber laser (EDFL) 339
- error bars 199
- excite-probe geometry 220, 258, 353
- Fabry–Perot effects 91, 379
- Fast Fourier Transform (FFT) 294, 397
- Fast Fourier Transform relations 163
- “Femtosecond Oscilloscope” 362
- Femto-Nitpicker 88
- femtosecond time-resolved ellipsometry 385
- Fiber-FROG 339
geometry 337–8
signal 342
technique 341
trace 339–40
- field autocorrelation 62
- first-order SD 242
- Fourier Transform Shift Theorem 20
- Fourier-transform algorithm 316
- Fourier-Transform Spectral Interferometry (FTSI) 369
- Fourier-transform spectrometers 61
- four-wave-mixing (4WM) 37, 41
- frequency-domain interferometry 368
- frequency filters 229
- fringe-resolved autocorrelation (FRAC) 97, 251, 275
- “Fresnel bi-mirror” 235
- Fresnel biprism 230, 234
- FROG algorithm 84, 157, 181, 205, 252, 274, 287, 334, 336
- FROG apparatus 229, 297, 394
GRENOUILLE 229
- FROG error G 160, 181, 216–17
- FROG error Z 162
- “FROG matrices” 398
- FROG sampling rate (FSR) 213
- FROG limitations 209–11
digitizing FROG traces 198
redundancy in 106, 181, 204
removing systematic error 206–9
simulation of noise 182–4
- Gabor Transform 42
- gain-dispersion phase 248
- “gate” vectors 364
- generalized projections (GP) algorithm 158, 160–1, 163, 165, 307, 340, 342, 361, 400
- geometrical time-smearing 146–7, 274, 284
- Gerchberg–Saxton algorithm 82, 84
- Gires-Tournois-interferometer 291, 295
- GRENOUILLE 7, 203, 230, 232–5, 367
theory 233
- group delay vs. frequency 16
- group-delay dispersion (GDD) 309–10, 325
- group-velocity dispersion (GVD) 92, 233, 235, 259, 325, 339
- group-velocity mismatch (GVM) 56–7, 93, 235, 261
- heterodyne technique 368, 393
spectral interferometry 393
- high harmonic generation (HHG) 254, 257, 412
- highly-chirped pulses 310
- high-power pulse 237
- high-power ultrafast laser systems 248
- “home-brew” spectrometer 145
- imaging spectrometer 142
- induced birefringence 43
- induced grating effect 41
- induced polarization 331
- induced-grating process 79, 355
- instantaneous angular frequency 16
- intensity and phase
vs. frequency 13
vs. time 11
- intensity autocorrelation, $A^{(2)}(\tau)$
see autocorrelation
- intensity constraint 166
- interference fringes 84
- interferogram analysis 62, 406
- interferometric alignment 314
- ionization
ultrafast 403, 405
- Kerr-lens mode-locked laser 269
- Kerr-lens self-mode-locking 291
- Langmuir oscillations 393
- linear chirp 21

- longitudinal geometrical distortions 146, 150–5
longitudinal geometrical smearing 146, 150–5
low-pass filtering 189–91
low-power limits 209–10
- Mach-Zehnder interferometer 394
marginals 94, 205–9, 221–6, 258, 268, 270–297, 340–1, 394
material-characterization experiment 370
material phase 248
mathematical-form constraint 159, 162
measuring ultraweak pulses 367
Michelson interferometer 292, 401
microstructure-fiber continuum 327–8
microstructure optical fiber 323
MI-FROG 395
modelocked semiconductor lasers 311
multi-dimensional minimization 168, 170
multi-grid matrix 398
multiple quantum wells (MQWs) 376
multiplicative noise 183–4, 193, 196–7, 201
multi-pulse probe 401, 406
- negative-frequency component 14
non-instantaneous processes 331
nonlinearities
 non-instantaneous 331
non-linear Schrödinger equation (NLSE) 339
nonlinear-optical constraint 106
nonlinear-spectroscopic experiment 299
nonrandom error *see* systematic error
Nyquist criterion 213
- one-dimensional blind-deconvolution 348
one-dimensional phase-retrieval problem 63
optical fiber amplifiers 310
optical rectification 40
optimized filtering 192
over-correction method 167–8
- parabolic pulses 310
PCGP algorithm 358, 360–1, 308, 397, 400, 407
phase-blanking 18
phase-matching 48, 50
- phase-matching bandwidth 53, 55, 57, 93, 233, 238–9, 252, 259, 277, 287–8, 323–4 *see also* group-velocity mismatch (GVM)
phase-mismatch 48, 50, 243, 284
phase retrieval 63–74, 105–8, 347–50
 one-dimensional 63–74, 347–50
 “Trivial ambiguities” 63, 105
 two-dimensional 105–8, 347–50
phase-unwrapping 18
photo-isomerization 414
photon-echo signals 279
polarization gating (PG) 42, 53, 117
 FROG 117
POLKADOT FROG 221, 234
POLLIWOG 5, 9, 375–8, 385, 387–8
power method 365, 400
Principle Components Generalized
 Projection Algorithm (PCGPA) 159, 201, 307, 357, 363, 392, 399
pulse characteristics
 spatio-temporal 33, 95
pulse-front tilt 94
pulse length 29–31
pulse propagation 27–9
pulse-shaping techniques 254
pulse spectral bandwidth 11, 31–3, 93, 323–5
pulse spectrum
 spatial variations in 33, 95
- quadratic chirp *see* cubic spectral phase
quantization error 183
quantization noise 198
quartic spectral phase 23–5, 250
quintic spectral phase 26, 250
- Raman effects 335
Raman ringing effect 252
 see also non-instantaneous processes
real-time inversion 361
refractive index 28, 401
 frequency-dependent 28
rms intensity error 199
rms phase error
 intensity-weighted 192
- scalar approximation 11
SD FROG 174–6, 243, 245, 247, 283, 285–6

- SD geometries 241–2, 246
 second-order coherence function 62, 71, 81
 self- and cross-phase modulation 238
 self-diffraction (SD) 117, 240, 354 *see also*
 SD FROG
 self-phase modulated pulses 317
 self-phase modulation (SPM) 212, 249, 257,
 293, 338
 SFG XFROG 314, 317–18
 SHG FROG 127, 172–3, 223, 249, 252–3,
 259, 267, 274, 294, 299, 319, 337,
 341, 361, 376
 apparatus 291
 direction-of-time ambiguity 223
 SHG phase-matching
 noncollinear 52
 short-wavelength pulses 239, 244
 signal-efficiency Limit 210–11
 single-cycle pulses 260, 262–3, 267, 274,
 282
 single-mode fiber 269
 single-shot FROG 141, 230, 250
 single-shot geometries 141–6, 152, 231, 241
 single-shot spectral measurements 327
 single-shot third-order FROG geometries
 282
 singular value decomposition (SVD) 360,
 364, 400
 Slowly Varying Envelope Approximation
 (SVEA) 45, 257
 sonogram 113–14
 spatial chirp 34, 92, 95, 205, 252
 spatial light modulators (SLM) 253
 spatio-temporal distortions 34, 92, 95, 205,
 232, 237
 spectral clipping 252
 spectral filtering 273, 284–5
 spectral interferometry (SI) 4, 9, 367–9,
 375, 377
 data analysis 369
 Spectral Phase Interferometry for Direct
 Electric-field Reconstruction
 (SPIDER) 258
 spectral width 29–31 *see also* pulse spectral
 bandwidth
 spectrogram 102, 315, 392
 rigorous version of the musical score 102,
 315, 392
 spectrogram field 392
 spectrogram inversion algorithms 103–4
 spectrum autoconvolution 207
 Stokes parameters 386–7
 subfemtosecond response 331
 sum-frequency generation (SFG) 41,
 313, 346
 super-polished substrates 246
 Swamp Optics 236
 systematic error 90, 204
 Temporal Analysis by Dispersing a Pair Of
 Light E-fields (TADPOLE) 5, 9,
 313, 367, 370, 372, 375–7, 391–2,
 394, 396
 Temporal Information Via Intensity (TIVI)
 method 82
 thin-film polarizers 241
 third-harmonic generation (THG) FROG
 41, 43, 78, 117, 130–2, 176–7, 337
 third-order autocorrelations 76, 240
 three-photon fluorescence 79
 time-bandwidth product (TBP) 31–2, 233,
 323
 time-dependent phase shift 403
 time-frequency analysis 32
 time-frequency domain 6, 101, 109, 259, 412
 time-resolved ellipsometry (TRE) 378, 387
 trace preparation
 background subtraction 184
 Transient-Grating (TG) FROG 124–6,
 240–5, 283–4, 355
 transverse geometrical distortions 146, 149,
 154
 TREEFROG (*see also* Blind FROG) 391–2,
 399, 402–3
 triple correlation 81
 trivial ambiguities 63, 64, 67, 105, 108, 112,
 120, 314, 393, 394
 two-beam coupling 42, 53
 two-beam excite-probe experiments 354
 two-photon absorption 240
 two-photon fluorescence 240, 246
 Type I phase-matching 275, 277–8, 319, 321
 Type II phase-matching 220, 275, 319
 Type II SHG FROG 135–7, 278
 ultrabroadband continuum 323
 ultrabroadband pulses 269, 287
 second-harmonic spectrum FROG 269

- ultrafast BOXCAR integrator 391
ultrafast polarization dynamics 375
ultrafast time-dependent frequency shift 404
ultraweak ultrashort pulses 370
UV-pulse measurement 238, 247
UV ultrashort pulses 314
- van Cittert-Zernike Theorem 415
vanilla FROG algorithm 159–60, 165–6,
168, 170–1
- wavelet noise reduction 192
wavelet transform 112
- wave-packet motion 257
Wiener filtering 192
Wigner Distribution 112
- XFROG algorithm 316, 350
XFROG 315, 324–6, 330, 412
- zero-dispersion wavelength (ZDW) 305,
310, 339
zeroth-order phase 19